

# AJNR

## AMERICAN JOURNAL OF NEURORADIOLOGY

MARCH 2015  
VOLUME 36  
NUMBER 3  
[WWW.AJNR.ORG](http://WWW.AJNR.ORG)

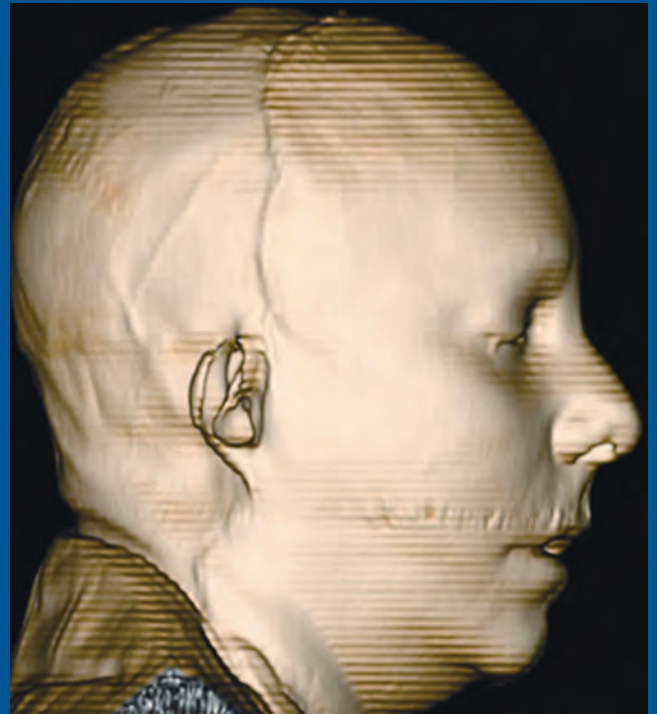
THE JOURNAL OF DIAGNOSTIC AND  
INTERVENTIONAL NEURORADIOLOGY

Abnormal brain metabolism in DVAs

Conscious sedation vs. general anesthesia for  
endovascular stroke treatment

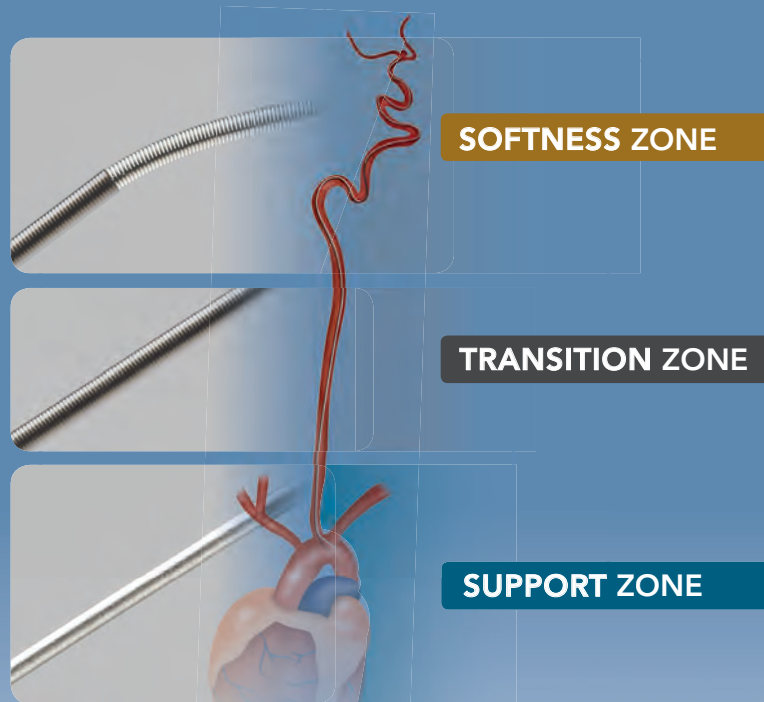
Treating disk herniations with percutaneous  
gelified ethanol

Official Journal ASNR • ASFNR • ASHNR • ASPNR • ASSR



# Advanced

by MicroVention



## ENHANCED CONTROL TO MAXIMIZE COIL PERFORMANCE

The **V-Trak® Advanced Coil System**, the next generation to power the performance of our most technically advanced line of coils. Offering the optimal combination of support and flexibility.

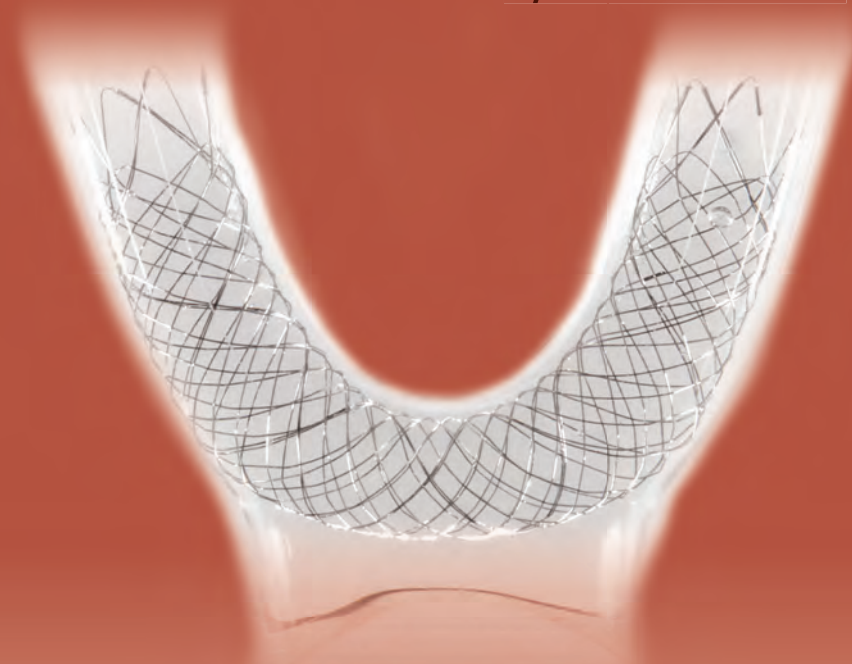
[microvention.com](http://microvention.com)

MICROVENTION, V-Trak, LVIS and Headway are registered trademarks of MicroVention, Inc. Scientific and clinical data related to this document are on file at MicroVention, Inc. Refer to Instructions for Use, contraindications and warnings for additional information. Federal (USA) law restricts this device for sale by or on the order of a physician. © 2015 MicroVention, Inc. 1/15

CE  
0297

# Support

by MicroVention



## LOW-PROFILE VISUALIZED INTRALUMINAL SUPPORT

The **LVIS®** and **LVIS® Jr. devices** are the next generation technology for optimal intraluminal support and coverage for stent-assist coil procedures.

Used with  **Headway**  
Microcatheter

RX only.

*Humanitarian Device:*

*Authorized by Federal Law for use with bare platinum embolic coils for the treatment of unruptured, wide neck (neck  $\geq$  4 mm or dome to neck ratio  $<$  2), intracranial, saccular aneurysms arising from a parent vessel with a diameter  $\geq$  2.5 mm and  $\leq$  4.5 mm. The effectiveness of this device for this use has not been demonstrated.*

For more information or a product demonstration,  
contact your local MicroVention representative:



**MicroVention, Inc.**

**Worldwide Headquarters**

1311 Valencia Avenue

Tustin, CA 92780 USA

MicroVention UK Limited

MicroVention Europe, S.A.R.L.

MicroVention Deutschland GmbH

PH +1.714.247.8000

PH +44 (0) 191 258 6777

PH +33 (1) 39 21 77 46

PH +49 211 210 798-0

# ASNR 53rd Annual Meeting & The Foundation of the Symposium 2015 in Chicago, April 25-30, 2015



ASFNR ASHNR ASPNR ASSR SNIS

THE FOUNDATION OF THE ASNR



**Stay connected with friends and colleagues.  
Get value-based neuroradiology that  
addresses best practices. Visit the ASNR  
2015 Meeting website to see the program!**

**Laurie A. Loevner, MD  
ASNR 2015 Program Chair and President-Elect**

## **Request Programming and Registration Materials for the ASNR 53<sup>rd</sup> Annual Meeting, Contact:**

ASNR 53<sup>rd</sup> Annual Meeting  
c/o American Society of Neuroradiology  
800 Enterprise Drive, Suite 205  
Oak Brook, Illinois 60523-4216  
Phone: 630-574-0220  
Fax: 630-574-0661  
Email: [meetings@asnr.org](mailto:meetings@asnr.org)  
Website: [www.asnr.org/2015](http://www.asnr.org/2015)

**Scan now to  
visit our website**



## **An exceptional Symposium and Meeting at the newly renovated Sheraton Chicago Hotel & Towers.**

**The weekend Symposium:** The Skull Base, will bridge the gap between the head and the spine. It will cover:

- Pertinent anatomy
- Optimization of imaging techniques
- Development and function of all the cranial nerves using a symptom-based approach
- Cutting edge intraoperative footage of transnasal endoscopic techniques which have redefined "surgical resectability", and have revolutionized the role of the neuroradiologist
- The posterior fossa, central hypertension and hypotension, and the craniovertebral junction

**Sunday afternoon,** the symposium continues with "Neuroradiologist-Clinician-Patient" Seminars. Breakout sessions include:

- Brain Tumors
- Head & Neck Cancer
- Thyroid Cancer
- Mild Traumatic Brain Injury
- MCI-Alzheimers Disease

Following these symposiums join us for an engaging game of Neuroradiology Jeopardy featuring Doctor-Patient teams, followed by a "mocktail reception" and Broadway entertainment!

ASNR Annual Meeting will provide informative updates on Neuroradiology and showcase specialty programming.

**Monday morning "Keynote Symposium: Getting Personal ....."** features Beth Daley Ullem, nationally-recognized Governance Expert; Grant Achatz, American chef, restaurateur, and head & neck cancer survivor; and Julian E. Bailes, Jr., MD, Neurosurgeon, consultant to NFL Players' Association, and advisor to NCAA Concussion Task Force.

Attend 5 Mini-Symposia throughout the week:

- Connectome and Genomics: Omics and Big Data for Neuroradiology
- Emergency Room Triage: Traumarama and Other Urgencies
- Neuroimaging Gently: Creating a Safe and Quality Environment for Neurodiagnostics & Neurointerventions
- Neuro-Nuclear Immersion
- Functional Neuroimaging Biomarkers of Psychiatric Disorders

# SAVE THE DATES....April 25-30, 2015

# AJNR

## AMERICAN JOURNAL OF NEURORADIOLOGY

MARCH 2015  
VOLUME 36  
NUMBER 3  
WWW.AJNR.ORG

Publication Preview at [www.ajnr.org](http://www.ajnr.org) features articles released in advance of print. Visit [www.ajnrblog.org](http://www.ajnrblog.org) to comment on AJNR content and chat with colleagues and AJNR's News Digest at <http://ajnrdigest.org> to read the stories behind the latest research in neuroimaging.

### EDITORIAL

#### PERSPECTIVES

- 423 **Crossing the Rubicon** *M. Castillo*

### REVIEW ARTICLES

- 425 **The Prognostic Utility of MRI in Clinically Isolated Syndrome: A Literature Review** *C. Odenthal and A. Coulthard*
- 432 **Subdural Hygromas in Abusive Head Trauma: Pathogenesis, Diagnosis, and Forensic Implications** *D. Wittschieber, B. Karger, T. Niederstadt, H. Pfeiffer, and M.L. Hahnemann*

### ACADEMIC PERSPECTIVES

- 440 **Differences in Neuroradiology Training Programs around the World** *T. Schneider, T.A.G.M. Huisman, J. Fiehler, L.J. Savic, and D.M. Yousem*

### GENETICS VIGNETTE

- 445 **Genetics of Parkinson Disease** *E. Ben-David and R. Tu*

### BRAIN

- 448 **White Matter Correlates of Cognitive Impairment in Essential Tremor** *K.S. Bhalsing, K.J. Kumar, J. Saini, R. Yadav, A.K. Gupta, and P.K. Pal*
- 454 **Susceptibility-Weighted Imaging Improves the Diagnostic Accuracy of 3T Brain MRI in the Work-Up of Parkinsonism** *F.J.A. Meijer, A. van Rumund, B.A.C.M. Fasen, I. Titulaer, M. Aerts, R. Esselink, B.R. Bloem, M.M. Verbeek, and B. Goraj*
- 461 **Comparison of 3T and 7T Susceptibility-Weighted Angiography of the Substantia Nigra in Diagnosing Parkinson Disease** *M. Cosottini, D. Frosini, I. Pesaresi, G. Donatelli, P. Cecchi, M. Costagli, L. Biagi, R. Ceravolo, U. Bonuccelli, and M. Tosetti*
- 467 **Quantitative Susceptibility Mapping of Human Brain at 3T: A Multisite Reproducibility Study** *P.-Y. Lin, T.-C. Chao, and M.-L. Wu*
- 475 **Brain Metabolic Abnormalities Associated with Developmental Venous Anomalies** *M. Larvie, D. Timerman, and J.A. Thum*
- 481 **Identification of Minimal Hepatic Encephalopathy in Patients with Cirrhosis Based on White Matter Imaging and Bayesian Data Mining** *H.-J. Chen, R. Chen, M. Yang, G.-J. Teng, and E.H. Herskovits*
- 488 **Strategies of Collateral Blood Flow Assessment in Ischemic Stroke: Prediction of the Follow-Up Infarct Volume in Conventional and Dynamic CTA** *S.E. Beyer, K.M. Thierfelder, L. von Baumgarten, M. Rottenkolber, F.G. Meinel, H. Janssen, B. Ertl-Wagner, M.F. Reiser, and W.H. Sommer*

★ Indicates Editor's Choices selection

📖 Indicates Fellows' Journal Club selection

🔑 Indicates open access to non-subscribers at [www.ajnr.org](http://www.ajnr.org)

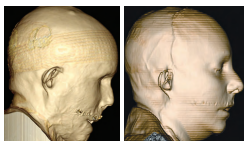
☰ Indicates article with supplemental on-line table

🖼️ Indicates article with supplemental on-line photo

📺 Indicates article with supplemental on-line video

EBM 1 Indicates Evidence-Based Medicine Level 1

EBM 2 Indicates Evidence-Based Medicine Level 2



Pre- and post-facial transplantation 3D surface-rendering CT.

# 2014 LUCIEN LEVY BEST RESEARCH ARTICLE

**Other nominated papers were:**

“Comparison of 3T and 7T Susceptibility-Weighted Angiography of the Substantia Nigra in Diagnosing Parkinson Disease” by M. Cosottini, D. Frosini, I. Pesaresi, G. Donatelli, P. Cecchi, M. Costagli, L. Biagi, R. Ceravolo, U. Bonuccelli, and M. Tosetti

“A Randomized Trial Comparing Balloon Kyphoplasty and Vertebroplasty for Vertebral Compression Fractures due to Osteoporosis” by M. Dohm, C.M. Black, A. Dacre, J.B. Tillman, G. Fueredi, on behalf of the KAVIAR investigators

“Diffusion-Weighted Imaging of the Head and Neck in Healthy Subjects: Reproducibility of ADC Values in Different MRI Systems and Repeat Sessions” by A.S. Kolff-Gart, P.J.W. Pouwels, D.P. Noij, R. Ljumanovic, V. Vandecaveye, F. de Keyzer, R. de Bree, P. de Graaf, D.L. Knol, and J.A. Castelijns

“The Maze-Making and Solving Technique for Coil Embolization of Large and Giant Aneurysms” by T. Ohta, I. Nakahara, R. Ishibashi, S. Matsumoto, M. Gomi, H. Miyata, H. Nishi, S. Watanabe, and I. Nagata

“MRI Surrogates for Molecular Subgroups of Medulloblastoma” by S. Perreault, V. Ramaswamy, A.S. Achrol, K. Chao, T.T. Liu, D. Shih, M. Remke, S. Schubert, E. Bouffet, P.G. Fisher, S. Partap, H. Vogel, M.D. Taylor, Y.J. Cho, and K.W. Yeom

“Mapping p53 Mutations in Low-Grade Glioma: A Voxel-Based Neuroimaging Analysis” by Y.Y. Wang, T. Zhang, S.W. Li, T.Y. Qian, X. Fan, X.X. Peng, J. Ma, L. Wang, and T. Jiang

## AWARD WINNER AND NOMINEES

The Editors of *AJNR* are pleased to announce the annual Lucien Levy Best Research Article Award has been presented to

### “Quantifying Intracranial Aneurysm Wall Permeability for Risk Assessment Using Dynamic Contrast-Enhanced MRI: A Pilot Study”

by P. Vakil, S.A. Ansari, C.G. Cantrell, C.S. Eddleman, F.H. Dehkordi, J. Vranic, M.C. Hurley, H.H. Batjer, B.R. Bendok, and T.J. Carroll.

This award is named for the late *AJNR* Senior Editor who championed its establishment and recognizes the best original research paper accepted in 2014. The winning paper, submitted by authors from Northwestern University, University of Texas-Southwestern, and Western Illinois University, was published electronically on February 5, 2015 and will appear in the May print issue. It was selected by a vote of the Journal’s Editor-in-Chief and Senior Editors.





495 **Impact of Time-to-Reperfusion on Outcome in Patients with Poor Collaterals** Y.-H. Hwang, D.-H. Kang, Y.-W. Kim, Y.-S. Kim, S.-P. Park, and D.S. Liebeskind



501 **MS Lesions Are Better Detected with 3D T1 Gradient-Echo Than with 2D T1 Spin-Echo Gadolinium-Enhanced Imaging at 3T** A. Crombé, M. Saranathan, A. Ruet, M. Durieux, E. de Roquefeuil, J.C. Ouallet, B. Brochet, V. Dousset, and T. Tourdias



508 **Pretreatment Diagnosis of Suprasellar Papillary Craniopharyngioma and Germ Cell Tumors of Adult Patients** H.-J. Lee, C.-C. Wu, H.-M. Wu, S.-C. Hung, J.-F. Lirng, C.-B. Luo, F.-C. Chang, and W.-Y. Guo

### FUNCTIONAL



518 **Crossed Cerebrocerebellar Language Lateralization: An Additional Diagnostic Feature for Assessing Atypical Language Representation in Presurgical Functional MR Imaging** C. Méndez Orellana, E. Visch-Brink, M. Vernooij, S. Kalloe, D. Satoer, A. Vincent, A. van der Lugt, and M. Smits

### INTERVENTIONAL *Published in collaboration with Interventional Neuroradiology*



525 **Conscious Sedation versus General Anesthesia during Endovascular Acute Ischemic Stroke Treatment: A Systematic Review and Meta-Analysis** W. Brinjikji, M.H. Murad, A.A. Rabinstein, H.J. Cloft, G. Lanzino, and D.F. Kallmes



530 **The Computational Fluid Dynamics Rupture Challenge 2013—Phase I: Prediction of Rupture Status in Intracranial Aneurysms** G. Janjiga, P. Berg, S. Sugiyama, K. Kono, and D.A. Steinman

537 **Patency of the Anterior Choroidal Artery after Flow-Diversion Treatment of Internal Carotid Artery Aneurysms** W. Brinjikji, D.F. Kallmes, H.J. Cloft, and G. Lanzino

542 **Silk Flow-Diverter Stent for the Treatment of Intracranial Aneurysms: A Series of 58 Patients with Emphasis on Long-Term Results** B. Lubicz, O. Van der Elst, L. Collignon, B. Mine, and F. Alghamdi



547 **Comparison of Modern Stroke Thrombectomy Approaches Using an In Vitro Cerebrovascular Occlusion Model** M. Mokin, S.V. Setlur Nagesh, C.N. Ionita, E.I. Levy, and A.H. Siddiqui



552 **Double Solitaire Mechanical Thrombectomy in Acute Stroke: Effective Rescue Strategy for Refractory Artery Occlusions?** J. Klisch, V. Sychra, C. Strasilla, C.A. Taschner, M. Reinhard, H. Urbach, and S. Meckel



557 **Small Pipes: Preliminary Experience with 3-mm or Smaller Pipeline Flow-Diverting Stents for Aneurysm Repair prior to Regulatory Approval** A.R. Martin, J.P. Cruz, C. O'Kelly, M. Kelly, J. Spears, and T.R. Marotta

### EXTRACRANIAL VASCULAR

562 **Attenuation of Blood Flow Pulsatility along the Atlas Slope: A Physiologic Property of the Distal Vertebral Artery?** T. Schubert, M. Pansini, O. Bieri, C. Stippich, S. Wetzel, S. Schaedelin, A. von Hessling, and F. Santini

### HEAD & NECK

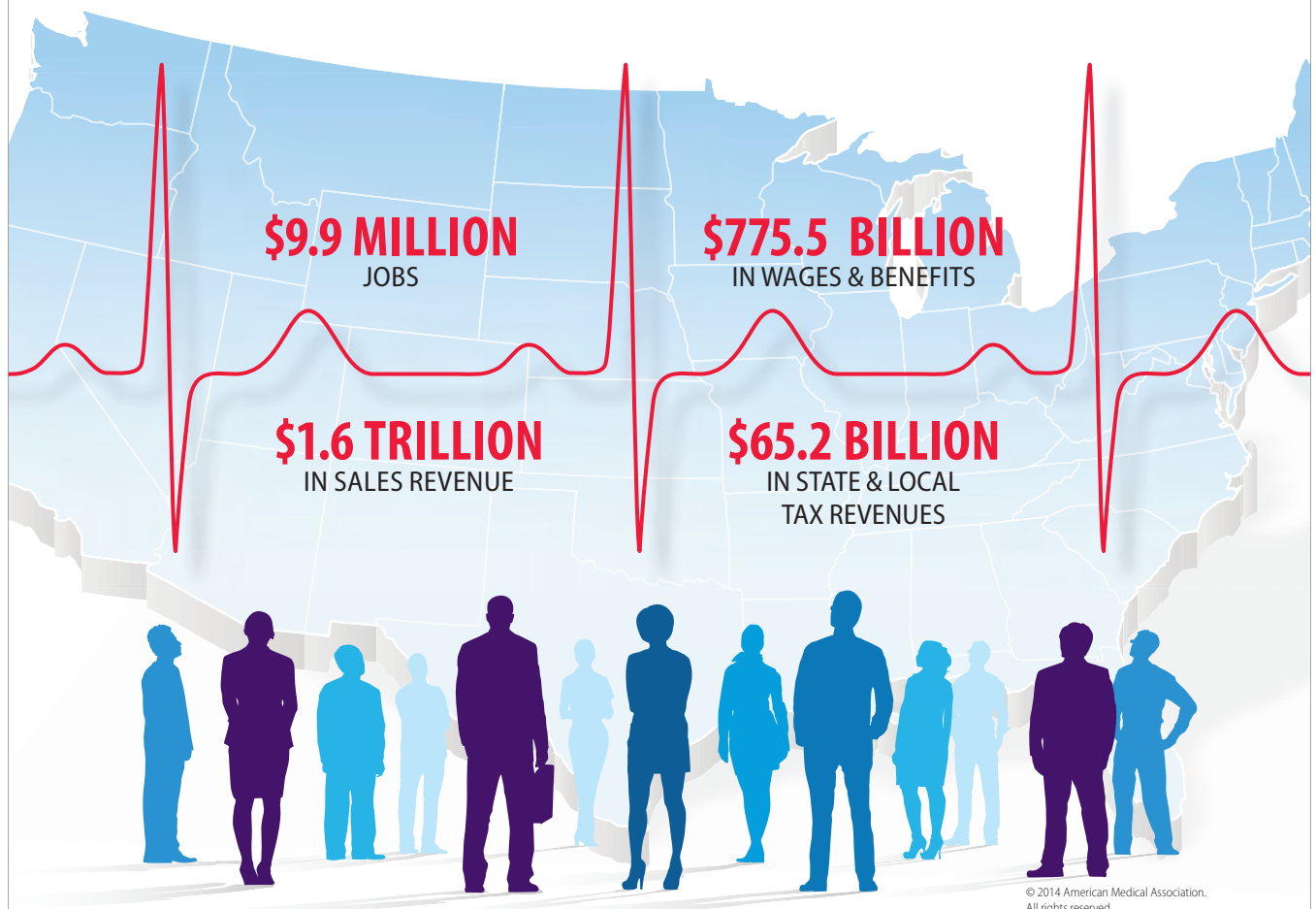


568 **Early Postoperative Imaging and Image-Guided Procedures on Patients with Face Transplants** T.C. Lee, T. Chansakul, R.Y. Huang, G.L. Wrubel, S. Mukundan, D.J. Annino, J.J. Pribaz, and B. Pomahac

### PEDIATRICS

575 **Physiologic Pineal Region, Choroid Plexus, and Dural Calcifications in the First Decade of Life** M.T. Whitehead, C. Oh, A. Raju, and A.F. Choudhri

# PHYSICIANS BOOST THE ECONOMY.



© 2014 American Medical Association. All rights reserved.

## See the effects across the nation.

The American Medical Association 2014 Economic Impact Study shows how much physicians add to the economic health of our nation.

Check the effect physicians have on the U.S. economy by viewing the entire national report from the AMA Advocacy Resource Center at [ama-assn.org/go/eis](http://ama-assn.org/go/eis). Visit the AMA at the American Society of Neuroradiology 2015 Annual Meeting to learn more about this study and other AMA resources.



Please activate your 2015 AMA membership by calling (800) 262-3211 or visit [ama-assn.org/go/join](http://ama-assn.org/go/join).

- 581 **Comparing 3T T1-Weighted Sequences in Identifying Hyperintense Punctate Lesions in Preterm Neonates** *D. Tortora, V. Panara, P.A. Mattei, A. Tartaro, R. Salomone, S. Domizio, A.R. Cotroneo, and M. Caulo*

#### SPINE

- 587 **Intramedullary Spinal Cord Metastases: Prognostic Value of MRI and Clinical Features from a 13-Year Institutional Case Series** *F.E. Diehn, J.B. Rykken, J.T. Wald, C.P. Wood, L.J. Eckel, C.H. Hunt, K.M. Schwartz, R.K. Lingineni, R.E. Carter, and T.J. Kaufmann*
- 594 **Correlation of the Patient Reported Outcomes Measurement Information System with Legacy Outcomes Measures in Assessment of Response to Lumbar Transforaminal Epidural Steroid Injections** *L. Shahgholi, K.J. Yost, R.E. Carter, J.R. Geske, C.E. Hagen, K.K. Amrami, F.E. Diehn, T.J. Kaufmann, J.M. Morris, N.S. Murthy, J.T. Wald, K.R. Thielen, D.F. Kallmes, and T.P. Maus*
- 600 **Percutaneous Injection of Radiopaque Gelified Ethanol for the Treatment of Lumbar and Cervical Intervertebral Disk Herniations: Experience and Clinical Outcome in 80 Patients** *M. Bellini, D.G. Romano, S. Leonini, I. Grazzini, C. Tabano, M. Ferrara, P. Piu, L. Monti, and A. Cerase*
- 606 **T1 $\rho$  and T2 Mapping of the Intervertebral Disk: Comparison of Different Methods of Segmentation** *R. Menezes-Reis, C.E.G. Salmon, C.S. Carvalho, G.P. Bonugli, C.B. Chung, and M.H. Nogueira-Barbosa*

#### ONLINE FEATURES ([www.ajnr.org](http://www.ajnr.org))

#### RESEARCH PERSPECTIVES

- E12 **Traumatic Brain Injury Imaging Research Roadmap** *M. Wintermark, L. Coombs, T.J. Druzgal, A.S. Field, C.G. Filippi, R. Hicks, R. Horton, Y.W. Lui, M. Law, P. Mukherjee, A. Norbash, G. Riedy, P.C. Sanelli, J.R. Stone, G. Sze, M. Tilkin, C.T. Whitlow, E.A. Wilde, G. York, and J.M. Provenzale; on behalf of the American College of Radiology Head Injury Institute*

#### LETTER

- E24 **Predictive Value of Calvarial Fracture for Delayed Epidural Hematoma following Decompressive Craniectomy** *Q.-p. Wang and C. You*
- E25 **Reply** *J.F. Talbott, A. Gean, E.L. Yuh, and S.I. Stiver*

#### ERRATA

E26

#### BOOK REVIEWS *R.M. Quencer, Section Editor*

Please visit [www.ajnrblog.org](http://www.ajnrblog.org) to read and comment on Book Reviews.

## Trevo® XP ProVue Retrievers

See package insert for complete indications, complications, warnings, and instructions for use.

### INDICATIONS FOR USE

The Trevo Retriever is intended to restore blood flow in the neurovasculature by removing thrombus in patients experiencing ischemic stroke within 8 hours of symptom onset. Patients who are ineligible for intravenous tissue plasminogen activator (IV t-PA) or who fail IV t-PA therapy are candidates for treatment.

### COMPLICATIONS

Procedures requiring percutaneous catheter introduction should not be attempted by physicians unfamiliar with possible complications which may occur during or after the procedure. Possible complications include, but are not limited to, the following: air embolism; hematoma or hemorrhage at puncture site; infection; distal embolization; pain/headache; vessel spasm, thrombosis, dissection, or perforation; emboli; acute occlusion; ischemia; intracranial hemorrhage; false aneurysm formation; neurological deficits including stroke; and death.

### COMPATIBILITY

3x20 mm retrievers are compatible with Trevo® Pro 14 Microcatheters (REF 90231) and Trevo® Pro 18 Microcatheters (REF 90238). 4x20 mm retrievers are compatible with Trevo® Pro 18 Microcatheters (REF 90238). Compatibility of the Retriever with other microcatheters has not been established. Performance of the Retriever device may be impacted if a different microcatheter is used. The Merci® Balloon Guide Catheters are recommended for use during thrombus removal procedures. Retrievers are compatible with the Abbott Vascular DOC® Guide Wire Extension (REF 22260)

### WARNINGS

- Contents supplied STERILE, using an ethylene oxide (EO) process. Nonpyrogenic.
- To reduce risk of vessel damage, adhere to the following recommendations:
  - Take care to appropriately size Retriever to vessel diameter at intended site of deployment.
  - Do not perform more than six (6) retrieval attempts in same vessel using Retriever devices.
  - Maintain Retriever position in vessel when removing or exchanging Microcatheter.
- To reduce risk of kinking/fracture, adhere to the following recommendations:
  - Immediately after unsheathing Retriever, position Microcatheter tip marker just proximal to shaped section. Maintain Microcatheter tip marker just proximal to shaped section of Retriever during manipulation and withdrawal.
  - Do not rotate or torque Retriever.
  - Use caution when passing Retriever through stented arteries.
- Do not resterilize and reuse. Structural integrity and/or function may be impaired by reuse or cleaning.
- The Retriever is a delicate instrument and should be handled carefully. Before use and when possible during procedure, inspect device carefully for damage. Do not use a device that shows signs of damage. Damage may prevent device from functioning and may cause complications.
- Do not advance or withdraw Retriever against resistance or significant vasospasm. Moving or torquing device against resistance or significant vasospasm may result in damage to vessel or device. Assess cause of resistance using fluoroscopy and if needed resheath the device to withdraw.

- If Retriever is difficult to withdraw from the vessel, do not torque Retriever. Advance Microcatheter distally, gently pull Retriever back into Microcatheter, and remove Retriever and Microcatheter as a unit. If undue resistance is met when withdrawing the Retriever into the Microcatheter, consider extending the Retriever using the Abbott Vascular DOC guidewire extension (REF 22260) so that the Microcatheter can be exchanged for a larger diameter catheter such as a DAC® catheter. Gently withdraw the Retriever into the larger diameter catheter.
- Administer anti-coagulation and anti-platelet medications per standard institutional guidelines.

### PRECAUTIONS

- Prescription only – device restricted to use by or on order of a physician.
- Store in cool, dry, dark place.
- Do not use open or damaged packages.
- Use by “Use By” date.
- Exposure to temperatures above 54°C (130°F) may damage device and accessories. Do not autoclave.
- Do not expose Retriever to solvents.
- Use Retriever in conjunction with fluoroscopic visualization and proper anti-coagulation agents.
- To prevent thrombus formation and contrast media crystal formation, maintain a constant infusion of appropriate flush solution between guide catheter and Microcatheter and between Microcatheter and Retriever or guidewire.
- Do not attach a torque device to the shaped proximal end of DOC® Compatible Retriever. Damage may occur, preventing ability to attach DOC® Guide Wire Extension.



**Concentric Medical**  
301 East Evelyn  
Mountain View, CA 94041



EMERGO Europe  
Molenstraat 15  
2513 BH, The Hague  
The Netherlands



**Stryker Neurovascular**  
47900 Bayside Parkway  
Fremont, CA 94538

[stryker.com/neurovascular](http://stryker.com/neurovascular)  
[stryker.com/emea/neurovascular](http://stryker.com/emea/neurovascular)

Date of Release: JUN/2014

EX\_EN\_GL

### Official Journal:

American Society of Neuroradiology  
American Society of Functional Neuroradiology  
American Society of Head and Neck Radiology  
American Society of Pediatric Neuroradiology  
American Society of Spine Radiology

### EDITOR-IN-CHIEF

#### Mauricio Castillo, MD

Professor of Radiology and Chief, Division of Neuroradiology, University of North Carolina, School of Medicine, Chapel Hill, North Carolina

### SENIOR EDITORS

#### Harry J. Cloft, MD, PhD

Professor of Radiology and Neurosurgery, Department of Radiology, Mayo Clinic College of Medicine, Rochester, Minnesota

#### Nancy J. Fischbein, MD

Professor of Radiology, Otolaryngology-Head and Neck Surgery, Neurology, and Neurosurgery and Chief, Head and Neck Radiology, Department of Radiology, Stanford University Medical Center, Stanford, California

#### Jeffrey S. Ross, MD

Staff Neuroradiologist, Barrow Neurological Institute, St. Joseph's Hospital, Phoenix, Arizona

#### Pamela W. Schaefer, MD

Clinical Director of MRI and Associate Director of Neuroradiology, Massachusetts General Hospital, Boston, Massachusetts, and Associate Professor, Radiology, Harvard Medical School, Cambridge, Massachusetts

#### Charles M. Strother, MD

Professor of Radiology, Emeritus, University of Wisconsin, Madison, Wisconsin

#### Jody Tanabe, MD

Professor of Radiology and Psychiatry, Chief of Neuroradiology, University of Colorado, Denver, Colorado

### EDITORIAL BOARD

Ashley H. Aiken, *Atlanta, Georgia*  
A. James Barkovich, *San Francisco, California*  
Walter S. Bartynski, *Charleston, South Carolina*  
Barton F. Branstetter IV, *Pittsburgh, Pennsylvania*  
Jonathan L. Brisman, *Lake Success, New York*  
Julie Bykowski, *San Diego, California*  
Donald W. Chakeres, *Columbus, Ohio*  
Alessandro Cianfoni, *Lugano, Switzerland*  
Colin Derdeyn, *St. Louis, Missouri*  
Rahul S. Desikan, *San Diego, California*  
Richard du Mesnil de Rochemont, *Frankfurt, Germany*  
Clifford J. Eskey, *Hanover, New Hampshire*  
Massimo Filippi, *Milan, Italy*  
David Fiorella, *Cleveland, Ohio*  
Allan J. Fox, *Toronto, Ontario, Canada*  
Christine M. Glastonbury, *San Francisco, California*

John L. Go, *Los Angeles, California*  
Wan-Yuo Guo, *Taipei, Taiwan*  
Rakesh K. Gupta, *Lucknow, India*  
Lotfi Hacein-Bey, *Sacramento, California*  
David B. Hackney, *Boston, Massachusetts*  
Christopher P. Hess, *San Francisco, California*  
Andrei Holodny, *New York, New York*  
Benjamin Huang, *Chapel Hill, North Carolina*  
Thierry A.G.M. Huisman, *Baltimore, Maryland*  
George J. Hunter, *Boston, Massachusetts*  
Mahesh V. Jayaraman, *Providence, Rhode Island*  
Valerie Jewells, *Chapel Hill, North Carolina*  
Timothy J. Kaufmann, *Rochester, Minnesota*  
Kenneth F. Layton, *Dallas, Texas*  
Ting-Yim Lee, *London, Ontario, Canada*  
Michael M. Lell, *Erlangen, Germany*  
Michael Lev, *Boston, Massachusetts*  
Karl-Olof Lovblad, *Geneva, Switzerland*  
Franklin A. Marden, *Chicago, Illinois*  
M. Gisele Matheus, *Charleston, South Carolina*  
Joseph C. McGowan, *Merion Station, Pennsylvania*  
Kevin R. Moore, *Salt Lake City, Utah*  
Christopher J. Moran, *St. Louis, Missouri*  
Takahisa Mori, *Kamakura City, Japan*

Suresh Mukherji, *Ann Arbor, Michigan*  
Amanda Murphy, *Toronto, Ontario, Canada*  
Alexander J. Nemeth, *Chicago, Illinois*  
Laurent Pierot, *Reims, France*  
Jay J. Pillai, *Baltimore, Maryland*  
Whitney B. Pope, *Los Angeles, California*  
M. Judith Donovan Post, *Miami, Florida*  
Tina Young Poussaint, *Boston, Massachusetts*  
Joana Ramalho, *Lisbon, Portugal*  
Otto Rapalino, *Boston, Massachusetts*  
Álex Rovira-Cañellas, *Barcelona, Spain*  
Paul M. Ruggieri, *Cleveland, Ohio*  
Zoran Rumboldt, *Rijeka, Croatia*  
Amit M. Saindane, *Atlanta, Georgia*  
Erin Simon Schwartz, *Philadelphia, Pennsylvania*  
Aseem Sharma, *St. Louis, Missouri*  
J. Keith Smith, *Chapel Hill, North Carolina*  
Maria Vittoria Spampinato, *Charleston, South Carolina*  
Gordon K. Sze, *New Haven, Connecticut*  
Krishnamoorthy Thamburaj, *Hershey, Pennsylvania*  
Kent R. Thielen, *Rochester, Minnesota*  
Cheng Hong Toh, *Taipei, Taiwan*  
Thomas A. Tomsick, *Cincinnati, Ohio*  
Aquila S. Turk, *Charleston, South Carolina*  
Willem Jan van Rooij, *Tilburg, Netherlands*  
Arastoo Vossough, *Philadelphia, Pennsylvania*  
Elysa Widjaja, *Toronto, Ontario, Canada*  
Max Wintermark, *Charlottesville, Virginia*  
Ronald L. Wolf, *Philadelphia, Pennsylvania*  
Kei Yamada, *Kyoto, Japan*

### EDITORIAL FELLOW

Asim F. Choudhri, *Memphis, Tennessee*

### YOUNG PROFESSIONALS ADVISORY COMMITTEE

Asim K. Bag, *Birmingham, Alabama*  
Anna E. Nidecker, *Sacramento, California*  
Peter Yi Shen, *Sacramento, California*

### HEALTH CARE AND SOCIOECONOMICS EDITOR

Pina C. Sanelli, *New York, New York*

Founding Editor

Juan M. Taveras

Editors Emeriti

Robert I. Grossman, Michael S. Huckman,  
Robert M. Quencer

Special Consultants to the Editor  
Sandy Cheng-Yu Chen, Girish Fatterpekar,  
Ryan Fitzgerald, Katherine Freeman,  
Yvonne Lui, Greg Zaharchuk

INR Liaisons

Timo Krings, Karel terBrugge

Managing Editor

Karen Halm

Electronic Publications Manager

Jason Gantenberg

Editorial Assistant

Mary Harder

Executive Director, ASNR

James B. Gantenberg

Director of Communications, ASNR

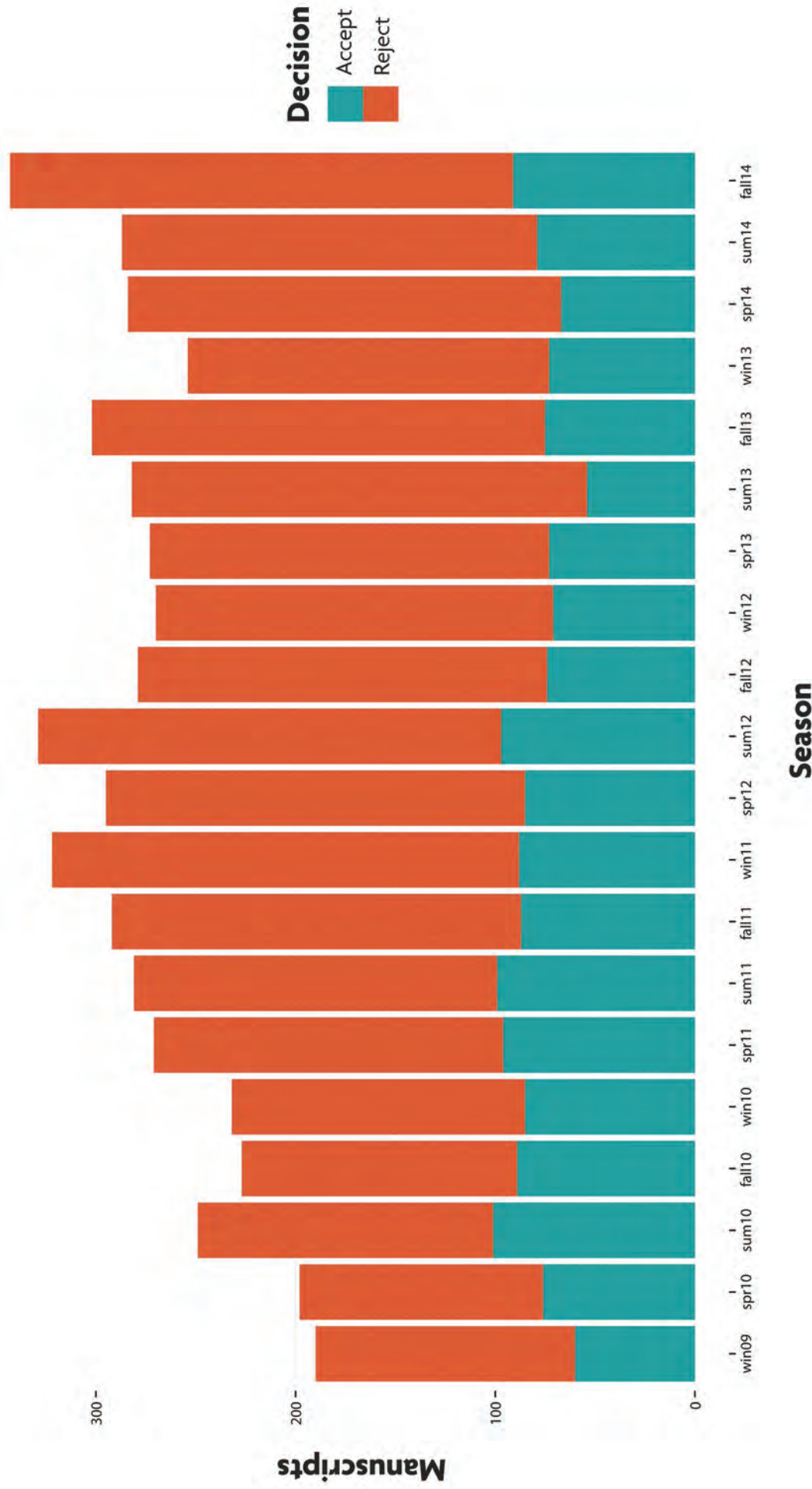
Angelo Artemakis



**AJNR (Am J Neuroradiol)** (ISSN 0195–6108) is a journal published monthly, owned and published by the American Society of Neuroradiology (ASNR), 800 Enterprise Drive, Suite 205, Oak Brook, IL 60523. Annual dues for the ASNR include \$170.00 for journal subscription. The journal is printed by Cadmus Journal Services, 5457 Twin Knolls Road, Suite 200, Columbia, MD 21045; Periodicals postage paid at Oak Brook, IL and additional mailing offices. Printed in the U.S.A. POSTMASTER: Please send address changes to American Journal of Neuroradiology, P.O. Box 3000, Denville, NJ 07834, U.S.A. Subscription rates: nonmember \$380 (\$450 foreign) print and online, \$305 online only; institutions \$440 (\$510 foreign) print and basic online, \$875 (\$940 foreign) print and extended online, \$365 online only (basic), extended online \$790; single copies are \$35 each (\$40 foreign). Indexed by PubMed/Medline, BIOSIS Previews, Current Contents (Clinical Medicine and Life Sciences), EMBASE, Google Scholar, HighWire Press, Q-Sensei, RefSeek, Science Citation Index, and SCI Expanded. Copyright © American Society of Neuroradiology.

# PUBLICATION METRICS

AMERICAN JOURNAL OF NEURORADIOLOGY



## Crossing the Rubicon

 M. Castillo, *Editor-in-Chief*

If you commit a crime, it is well-known that it is better to face the judge in the morning than later in the day. Studies show that criminals are less likely to be convicted if their case is heard in the early morning than in the late afternoon.<sup>1</sup> Although the above scenario will hopefully never affect any of us neuroradiologists, I do wonder how it affects our daily work. Am I more likely to make the wrong decision at the end of a long day in the reading room? As an editor, am I more likely to accept or reject articles late in the evening?\*

Repeated judgments and decisions exhaust one's mental resources, especially those related to executive functions and thus influence the way we make choices leading to intuitive rather than rational decision-making. Lesson: never buy a car late in the afternoon; do it early, during the weekend, and after sleeping well the night before. Individuals who buy their cars when tired are more likely to accept whatever the manufacturers say about their products.<sup>2</sup> Car salespersons know how to play the game as they go back and forth to their managers, each time forcing you to make new decisions (paint type, type of wheels, leather or standard cloth, and so forth) that wear you down so that when the time to make the final decision to buy the car comes, you are exhausted and just buy it as is. Candy manufacturers are also experts at decision fatigue, and they generally place their (junkier and cheaper) products by the supermarket cashier, so when one is exhausted from shopping, poor decision-making kicks in and one ends up buying all sorts of junk food. Making more decisions during one's day does not make one better at them; on the contrary, it makes for worse choices. The impulsive decision to answer a controversial e-mail when fatigued is nearly always the wrong one; something that I learned the painful way.

The Rubicon decision model states that there are 3 stages to decision-making: first a predecisional (orientation) stage and last a postdecisional stage (also called emergence and reinforcement stages), which are separated by a Rubicon (named after the river in northern Italy that Caesar crossed resulting in a civil war between Gaul and Rome). Thus, the expression "crossing the Rubicon" refers to making an irreversible decision. When one makes the decision to click on the approve button for an imaging report, the "imaging interpretation Rubicon" has been crossed. Crossing the Rubicon is one of the most exhausting stages of decision-making, so it should not be surprising that we radiologists feel drained by the end of the day.

The Rubicon process is even more complicated when a clear-cut decision cannot be made and one must make trade-offs (called the conflict stage). Compromise and trade-offs in the predecisional stage are also exhausting. If one cannot afford to buy an item, trade-offs lead to exhaustion and not uncommonly one

ends up making a decision based only on price rather than other important features such as quality. Marketing strategies also take advantage of this type of fatigue to time the sale of items when you are indecisive. Fatigue can also work in other ways when you are trying to decide. Many choices, conversely, may not make decisions easier but rather lead to no decisions at all.

Some studies have shown that medical-decision errors often occur under the effects of stress and fatigue. In addition, medical teams are unlikely to discuss these errors and to accept the role that decision fatigue played in them. However, airline cockpit crews are prone to report these errors to help improve their performance.<sup>3</sup> In the 1950s, commercial airline accidents dropped significantly when it became obvious that many errors arose from incorrect decision-making by pilots and crew. Critical personality features that airlines look for in their pilots include the ability to learn from errors, recognize them in others, and contribute to solving them. Today, more than 7 generations of airline crews have been trained with these features in mind, and aviation accidents are at an all-time low.

Work hours may be limited to avoid fatigue and errors in decision-making. We are all familiar with the application of this concept in regard to the maximum hours that trainees in medicine can work (80 per week). These hours include hospital day work, call hours, and time spent in academic activities related to training. Additionally, any other activity for which "attendance is strongly encouraged" (such as off-hours journal clubs) needs to be counted within the allowed 80 hours. When a resident travels to present work at a meeting, this travel also counts as active duty time. Why does this requirement apply to trainees and not us, full-fledged radiologists? I spend about 10–12 hours per day at the hospital, plus an additional 2–3 per day working on *AJNR*, and countless others doing service and volunteer work. Yet, the ultimate responsibility of making a decision in reporting imaging studies falls on me. Are younger individuals more resilient to fatigue than us older ones? Airline rules apply equally to senior and less experienced crew members.

The origin of limiting the hours trainees can work arose from recommendations made by the Institute of Medicine in 2008 with the intention of limiting trainee fatigue and decision-making errors. Younger trainees are thought to be more affected by fatigue; therefore, they are allowed to work fewer hours than senior ones (16 versus 28 continuous hours).<sup>4</sup> A study published in the *New England Journal of Medicine* points out how these new rules made a bad situation even worse. Data from a survey completed by more than 6200 residents showed that residents believed that their schedules, education, and quality of life were actually worse and that patient care was suffering after implementation of the new hour policy in 2011.<sup>5</sup> This finding makes perfect sense because while it relieved fatigue in first-year trainees, the bulk of the work was shifted to more senior residents who actually compose the largest pool. Another study reported that despite the new work hour requirements, the amount of sleep residents got did not improve.<sup>6</sup> If limiting duty hours was an attempt to improve patient safety, this also failed and intensive care unit stays are more likely than before the reform.<sup>7</sup> To be fair, I must mention that

\* Don't worry; I do most of my editor work in the early morning.

<http://dx.doi.org/10.3174/ajnr.A4107>

many other studies (too many to quote here) have shown that errors in laparoscopy and electrocardiogram interpretation, unnecessary prolongation of procedures, and lesser quality physical examinations occur more often when chronically sleep-deprived residents have been involved.

Why limiting duty hours for our trainees failed is difficult to understand. Airline pilots are allowed only 8 hours of flight time in a 24-hour period, and all pilots must rest a minimum of 8 hours between assignments.<sup>8</sup> For flights lasting more than 12 hours, adequate sleeping facilities outside the flight deck must be provided. Airlines also provide their pilots with “fatigue” training. If pilots nap, why not our residents? The Accreditation Council for Graduate Medical Education actually says, “Strategic napping is strongly suggested in the program requirements . . . and should not be scheduled but based upon resident fatigue.”<sup>9</sup>

Although intuition tells us that working overtime leads to fatigue, this is not always the case. In a survey of 4000 other workers, the amount of nonextreme overtime did not correlate with fatigue.<sup>10</sup> Moreover, overtime workers had favorable characteristics such as high decision latitude, high job variety, high job demands, and, most important, a high job satisfaction. It appears that personal motivation is what leads these workers to work more while maintaining high satisfaction. This, however, may not be the case in Asia where doctors are exposed to extreme overtime (more than 60 additional hours per week) and chronic fatigue is common.<sup>10</sup>

The key to the failure of the new resident work hour requirements to improve fatigue and decision-making errors may lie in our working environments. In an above-cited study, a positive psychosocial environment was critical to ameliorate the effects of fatigue.<sup>10</sup> This may be why all of these policies work better in the cockpit than in our reading rooms. Cockpits are highly structured, relatively quiet, free of inconsequential interruptions, and respectful places to work, while our reading rooms with their myriad interruptions by telephone, secretaries, clerks, technologists, students, and other physicians have become stressful, nightmarish environments in which it is difficult to complete the assigned tasks and concentrate on making the correct decisions.

Below are some of the most common problems leading to decision-making mistakes and how I think they relate to radiologists:

- 1) Not taking enough time. A common problem in my reading room in which 1 fellow, 1 resident, and 1 attending interpret upwards of 100 head CTs and MRIs during the workday (spine and ear, nose, and throat studies are interpreted in different reading rooms that have the same problems).
- 2) Lacking a peaceful environment (see above). Business folks put it in different language: wallowing in chaos.
- 3) Not considering priorities. In marketing, this is akin to not doing what is best for you, neglecting your values, avoiding the truth, procrastinating, and ignoring what is right.

- 4) Learning how to say no. I think that learning when to stop interpreting studies and realizing and accepting fatigue are essential to avoid mistakes. Item 3 comes into play here. In the late afternoon, one must prioritize the studies that need to be read and leave others for later. I have learned something else: There is no reason why a case that one does not understand must be immediately interpreted. Now, I place a preliminary report with a note stating that I would like to think about it for a while. This pause allows me to go to my office and do some research, which has always been a good decision, resulting in more intelligent reports. This is what experts call “timing” your decision.

Well, most of this advice is easier said (written) than done. Fatigue will always affect the way we make decisions, and as our existing medical delivery systems come under stress, more work and fatigue will be the rule rather than the exception. Remember that a good and timely decision does not guarantee a good outcome. Decisions must be plastic; they should be able to change and mold when new information becomes available. An irrevocable decision to cross the Rubicon always carries with it the risk of the Ides of March.

## REFERENCES

1. Danziger S, Levav J, Avnaim-Pesso L. **Extraneous factors in judicial decisions.** *Proc Natl Acad Sci U S A* 2011;108:6889–92
2. Levav J, Heitmann H, Herrmann A, et al. **Order in product customization decisions: evidence from field experiments.** *J Polit Econ* 2010;118:274–99
3. Sexton JB, Thomas EJ, Halmrieck RL. **Error, stress, and teamwork in medicine and aviation: cross sectional surveys.** *BMJ* 2000;320:745–49
4. Fodeman JD. **The new resident duty hours fail.** *National Review Online.* August 12, 2012. <http://www.nationalreview.com/critical-condition/313022/new-resident-duty-hours-fail-jason-d-fodeman>. Accessed March 19, 2014
5. Drolet BC, Christopher DA, Fischer SA. **Resident’s response to duty-hour regulations: a follow-up national survey.** *N Engl J Med* 2010;363:e34
6. Schumacher DJ, Frintner MP, Jain A, et al. **The 2011 ACGME standards: impact report by graduating residents on the working and learning environment.** *Acad Pediatr* 2014;14:149–54
7. Block L, Jarlenski M, Wu AW, et al. **Inpatient safety outcomes following the 2011 residency work-hour reform.** *J Hosp Med* 2014;9:347–52
8. Federal Aviation Administration. **Fact sheet—pilot flight times, rest, and fatigue.** January 27, 2010. [http://www.faa.gov/news/fact\\_sheets/news\\_story.cfm?newsId=6762](http://www.faa.gov/news/fact_sheets/news_story.cfm?newsId=6762). Accessed March 19, 2014
9. Accreditation Council for Graduate Medical Education. **Frequently asked questions: ACGME common duty hour requirements.** <https://www.acgme.org/acgmeweb/Portals/0/PDFs/dh-faqs2011.pdf>. Updated June 18, 2014. Accessed September 19, 2014
10. Beckers D, van der Linden D, Smulders P, et al. **Working overtime hours: relations with fatigue, work motivation, and the quality of work.** *J Occup Environ Med* 2004;46:1282–89

# The Prognostic Utility of MRI in Clinically Isolated Syndrome: A Literature Review

C. Odenthal and A. Coulthard



## ABSTRACT

**SUMMARY:** For patients presenting with clinically isolated syndrome, the treating clinician needs to advise the patient on the probability of conversion to clinically definite multiple sclerosis. MR imaging may give useful prognostic information, and there is large body of literature pertaining to the use of MR imaging in assessing patients presenting with clinically isolated syndrome. This literature review evaluates the accuracy of MR imaging in predicting which patients with clinically isolated syndrome will go on to develop long-term disease and/or disability. New and emerging MR imaging technologies and their applicability to patients with clinically isolated syndrome are also considered.

**ABBREVIATIONS:** CDMS = clinically definite multiple sclerosis; CIS = clinically isolated syndrome; EDSS = Expanded Disability Status Scale; T2LV = T2 lesion volume

**M**ultiple sclerosis is a chronic autoimmune inflammatory disease of the CNS, which may have long-term consequences on patients quality of life. In 85% of patients with MS, the first presentation is in the form of clinically isolated syndrome (CIS).<sup>1</sup> It is important to identify which patients presenting with CIS will go on to develop MS to expedite treatment initiation with the goal of reducing future morbidity.

MR imaging has a central role in the investigation of patients presenting with a suspected demyelinating illness. In addition to excluding other diseases, MR imaging allows clinicians to observe the pathologic processes underpinning the clinical manifestations *in vivo*. In individuals with established MS, MR imaging appearances are considered predictive of future disability and disease progression. However, the prognostic value of MR imaging in subjects presenting with CIS is less clear.

This review will address whether MR imaging data from subjects presenting with CIS is predictive of future disease and disability. New and emerging MR imaging technologies will also be reviewed.

## MATERIALS AND METHODS

References were identified by PubMed and MEDLINE searches, between 1993 and February 2013, and further references were identified from relevant articles. The search terms “clinically iso-

lated syndrome,” “CIS,” “first demyelinating event,” “FDE,” “multiple sclerosis,” “MS,” “MR imaging,” and “MRI” were used. Articles were limited to English language.

Studies for inclusion were to meet the following criteria: 1) the study must address the ability of MR imaging to predict MS and/or disability in subjects with CIS, 2) MR imaging must be performed at initial presentation, 3) CIS must be statistically analyzed separately from other phenotypes. The following exclusion criteria were applied: 1) MR imaging features not included as independent or dependent variables in statistical analysis, 2) subject group with single-category symptoms only, 3) spinal cord MR imaging investigation only, and 4) pediatric studies.

A single reviewer with experience in research design and methodology performed the literature search and collated data.

## Definition of CIS

CIS is defined as a monophasic presentation with suspected underlying inflammatory demyelination. Symptoms are typically of rapid onset, and last for more than 24 hours. CIS is divided into 4 categories, based on whether presentation demonstrates mono- or multifocal clinical or MR imaging features.<sup>2</sup> MR imaging lesions should appear typical for demyelination, may be located in the brain or spinal cord, and an alternative diagnosis should be considered less likely.<sup>2</sup>

Published rates of conversion from CIS to clinically definite MS (CDMS) differ according to length of study follow-up. Five studies were identified in which subjects were followed for greater than 6 years. For follow-up of 6.9, 7.2, 7.3, 14.0, and 20.0 years, total conversion rates were 48%, 60%, 85%, 68%, and 63%, respectively.<sup>3-7</sup>

From the School of Medicine (C.O.), University of Queensland, Brisbane, Queensland, Australia; and Department of Medical Imaging (A.C.), Royal Brisbane and Women's Hospital, Brisbane, Queensland, Australia.

Please address correspondence to Cara Odenthal, Research Office, Department of Medical Imaging, Royal Brisbane and Women's Hospital, Herston, Queensland, Australia, 4006; e-mail: caraodenthal@yahoo.com.au

Indicates open access to non-subscribers at www.ajnr.org

<http://dx.doi.org/10.3174/ajnr.A3954>

### Conventional MR Imaging

Conventional MR imaging has a well-established role in the initial assessment of subjects with CIS. The risk of conversion to CDMS is greater in patients presenting with abnormal T2WI. Subjects with CIS subjects in the range of 50%–70% present with abnormal T2WI.<sup>1</sup> Two studies were identified which observed subjects for over 10 years. Fisniku et al<sup>7</sup> followed 107 subjects with CIS to 20.2 years; 82% with abnormal baseline MR imaging converted to CDMS, compared with 21% with normal MR imaging. In another study, 88% of subjects with abnormal MR imaging converted by 14 years, compared with 19% of those with normal scans.<sup>6</sup>

T2 lesion number at presentation has been associated with increased risk of conversion to CDMS.<sup>8–17</sup> However, a recent meta-analysis concluded that abnormal T2WI, regardless of lesion number, was associated with increased risk of conversion.<sup>18</sup> However, the review was limited, with nonuniform definitions of conversion to MS, and varied length of follow-up among the included studies.

In addition to T2 lesions, increased risk of conversion to MS is associated with the presence of gadolinium-enhancing lesions.<sup>8,12–14,16,19–23</sup> Accurate estimation of the incidence of Gd-enhancing lesions at CIS presentation is difficult because of inconsistent administration of contrast across studies. Gd-enhancing lesions may only be present in subjects with abnormal T2WI.<sup>8,24</sup> The presence of at least 1 Gd-enhancing lesion is predictive of time to CDMS in monofocal, but not in multifocal, presentations.<sup>25</sup>

The prognostic significance of T1 lesions has been infrequently addressed. Summers et al<sup>4</sup> found that in addition to Gd-enhancing lesions, T1 lesions were predictive of cognitive dysfunction after 7 years.

Few studies have addressed the association between conventional MR imaging measures and disability. A number of disability scales are used in subjects with CIS. The most frequently used is the Expanded Disability Status Scale (EDSS), which primarily assesses ambulation.<sup>26</sup> Another scale, the Multiple Sclerosis Functional Composite, addresses cognition in addition to mobility.<sup>27,28</sup> Baseline T2 lesion number is associated with EDSS at long-term follow-up of up to 14 years.<sup>6,9</sup> A recent study found that baseline Gd-enhancing lesion number was predictive of both EDSS and Multiple Sclerosis Functional Composite at 6 years. The authors also found that while baseline T2 lesion number was not associated with disability, the increase in T2 lesion number over the first year after presentation was predictive of EDSS at 6 years.<sup>29</sup>

Similar to subjects with MS, lesions are primarily distributed around the ventricular system in subjects with CIS.<sup>30,31</sup> The risk of disease progression is associated with lesion location, with periventricular,<sup>32</sup> callosal,<sup>32,33</sup> and cerebellar<sup>34</sup> distributions being most associated with conversion to CDMS.

Infratentorial lesion location may be associated with increased risk of disease and disability.<sup>34,35</sup> Since infratentorial lesions are likely to affect clinically eloquent areas, they may have greater contribution to future disability.<sup>34</sup> However, brain stem syndromes are represented infrequently in the literature. In a large multicenter study of 468 subjects with CIS, infratentorial lesions (including the brain stem and cerebellum) were not associated with increased risk of conversion.<sup>12</sup>

### MR Imaging Volumetrics

Brain volume measurement is considered a surrogate marker for neurodegeneration in patients with MS.<sup>36</sup> It is uncertain whether neurodegeneration is present in subjects with CIS.

Techniques for MR imaging volumetrics may be 2D or 3D, and range from fully manual to fully automatic. Numerous software packages are available, including Statistical Parametric Mapping (SPM; Wellcome Department of Imaging Neuroscience, London, UK),<sup>37</sup> FreeSurfer (<http://surfer.nmr.mgh.harvard.edu>),<sup>38,39</sup> and the FMRIB Software Library (FSL; <http://www.fmrib.ox.ac.uk/fsl>).<sup>40,41</sup> After removing the skull, automated segmentation algorithms are applied to MR imaging data to obtain GM,<sup>42</sup> WM,<sup>43</sup> CSF, and whole-brain volumes. In addition to absolute values, volumes may be expressed as a fraction of total intracranial volume.

Estimates of baseline lesion volumes are heterogeneous. Mean T2 lesion volume (T2LV) has been estimated to be between 2.0 mL to 6.2 mL,<sup>21,29,44–48</sup> whereas T1 lesion volume estimates range from 0.4 mL to 0.5 mL.<sup>29,46,48</sup> Gd-enhancing lesion volume has been inconsistently reported because of nonuniform use of contrast. Baseline lesion volumes have been noted to differ considerably depending on patient symptoms.<sup>21,45</sup>

Subjects with CIS who convert to CDMS demonstrate a greater T2LV at presentation compared with those who do not convert.<sup>11,16,22,29,49</sup> From multivariate regression analysis, Calabrese et al<sup>50</sup> found that baseline T2LV was an independent predictor of conversion to MS by 4 years. A study by Paolillo et al,<sup>51</sup> on the other hand, did not demonstrate either T1 lesion volume or T2LV to be associated with conversion; however, in that study, follow-up was limited to 18 months.

T2LV is associated with the development of future disability. An early study by Brex et al<sup>6</sup> found that baseline T2LV was associated with EDSS at 14 years, with the increase in T2LV over the first 5 years also being associated with disability at follow-up. Similarly, other studies have found that the rate of increase in T2LV in the first year is associated with greater long-term disability.<sup>7,29</sup>

T1 lesion volume may be better suited to the prediction of disability scales other than the EDSS. Di Filippo et al<sup>29</sup> found that while baseline T1 lesion volume was not associated with EDSS, it did correlate with Multiple Sclerosis Functional Composite at 6 years. Another study found that both T1 lesion number and volume were predictive of future cognitive dysfunction.<sup>4</sup>

Baseline measures of whole-brain volume have not been consistently demonstrated to differentiate subjects with CIS from healthy controls, with a number of studies finding no significant difference at baseline.<sup>22,31,45,46,49,52–54</sup> These findings are in contrast to that of Sbardella et al<sup>55</sup>; however, subjects with CIS included in their study had a high lesion load (mean T2 lesion number 15.5). To date, no study has demonstrated any significant difference in global measures of WM or GM volumes in patients with CIS compared to healthy controls.

In a cross-sectional study, Henry et al<sup>52</sup> reported volume reduction in a number of deep GM structures of subjects with CIS, compared with controls, including the thalamus and caudate nucleus. Although deep GM volumes were not correlated with EDSS, cerebellar volume was associated with baseline tests of cerebellar function.<sup>52</sup> In another study, reduced thalamic volume in subjects

with CIS was not retained after correction for multiple comparisons.<sup>56</sup> Numerous other authors have since failed to demonstrate any convincing GM volume reduction in subjects with CIS.<sup>16,31,47,50,57</sup> A recent study of 212 subjects did find that increased T2LV was associated with reduced volume of a number of deep GM structures; however, the study lacked healthy controls.<sup>45,52</sup>

A fundamental flaw in regional volumetric analysis is inaccurate segmentation of deep GM structures.<sup>58</sup> Greater lesion burden leads to more problems in tissue misclassification.<sup>59</sup> More accurate estimation of atrophy is possible when volume change is measured directly from serially acquired MR imaging scans by using registration-based methods.<sup>58</sup>

Structural Image Evaluation by using Normalization of Atrophy is a robust, well-validated tool that uses registration-based methods to estimate percentage brain volume change between 2 time points.<sup>40,41</sup> Although it does not allow estimation of regional volumes, Structural Image Evaluation by using Normalization of Atrophy is highly reproducible.<sup>60</sup> Estimates of percentage brain volume change range from  $-0.35\%$  to  $-0.73\%$  per year in subjects with CIS.<sup>29,51,60,61</sup> Subjects who convert to CDMS have been demonstrated to have greater percentage brain volume change than those who do not.<sup>29,61</sup> Kalincik et al,<sup>22</sup> in contrast, found that percentage brain volume change was not significantly different in subjects with CIS who converted. However, in their study all subjects with CIS had abnormal T2WI.<sup>22</sup>

The corpus callosum is a structure of interest in demyelinating illnesses. In a longitudinal study of 24 subjects with CIS, Audoin et al<sup>62</sup> found that the midsagittal corpus callosal area was significantly reduced at 12 months, when compared with healthy controls. Callosal area also correlated with progression in EDSS. More recently, in a larger cohort of 220 subjects with CIS, change in callosal area in the first 6 months after presentation was predictive of conversion to CDMS by 2 years.<sup>22</sup>

### **Diffusion Tensor Imaging**

DTI allows assessment of the structural integrity of tissues, with water diffusivity being affected by various CNS tissue barriers, including microtubules and cell membranes. Descriptive parameters include fractional anisotropy, reflective of the fraction of anisotropy along 1 direction, and mean diffusivity or apparent diffusion coefficient, which is the average diffusion per voxel, regardless of direction. In WM, fiber organization is reflected by the anisotropy, with the quantity of anisotropy being augmented by the integrity of surrounding myelin.<sup>63</sup>

Although histogram analysis of mean diffusivity has been shown to differentiate subjects with CIS from healthy controls,<sup>64</sup> region-of-interest approaches have not.<sup>65</sup>

Using tractography, Pagani et al<sup>66</sup> found that subjects with CIS with pyramidal symptoms had increased mean diffusivity in the pyramidal tract, compared with both patients without symptoms, and control subjects. On the other hand, another study found that patients with CIS had increased mean diffusivity in all WM tracts.<sup>67</sup> Neither study found a difference in baseline fractional anisotropy in subjects with CIS.<sup>66,67</sup> In contrast, another study using tract-based spatial statistics demonstrated widespread reduced fractional anisotropy in the WM of subjects with CIS.<sup>56</sup>

Tract-based spatial statistics is a recently developed technique that allows analysis of microstructural fiber damage,<sup>68</sup> and may be more sensitive to detect subtle anisotropy changes. However, while baseline fractional anisotropy was correlated with GM atrophy at 1 year in the same cohort, there was no association with disability.<sup>56,69</sup>

### **Magnetization Transfer Imaging**

Magnetization transfer imaging measures the transfer of magnetization from hydrogen nuclei of water with restricted motion (bound pool), to hydrogen nuclei of freely moving water (free pool). This allows imaging of the bound pool, which includes protons in macromolecules, including myelin. The magnetization transfer ratio thus represents pathologic changes to macromolecules.<sup>70</sup>

Results of studies by using magnetization transfer imaging have been mixed. Iannucci et al<sup>49</sup> found that the magnetization transfer ratio of patients with CIS differed significantly from healthy controls; however, all patients had  $\geq 4$  lesions. In a large multicenter study, magnetization transfer ratio differentiated patients from controls in only 1 of 3 study centers.<sup>46</sup> Therefore, magnetization transfer ratio abnormalities are likely associated with increased lesion number at presentation.<sup>53,71</sup>

Magnetization transfer ratio has been shown to be predictive of conversion to CDMS<sup>49</sup> and future cognitive decline.<sup>72</sup> However, some studies have found conflicting results.<sup>46,73</sup> Another magnetization transfer imaging technique, magnetization transfer ratio texture analysis, has not been demonstrated to have prognostic utility in patients with CIS.<sup>3</sup>

### **MR Imaging Spectroscopy**

NAA is a metabolite considered to be exclusive to neurons. Watjes et al<sup>74</sup> identified a significant reduction in tNAA (summed NAA and its moiety, N-acetyl-aspartyl-glutamate) in the normal-appearing WM of subjects with CIS compared with healthy controls. Subsequent studies have had conflicting results.<sup>32,75</sup> Other studies found that only those patients with clinical progression demonstrated reduced NAA at presentation.<sup>55,76</sup>

Myo-inositol (mIns or Ins) is a metabolite primarily concentrated in glial cells. As with NAA, studies of this metabolite have demonstrated mixed results. In 1 study, when subjects with CIS were compared with controls, baseline mIns of normal-appearing WM discriminated only those who went on to convert to CDMS.<sup>76</sup> On the other hand, another study of a larger cohort found that mIns concentration was higher across the entire CIS group.<sup>75</sup>

Metabolite concentrations have a temporal evolution after CIS presentation. Audoin et al<sup>62</sup> performed serial MR spectroscopy, with metabolite concentrations measured in the corpus callosum. They demonstrated baseline reduced NAA and increased choline (Cho, associated with myelin), both of which normalized by 6 months. In another study, the rate of increase in mIns concentration in normal-appearing WM over the first year was predictive of poor executive function at 7.2 years.<sup>4</sup>

Although metabolite concentrations may be associated with long-term cognitive change, no single metabolite has demonstrated a correlation with disability, either at baseline or follow-up.<sup>4,75</sup> However, a model combining metabolite concentrations

with other MR imaging variables was shown to demonstrate superior utility in predicting disability at 1 year compared with any variable alone.<sup>55</sup>

### **Functional MR Imaging**

Functional cortical changes are present from the earliest stages of CIS. Compared with healthy controls, subjects with CIS demonstrate increased cortical activation in both cerebral hemispheres,<sup>77,78</sup> with the extent of activation being related to motor task difficulty.<sup>79</sup> Patterns of activation are associated with short-term disease evolution, with converters demonstrating recruitment of a more extensive sensorineural network at baseline.<sup>80</sup> In a study assessing cognitive changes in CIS, more widespread activation on fMRI was associated with improved cognition scores, both at baseline and 1-year follow-up.<sup>81</sup>

Using a novel fMRI technique called dynamic causal modeling, Rocca et al<sup>82</sup> found that subjects with CIS had increased interconnectivity between the left and right sensorimotor cortex. However, subjects were not followed longitudinally.

A recent study measured the amplitude of low frequency alteration in resting-state fMRI. Compared with healthy controls, subjects with CIS demonstrated decreased amplitude of low frequency alteration in numerous cerebral regions.<sup>83</sup> In contrast, subjects with MS have previously been shown to have areas of increased cerebral amplitude of low frequency alteration.<sup>84</sup> The authors hypothesized that amplitude of low frequency alteration may evolve as time passes from the initial presentation.<sup>83</sup>

### **MR Imaging Perfusion**

Varga et al<sup>85</sup> quantified cerebral blood flow with MR perfusion in a mixed cohort of subjects with CIS and MS. Compared with healthy controls, they found hypoperfusion in the periventricular normal-appearing WM of subjects with CIS. However, none of the perfusion parameters were associated with disability measures in either subgroup.

### **Brain Iron Quantification**

T2 hypointensity, attributable to iron deposition, is a frequent finding in subjects with MS.<sup>86</sup> In subjects with CIS, T2 hypointensity has been identified in the left caudate nucleus.<sup>87</sup> Khalil et al<sup>88</sup> used R2\* relaxometry to quantify brain iron deposition in a cohort of subjects with CIS and MS. Compared with subjects with MS, patients with CIS had significantly reduced R2\* values in a number of deep GM regions. While R2\* values correlated with regional brain volumes, there was no association with disability.<sup>88</sup> In another study, patients with CIS had significantly reduced R2\* values in the basal ganglia and thalamus.<sup>89</sup> However, this study was limited, as age was not considered in the methodology, despite control subjects being 3 years older than those with CIS.

Hagemer et al<sup>47</sup> used an SWI phase approach to obtain mean phase of the abnormal phase tissue, a metric for quantification of iron levels. Compared with healthy controls, subjects with CIS had significantly increased abnormal phase and abnormal phase volume in a number of deep GM regions. However, iron deposition was noted in the absence of any significant volume change.

In addition to R2\* relaxometry, Langkammer et al<sup>90</sup> performed quantitative susceptibility mapping on 26 subjects with

CIS. Quantitative susceptibility mapping detects magnetic charge variations attributable not only to iron, but also but also to myelin. Although R2\* relaxometry did not differentiate between subjects with CIS and controls, quantitative susceptibility mapping revealed abnormality in the caudate, putamen, and basal ganglia in subjects with CIS. In apparent contrast, a recently published study by Quinn et al<sup>91</sup> showed that subjects with CIS had increased R2\* compared with age-matched healthy controls in a number of regions, including the medial thalamus and right putamen. Furthermore, thalamic R2\* relaxometry indices were positively correlated with EDSS ( $r = 0.47, P = .028$ ). Apparently conflicting results by these 2 recently published studies may be attributable to differences in image processing techniques. Langkammer et al<sup>90</sup> calculated the mean R2\* of segmented cerebral structures, while Quinn et al<sup>91</sup> used voxelwise analysis.

### **MR Imaging in Clinical Trials**

MR imaging features have been included as outcome measures in a number of therapeutic trials. Treatments tested included: plasma exchange,<sup>92</sup> intramuscular interferon  $\beta$ -1a,<sup>93</sup> and interferon  $\beta$ -1b.<sup>94,95</sup> Patients with CIS with abnormal baseline T2-weighted MR imaging are ideal candidates to include in therapeutic trials because of increased risk of conversion to MS.<sup>96</sup>

### **Emerging MR Imaging Technologies**

Multicomponent driven equilibrium single pulse observation of T1 and T2 is a newly developed MR imaging technique used to quantify myelin tissue content in vivo.<sup>97</sup> Kitzler et al<sup>98</sup> examined the utility of multicomponent driven equilibrium single pulse observation for measurement of myelin water fraction across a range of MS subtypes. In subjects with CIS, the total volume of voxels demonstrating deficient myelin water fraction was statistically significant compared with healthy controls. To date, there are no longitudinal studies on subjects with CIS using this technique.

## **CONCLUSIONS**

In subjects presenting with CIS, the primary concern of clinicians and patients is the probability of conversion to CDMS. MR imaging plays a key role in the initial assessment of subjects with CIS.

A number of MR imaging markers have demonstrated prognostic potential. Abnormal T2WI is associated with increased risk of conversion. The number and volume of T2 and Gd-enhancing lesions may be predictive of disability. Changes in corpus callosum area and whole-brain volume over the first year from diagnosis of CIS have also shown prognostic utility; however, studies are limited.

Although new and emerging technologies have not demonstrated any convincing prognostic potential at this stage, they do give insight into the mechanisms underlying the pathology of CIS. While regional atrophy is not present at patient presentation, changes in DTI and MR spectroscopy parameters demonstrate that there is functional change occurring in normal-appearing brain tissue. Widespread increased motor cortical activation visualized on fMRI suggests that neuroplasticity is already a factor at initial presentation. Furthermore, subjects with CIS demonstrate brain iron deposition, a feature that is characteristic of MS.

There are a number of limitations within the published liter-

ature, and thus, of this review. In general, cohort sizes are small, with heterogeneous subject selection criteria. Many studies are cross-sectional, or have limited length of follow-up. Further studies of robust design and long-term follow-up are needed to investigate the utility of MR imaging techniques in the prediction of disease and disability in subjects with CIS.

## REFERENCES

- Miller DH, Chard DT, Ciccarelli O. Clinically isolated syndromes. *Lancet Neurol* 2012;11:157–69
- Miller DH, Weinshenker BG, Filippi M, et al. Differential diagnosis of suspected multiple sclerosis: a consensus approach. *Mult Scler* 2008;14:1157–74
- Tozer DJ, Marongiu G, Swanton JK, et al. Texture analysis of magnetization transfer maps from patients with clinically isolated syndrome and multiple sclerosis. *J Magn Reson Imaging* 2009;30:506–13
- Summers M, Swanton J, Fernando K, et al. Cognitive impairment in multiple sclerosis can be predicted by imaging early in the disease. *J Neurol Neurosurg Psychiatry* 2008;79:955–58
- Patrucco L, Rojas JL, Miguez JS, et al. Application of the McDonald 2010 criteria for the diagnosis of multiple sclerosis in an Argentinian cohort of patients with clinically isolated syndromes. *Mult Scler* 2013;19:1297–301
- Brex PA, Ciccarelli O, O’Riordan JI, et al. A longitudinal study of abnormalities on MRI and disability from multiple sclerosis. *N Engl J Med* 2002;346:158–64
- Fisniku LK, Brex PA, Altmann DR, et al. Disability and T2 MRI lesions: a 20-year follow-up of patients with relapse onset of multiple sclerosis. *Brain* 2008;131:808–17
- Brex PA, O’Riordan JI, Miszkiel KA, et al. Multisequence MRI in clinically isolated syndromes and the early development of MS. *Neurology* 1999;53:1184–90
- Tintoré M, Rovira A, Río J, et al. Baseline MRI predicts future attacks and disability in clinically isolated syndromes. *Neurology* 2006;67:968–72
- Alroughani R, Al Hashel J, Lamdhade S, et al. Predictors of conversion to multiple sclerosis in patients with clinical isolated syndrome using the 2010 revised McDonald criteria. *ISRN Neurol* 2012;2012:792192
- Dalton CM, Brex PA, Jenkins R, et al. Progressive ventricular enlargement in patients with clinically isolated syndromes is associated with the early development of multiple sclerosis. *J Neurol Neurosurg Psychiatry* 2002;73:141–47
- Moraal B, Pohl C, Uitdehaag BM, et al. Magnetic resonance imaging predictors of conversion to multiple sclerosis in the BENEFIT study. *Arch Neurol* 2009;66:1345–52
- Brex PA, Miszkiel KA, O’Riordan JI, et al. Assessing the risk of early multiple sclerosis in patients with clinically isolated syndromes: the role of a follow up MRI. *J Neurol Neurosurg Psychiatry* 2001;70:390–93
- Pestalozza IF, Pozzilli C, Di Legge S, et al. Monthly brain magnetic resonance imaging scans in patients with clinically isolated syndrome. *Mult Scler* 2005;11:390–94
- Dalton CM, Brex PA, Miszkiel KA, et al. Application of the new McDonald criteria to patients with clinically isolated syndromes suggestive of multiple sclerosis. *Ann Neurol* 2002;52:47–53
- Zivadinov R, Havrdová E, Bergsland N, et al. Thalamic atrophy is associated with development of clinically definite multiple sclerosis. *Radiology* 2013;268:831–41
- Brex PA, Leary SM, Plant GT, et al. Magnetization transfer imaging in patients with clinically isolated syndromes suggestive of multiple sclerosis. *AJNR Am J Neuroradiol* 2001;22:947–51
- Zhang WY, Hou YL. Prognostic value of magnetic resonance imaging in patients with clinically isolated syndrome conversion to multiple sclerosis: a meta-analysis. *Neurol India* 2013;61:231–38
- Predictors of short-term disease activity following a first clinical demyelinating event: analysis of the CHAMPS placebo group. *Mult Scler* 2002;8:405–09
- CHAMPS Study Group. MRI predictors of early conversion to clinically definite MS in the CHAMPS placebo group. *Neurology* 2002;59:998–1005
- Baseline MRI characteristics of patients at high risk for multiple sclerosis: results from the CHAMPS trial. Controlled high-risk subjects Avonex multiple sclerosis prevention study. *Mult Scler* 2002;8:330–38
- Kalincik T, Vaneckova M, Tyblova M, et al. Volumetric MRI markers and predictors of disease activity in early multiple sclerosis: a longitudinal cohort study. *PLoS One* 2012;7:e50101
- Polman C, Kappos L, Freedman MS, et al. Subgroups of the BENEFIT study: risk of developing MS and treatment effect of interferon beta-1b. *J Neurol* 2008;255:480–87
- Rovira A, Swanton J, Tintore M, et al. A single, early magnetic resonance imaging study in the diagnosis of multiple sclerosis. *Arch Neurol* 2009;66:587–92
- Nielsen JM, Pohl C, Polman CH, et al. MRI characteristics are predictive for CDMS in monofocal, but not in multifocal patients with a clinically isolated syndrome. *BMC Neurol* 2009;9:19
- Kurtzke JF. Rating neurologic impairment in multiple sclerosis: an expanded disability status scale (EDSS). *Neurology* 1983;33:1444–52
- Whitaker JN, McFarland HF, Rudge P, et al. Outcomes assessment in multiple sclerosis clinical trials: a critical analysis. *Mult Scler* 1995;1:37–47
- Rudick R, Antel J, Confavreux C, et al. Clinical outcomes assessment in multiple sclerosis. *Ann Neurol* 1996;40:469–79
- Di Filippo M, Anderson VM, Altmann DR, et al. Brain atrophy and lesion load measures over 1 year relate to clinical status after 6 years in patients with clinically isolated syndromes. *J Neurol Neurosurg Psychiatry* 2010;81:204–08
- Kincses ZT, Ropele S, Jenkinson M, et al. Lesion probability mapping to explain clinical deficits and cognitive performance in multiple sclerosis. *Mult Scler* 2011;17:681–89
- Ceccarelli A, Rocca MA, Pagani E, et al. A voxel-based morphometry study of grey matter loss in MS patients with different clinical phenotypes. *NeuroImage* 2008;42:315–22
- Brex PA, Gomez-Anson B, Parker GJ, et al. Proton MR spectroscopy in clinically isolated syndromes suggestive of multiple sclerosis. *J Neurol Sci* 1999;166:16–22
- Jafari N, Kreft KL, Flach HZ, et al. Callosal lesion predicts future attacks after clinically isolated syndrome. *Neurology* 2009;73:1837–41
- Tintore M, Rovira A, Arrambide G, et al. Brainstem lesions in clinically isolated syndromes. *Neurology* 2010;75:1933–38
- Minneboo A, Barkhof F, Polman CH, et al. Infratentorial lesions predict long-term disability in patients with initial findings suggestive of multiple sclerosis. *Arch Neurol* 2004;61:217–21
- Frischer JM, Bramow S, Dal-Bianco A, et al. The relation between inflammation and neurodegeneration in multiple sclerosis brains. *Brain* 2009;132:1175–89
- Ashburner J, Friston KJ. Unified segmentation. *NeuroImage* 2005;26:839–51
- Dale AM, Fischl B, Sereno MI. Cortical surface-based analysis—I. Segmentation and surface reconstruction. *NeuroImage* 1999;9:179–94
- Dale AM, Sereno MI. Improved localization of cortical activity by combining EEG and MEG with MRI cortical surface reconstruction—a linear approach. *J Cogn Neurosci* 1993;5:162–76
- Smith SM, Jenkinson M, Woolrich MW, et al. Advances in functional and structural MR image analysis and implementation as FSL. *NeuroImage* 2004;23 Suppl 1:S208–19
- Smith SM, Zhang Y, Jenkinson M, et al. Accurate, robust, and automated longitudinal and cross-sectional brain change analysis. *NeuroImage* 2002;17:479–89
- Hagman S, Raunio M, Rossi M, et al. Disease-associated inflammatory biomarker profiles in blood in different subtypes of multiple

- sclerosis: prospective clinical and MRI follow-up study. *J Neuroimmunol* 2011;234:141–47
43. Teunissen CE, Iacobaeus E, Khademi M, et al. **Combination of CSF N-acetylaspartate and neurofilaments in multiple sclerosis.** *Neurology* 2009;72:1322–29
  44. Roosendaal SD, Bendfeldt K, Vrenken H, et al. **Grey matter volume in a large cohort of MS patients: relation to MRI parameters and disability.** *Mult Scler* 2011;17:1098–106
  45. Bergsland N, Horakova D, Dwyer MG, et al. **Subcortical and cortical gray matter atrophy in a large sample of patients with clinically isolated syndrome and early relapsing-remitting multiple sclerosis.** *AJNR Am J Neuroradiol* 2012;33:1573–78
  46. Rocca MA, Agosta F, Sormani MP, et al. **A three-year, multi-parametric MRI study in patients at presentation with CIS.** *J Neurol* 2008;255:683–91
  47. Hagemeyer J, Weinstock-Guttman B, Bergsland N, et al. **Iron deposition on SWI-filtered phase in the subcortical deep gray matter of patients with clinically isolated syndrome may precede structure-specific atrophy.** *AJNR Am J Neuroradiol* 2012;33:1596–601
  48. Tavazzi E, Dwyer MG, Weinstock-Guttman B, et al. **Quantitative diffusion weighted imaging measures in patients with multiple sclerosis.** *NeuroImage* 2007;36:746–54
  49. Iannucci G, Tortorella C, Rovaris M, et al. **Prognostic value of MR and magnetization transfer imaging findings in patients with clinically isolated syndromes suggestive of multiple sclerosis at presentation.** *AJNR Am J Neuroradiol* 2000;21:1034–38
  50. Calabrese M, Rinaldi F, Mattisi I, et al. **The predictive value of gray matter atrophy in clinically isolated syndromes.** *Neurology* 2011;77:257–63
  51. Paolillo A, Piattella MC, Pantano P, et al. **The relationship between inflammation and atrophy in clinically isolated syndromes suggestive of multiple sclerosis: a monthly MRI study after triple-dose gadolinium-DTPA.** *J Neurol* 2004;251:432–39
  52. Henry RG, Shieh M, Okuda DT, et al. **Regional grey matter atrophy in clinically isolated syndromes at presentation.** *J Neurol Neurosurg Psychiatry* 2008;79:1236–44
  53. Traboulsee A, Dehmeshki J, Brex PA, et al. **Normal-appearing brain tissue MTR histograms in clinically isolated syndromes suggestive of MS.** *Neurology* 2002;59:126–28
  54. Rudick RA, Lee JC, Nakamura K, et al. **Gray matter atrophy correlates with MS disability progression measured with MSFC but not EDSS.** *J Neurol Sci* 2009;282:106–11
  55. Sbardella E, Tomassini V, Stromillo ML, et al. **Pronounced focal and diffuse brain damage predicts short-term disease evolution in patients with clinically isolated syndrome suggestive of multiple sclerosis.** *Mult Scler* 2011;17:1432–40
  56. Raz E, Cercignani M, Sbardella E, et al. **Clinically isolated syndrome suggestive of multiple sclerosis: voxelwise regional investigation of white and gray matter.** *Radiology* 2010;254:227–34
  57. Ceccarelli A, Rocca MA, Perego E, et al. **Deep grey matter T2 hypointensity in patients with paediatric multiple sclerosis.** *Mult Scler* 2011;17:702–07
  58. Derakhshan M, Caramanos Z, Giacomini PS, et al. **Evaluation of automated techniques for the quantification of grey matter atrophy in patients with multiple sclerosis.** *NeuroImage* 2010;52:1261–67
  59. Battaglini M, Jenkinson M, De Stefano N. **Evaluating and reducing the impact of white matter lesions on brain volume measurements.** *Hum Brain Mapp* 2012;33:2062–71
  60. Rovaris M, Judica E, Ceccarelli A, et al. **A 3-year diffusion tensor MRI study of grey matter damage progression during the earliest clinical stage of MS.** *J Neurol* 2008;255:1209–14
  61. De Stefano N, Giorgio A, Battaglini M, et al. **Assessing brain atrophy rates in a large population of untreated multiple sclerosis subtypes.** *Neurology* 2010;74:1868–76
  62. Audoin B, Ibarrola D, Malikova I, et al. **Onset and underpinnings of white matter atrophy at the very early stage of multiple sclerosis—a 2-year longitudinal MRI/MRSI study of corpus callosum.** *Mult Scler* 2007;13:41–51
  63. Beaulieu C, Allen PS. **Determinants of anisotropic water diffusion in nerves.** *Magn Reson Med* 1994;31:394–400
  64. Yu CS, Lin FC, Liu Y, et al. **Histogram analysis of diffusion measures in clinically isolated syndromes and relapsing-remitting multiple sclerosis.** *Eur J Radiol* 2008;68:328–34
  65. Caramia F, Pantano P, Di Legge S, et al. **A longitudinal study of MR diffusion changes in normal appearing white matter of patients with early multiple sclerosis.** *Magn Reson Imaging* 2002;20:383–88
  66. Pagani E, Filippi M, Rocca MA, et al. **A method for obtaining tract-specific diffusion tensor MRI measurements in the presence of disease: application to patients with clinically isolated syndromes suggestive of multiple sclerosis.** *NeuroImage* 2005;26:258–65
  67. Preziosa P, Rocca MA, Mesaros S, et al. **Intrinsic damage to the major white matter tracts in patients with different clinical phenotypes of multiple sclerosis: a voxelwise diffusion-tensor MR study.** *Radiology* 2011;260:541–50
  68. Smith SM, Jenkinson M, Johansen-Berg H, et al. **Tract-based spatial statistics: voxelwise analysis of multi-subject diffusion data.** *NeuroImage* 2006;31:1487–505
  69. Raz E, Cercignani M, Sbardella E, et al. **Gray- and white-matter changes 1 year after first clinical episode of multiple sclerosis: MR imaging.** *Radiology* 2010;257:448–54
  70. Pike GB. **Pulsed magnetization transfer contrast in gradient echo imaging: a two-pool analytic description of signal response.** *Magn Reson Med* 1996;36:95–103
  71. Fernando KT, Tozer DJ, Miszkiel KA, et al. **Magnetization transfer histograms in clinically isolated syndromes suggestive of multiple sclerosis.** *Brain* 2005;128:2911–25
  72. Khalil M, Enzinger C, Langkammer C, et al. **Cognitive impairment in relation to MRI metrics in patients with clinically isolated syndrome.** *Mult Scler* 2011;17:173–80
  73. Gallo A, Rovaris M, Benedetti B, et al. **A brain magnetization transfer MRI study with a clinical follow up of about four years in patients with clinically isolated syndromes suggestive of multiple sclerosis.** *J Neurol* 2007;254:78–83
  74. Wattjes MP, Harzheim M, Lutterbey GG, et al. **Axonal damage but no increased glial cell activity in the normal-appearing white matter of patients with clinically isolated syndromes suggestive of multiple sclerosis using high-field magnetic resonance spectroscopy.** *AJNR Am J Neuroradiol* 2007;28:1517–22
  75. Fernando KT, McLean MA, Chard DT, et al. **Elevated white matter myo-inositol in clinically isolated syndromes suggestive of multiple sclerosis.** *Brain* 2004;127:1361–69
  76. Wattjes MP, Harzheim M, Lutterbey GG, et al. **Prognostic value of high-field proton magnetic resonance spectroscopy in patients presenting with clinically isolated syndromes suggestive of multiple sclerosis.** *Neuroradiology* 2008;50:123–29
  77. Pantano P, Iannetti GD, Caramia F, et al. **Cortical motor reorganization after a single clinical attack of multiple sclerosis.** *Brain* 2002;125:1607–15
  78. Rocca MA, Colombo B, Falini A, et al. **Cortical adaptation in patients with MS: a cross-sectional functional MRI study of disease phenotypes.** *Lancet Neurol* 2005;4:618–26
  79. Filippi M, Rocca MA, Mezzapesa DM, et al. **Simple and complex movement-associated functional MRI changes in patients at presentation with clinically isolated syndromes suggestive of multiple sclerosis.** *Hum Brain Mapp* 2004;21:108–17
  80. Rocca MA, Mezzapesa DM, Ghezzi A, et al. **A widespread pattern of cortical activations in patients at presentation with clinically isolated symptoms is associated with evolution to definite multiple sclerosis.** *AJNR Am J Neuroradiol* 2005;26:1136–39
  81. Audoin B, Reuter F, Duong MV, et al. **Efficiency of cognitive control recruitment in the very early stage of multiple sclerosis: a one-year fMRI follow-up study.** *Mult Scler* 2008;14:786–92
  82. Rocca MA, Absinta M, Moiola L, et al. **Functional and structural connectivity of the motor network in pediatric and adult-onset relapsing-remitting multiple sclerosis.** *Radiology* 2010;254:541–50
  83. Liu Y, Duan Y, Liang P, et al. **Baseline brain activity changes in**

- patients with clinically isolated syndrome revealed by resting-state functional MRI. *Acta Radiol* 2012;53:1073–78
84. Liu Y, Liang P, Duan Y, et al. **Brain plasticity in relapsing-remitting multiple sclerosis: evidence from resting-state fMRI.** *J Neurol Sci* 2011;304:127–31
  85. Varga AW, Johnson G, Babb JS, et al. **White matter hemodynamic abnormalities precede sub-cortical gray matter changes in multiple sclerosis.** *J Neurol Sci* 2009;282:28–33
  86. Ge Y, Jensen JH, Lu H, et al. **Quantitative assessment of iron accumulation in the deep gray matter of multiple sclerosis by magnetic field correlation imaging.** *AJNR Am J Neuroradiol* 2007;28:1639–44
  87. Ceccarelli A, Rocca MA, Neema M, et al. **Deep gray matter T2 hypointensity is present in patients with clinically isolated syndromes suggestive of multiple sclerosis.** *Mult Scler* 2010;16:39–44
  88. Khalil M, Enzinger C, Langkammer C, et al. **Quantitative assessment of brain iron by R(2)\* relaxometry in patients with clinically isolated syndrome and relapsing-remitting multiple sclerosis.** *Mult Scler* 2009;15:1048–54
  89. Khalil M, Langkammer C, Ropele S, et al. **Determinants of brain iron in multiple sclerosis: a quantitative 3T MRI study.** *Neurology* 2011;77:1691–97
  90. Langkammer C, Liu T, Khalil M, et al. **Quantitative susceptibility mapping in multiple sclerosis.** *Radiology* 2013;267:551–59
  91. Quinn MP, Gati JS, Klassen ML, et al. **Increased deep grey matter iron is present in clinically isolated syndromes.** *Mult Scler* 2014;3:194–202
  92. Meca-Lallana JE, Hernandez-Clares R, Leon-Hernandez A, et al. **Plasma exchange for steroid-refractory relapses in multiple sclerosis: an observational, MRI pilot study.** *Clin Ther* 2013;35:474–85
  93. Kinkel RP, Dontchev M, Kollman C, et al. **Association between immediate initiation of intramuscular interferon beta-1a at the time of a clinically isolated syndrome and long-term outcomes: a 10-year follow-up of the controlled high-risk Avonex multiple sclerosis prevention study in ongoing neurological surveillance.** *Arch Neurol* 2012;69:183–90
  94. Kappos L, Polman CH, Freedman MS, et al. **Treatment with interferon beta-1b delays conversion to clinically definite and McDonald MS in patients with clinically isolated syndromes.** *Neurology* 2006;67:1242–49
  95. Barkhof F, Polman CH, Radue EW, et al. **Magnetic resonance imaging effects of interferon beta-1b in the BENEFIT study: integrated 2-year results.** *Arch Neurol* 2007;64:1292–98
  96. Kinkel RP, Simon JH, Baron B. **Bimonthly cranial MRI activity following an isolated monosymptomatic demyelinating syndrome: potential outcome measures for future multiple sclerosis 'prevention' trials.** *Mult Scler* 1999;5:307–12
  97. Deoni SC, Rutt BK, Jones DK. **Investigating exchange and multi-component relaxation in fully balanced steady-state free precession imaging.** *J Magn Reson Imaging* 2008;27:1421–29
  98. Kitzler HH, Su J, Zeineh M, et al. **Deficient MWF mapping in multiple sclerosis using 3D whole-brain multi-component relaxation MRI.** *NeuroImage* 2012;59:2670–77

# Subdural Hygromas in Abusive Head Trauma: Pathogenesis, Diagnosis, and Forensic Implications

D. Wittschieber, B. Karger, T. Niederstadt, H. Pfeiffer, and M.L. Hahnemann



## ABSTRACT

**SUMMARY:** Are subdural hygromas the result of abusive head trauma? CT and MR imaging represent important tools for the diagnosis of abusive head trauma in living infants. In addition, in-depth understanding of the pathogenesis of subdural hygromas is increasingly required by neuroradiologists, pediatricians, and forensic physicians. Therefore, the current knowledge on subdural hygromas is summarized and forensic conclusions are drawn. The most important diagnostic pitfalls, benign enlargement of the subarachnoid space, and chronic subdural hematoma, are discussed in detail. Illustrative cases from forensic practice are presented. Literature analysis indicates that subdural hygromas can occur immediately or be delayed. If other infrequent reasons can be excluded, the presence of subdural hygromas strongly suggests a posttraumatic state and should prompt the physician to search for other signs of abuse. To differentiate subdural hygromas from other pathologies, additional MR imaging of the infant's head is indispensable after initial CT scan.

**ABBREVIATIONS:** AHT = abusive head trauma; BESS = benign enlargement of subarachnoid space; BV = bridging vein; cSDH = chronic subdural hematoma; SDH = subdural hematoma; SDHy = subdural hygroma

Child abuse represents a very heterogeneous, unfortunately still present, and therefore well-established research field within the forensic sciences.<sup>1-6</sup> According to the Committee on Child Abuse and Neglect of the American Academy of Pediatrics, abusive head trauma (AHT), also referred to as nonaccidental head injury, is still the leading cause of child abuse fatalities.<sup>7-9</sup> The incidence of AHT in children under 1 year of age ranges between 14 and 28 per 100,000 live births in Western countries.<sup>10-15</sup> Direct blunt force to the head and the so-called Shaken Baby syndrome are currently assumed to be the main etiologic factors of AHT.<sup>9,16-18</sup> The full-blown clinical picture of Shaken Baby syndrome is characterized by the triad of subdural hematomas (SDHs), retinal hemorrhages, and encephalopathy. In some cases, metaphyseal fractures, rib fractures, or small hematomas on arms or thorax may be encountered.<sup>18-22</sup> The caregiver's explanation provided for the injuries is frequently inadequate or inconsistent.<sup>9,18</sup>

The diagnosis and dating of AHT in living infants predominantly relies on neuroimaging by means of CT and/or MR imaging.<sup>23-30</sup> An important indicator for AHT is the presence of SDHs attributed to defects of the bridging veins (BVs). Moreover, in some cases suspected for AHT, radiologists are confronted with almost homogeneous fluid collections within the subdural space, which appear isodense/isointense or nearly isodense/isointense to CSF. These collections are then interchangeably termed as subdural hygromas (SDHys), chronic subdural hematomas (cSDHs), or a terminologic mixture of both: chronic hygromas. This radiologic diagnosis has often resulted in difficulties with regard to the medicolegal assessment of such cases because the exact pathogenesis, diagnosis, and significance of SDHys are still a matter of debate and uncertainty, particularly in infants.<sup>31,32</sup> However, these issues can be decisive in court, for example, when SDHys are considered as evidence for the age of injury.

Therefore, the present review addresses the following questions:

1. What are SDHys?
2. What are the current theories regarding the pathogenesis of SDHy?
3. Which alternative explanations and differential diagnoses have to be considered?
4. What forensic implications arise concerning AHT?

From the Departments of Forensic Medicine (D.W., B.K., H.P.) and Clinical Radiology (T.N.), University Hospital Münster, Münster, Germany; and Department of Diagnostic and Interventional Radiology and Neuroradiology (M.L.H.), University Hospital Essen, Essen, Germany.

Please address correspondence to Daniel Wittschieber, MD, Department of Forensic Medicine, University Hospital Münster, Röntgenstraße 23, 48149 Münster, Germany; e-mail: daniel.wittschieber@ukmuenster.de

Indicates open access to non-subscribers at [www.ajnr.org](http://www.ajnr.org)

<http://dx.doi.org/10.3174/ajnr.A3989>

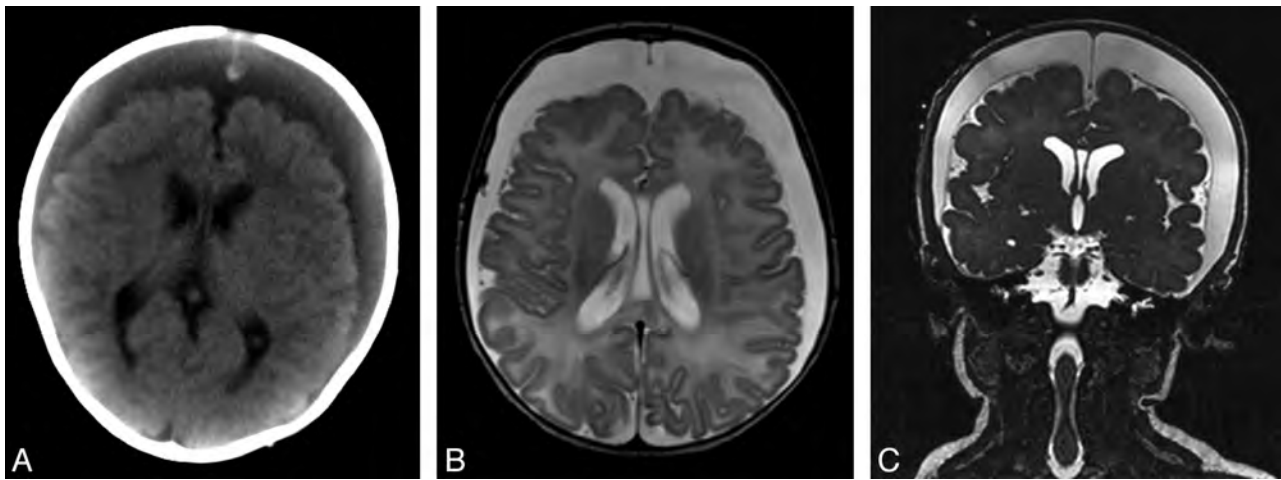


**FIG 1.** Two-month-old boy with huge hypodense, CSF-like, subdural collections lacking encapsulating membranes (A, cranial CT). MR imaging confirmed the diagnosis of frontoparietal SDHys on both sides (B, axial T2-weighted image; C, coronal T2-weighted image).

### What are Subdural Hygromas?

Pathology is always based on anatomy. Under physiologic conditions, the subdural space does not exist in humans. It does not open until the dura-arachnoid interface is mechanically separated, for instance due to brain shrinking, trauma, or neurosurgical interventions.<sup>33-35</sup> This opening is actually regarded as a cleaving of the so-called dural border cell layer—the innermost zone of the dura mater—and therefore also referred to as intradural lesion.<sup>33,36</sup> Nevertheless, in this article, the traditional term subdural is used to describe accordant pathologies within that space such as SDHy.

SDHys can be regarded and examined from 2 different points of view: first, the traditional perspective of the neuropathologist, forensic pathologist, or neurosurgeon who directly investigate or treat colorful 3D pathologies in the human head; and second, the perspective of the neuroradiologist who indirectly evaluates and interprets 2D black-and-white cross-sectional images from CT, MR imaging, or sonography.

With respect to the traditional macroscopic perspective, the term *Hygroma durae matris* (hygrós [gr.] = wet, moist) was first introduced by Rudolph Virchow in 1856.<sup>37</sup> Many other terms, such as subdural hydroma, *Meningitis serosa traumatica*, traumatic subdural effusion, or simply subdural fluid accumulation have also been used.<sup>33,38-42</sup> SDHys are classically described as protein-rich, clear, pink-tinged, or xanthochromic fluid collections within the subdural space.<sup>22,37,42-47</sup> Likewise, if the principal component of a subdural collection appears to be CSF-like, the term SDHy is used.<sup>44,48-50</sup> A mixture of blood and CSF is referred to as hematohygroma.<sup>51-54</sup>

The heterogeneous appearances of SDHys prompted Unterharnscheidt<sup>37</sup> to differentiate between 2 general morphologic types:

1. Cystic and often multichambered formations encapsulated by a membrane.
2. “Free” fluid collections without any capsule.

In radiology, the definition of SDHy is more difficult, and the terminology is very heterogeneous. While acute SDH, representing 1 of the leading indicators for Shaken Baby syndrome,

can be reliably diagnosed by means of CT and MR imaging, other pathologic fluid collections are often termed interchangeably as SDHys, cSDHs, subdural effusions, chronic hygromas, or simply subdural collections.

The term subdural collection is used as an unspecific umbrella term for pathologically formed subdural fluid, whereas the term chronic hygromas should be principally avoided as it is a very imprecise and pathogenetically insufficient description. If there is a mass of proteinaceous liquid within the subdural space that appears to be associated with bacterial meningitis, it is generally spoken of as a subdural effusion.<sup>54-56</sup>

But what about SDHy versus cSDH? A current neuroradiologic textbook by Osborn<sup>55</sup> defines SDHys as “hypodense, CSF-like, crescentic extraaxial collections that consists purely of CSF, have no blood products, lack encapsulating membranes, and show no enhancement following contrast administration” (Fig 1). This description is strikingly similar to the second morphologic type of SDHy suggested above by Unterharnscheidt.<sup>37</sup> However, this CSF-like appearance is also the reason why SDHys harbor a high potential to be confused with cSDHs.<sup>57</sup> According to Osborn,<sup>55</sup> cSDHs may be defined as “encapsulated collections of sanguineous or serosanguineous fluid confined within the subdural space.” This description, on the other hand, closely resembles the first of Unterharnscheidt’s<sup>37</sup> morphologic types of SDHy suggesting that cSDHs diagnosed by radiologists can also be termed as SDHys. In fact, the terms cSDH (in the meaning of old SDH) and SDHy are frequently used as synonyms in radiologic reports as well as in recent scientific literature.<sup>34</sup> Thereby, it is implied that SDHys solely indicate remnants of SDHs.

But is this simplification true? This may become an important issue for the forensic expert in court. Once the radiologic diagnosis of SDHy is made, the forensic expert will likely be confronted with 2 questions: Does the SDHy represent a result of AHT? And if yes, does it indicate recent injury, old injury, or, when in combination with other types of subdural collections, the presence of multiple injuries that occurred at different times? Therefore, it is important to understand how SDHys develop or what they originate from.

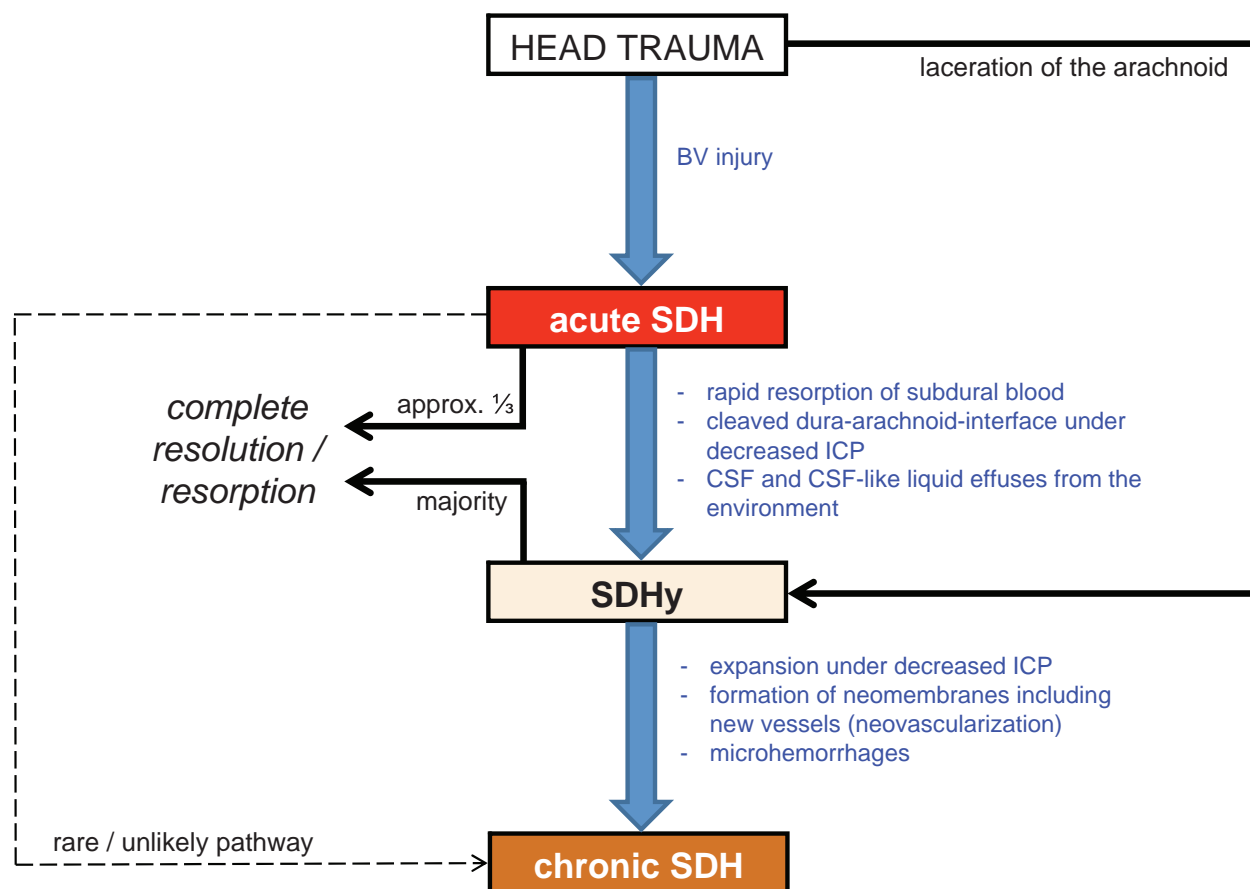


**FIG 2.** Simplified schematic drawing of the pathogenetic pathways of the origin and fate of SDHys. ICP indicates intracranial pressure.

**The Pathogenesis of Subdural Hygromas:  
An Ongoing Odyssey**

Among neurotraumatologists it is generally known that SDHys usually derive from head injuries and represent rare posttraumatic complications that may coexist with epidural or subdural hematomas.<sup>33,42,43,57-60</sup> Unfortunately, the causes of SDHys cannot always be read directly from the CT or MR images. Numerous scientists from different disciplines sought to address this problem in the last decades. Particularly in infants, SDHys are not well described and only little understood. Children were even excluded in a recent radiologic SDHy study because their pathogenetic aspects were considered a priori as different from adults.<sup>61</sup>

Hereafter, the 2 current basic concepts of SDHy formation with their different medicolegal implications, as well as important alternative explanations, are presented.

**Concept 1: Delayed Formation of Subdural Hygromas**

It appears to be widely presumed that SDHys represent liquefied and/or deposited remnants of a previous acute SDH<sup>52,62-65,82</sup> suggesting that, in a case of suspected child abuse, the baby could have been abused weeks ago. In 1857, Rudolph Virchow considered SDHys as “final stages of subdural hemorrhages.”<sup>37</sup> But are SDHys really direct remnants of acute SDHs?

An advanced approach was developed considering additional aspects of SDHy formation. The suggested process describes the conversion of acute SDH into cSDH via SDHy as an intermediate stage (blue pathway in Fig 2).<sup>47,66</sup> Because most acute SDHs re-

solve rapidly, reflecting the high levels of tissue thromboplastin in brain tissue and CSF,<sup>67</sup> this approach has been refined by other authors. During the dissolving of the acute SDH, especially if decreased intracranial pressure is present, the cleaved dura-arachnoid interface is assumed to remain as persistent posttraumatic space. Liquid remnants of the acute SDH or CSF might then pass into that opened space by effusion from surrounding vessels or even the subarachnoid space, forming the SDHy.<sup>50,52</sup> It should be noticed that in this approach, the SDHy is considered as a consequence of the SDH but not as a directly transformed remnant of it.

Alternatively, Mack et al<sup>36</sup> suggested that CSF could physiologically move from the subarachnoid space into interstitial spaces of the dura mater and subsequently via the dural venous plexus into the dural sinuses. CSF might therefore be present in small amounts in the dura at all times. In any cases of alteration of this CSF absorption pathway—for instance from bleeding into the dural layers—a disruption of the transport mechanism may result in delayed accumulation of CSF within the subdural space producing imaging findings of SDHy. Approximately 30 years earlier, it was hypothesized that concurrent traumatic subarachnoid hemorrhages, that are frequently found together with SDHy, may secondarily predispose to defective CSF resorption leading to enlargement of subdural CSF collections as well.<sup>43,68,69</sup> In the end, SDHys represent a subsequent result of acute SDHs.

Following the concept of delayed SDHy formation, the pres-

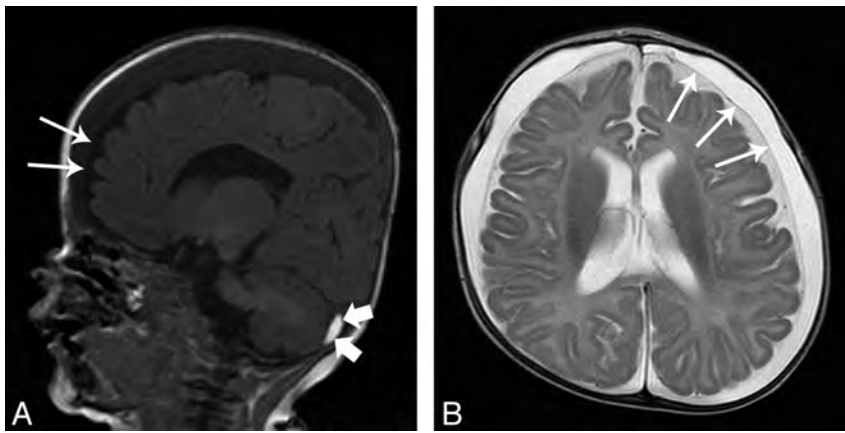


**FIG 3.** MR imaging scan of a 5-month-old female infant who showed a sudden increase of head circumference (from 50th to 97th percentile within 1 month). Frontoparietal SDHs (maximum width of 11 mm) as well as enlarged subarachnoid spaces (maximum width of 4 mm) were found on both sides (A, sagittal T1-weighted image; B, axial T2-weighted image; *thin arrows* indicate position of the subarachnoid membrane). In addition, a small subacute SDH was diagnosed in the left posterior cranial fossa beneath the tentorium cerebelli (A, *small thick arrows* indicate subdural blood). In the preceding months, periodic sonography scans of the head did not ever show any abnormalities with respect to the subdural or subarachnoid space. Ophthalmologic examination revealed sub- and epiretinal hemorrhages distributed over the whole fundus area of both eyes. These retinal hemorrhages were not present yet in a check-up examination 1 month after birth. As further clinical diagnostics have ruled out coagulopathies, neoplastic diseases, and metabolic disorders, the presence of SDH and retinal hemorrhage prove substantial (sub)acute head trauma and therefore strongly suggest child abuse (AHT). The enlarged subarachnoid spaces, found after the trauma diagnosis, have rather to be regarded as consequence and not as source (see “BESS” section). Hence, the SDHy in this well-documented case can be regarded as a result of acute injury.

ence of SDHy may be medicolegally interpreted as later consequence of AHT that occurred some days or a few weeks before.

### Concept 2: Rapid Formation of Subdural Hygromas

This theory suggests SDHy to be caused by a laceration in the arachnoid.<sup>33,37–39,49–51,53,70–72</sup> Hence, SDHy can result from trauma and from cranial operations in which the arachnoid membrane is opened, leading to CSF transfer into the subdural space.<sup>33</sup> For this, the term acute SDHy has been suggested.<sup>52</sup> A ball-valve mechanism of the arachnoid is assumed to prevent a backflow of CSF into the subarachnoid space.<sup>33,72</sup>

In regard to a 74-year-old woman with acute SDHy and subarachnoid hemorrhage after accidental head injury, Kamezaki et al<sup>73</sup> discussed a tear of the arachnoid membrane as possible reason for the SDHy. Radiotracer and cisternography studies performed in infants with SDHy were able to show that radioisotopes (eg, indium-111) injected into the subarachnoid space move into the subdural compartment.<sup>44,53</sup> In addition, the CSF-specific  $\beta$ -trace protein and other proteins have been found up to 100% of SDHs,<sup>74,75</sup> indicating that there really is CSF in the subdural space.

Zouros et al<sup>53</sup> reported on 5 infants with suspected AHT showing acute hematoxygromas. Encapsulating neomembranes, possibly indicating the presence of cSDH (see below: “Differential Diagnoses of Subdural Hygromas”), were not found either on MR imaging or at surgery. In addition, free CSF communication between subarachnoid and subdural space was proved in all cases by radiotracer injection. The authors proposed a mechanism whereby SDHy directly originates from shaking the baby: during acceleration and deceleration of the brain, acute shear strains be-

tween arachnoid and dura may disrupt both the BVs and the weak arachnoid attachments to the parasagittal dura (Pacchioni granulations). Thereby, a mixture of CSF and blood products can flow into the traumatically opened subdural space resulting in an acute subdural hematoxygroma.<sup>53</sup>

This is not only a plausible explanation for the known mixed-density appearance of subdural collections frequently seen in AHT cases. The injured arachnoid granulations also explain the often-described occurrence of enlarged subarachnoid spaces because of suboptimal CSF absorption.

Following this concept of rapid formation, SDHs must not be considered automatically as direct remnants or delayed consequence of acute SDHs but SDHy and acute SDH may develop simultaneously as exemplified in Figure 3. Medicolegal expert opinions should therefore consider the possibility of a rapid formation of SDHy as an additional symptom indicating AHT.

### Alternative Explanations

Besides the 2 main theories introduced above, additional theories regarding the formation of SDHs are discussed. In terms of forensic issues, 2 in particular are noteworthy:

1. Glutaric aciduria type I: this hereditary disease is caused by a deficiency of the enzyme glutaryl CoA-dehydrogenase and leads to increased urinary excretion of glutaric and 3-hydroxy-glutaric acid.<sup>76</sup> Clinically, macrocephalia and extrapyramidal movement disorders are described. In neuro-radiology, frontotemporal atrophy as well as SDHs and/or SDHs are diagnosed.<sup>77,78</sup> Glutaric aciduria type I should therefore be diagnostically excluded in infants with SDHy, because misdiagnosing as AHT may occur in exceptional cases.<sup>79,80</sup>
2. Rupture of pre-existing arachnoid cysts: arachnoid cysts are congenital or acquired intra-arachnoidal CSF collections occurring infrequently. These may rupture because of minor, but identifiable, head trauma, or sudden temporary rise in intracranial pressure.<sup>48,81</sup> Ruptures result in SDHs rather than in SDHs.<sup>48</sup> However, this phenomenon has not been described in infants yet. A review of the literature by Gelabert-González et al<sup>81</sup> demonstrated ages of occurrence ranging from 5 to 25 years. It seems conceivable that arachnoid cysts also rupture in infants and are not yet acknowledged as such. However, as long as scientific data do not support this possibility, this remains mere speculation.

### Differential Diagnoses of Subdural Hygromas

**Chronic Subdural Hematoma.** Surgeons and pathologists know cSDH as subdural liquid with a dark brown “crank case oil” ap-

pearance.<sup>47</sup> Many cSDHs also contain a mixture of both CSF and blood, such as breakdown products of hemoglobin or other proteins.<sup>55,82</sup> Furthermore, multiple hemorrhages of different ages are supposed to be common (so-called mixed-age SDH).<sup>55</sup> This may sometimes also lead to an attenuation approximating that of CSF.

The pathogenesis of cSDH is not yet clear. cSDHs were observed to evolve directly from acute SDHs in only very few cases (reviewed in<sup>52</sup>). Moreover, experimental studies failed to reproduce cSDH from acute subdural blood.<sup>83,84</sup> It has also been reported that, based on histopathology<sup>85</sup> and CT,<sup>66</sup> chronic and acute SDH should actually be regarded as different entities. cSDH might therefore not be (at least not directly) the last stage of an old acute SDH.

A direct transformation from remnants of an acute SDH into a cSDH is therefore not plausible in all cases. Instead, a more complex pathomechanism must be assumed. As mentioned above (Fig 2), cSDHs were commonly shown, at least in adult trauma cases (mostly traffic crashes), to derive from SDHs with incidence rates between 8% and 58%.<sup>33,47,58,59</sup> Thus, the fate of SDHy is either resolution or cSDH formation.<sup>33,59,75</sup> Under a normal pressure situation, the SDHy resolves. If the decreased intracranial pressure that had led to SDHy formation continues, the SDHy may expand.<sup>50,52</sup> This can enlarge the intradural cleavage (= subdural space filled with SDHy) up to the opposite brain side opening a subdural space even above the falx cerebri. Accordingly, SDHs were frequently observed not to be restricted to the brain side of the “original pathology” (eg, acute SDH).<sup>45</sup>

SDHy can then develop neomembranes from the proliferating dural border cells that are principally able to proliferate in any pathologic process with cleavage of the dural borderzone tissues.<sup>50</sup> Forming of neomembranes is accompanied by neovascularization. Spontaneous microhemorrhages from these fragile new vessels may then occur and lead to a mixture of CSF and blood.<sup>86,87</sup> Therefore, it has been suggested that repeated microhemorrhages possibly convert an SDHy into an expanding cSDH.<sup>33,50,52,57,66</sup>

These pathogenetic considerations show why it is important for the forensic expert to differentiate between cSDH and SDHy. While cSDHs appear to be very rare and delayed consequences of subdural collections, SDHys can apparently develop delayed or rapidly. However, differentiation can be impossible for the radiologist in cases of cSDH appearing CSF-like in CT or MR imaging. These cSDHs are particularly vulnerable to be accidentally referred to as SDHys. Consequently, the terms cSDH and SDHy are often used as synonyms in practice.

Some authors describe the differences between cSDH and SDHy as follows: SDHys are thought to be less than 3 weeks old, static or decreasing, and do not or rarely produce a mass effect, whereas cSDHs are thought to be older than 3 weeks, enlarging, and may cause a mass effect.<sup>50,51,88</sup> However, all these smooth differentiating criteria should be handled with care. “Three weeks” cannot be a strict borderline, and most of the aforementioned pathophysiologic data regarding cSDH rely on studies in adults. Thus, it remains at least questionable whether these results can be applied to infants at all.

As SDHys mostly lack neomembranes, this aspect could be

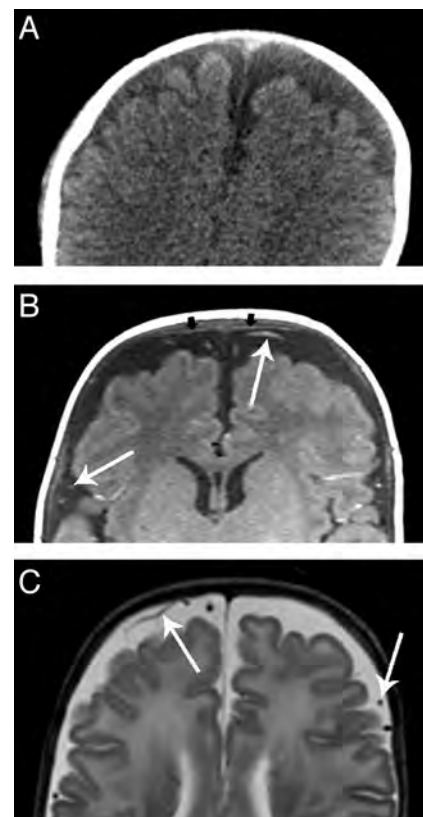


**FIG 4.** Benign enlargement of the subarachnoid space. While in CT (A), BESS could be misdiagnosed as SDHy, MR imaging (B, T1-weighted image; C, T2-weighted image) clearly demonstrates the presence of BESS. Note the vessels (*thin arrows*) spanning through the subarachnoid space. The small black arrows in B point at the subarachnoid membrane.

another morphologic criterion for differentiation. Neomembranes are usually present in cSDHs and encapsulate the subdural collection as a result of tissue response and may even subdivide it into different chambers.<sup>34,50,55</sup> Although neomembranes are described as becoming visible to the naked eye after approximately 10 days<sup>34</sup> and were shown to aid in dating injuries,<sup>89</sup> diagnosing such membranes in CT or MR imaging can be very challenging.

**Benign Enlargement of the Subarachnoid Space.** The benign enlargement of the subarachnoid space (BESS) represents an important differential diagnosis for both SDHy and cSDH (Fig 4).<sup>48,51,52,90</sup> These subarachnoid fluid collections are frequently observed and often termed confusingly as “benign hygromas of infancy.” BESS probably results from immaturity of the arachnoid villi leading to a transient form of communicating or external hydrocephalus.<sup>52</sup> Infants concerned are usually neurologically uneventful without evidence of prior brain injury.<sup>91</sup> Nowadays, BESS can clearly be distinguished from SDHy (Fig 5), particularly because of improvements in MR imaging technology. In the presence of BESS, the vessels, which run through the subarachnoid space, are localized away from the brain. On the other hand, in the presence of a subdural fluid collection, the vessels can be found near the surface of the brain.

Forensically, it is important to know that long-term observations of infants with BESS as well as a finite element study indicated no increased risk for developing SDH.<sup>92-95</sup> The hypothesis

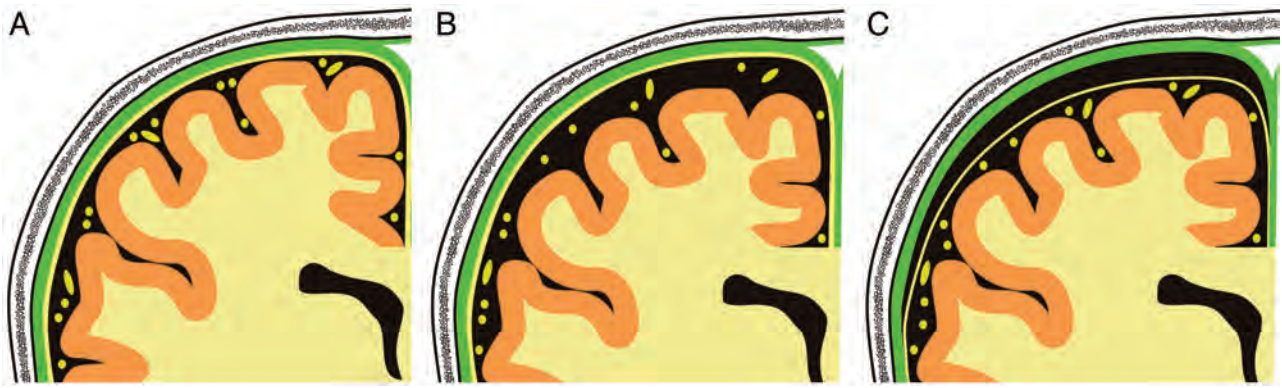


**FIG 5.** Schematic drawing of the right parietal region as seen in the coronal view imaging. Note the position of the subarachnoid membrane and the subarachnoid vessels (both in yellow). The dura mater is presented in green. A, normal situation; B, enlarged subarachnoid spaces and C, subdural hygroma.

was that stretching of the BV due to enlargement of the subarachnoid space may result in a predisposition to developing SDH. Accordingly, it has been reported that SDHs may occur either spontaneously or as a result of minor trauma in infants with BESS.<sup>96</sup> By contrast, it has been frequently discussed that enlarging of the head circumference because of external hydrocephalus is rather a consequence and not the cause of bleeding, for instance, due to impaired CSF absorption caused by subarachnoid pus, cells, or hemorrhage, or by SDH.<sup>51,54,95</sup>

Besides BESS, it is essential to know that, in general, the subarachnoid spaces are relatively larger in the first 2 years of life than in older children or adults.<sup>52,82,87</sup> According to Libicher and Tröger,<sup>97</sup> head sonography of 89 healthy American infants revealed the distances between the inner calvarian table and the cerebral cortex to range from 0.3 to 6.3 mm (upper limit proposed based on the 95th percentile: 4 mm). The infants' head circumferences of that study were found to be between the 3rd and 97th percentile. In addition, cerebral atrophy, for example, as a result of AHT, may also lead to the impression of enlarged subarachnoid spaces.<sup>52,82</sup>

## CONCLUSIONS

SDHy and cSDH are often difficult to distinguish from each other and are often used synonymously in daily case work. While cSDHs in infants are rare and rather implicate a delayed and non-acute process, SDHys may develop rapidly or be delayed. Accordingly, early hypodensity in infantile SDH has also been observed by others<sup>51,98-100</sup> arguing against an overhasty diagnosis of a chronic process but suggesting a significant role of CSF.

On one hand, SDHys are classically considered as remains of a previous SDH, directly or indirectly, which strongly suggests a trauma of cortical BVs and a delayed formation of SDHys (see Concept 1 section). On the other hand, acute pathogenesis of SDHys has been verified by traumatically induced tears in the arachnoid membrane (see Concept 2 section). In all probability, multiple mechanisms exist and also coexist. Accordingly, it is not adequate to state different ages of injuries when SDH and SDHy are present concomitantly.

Both concepts presented have 1 thing in common: if other infrequent reasons and differential diagnoses have been excluded, the presence of SDHy strongly suggests trauma, or more precisely:

a posttraumatic state. The presence of SDHy in infants therefore represents compelling reason to search for other signs of AHT such as retinal hemorrhages, fractures, bruises, or inadequate explanations for trauma.

The usage of SDHy for age estimation of head trauma is difficult and should not be considered as the most important factor in determining the time of injury.<sup>53</sup> Hence, as already proposed by Vezina,<sup>51</sup> in initial CT investigations, it is best to describe subdural collections only in terms of density (hypo-, hyper-, isodense, or mixed) and strongly avoid labels such as "acute" or "chronic."

If additional presurgical MR imaging scans of the head exist, further assessment is possible. MR imaging is clearly more sensitive to the presence of SDH, BESS, neomembranes, and injuries of the cerebrum, brain stem, or upper cervical cord. Furthermore, temporal development of intracranial hemorrhages by means of MR imaging is well studied.<sup>51,52</sup>

To conclude, evaluation of SDHy cases should ideally be done in close cooperation between neuroradiology, pediatrics, and forensic medicine. The initial neuroradiologic evaluation is of particular importance and indispensable for correct medicolegal conclusions.

## REFERENCES

- Jacobi G, Dettmeyer R, Banaschak S, et al. **Child abuse and neglect: diagnosis and management.** *Dtsch Arztebl Int* 2010;107:231-39
- Friedrich K, Becker K, Rothschild MA, et al. **Child abuse inflicted by small children.** *Int J Legal Med* 2013;127:627-30
- Bilo RAC, Robben SGF, van Rijn RR. **General aspects of fractures in child abuse.** In: Bilo RAC, Robben SGF, van Rijn RR, eds. *Forensic Aspects of Paediatric Fractures. Differentiating Accidental Trauma From Child Abuse.* New York: Springer-Verlag; 2010:1-13
- Trübner K, Schubries M, Beintker M, et al. **Genital findings in boys suspected for sexual abuse.** *Int J Legal Med* 2013;127:967-70
- Modelli ME, Galvão MF, Pratesi R. **Child sexual abuse.** *Forensic Sci Int* 2012;217:1-4
- Schulte B, Rothschild MA, Vennemann M, et al. **Examination of (suspected) neonaticides in Germany: a critical report on a comparative study.** *Int J Legal Med* 2013;127:621-25
- Duhaime AC, Christian CW, Rorke LB, et al. **Nonaccidental head injury in infants—the "shaken-baby syndrome."** *N Engl J Med* 1998;338:1822-29
- American Academy of Pediatrics: Committee on Child Abuse and

- Neglect. **Shaken baby syndrome: rotational cranial injuries—technical report.** *Pediatrics* 2001;108:206–10
9. Herrmann B. **Nichtakzidentelle kopfverletzungen und schütteltraumaklinische und pathophysiologische aspekete.** *Rechtsmedizin* 2007;18:9–16
  10. Jayawant S, Rawlinson A, Gibbon F, et al. **Subdural haemorrhages in infants: population based study.** *BMJ* 1998;317:1558–61
  11. Barlow KM, Minns RA. **Annual incidence of shaken impact syndrome in young children.** *Lancet* 2000;356:1571–72
  12. Keenan HT, Runyan DK, Marshall SW, et al. **A population-based study of inflicted traumatic brain injury in young children.** *JAMA* 2003;290:621–26
  13. Hobbs C, Childs AM, Wynne J, et al. **Subdural haematoma and effusion in infancy: an epidemiological study.** *Arch Dis Child* 2005;90:952–55
  14. Talvik I, Metsvaht T, Leito K, et al. **Inflicted traumatic brain injury (ITBI) or shaken baby syndrome (SBS) in Estonia.** *Acta Paediatr* 2006;95:799–804
  15. Fanconi M, Lips U. **Shaken baby syndrome in Switzerland: results of a prospective follow-up study, 2002–2007.** *Eur J Pediatr* 2010;169:1023–28
  16. Christian CW, Block R, Committee on Child Abuse, et al. **Abusive head trauma in infants and children.** *Pediatrics* 2009;123:1409–11
  17. Gill JR, Goldfeder LB, Armbrustmacher V, et al. **Fatal head injury in children younger than 2 years in New York City and an overview of the shaken baby syndrome.** *Arch Pathol Lab Med* 2009;133:619–27
  18. Matschke J, Herrmann B, Spermhake J, et al. **Shaken baby syndrome: a common variant of non-accidental head injury in infants.** *Dtsch Arztebl Int* 2009;106:211–17
  19. Matschke J, Püschel K, Glatzel M. **Ocular pathology in shaken baby syndrome and other forms of infantile non-accidental head injury.** *Int J Legal Med* 2009;123:189–97
  20. Martrille L, Cattaneo C, Dorandeu A, et al. **A multicentre and prospective study of suspected cases of child physical abuse.** *Int J Legal Med* 2006;120:73–78
  21. Herman BE, Makoroff KL, Corneli HM. **Abusive head trauma.** *Pediatr Emerg Care* 2011;27:65–69
  22. Squier W. **The “shaken baby” syndrome: pathology and mechanisms.** *Acta Neuropathol* 2011;122:519–42
  23. Fernando S, Obaldo RE, Walsh IR, et al. **Neuroimaging of nonaccidental head trauma: pitfalls and controversies.** *Pediatr Radiol* 2008;38:827–38
  24. Hedlund GL, Frasier LD. **Neuroimaging of abusive head trauma.** *Forensic Sci Med Pathol* 2009;5:280–90
  25. Choudhary AK, Bradford RK, Dias MS, et al. **Spinal subdural hemorrhage in abusive head trauma: a retrospective study.** *Radiology* 2012;262:216–23
  26. Ringl H, Stiassny F, Schima W, et al. **Intracranial hematomas at a glance: advanced visualization for fast and easy detection.** *Radiology* 2013;267:522–30
  27. Kemp AM, Rajaram S, Mann M, et al. **What neuroimaging should be performed in children in whom inflicted brain injury (IBI) is suspected? A systematic review.** *Clin Radiol* 2009;64:473–83
  28. Kemp AM, Jaspán T, Griffiths J, et al. **Neuroimaging: what neuro-radiological features distinguish abusive from non-abusive head trauma? A systematic review.** *Arch Dis Child* 2011;96:1103–12
  29. Di Pietro MA, Brody AS, Cassidy CI, et al. **Section on radiology; American Academy of Pediatrics. Diagnostic imaging of child abuse.** *Pediatrics* 2009;123:1430–35
  30. Sieswerda-Hoogendoorn T, Boos S, Spivack B, et al. **Abusive head trauma part II: radiological aspects.** *Eur J Pediatr* 2012;171:617–23
  31. Debertin AS, Spermhake JP. **Untersuchung und dokumentation des nichtakzidentellen schädel-hirn-traumas im säuglings- und kleinkindalter.** *Rechtsmedizin* 2008;18:17–22
  32. Bajanowski T, Neuen-Jacob E, Schubries M, et al. **Nichtakzidentelles schädel-hirn-trauma und schütteltrauma.** *Rechtsmedizin* 2008;18:23–28
  33. Lee KS. **The pathogenesis and clinical significance of traumatic subdural hygroma.** *Brain Inj* 1998;12:595–603
  34. Squier W, Mack J. **The neuropathology of infant subdural haemorrhage.** *Forensic Sci Int* 2009;187:6–13
  35. v. Düring M, Dermietzel, Drenckhahn D. **Hirnhäute, ventrikelauskleidung, liquor cerebrospinalis.** In: Benninghoff A, Drenckhahn D, eds. *Anatomie, Band 2.* 16th ed. München: Urban&Fischer/Elsevier; 2004:266–83
  36. Mack J, Squier W, Eastman JT. **Anatomy and development of the meninges: implications for subdural collections and CSF circulation.** *Pediatr Radiol* 2009;39:200–10
  37. Unterharnscheidt F. **Subdurales hydrom oder hygrom.** In: Doerr W, Seifert G, eds. *Spezielle Pathologische Anatomie, Band 13/VI.A Traumatologie von Hirn und Rückenmark—Traumatische Schäden des Gehirns (Forensische Pathologie).* Berlin Heidelberg: Springer-Verlag;1993: 312–22
  38. Dandy WE. **Chronic subdural hydroma and serous meningitis (pachymeningitis serosa; localized external hydrocephalus).** In: Lewis D, ed. *Practice of Surgery.* Hagerstown, Maryland: WF Proir Co.; 1932:306–09
  39. Dandy WE. **Chronic subdural hydroma and serous meningitis (pachymeningitis serosa; localized external hydrocephalus).** In: Lewis D, ed. *Practice of Surgery.* Hagerstown, Maryland: WF Proir Co.; 1955:291–93
  40. Payr E. **Meningitis serosa bei und nach schädelverletzungen (traumatica).** *Med Klin* 1916;12:841–46
  41. McConnell AA. **Traumatic subdural effusions.** *J Neurol Neurosurg Psychiatry* 1941;4:273–74
  42. Oka H, Motomochi M, Suzuki Y, et al. **Subdural hygroma after head injury. A review of 26 cases.** *Acta Neurochir (Wien)* 1972;26:265–73
  43. Stone JL, Lang RG, Sugar O, et al. **Traumatic subdural hygroma.** *Neurosurgery* 1981;8:542–50
  44. Hoff J, Bates E, Barnes B, et al. **Traumatic subdural hygroma.** *J Trauma* 1973;13:870–76
  45. French BN, Cobb CA III, Corkill G, et al. **Delayed evolution of post-traumatic subdural hygroma.** *Surg Neurol* 1978;9:145–48
  46. Wetterling T, Demierre B, Rama B, et al. **The clinical course of surgically treated post-traumatic subdural hygromas.** *Acta Neurochir (Wien)* 1986;83:99–104
  47. Lee KS, Bae WK, Park YT, et al. **The pathogenesis and fate of traumatic subdural hygroma.** *Br J Neurosurg* 1994;8:551–58
  48. Punt J. **Mechanisms and management of subdural hemorrhage.** In: Minns RA, Brown JK, eds. *Shaking and Other Non-Accidental Head Injuries in Children.* London: Mac Keith Press; 2005:290–313
  49. Livingston JH, Childs AM. **The epidemiology of non-accidental head injury.** In: Minns RA, Brown JK, eds. *Shaking and Other Non-Accidental Head Injuries in Children.* London: Mac Keith Press; 2005:147–53
  50. Case ME. **Inflicted traumatic brain injury in infants and young children.** *Brain Pathol* 2008;18:571–82
  51. Vezina G. **Assessment of the nature and age of subdural collections in nonaccidental head injury with CT and MRI.** *Pediatr Radiol* 2009;39:586–90
  52. Hymel KP, Jenny C, Block RW. **Intracranial hemorrhage and re-bleeding in suspected victims of abusive head trauma: addressing the forensic controversies.** *Child Maltreat* 2002;7:329–48
  53. Zouros A, Bhargava R, Hoskinson M, et al. **Further characterization of traumatic subdural collections of infancy. Report of five cases.** *J Neurosurg* 2004;100(5 Suppl):512–18
  54. Hedlund GL. **Subdural hemorrhage and abusive head trauma: challenges and controversies.** Paper presented at: 98th Scientific Assembly and Annual Meeting of the Radiological Society of North America (RSNA), November 25–30, 2012; McCormick Place, Chicago, Illinois.
  55. Osborn AG. **Part one: trauma.** In: Osborn AG, ed. *Osborn’s Brain: Imaging, Pathology, and Anatomy.* 2nd ed. Salt Lake City: Amirsys; 2013:1–72

56. Hedlund G, Bale JF, Barkovich AJ. **Infections of the developing and mature nervous system.** In: Barkovich AJ, Raybaud, eds. *Pediatric Neuroimaging*. 5th ed. Philadelphia: Lippincott Williams & Wilkins; 2012:954–1050
57. Lee KS, Bae WK, Doh JW, et al. **Origin of chronic subdural haematoma and relation to traumatic subdural lesions.** *Brain Inj* 1998; 12:901–10
58. Ohno K, Suzuki R, Masaoka H, et al. **Chronic subdural haematoma preceded by persistent traumatic subdural fluid collection.** *J Neurol Neurosurg Psychiatry* 1987;50:1694–97
59. Lee KS, Bae WK, Bae HG, et al. **The fate of traumatic subdural hygroma in serial computed tomographic scans.** *J Korean Med Sci* 2000;15:560–68
60. Lee KS. **Natural history of chronic subdural haematoma.** *Brain Inj* 2004;18:351–58
61. Zanini MA, de Lima Resende LA, de Souza Faleiros AT, et al. **Traumatic subdural hygromas: proposed pathogenesis based classification.** *J Trauma* 2008;64:705–13
62. Maxeiner H. **Subduralblutungen: ursachen, arten, folgen und forensische aspekte.** *Rechtsmedizin* 2009;19:111–28
63. Tutsch-Bauer E, Meyer HJ, Monticelli F. **Schütteltrauma.** *Rechtsmedizin* 2005;15:399–408
64. Punt N. **Glossary of terms.** In: Minns RA, Brown JK, eds. *Shaking and Other Non-Accidental Head Injuries in Children*. London: Mac Keith Press; 2005:479–97
65. Minns RA, Jones PA, Barlow KM. **Outcome and prognosis of non-accidental head injury in infants.** In: Minns RA, Brown JK, eds. *Shaking and Other Non-Accidental Head Injuries in Children*. London: Mac Keith Press; 2005:364–414
66. Lee KS, Doh JW, Bae HG, et al. **Relations among traumatic subdural lesions.** *J Korean Med Sci* 1996;11:55–63
67. Astrup T. **Assay and content of tissue thromboplastin in different organs.** *Thromb Diath Haemorrh* 1965;14:401–16
68. Kapila A, Trice J, Spies WG, et al. **Enlarged cerebrospinal fluid spaces in infants with subdural hematomas.** *Radiology* 1982;142: 669–72
69. Orrison WW, Robertson WC, Sackett JF. **Computerized tomography in chronic subdural hematomas (effusions) of infancy.** *Neuroradiology* 1978;16:79–81
70. Naffziger HC. **Subdural fluid accumulations following head injury.** *JAMA* 1924;82:1751–52
71. Todorow S, Happe M. **Traumatic subdural hygromas.** *Neurochirurgia (Stuttg)* 1981;24:131–36
72. Borzone M, Capuzzo T, Perria C, et al. **Traumatic subdural hygromas: a report of 70 surgically treated cases.** *J Neurosurg Sci* 1983;27:161–65
73. Kamezaki T, Yanaka K, Fujita K, et al. **Traumatic acute subdural hygroma mimicking acute subdural hematoma.** *J Clin Neurosci* 2004;11:311–13
74. Kristof RA, Grimm JM, Stoffel-Wagner B. **Cerebrospinal fluid leakage into the subdural space: possible influence on the pathogenesis and recurrence frequency of chronic subdural hematoma and subdural hygroma.** *J Neurosurg* 2008;108:275–80
75. Wetterling T, Demierre B, Rama B, et al. **Protein analysis of subdural hygroma fluid.** *Acta Neurochir (Wien)* 1988;91:79–82
76. Hoffmann GF, Trefz FK, Barth PG, et al. **Glutaryl-coenzyme A dehydrogenase deficiency: a distinct encephalopathy.** *Pediatrics* 1991; 88:1194–203
77. Osaka H, Kimura S, Nezu A, et al. **Chronic subdural hematoma, as an initial manifestation of glutaric aciduria type-1.** *Brain Dev* 1993;15:125–27
78. Drigo P, Burlina AB, Battistella PA. **Subdural hematoma and glutaric aciduria type 1.** *Brain Dev* 1993;15:460–61
79. Muntau AC, Röschinger W, Pfluger T, et al. **Subdurale hygrome und hämatome im säuglingsalter als initialmanifestation der glutarazidurie typ I.** *Monatsschr Kinderheilkd* 1997;145:646–51
80. Bishop FS, Liu JK, McCall TD, et al. **Glutaric aciduria type 1 presenting as bilateral subdural hematomas mimicking nonaccidental trauma. Case report and review of the literature.** *J Neurosurg* 2007;106(3 Suppl):222–26
81. Gelabert-González M, Fernández-Villa J, Cutrín-Prieto J, et al. **Arachnoid cyst rupture with subdural hygroma: report of three cases and literature review.** *Childs Nerv Syst* 2002;18:609–13
82. Kleinman PK, Barnes PD. **Head trauma.** In: Kleinman PK, ed. *Diagnostic Imaging of Child Abuse*. 2nd ed. St. Louis: Mosby; 1998:285–342
83. Goodell CL, Mealey J Jr. **Pathogenesis of chronic subdural hematoma. Experimental studies.** *Arch Neurol* 1963;8:429–37
84. Watanabe S, Shimada H, Ishii S. **Production of clinical form of chronic subdural hematoma in experimental animals.** *J Neurosurg* 1972;37:552–61
85. Poljaković Z, Petrusić I, Kalousek M, et al. **Correlative pathology of subdural hematoma with computerized tomography.** *Neurol Croat* 1991;41:21–32
86. Sargent S, Kennedy JG, Kaplan JA. **“Hyperacute” subdural hematoma: CT mimic of recurrent episodes of bleeding in the setting of child abuse.** *J Forensic Sci* 1996;41:314–16
87. Caré MM. **Neuroradiology.** In: Frasier L, Rauth-Farley K, Alexander R, et al, eds. *Abusive Head Trauma in Infants and Children—A Medical, Legal, and Forensic Reference*. St. Louis: G.W. Medical Publishing; 2006:73–98
88. Barnes PD, Krasnokutsky M. **Imaging of the central nervous system in suspected or alleged nonaccidental injury, including the mimics.** *Top Magn Reson Imaging* 2007;18:53–74
89. Walter T, Meissner C, Oehmichen M. **Pathomorphological staging of subdural hemorrhages: statistical analysis of post-traumatic histomorphological alterations.** *Leg Med (Tokyo)* 2009;11(Suppl 1):S56–62
90. Alper G, Ekinci G, Yilmaz Y, et al. **Magnetic resonance imaging characteristics of benign macrocephaly in children.** *J Child Neurol* 1999;14:678–82
91. Prassopoulos P, Cavouras D, Golfopoulos S, et al. **The size of the intra- and extraventricular cerebrospinal fluid compartments in children with idiopathic benign widening of the frontal subarachnoid space.** *Neuroradiology* 1995;37:418–21
92. Briner S, Bodensteiner J. **Benign subdural collections of infancy.** *Pediatrics* 1981;67:802–04
93. Robertson WC Jr, Chun RW, Orrison WW, et al. **Benign subdural collections of infancy.** *J Pediatr* 1979;94:382–86
94. Hamza M, Bodensteiner JB, Noorani PA, et al. **Benign extracerebral fluid collections: a cause of macrocrania in infancy.** *Pediatr Neurol* 1987;3:218–21
95. Raul JS, Roth S, Ludes B, et al. **Influence of the benign enlargement of the subarachnoid space on the bridging veins strain during a shaking event: a finite element study.** *Int J Legal Med* 2008; 122:337–40
96. McNeely PD, Atkinson JD, Saigal G, et al. **Subdural hematomas in infants with benign enlargement of the subarachnoid spaces are not pathognomonic for child abuse.** *AJNR Am J Neuroradiol* 2006; 27:1725–28
97. Libicher M, Tröger J. **US measurement of the subarachnoid space in infants: normal values.** *Radiology* 1992;184:749–51
98. Dias MS, Backstrom J, Falk M, et al. **Serial radiography in the infant shaken impact syndrome.** *Pediatr Neurosurg* 1998;29:77–85
99. Vinchon M, Noulé N, Tchofo PJ, et al. **Imaging of head injuries in infants: temporal correlates and forensic implications for the diagnosis of child abuse.** *J Neurosurg* 2004;101:44–52
100. Bradford R, Choudhary AK, Dias MS. **Serial neuroimaging in infants with abusive head trauma: timing abusive injuries.** *J Neurosurg Pediatrics* 2013;12:110–19

# Differences in Neuroradiology Training Programs around the World

T. Schneider, T.A.G.M. Huisman, J. Fiehler, L.J. Savic, and D.M. Yousem



## ABSTRACT

**BACKGROUND AND PURPOSE:** No previous study compares neuroradiology training programs and teaching schedules across the globe, to our knowledge. This study was conducted to better understand international program requisites.

**MATERIALS AND METHODS:** Data from 43 countries were collected by an e-mail-based questionnaire (response rate, 84.0%). Radiologists across the world were surveyed regarding the neuroradiology training schemes in their institutions. Answers were verified by officers of the national neuroradiology societies.

**RESULTS:** While many countries do not provide fellowship training in neuroradiology ( $n = 16$ ), others have formal postresidency curricula ( $n = 27$ ). Many programs have few fellows and didactic sessions, but the 1- or 2-year duration of fellowship training is relatively consistent ( $n = 23/27, 85\%$ ).

**CONCLUSIONS:** There is a wide variety of fellowship offerings, lessons provided, and ratios of teachers to learners in neuroradiology training programs globally.

**ABBREVIATIONS:** ACGME = Accreditation Council for Graduate Medical Education; DNR = diagnostic neuroradiology; ESNR = European Society of Neuroradiology; INR = interventional neuroradiology; NR = neuroradiology

The United States considers itself a leader in medical education and training among nations.<sup>1</sup> Generally speaking, American medical school, residency, and fellowship programs are considered globally as being well-structured, highly competitive, and outstanding in the quality of education and instruction. As of the 2013–2014 academic year, 185 radiology residency programs and 85 neuroradiology (NR) fellowship programs in the United States are voluntarily supervised by the Accreditation Council for Graduate Medical Education (ACGME). This private, nonprofit organization sets educational standards and periodically reviews their implementation within the respective graduate medical educa-

tion programs.<sup>2</sup> In addition, completion of programs accredited by the ACGME is a prerequisite to becoming board-certified in diagnostic radiology and subspecialty certified in neuroradiology. Examinations are offered by the American Board of Radiology annually through the American Board of Medical Specialties. It oversees specialty and subspecialty certification in radiology and 23 other medical specialties in the United States.

The educational path for an aspiring American neuroradiologist typically begins by matching in a first-postgraduate-year prerequisite clinical year (internship year) and an ACGME-accredited postgraduate year 2- to 5-year diagnostic radiology residency program.<sup>3</sup> The first 3 years of residency focus on diagnostic radiology (postgraduate years 2–4) and include 9 core rotations in abdominal radiology, breast imaging, cardiothoracic radiology, musculoskeletal radiology, neuroradiology, nuclear radiology, pediatric radiology, sonography, and vascular and interventional radiology. In postgraduate year 5, residents may participate in subspecialty rotations of their choice.<sup>4</sup> The trainees' diagnostic experience in the different imaging modalities is assessed through a case/procedure log system, which is annually reviewed by the faculty of the program and the ACGME.<sup>5</sup>

After finishing residency, graduating radiologists have the opportunity to start additional fellowship training within their discipline of choice if they desire subspecialty expertise.<sup>6</sup> Contributing factors that

Received June 28, 2014; accepted after revision August 15.

From the Divisions of Neuroradiology (T.S., D.M.Y.), Pediatric Radiology (T.A.G.M.H.), and Interventional Radiology (L.J.S.), Russell H. Morgan Department of Radiology and Radiological Science, The Johns Hopkins University School of Medicine, Baltimore, Maryland; and Department of Diagnostic and Interventional Neuroradiology (T.S., J.F.), University Medical Center Hamburg-Eppendorf, Hamburg, Germany.

Paper previously presented at: American Society of Neuroradiology Annual Meeting and the Foundation of the ASNR Symposium, May 17–22, 2014; Montréal, Quebec, Canada.

Please address correspondence to Tanja Schneider, MD, Universitätsklinikum Hamburg-Eppendorf, Martinistr 52, Haus O22, 20246 Hamburg, Germany; e-mail: tan.schneide@uke.de



Indicates article with supplemental on-line tables.

<http://dx.doi.org/10.3174/ajnr.A4132>

promote the implementation of fellowship programs in radiology are the rapid development of new imaging techniques, the need for appropriate interpretation skills and expertise to compete in the job market, and the trend toward endovascular and percutaneous therapies.<sup>1</sup>

The first NR fellowship positions were offered in Stockholm and London in the 1950s and approximately 10 years later in New York (1960).<sup>7</sup> Regarding neuroradiology, 2 fellowships are offered in the United States currently: diagnostic neuroradiology (DNR) and interventional neuroradiology (INR), with the latter, by ACGME regulations, requiring a previous DNR year. However, very few of the offered neurointerventional programs are currently ACGME-accredited, so this requirement is often not completed.

Because there is a trend toward greater subspecialization in radiology globally, we conducted a survey to investigate differences in radiology training programs across the world with regard to the general curriculum, focusing on neuroradiology fellowships in particular. Therefore, departments in countries on all continents were asked to complete a standardized questionnaire about their training programs. Hence, differences in international educational structures could be revealed.

## MATERIALS AND METHODS

The parameters of radiology residency and fellowship training at institutions across the globe (both university hospitals and community teaching hospitals) were analyzed. From December 2013 through February 2014, a 16-item questionnaire was sent via e-mail to members of 50 non-US neuroradiology societies, neuroradiologists, neuroradiology fellows, and residents (On-line Table 1). To check the accuracy of information submitted, in a second step, we contacted representatives of national radiology and neuroradiology societies, who validated the responses.

The items were related to 3 topics: general information about the structure of medical education, features of general radiology residency, and neuroradiology fellowship programs. Responders were further contacted by e-mail to clarify specific issues if necessary.

To evaluate the structure of the trainee didactic and clinical education, we asked for the weekly number of neuroradiology teaching sessions in the programs. In addition, a ratio of the number of residents/fellows to the number of attending physicians was calculated for each department.

## RESULTS

The response rate was 86.0% (43/50 countries). Members of national neuroradiology societies helped to verify 76.7% of the initial results ( $n = 33/43$  countries). Representative information was obtained from the following 43 countries:

- North America: United States and Canada
- South America: Argentina, Brazil, Colombia, and Guatemala
- Europe: Albania, Austria, Belgium, Denmark, Finland, France, Germany, Greece, Iceland, Ireland, Italy, Lithuania, Norway, Portugal, Spain, Sweden, Switzerland, the Netherlands, Turkey, and United Kingdom
- Africa: Egypt, South Africa, and Tunisia

- Asia: China, India, Indonesia, Iran, Israel, Japan, Lebanon, Pakistan, Philippines, Saudi Arabia, South Korea, and Thailand
- Australia
- New Zealand.

As for general categorization of responses, the countries were divided into those who do not provide neuroradiology fellowship programs and those who do.

### Countries That Do Not Provide Fellowship Training

On-line Table 2 provides information about the 16 countries reporting that they do not offer a fellowship program for either diagnostic or interventional neuroradiology ( $n = 16/43$ ).

The duration of medical school, including an internship period before graduation, ranges from 4 years in Lebanon (an American system with a 3-year bachelor of science degree required) to up to 7 years in Iceland, Egypt, and Tunisia.

Internships as part of general radiology residency are mandatory in Albania, Denmark, Lebanon, New Zealand, Pakistan, and South Africa. The shortest radiology residency program (3 years) of all surveyed countries without neuroradiology fellowships was in Egypt. Only in Egypt (1:1), and New Zealand (1:1.5) are there official requirements for a resident/faculty ratio.

In Spain, no official fellowship programs are provided, and instead, candidates are obliged to get a 2- or 3-year grant for a specific project from the national government, a hospital, or the pharmaceutical industry. In Turkey, a few hospitals have formal approval to offer fellowships for interventional neuroradiology, but there are no public tenders for diagnostic neuroradiology fellowships.

None of the surveyed African nations (Egypt, South Africa, and Tunisia) offer neuroradiology fellowships. A unique feature of the Tunisian radiology residency program is that the residents rotate through different departments in various cities and hospitals across the country.

Pakistan offers 1-year fellowships in vascular and interventional radiology during which the fellows likely get some interventional neuroradiology exposure, but there is no dedicated program per se.

### Countries with a Formal Neuroradiology Fellowship Program

On-line Tables 4 and 5 show information about the 27 countries that provide postresidency training in DNR and/or INR.

If one looks at the ratio of the number of residents/number of attending physicians, there is a large difference among the surveyed departments: on the one hand, countries such as Finland (ratio 0.2), Norway (0.3), the United States (0.3), and Canada (0.5) have a surplus of attendings (attendings exceed residents by far). On the other hand, Germany (ratio: 2.9), Brazil (3.2), Iran (3.2), and Indonesia (8.3–10.0) have a high number of residents compared with the number of attendings. National requirements regarding the number of faculty members are available only in a few countries (Austria, Australia, India, the Netherlands, and the United States).

Of those countries with a neuroradiology training program, almost every department offers regular neuroradiology lectures or at least the opportunity for residents to attend otolaryngology,

neurosurgery, or neurology case conferences. Case logs for tracking the residents' experience are used by most departments (63%).

Thirteen of 27 analyzed hospitals offer diagnostic and interventional neuroradiology fellowship programs; 9 departments provide only a diagnostic ( $n = 8$ ) or a neurointerventional program ( $n = 1$ ). The neuroradiology fellowships in Germany (2–3 years), India (3 years), Ireland (1 year), and South Korea (2 years) include both diagnostic and interventional NR in 1 curriculum (see “NR” in On-line Table 5).

The largest fellowship program is offered by the representative United States department (Johns Hopkins University) with 8 places for diagnostic NR and 2–3 places for interventional NR yearly. This program offers 1–2 teaching sessions daily (case presentations, journal clubs, grand rounds) given by neuroradiology, neurosurgery, neurology, and otolaryngology faculty or by the fellows themselves. There is a wide variety in terms of the number of scheduled lectures among other countries (only sporadic lectures in the Swedish, British, Chinese, Iranian, and Korean departments; 1–5 lectures per week in all other departments).

Ten of these 27 countries do not require a written or oral examination at the end of the neuroradiology fellowship.

Because of a lack of specialized interventional neuroradiologists, interventional neuroradiology procedures in Indonesia are performed by general interventional radiologists. A fellowship program for INR is currently in the planning phase.

The Tehran University of Medical Sciences is the only hospital in Iran that offers a fellowship for INR. The DNR postresidency program in Israel has been recently approved by the Israeli Medical Association and was reported to start in 2014.

Compared with the aforementioned countries, Portugal is an exception. After 6 years of medical school, the trainee must complete 18 months of an internship and can then start a 5-year neuroradiology fellowship program without doing a general radiology residency beforehand. Currently 7 teaching centers with 30 trainees offer a program solely focusing on diagnostic and interventional neuroradiology, including rotations in neurology, neurosurgery, and neuropediatrics. Fellows have a case log and must pass an oral examination at the end of the 5 years.

Taken together, nearly half of the European countries analyzed provide formal postresidency training in neuroradiology ( $n = 11/20$ ). To obtain an official degree in neuroradiology in a country without a fellowship program, one can complete a special course program organized by the European Society of Neuroradiology (ESNR, On-line Table 3). The first-level course is held on a yearly basis as a 2-day course in varying European cities, reviewing the most common cerebral pathologies, and is designed for residents in their first, second, or third year. The second-level course is organized every 6 months and is designed for certified radiologists with a 2-year minimum of neuroradiology training. Each of the 4 modules (first course: embryology/anatomy/malformations/genetics; second course: tumors and tumorlike lesions; third course: vascular diseases; and fourth course: trauma/degenerative/metabolic/inflammatory) lasts 5 days. The location is selected by the ESNR executive committee. Eligible candidates for the final European Diploma in Neuroradiology are certified radiologists with a 2-year minimum training in neuroradiology, who

need to successfully pass the written examinations associated with the second-level course modules. The ESNR also organizes third-level courses (European Advanced Courses/European Diploma of Higher Qualification). The duration of these programs varies, but usually 1 course lasts several days and is offered in different cities. In doing so, the ESNR aims to achieve standardization of neuroradiology education throughout Europe.<sup>8</sup>

Regarding training in general radiology in Europe, the European Society of Radiology recently published the revised version of the European Training Curriculum for Radiology. It aims to harmonize radiology training in Europe because it describes the objectives in knowledge, skills, and competences and attitudes for radiology residents. The curriculum does not include details about lecture hours, case log minimums, or the number of faculty members.<sup>9</sup> Comparable with the European Society of Radiology work, the ESNR implemented the “European Charter for Education and Training in Clinical Neuroradiology (Diagnostic and Interventional),” attempting to standardize neuroradiology subspecialization training in Europe.<sup>10</sup>

## DISCUSSION

In this study, data about neuroradiology training programs in various countries worldwide were collected, though it is virtually impossible to realistically compare their quality. Socioeconomic factors, local culture/preferences, historic precedents, and financial factors may explain differences in educational structures in these countries more than any other condition. However, this survey was primarily conducted to give an impression of the educational concepts in different countries and to show how their training schemes are organized.

### Preresidency

Despite the varying structure of medical school curricula (eg, undergraduate/graduate education in the United States, Canada, or Australia versus direct-entry medical programs in Germany, Brazil, or Thailand; and inclusion of an internship within the medical school curriculum versus noninclusion), the duration of medical school is roughly equal in all countries studied (4–6 years). In almost all the analyzed countries, it is mandatory to complete an internship, which is either included in the medical school curriculum or has to be performed after graduation from medical school before a radiology residency. On the other hand, there is an ongoing debate in America as to whether the year of internship should be spent in other activities for future radiologists. Shortening the US radiology residency program to 3 years and potentially completing clinical months instead of a preresidency internship as part of subspecialty fellowship training after the residency has been suggested in editorials.<sup>1,11</sup>

### Residency

There was a wide variation in the duration of radiology residency, ranging from 3 years (Egypt, Brazil, Colombia, India, Thailand, and Japan; 6/43 = 14%) to 5 years ( $n = 17/43$  departments = 39.5%). Iceland, with the lowest population density of all European countries, provides formal residency programs for general medicine and psychiatry, but not for radiology. All 3 neuroradi-

ologists working there obtained their training in mainland Scandinavia.

Because new imaging techniques are developing more rapidly, whether the shorter programs would be able to cover the same teaching modules as the longer programs has been questioned. However, the current trend is toward greater subspecialization. In this setting, it may be feasible for even a short general program to provide a sufficient basis for proceeding to more focused subspecialty expertise.

A striking difference was observed for the ratio of the number of residents to faculty members, which was lowest in the US department (0.3 residents/1 attending) and highest in Germany (2.9 residents/1 attending), Brazil (3.2 residents/1 attending), Iran (3.2 residents/1 attending), and Indonesia (8.3–10 residents/1 attending). A high number of attending physicians are suggested as the basis for maintaining a high standard of teaching, educating young radiologists, and conducting high-quality research. Consequently, in the United States, the ACGME requires at least 1 full-time equivalent physician faculty in each of the 9 core subspecialties for US radiology residency programs (see the first paragraph).<sup>4</sup>

Furthermore, a unique feature of US general radiology programs is that they must offer a minimum of 5 hours of lectures, case conferences, and journal clubs per week (mandated by the ACGME). As required by the ACGME, residents are not responsible for covering clinical service during that time.<sup>3,4</sup> No other country mandates such extensive protected teaching/learning time.

Most neuroradiology lectures during residency are included in the general diagnostic radiology conference schedule, but ambitious residents may have the opportunity to plan extra rotations in neuroradiology. An additional focused lecture series in neuroradiology (4 weeks) for residents is provided once a year in some US and Turkish departments.

### **Fellowship**

Regarding specialized training in neuroradiology, a wide spectrum of programs was observed, ranging from solely DNR (7 countries) or INR training (1 country) versus both DNR and INR fellowships (13 countries including the United States plus 4 countries with a joint DNR/INR [both diagnostic and interventional NR in 1 curriculum fellowship]) to a program that does not require completion of residency in general radiology but rather provides exclusive DNR/INR neuroradiology training for 5 years (Portugal).

The departments of 5/27 countries (18.5%) that provide neuroradiology fellowship training do not provide regularly scheduled didactic sessions. In contrast, daily teaching is strongly encouraged in some countries, where fellowship lectures are also provided by the clinical services (ie, neurosurgeons, neurologists, and otolaryngologists). The Philippine, Australian, and the Saudi Arabian departments also offer daily teaching. To encourage education and self-improvement of fellows (and residents), the didactic curriculum may also include a variety of formats (case series, journal clubs, noon conferences, grand rounds, and morbidity and mortality conferences).

To maintain the highest standards of neuroradiology educa-

tion and ensure competent guidance of the US trainees, a faculty-to-fellow ratio exceeding 1:1 is suggested by the ACGME. Except for the Chinese hospital (6 DNR fellows to 4 faculty members), each non-US department analyzed met this requirement (26/27 = 96.3%).<sup>12</sup>

The limitations of this survey are based on sampling bias for those respondents that replied to the survey and the results provided particularly for that institution. Because national regulations are not widely disseminated across each country, one could not tell whether the results from 1 institution truly represent the whole nation. We aimed to cross-check the validity of the answers (regarding general information) submitted by interviewing national representatives of neuroradiology and radiology societies, but not all officials responded. However, the information we obtained was provided by radiology residents, neuroradiology fellows, or radiology faculty members. Because the comparison with the representative American program was also based on a single large university hospital (Johns Hopkins), we used the ACGME regulations to provide the requirements of all American programs.

### **CONCLUSIONS**

Several differences were observed with regard to the organization of neuroradiology training in the nations examined. The spectrum ranges from the complete absence of neuroradiology fellowships to highly specialized and elaborate programs in several countries. These variations across the globe may be primarily related to financial and economic factors; historical precedents, politics, and turf battles among medical specialties; the volume of candidates available; the job market; and the teaching expertise available.

ACGME-approved radiology residency programs in the United States are structured educational experiences, because they are based on concrete enforceable guidelines.<sup>4,5,12</sup> These include scheduled rotations with specified goals and objectives, requirements for qualification of personnel, the necessity of a case log as an accurate trainee experiential record, teaching standards with scheduled conferences and lectures relating to a core didactic curriculum, periodic review of the resident, and the implementation of objective national certifying examinations.<sup>4</sup> As well, ACGME-accredited neuroradiology fellowship training is offered in the United States and also provides analogous guidelines requiring faculty-to-fellow ratios that exceed 1:1. Non-ACGME-approved fellowships in neuroradiology are also offered. However, because they may not lead to US subspecialty certification and may not be recognized for state licensure, those programs remain less desirable.

The ESNR has recently endeavored to coordinate training courses in neuroradiology, implement standardized European examinations, and create a “European Charter for Education and Training in Clinical Neuroradiology”.<sup>10</sup> Primarily, it aims to harmonize subspecialization training in neuroradiology throughout Europe and to create common standards of knowledge.

In summary, many different philosophies and methods for training radiologists and neuroradiologists can be found across the globe. While the duration of diagnostic neuroradiology train-

ing varies only minimally, the structure of that training and the regulations and oversight vary widely.

Disclosures: Thierry A.G.M. Huisman—UNRELATED: *Expert Testimony*: defense; Jens Fiehler—UNRELATED: *Consultancy*: MicroVention, Stryker, Codman, Acandis; *Grants/Grants Pending*: MicroVention,\* Philips Healthcare\*; *Payment for Lectures (including service on Speakers Bureaus)*: Covidien, Penumbra; *Travel/Accommodations/Meeting Expenses Unrelated to Activities Listed*: Covidien. David M. Yousem—UNRELATED: *Consultancy*: medicolegal; *Expert Testimony*: medicolegal; *Payment for Lectures (including service on Speakers Bureaus)*: American College of Radiology Education Center, *Comments*: revenue shared with Johns Hopkins School of Medicine; *Royalties*: 3 Elsevier books; *Payment for Development of Educational Presentations*: CMEInfo.com,\* *Comments*: revenue to Johns Hopkins. \*Money paid to the institution.

## REFERENCES

1. Arenson R, Dunnick NR. **Training a better radiologist.** *J Am Coll Radiol* 2006;3:389–93
2. ACGME. Number of accredited programs for the current academic year (2013–2014). <http://www.acgme.org/ads/Public/Reports/ReportRun?ReportId=3&CurrentYear=2013&AcademicYearId=2013>. Accessed May 29, 2014
3. Rumack CM. **American diagnostic radiology residency and fellowship programmes.** *Ann Acad Med Singapore* 2011;40:126–31
4. ACGME program requirements for graduate medical education in diagnostic radiology. [http://www.acgme.org/acgmeweb/Portals/0/PFAssets/2013-PR-FAQ-PIF/420\\_diagnostic\\_radiology\\_07012013.pdf](http://www.acgme.org/acgmeweb/Portals/0/PFAssets/2013-PR-FAQ-PIF/420_diagnostic_radiology_07012013.pdf). Accessed December 17, 2013
5. ACGME. Case log categories and required minimum numbers. [http://www.acgme.org/acgmeweb/Portals/0/PFAssets/ProgramResources/420\\_DR\\_Case\\_Log\\_Minimums.pdf](http://www.acgme.org/acgmeweb/Portals/0/PFAssets/ProgramResources/420_DR_Case_Log_Minimums.pdf). Accessed December 17, 2013
6. Smith GG, Thrall JH, Pentecost M, et al. **Subspecialization in radiology and radiation oncology.** *J Am Coll Radiol* 2009;6:147–59 e4
7. Taveras JM. **Development of the first fellowship training program in neuroradiology in North America.** *AJNR Am J Neuroradiol* 1991;12:587–90
8. European Society of Neuroradiology, diplomas and exams. <http://www.esnr.org/en/diplomas-exams/>. Accessed June 3, 2014
9. The European Society of Radiology. Revised European training curriculum for radiology. [http://www.myesr.org/html/img/pool/Rev\\_April\\_9,\\_2014\\_ESR\\_2013\\_ESR-EuropeanTrainingCurriculum\\_web\\_aktualisiert\\_April\\_9,\\_2014.pdf](http://www.myesr.org/html/img/pool/Rev_April_9,_2014_ESR_2013_ESR-EuropeanTrainingCurriculum_web_aktualisiert_April_9,_2014.pdf). Accessed August 2, 2014
10. The European Society of Radiology. European Charter for Education and Training in Clinical Neuroradiology (Diagnostic and Interventional). <http://www.esnr.org/en/education-training/charter-standards/>. Accessed August 10, 2014
11. Baker SR, Tilak GS, Geannette C, et al. **The value of the internship year for radiologists: a retrospective analysis as assessed by current residents and fellows.** *Acad Radiol* 2008;15:1205–10
12. ACGME program requirements for graduate medical education in neuroradiology. <http://www.esnr.org/en/education-training/charter-standards/>. Accessed May 31, 2014

# Genetics of Parkinson Disease

E. Ben-David and R. Tu

**ABBREVIATION:** PD = Parkinson disease

**P**arkinson disease (PD) is a degenerative disorder of the nervous system. It is characterized by loss of dopamine-producing cells which, in time, develops into motor system dysfunction. A small portion of PD cases are purely genetic. Currently, diagnosis is based on clinical examination. Molecular imaging is most sensitive and novel techniques are promising; however, their use is largely limited to research. Anatomic imaging is not disease-specific in this disorder, though it may be used to rule out alternative diagnoses known to mimic PD.

## HISTORY OF PARKINSON DISEASE

The description of tremors and other symptoms of PD is found in ancient texts.<sup>1,2</sup> The eponym of the disease was bestowed posthumously, in the late 1800s, by Jean-Martin Charcot upon James Parkinson, a British apothecary and surgeon, who described “paralysis agitans” in a monograph entitled *An Essay on the Shaking Palsy* in 1817.<sup>3</sup> PD is the second most common neurodegenerative disorder after Alzheimer disease.<sup>4</sup> It is caused by impairment of the dopaminergic system, initially affecting movement. In later stages, cognition and behavior may also be affected.

Pathologically, PD is associated with dopaminergic neuronal cell loss and accumulation of Lewy bodies and Lewy neuritis within affected cells. Clinical symptoms develop when between 70%–80% of the involved nerve terminals have degenerated.<sup>5</sup> Prevalence of PD is approximately 1% of the population over the age of 50.<sup>6,7</sup> Its reported annual incidence rate is 13.4 per 100,000 in the general population; however, over the age of 60 years, the incidence rate greatly increases.<sup>8</sup>

## WHAT ARE THE CLINICAL MANIFESTATIONS OF PARKINSON DISEASE?

PD is a movement disorder with a slow onset, frequently presenting initially with coordination difficulties. Later, bradykinesia, rigidity, postural instability, and resting tremors are the dominant features of the disease.<sup>9</sup> The time lag between the initial symptoms and diagnosis may be several years.<sup>10</sup>

A depletion of dopaminergic production may be seen in other diseases as well. Atypical PD, also known as Parkinson Plus Syndromes, represents 15% of patients presenting with Parkinson-like symptoms. However, these syndromes (multiple system atrophy, Lewy body dementia, progressive supranuclear palsy, and corticobasal degeneration) do not respond to dopamine therapy.

## ARE THERE GENETIC TYPES OF PD?

Initially, the genetic component of PD was questioned, especially in PD occurring after the age of 60.<sup>11</sup> In a large twin study examining concordance for PD in twins, no concordance was found.<sup>12</sup> However, additional studies found a Mendelian inheritance pattern, especially in early onset PD.<sup>13,14</sup> Currently, monogenic PD is thought to cause 3%–5% of all PD.<sup>15</sup> Detection of the genes was performed using linkage analysis and positional cloning in families suspected of having a genetic component. The genes discovered to have a link to PD were designated the “PARK” genes.<sup>16</sup> The inheritance patterns may be autosomal dominant, as is seen in the *PARK1*, 3, 5, and 8 genes. Autosomal recessive PD is linked to *PARK2*, 6, and 7. A polymorphic or multiple genetic form of late onset PD has been described as well.<sup>17</sup>

## THE PRION DISEASE HYPOTHESIS

In recent years, there has been an increasing body of research suggesting that  $\alpha$ -synuclein, which accumulates in Lewy bodies in patients with PD, is a prionlike protein. The protein aggregates in a misfolded configuration and demonstrates properties of self-propagation to adjacent cells.<sup>18–20</sup> The similarity of genetic forms of PD and prion diseases is stated as an argument on behalf of this hypothesis.<sup>21</sup>

From the Department of Radiology, George Washington University Hospital, Washington, DC.

Please address correspondence to Raymond Tu, MD, MS, FACR, Department of Radiology, George Washington University Hospital, 901 23rd St NW, Washington, DC 20037; e-mail: Raymond.Tu@progressiveradiology.net

<http://dx.doi.org/10.3174/ajnr.A4092>

## IS THERE DIAGNOSTIC TESTING FOR PD?

Currently, diagnosis of Parkinson disease is based on the clinically characteristic signs of bradykinesia, rigidity, and resting tremor. Asymmetric onset of symptoms and a response to levodopa are considered supporting diagnostic features.<sup>16</sup>

## WHAT IS THE ROLE OF IMAGING IN PD?

**MR Imaging.** The role of iron in the pathogenesis of Parkinson disease has been and continues to be investigated.<sup>22,23</sup> Iron, which has ferromagnetic properties and is excessively deposited in the substantia nigra of patients with PD, led many to believe that this could potentially be an imaging marker of the disease, especially with T2/T2\* imaging.<sup>24–26</sup> In addition, more advanced MR imaging techniques have been evaluated, such as SWI<sup>27,28</sup> and magnetic transfer imaging.<sup>29,30</sup> One limitation of iron-based imaging is that it is nonspecific and may be seen in myriad normal or non-PD patients with parkinsonism.

Voxel-based morphometry uses high-resolution images for the assessment of brain structure. In a study of carriers of *PARK2* and 6 heterozygous carriers, an increase in volume of the posterior putamen and the internal globus pallidus was seen, possibly a compensatory reaction to dopaminergic dysfunction.<sup>31</sup>

Evaluation of white matter tracts, basal ganglia, and substantia nigra integrity using regional apparent diffusion coefficients and fractional anisotropy can be performed using DTI.<sup>32–35</sup>

Resting-state MR imaging shows promise in the evaluation of abnormal neural networks, which is seen as hypersynchronicity in basal ganglia-thalamo-cortical loops.<sup>36,37</sup>

High-field (7T) MRS demonstrates elevated putaminal and pontine gamma-aminobutyric acid levels.<sup>38</sup> This is promising; however, larger studies are required to validate this technique for clinical use.

**Molecular Imaging.** Radionuclide (<sup>18</sup>F)fluoro-L-dopa or FDOPA uptake by dopaminergic neurons makes this molecule particularly useful as a sensitive tool for assessing the dopaminergic pathway.

In a comprehensive review, van der Vegt et al<sup>15</sup> discussed, at length, the use of molecular as well as structural imaging in genetic forms of PD. The use of [<sup>18</sup>F]FDOPA PET and SPECT imaging is characteristic for sporadic PD but is nonspecific for genetic PD. A pattern similar to idiopathic PD of presynaptic dopaminergic dysfunction was seen in most genetic forms of PD.

## CONCLUSIONS

Diagnosis of PD still rests on a characteristic clinical examination. Only a fraction of these patients will have a monogenetic etiology. Of the imaging modalities, radionuclide studies appear to be the most sensitive diagnostic tool. Structural imaging is currently noncontributory for diagnosis; however, it may be used to rule out other diseases that may have a similar clinical presentation. Genetic and idiopathic forms of PD have similar imaging appearances, suggesting a common pathophysiology.

## REFERENCES

1. García Ruiz PJ. **Prehistory of Parkinson's disease** [in Spanish]. *Neurología* 2004;19:735–37
2. Stern G. **Did parkinsonism occur before 1817?** *J Neurol Neurosurg Psychiatry* 1989;52(suppl):11–12
3. Olanow CW, Stern MB. **Parkinson's disease: unresolved issues.** *Ann Neurol* 2008;64(suppl 2):S1–2
4. Nussbaum RL, Ellis CE. **Alzheimer's disease and Parkinson's disease.** *N Engl J Med* 2003;348:1356–64
5. Bernheimer H, Birkmayer W, Hornykiewicz O, et al. **Brain dopamine and the syndromes of Parkinson and Huntington. Clinical, morphological and neurochemical correlations.** *J Neurol Sci* 1973;20:415–55
6. de Lau LM, Breteler MM. **Epidemiology of Parkinson's disease.** *Lancet Neurol* 2006;5:525–35
7. Polymeropoulos MH, Higgins JJ, Golbe LI, et al. **Mapping of a gene for Parkinson's disease to chromosome 4q21–q23.** *Science* 1996;274:1197–99
8. Van Den Eeden SK, Tanner CM, Bernstein AL, et al. **Incidence of Parkinson's disease: variation by age, gender, and race/ethnicity.** *Am J Epidemiol* 2003;157:1015–22
9. Hoehn MM, Yahr MD. **Parkinsonism: onset, progression and mortality.** *Neurology* 1967;17:427–42
10. Lees AJ, Hardy J, Revesz T. **Parkinson's disease.** *Lancet* 2009;373:2055–66
11. Tanner CM, Ottman R, Goldman SM, et al. **Parkinson disease in twins: an etiologic study.** *JAMA* 1999;281:341–46
12. Ward CD, Duvoisin RC, Ince SE, et al. **Parkinson's disease in 65 pairs of twins and in a set of quadruplets.** *Neurology* 1983;33:815–24
13. Barbeau A, Pourcher E. **New data on the genetics of Parkinson's disease.** *Can J Neurol Sci* 1982;9:53–60
14. Lazzarini AM, Myers RH, Zimmerman TR, et al. **A clinical genetic study of Parkinson's disease: evidence for dominant transmission.** *Neurology* 1994;44:499–506
15. van der Vegt JP, van Nuenen BF, Bloem BR, et al. **Imaging the impact of genes on Parkinson's disease.** *Neuroscience* 2009;164:191–204
16. Farlow J, Pankratz ND, Wojcieszek J, et al. **Parkinson disease overview.** In: Pagon RA, Adam MP, Ardinger HH, et al, eds. *GeneReviews* [Internet]. Seattle: University of Washington; 1993–2014. 2004 May 25 [updated 2014 Feb 27]
17. Hamza TH, Zabetian CP, Tenesa A, et al. **Common genetic variation in the HLA region is associated with late-onset sporadic Parkinson's disease.** *Nat Genet* 2010;42:781–85
18. Olanow CW, Brundin P. **Parkinson's disease and alpha synuclein: is Parkinson's disease a prion-like disorder?** *Mov Disord* 2013;28:31–40
19. Hansen C, Angot E, Bergstrom A-L, et al. **α-Synuclein propagates from mouse brain to grafted dopaminergic neurons and seeds aggregation in cultured human cells.** *J Clin Invest* 2011;121:715–25
20. Angot E, Steiner JA, Lema Tome CM, et al. **Alpha-synuclein cell-to-cell transfer and seeding in grafted dopaminergic neurons in vivo.** *PLoS One* 2012;7:e39465
21. Hilker R, Brotchie JM, Chapman J. **Pros and cons of a prion-like pathogenesis in Parkinson's disease.** *BMC Neurol* 2011;11:74
22. Gotz ME, Double K, Gerlach M, et al. **The relevance of iron in the pathogenesis of Parkinson's disease.** *Ann N Y Acad Sci* 2004;1012:193–208
23. Zecca L, Youdim MB, Riederer P, et al. **Iron, brain ageing and neurodegenerative disorders.** *Nat Rev Neurosci* 2004;5:863–73
24. Rutledge JN, Hilal SK, Silver AJ, et al. **Study of movement disorders and brain iron by MR.** *AJR Am J Roentgenol* 1987;149:365–79
25. Gorell JM, Ordidge RJ, Brown GG, et al. **Increased iron-related MRI contrast in the substantia nigra in Parkinson's disease.** *Neurology* 1995;45:1138–43
26. Cho Z-H, Oh S-H, Kim J-M, et al. **Direct visualization of Parkinson's disease by in vivo human brain imaging using 7.0T magnetic resonance imaging.** *Mov Disord* 2011;26:713–18
27. Ashwell GJ, Urasinska-Wojcik B, Phillips LJ. **In situ stepwise synthesis of functional multijunction molecular wires on gold electrodes and gold nanoparticles.** *Angew Chem Int Ed Engl* 2010;49:3508–12

28. Wang Y, Butros SR, Shuai X, et al. **Different iron-deposition patterns of multiple system atrophy with predominant parkinsonism and idiopathic Parkinson diseases demonstrated by phase-corrected susceptibility-weighted imaging.** *AJNR Am J Neuroradiol* 2012;33:266–73
29. Michaeli S, Oz G, Sorce DJ, et al. **Assessment of brain iron and neuronal integrity in patients with Parkinson's disease using novel MRI contrasts.** *Mov Disord* 2007;22:334–40
30. Neustrasil I, Michaeli S, Liimatainen T, et al. **T1rho and T2rho MRI in the evaluation of Parkinson's disease.** *J Neurol* 2010;257:964–68
31. Binkofski F, Reetz K, Gaser C, et al. **Morphometric fingerprint of asymptomatic Parkin and PINK1 mutation carriers in the basal ganglia.** *Neurology* 2007;69:842–50
32. Le Bihan D. **Looking into the functional architecture of the brain with diffusion MRI.** *Nat Rev Neurosci* 2003;4:469–80
33. Scherfler C, Frauscher B, Schocke M, et al. **White and gray matter abnormalities in idiopathic rapid eye movement sleep behavior disorder: a diffusion-tensor imaging and voxel-based morphometry study.** *Ann Neurol* 2011;69:400–07
34. Bosnell R, Giorgio A, Johansen-Berg H. **Imaging white matter diffusion changes with development and recovery from brain injury.** *Dev Neurorehabil* 2008;11:174–86
35. Schocke MFH, Seppi K, Esterhammer R, et al. **Diffusion-weighted MRI differentiates the Parkinson variant of multiple system atrophy from PD.** *Neurology* 2002;58:575–80
36. Baudrexel S, Witte T, Seifried C, et al. **Resting state fMRI reveals increased subthalamic nucleus-motor cortex connectivity in Parkinson's disease.** *Neuroimage* 2011;55:1728–38
37. Skidmore FM, Yang M, Baxter L, et al. **Reliability analysis of the resting state can sensitively and specifically identify the presence of Parkinson disease.** *Neuroimage* 2013;75:249–61
38. Emir UE, Tuite PJ, Oz G. **Elevated pontine and putamenal GABA levels in mild-moderate Parkinson disease detected by 7 Tesla proton MRS.** *PLoS One* 2012;7:e30918

# White Matter Correlates of Cognitive Impairment in Essential Tremor

K.S. Bhalsing, K.J. Kumar, J. Saini, R. Yadav, A.K. Gupta, and P.K. Pal



## ABSTRACT

**BACKGROUND AND PURPOSE:** Impairment of cognitive functions occurs in essential tremor, though the mechanism is largely unknown. The aim of this study was to find microstructural correlates of cognitive dysfunction seen in essential tremor by using DTI and neuropsychological assessment.

**MATERIALS AND METHODS:** Fifty-five patients with essential tremor and 55 matched healthy controls were evaluated. Essential tremor was diagnosed by using the National Institutes of Health criteria. Subjects were assessed by using a structured neuropsychological battery. DTI data were acquired by using 3T MR imaging and were analyzed by using tract-based spatial statistics. Fractional anisotropy, mean diffusivity, radial diffusivity, and axial diffusivity were analyzed.

**RESULTS:** Patients were considered cognitively impaired when the test score was 1.5 SDs below or above the mean of healthy controls (depending on the type of test) in  $\geq 3$  neuropsychological tests. Patients with cognitive impairment had significantly higher mean diffusivity, radial diffusivity, and axial diffusivity values in the bilateral frontoparietal regions. In patients with cognitive impairment, mean diffusivity, radial diffusivity, and axial diffusivity showed correlations with various neuropsychological test scores. Executive function correlated with DTI measures of the frontal white matter, cingulum, inferior superior longitudinal and uncinate fasciculi, anterior thalamic radiations, and posterior lobe of the cerebellum. Visuospatial function correlated with the right parieto-occipital lobe, whereas visual-verbal memories correlated with the anterior thalamic radiations, inferior longitudinal and uncinate fasciculi, and the posterior lobe of the cerebellum. No significant correlations were found between fractional anisotropy and any of the neuropsychological test scores.

**CONCLUSIONS:** The present study demonstrates a correlation between neuropsychological test scores and DTI measures, suggesting a neuroanatomic basis for cognitive impairment seen in patients with essential tremor.

**ABBREVIATIONS:** ET = essential tremor; ETCI = ET with cognitive impairment; ETNCI = ET without cognitive impairment; HC = healthy controls; TBSS = tract-based spatial statistics

Essential tremor (ET) is the most common movement disorder. It is associated with cognitive impairments<sup>1</sup> and behavioral and sleep disturbances,<sup>2</sup> in addition to tremor. Various studies have shown cognitive impairment, especially executive-visuospatial dysfunction and attention deficits, in patients with ET.<sup>3,4</sup> Voxel-based morphometry studies in ET have found volume reductions in the cerebellum and cerebrum (frontal lobe, insula, and cingulum).<sup>5,6</sup> While voxel-based morphometry analysis is

useful for demonstrating regional GM changes, DTI provides information about the microstructural organization of WM. The most widely used measurements are fractional anisotropy and mean diffusivity. Variations in these measures within WM structures are thought to reflect structural changes such as myelin abnormalities, neuronal damage, microtubule breakdown, and/or axonal loss. The involvement of WM is controversial in ET. In particular, the first diffusion study in ET did not report WM abnormalities,<sup>7</sup> while Shin et al<sup>8</sup> showed fractional anisotropy reduction in the cerebellum, brain stem, and cerebral hemispheres in patients with ET. Recently, a few studies have reported the presence of WM abnormalities in the frontoparietal region and cerebellar peduncles.<sup>9,10</sup> Thus, structural studies in ET suggest involvement of the cerebellofrontal network, which is known to play an important role in higher level cognitive functions.<sup>11</sup>

The aim of the present study was to characterize the brain localization of cognitive dysfunction in ET. To characterize cognitive dysfunction, we used a structured neuropsychological bat-

Received May 9, 2014; accepted after revision August 22.

From the Departments of Neurology (K.S.B., R.Y., P.K.P.), Clinical Psychology (K.J.K.), and Neuroimaging and Interventional Radiology (J.S., A.K.G.), National Institute of Mental Health and Neurosciences, Karnataka, India.

Please address correspondence to Pramod Kumar Pal, DM, Department of Neurology, National Institute of Mental Health and Neurosciences, Hosur Rd, Bangalore-560029, Karnataka, India; e-mail: pal.pramod@rediffmail.com



Indicates article with supplemental on-line tables.



Evidence-Based Medicine Level 2.

<http://dx.doi.org/10.3174/ajnr.A4138>

tery. Tract-based spatial statistics (TBSS; <http://fsl.fmrib.ox.ac.uk/fsl/fslwiki/TBSS>) analysis on DTI images was performed to characterize the microstructural correlates of cognitive performance. Such correlation analysis offers an opportunity to detect the role of WM microstructural damage in cognitive deficits seen in ET.

## MATERIALS AND METHODS

We studied 55 patients with ET (mean age,  $45.6 \pm 11.7$  years) and 55 age-, sex-, education-, and handedness-matched healthy controls (HC) (mean age,  $46.2 \pm 11.4$  years) at the National Institute of Mental Health and Neurosciences, India, from December 2011 to August 2013. All subjects were screened with the Mini-Mental State Examination scale and were included if the score was  $\geq 25$ .

### Patient Group

All patients recruited in our study were carefully examined by a movement disorder specialist (P.K.P.). The diagnosis of ET was confirmed by using the National Institutes of Health Collaborative Genetic Criteria.<sup>12</sup> The severity of the tremor was assessed by using the Fahn-Tolosa-Marin tremor rating scale. In all patients, arm tremors were assessed at rest, with their arms extended, and while performing finger-to-nose movements. Head, voice, leg, and trunk tremors were also assessed in addition to arm tremor. Tremor severity was also assessed while writing and performing activities of daily living (such as pouring water and buttoning and unbuttoning a shirt).

The half-life of the commonly used medications for tremor ranges from 5 to 50 hours, and it takes 3–5 plasma half-lives to eliminate a drug from a body. Therefore, patients who were on medications for tremor were asked to stop the medications 2 weeks before the study.

### Control Group

Hospital staff, spouses, and nonfamily attendants of patients were recruited as controls. Each control was carefully interviewed and examined to rule out any neurologic conditions and family history of neurodegenerative disorders. The Modified Mini Screen was applied to all of them to rule out the presence of any psychiatric disorder.

The study was approved by the ethics committee of the institution, and all subjects consented to participate in this study.

### Neuropsychological Evaluation

All subjects underwent neuropsychological assessment with tests assessing attention, executive functions, memory (visual, verbal, and working memory), and visuospatial functions. In patients, depending on the type of test, a test finding was considered abnormal if the score was 1.5 SDs below or above the mean of the healthy controls.<sup>13</sup> A patient was recognized as cognitively impaired if  $\geq 3$  neuropsychological test findings were abnormal. We considered  $\geq 3$  tests to increase the stringency of the criteria. Patients were further divided into 2 groups, namely ET with cognitive impairment (ETCI) and ET without cognitive impairment (ETNCI).

### Test for Attention and Executive Functions

**Wisconsin Card Sorting Test.** A computerized version of the Wisconsin Card Sorting Test (Berg's Card Sorting Test; [\[pebl.sourceforge.net/battery.html\]\(http://pebl.sourceforge.net/battery.html\)\), which consists of 64 trials, was used. Performance was evaluated on the basis of categories completed, perseverative response, and perseverative errors.](http://</a></p></div><div data-bbox=)

**Stroop Test.** The Stroop Test is a test of response inhibition. It consists of 3 subtasks having 100 stimuli each. The first subtask shows names of colors printed in black ink in random order. The second subtask displays 1 of 4 basic colors. The third subtask contains names of colors printed in an incongruous ink color; for example, the word "yellow" printed in red ink. The subject is required to inhibit the prepotent or habitual response of reading the word and instead give a new response, which is to name the color of the ink. This is known as Stroop effect.

The time needed to complete each subtask was recorded. Performance was evaluated on the basis of "interference" because it is considered a measure of cognitive flexibility and executive functioning.<sup>14</sup> It was calculated by subtracting the average time needed to complete the first 2 subtasks from the time needed to complete the third subtask.

**Color Trails Tests I and II.** The Color Trails Test has 3 parts. The time required to perform each part was recorded.

### Test for Visuospatial Functions

**Line Orientation Test.** The Benton's Judgment of Line Orientation Test is considered a valid task for the assessment of visuospatial function.<sup>15</sup> In the present study, we used a self-designed short form of the test (15 items instead of 30), keeping all the parameters similar to those in the original test.

### Test for Working Memory

**Wechsler Memory Scale III Spatial Span Test.** We performed both forward and backward Spatial Span tests to judge the performance.

### Test for Verbal and Visual Memory

We used the Rey Auditory Verbal Learning Test and Wechsler Memory Scale III Face Recognition test for evaluation of verbal and visual memories, respectively. In both tests, performance was evaluated on the basis of immediate and delayed recall.

### MR Imaging Acquisition

Imaging was performed in all subjects by using an Achieva (Philips Healthcare, Best, the Netherlands) 3T MR imaging scanner. Diffusion-weighted data with 16 directions were acquired by using a 32-channel head coil. In case of severe head tremors, additional cushions were used to stabilize the head. The acquisition parameters were the following: TR/TE = 8782/62 ms, flip angle =  $90^\circ$ ,  $b = 1000 \text{ s/mm}^2$ , section thickness = 2 mm, number of sections = 60, intersection gap = 0, acquisition matrix =  $112 \times 112$ . FLAIR images were also acquired. Before the analysis, all images were screened by a neuroradiologist for the presence of structural abnormalities.

### Tract-Based Spatial Statistics

The fMRI of the Brain Software Library (FSL; <http://www.fmrib.ox.ac.uk/fsl/>), Tract-Based Spatial Statistics tool,<sup>16</sup> was used to

### Clinical and demographic details of study subjects

	ETCI (n = 33)	ETNCI (n = 22)	HC (n = 55)	P Value
Age (yr)	47.03 ± 10.4	43.4 ± 13.4	46 ± 11	.2 <sup>a</sup>
Sex (female/male)	1:2.8	1:2.5	1:2.6	.4 <sup>a</sup>
MMSE score	29.2 ± 0.86	29.6 ± 0.7	29.9 ± 0.2	.1 <sup>a</sup>
Family history of disease (No.)	18	13	NA	.6 <sup>b</sup>
Disease duration (yr)	10.2 ± 7.4	9.5 ± 8.2	NA	.8 <sup>b</sup>
Fahn-Tolosa-Marin score	34.8 ± 14.3	33.9 ± 15.4	NA	.8 <sup>b</sup>

Note:—NA indicates not applicable; MMSE, Mini-Mental State Examination.

<sup>a</sup> ANOVA.

<sup>b</sup> Unpaired *t* test.

compare diffusion measures among ETCI, ETNCI, and HC groups and to correlate diffusion measures with neuropsychological assessment scores. DTI data were first corrected for eddy current and head motion. Fractional anisotropy images were then created by fitting a tensor model to the raw diffusion data by using the FMRIB Diffusion Toolbox (<http://www.fmrib.ox.ac.uk/fsl/fdt/index.html>) and were extracted by using the Brain Extraction Tool.<sup>17,18</sup> The fractional anisotropy data of all the subjects were then aligned into a common space by using the FMRIB Nonlinear Registration Tool (FNIRT; <http://fsl.fmrib.ox.ac.uk/fsl/fslwiki/FNIRT>). In the next step, the mean fractional anisotropy image was created and thinned to create a mean fractional anisotropy skeleton, which represented the centers of all tracts common to the whole group. To exclude GM or cerebrospinal fluid, the mean fractional anisotropy skeleton was thresholded at 0.2. The aligned fractional anisotropy data of each subject were then projected onto this fractional anisotropy skeleton. In addition to fractional anisotropy, mean diffusivity, radial diffusivity, and axial diffusivity images were also generated.

### Statistical Analysis

**F-test and Post Hoc Analysis.** The *F*-test was performed among the 3 groups (ETCI, ETNCI, and HC) to investigate differences in DTI measures within the groups. Post hoc analysis was then performed (when appropriate) to evaluate the differences among ETCI versus HC, ETCI versus ETNCI, and ETNCI versus HC. Age, sex, total intracranial volume, disease duration, and Fahn-Tolosa-Marin scale scores were entered as nuisance regressors in the design matrix throughout the analysis. Statistical analysis was performed by using the FSL Randomize Tool (<http://fsl.fmrib.ox.ac.uk/fsl/fslwiki/Randomise/UserGuide>) with 5000 permutations.

**Correlation Analysis.** Correlation analysis was performed to study the relationship between neuropsychological test scores and each of the DTI measures. Neuropsychological test scores were used as a covariate of interest in the framework of a general linear model. Age, sex, total intracranial volume, disease duration, and Fahn-Tolosa-Marin scale scores were entered as nuisance regressors in the design matrix throughout the analysis. Statistical analysis was performed by using the FSL Randomize Tool with 5000 permutations.

Threshold-free cluster enhancement was performed to enhance cluster-like structures.<sup>19</sup> Family-wise error correction with  $P < .05$  was considered significant. In correlation analysis, we did not find any surviving clusters or voxels with analysis corrected for multiple comparisons (family-wise error or false discovery rate correction), so we decided to report the

correlation results with  $P < .001$  (uncorrected for multiple comparisons) as statistically significant.

### RESULTS

Thirty-three patients were classified as ETCI. A comparison of the 3 groups with respect to demographic and clinical characteristics is presented in the Table. Inter-group analysis among ETCI, ETNCI, and HC by using ANOVA and between ETCI and ETNCI by using a *t* test did not show

any statistically significant differences in any of the demographic and clinical parameters.

### ANOVA and Post Hoc T Test

An *F*-test performed among the 3 groups was found to be statistically significant in mean diffusivity, radial diffusivity, and axial diffusivity, while it was not significant for fractional anisotropy. On post hoc *t* test analysis (family-wise error-corrected,  $P < .05$ ), the ETCI group compared with HC group showed increased mean diffusivity in the right cingulum and left precuneus (parietal lobe), increased radial diffusivity in the right medial frontal white matter and left cingulum, and increased axial diffusivity in the right cingulum and left medial frontal white matter. The Figure shows the results of *t* test analysis performed in ETCI versus HC.

There was no statistically significant difference in any of the diffusion measures for comparisons between ETCI versus ETNCI and ETNCI versus HC groups.

### Correlation Analysis

The following correlations (uncorrected for multiple comparisons,  $P < .001$ ) between diffusion measures and neuropsychology assessment scores were observed in the ETCI group (On-line Tables 1–3):

- 1) The number of categories completed on the Wisconsin Card Sorting Test showed a negative correlation with mean diffusivity, radial diffusivity, and axial diffusivity of the right medial frontal gyrus, right cingulum, left anterior thalamic radiations, and bilateral cerebellum (posterior lobe), whereas the number of perseverative errors on the Wisconsin Card Sorting Test positively correlated with mean diffusivity of bilateral anterior thalamic radiations, bilateral superior longitudinal fasciculus, left uncinate fasciculus, left cerebellum (posterior lobe) and radial diffusivity of left anterior thalamic radiations, right superior and inferior longitudinal fasciculus and left uncinate fasciculus.
- 2) The Stroop Test score showed a positive correlation with mean diffusivity, radial diffusivity, and axial diffusivity of the left anterior thalamic radiations, bilateral superior longitudinal fasciculus, left uncinate fasciculus, and left cerebellum (posterior lobe).
- 3) The Color Trails Test score positively correlated with mean diffusivity, radial diffusivity, and axial diffusivity of the left anterior thalamic radiations and bilateral superior longitudinal fasciculus.
- 4) Working memory scores showed a negative correlation with

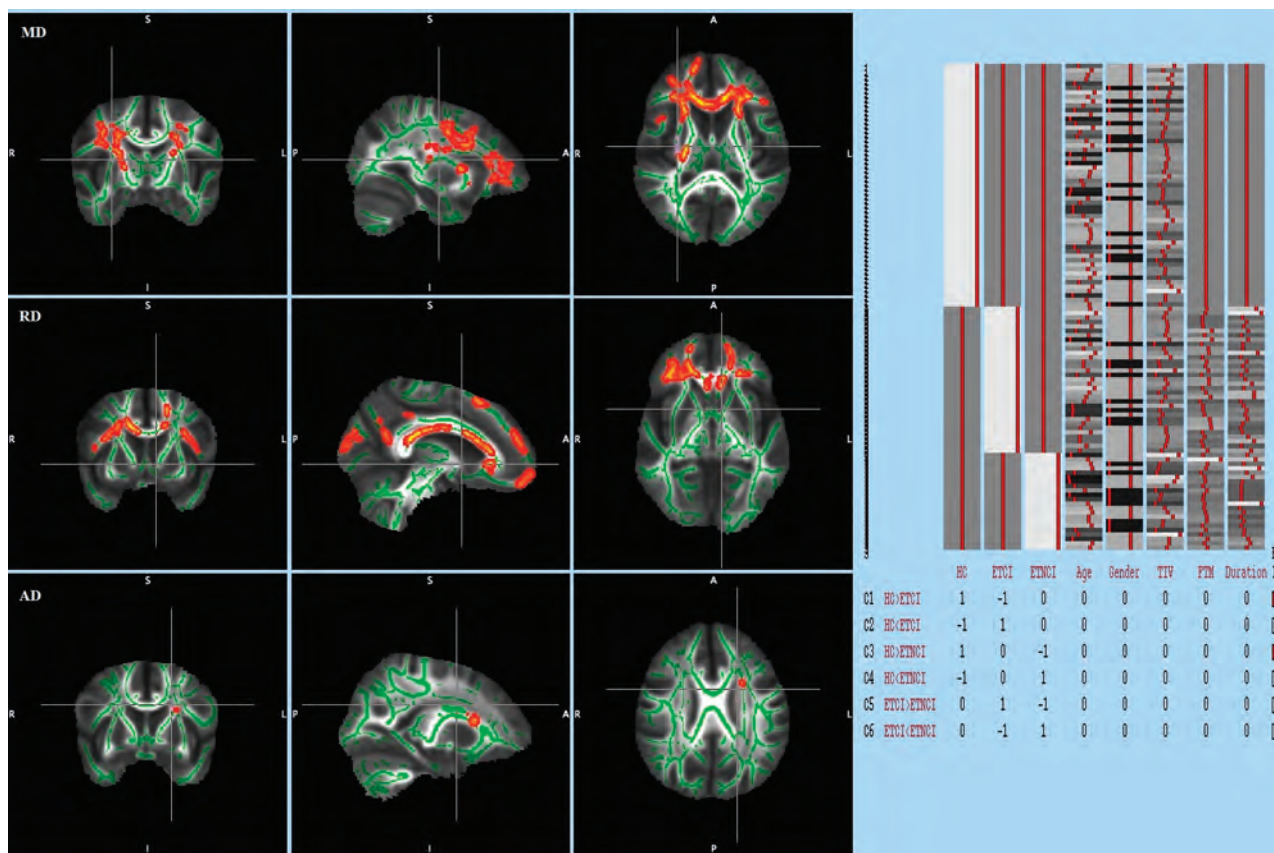


**FIGURE.** TBSS analysis ( $t$  test) performed in those with ETCI versus HC. Voxels demonstrating significantly (family-wise error–corrected  $P < .05$ ) increased mean diffusivity, radial diffusivity, and axial diffusivity in ETCI compared with HC are shown in red-yellow. Voxels are thickened into local tracts and overlaid on the white matter skeleton (green). The design matrix used for the TBSS analysis is shown on the right.

mean diffusivity and radial diffusivity of the right medial frontal gyrus, right cingulum, bilateral anterior thalamic radiations, right superior longitudinal fasciculus, and right cerebellum (posterior lobe).

- 5) Visuospatial scores negatively correlated with mean diffusivity, radial diffusivity of the right parietal lobe (supramarginal), and the right occipital lobe.
- 6) Verbal memory immediate recall showed a negative correlation with mean diffusivity, radial diffusivity, and axial diffusivity of the bilateral inferior longitudinal fasciculus, right uncinate fasciculus, and bilateral cerebellum (posterior lobe), whereas delayed recall showed a negative correlation with the right anterior thalamic radiations, right inferior longitudinal fasciculus, and right uncinate fasciculus.
- 7) Visual memory immediate recall showed a negative correlation with mean diffusivity, radial diffusivity, and axial diffusivity of the right inferior longitudinal fasciculus, whereas delayed recall negatively correlated with diffusivity measurements of the right anterior thalamic radiations and bilateral inferior longitudinal fasciculus.

There was no statistically significant correlation between fractional anisotropy and any of the neuropsychology assessment scores in the ETCI group. No significant correlation was found between neuropsychological test scores and any of the diffusion measures in the ETNCI and HC groups.

## DISCUSSION

Cognitive impairments often accompany typical motor symptoms of ET. Cognitive impairments related to impairments in the frontal-cerebellar circuit appear to be the most prominent feature of ET.<sup>4</sup> Despite the high prevalence of ET and the impact of cognitive impairments on quality of life, the spectrum and neural basis of these impairments are not fully characterized. Although a number of DTI studies have been conducted to better understand ET pathology, none have focused on the cognitive correlates of the disease. To our knowledge, our study is the first to comprehensively study the broad range of cognitive deficits in ET by using a structured neuropsychological battery and to correlate them with the structural abnormalities identified by using DTI.

We analyzed DTI measures that are thought to reflect the following: 1) directional WM integrity (fractional anisotropy), 2) tissue breakdown with increased water content (mean diffusivity), and 3) the integrity of axons versus their adjacent myelin sheaths (radial diffusivity and axial diffusivity).<sup>20</sup> Diffusion anisotropy (fractional anisotropy) may not be enough to better characterize the tissue microstructure. If diffusion changes along the direction of the semi-major axis (axial diffusivity) are proportional to those of the semi-minor axes (radial diffusivity), then fractional anisotropy, which is the ratio of axial diffusivity and radial diffusivity, would remain relatively unchanged.<sup>21</sup> Thus, it is recommended that studies use multiple diffusion tensor measures

to assess WM integrity comprehensively.<sup>21</sup> Our analysis revealed changes in the ETCI group mainly involving the bilateral frontal parietal WM. The changes were mainly observed in mean diffusivity, radial diffusivity, and axial diffusivity. This finding is similar to those in studies performing whole-brain analysis by using TBSS in patients with ET.<sup>9,10</sup> Significant changes in fractional anisotropy of the cerebrum and cerebellum have been reported in various region-of-interest-based studies in patients with ET.<sup>8,9</sup> The reason for these changes is unclear, but a possible explanation might be attributable to subtle changes in fractional anisotropy that can be detected within ROIs, which however may not survive stringent whole-brain statistical analysis. A region-of-interest approach can be artifactual because even a subtle amount of atrophy in a tract of interest could lead to wrong placement of ROIs.<sup>21</sup> Thus, region-of-interest results need to be interpreted with caution.

Executive function is often regarded as the most common cognitive deficit in patients with ET.<sup>4</sup> In the present study, executive and working memory dysfunction showed a correlation with DTI measures in the right medial frontal gyrus, right cingulum, bilateral anterior thalamic radiations, bilateral superior longitudinal fasciculus, left uncinate fasciculus, and bilateral cerebellum (posterior lobe). Our results revealed that executive dysfunction in ET was largely associated with changes in frontal WM. Lesion studies have demonstrated that the frontal lobe is crucial for executive functions.<sup>22</sup> Zheng et al<sup>23</sup> also reported involvement of frontal connections while testing DTI correlates of executive dysfunction in Parkinson disease. However, a meta-analysis of neuroimaging and lesion studies revealed that executive functions are sensitive, but not specific, to frontal lobe functioning, meaning that both frontal and nonfrontal brain regions are necessary for executive functions.<sup>24</sup>

Our results are in agreement with this finding. We also found correlation of executive dysfunction with temporal lobe projections. The temporal lobe has several WM projections, including the cingulum, which are involved in many brain functions, such as working memory and attention.<sup>25</sup> The superior longitudinal fasciculus, inferior longitudinal fasciculus, and uncinate fasciculus have an important role in executive function, language, and memory.<sup>26</sup> Our results are suggestive of a possible relationship between WM integrity in the anterior thalamic radiations and executive performance. This finding is consistent with the role of the anterior thalamic radiations in cognition because the anterior thalamic radiations carry fibers from the thalamic nuclei to the prefrontal cortex, which are involved in executive function and planning complex behaviors.<sup>27-30</sup> Thalamic atrophy has been related to cognitive performance in many neurodegenerative disorders, such as Huntington disease, mostly affecting the executive functioning of patients.<sup>31</sup> Thus, our finding of a correlation between anterior thalamic radiations–impaired diffusivity and executive dysfunction is consistent with prior work, suggesting the importance of thalamic-prefrontal connections in executive control.

Neuropathologic research supports the role of cerebellar degeneration in the pathogenesis of ET, but its role in cognitive dysfunction remains unclear.<sup>32</sup> Research in patients with focal lesions (strokes or tumors) and fMRI in healthy subjects has

shown the role of the cerebellum in a variety of cognitive functions.<sup>11</sup> An fMRI study by Passamonti et al<sup>33</sup> showed abnormal activation of the cingulum and cerebellum (posterior lobe) in patients with ET during working memory trials. In our previous study on the correlation of GM volume with cognitive dysfunction in ET, we found that executive dysfunction correlated with GM volume values in the frontal lobe, cingulum, and cerebellum (posterior lobe).<sup>34</sup> The overactivation of the cingulum and cerebellum during working memory trials in an fMRI study<sup>33</sup> may represent compensation for volume loss and loss of WM integrity of these areas observed in our study.

We observed significant impairment of the visuospatial functions in ETCI, an observation similar to that reported by Sahin et al.<sup>3</sup> Daniels et al<sup>35</sup> reported relative expansion of GM volume bilaterally in the region of the temporal parietal junction in patients with ET and attributed this to adaptive reorganization for compromised visuospatial functioning. In the present study, visuospatial dysfunction was correlated with diffusion measures of the right parieto-occipital lobe. Our previous study also found a correlation of visuospatial dysfunction with GM volume values in the parietal, temporal, and occipital lobes.<sup>34</sup> The right occipital and right parietal cortices are specialized for visuospatial function.<sup>36</sup> The correlation of the visuospatial dysfunction score with GM volume changes and diffusion parameters in these areas may suggest that structural damage in these areas may contribute to underlying dysfunction.

In the present study, we also found impairment in visual and verbal memory correlating with diffusion measures of the right anterior thalamic radiations, bilateral inferior longitudinal fasciculus, right uncinate fasciculus, and posterior lobe of the cerebellum. The inferior longitudinal fasciculus is known to play an important role in visual memory as demonstrated by previous postmortem, lesion, and imaging studies.<sup>26</sup> The uncinate fasciculus plays a role in the formation and retrieval of memories.<sup>26</sup> Thus, memory impairment seen in patients with ET may represent involvement of the cerebellothalamocortical loop. The involvement of memory seen in our study may help explain the risk of dementia in patients with ET, as demonstrated by a few previous studies.<sup>37,38</sup>

In our study, an association was observed between cognition and WM microstructure in ET. Such an association has been demonstrated in different degenerative disorders such as Parkinson disease and Alzheimer disease.<sup>23,39</sup> It suggests a role of neurodegeneration in cognitive deficits seen in ET. Neuropathologic studies also provide evidence of neurodegeneration in ET.<sup>32</sup> Novellino et al,<sup>40</sup> for the first time, demonstrated increased iron accumulation in a group of patients with ET by using T2\* MR imaging, further strengthening the role of neurodegeneration in ET. Prospective longitudinal neuroimaging studies coupled with neuropathology are needed to substantiate the role of neurodegeneration in ET.

### Limitations

Even though careful clinical examination was performed to exclude Parkinson disease, a dopamine transporter scan to demonstrate the integrity of the nigrostriatal network was not performed. TBSS definitely has its advantages in DTI analysis;

nonetheless, it is not without limitations. In regions of crossing tracts or junctions, it may be inefficient in detecting changes in DTI parameters. Finally, the results of our correlation analysis should be interpreted carefully because they were not controlled for multiple comparisons, which may lead to false-positives. Moreover, in view of the cross-sectional design of the present study, future longitudinal studies would be needed to better assess the course of neuroanatomic changes and cognitive impairment in ET.

## CONCLUSIONS

This study demonstrates microstructural changes in the WM of patients with ET with cognitive impairment. These changes correlated with abnormal neuropsychological test scores in various brain regions. Such mapping of WM networks may provide insight into the etiology of cognitive impairment in ET.

## REFERENCES

- Lombardi WJ, Woolston DJ, Roberts JW, et al. **Cognitive deficits in patients with essential tremor.** *Neurology* 2001;57:785–90
- Chandran V, Pal PK, Reddy JY, et al. **Non-motor features in essential tremor.** *Acta Neurol Scand* 2012;125:332–37
- Sahin HA, Terzi M, Ucak S, et al. **Frontal functions in young patients with essential tremor: a case comparison study.** *J Neuropsychiatry Clin Neurosci* 2006;18:64–72
- Gasparini M, Bonifati V, Fabrizio E, et al. **Frontal lobe dysfunction in essential tremor: a preliminary study.** *J Neurol* 2001;248:399–402
- Bagepally BS, Bhatt MD, Chandran V, et al. **Decrease in cerebral and cerebellar gray matter in essential tremor: a voxel-based morphometric analysis under 3T MRI.** *J Neuroimaging* 2012;22:275–78
- Benito-León J, Alvarez-Linera J, Hernandez-Tamames JA, et al. **Brain structural changes in essential tremor: voxel-based morphometry at 3-Tesla.** *J Neurol Sci* 2009;287:138–42
- Martinelli P, Rizzo G, Manners D, et al. **Diffusion-weighted imaging study of patients with essential tremor.** *Mov Disord* 2007;22:1182–85
- Shin DH, Han BS, Kim HS, et al. **Diffusion tensor imaging in patients with essential tremor.** *AJNR Am J Neuroradiol* 2008;29:151–53
- Klein JC, Lorenz B, Kang JS, et al. **Diffusion tensor imaging of white matter involvement in essential tremor.** *Hum Brain Mapp* 2011;32:896–904
- Saini J, Bagepally BS, Bhatt MD, et al. **Diffusion tensor imaging: tract based spatial statistics study in essential tremor.** *Parkinsonism Relat Disord* 2012;18:477–82
- Schmahmann JD. **From movement to thought: anatomic substrates of the cerebellar contribution to cognitive processing.** *Hum Brain Mapp* 1996;4:174–98
- Chouinard S, Louis ED, Fahn S. **Agreement among movement disorder specialists on the clinical diagnosis of essential tremor.** *Mov Disord* 1997;12:973–76
- Petersen RC, Doody R, Kurz A, et al. **Current concepts in mild cognitive impairment.** *Arch Neurol* 2001;58:1985–92
- Moering RG, Schinka JA, Mortimer JA, et al. **Normative data for elderly African Americans for the Stroop Color and Word Test.** *Arch Clin Neuropsychol* 2004;19:61–71
- Benton AL, Varney NR, Hamsher KD. **Visuospatial judgment: a clinical test.** *Arch Neurol* 1978;35:364–67
- Smith SM, Jenkinson M, Johansen-Berg H, et al. **Tract-based spatial statistics: voxelwise analysis of multi-subject diffusion data.** *Neuroimage* 2006;31:1487–505
- Behrens TE, Woolrich MW, Jenkinson M, et al. **Characterization and propagation of uncertainty in diffusion-weighted MR imaging.** *Magn Reson Med* 2003;50:1077–88
- Smith SM, Jenkinson M, Woolrich MW, et al. **Advances in functional and structural MR image analysis and implementation as FSL.** *Neuroimage* 2004;23(suppl 1):S208–19
- Smith SM, Johansen-Berg H, Jenkinson M, et al. **Acquisition and voxelwise analysis of multi-subject diffusion data with tract-based spatial statistics.** *Nat Protoc* 2007;2:499–503
- Oertel-Knöchel V, Reinke B, Alves G, et al. **Frontal white matter alterations are associated with executive cognitive function in euthymic bipolar patients.** *J Affect Disord* 2014;155:223–33
- Acosta-Cabronero J, Williams GB, Pengas G, et al. **Absolute diffusivities define the landscape of white matter degeneration in Alzheimer's disease.** *Brain* 2010;133:529–39
- Rowe AD, Bullock PR, Polkey CE, et al. **"Theory of mind" impairments and their relationship to executive functioning following frontal lobe excisions.** *Brain* 2001;124:600–16
- Zheng Z, Shemmassian S, Wijekoon C, et al. **DTI correlates of distinct cognitive impairments in Parkinson's disease.** *Hum Brain Mapp* 2014;35:1325–33
- Alvarez JA, Emory E. **Executive function and the frontal lobes: a meta-analytic review.** *Neuropsychol Rev* 2006;16:17–42
- Sepulcre J, Masdeu JC, Pastor MA, et al. **Brain pathways of verbal working memory: a lesion-function correlation study.** *Neuroimage* 2009;47:773–78
- Sasson E, Doniger GM, Pasternak O, et al. **White matter correlates of cognitive domains in normal aging with diffusion tensor imaging.** *Front Neurosci* 2013;7:32
- Floresco SB, Grace AA. **Gating of hippocampal-evoked activity in prefrontal cortical neurons by inputs from the mediodorsal thalamus and ventral tegmental area.** *J Neurosci* 2003;23:3930–43
- Mamah D, Conturo TE, Harms MP, et al. **Anterior thalamic radiation integrity in schizophrenia: a diffusion-tensor imaging study.** *Psychiatry Res* 2010;183:144–50
- Van der Werf YD, Jolles J, Witter MP, et al. **Contributions of thalamic nuclei to declarative memory functioning.** *Cortex* 2003;39:1047–62
- Zoppelt D, Koch B, Schwarz M, et al. **Involvement of the mediodorsal thalamic nucleus in mediating recollection and familiarity.** *Neuropsychologia* 2003;41:1160–70
- Kassubek J, Juengling FD, Ecker D, et al. **Thalamic atrophy in Huntington's disease co-varies with cognitive performance: a morphometric MRI analysis.** *Cereb Cortex* 2005;15:846–53
- Louis ED, Faust PL, Vonsattel JP, et al. **Neuropathological changes in essential tremor: 33 cases compared with 21 controls.** *Brain* 2007;130:3297–307
- Passamonti L, Novellino F, Cerasa A, et al. **Altered cortical-cerebellar circuits during verbal working memory in essential tremor.** *Brain* 2011;134:2274–86
- Bhalsing KS, Upadhyay N, Kumar KJ, et al. **Association between cortical volume loss and cognitive impairments in essential tremor.** *Eur J Neurol* 2014;21:874–83
- Daniels C, Peller M, Wolff S, et al. **Voxel-based morphometry shows no decreases in cerebellar gray matter volume in essential tremor.** *Neurology* 2006;67:1452–56
- Nobre AC, Sebestyen GN, Gitelman DR, et al. **Functional localization of the system for visuospatial attention using positron emission tomography.** *Brain* 1997;120(pt 3):515–33
- Benito-León J, Louis ED, Bermejo-Pareja F. **Elderly-onset essential tremor is associated with dementia.** *Neurology* 2006;66:1500–05
- Bermejo-Pareja F, Louis ED, Benito-Leon J. **Risk of incident dementia in essential tremor: a population-based study.** *Mov Disord* 2007;22:1573–80
- Fellgiebel A, Schermuly I, Gerhard A, et al. **Functional relevant loss of long association fibre tracts integrity in early Alzheimer's disease.** *Neuropsychologia* 2008;46:1698–706
- Novellino F, Cherubini A, Chiriaco C, et al. **Brain iron deposition in essential tremor: a quantitative 3-Tesla magnetic resonance imaging study.** *Mov Disord* 2013;28:196–200

# Susceptibility-Weighted Imaging Improves the Diagnostic Accuracy of 3T Brain MRI in the Work-Up of Parkinsonism

F.J.A. Meijer, A. van Rumund, B.A.C.M. Fassen, I. Titulaer, M. Aerts, R. Esselink, B.R. Bloem, M.M. Verbeek, and B. Goraj



## ABSTRACT

**BACKGROUND AND PURPOSE:** The differentiation between Parkinson disease and atypical parkinsonian syndromes can be challenging in clinical practice, especially in early disease stages. Brain MR imaging can help to increase certainty about the diagnosis. Our goal was to evaluate the added value of SWI in relation to conventional 3T brain MR imaging for the diagnostic work-up of early-stage parkinsonism.

**MATERIALS AND METHODS:** This was a prospective observational cohort study of 65 patients presenting with parkinsonism but with an uncertain initial clinical diagnosis. At baseline, 3T brain MR imaging with conventional and SWI sequences was performed. After clinical follow-up, probable diagnoses could be made in 56 patients, 38 patients diagnosed with Parkinson disease and 18 patients diagnosed with atypical parkinsonian syndromes, including 12 patients diagnosed with multiple system atrophy–parkinsonian form. In addition, 13 healthy controls were evaluated with SWI. Abnormal findings on conventional brain MR imaging were grouped into disease-specific scores. SWI was analyzed by a region-of-interest method of different brain structures. One-way ANOVA was performed to analyze group differences. Receiver operating characteristic analyses were performed to evaluate the diagnostic accuracy of conventional brain MR imaging separately and combined with SWI.

**RESULTS:** Disease-specific scores of conventional brain MR imaging had a high specificity for atypical parkinsonian syndromes (80%–90%), but sensitivity was limited (50%–80%). The mean SWI signal intensity of the putamen was significantly lower for multiple system atrophy–parkinsonian form than for Parkinson disease and controls ( $P < .001$ ). The presence of severe dorsal putaminal hypointensity improved the accuracy of brain MR imaging: The area under the curve was increased from 0.75 to 0.83 for identifying multiple system atrophy–parkinsonian form, and it was increased from 0.76 to 0.82 for identifying atypical parkinsonian syndromes as a group.

**CONCLUSIONS:** SWI improves the diagnostic accuracy of 3T brain MR imaging in the work-up of parkinsonism by identifying severe putaminal hypointensity as a sign indicative of multiple system atrophy–parkinsonian form.

**ABBREVIATIONS:** AP = atypical parkinsonian syndromes; AUC = area under the curve; CBS = corticobasal syndrome; DLB = dementia with Lewy bodies; HC = healthy controls; MSA = multiple system atrophy; MSA-P = multiple system atrophy–parkinsonian form; PD = Parkinson disease; PSP = progressive supranuclear palsy; ROC = receiver operating characteristic; SI = signal intensity

In clinical practice, the differentiation between Parkinson disease (PD) and atypical parkinsonian syndromes (AP), such as multiple system atrophy (MSA), progressive supranuclear palsy (PSP), corticobasal syndrome (CBS), and dementia with Lewy bodies (DLB), can be challenging. For adequate patient counsel-

ing and treatment planning, it is important to make the correct diagnosis at an early disease stage. Ancillary investigations such as brain MR imaging can be performed to increase certainty about the diagnosis. In the diagnostic work-up of parkinsonism, performing brain MR imaging is advised because it can support the diagnosis of AP or vascular parkinsonism.<sup>1</sup> Also, brain MR imaging can demonstrate other more rare causes of parkinsonism such as normal pressure hydrocephalus or multiple sclerosis.

Conventional brain MR imaging findings, including those of T1, T2, T2 FLAIR, and proton-attenuation sequences, are usually normal in PD or will show age-related changes.<sup>2</sup> Atrophy or

Received June 16, 2014; accepted after revision August 10.

From the Departments of Radiology and Nuclear Medicine (F.J.A.M., B.A.C.M.F., B.G.) and Laboratory Medicine (M.M.V.), and Department of Neurology (A.v.R., I.T., M.A., R.E., B.R.B., M.M.V.), Donders Institute for Brain, Cognition and Behavior, Radboud University Nijmegen Medical Center, Nijmegen, the Netherlands; and Department of Diagnostic Imaging (B.G.), Medical Center of Postgraduate Education, Warsaw, Poland.

This work was supported by Stichting Internationaal Parkinson Fonds and het Van Alkemade Keuls Fonds.

Please address correspondence to Frederick J.A. Meijer, MD, Radboud University Nijmegen Medical Center, Department of Radiology and Nuclear Medicine, Postbus 9101, 6500 HB Nijmegen, the Netherlands; e-mail: Anton.Meijer@radboudumc.nl

 Indicates article with supplemental on-line tables.

 Indicates article with supplemental on-line photo.

<http://dx.doi.org/10.3174/ajnr.A4140>

**Table 1: MRI scanning protocol**

Sequence	TR (ms)	TE (ms)	Flip Angle	Voxel Size (mm)	No. and Direction of Sections	iPAT Factor	Acquisition Time (min:sec)
T2 TSE	5830	120	120°	0.6 × 0.6 × 3	48 Axial	—	3:43
T1 MPRAGE	2300	4.71	12°	1 × 1 × 1	192 Sagittal	2	5:47
T2 FLAIR	9000	86	150°	0.7 × 0.6 × 5	28 Axial	2	2:44
Proton-attenuation	2000	20	90°	0.9 × 0.9 × 3	48 Axial	—	7:16
DWI-EPI ( <i>b</i> =0 and <i>b</i> =1000)	3900	89	90°	1.3 × 1.3 × 5	48 Axial	2	2:10
SWI gradient-echo	29	20	15°	0.6 × 0.6 × 3	48 Axial	2	4:42

**Note:**—iPAT indicates integrated parallel acquisition technique.

signal-intensity (SI) changes of specific regions of the brain identified on brain MR imaging can have high specificity for the different forms of AP. Examples include putaminal or pontine atrophy in MSA and midbrain atrophy (hummingbird sign) in PSP. The sensitivity of brain MR imaging for AP is generally limited, especially in early disease stages.<sup>3-5</sup>

New MR imaging techniques have become available for clinical practice in recent years, including susceptibility-weighted imaging. SWI is sensitive to magnetic susceptibility differences in tissues such as blood, calcification, and iron deposition. Because SWI makes use of both magnitude and phase information during image acquisition, it is superior in detecting brain susceptibility changes in comparison with T2\* gradient-echo sequences.<sup>6,7</sup> SWI is emerging as a useful technique in a wide variety of intracranial pathologies, including neurodegenerative diseases.<sup>8</sup> In parkinsonian syndromes, there are different patterns of abnormal brain iron metabolism in PD and AP. Examples include increased iron accumulation in the substantia nigra in PD and increased striatal iron content in MSA.<sup>9</sup> These patterns of abnormal brain iron content should be differentiated from physiologic age-related iron accumulation.<sup>10,11</sup> Also, there still is debate about whether disturbances in iron levels in PD constitute representation of the primary pathologic process or are a secondary consequence.<sup>12</sup> This debate is highly relevant for SWI because it influences whether abnormal iron content in brain structures can be identified in early-stage PD or AP. Initial reports on SWI in parkinsonism indicate that SWI may provide new diagnostic markers for clinical use.<sup>13,14</sup>

The goal of our study was to evaluate whether SWI is of added value in relation to conventional 3T brain MR imaging in the diagnostic work-up of early-stage parkinsonism.

## MATERIALS AND METHODS

### Study Group

We performed a prospective observational study in 65 patients presenting with parkinsonism with a disease duration of <3 years, with major uncertainty of the underlying diagnosis on inclusion. Patients were consecutively recruited at our outpatient movement disorder clinic during 2010–2012. Study inclusion criteria were clinical signs and symptoms of parkinsonism (hypokinetic-rigid syndrome) with an uncertain clinical diagnosis and disease duration of <3 years. Exclusion criteria were age younger than 18 years, prior brain surgery, the presence of another neurodegenerative disorder, and unstable comorbidity. The medical ethics committee of our hospital approved the study, and all participants gave written informed consent. For the sake of the SWI analyses, we also enrolled 13 age- and sex-matched healthy controls, who were scanned with the SWI sequence.

### Study Design

Patients had a clinical assessment at baseline by standardized history taking and neurologic examination by an experienced physician (M.A., A.v.R.). Cardiovascular risk factors, activities in daily living, medication use, disease onset, clinical signs, most affected body site, and balance and fear of falling were assessed. Clinical neurologic scores were applied, including the Non-Motor Symptoms Scale<sup>15</sup> and the Mini-Mental State Examination<sup>16</sup> to evaluate global cognitive status and the Unified Parkinson's Disease Rating Scale<sup>17</sup> and the Hoehn and Yahr Staging Scale<sup>18</sup> to evaluate motor function.

At baseline, all patients underwent brain MR imaging. After clinical follow-up, final diagnoses could be made by 2 experienced clinicians (A.v.R., R.E.). These diagnoses were made according to international diagnostic criteria<sup>19-24</sup> based on neurologic signs that developed during the course of the disease (as identified during repeat neurologic examinations), rate of disease progression, and treatment response. Our primary interest was to evaluate the added value of SWI in relation to conventional 3T brain MR imaging performed in the early disease stage in differentiating PD and the various forms of AP.

### Brain MR Imaging Protocol

At baseline, all patients underwent 3T MR imaging of the brain (Magnetom Trio; Siemens, Erlangen, Germany). The scanning protocol included 3D T1 MPRAGE, T2 TSE, T2 FLAIR, proton-attenuation, and DWI sequences. The SWI sequence was a 3D gradient echo acquisition; magnitude and phase images were obtained in the axial plane. Details of the scanning protocol are provided in Table 1. In addition to our patient cohort, 13 age-matched healthy controls (HC) were scanned with the SWI sequence.

### Imaging Analysis

Two neuroradiologists (F.J.A.M. and B.G.) evaluated conventional brain MR imaging studies in a standardized manner, blinded to clinical information. First, abnormalities that have been validated for the evaluation of parkinsonian syndromes were scored.<sup>3-5,25</sup> Second, selected abnormalities were grouped in a score typical for a given disease. Atrophy and T2 hypointensity changes of the putamen, pontine atrophy, hot cross bun sign, cerebellar atrophy, and T2 hyperintense signal changes of the middle cerebellar peduncle were combined in the "MSA" score. Midbrain atrophy, hummingbird sign, and a reduced AP midbrain diameter of <14 mm were scored and combined in the "PSP" score. Cortical atrophy and third and lateral ventricle dilation were scored and combined in the "Atrophy" score as a manifestation of CBS or DLB. The "MSA," "PSP," and "Atrophy" scores combined resulted in the "Sum" score, which was used to

evaluate AP as a group. Several thresholds (eg, the presence of 1, 2, 3, or 4 abnormalities) were applied to these scores to evaluate the diagnostic accuracy of conventional brain MR imaging for the different forms of AP. Furthermore, white matter changes and the presence of infarction were scored.

The region-of-interest method was used to evaluate the SWI sequences on an Impax workstation, Version 6.5.3 (Agfa-Gevaert, Mortsel, Belgium). A 4.9-mm<sup>2</sup> circular region of interest was placed bilaterally in the following structures: caudate nucleus, putamen (anterior and posterior), red nucleus, substantia nigra (anterior and posterior), globus pallidus, thalamus, pulvinar thalamus, and dentate nucleus. The region of interest was placed in the most hypointense part of the brain structure, avoiding vessels and not including the edges of the structure. Additionally, the signal intensity of CSF was measured by region-of-interest placement in the fourth ventricle. SWI signal intensity of the different brain structures was normalized to CSF with a signal intensity of 200, to correct for inconsistencies in the reference standard. Two readers (F.J.A.M. and B.A.C.M.F.), blinded to the clinical symptoms and diagnoses, performed the region-of-interest analysis of the SWI sequences. One reader (B.A.C.M.F.) performed the region-of-interest analysis twice to evaluate intrarater variability.

Increased susceptibility is defined here as decreased SWI signal intensity. On the basis of the mean signal intensity values obtained, the hypointensity was graded according to the criteria proposed by Gupta et al (Fig 1)<sup>13</sup>:

Grade 0: SI similar to CSF intensity (SI > 200)

Grade 1: mild hypointensity (SI > 150 but < 200)

Grade 2: moderate hypointensity (SI > 75 but < 150)

Grade 3: severe hypointensity (SI < 75).

### Statistical Analyses

The diagnostic accuracy of the conventional brain MR imaging “MSA,” “PSP,” “Atrophy,” and “Sum” scores to identify the different forms of AP was calculated. Cohen  $\kappa$  coefficient was used to evaluate interrater variability of abnormalities scored on conventional brain MR imaging. For SWI, both intra- and interrater agreement was evaluated. Agreement was graded as the following:  $\kappa < 0.20$ , poor agreement; 0.21–0.40, fair agreement; 0.41–0.60, moderate agreement; 0.61–0.80, good agreement;  $> 0.80$ , perfect agreement.

The mean SWI signal intensity of the brain structures was calculated for each diagnosis, and 1-way ANOVA, corrected for multiple comparisons with a Bonferroni correction, was performed to analyze group differences. A *P* value < .05 was considered statistically significant for disease-specific SWI changes.

Finally, the area under the curve (AUC) of the receiver operating characteristic (ROC) was used to evaluate the discriminative power of conventional brain MR imaging alone and in combination with selected SWI measures.

All statistical analyses were performed with SPSS (Version 20; IBM, Armonk, New York).

## RESULTS

### Study Group

Patients had a mean follow-up of 24.8 ± 12 months. Of the 65 patients, 9 were excluded for the following reasons: brain MR

imaging with severe artifacts (*n* = 2), uncertain diagnosis (*n* = 4), diagnosis other than PD or AP (*n* = 1), and diagnosis of vascular parkinsonism (*n* = 2).

Of the remaining 56 patients, 38 patients were diagnosed with PD, and 18 patients, with AP (12 with multiple system atrophy-parkinsonian form [MSA-P], 3 with PSP, and 3 with DLB). Demographic data of the study population and control group are shown in Table 2.

### Conventional Brain MR Imaging Results

Abnormalities scored on conventional brain MR imaging are summarized in On-line Table 1. Overall there was good interrater agreement for the abnormalities scored on brain MR imaging with perfect interrater agreement ( $\kappa > 0.8$ ) for atrophy and signal-intensity changes of the putamen and midbrain. Pontine and cerebellar atrophy and T2 hyperintensity changes of the middle cerebellar peduncle showed moderate interrater agreement ( $\kappa = 0.47$ –0.54). There was poor agreement for the putaminal rim sign. The putaminal rim sign proved not to be indicative of MSA on 3T MR imaging (sensitivity, 42%; specificity, 48% for MSA), which is in line with a previous report.<sup>26</sup> Therefore, we did not include the putaminal rim sign in further analyses.

The diagnostic accuracy of conventional brain MR imaging abnormalities combined in group scores to identify the different forms of AP is shown in Table 3. Sensitivity and specificity can be influenced by choosing a threshold—eg, the presence of at least 1 abnormality for the “MSA” score to identify MSA-P results in 83% sensitivity with 66% specificity, while the presence of at least 2 abnormalities results in 25% sensitivity with 93% specificity. The presence of at least 2 abnormalities on conventional brain MR imaging has reasonable sensitivity (78%) and specificity (76%) to identify AP as a group. The specificity for AP can be increased (89%) by considering the presence of at least 4 abnormalities for the diagnosis of AP, though at the cost of sensitivity (50%).

### MR Imaging SWI Analysis

Significantly lower mean SWI signal intensity of the putamen was found in MSA-P, in comparison with PD and HC (On-line Table 2). This finding was consistent for both sides and the anterior and posterior parts of the putamen (all regions, *P* < .001 for MSA-P versus PD, for both readers). Signal intensity of the posterior putamen was compared with that of the anterior part. The distribution of putaminal signal intensities for the different disease groups demonstrated that grade 3 hypointensity changes of the posterior putamen discriminated MSA-P from the other groups (boxplots in On-line Fig 1). For the anterior putamen, the presence of grade 2 or 3 hypointensity changes discriminated MSA-P from the other groups. There was good intrarater ( $\kappa = 0.76$ ) and interrater ( $\kappa = 0.80$ ) agreement for the putaminal SWI hypointensity grading.

Lower mean SWI signal intensity of the caudate nucleus was seen in MSA-P; the difference in signal intensity was statistically significant on the left side in comparison to PD. Caudate nucleus signal intensity (mean grade 1 hypointensity) was not as low as that for the putamen. In PSP, significantly decreased mean SWI

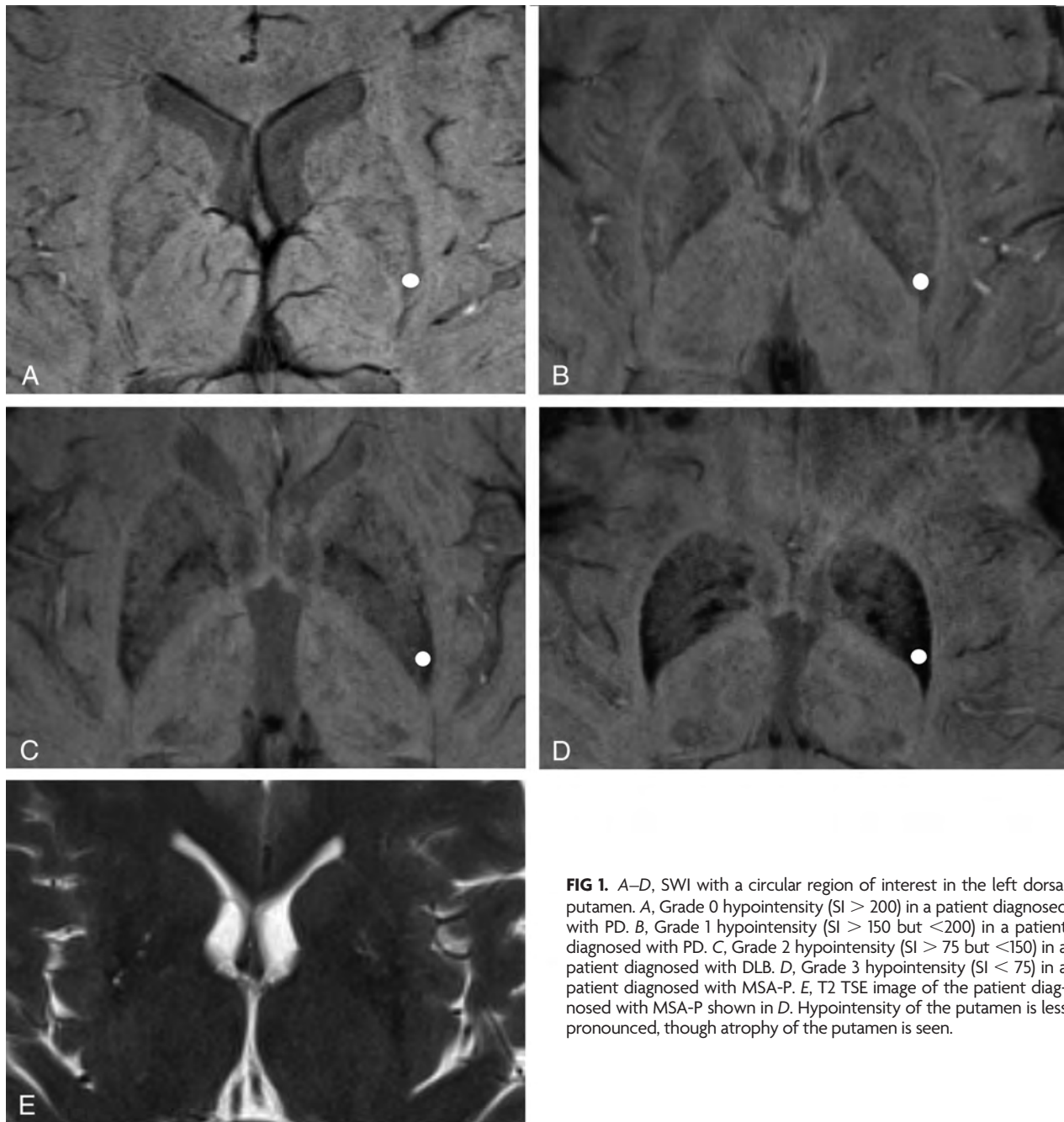


**FIG 1.** A–D, SWI with a circular region of interest in the left dorsal putamen. A, Grade 0 hypointensity (SI > 200) in a patient diagnosed with PD. B, Grade 1 hypointensity (SI > 150 but <200) in a patient diagnosed with PD. C, Grade 2 hypointensity (SI > 75 but <150) in a patient diagnosed with DLB. D, Grade 3 hypointensity (SI < 75) in a patient diagnosed with MSA-P. E, T2 TSE image of the patient diagnosed with MSA-P shown in D. Hypointensity of the putamen is less pronounced, though atrophy of the putamen is seen.

**Table 2: Patient characteristics<sup>a</sup>**

	PD (n = 38)	AP (n = 18)	MSA-P (n = 12)	PSP (n = 3)	DLB (n = 3)	HC (n = 13)
Age (yr)	61 (9)	65 (8)	63 (9)	67 (5)	69 (3)	67 (7)
Sex (M/F)	23:15	9:9	6:6	1:2	2:1	9:4
Disease duration (mo)	19.1 (14)	15.2 (12)	15.5 (11)	23.0 (20)	6.7 (7)	–
UPDRS-III	32.1 (12)	45.2 (11)	45.5 (12)	47.5 (13)	42.7 (11)	–
H&Y	1.7 (0.7)	2.6 (0.9)	2.6 (1.0)	3.0 (0)	2.3 (0.6)	–
MMSE	28.5 (1.6)	28.1 (1.6)	28.4 (1.4)	28.7 (0.6)	26.0 (1.0)	–

**Note:**—UPDRS-III indicates Unified Parkinson’s Disease Rating Scale—III; H&Y, Hoehn and Yahr Staging Scale; MMSE, Mini-Mental State Examination.

<sup>a</sup> Data are mean or number (SD).

signal intensities (grade 2 hypointensity) of the red and dentate nuclei on the left side were found in comparison with those in PD and HC.

In comparison with the different forms of AP and HC, no

statistically significant SWI signal-intensity changes of the different brain structures were found for PD.

On the basis of the findings above, SWI hypointensity grading of the putamen was used for further analyses in eval-

**Table 3: Frequency (%) of positive results<sup>a</sup>**

	PD (n = 38)	MSA-P (n = 12)	PSP (n = 3)	DLB (n = 3)	Sensitivity/Specificity	$\kappa$ (Interrater)
"MSA" score, threshold 1	11 (29)	10 (83)	1 (33)	3 (100)	83%/66% for MSA	0.64
"MSA" score, threshold 2	2 (5)	3 (25)	0 (0)	1 (33)	25%/93% for MSA	0.59
"PSP" score, threshold 1	0 (0)	1 (8)	3 (100)	0 (0)	100%/98% for PSP	0.88
"Atrophy" score, threshold 2	7 (18)	4 (33)	3 (100)	2 (67)	67%/74% for DLB	0.86
"Sum" score, threshold 2	9 (24)	8 (67)	3 (100)	3 (100)	78%/76% for AP	0.75
"Sum" score, threshold 3	8 (21)	5 (42)	3 (100)	2 (67)	56%/79% for AP	0.80
"Sum" score, threshold 4	4 (11)	4 (33)	3 (100)	2 (67)	50%/89% for AP	0.64

<sup>a</sup>Threshold criteria defined as the presence of either 1, 2, 3, or 4 abnormalities on conventional brain MRI for the different scores.

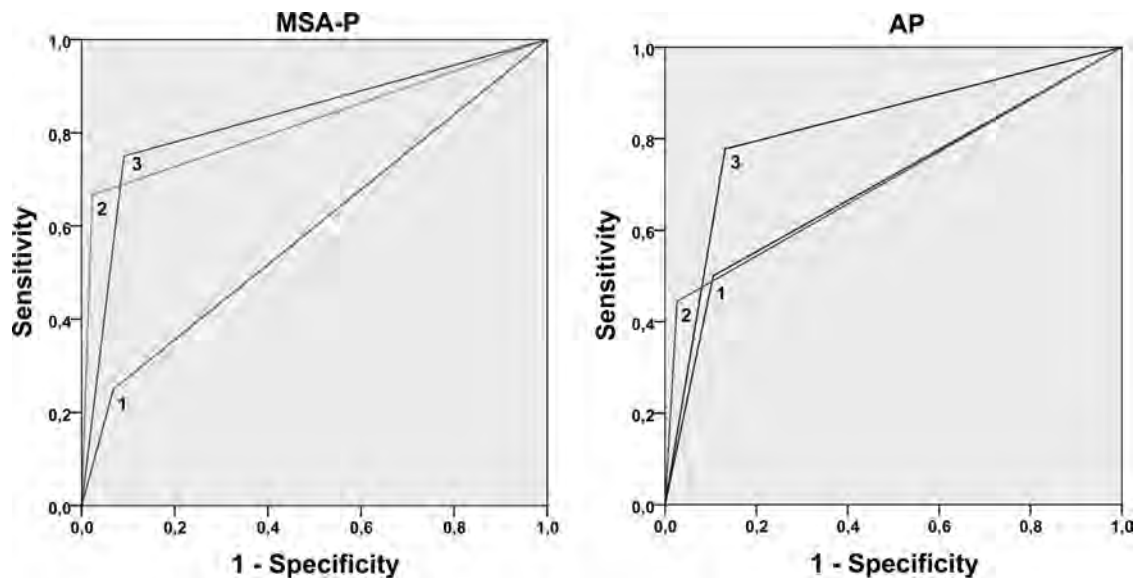


**FIG 2.** ROC curves to evaluate diagnostic accuracy. Point 1 indicates the brain MR imaging "MSA" score to identify MSA-P, threshold 2 abnormalities (left figure), and the MR imaging "Sum" score to identify AP as a group, threshold 4 abnormalities (right figure). Point 2 is the grade 3 SWI hypointensity of the dorsal putamen. Point 3 indicates points 1 and 2 combined. SWI increases sensitivity with preservation of high specificity.

uating the diagnostic accuracy of brain MR imaging and SWI.

### Evaluation of Diagnostic Accuracy

SWI grade 3 hypointensity of the posterior putamen proved to be superior to grade 2 or 3 hypointensity of the anterior putamen for identifying MSA-P (AUC, 0.82 versus 0.69). The results of the ROC analyses to evaluate the diagnostic accuracy of conventional brain MR imaging alone and in combination with SWI grade 3 hypointensities of the putamen are shown in Fig 2 and On-line Tables 3 and 4.

### Diagnosis of MSA-P

Conventional brain MR imaging "MSA" score, with a threshold of at least 2 abnormalities present, results in an AUC of 0.59 (confidence interval, 0.40–0.79) to identify MSA-P. Threshold 1 results in an AUC of 0.75 (confidence interval, 0.60–0.90). The AUC is increased to 0.83 (confidence interval, 0.68–0.98) when combining the conventional brain MR imaging threshold 2 with the presence of SWI grade 3 hypointensity of the posterior putamen. This increase in AUC is explained by a significant improvement in sensitivity (25%–75%) with preservation of high specificity (91%).

### Diagnosis of AP

The conventional brain MR imaging "Sum" score, when at least 2 abnormalities are present, results in the highest AUC of 0.76 (confidence interval, 0.62–0.90) to identify AP as a group. The AUC can be

increased to 0.82 (confidence interval, 0.69–0.95) when combining the conventional brain MR imaging "Sum" score with at least 4 abnormalities present with SWI grade 3 hypointensity of the posterior putamen. The improved diagnostic accuracy results from improved sensitivity (50%–78%) with preservation of high specificity (87%).

## DISCUSSION

Unlike previous studies, we prospectively evaluated both conventional brain MR imaging and SWI in patients presenting with parkinsonism with an initial uncertain diagnosis, in whom increase of certainty about the diagnosis is of the most clinical relevance. In our study population, the ability of conventional 3T brain MR imaging to differentiate PD and the different atypical parkinsonian syndromes was limited and depended on defined diagnostic criteria. When combined with SWI, the diagnostic accuracy was improved, mainly by identifying severe hypointensity of the putamen, which is indicative of MSA-P.

Patterns of normal age-related iron content of the different brain structures have been described in literature, including age-related increase in iron content of the putamen.<sup>27,28</sup> Because we included a group of age-matched healthy controls, it is more likely that the increased putaminal susceptibility in MSA-P found in our study reflects pathologic mineralization rather than a result of aging.

Increased iron concentrations and decreased signal intensity on T2 spin-echo and T2\* gradient echo-weighted sequences of

the putamen, but also of the caudate nucleus, have been reported previously in MSA.<sup>9,29-33</sup> Susceptibility changes of the putamen are depicted more accurately by SWI than by a T2 spin-echo sequence (Fig 1D, -E). With regard to SWI, decreased signal intensity of the putamen in MSA has been described,<sup>14</sup> though not confirmed by others.<sup>34</sup> Gupta et al<sup>13</sup> found higher putaminal SWI hypointensity scores in MSA-P, though this difference was not statistically significant. Wang et al<sup>14</sup> found increased iron deposition in the putamen in MSA-P, as we did, and reported that the lower inner region of the putamen was the most valuable subregion in differentiating MSA-P from PD, while in our study, this finding is valid for the posterior part of the putamen.

Gupta et al<sup>13</sup> reported higher hypointensity scores of the putamen and red nucleus in PSP, in comparison with PD and MSA. In our study population, the SWI signal intensities of the red nucleus and dentate nucleus were lower in PSP compared with PD, with statistical significance on the left side. This finding is in line with observed neuropathologic changes of these structures in PSP.<sup>35</sup> SWI hypointensity changes of these nuclei could therefore possibly provide a new diagnostic marker for PSP. Increased iron content in the substantia nigra and putamen have been reported in PSP mainly in advanced disease stages, but not in the amount seen in MSA.<sup>9</sup> According to the literature, there is little evidence of increased brain iron levels in DLB, but possibly the substantia nigra is affected.<sup>9</sup>

SWI signal intensity is influenced by many factors besides iron content of brain structures, including acquisition parameters and magnetic field strength but also by spatial position and reconstruction algorithms (which differ across MR imaging vendors). For reproducibility of quantitative analyses, it is important to apply a normalization technique. Our study population was scanned by using a 3T MR imaging scanner, while others used a 1.5T scanner.<sup>13,14</sup> It is likely that differences in magnetic field strengths could partly explain discrepancies in study results because a 3T MR imaging scanner is more sensitive to susceptibility changes than a 1.5T scanner.<sup>36,37</sup>

On the basis of their 3T MR imaging SWI study, Haller et al<sup>34</sup> found increased susceptibility in the thalamus and left substantia nigra in PD, and they reported good discrimination between PD and AP by using a support-vector analysis. Unfortunately, they did not include a healthy control group to evaluate whether the observed increased susceptibility in the substantia nigra and thalamus is PD-specific. In our study population, we did not observe changes in the susceptibility of the substantia nigra or other brain structures in PD in comparison with patients with AP or matched healthy control subjects. A possible explanation could be that our patients with PD were scanned in earlier disease stages. In previous studies however, no clear evidence was found of substantia nigra iron content being related to disease duration.<sup>38,39</sup> In recent in vivo and postmortem SWI studies, a subregion of the substantia nigra pars compacta, called nigrosome 1, was reported to be absent in PD.<sup>40,41</sup> A “swallow tail” appearance of the healthy nigrosome 1 and its absence in PD have recently been evaluated in a case control study with observed good discrimination between patients with PD and HC.<sup>42</sup> It is not known whether the absence of nigrosome 1 on SWI could discriminate PD from AP.

There are some limitations to our study. First, our study population was relatively small, especially for the AP group, and conclusions were mainly based on a comparison among PD, MSA-P,

and HC. Therefore, definite conclusions regarding other forms of AP cannot be made. On the other hand, the prevalence of less frequent parkinsonian syndromes in our cohort does reflect clinical practice and draws attention to the need for ancillary investigations aiming to improve certainty about the diagnosis in a patient presenting with parkinsonism. The subjects of our study were patients with parkinsonism and uncertain clinical diagnosis, which could explain the relatively low frequency of the different forms of atypical parkinsonism in our study population.

The small number of patients diagnosed with PSP could explain why the lower signal intensity values of the red nucleus and dentate nucleus were only statistically significant unilaterally. Whether the SWI sequence is of added value for the diagnosis of PSP, CBS, DLB, or other forms of AP not included in our study, such as multiple system atrophy—cerebellar form and CBS, remains to be determined. In vascular parkinsonism, SWI could be of additional value to identify microbleeds as a sign of microangiopathy, but this possibility was beyond the scope of our study.

Second, we did not have postmortem confirmation of the diagnoses; therefore, we cannot fully rule out misdiagnosis in our study population. The diagnoses were made by a movement-disorder specialist on the basis of accepted diagnostic criteria, after a mean follow-up of 24.5 months. This approach proved to yield high accuracy (>90%) as shown in a previous clinical-pathologic study.<sup>43</sup>

Third, because there are only a few studies available in which SWI has been evaluated in parkinsonism, validation of diagnostic criteria is crucial for optimal use in daily clinical practice. This validation also applies to the conventional brain sequences because diagnostic criteria have not been standardized. Because abnormalities on brain MR imaging differ for the various forms of AP, disease-specific diagnostic criteria give a more accurate estimation of the diagnostic accuracy of brain MR imaging rather than grouping all the forms of AP together. Standardization of the scanning protocol, with the magnetic field strength of the MR imaging study taken into account, and postprocessing methods is necessary for validation of diagnostic criteria.

Other advanced MR imaging techniques, including diffusion (tensor) imaging, magnetization transfer imaging, and functional MR imaging could possibly provide new diagnostic markers for PD or AP. In future clinical cohort studies, it would be interesting to study the diagnostic value of SWI in relation to these advanced imaging techniques.

## CONCLUSIONS

SWI proved a useful sequence in addition to conventional 3T brain MR imaging in the diagnostic work-up of early-stage parkinsonism. SWI improves the diagnostic accuracy of 3T brain MR imaging by detecting severe hypointensity of the putamen as a sign indicative of MSA-P.

Disclosures: Bastiaan R. Bloem—UNRELATED: Board Membership: ZonMw\*; Consultancy: UCB,\* Glaxo-Smith-Kline,\* Danone\*; Grants/Grants Pending: ZonMw\*, Michael J. Fox Foundation,\* Davis Phinney Foundation\*; Payment for Lectures (including service on Speakers Bureaus): AbbVie\*; OTHER RELATIONSHIPS: B.R. Bloem was an Editorial Board member of *Movement Disorders* (earlier) and Associate Editor for the *Journal of Parkinson's Disease* (currently), and received funds from the Alkemade Keuls fund, the Michael J. Fox Foundation, the Netherlands Organization of Scientific Research, the Prinses Beatrix Foundation, and the Stichting International Parkinson Fonds. Marcel M. Verbeek—RELATED: Grant: Stichting International Parkinson Fonds\*; OTHER RELATIONSHIPS: Associate Editor of the *Journal of Alzheimer's*

mer's Disease; Editorial Board member, *International Journal of Molecular Epidemiology and Genetics*; Editorial Board member, *American Journal of Neurodegenerative Diseases*; Editorial Board member, *Molecular Neurodegeneration*; received funding from Internationale Stichting Alzheimer Onderzoek; Joint Programming in Neurodegenerative Disease, Alzheimer's Drug Discovery Foundation. \*Money paid to the institution.

## REFERENCES

- Berardelli A, Wenning GK, Antonini A, et al. EFNS/MDS-ES/ENS [corrected] recommendations for the diagnosis of Parkinson's disease. *Eur J Neurol* 2013;20:16–34
- Brooks DJ. Morphological and functional imaging studies on the diagnosis and progression of Parkinson's disease. *J Neurol* 2000; 247(suppl 2):11–18
- Schrag A, Good CD, Miskiel K, et al. Differentiation of atypical parkinsonian syndromes with conventional brain MRI. *Neurology* 2000;54:697–702
- Mahlknecht P, Hotter A, Hussl A, et al. Significance of MRI in diagnosis and differential diagnosis of Parkinson's disease. *Neurodegener Dis* 2010;7:300–18
- Meijer FJ, Aerts MB, Abdo WF, et al. Contribution of conventional brain MRI to the differential diagnosis of parkinsonism: a 3-year prospective follow-up study. *J Neurol* 2012;259:929–35
- Haacke EM, Xu Y, Cheng YC, et al. Susceptibility weighted imaging (SWI). *Magn Reson Med* 2004;52:612–18
- Haacke EM, Cheng NY, House MJ, et al. Imaging iron stores in the brain using magnetic resonance imaging. *Magn Reson Imaging* 2005;23:1–25
- Sehgal V, Delproposto Z, Haacke EM, et al. Clinical applications of neuroimaging with susceptibility-weighted imaging. *J Magn Reson Imaging* 2005;22:439–50
- Berg D, Hochstrasser H. Iron metabolism in Parkinsonian syndromes. *Mov Disord* 2006;21:1299–310
- Haacke EM, Ayaz M, Khan A, et al. Establishing a baseline phase behavior in magnetic resonance imaging to determine normal vs. abnormal iron content in brain. *J Magn Reson Imaging* 2007;26:256–64
- Harder SL, Hopp KM, Ward H, et al. Mineralization of the deep gray matter with age: a retrospective review with susceptibility-weighted MR imaging. *AJNR Am J Neuroradiol* 2008;29:176–83
- Friedman A, Galazka-Friedman J, Kozirowski D. Iron as a cause of Parkinson disease: a myth or a well-established hypothesis? *Parkinsonism Relat Disord* 2009;15(suppl 3):212–14
- Gupta D, Saini J, Kesavadas C, et al. Utility of susceptibility-weighted MRI in differentiating Parkinson's disease and atypical parkinsonian syndromes. *Neuroradiology* 2010;52:1087–94
- Wang Y, Butros SC, Shuai X, et al. Different iron-deposition patterns of multiple system atrophy with predominant parkinsonism and idiopathic Parkinson diseases demonstrated by phase-corrected susceptibility-weighted imaging. *AJNR Am J Neuroradiol* 2012;33:266–73
- Chaudhuri KR, Martinez-Martin P. Quantitation of non-motor symptoms in Parkinson's disease. *Eur J Neurol* 2008;15(suppl 2):2–7
- Folstein MF, Robins LN, Helzer JE. The Mini-Mental State Examination. *Arch Gen Psychiatry* 1983;40:812
- Fahn S, Elton RL. Unified Parkinson's Disease Rating Scale. In: Fahn S, Marsden CD, Calne D, eds. *Recent Developments in Parkinson's Disease*. Vol 2. Florham Park: MacMillan Healthcare Information; 1987:153–63
- Hoehn MM, Yahr MD. Parkinsonism: onset, progression, and mortality. *Neurology* 1967;17:427–42
- Gelb DJ, Oliver E, Gilman S. Diagnostic criteria for Parkinson disease. *Arch Neurol* 1999;56:33–39
- Gilman S, Wenning GK, Low PA, et al. Second consensus statement on the diagnosis of multiple system atrophy. *Neurology* 2008;71:670–76
- Litvan I, Agid Y, Calne D, et al. Clinical research criteria for the diagnosis of progressive supranuclear palsy (Steele-Richardson-Olszewski syndrome): report of the NINDS-SPSP international workshop. *Neurology* 1996;47:1–9
- McKeith IG, Dickson DW, Lowe J, et al. Consortium on DLB: diagnosis and management of dementia with Lewy bodies: third report of the DLB Consortium. *Neurology* 2005;65:1863–72
- Boeve BF, Lang AE, Litvan I. Corticobasal degeneration and its relationship to progressive supranuclear palsy and frontotemporal dementia. *Ann Neurol* 2003;54(suppl 5):15–19
- Zijlmans JC, Daniel SE, Hughes AJ, et al. Clinicopathological investigation of vascular parkinsonism, including clinical criteria for diagnosis. *Mov Disord* 2004;19:630–40
- Yekhlef F, Ballan G, Macia F, et al. Routine MRI for the differential diagnosis of Parkinson's disease, MSA, PSP, and CBD. *J Neural Transm* 2003;110:151–69
- Lee WH, Lee CC, Shyu WC, et al. Hyperintense putaminal rim sign is not a hallmark of multiple system atrophy at 3T. *AJNR Am J Neuroradiol* 2005;26:2238–42
- Hallgren B, and Sourander P. The effect of age on the non-haem iron in the human brain. *J Neurochem* 1958;3:41–51
- Martin WW, Ye FQ, Allen PS. Increasing striatal iron content associated with normal aging. *Mov Disord* 1998;13:281–86
- Drayer BP, Olanow W, Burger P, et al. Parkinson plus syndrome: diagnosis using high field MR imaging of brain iron. *Radiology* 1986;159:493–98
- Martin WR, Roberts TE, Ye FQ, et al. Increased basal ganglia iron in striatonigral degeneration: in vivo estimation with magnetic resonance. *Can J Neurol Sci* 1998;25:44–47
- Vymazal J, Righini A, Brooks RA, et al. T1 and T2 in the brain of healthy subjects, patients with Parkinson disease and patients with multiple system atrophy: relation to iron content. *Radiology* 1999;211:489–95
- Kraft E, Schwarz J, Trenkwalder C, et al. The combination of hypointense and hyperintense signal changes on T2-weighted magnetic resonance imaging sequences: a specific marker of multiple system atrophy? *Arch Neurol* 1999;56:225–28
- Kraft E, Trenkwalder C, Auer DP. T2\*-weighted MRI differentiates multiple system atrophy from Parkinson's disease. *Neurology* 2002;59:1256–67
- Haller S, Badoud S, Nguyen D, et al. Differentiation between Parkinson disease and other forms of Parkinsonism using support vector machine analysis of susceptibility-weighted imaging (SWI): initial results. *Eur Radiol* 2013;23:12–19
- Collins SJ, Ahlskog JE, Parisi JE, et al. Progressive supranuclear palsy: neuropathologically based diagnostic clinical criteria. *J Neurol Neurosurg Psychiatry* 1995;58:167–73
- Nandigam RN, Viswanathan A, Delgado P, et al. MR imaging detection of cerebral microbleeds: effect of susceptibility-weighted imaging, section thickness, and field strength. *AJNR Am J Neuroradiol* 2009;30:338–43
- Wardlaw JM, Brindle W, Casado AM, et al. A systematic review of the utility of 1.5 versus 3 Tesla magnetic resonance brain imaging in clinical practice and research. *Eur Radiol* 2012;22:2295–303
- Martin WR, Wieler M, Gee M. Midbrain iron content in early Parkinson disease: a potential biomarker of disease status. *Neurology* 2008;70:1411–17
- Rossi ME, Ruottinen H, Saunamäki T, et al. Imaging brain iron and diffusion patterns: a follow-up study of Parkinson's disease in the initial stages. *Acad Radiol* 2014;21:64–71
- Blazejewska AI, Schwarz ST, Pitiot A, et al. Visualization of nigrosome 1 and its loss in PD: pathoanatomical correlation and in vivo 7 T MRI. *Neurology* 2013;81:534–40
- Kwon DH, Kim JM, Oh SH, et al. Seven-Tesla magnetic resonance images of the substantia nigra in Parkinson disease. *Ann Neurol* 2012;71:267–77
- Schwarz ST, Afzal M, Morgan PS, et al. The 'swallow tail' appearance of the healthy nigrosome: a new accurate test of Parkinson's disease—a case-control and retrospective cross-sectional MRI study at 3T. *PLoS One* 2014;9:e93814
- Hughes AJ, Daniel SE, Ben Shlomo Y, et al. The accuracy of diagnosis of parkinsonian syndromes in a specialist movement disorder service. *Brain* 2002;125:861–70

# Comparison of 3T and 7T Susceptibility-Weighted Angiography of the Substantia Nigra in Diagnosing Parkinson Disease

M. Cosottini, D. Frosini, I. Pesaresi, G. Donatelli, P. Cecchi, M. Costagli, L. Biagi, R. Ceravolo, U. Bonuccelli, and M. Tosetti



## ABSTRACT

**BACKGROUND AND PURPOSE:** Standard neuroimaging fails in defining the anatomy of the substantia nigra and has a marginal role in the diagnosis of Parkinson disease. Recently 7T MR target imaging of the substantia nigra has been useful in diagnosing Parkinson disease. We performed a comparative study to evaluate whether susceptibility-weighted angiography can diagnose Parkinson disease with a 3T scanner.

**MATERIALS AND METHODS:** Fourteen patients with Parkinson disease and 13 healthy subjects underwent MR imaging examination at 3T and 7T by using susceptibility-weighted angiography. Two expert blinded observers and 1 neuroradiology fellow evaluated the 3T and 7T images of the sample to identify substantia nigra abnormalities indicative of Parkinson disease. Diagnostic accuracy and intra- and interobserver agreement were calculated separately for 3T and 7T acquisitions.

**RESULTS:** Susceptibility-weighted angiography 7T MR imaging can diagnose Parkinson disease with a mean sensitivity of 93%, specificity of 100%, and diagnostic accuracy of 96%. 3T MR imaging diagnosed Parkinson disease with a mean sensitivity of 79%, specificity of 94%, and diagnostic accuracy of 86%. Intraobserver and interobserver agreement was excellent at 7T. At 3T, intraobserver agreement was excellent for experts, and interobserver agreement ranged between good and excellent. The less expert reader obtained a diagnostic accuracy of 89% at 3T.

**CONCLUSIONS:** Susceptibility-weighted angiography images obtained at 3T and 7T differentiate controls from patients with Parkinson disease with a higher diagnostic accuracy at 7T. The capability of 3T in diagnosing Parkinson disease might encourage its use in clinical practice. The use of the more accurate 7T should be supported by a dedicated cost-effectiveness study.

**ABBREVIATIONS:** HS = healthy subjects; PD = Parkinson disease; SN = substantia nigra; SWAN = susceptibility-weighted angiography; UHF = ultra-high-field

Parkinson disease (PD) is a common neurodegenerative disease whose pathologic substrate is nigrostriatal dopaminergic degeneration due to the neuronal loss in the pars compacta of the substantia nigra (SN).<sup>1</sup>

On the basis of the correlation between MR signal intensity at conventional field strengths and Perls staining for iron distribution, the medial portion of the midbrain with lower MR signal is attributed to the pars reticulata of the substantia nigra, and the lateral region (with higher MR signal), to the substantia nigra pars compacta.<sup>2</sup> However, Perls staining and T2WI signal hypointensity do not match precisely,<sup>3</sup> and the hypointense area on T2WI does not match the substantia nigra pars reticulata.<sup>4</sup> Moreover, conventional MR imaging techniques, including segmented inversion recovery ratio imaging,<sup>5</sup> fail to distinguish the inner structure of the substantia nigra.<sup>6</sup> More advanced and recently proposed SN-derived biomarkers such as relaxometry,<sup>7,8</sup> DTI,<sup>9</sup> and neuromelanin imaging<sup>10</sup> are currently not yet accepted in evaluating patients with PD in clinical practice.<sup>11</sup>

Recently, by using high-resolution 3D susceptibility-weighted angiography (SWAN),<sup>12</sup> the ultra-high-field (UHF) anatomy of the SN with its inner organization has been described<sup>13</sup> as a 3-layer structure of different signal intensities along the posterior-

Received May 31, 2014; accepted after revision August 29.

From the IMAGO7 Foundation (M. Cosottini, M. Costagli), Pisa, Italy; Department of Translational Research and New Technologies in Medicine and Surgery (M. Cosottini, G.D.) and Neurology Unit (D.F., R.C., U.B.), Department of Clinical and Experimental Medicine, University of Pisa, Pisa, Italy; Neuroradiology Unit (I.P., P.C.), Department of Diagnostic and Interventional Radiology, Azienda Ospedaliero Universitaria Pisana, Pisa, Italy; and Stella Maris Scientific Institute (L.B., M.T.), Pisa, Italy.

The study is part of an experimental protocol named "Clinical Impact of Ultra-High-Field MRI in Neurodegenerative Diseases Diagnosis," RF-2009-1546281, approved and funded by Italian Ministry of Health and co-funded by the Health Service of Tuscany.

Please address correspondence to Mirco Cosottini, MD, Via Paradisa 2, 56124 Cisanello Pisa, Italy; e-mail: mircocosottini@libero.it

 Indicates open access to non-subscribers at [www.ajnr.org](http://www.ajnr.org)

 Indicates article with supplemental on-line photo.

<http://dx.doi.org/10.3174/ajnr.A4158>

anterior axis of the midbrain, resembling the dorsal and ventral components of the substantia nigra pars compacta and the substantia nigra pars reticulata, respectively. By using calbindin immunostaining, one can distinguish calbindin-positive (matrix) and calbindin-negative structures (nigrosomes)<sup>14</sup> within the substantia nigra. In a recent MR imaging study at 7T,<sup>15</sup> nigrosome 1, the largest and highly attenuated cluster of calbindin-negative neurons within the substantia nigra pars compacta ventralis, corresponded to the round hyperintense area observed in the intermediate and lateral portion of the substantia nigra pars compacta.<sup>16</sup>

In patients with PD the 3-layer organization and the hyperintense lateral spot within the SN (nigrosome 1) are lost, and this radiologic sign distinguishes patients with PD from healthy subjects (HS) on an individual basis with high accuracy.<sup>13</sup>

The diagnostic gain provided by 7T imaging is a prerequisite for the clinical acceptance of UHF, but until now, 7T MR imaging examinations have been confined to the research environment. The neuroimaging-based diagnosis of PD might constitute an important addition to the clinical diagnosis of extrapyramidal disorders. Therefore, the diagnostic role of SWI performed with a clinical MR imaging scanner at 3T has been tested recently,<sup>17,18</sup> with promising results. A direct comparison of 3T and 7T evaluation of the SN is mentioned in a pilot experience including 2 patients with PD.<sup>15</sup>

Here, we describe a comparative study with a case control design that prospectively evaluates the diagnostic accuracy of SWAN at 3T and 7T.

## MATERIALS AND METHODS

### Subjects

Fourteen patients with PD according to the clinical criteria for probable PD of the UK Parkinson's Disease Society Brain Bank<sup>19</sup> were consecutively enrolled from a tertiary movement disorder center.

Patients (6 women and 8 men; mean age, 57.4 years; range, 39–69 years) had a disease mean duration at the moment of enrollment of 58 months (range, 6–120 months); the range of Hoehn and Yahr Scale<sup>20</sup> was 1–2, and the motor part of the Unified Parkinson Disease Rating Scale<sup>21</sup> was 18.3 (range, 9–37).

Thirteen right-handed HS (4 women and 9 men; mean age, 54.8 years; range, 41–66 years) were enrolled to test the diagnostic accuracy of the SN MR imaging examination in discriminating patients with PD from controls. All HS were volunteers and had no personal or family history of psychiatric and neurologic disorders; their general and neurologic examination findings were unremarkable.

All patients and controls gave their informed consent to the enrollment and diagnostic procedures on the basis of the adherence to an experimental protocol called "Clinical Impact of Ultra-High-Field MRI in Neurodegenerative Diseases Diagnosis," RF-2009-1546281, approved and funded by the Italian Ministry of Health and co-funded by the Health Service of Tuscany. The local competent ethics committee approved the study.

### MR Imaging Acquisition

MR imaging examinations were performed in patients and controls by using a Discovery MR 950 7T imaging scanner (GE

Healthcare, Milwaukee, Wisconsin) equipped with a 2CH-TX/32CH-RX head coil (Nova Medical, Wilmington, Massachusetts) and a Discovery MR 750 3T scanner (GE Healthcare) equipped with an 8-channel head coil. Patients and controls underwent both 7T and 3T examination in a random order but within 1 month of recruitment.

The same technicians optimized the 3D multiecho gradient-recalled sequence (SWAN) at 7T and 3T.

The MR imaging parameters at 7T were TE = 5.57, 10.7, 15.84, 20.97, 26.1, 31.23, 36.36, 41.5 ms; TR = 55.7 ms; flip angle = 8°; NEX = 0.67; in-plane resolution = 312  $\mu$ m; thickness = 1.2 mm; 18 partitions; receiver bandwidth = 67 KHz.

The MR imaging parameters at 3T were TE = 13, 17.96, 22.93, 27.89, 32.86, 37.82, 42.78, 47.75, 52.71, 57.68, 62.64 ms; TR = 67.2 ms; flip angle = 15°; NEX = 0.68; in-plane resolution = 394  $\mu$ m; thickness = 1.2 mm; 18 partitions; receiver bandwidth = 62.5 KHz.

The SWAN acquisitions on both MR imaging systems targeted the midbrain and were oriented perpendicularly to the fourth ventricle floor.

The final output image was reconstructed into a 512  $\times$  512  $\times$  18 matrix by averaging the images obtained for each single echo. The SWAN acquisition time was 4 minutes 2 seconds at 7T and 4 minutes 20 seconds at 3T.

### Image Analysis

According to the methodology of a previous study,<sup>13</sup> the SN anatomy was evaluated along the rostrocaudal axis at the level of the inferior third of the red nucleus (level I) and at the level of the superior cerebellar peduncle decussation (level II), where the signal changes were more informative for diagnosing PD. Anatomy was considered normal if the SN at level I was characterized by a medial homogeneous hypointense region and by a lateral hyperintense spot between 2 hypointense layers and if a trilaminar organization characterized by a central hyperintense layer between 2 hypointense laminae was detectable at level II.

The criteria for abnormal SN anatomy were the loss of the hyperintense lateral spot at level I or/and the loss of the 3-layer organization at level II on at least 1 side of the midbrain.

Two experienced neuroradiologists were invited to identify "abnormal" SN in SWAN-targeted images acquired in the sample of patients and controls. Images acquired at 7T and 3T were separately loaded into a data base and presented in a blinded and randomized fashion. This process ensured that the readers were unaware of the clinical diagnosis. Readers were asked to identify patients with PD according to the "abnormal" appearance of the SN. Images of each subject were presented twice after an interval of 7 days to calculate intra- and interrater reliability separately for 7T and 3T imaging. Intra- and interobserver reliability of responses from each reader were cross-tabulated to enable the calculation of agreement and the Cohen  $\kappa$  statistic.<sup>22</sup> The strength of agreement was considered low for  $\kappa$  values of 0.21–0.40, moderate for  $\kappa$  values of 0.41–0.60, good for  $\kappa$  values of 0.61–0.80, and excellent for  $\kappa$  values of  $\geq$ 0.81. Sensitivity, specificity, positive predictive value, negative predictive value, and diagnostic accuracy with respect to the clinical diagnosis were calculated.

**Sensitivity, specificity, PPV and NPV, diagnostic accuracy, and true-positive/true-negative results for each reader in each reading session**

	7T						3T					
	R1 1st	R1 2nd	R2 1st	R2 2nd	R3 1st	R3 2nd	R1 1st	R1 2nd	R2 1st	R2 2nd	R3 1st	R3 2nd
Sensitivity	93	93	93	93	77	86	79	79	71	86	79	79
Specificity	100	100	100	100	100	100	92	100	92	92	100	100
PPV	100	100	100	100	100	100	92	100	91	92	100	100
NPV	93	93	93	93	81	87	80	81	75	86	81	81
Accuracy	96	96	96	96	85	93	85	89	81	89	89	89
TP/TN	13/13	13/13	13/13	13/13	10/13	12/13	11/12	11/13	10/12	12/12	11/13	11/13

**Note:**—R indicates reader; TP, true-positive; TN, true-negative; 1st, first reading; 2nd, second reading; NPV, negative predictive value; PPV, positive predictive value.

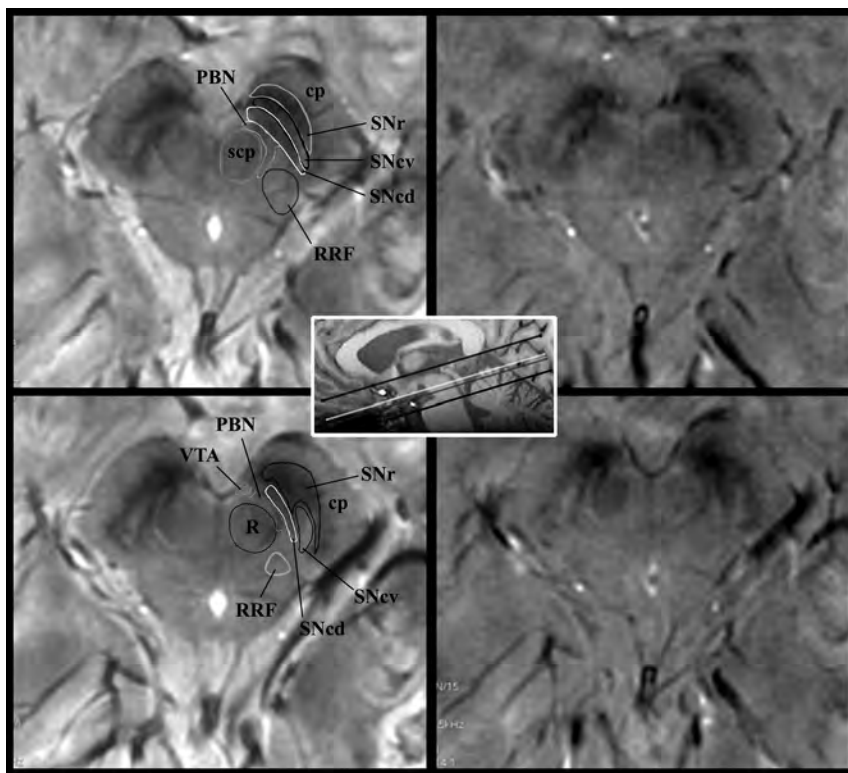


**FIG 1.** SWAN-targeted axial image of the midbrain in a healthy subject evaluated at 3T (right column) and at 7T (left column). The trilaminar organization of the SN at level II (upper row) and the nigrosome formation at level I (lower row) are clearly shown with 3T and 7T magnets. Levels I and II of image acquisition are represented by white and gray lines in the scout image. On 7T images, we overlaid a diagram of the trilaminar structure of the SN derived by anatomic atlases.<sup>41</sup> The diagnostic accuracy is elevated for both high- and ultra-high-field-strength magnets. cp indicates cerebral peduncle; PBN, parabrachial nucleus; RRF, retrorubral field; scp, superior cerebellar peduncle; SNcv, substantia nigra pars compacta ventralis; SNcd, substantia nigra pars compacta dorsalis; SNr, substantia nigra pars reticularis; VTA, ventral tegmental area; R, red nucleus.

To test the role of radiologic signs in diagnosing PD and to reduce the bias of previous experiences at high and ultra-high-field strength magnets, we presented the entire data base of patients and controls to a third blinded observer with 5 years' experience in radiology at our university and whose experience in the neuroradiology unit included CT and 1.5T MR imaging studies of patients with neurodegenerative and movement disorders but not with acquisitions on 3T or 7T MR imaging systems. The third rater was invited to study the SN anatomy and its changes according to the most recent literature<sup>13,15</sup> regarding the semiology of the SN in PD. A dataset consisting of 8 midbrain images at 3T (4 HS) and at 7T (4 HS) was used for training purposes. The images belonging to this training dataset were not included in the rest of

this study. After training, the third rater evaluated all the 3T and 7T midbrain images previously presented to the 2 experienced neuroradiologists in a blinded and randomized fashion at 2 different times to calculate sensitivity, specificity, accuracy, and intraobserver agreement for 3T and 7T acquisitions.

**RESULTS**

The diagnostic accuracy, sensitivity, specificity, positive predictive value, and negative predictive value for each rater in each reviewing session are separately reported in the Table. In the next 2 paragraphs, the diagnostic parameters are reported as the mean value obtained by the 2 expert raters in the 2 reviewing sessions.

**7T MR Imaging of the SN**

Sensitivity, specificity, positive predictive value, and negative predictive value for the diagnosis of PD were 93%, 100%, 100%, and 93%, respectively. Diagnostic accuracy was 96%. Intraobserver agreement ( $\kappa = 1$ ) and interobserver agreement ( $\kappa = 1$ ) were excellent.

**3T MR Imaging of the SN**

Sensitivity, specificity, positive predictive value, and negative predictive value for the diagnosis of PD were 79%, 94%, 94%, and 81%, respectively. Diagnostic accuracy was 86%. At 3T, intraobserver

agreement was excellent for both raters ( $\kappa = 0.924$  for rater 1 and  $\kappa = 0.851$  for rater 2) and interobserver agreement was good for the first reviewing session ( $\kappa = 0.773$ ) and excellent for the second reviewing session ( $\kappa = 0.851$ ).

**Performance of the Third, Less Expert Rater**

For the third rater, sensitivity, specificity, positive predictive value, negative predictive value, and accuracy were 82%, 100%, 100%, 84%, and 89% at 7T and 79%, 100%, 100%, 81%, and 89% at 3T, respectively. Intraobserver agreement was good ( $\kappa = 0.773$ ) at 7T and excellent ( $\kappa = 1$ ) at 3T.

Examples of 3T correct, false-positive, and false-negative readings as classified by rater 2 are shown respectively in Figs 1–3.

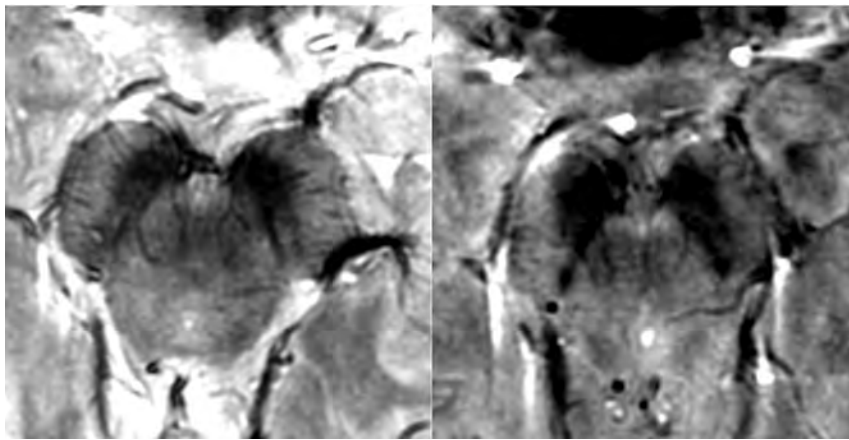


**FIG 2.** SWAN-targeted axial image of the midbrain in a healthy subject evaluated at 3T (right) and 7T (left). The nigrosome formation appreciable at 7T is interpreted as lost at 3T, generating a false-positive.

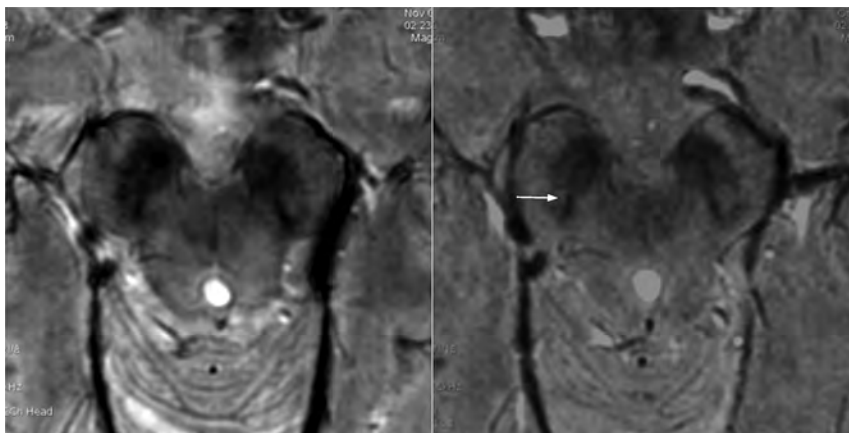


**FIG 3.** SWAN-targeted axial image of the midbrain in a patient with PD evaluated at 3T (right) and 7T (left). The nigrosome formation seems recognizable in the left SN. On the right SN, the nigrosome formation is lost at 7T, while at 3T the slight hyperintense component (arrow) has been erroneously interpreted as a nigrosome, leading to a false-negative finding.

## DISCUSSION

Our results confirm the capability of 7T MR imaging to reveal, through visual inspection of SWAN images, the loss of the 3-layer organization<sup>13</sup> and of the lateral bright spot of the SN<sup>13,15,16</sup> in patients with PD, allowing high diagnostic accuracy.

MR imaging at 7T is being tested in different clinical conditions<sup>23</sup> to assess its clinical importance for specific situations.<sup>24</sup> UHF MR imaging examinations provide encouraging results in terms of tolerability and acceptance.<sup>25,26</sup> At present, around the world, there are approximately 40 UHF MR imaging systems that are still confined to the research environment. In this study, we transferred the semiology adopted at 7T in diagnosing PD to 3T and verified that the diagnostic gain permitted by UHF could be extended, at least to some relevant extent, to a clinical scanner that is more easily accessible for patient care (Fig 1).

With high-resolution target imaging at 3T, we detected a partition of the SN in HS and identified patients with PD as reported in other recent experiences.<sup>17,18</sup> Nevertheless as demonstrated by the lower intra- and interobserver agreement at 3T, the confidence in revealing the inner structure of the SN was inferior to that of 7T. The loss of the 3-layer organization of the SN or the loss

of the hyperintense spot in the lateral component of the intermediate tier of the SN is less evident at 3T and leaves some uncertainty in defining the pathologic aspect of the SN in PD. As demonstrated by the higher number of false-positives and false-negatives at 3T, identifying the hyperintense central component of the normal SN (Fig 2) is more difficult, and the raters tended to overestimate subtle SN hyperintensities, which were misinterpreted as normal (Fig 3). The global effect is the reduction of the diagnostic accuracy of SWAN sequences at 3T with respect to 7T.

Because the MR imaging signal increases quadratically with the field strength while noise increases only linearly, the SNR is theoretically more than double at 7T with respect to 3T, and this difference can be exploited to increase the spatial resolution.<sup>27</sup> In our protocol, the 7T and 3T images have a similar spatial resolution (312  $\mu\text{m}$  at 7T versus 364  $\mu\text{m}$  at 3T); therefore, this is unlikely to be the reason for the better performance of 7T. The superior imaging performance of 7T is more likely from the increased T2\* contrast and magnetic susceptibility effects of paramagnetic substances, which are enhanced at higher magnetic fields.<sup>28-30</sup> The magnetic susceptibility effects of iron contained in the SN scale linearly with magnetic field strength. At 7T, the larger susceptibility effect compared with 3T results in more informative images of

the midbrain with an increased contrast between the 2 hypointense iron-containing components of the SN and the intermediate hyperintense part that is preserved in HS (On-line Figure).

From a clinical point of view, a diagnostic error occurs in 10%–25% of patients with parkinsonism; and 20% of patients with PD coming to medical attention are not diagnosed as such.<sup>31</sup> These diagnoses result in delayed or inappropriate therapy initiation.<sup>32</sup> The accuracy of the clinical diagnosis of PD is 90% in a 5-year observation period,<sup>33</sup> and the rate of re-diagnosis from PD to an alternative disease is 5.9%.<sup>34</sup> The most frequent wrong differential diagnosis is related to atypical parkinsonism<sup>35</sup> but also to nondegenerative movement disorders such as essential tremor, dystonic tremor, and vascular pseudoparkinsonism.<sup>36</sup> More rare but crucial misdiagnoses are normal pressure hydrocephalus<sup>37</sup> and neoplastic lesions.<sup>38</sup> The total annual cost of anti-Parkinson medication for these misdiagnosed patients has been estimated at £13,400 (US \$21,722).<sup>34</sup> The potential role of MR imaging would be to provide an earlier and more accurate diagnosis than the standard clinical assessment, improving the cost-effectiveness. The diagnostic accuracy of SWAN imaging at 3T is lower than that

at 7T but is still high enough to suggest a role in a clinical setting. Because the sensitivity of the clinical evaluation is high (96%) and the specificity of the 3T MR imaging is higher than that of the clinical evaluation in a 5-year period (82%),<sup>36</sup> 3T MR imaging can be used in clinical practice as a confirmatory method. In a population with a clinical suspicion of PD, the high specificity of 3T MR imaging allows identifying true-negative subjects, similar to nuclear medicine with radiotracers for dopamine transporters.<sup>39</sup> Because MR imaging is a fundamental step in excluding pseudoparkinsonism or atypical parkinsonism,<sup>40</sup> the use of a 3T clinical scanner, including the imaging of the SN, seems to be justified in extrapyramidal disorders.

Unfortunately SN imaging at 3T is less effective than at 7T in identifying true-positive cases, attenuating its impact. We hypothesize that patients with high clinical suspicion of PD and negative imaging findings of the SN at 3T might benefit from an evaluation at 7T. A dedicated study would be necessary to calculate whether the use of the more accurate diagnosis obtained with 7T MR imaging is cost-effective compared with to the use of 3T MR imaging only.

Regarding the results of the less expert rater unbiased by previous UHF MR imaging experiences, the high diagnostic accuracy and intrarater reproducibility at 7T and 3T confirm the robustness of the radiologic semiology consisting of simple and reproducible signs.<sup>17</sup>

The diagnostic accuracy is inferior at 3T in both expert and less expert raters, indicating that the confidence in expressing a diagnostic judgment depends more on the magnetic field strength than on the rater's ability.

Some major limitations should be taken into account. First, the number of enrolled patients is limited mostly due to the limited number of patients available for evaluation at 7T. Patients and controls are not perfectly matched, though they do not differ significantly. The sequence parameters (TE and flip angle) slightly differ between the 2 MR imaging scanners. TEs are automatically determined by the software and cannot be set by the operators, while the flip angle at 7T is reduced to limit the signal drop related to the T2 relaxation time shortening at UHF. Finally, although images were randomly presented, the quality of images obtained at 7T and 3T is clearly different, and the 2 datasets can be clearly recognized by the readers, who therefore cannot be considered blinded with respect to the scanner but only with respect to the subject's condition.

## CONCLUSIONS

The experience acquired in the research environment by using 7T systems allowed us to develop and refine targeted MR imaging acquisitions for 3T scanners, improving the role of imaging in the diagnosis of PD at a single-subject level in clinical practice. However if the higher diagnostic accuracy of SWAN at 7T with respect to 3T could justify the use of the 7T in clinical practice, a cost-effectiveness study to support this possibility should be performed.

## ACKNOWLEDGMENTS

We wish to acknowledge the help provided by Mark Symms.

Disclosures: Ubaldo Bonuccelli—UNRELATED: Grants/Grants Pending: Regione Toscana Health Authority, for a Parkinson disease study (€200,000 [US \$253,165]); Payment for Lectures (including service on Speakers Bureaus): Lundbeck, Chiesi, GlaxoSmithKline, Novartis, Comments: For speeches at meetings (€2000 [US \$2530]); Travel/Accommodations/Meeting Expenses Unrelated to Activities Listed: Lundbeck, Chiesi,\* GlaxoSmithKline,\* Novartis,\* Comments: for participation at neurology meetings (€2000 [US \$2530]). \*Money paid to the institution.

## REFERENCES

1. Fearnley JM, Lees AJ. Ageing and Parkinson's disease: substantia nigra regional selectivity. *Brain* 1991;114:2283–301
2. Drayer BP. Imaging of the aging brain. Part II. Pathologic conditions. *Radiology* 1988;166:797–806
3. Rutledge JN, Hilal SK, Silver AJ, et al. Study of movement disorders and brain iron by MR. *AJR Am J Roentgenol* 1987;149:365–79
4. Oikawa H, Sasaki M, Tamakawa Y, et al. The substantia nigra in Parkinson disease: proton density-weighted spin-echo and fast short inversion time inversion-recovery MR findings. *AJNR Am J Neuroradiol* 2002;23:1747–56
5. Hutchinson M, Raff U, Lebedev S. MRI correlates of pathology in parkinsonism: segmented inversion recovery ratio imaging (SIRIM). *Neuroimage* 2003;20:1899–902
6. Minati L, Grisoli M, Carella F, et al. Imaging degeneration of the substantia nigra in Parkinson disease with inversion-recovery MR imaging. *AJNR Am J Neuroradiol* 2007;28:309–13
7. Ordidge RJ, Gorell JM, Deniau JC, et al. Assessment of relative brain iron concentrations using T2-weighted and T2\*-weighted MRI at 3 Tesla. *Magn Reson Med* 1994;32:335–41
8. Martin WR, Wieler M, Gee M. Midbrain iron content in early Parkinson disease: a potential biomarker of disease status. *Neurology* 2008;70:1411–17
9. Vaillancourt DE, Spraker MB, Prodoehl, et al. High-resolution diffusion tensor imaging in the substantia nigra of de novo Parkinson disease. *Neurology* 2009;72:1378–84
10. Sasaki M, Shibata E, Tohyama K, et al. Neuromelanin magnetic resonance imaging of locus ceruleus and substantia nigra in Parkinson's disease. *Neuroreport* 2006;17:1215–18
11. Lehérycy S, Sharman MA, Dos Santos CL, et al. Magnetic resonance imaging of the substantia nigra in Parkinson's disease. *Mov Disord* 2012;27:822–30
12. Haacke EM, Xu Y, Cheng YC, et al. Susceptibility weighted imaging (SWI). *Magn Reson Med* 2004;52:612–18
13. Cosottini M, Frosini D, Pesaresi I, et al. MR imaging of the substantia nigra at 7 T enables diagnosis of Parkinson disease. *Radiology* 2014;271:831–38
14. Damier P, Hirsch EC, Agid Y, et al. The substantia nigra of the human brain. I. Nigrosomes and the nigral matrix, a compartmental organization based on calbindin D(28K) immunohistochemistry. *Brain* 1999;122:1421–36
15. Blaziejewska AI, Schwarz ST, Pitiot A, et al. Visualization of nigrosome 1 and its loss in PD: pathoanatomical correlation and in vivo 7 T MRI. *Neurology* 2013;81:534–40
16. Kwon DH, Kim JM, Oh SH, et al. Seven-Tesla magnetic resonance images of the substantia nigra in Parkinson disease. *Ann Neurol* 2012;71:267–77
17. Schwarz ST, Afzal M, Morgan PS, et al. The “swallow tail” appearance of the healthy nigrosome: a new accurate test of Parkinson's disease—a case-control and retrospective cross-sectional MRI study at 3T. *PLoS One* 2014;9:e93814
18. Mueller CI, Pinter B, Reiter E, et al. Visualization of nigrosome 1 and its loss in PD: pathoanatomical correlation and in vivo 7T MRI. *Neurology* 2014;82:1752
19. Gibb WR, Lees AJ. The relevance of the Lewy body to the pathogenesis of idiopathic Parkinson's disease. *J Neurol Neurosurg Psychiatry* 1988;51:745–52
20. Hoehn MM, Yahr MD. Parkinsonism: onset, progression and mortality. *Neurology* 1967;17:427–42
21. Fahn S, Elton RL, members of the UPDRS Development Committee.

- Unified Parkinson's Disease Rating Scale.** In: Fahn D, Marsden CD, Calne D, et al, eds. *Recent Development in Parkinson's Disease*. Vol. 2. Florham Park: Macmillan Healthcare Information; 1987
22. Landis JR, Koch GG. **The measurement of observer agreement for categorical data.** *Biometrics* 1977;33:159–74
  23. van der Kolk AG, Hendrikse J, Zwanenburg JJ, et al. **Clinical applications of 7 T MRI in the brain.** *Eur J Radiol* 2013;82:708–18
  24. Knopp MV. **Clinical applications of ultra-high field 7T MR: moving to FDA/EU approval—potential clinical applications for ultra-high field MR.** In: *Proceedings of the International Society Magnetic Resonance Medicine Weekday Educational Course*, Montreal, Quebec, Canada. May 11, 2011
  25. Theysohn JM, Maderwald S, Kraff O, et al. **Subjective acceptance of 7 Tesla MRI for human imaging.** *MAGMA* 2008;21:63–72
  26. Cosottini M, Frosini D, Biagi L, et al. **Short-term side-effects of brain MR examination at 7 T: a single-centre experience.** *Eur Radiol* 2014;24:1923–28
  27. Kuhl CK, Traber F, Schild HH. **Whole-body high-field-strength (3.0-T) MR imaging in clinical practice. Part I. Technical considerations and clinical applications.** *Radiology* 2008;246:675–96
  28. Haacke EM, Mittal S, Wu Z, et al. **Susceptibility-weighted imaging: technical aspects and clinical applications, part 1.** *AJNR Am J Neuroradiol* 2009;30:19–30
  29. Haller S, Badoud S, Nguyen D, et al. **Differentiation between Parkinson disease and other forms of Parkinsonism using support vector machine analysis of susceptibility-weighted imaging (SWI): initial results.** *Eur Radiol* 2013;23:12–19
  30. Wang Y, Butros SR, Shuai X, et al. **Different iron-deposition patterns of multiple system atrophy with predominant parkinsonism and idiopathic Parkinson diseases demonstrated by phase-corrected susceptibility-weighted imaging.** *AJNR Am J Neuroradiol* 2012;33:266–73
  31. Schrag A, Ben-Shlomo Y, Quinn N. **How valid is the clinical diagnosis of Parkinson's disease in the community?** *J Neurol Neurosurg Psychiatry* 2002;73:529–34
  32. Jankovic J, Rajput AH, McDermott MP, et al. **The evolution of diagnosis in early Parkinson disease.** *Arch Neurol* 2000;57:369–72
  33. Hughes AJ, Daniel SE, Lees AJ. **Improved accuracy of clinical diagnosis of Lewy body Parkinson's disease.** *Neurology* 2001;57:1497–99
  34. Newman EJ, Breen K, Patterson J, et al. **Accuracy of Parkinson's disease diagnosis in 610 general practice patients in the West of Scotland.** *Mov Disord* 2009;24:2379–85
  35. Hughes AJ, Daniel SE, Ben-Shlomo Y, et al. **The accuracy of diagnosis of parkinsonian syndromes in a specialist movement disorder service.** *Brain* 2002;125:861–70
  36. Meara J, Bhowmick BK, Hobson P. **Accuracy of diagnosis in patients with presumed Parkinson's disease.** *Age Ageing* 1999;28:99–102
  37. Curran T1, Lang AE. **Parkinsonian syndromes associated with hydrocephalus: case reports, a review of the literature, and pathophysiological hypotheses.** *Mov Disord* 1994;9:508–20
  38. Frosini D, Ceravolo R, Rossi C, et al. **Bilateral thalamic glioma presenting with parkinsonism.** *Mov Disord* 2009;24:2168–69
  39. Bajaj N, Hauser RA, Grachev ID. **Clinical utility of dopamine transporter single photon emission CT (DaT-SPECT) with (123I) ioflupane in diagnosis of parkinsonian syndromes.** *J Neurol Neurosurg Psychiatry* 2013;84:1288–95
  40. Berardelli A, Wenning GK, Antonini A, et al. **EFNS/MDS-ES/ENS recommendations for the diagnosis of Parkinson's disease.** *Eur J Neurol* 2013;20:16–34
  41. Halliday G, Reyes S, Double K. **Substantia nigra, ventral tegmental area, and retrorubral fields.** In: Main JK, Paxinos G, eds. *The Human Nervous System*. 3rd ed. London: Academic Press; 2012: 439–55, chap 3

# Quantitative Susceptibility Mapping of Human Brain at 3T: A Multisite Reproducibility Study

P.-Y. Lin, T.-C. Chao, and M.-L. Wu



## ABSTRACT

**BACKGROUND AND PURPOSE:** Quantitative susceptibility mapping of the human brain has demonstrated strong potential in examining iron deposition, which may help in investigating possible brain pathology. This study assesses the reproducibility of quantitative susceptibility mapping across different imaging sites.

**MATERIALS AND METHODS:** In this study, the susceptibility values of 5 regions of interest in the human brain were measured on 9 healthy subjects following calibration by using phantom experiments. Each of the subjects was imaged 5 times on 1 scanner with the same procedure repeated on 3 different 3T systems so that both within-site and cross-site quantitative susceptibility mapping precision levels could be assessed. Two quantitative susceptibility mapping algorithms, similar in principle, one by using iterative regularization (iterative quantitative susceptibility mapping) and the other with analytic optimal solutions (deterministic quantitative susceptibility mapping), were implemented, and their performances were compared.

**RESULTS:** Results show that while deterministic quantitative susceptibility mapping had nearly 700 times faster computation speed, residual streaking artifacts seem to be more prominent compared with iterative quantitative susceptibility mapping. With quantitative susceptibility mapping, the putamen, globus pallidus, and caudate nucleus showed smaller imprecision on the order of 0.005 ppm, whereas the red nucleus and substantia nigra, closer to the skull base, had a somewhat larger imprecision of approximately 0.01 ppm. Cross-site errors were not significantly larger than within-site errors. Possible sources of estimation errors are discussed.

**CONCLUSIONS:** The reproducibility of quantitative susceptibility mapping in the human brain in vivo is regionally dependent, and the precision levels achieved with quantitative susceptibility mapping should allow longitudinal and multisite studies such as aging-related changes in brain tissue magnetic susceptibility.

**ABBREVIATIONS:** PDF = projection onto dipole fields; QSM = quantitative susceptibility mapping; SHARP = sophisticated harmonic artifact reduction for phase data

Quantitative susceptibility mapping (QSM) of the human brain has recently drawn increasing research interest because of its strong potential in neurologic applications.<sup>1-12</sup> The magnetic susceptibility reflects the amount of induced magnetization in a certain tissue when placed in an external magnetic field such as that of an

MR imaging scanner.<sup>11</sup> As a result, measurements of magnetic susceptibility allow an examination of the difference in tissue ion content in the generally diamagnetic brain parenchyma. Previous reports by using QSM in the brain have demonstrated its capability to quantify cerebral iron deposition and, therefore, to assess brain pathology, including Parkinson disease and multiple sclerosis.<sup>2,13,14</sup>

The procedures to reconstruct the susceptibility maps comprise multiple data-processing steps, each of which could contribute to variations in the numeric results. For instance, the effectiveness of background gradient removal may be variable on different shimming conditions before image acquisition, and the convergence condition in the iterative regularization may be prone to parameter-selection bias. Consequently, it would be useful to assess the reproducibility and consistency of QSM results on a cross-site and within-subject basis so that the QSM approaches could be extended for longitudinal investigations of brain diseases with an increased patient pool.

In this study, we aimed to investigate the reproducibility of

Received March 19, 2014; accepted after revision August 28.

From the Department of Computer Science and Information Engineering (P.-Y.L., T.-C.C., M.-L.W.) and Institute of Medical Informatics (T.-C.C., M.-L.W.), National Cheng Kung University, Tainan, Taiwan.

The authors were supported in part under grant Nos. NSC-101-2221-E-006-063-MY2 (P.-Y.L. and M.-L.W.), NSC-100-2218-E-006-038-MY2 (T.-C.C.), and MOST-102-2221-E-006-017 (T.-C.C.) from the National Science Council, Taiwan; and the Aim for the Top University Project to the National Cheng Kung University, Ministry of Education, Taiwan (M.-L.W.).

Please address correspondence to Ming-Long Wu, PhD, Department of Computer Science and Information Engineering, National Cheng Kung University, No. 1, University Rd, Tainan 70101, Taiwan; e-mail: minglong.wu@csie.ncku.edu.tw

Indicates open access to non-subscribers at www.ajnr.org

<http://dx.doi.org/10.3174/ajnr.A4137>

QSM within healthy adult subjects and the consistency of QSM among multiple sites in different brain regions. The results would provide implications regarding the precision levels of QSM before being widely applied in clinical brain studies. We compared results from both the iterative and deterministic methods, showing opportunities for higher computation efficiency by using fewer freely adjustable parameters, along with its possible limits. In all, this study is expected to increase the practicality of QSM for clinical neurologic applications, especially those in multisite and longitudinal studies.

## MATERIALS AND METHODS

### Phantom Experiment Validation

A cylindrical phantom (diameter = 20 cm, height = 16 cm) containing water was made with 6 test tubes (diameter = 1.8 cm, height = 20 cm) inserted into the container. Gadolinium, gadopentetate dimeglumine solution (Magnevist; Bayer HealthCare, Wayne, New Jersey), was prepared at 0%, 0.25%, 0.5%, 0.75, 1%, and 1.25% of the raw solution. The test tubes were placed parallel to the main magnetic field in the cylindrical container and were filled with gadolinium solution, generating susceptibility changes of 0, 0.41, 0.82, 1.22, 1.63, and 2.04 ppm, respectively.<sup>15</sup>

Phantom scans were performed on the 3T MR imaging scanners used for human subject experiments (to be detailed in the next section). Data were acquired by using multichannel head coils identical to those used in human experiments, with a 3D multiecho gradient-echo sequence (axial slices: matrix size =  $224 \times 216 \times 92$ ; voxel =  $1 \times 1 \times 2 \text{ mm}^3$ ; flip angle =  $30^\circ$ ; TR = 30 ms; unipolar readout gradient, TE = 2.6, 6.6, 10.6, 14.6, 18.6, and 22.6 ms).

### Human Subject Experiments

Nine healthy subjects (7 men, 2 women; age range, 23–37 years; mean,  $28 \pm 5$  years) participated in the MR imaging brain scans of this study. Each subject underwent 15 QSM scans, with 5 scans in each of the three 3T scanners tested in this study. The 5 scans in each scanner were acquired in the same scan session for all subjects. For each subject, the time span to complete the scans at 3 sites ranged from 3 to 68 days. Subject scans were performed following an institutional review board protocol. One hundred thirty-five datasets were collected and analyzed.

Three 3T MR imaging scanners (site A and site B: Magnetom Skyra; Siemens, Erlangen, Germany; Site C: Discovery MR750; GE Healthcare, Milwaukee, Wisconsin) at 3 sites separated from one another by 40–350 km were used in this multisite study. Multiecho gradient-echo images (axial slices: matrix size =  $256 \times 256 \times 64$ ; FOV = 256 mm; slice thickness = 2 mm; TR/TE1 = 45/6 ms; echo spacing = 6 ms; 6 echoes with unipolar readout; flip angle =  $5^\circ$ ; bandwidth = 31.25 KHz; 16-channel head coil at sites A and B; 8-channel head coil at site C) were acquired for QSM reconstruction. The scanning time for each single scan was approximately 12 minutes. Typical values of the signal-to-noise ratio for the first TE images were approximately 185, 165, and 260 for sites A, B, and C, respectively.

All datasets were first preprocessed and then went through the QSM computation algorithms. Susceptibility maps from iterative QSM and deterministic QSM were compared both in phantom and in human subject data. For region-of-interest analysis, 15 sets

of susceptibility maps from each subject were registered in SPM8 software (<http://www.fil.ion.ucl.ac.uk/spm/software/spm8>). Five ROIs, including the caudate nucleus, putamen, globus pallidus, red nucleus, and substantia nigra, were then manually selected in all subjects to calculate the mean susceptibility values in each region of interest. Within-subject variability of the susceptibility values was then calculated with data from both a single site and 3 sites. As a result, 3 within-site variability values (each corresponding to the SD in a particular site) and 5 cross-site variability values (each corresponding to the SD from 1 of the 5 scans in 3 scanners) were obtained for each subject. Within-site and cross-site imprecision levels were calculated by averaging 3 within-site and 5 cross-site variability values, separately. Subsequently, within-site and cross-site imprecision levels were tested for significance of the difference in 5 ROIs by using paired Student *t* tests with a Bonferroni correction ( $P = .05/5 = .01$ ).

In addition, susceptibility values in the 5 ROIs, with reference to those of the CSF in the lateral ventricles, were plotted versus ages of the recruited subjects. To examine whether the precision level of QSM allows an investigation of possible correlation of susceptibility values with age, we performed linear regression with average susceptibility values obtained from iterative QSM versus subject ages in each region of interest. One hundred thirty-five datasets were included.

### Data-Preprocessing Procedures

Multiecho gradient-echo images were used for calculating quantitative susceptibility maps. In the data-preprocessing stage, 3D phase unwrapping was first applied for images obtained at each TE.<sup>16</sup> Subsequently, magnetic field distribution was estimated by weighted least-squares fitting of the phase values versus the TE on a voxel-by-voxel basis.<sup>17</sup> The background magnetic field was removed from the total magnetic field by using the projection onto dipole fields (PDF) method.<sup>18</sup>

### Quantitative Susceptibility Mapping

In susceptibility mapping, a magnetic dipole model was used to model the magnetic field  $B_{\text{local}}$  contributed from all tiny magnetic substances with susceptibility distribution of  $\chi_{\text{local}}$  in a 3D space.<sup>2,15,19–22</sup> An inverse problem was solved from the magnetic field  $B_{\text{local}}$  by using a regularized equation to obtain the tissue susceptibility distribution  $\chi_{\text{local}}$ . Two QSM methods, iterative and deterministic, by using similar regularized equations, were compared in this study.<sup>1,23</sup>

### Iterative QSM

Regularization was applied so that the optimal solution converged under the constraint of consistency with the magnitude image as in the following equation<sup>1</sup>:

$$1) \quad \min \chi_{\text{local}} (\| (F^H D F \chi_{\text{local}} - B_{\text{local}}) \|_2^2 + \lambda^2 \| W_e G \chi_{\text{local}} \|_2^2),$$

where  $F$  is the Fourier transform operator,  $D$  is the matrix expression of the dipole model,  $B_{\text{local}}$  denotes the local magnetic field obtained from the PDF method,  $\lambda$  is the associated regularization parameter;  $G$  represents a gradient operator; and  $W_e$  is a binary mask containing nonedge regions of the magnitude images, respectively. The minimization problem was solved by using the conjugate gradient method.

In equation 1, the first term  $\|(F^H DF\chi_{local} - B_{local})\|_2^2$  was used to ensure the fidelity between the magnetic field generated from  $\chi_{local}$  and the local magnetic field  $B_{local}$ . To reduce streaking artifacts in  $\chi_{local}$  maps, we added  $\lambda^2 \|W_e G\chi_{local}\|_2^2$  as the regularization term, in which edges in susceptibility maps ( $G\chi_{local}$ ) were suppressed when appearing at nonedge regions of the magnitude image ( $W_e$ ).

To determine the optimal  $\lambda$  value from a given range, for each  $\lambda$ , we recorded the fitted error  $\|(F^H DF\chi_{local} - B_{local})\|_2^2$ . The optimal  $\lambda$  was chosen so that the fitted error reached the expected noise variance.<sup>24</sup>

### Deterministic QSM

In addition to the iterative method, a deterministic QSM method has been proposed to calculate the susceptibility maps with improved computational efficiency.<sup>23</sup> Similar to the iterative QSM, the deterministic QSM involves minimization of the following equation:

$$2) \quad \min \chi_{local} (\|(F^H DF\chi_{local} - B_{local})\|_2^2 + \lambda^2 \|G\chi_{local}\|_2^2),$$

where  $F$  is the Fourier transform operator,  $D$  is the matrix expression of the dipole model,  $B_{local}$  denotes the local magnetic field obtained from the PDF method,  $\lambda$  is the associated regularization parameter, and  $G$  represents a gradient operator, respectively. The minimization equation in deterministic QSM is similar to that of iterative QSM except that the edge information from magnitude images (ie,  $W_e$  of equation 1) is not included. Through mathematical derivation, when equation 2 is minimized, an analytic solution for  $\chi_{local}$  can be obtained as in the following<sup>23</sup>:

$$3) \quad \chi_{local} = F^H [D^2 + \lambda^2 (E_x^2 + E_y^2 + E_z^2)]^{-1} DFB_{local}$$

where  $E_x$ ,  $E_y$ , and  $E_z$  are alternative forms of the gradient operator  $G$  in equation 2, expressed in 3 directions. Equation 3 shows that the optimal solution of  $\chi_{local}$  can be calculated by using Fourier transform and matrix multiplication, which greatly reduce computation time compared with the iterative approach. The optimal  $\lambda$  was determined in a manner identical to that used in iterative QSM as stated above.

Minimization problems in iterative and deterministic QSM were solved by using Matlab (MathWorks, Natick, Massachusetts) R2012a (central processing unit: Intel i7-3930K; RAM 64GB; Microsoft Windows 7). The computation time for calculating susceptibility maps was recorded to compare the 2 QSM methods.

## RESULTS

### Phantom Experiment

Results from the phantom scan comparing the experimental susceptibility values in the 6 tubes against the ideal susceptibility values predicted from the concentrations of the gadolinium solutions<sup>15</sup> are shown in Fig 1. Good linearity exists between the measured susceptibility and the true values ( $R^2 = 0.999$ ). The fitted line between the 2 susceptibility values has a slope of 0.91 and an intercept of  $-0.04$  ppm, respectively. Due to excellent linearity, the regression equation is used as calibration to adjust the susceptibility values obtained in subsequent in vivo studies. Figure 2 shows the susceptibility maps in a view plane covering the long axes of 2 tubes to compare the results from both the iterative (Fig 2A) and the deterministic (Fig 2B) QSM. The susceptibility map

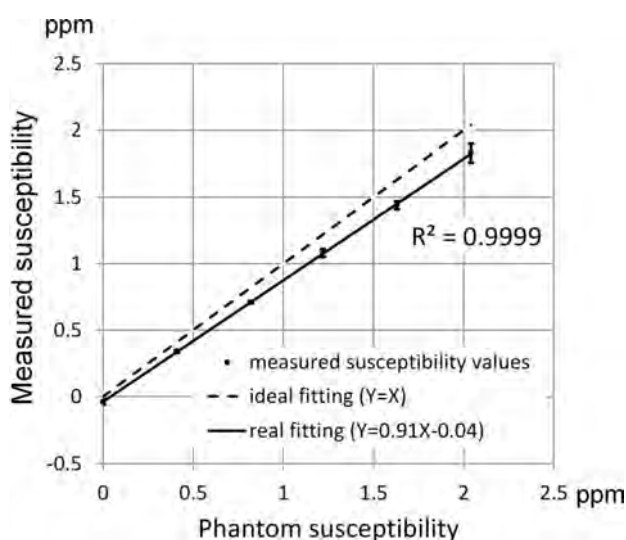


**FIG 1.** Measured susceptibility versus the phantom susceptibility values. Good linearity exists between measured susceptibility values and phantom susceptibility values in 6 test tubes of the phantom. The regression line has a slope of 0.91.

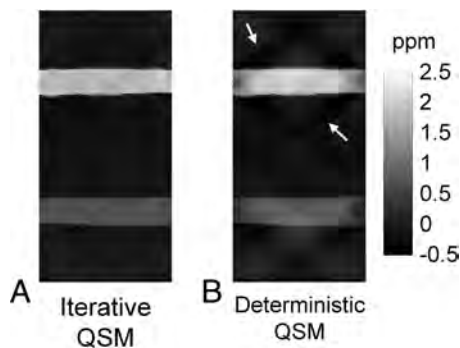


**FIG 2.** Comparison of iterative QSM and deterministic QSM in a sagittal view of the phantom. The susceptibility map from deterministic QSM presents a higher level of streaking artifacts as indicated by the white arrows.

from deterministic QSM presents a visually higher level of streaking artifacts, as indicated by white arrows in Fig B, than that from the iterative QSM in Fig 2A. Further adjustments of the  $\lambda$  value in deterministic QSM show that the reconstructed susceptibility map exhibits either streaking at a small  $\lambda$  (under-regularized) or blurring at a large  $\lambda$  (over-regularized). At the  $\lambda$  value chosen in our study, the presence of both artifacts albeit at lower levels is visually discernible (not shown).

### Human Subject Experiments

Susceptibility maps from a human subject reconstructed by iterative QSM and deterministic QSM are shown in Fig 3A, -B, respectively. In 3 displayed views, both image contrast and brain structures are very similar in the susceptibility maps of Fig 3A, -B, for which no visually prominent streaking artifacts are present. For examining the difference in susceptibility maps generated from the 2 QSM methods more closely, Fig 3C shows subtraction of Fig 3A, -B. Note that most of the streaking patterns are centered at locations with highly distinct susceptibility values from the vicinity, such as the superior sagittal sinus and regions close to the skull base, as indicated by white arrows. The average reconstruc-

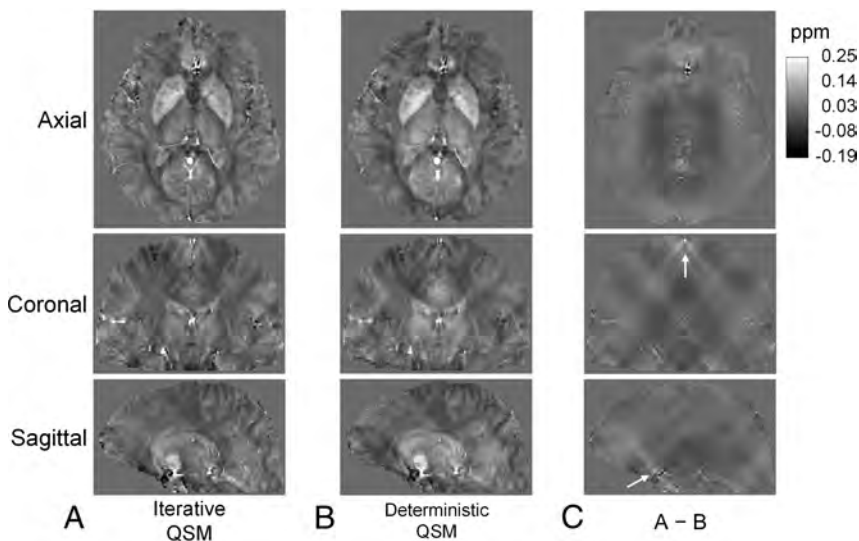


**FIG 3.** Susceptibility maps reconstructed by iterative QSM (A) and deterministic QSM (B) in 3 different views. Susceptibility maps from both methods are very similar in contrast and brain structures. C, The difference images of A and B. Note that most streaking patterns in C are centered at locations with high susceptibility values, such as the sagittal sinus and regions close to the skull base, as indicated by white arrows.

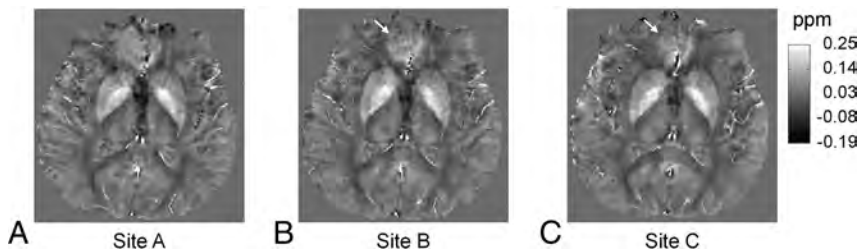


**FIG 4.** Susceptibility maps reconstructed by using iterative QSM with data from 3 scanners at sites A, B, and C. A–C, Good consistency in brain structures and susceptibility values is shown. Some difference is found at the frontal lobe as indicated by white arrows in B and C, likely due to different shimming conditions in this region.

tion durations for a dataset using iterative QSM and deterministic QSM are 123 seconds and 0.17 seconds, respectively.

Data from multiple sites are also compared in all subjects. Figure 4 shows the susceptibility maps of another subject reconstructed with data from 3 tested scanners at sites A, B, and C by using iterative QSM. Figure 4 presents good consistency in brain structures and susceptibility values. Some difference can be observed at the frontal lobe as indicated by white arrows in Fig 4B, -C. Figures 5 and 6 show the region-of-interest analysis results from iterative QSM and deterministic QSM, respectively, of the within-site and cross-site variations for all 9 subjects. Among the 5 ROIs, the putamen and globus pallidus show comparably less imprecision in the susceptibility values, whereas the red nucleus and substantia nigra exhibit relatively larger imprecision ( $P < .001$  for all pairs of comparison). Generally, for each subject, cross-site variation of susceptibility values is no larger than within-site variation in all ROIs statistically ( $P > .01$  after Bonferroni correction). The Table summarizes results in Figs 5 and 6 by showing within-site and cross-site imprecisions averaged from 9 subjects. Iterative QSM and deterministic QSM perform equally well in these regions. The caudate nucleus is the only exception among the 5 ROIs, in which iterative QSM (0.0054 and 0.0059 ppm for within-site and cross-site imprecisions, respectively) is found to outperform

deterministic QSM (0.0087 and 0.0107 ppm for within-site and cross-site imprecisions, respectively).

Figure 7 plots the susceptibility values versus age with the preliminary linear regression results. Among the 5 selected ROIs, the putamen, globus pallidus, and red nucleus present correlation coefficients of 0.40, 0.35, and 0.47 ( $P < .001$ ), respectively, which reach statistical significance. The caudate nucleus, on the other hand, shows no age association ( $P > .5$ ). The substantia nigra exhibits marginal association with age, showing a correlation coefficient of 0.20 and  $P = .02$ , which does not reach statistical significance after Bonferroni correction.

## DISCUSSION

Quantitative susceptibility mapping provides an important opportunity for measuring pathologic changes in iron content to improve the diagnosis of brain diseases.<sup>25</sup> Before one fully uses the potential of QSM, it should be understood that settings of the parameters in the data-preprocessing procedures and the susceptibility-mapping algorithms could both lead to variations in the quantitative results. Therefore, it is essential to establish the precision level of QSM in terms of both within-site and cross-site reproducibility before wide application of this technique to clinical studies.

The results from our study show that while within-site and cross-site yield sim-

ilar reproducibility levels in general, the caudate nucleus, putamen, and globus pallidus show significantly higher precision in susceptibility values (average variations on the order of 0.005 ppm) than the red nucleus and substantia nigra (average variations on the order of 0.01 ppm) when computed by using iterative QSM. This regional dependency of QSM precision is anticipated to arise from the influences of air-tissue interfaces. In fact, the shimming condition is expected to alter in different scans particularly near the air-tissue interfaces, which in turn, could cause inconsistencies in background field removal via the PDF method. Moreover, the PDF approach, though relatively robust compared with the high-pass-filtering approach, is known to exhibit difficulties in the object boundaries, which also correspond to regions adjacent to the air cavities.<sup>18</sup> Our experimental observation of the somewhat larger cross-site discrepancy in the frontal region, as shown in Fig 4, is also consistent with the inference that boundaries of large susceptibility changes remain the major challenging regions for QSM. The red nucleus and substantia nigra are 2 examples of tissues at the skull base level, hence exhibiting relatively lower precision than other regions investigated in this study.

One recent study reported aging-related increases in suscepti-

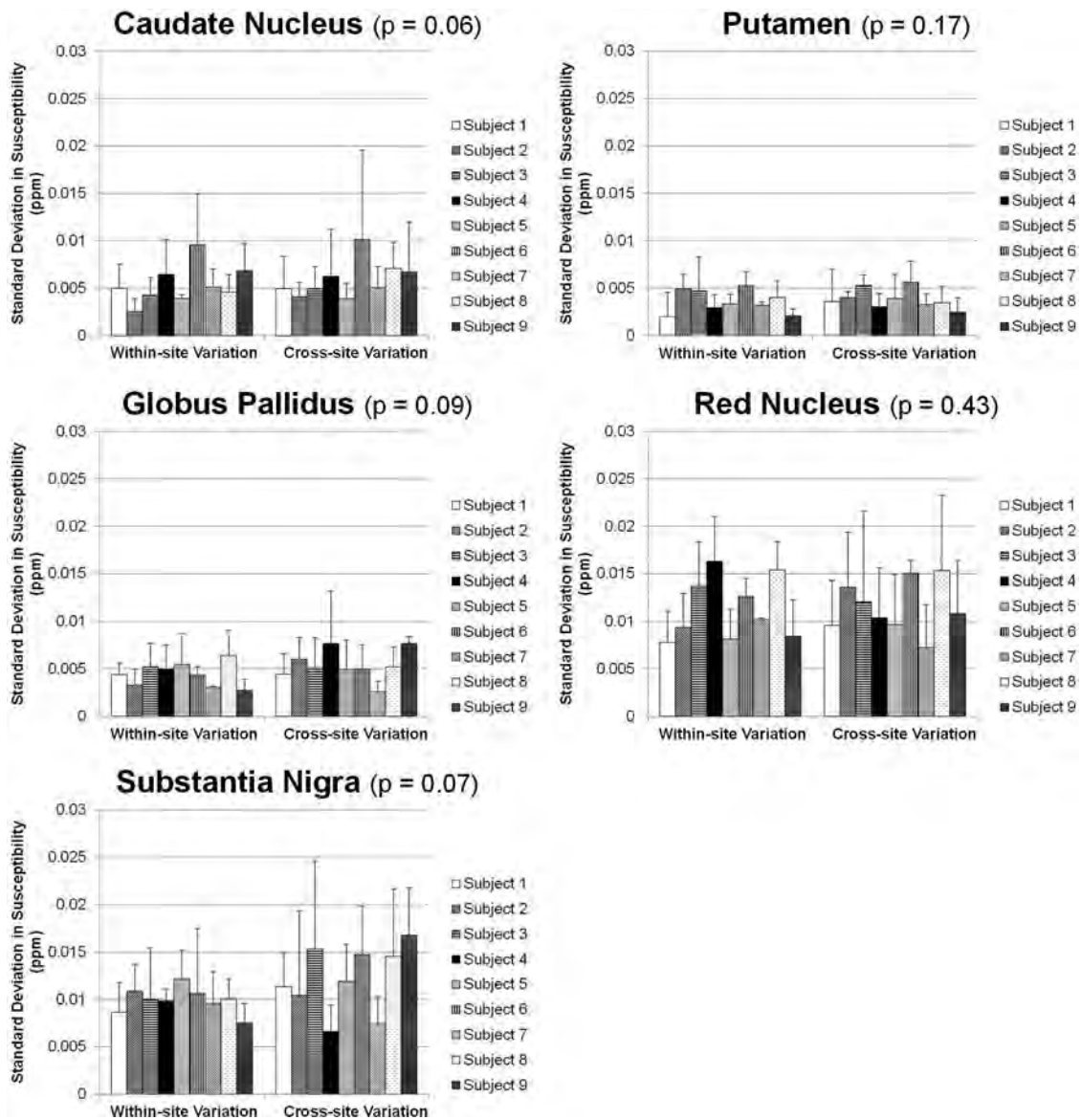


**FIG 5.** Within-site (*left*) and cross-site (*right*) imprecisions shown as SDs from multiple measurements on the 9 subjects by using the iterative QSM algorithm. The *P* values shown in the subplot titles stand for the difference between within-site and cross-site precisions (paired Student *t* test). For all 5 regions, cross-site variations are not larger than within-site variations. The putamen and globus pallidus show the highest precision, followed by the caudate nucleus, red nucleus, and substantia nigra.

bility values in healthy human subjects, with stronger statistical significance found in the putamen, globus pallidus, and red nucleus than in the substantia nigra, and insignificant changes in the caudate nucleus,<sup>7</sup> all in very good agreement with findings from our study. In the study by Bilgic et al,<sup>7</sup> the analysis was performed on 2 groups of subjects whose age ranges were far separated (21–29 years for the young population versus 64–86 years for the elderly population, respectively), as opposed to our preliminary investigation in which the subject age range was relatively narrow (23–37 years). Nevertheless, the ranges of the numeric values of the magnetic susceptibility found for these brain regions in our data are consistent with those in previous investigations.<sup>7,26</sup> More important, with the levels of precision achieved in our study, future examinations of the aging-related susceptibility changes on the basis of regression analysis as opposed to categoric analysis should be highly feasible.

In the phantom experiment, the slope between measured and expected susceptibility values in Fig 1 is 0.91, which reveals 9% of the inaccuracy in QSM. The inaccuracy of QSM in this study was found to be at a level similar to that found in another study (Fig 2 in de Rochefort et al, slope = 0.93).<sup>1</sup> Although the slope is found to deviate from the ideal value of unity, the *R*<sup>2</sup> value of 0.9999 between measured and expected susceptibility values demonstrates the high linearity of susceptibility mapping within the range of 0–2.04 ppm. Thus, the precision and reproducibility are not affected, even if the nonunity slope currently remains an unsolved issue if absolute accuracy is required.

Comparison of iterative and deterministic QSM shows that both algorithms are capable of solving the inverse problem of susceptibility mapping with good consistency, at least for region-of-interest-based analysis. However, deterministic QSM may be more susceptible to streaking artifacts at regions surrounding strong susceptibility

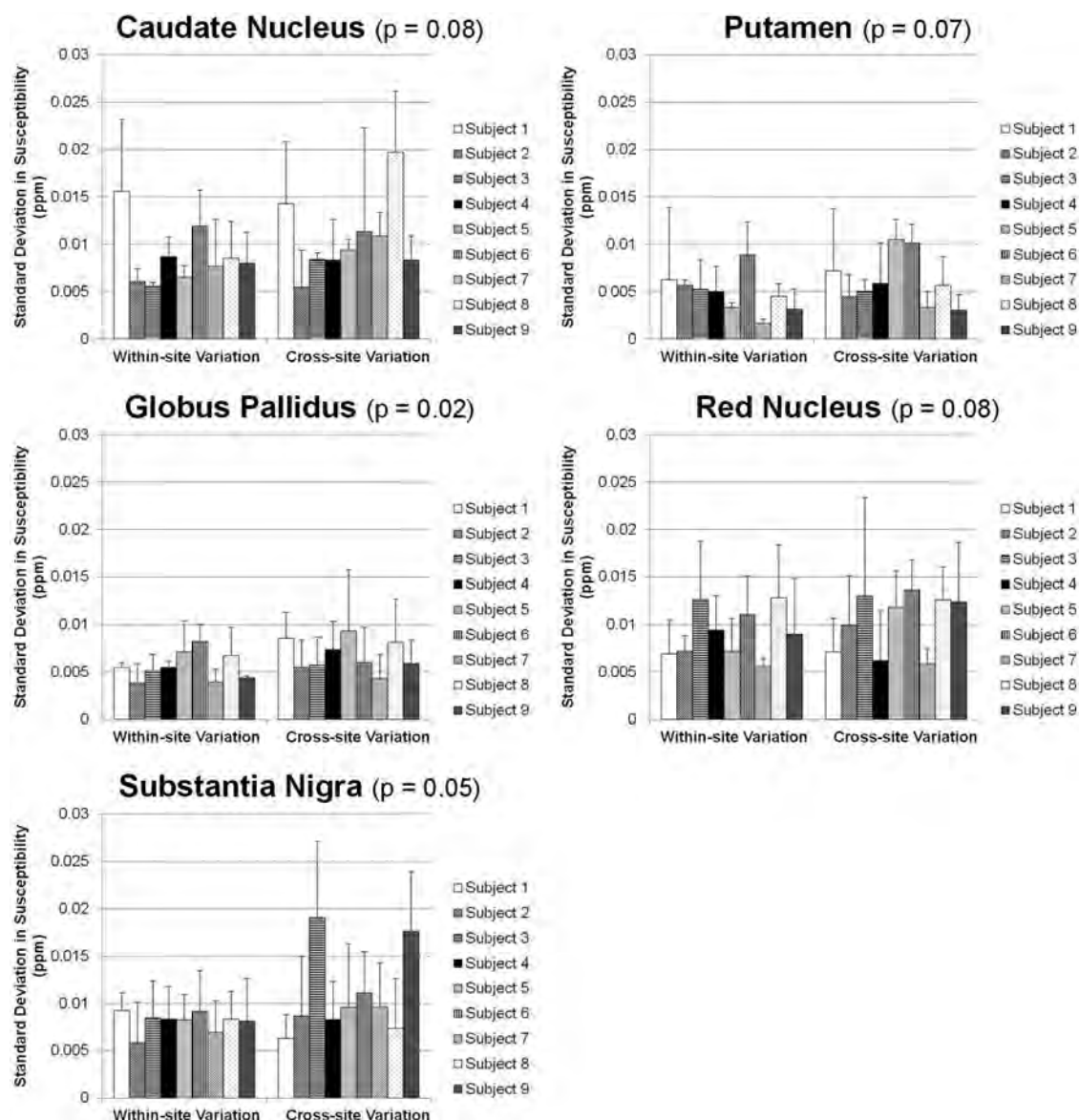


**FIG 6.** Within-site (*left*) and cross-site (*right*) imprecisions shown as SDs from multiple measurements on the 9 subjects by using the deterministic QSM algorithm. The *P* values shown in the subplot titles stand for the difference between within-site and cross-site precisions (paired Student *t* test). For all 5 regions, cross-site variations are not larger than within-site variations. The putamen and globus pallidus show the highest precision, followed by the caudate nucleus, red nucleus, and substantia nigra.

**Within-site and cross-site imprecisions averaged from 9 subjects**

ROI	Method	Within-Site Imprecision (ppm)	Cross-Site Imprecision (ppm)
Caudate nucleus	Iterative QSM	0.0054 (10.0%)	0.0059 (11.0%)
	Deterministic QSM	0.0087 (17.9%)	0.0107 (21.9%)
Putamen	Iterative QSM	0.0037 (9.3%)	0.0038 (9.5%)
	Deterministic QSM	0.0048 (8.3%)	0.0061 (10.6%)
Globus pallidus	Iterative QSM	0.0044 (3.4%)	0.0054 (4.1%)
	Deterministic QSM	0.0056 (3.4%)	0.0068 (4.1%)
Red nucleus	Iterative QSM	0.0113 (18.4%)	0.0115 (18.7%)
	Deterministic QSM	0.0091 (9.3%)	0.0103 (10.6%)
Substantia nigra	Iterative QSM	0.0099 (15.2%)	0.0121 (18.6%)
	Deterministic QSM	0.0081 (8.2%)	0.0108 (11.1%)

equations 1 and 2 suggests that the inclusion of the edge mask from the magnitude image in the regularization term is the major cause for the difference in the performance for the 2 QSM algorithms. Most interesting, on human brain susceptibility maps obtained in vivo by using deterministic QSM, streaking artifacts are not as visually prominent as on the phantom images, where the possible presence of the streaking artifacts may have been masked by the texture of brain tissues. While for these human data, the comparative superiority of the 2 QSM algorithms

changes, as shown in the phantom images. This susceptibility could also explain the somewhat inferior reproducibility of deterministic QSM to iterative QSM in the caudate nucleus. An examination of

cannot be assessed because no ground truth could be obtained for validation, causing difficulty in determining which of the 2 QSM methods gives a lower level of streaking artifacts in Fig 3, the

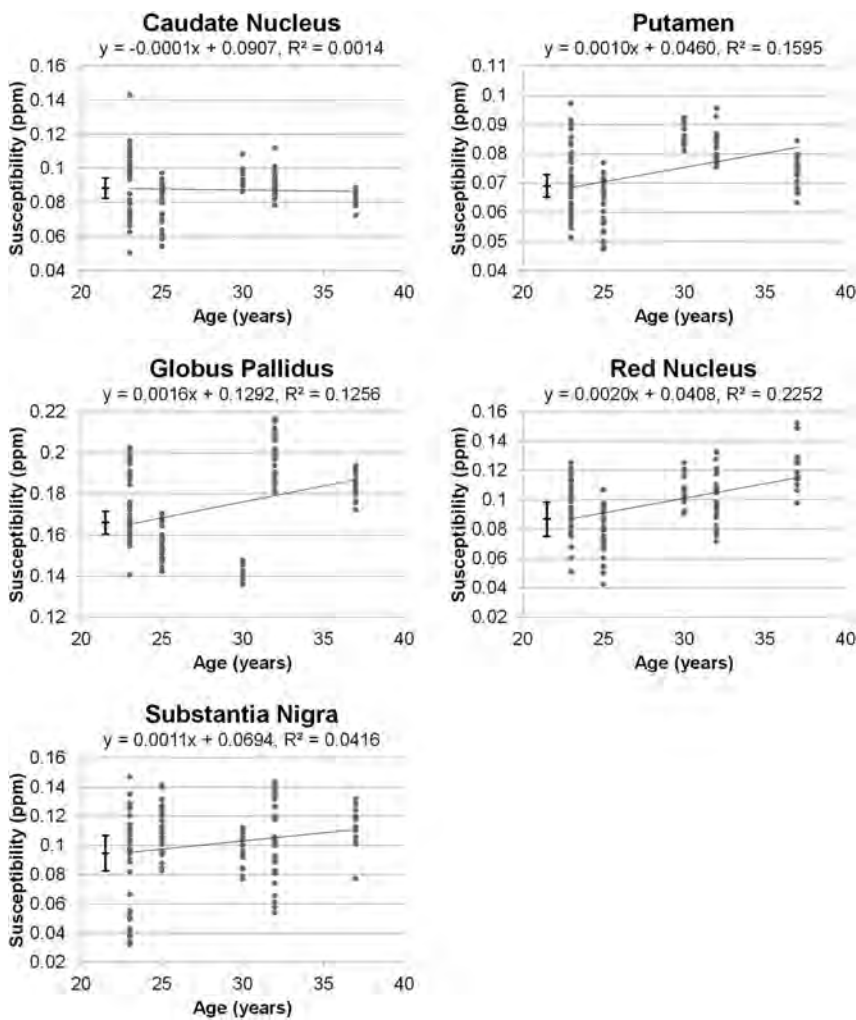


**FIG 7.** Linear regression results comparing susceptibility values versus age by using 135 datasets collected in this study. Among the 5 ROIs, the putamen, globus pallidus, and red nucleus present correlation coefficients of 0.40, 0.35, and 0.47, respectively ( $P < .001$ ). The caudate nucleus shows no age association ( $P > .5$ ), and the substantia nigra exhibits a marginal association that does not reach statistical significance after Bonferroni correction ( $P = .02$ ). The vertical error bars shown on the left stand for the cross-site variability values of iterative QSM found for these regions.

phantom results are certainly in favor of iterative QSM. Consequently, although the deterministic QSM is found to be at least 700 times faster than iterative QSM and thus opening an opportunity for on-line reconstruction of susceptibility maps at the MR imaging console, for detailed quantitative analysis such as aging-related changes, the iterative QSM approach is still recommended.

In data preprocessing, the purpose of background field removal is to extract local magnetic field variation generated by brain tissues, which is subsequently used for QSM. The high-pass filtering method is not preferred for quantitative susceptibility mapping, even though it is one of the most frequently used methods for background field removal in MR imaging (eg, in susceptibility-weighted imaging). One of the major limitations of applying high-pass filtering in QSM is that part of the local field information could be mistakenly filtered out, because the distributions of spatial frequency in local field and in background field cannot be cleanly separated by a single high-pass-filtering kernel size. Therefore, new methods, including the PDF<sup>18</sup> and the sophisticated harmonic artifact reduction for phase data (SHARP)<sup>22</sup> methods, have been proposed for background field

removal in QSM. The idea of both the PDF and the SHARP methods is to decompose local field and background field by using their physical properties. While the PDF method uses a projection theorem, the SHARP method applies the Laplace equation to separate background field. In previous studies, both the PDF and the SHARP methods have been demonstrated to be superior to the high-pass-filtering method for background field removal in QSM.<sup>18,22</sup> From numeric simulation, we have also confirmed that local field obtained by the PDF method preserves subtle field changes from brain tissues better than that obtained by the high-pass-filtering method (data not shown). We, therefore, think that both the PDF and the SHARP methods are adequate for background field removal in QSM. The comparison between the PDF and the SHARP methods, however, is beyond the scope of this study.

This study is limited by the absence of flow compensation to reduce flow-related phase accumulations in vessels and the ventricles. Because our study used commercial 3D multiecho gradient-echo sequences on the tested scanners, full flow compensation for all echoes was unavailable at the time of this study. This scenario may have affected the reference susceptibility values calculated for the flowing CSF in the lateral ventricles. Nonetheless, this minor weakness influences only the absolute susceptibility values reported for the 5 ROIs and is relatively unimportant to our investigation focused on within-site and cross-site precision assessment.

Some investigators used the splenium as a reference<sup>7</sup> instead of using CSF.<sup>26</sup> Yet in our experience, the regional variations of susceptibility in the splenium are no smaller than those found for the lateral ventricles. This potential limitation of uncertain susceptibility values for the CSF could be alleviated with pulse sequence modifications to include flow compensation for all echoes.<sup>17,27</sup> As a last note, the statistical sensitivity of cross-site imprecisions may be somewhat limited by the derivation of SDs by using only 3 numbers. However, this limitation is because we could only access the three 3T scanners. Moreover, even with this statistical limitation, results from this study could still serve as a reference for the imprecision level to be expected in future multisite QSM studies.

## CONCLUSIONS

In summary, quantitative susceptibility mapping is a technique of high potential to measure changes in iron content in human brain tissues. This study demonstrates that an average imprecision level of approximately 0.005–0.01 ppm, depending on the location

within the brain, could be achieved at 3T for QSM when used with careful control, even on different scanners. Results from our study may further increase the practicality and applicability of QSM in longitudinal and cross-site human brain studies.

## ACKNOWLEDGMENTS

The authors thank the following institutions for their research support: Research Center for Mind, Brain & Learning, National Chengchi University; Mind Research and Imaging Center, National Cheng Kung University; and the Department of Radiology, Kaohsiung Veterans General Hospital.

Disclosures: Po-Yu Lin, Tzu-Cheng Chao, Ming-Long Wu—RELATED: Grant: This study was partially supported by research funding from the National Science Council, Taiwan; Support for Travel to Meetings for the Study or Other Purposes: National Science Council, Taiwan, Comments: The traveling expense among multiple MRI sites to collect data was supported by research grants from the National Science Council, Taiwan.

## REFERENCES

1. de Rochefort L, Liu T, Kressler B, et al. **Quantitative susceptibility map reconstruction from MR phase data using Bayesian regularization: validation and application to brain imaging.** *Magn Reson Med* 2010;63:194–206
2. Liu T, Liu J, de Rochefort L, et al. **Morphology enabled dipole inversion (MEDI) from a single-angle acquisition: comparison with COSMOS in human brain imaging.** *Magn Reson Med* 2011;66:777–83
3. Schweser F, Deistung A, Sommer K, et al. **Toward online reconstruction of quantitative susceptibility maps: superfast dipole inversion.** *Magn Reson Med* 2013;69:1582–94
4. Shmueli K, de Zwart JA, van Gelderen P, et al. **Magnetic susceptibility mapping of brain tissue in vivo using MRI phase data.** *Magn Reson Med* 2009;62:1510–22
5. Wharton S, Schafer A, Bowtell R. **Susceptibility mapping in the human brain using threshold-based k-space division.** *Magn Reson Med* 2010;63:1292–304
6. Wu B, Li W, Guidon A, et al. **Whole brain susceptibility mapping using compressed sensing.** *Magn Reson Med* 2012;67:137–47
7. Bilgic B, Pfefferbaum A, Rohlfing T, et al. **MRI estimates of brain iron concentration in normal aging using quantitative susceptibility mapping.** *Neuroimage* 2012;59:2625–35
8. Deistung A, Schafer A, Schweser F, et al. **Toward in vivo histology: a comparison of quantitative susceptibility mapping (QSM) with magnitude-, phase-, and R2\*-imaging at ultra-high magnetic field strength.** *Neuroimage* 2013;65:299–314
9. Li W, Wu B, Liu C. **Quantitative susceptibility mapping of human brain reflects spatial variation in tissue composition.** *Neuroimage* 2011;55:1645–56
10. Lim IA, Faria AV, Li X, et al. **Human brain atlas for automated region of interest selection in quantitative susceptibility mapping: application to determine iron content in deep gray matter structures.** *Neuroimage* 2013;82:449–69
11. Liu J, Liu T, de Rochefort L, et al. **Morphology enabled dipole inversion for quantitative susceptibility mapping using structural consistency between the magnitude image and the susceptibility map.** *Neuroimage* 2012;59:2560–68
12. Wu B, Li W, Avram AV, et al. **Fast and tissue-optimized mapping of magnetic susceptibility and T2\* with multi-echo and multi-shot spirals.** *Neuroimage* 2012;59:297–305
13. Langkammer C, Schweser F, Krebs N, et al. **Quantitative susceptibility mapping (QSM) as a means to measure brain iron? A post mortem validation study.** *Neuroimage* 2012;62:1593–99
14. Zheng W, Nichol H, Liu S, et al. **Measuring iron in the brain using quantitative susceptibility mapping and X-ray fluorescence imaging.** *Neuroimage* 2013;78:68–74
15. de Rochefort L, Brown R, Prince MR, et al. **Quantitative MR susceptibility mapping using piece-wise constant regularized inversion of the magnetic field.** *Magn Reson Med* 2008;60:1003–09
16. Cusack R, Papadakis N. **New robust 3-D phase unwrapping algorithms: application to magnetic field mapping and undistorting echoplanar images.** *Neuroimage* 2002;16:754–64
17. Gilbert G, Savard G, Bard C, et al. **Quantitative comparison between a multiecho sequence and a single-echo sequence for susceptibility-weighted phase imaging.** *Magn Reson Imaging* 2012;30:722–30
18. Liu T, Khalidov I, de Rochefort L, et al. **A novel background field removal method for MRI using projection onto dipole fields (PDF).** *NMR Biomed* 2011;24:1129–36
19. Cheng YC, Neelavalli J, Haacke EM. **Limitations of calculating field distributions and magnetic susceptibilities in MRI using a Fourier based method.** *Phys Med Biol* 2009;54:1169–89
20. Haacke EM, Tang J, Neelavalli J, et al. **Susceptibility mapping as a means to visualize veins and quantify oxygen saturation.** *J Magn Reson Imaging* 2010;32:663–76
21. Liu T, Spincemaille P, de Rochefort L, et al. **Calculation of susceptibility through multiple orientation sampling (COSMOS): a method for conditioning the inverse problem from measured magnetic field map to susceptibility source image in MRI.** *Magn Reson Med* 2009;61:196–204
22. Schweser F, Deistung A, Lehr BW, et al. **Quantitative imaging of intrinsic magnetic tissue properties using MRI signal phase: an approach to in vivo brain iron metabolism?** *Neuroimage* 2011;54:2789–807
23. Bilgic B, Chatnuntawech I, Fan AP, et al. **Fast image reconstruction with L2-regularization.** *J Magn Reson Imaging* 2014;40:181–91
24. Kressler B, de Rochefort L, Liu T, et al. **Nonlinear regularization for per voxel estimation of magnetic susceptibility distributions from MRI field maps.** *IEEE Trans Med Imaging* 2010;29:273–81
25. Wang S, Lou M, Liu T, et al. **Hematoma volume measurement in gradient echo MRI using quantitative susceptibility mapping.** *Stroke* 2013;44:2315–17
26. Wharton S, Bowtell R. **Whole-brain susceptibility mapping at high field: a comparison of multiple- and single-orientation methods.** *Neuroimage* 2010;53:515–25
27. Liu T, Wisnieff C, Lou M, et al. **Nonlinear formulation of the magnetic field to source relationship for robust quantitative susceptibility mapping.** *Magn Reson Med* 2013;69:467–76

# Brain Metabolic Abnormalities Associated with Developmental Venous Anomalies

M. Larvie, D. Timerman, and J.A. Thum



## ABSTRACT

**BACKGROUND AND PURPOSE:** Developmental venous anomalies are the most common intracranial vascular malformation and are typically regarded as inconsequential, especially when small. While there are data regarding the prevalence of MR imaging findings associated with developmental venous anomalies, FDG-PET findings have not been well-characterized.

**MATERIALS AND METHODS:** Clinical information systems were used to retrospectively identify patients with developmental venous anomalies depicted on MR imaging examinations who had also undergone FDG-PET. Both the MR imaging and FDG-PET scans were analyzed to characterize the developmental venous anomalies and associated findings on the structural and functional scans. Qualitative and quantitative assessments were performed, including evaluation of the size of the developmental venous anomaly, associated MR imaging findings, and characterization of the FDG uptake in the region of the developmental venous anomaly.

**RESULTS:** Twenty-five developmental venous anomalies in 22 patients were identified that had been characterized with both MR imaging and FDG-PET, of which 76% (19/25) were associated with significant metabolic abnormality in the adjacent brain parenchyma, most commonly hypometabolism. Patients with moderate and severe hypometabolism were significantly older (moderate: mean age,  $65 \pm 7.4$  years,  $P = .001$ ; severe: mean age,  $61 \pm 8.9$  years,  $P = .008$ ) than patients with developmental venous aberrancies that did not have abnormal metabolic activity (none: mean age,  $29 \pm 14$  years).

**CONCLUSIONS:** Most (more than three-quarters) developmental venous anomalies in our series of 25 cases were associated with metabolic abnormality in the adjacent brain parenchyma, often in the absence of any other structural abnormality. Consequently, we suggest that developmental venous anomalies may be better regarded as developmental venous aberrancies.

**ABBREVIATION:** DVA = developmental venous anomaly

A developmental venous anomaly (DVA) is a transparenchymal vein of greater than usual size into which coalesces a network of smaller veins, a configuration described as a caput

medusa. DVAs may drain into either the superficial or deep venous systems and may occur in the cerebrum, cerebellum, brain stem, and spinal cord. DVAs are the most common intracranial vascular malformation, with a reported incidence of 2.6%.<sup>1,2</sup> The mechanism of DVA formation is still controversial. The term “developmental venous anomaly” was first coined by Lasjaunias et al<sup>3</sup> to emphasize their belief that these are embryologic variants of venous drainage rather than true vascular anomalies.

Brain parenchymal lesions have been widely reported in association with DVAs, with abnormalities apparent on angiography,<sup>4</sup> CT<sup>5</sup> and MR structural imaging,<sup>6–8</sup> and functional imaging methods such as perfusion and diffusion-weighted imaging.<sup>9–12</sup> Several case reports further exemplify how DVAs can be associated with clinical pathologies such as hemorrhagic transformation, ischemic complications, and epileptogenic foci.<sup>13–16</sup> Recent studies also indicate the possible role of DVAs in the formation of cavernous malformations.<sup>9</sup> These findings suggest that the clinical significance of abnormal brain anatomy and activity near a DVA

Received July 31, 2014; accepted after revision September 18.

From the Harvard Medical School (M.L.), Boston, Massachusetts; Divisions of Neuroradiology and Nuclear Medicine and Molecular Imaging (M.L., D.T., J.A.T.), Department of Radiology, Massachusetts General Hospital, Boston, Massachusetts; and Division of Health Sciences and Technology (D.T., J.A.T.), Harvard–Massachusetts Institute of Technology, Cambridge, Massachusetts.

This work was supported in part by the National Institutes of Health (P01 AG036694-01, 2R01 AG026484-06A1).

Paper previously presented in abstract form at: Annual Meeting of the American Society of Neuroradiology and the Foundation of the ASNR Symposium, May 17–22, 2014; Montreal, Quebec, Canada.

Please address correspondence to Mykol Larvie, MD, PhD, Department of Radiology, Massachusetts General Hospital, 55 Fruit St, Boston, MA 02114; e-mail: mlarvie@gmail.com

 Indicates open access to non-subscribers at www.ajnr.org

 Indicates article with supplemental on-line table.

<http://dx.doi.org/10.3174/ajnr.A4172>

is uncertain and has yet to be accurately evaluated. Furthermore, our clinical experience has revealed metabolic abnormality associated with DVAs, as determined by FDG-PET. These findings led us to the hypothesis that the metabolic activity in brain parenchyma in the region of a DVA is abnormal. In this study, we sought to better understand metabolic activity in the region of DVAs as assessed by FDG-PET.

## MATERIALS AND METHODS

### Patient Population

This study was performed at a tertiary care academic medical center for adult and pediatric patients and was approved by the institutional review board and ethics committee. A retrospective search for patients with DVAs identified on radiologic examinations during January 2000 to August 2013 at our institution was performed. The reports were analyzed for key terms by using an internal radiology report data base. There were 9337 radiology reports that included the phrases “developmental venous abnormality,” “developmental venous anomaly,” “venous angioma,” “cerebral venous malformation,” “cerebral venous medullary malformation,” or “DVA” in the findings. Criteria for inclusion in the study were the following: 1) patients with at least 1 cerebral or cerebellar DVA identified by MR imaging and reconfirmed by a neuroradiologist (M.L.); 2) positive confirmation of the DVA, as defined by the presence of dilated medullary veins (caput medusa) converging to a large transparenchymal vein draining into a deep or superficial vein; and 3) availability of an FDG-PET scan performed within 1 year of the MR imaging examination demonstrating the DVA. Consequently, all included cases were initially identified and reported by a clinical staff radiologist and subsequently confirmed by a trained neuroradiologist for inclusion in this study. Exclusion criteria for this study were the following: 1) PET or MR imaging findings suggestive of a neurodegenerative disease; or 2) a confounding lesion, such as a tumor, in the region of the DVA or the anatomically equivalent contralateral cortex. One subject had a seizure at the time of PET imaging: This case is presented independently and was not included in the statistical data analysis of the correlates of hypometabolism. Of the 22 patients who qualified for this study, 25 DVAs were identified. The medical histories of the 22 patients were reviewed to identify demographic information, the initial reason for obtaining the imaging studies, and DVA characteristics (Table and On-line Table).

### MR Imaging

The included MR imaging examinations were performed using a variety of imaging protocols that were prescribed according to the clinical indication for the scan. All MR imaging was performed at our institution using 1.5T (Signa, GE Healthcare, Milwaukee, Wisconsin; and Avanto, Siemens, Erlangen, Germany), 3T (Discovery, GE Healthcare; and Trio and Skyra, Siemens), and 7T (Siemens) scanners. When available, postcontrast T1-weighted imaging was used for the evaluation and confirmation of the DVA. In those cases in which postcontrast imaging was not available, sequences that reliably depicted flow voids, including T1- and T2-weighted sequences, were used for evaluation of the DVAs. Any additional MR imaging sequences were also reviewed to assess the presence of additional findings in the area affected by

### Summary of characteristics of all patients and DVAs<sup>a</sup>

Characteristic	
Total No. of patients	22
No. of DVAs per patient	
1	19 (86%)
2	3 (14%)
Age (yr) (mean)	41.5 ± 19.8
Male, female sex	11 (50%), 11 (50%)
DVA hemisphere: left, right	
Cerebral	8 (32%), 11 (44%)
Cerebellar	2 (8%), 4 (16%)
Indication for imaging patient	
Seizure	11 (50%)
Tumor	5 (23%)
Memory loss	1 (5%)
Infection	1 (5%)
Other	4 (18%)
Metabolic activity near DVA	
Isometabolic	6 (24%)
Hypometabolic	18 (72%)
Mild	11 (44%)
Moderate	4 (16%)
Severe	3 (12%)
Hypermetabolic	1 (4%)
Mild	0 (0%)
Moderate	0 (0%)
Severe	1 (4%)

<sup>a</sup> Each DVA was counted separately in the 3 patients with multiple DVAs.

the DVA. The specific associated findings identified were the following: atrophy, calcification, hemorrhage, cavernous malformations, and abnormal T2 hyperintensity. Thirteen patients also had CT scans, which were reviewed to aid in the identification of calcification.

### FDG-PET Imaging

All PET was performed at our institution using a standard protocol. Imaging was performed approximately 45 minutes following intravenous injection of 5.0-mCi of [<sup>18</sup>F] fluorodeoxyglucose by using an ECAT HR+ scanner (CTI-Seimens, Knoxville, Tennessee). Sixty-three planes were acquired simultaneously during a 15.5-cm FOV. Images were acquired in 3D mode. Attenuation correction was performed using a transmission scan obtained with a germanium-68 source. A maximum likelihood reconstruction method was used, yielding images with an in-plane resolution of approximately 4.6 mm (full width at half maximum). All patients were screened with fingerstick blood glucose measurement, and PET was not performed in those patients with blood glucose of >150 mg/dL.

### Image Analysis

MR images and PET images were reviewed independently and coregistered using a PACS. PET images were also evaluated by comparison with normal standards to assess regional hypometabolism and hypermetabolism using internally developed software. FDG-PET findings in the brain parenchyma affected by DVAs was qualitatively evaluated and classified as normal, hypometabolic, or hypermetabolic in comparison with parenchyma in the contralateral brain hemisphere. Hypometabolism was further characterized as mild, moderate, and severe with respect to the range of findings in this study. This qualitative assessment of metabolism included both the extent of the lesion and the degree of met-

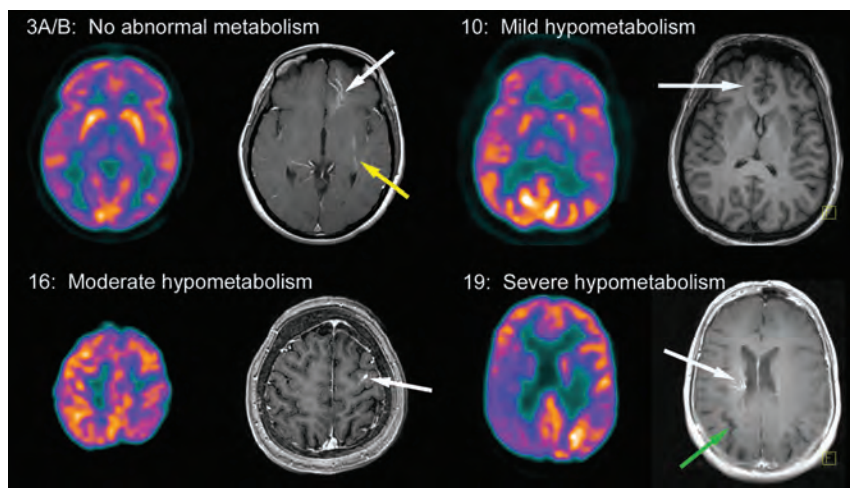


**FIG 1.** Representative FDG-PET and MR images demonstrating DVAs and associated metabolic activity. The numbering in the upper left of each image pair corresponds to the cases in the On-line Table. Cases 3A (white arrow) and 3B (yellow arrow) both do not demonstrate abnormal metabolism with respect to the contralateral cerebral hemisphere. Case 10 demonstrates mild hypometabolism in the anterior right frontal lobe corresponding to an area drained by a DVA. Case 16 demonstrates moderate hypometabolism in the posterior left frontal lobe corresponding to a DVA. Case 19 demonstrates severe hypometabolism distributed over the right frontal and parietal lobes and involving both cortical and deep gray matter in the region of a large DVA, which is not completely depicted on this single axial section. The green arrow in case 19 indicates atrophy.

abolic abnormality. We approximated the size of DVAs as the longest dimension on axial, sagittal, or coronal images, taking into account any visible feature of the DVA, including a caput medusae, if present, and the draining vein. This approximate measurement was obtained from the available imaging that best depicted the DVA, which was predominantly T1 postcontrast images, though other sequences that demonstrated the DVA were reviewed, including T1 precontrast, T2 and SWI, and T2\* gradient recalled-echo images. Both qualitative and quantitative assessments were assigned by the consensus of the 3 authors. Representative MR images and PET images were obtained of each DVA (Fig 1).

### Statistical Analysis

The relationship between DVA size (in centimeters) and the qualitative degree of hypometabolism (normal, mild, moderate, or severe) was statistically analyzed for 24 cases. One of the 25 cases included in this study showed hypermetabolism in the clinical context of a seizure and was excluded from this analysis. Each of the datasets for the degree of hypometabolism was tested for equal variance. An ANOVA test was performed to determine whether the DVA sizes of the hypometabolic groups were significantly different, and pair-wise *t* tests for equal variance among the 6 paired combinations of the 4 groups were performed to determine which groups had significantly different DVA sizes compared with each other. Differences with  $P < .05$  were considered statistically significant.

### RESULTS

Twenty-five DVAs were identified and characterized in 22 patients. A summary of the DVA characteristics and associated findings is presented in the On-line Table. Three patients each had 2 DVAs identified. The other 19 patients each had 1 DVA identified.

Clinical and demographic features of the patient cohort in this

study are presented in the Table. Eleven patients were male, and 11 were female; ages at the time of PET imaging ranged from 14 to 76 years (mean,  $41.5 \pm 19.8$  years). Ten of the 25 DVAs (40%) were identified on the patient's left side. Nineteen of the 25 DVAs (76%) were supratentorial.

Among the 22 patients, the most common indications for imaging were seizure ( $n = 11$ , 50%), tumor ( $n = 5$ , 23%), memory loss ( $n = 1$ , 5%), infection ( $n = 1$ , 5%), and other (including paresthesias, motor deficits, and blurred vision;  $n = 4$ , 18%), as shown in the Table. At least 2 of the patients had symptoms that may have been due to the DVA. One of these patients had a DVA in the left perirolandic region that may have been a causative factor in the patient's reported right-sided paresthesias (case 16). Another patient (case 22) with a left temporo-occipital DVA had a seizure immediately following

injection of FDG. The subsequent PET scan showed severe hypermetabolism associated with the DVA, which may reflect an underlying epileptogenic abnormality.

Qualitatively, 18 DVAs (72%) exhibited some degree of hypometabolism, 6 DVAs (24%) showed no visibly discernible metabolic difference between the cortical region drained by the DVA and the homologous contralateral brain, and 1 DVA (4%) exhibited severe hypermetabolism (case 22, On-line Table).

Examples of the range of metabolic abnormalities seen in association with DVAs are shown in Fig 1, with the case numbering (top left of the image pairs) corresponding to the On-line Table. Cases 3A and 3B both demonstrate no abnormal metabolism in the region of the DVA, which is similar in metabolic activity to the contralateral hemisphere. Case 3A is notable for a large DVA that has no associated metabolic abnormality. Cases 10, 16, and 19 demonstrate mild, moderate, and severe hypometabolism, respectively, compared with the contralateral cerebral hemisphere. Case 19 is a demonstration of hypometabolism involving both cortical and deep gray matter in the region of the DVA.

As shown in Fig 2, patients with DVAs that were associated with moderate and severe hypometabolism were significantly older (moderate: mean age,  $65 \pm 7.4$  years,  $P = .001$ ; and severe: mean age,  $61 \pm 8.9$  years,  $P = .008$ ) than patients with DVAs that were associated with normal metabolic activity (none: mean age,  $29 \pm 14$  years). Furthermore, patients with mild hypometabolism were younger (mild: mean age,  $33 \pm 16$  years) than those with moderate or severe hypometabolism, with  $P = .002$  and  $P = .013$  for the respective comparisons.

As shown in Fig 3, DVAs that were associated with severe hypometabolism were significantly larger (mean,  $5.0 \pm 1.5$  cm) than DVAs that were not associated with metabolic abnormality (mean,  $2.3 \pm 0.6$  cm,  $P = .011$ ) and were also significantly larger than DVAs with mild hypometabolism (mean,  $2.4 \pm 1.0$  cm,  $P =$

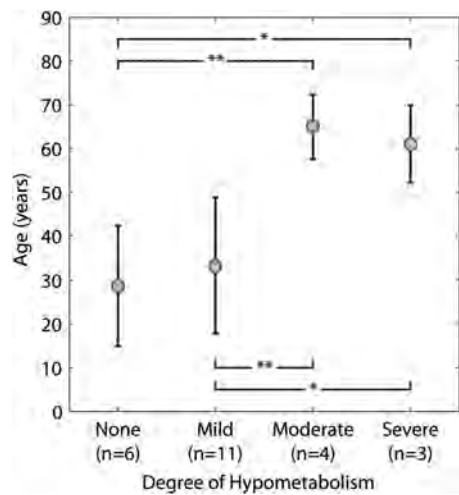


**FIG 2.** Relationship between age and degree of hypometabolism. Patients with DVAs with corresponding moderate and severe hypometabolism were significantly older (moderate: mean age,  $65 \pm 7.4$  years,  $P = .001$ ; severe: mean age,  $61 \pm 8.9$  years,  $P = .008$ ) than patients with DVAs that were not associated with abnormal metabolism (none: mean age,  $29 \pm 14$  years). Patients with a moderate ( $P = .002$ ) or severe ( $P = .013$ ) degree of hypometabolism were also older than patients with mild hypometabolism (mild: mean age,  $33 \pm 16$  years). All patients who were 50 years or older ( $n = 8$ ) had some degree of hypometabolism and included all cases with moderate ( $n = 4$ ) and severe ( $n = 3$ ) hypometabolism. A single asterisk indicates statistical significance at  $P < .05$ ; double asterisks indicate statistical significance at  $P < .005$ . Error bars indicate 2 SDs.

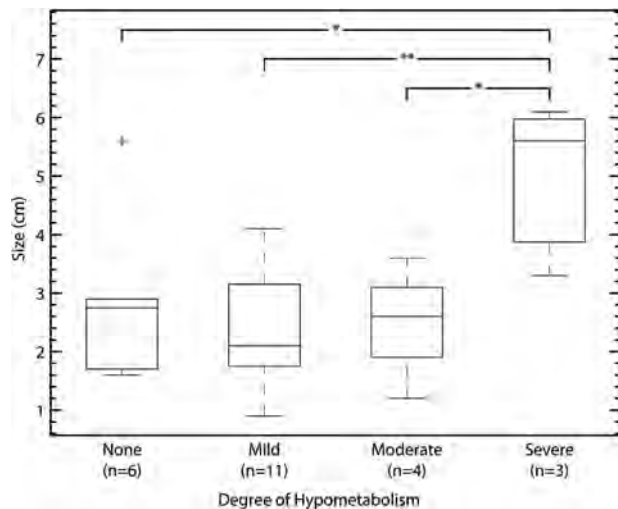


**FIG 3.** Size of the DVA versus the degree of hypometabolism in brain parenchyma drained by the DVA. DVAs associated with severe hypometabolism were larger (mean,  $5.0 \pm 1.5$  cm) than those not associated with abnormal metabolism (mean,  $2.3 \pm 0.6$  cm,  $P = .011$ ), mild hypometabolism (mean,  $2.4 \pm 1.0$  cm,  $P = .003$ ), and moderate hypometabolism (mean,  $2.5 \pm 1.0$  cm,  $P = .043$ ). Case 3A corresponds to the outlier, which was not included in the statistical analysis. This DVA was not associated with any degree of hypometabolism but had a large size measurement (indicated by a plus sign). DVA size was approximated by using the length of the single greatest dimension of the lesion. A single asterisk indicates statistical significance at  $P < .05$ ; double asterisks indicate statistical significance at  $P < .005$ . Error bars indicate 2 SDs.

.003) and moderate hypometabolism (mean,  $2.5 \pm 1.0$  cm,  $P = .043$ ). A statistically significant difference in DVA size was not observed between DVAs with no associated metabolic abnormality and those associated with mild or moderate hypometabolism.

The 1 DVA in our sample with corresponding hypermetabo-

lism is depicted in Fig 4 and corresponds to case 22 in the On-line Table. In this case, a relatively small DVA is associated with severe hypermetabolism in the adjacent brain parenchyma.

Other findings identified in association with the DVAs were atrophy (4 cases), calcifications (2 cases, one a large calcification measuring 5.5 cm and the other a 1.5-cm calcification), cavernous malformations (2 cases, both subcentimeter), hemorrhage (1 case), and elevated T2 hyperintensity (4 cases), as presented in the On-line Table. The hemorrhage, identified in a single case, was revealed by a 15-mm arc of mild susceptibility signal in the deep white matter along the course of the DVA that was distinct from the associated flow void and was not apparent on a CT scan. This hemorrhage was within the deep white matter and was not clearly associated with hypometabolism in the adjacent cortex. The other findings—atrophy, calcifications, and cavernous malformations—were contained within the area of abnormal metabolism on the PET scan. Overall, 10 of the 25 total DVAs (40%) were associated with a brain parenchymal lesion. Of the 24 nonhypermetabolic cases, all 6 DVAs that were scored as having normal metabolism in the cortex drained by the DVA had no additional abnormalities. Severe hypometabolism was observed in 1 of the 3 cases that exhibited atrophy, both of the 2 cases that had calcification, and 1 of the 4 cases with T2 hyperintensity. The 2 DVA cases with associated cavernous malformations also had corresponding hypometabolism.

## DISCUSSION

We have undertaken this qualitative analysis to evaluate a relatively large number of cases with both structural imaging (principally MR imaging) and metabolic functional imaging with FDG-PET. In this study, cortical hypometabolism associated with a DVA was observed in more than two-thirds of the 25 cases identified, supporting our hypothesis that the metabolic activity in the brain parenchyma in the region of a DVA is not necessarily definitively normal. This finding challenges the conventional understanding that DVAs are clinically inconsequential and do not affect adjacent brain parenchyma,<sup>3</sup> though the significance of any metabolic abnormality remains uncertain.

The etiology of hypometabolism in the brain parenchyma drained by a DVA is unclear and may reflect an intrinsic, possibly developmental, neuronal abnormality or an acquired abnormality secondary to derangement of blood flow. We observed an association between the degree of DVA-associated hypometabolism and increased age of the patient. This association between hypometabolism in the drainage region of a DVA and age suggests the hypothesis that DVAs result in cumulative brain parenchymal injury. In this study, all 8 patients who were 50 years or older had some degree of hypometabolism, including all 4 cases with moderate hypometabolism and all 3 cases with severe hypometabolism.

DVAs have been documented in neonates,<sup>17,18</sup> children,<sup>19</sup> and adults.<sup>7</sup> Risk stratification among age groups is challenging, given that the progression of brain abnormality and associated symptoms may be slow. One report showed that patients with signal-intensity changes associated with a DVA were significantly older than those without.<sup>7</sup>

Our case series included a large DVA with no associated meta-

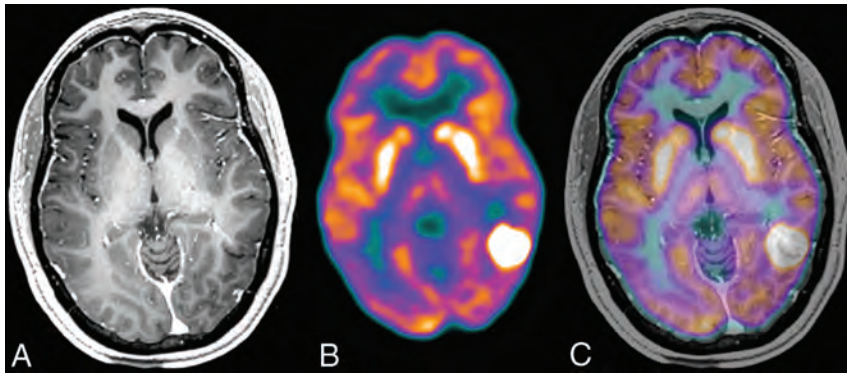


**FIG 4.** Case 22 is a patient who presented for evaluation of epilepsy. MR imaging (A) revealed a DVA in the left temporo-occipital region, seen here on postcontrast T1 images. Additional sequences (not shown) reveal elevated T2 signal in the region surrounding the DVA. The patient had seizure activity shortly after FDG administration, and FDG-PET (B) demonstrates focal severe hypermetabolism within the posterior left temporal lobe and anterior left occipital lobe that corresponds to the region of T2 hyperintensity on the MR imaging. Coregistration of the MR imaging and FDG-PET (C) demonstrates concordance between the PET abnormality and the DVA, suggesting the possibility that cortical abnormality related to the DVA may have resulted in an epileptogenic focus.

bolic abnormality (case 3A) in a 24-year-old patient. This stands as the single exception in this series, in which other large DVAs were associated with other brain parenchymal abnormalities. It would be informative to learn whether this lesion remains stable or additional brain parenchymal abnormalities develop with time.

Hemorrhagic or ischemic infarction around a DVA has been reported in multiple studies<sup>1,3,20</sup> and has been attributed to acute thrombosis of the collecting vein. Not all patients with DVAs in our study had observable hypometabolism near the DVA, suggesting that either not all DVAs result in decreased metabolic activity or that infarction and subsequent brain parenchymal injury have yet to occur in such patients.

Few reports have used FDG-PET to evaluate the metabolic activity in the brain parenchyma drained by DVAs. In one case report, a patient presented with a DVA with associated increased FDG uptake in a region of MR imaging enhancement, which was attributed to “vascular changes, microcalcifications, and chronic inflammatory changes.”<sup>20</sup> Although it is challenging to appreciate the complete FDG-PET findings without a thorough analysis of the data, it appears that the axial map provided in Fig 2A of that report could suggest marked hypometabolism associated with the DVA in the right cerebellum relative to the homologous contralateral region. In another case report, Planche et al<sup>21</sup> described a patient with a DVA and cortical hypometabolism demonstrated on FDG-PET, though this finding was confounded by superimposed pathology of Sturge-Weber syndrome, including extensive pial angiomatosis.

Brain metabolism has been previously evaluated by using FDG-PET in patients with cavernous malformations. Ryvlin et al<sup>22</sup> observed significantly reduced brain metabolism in 4 of 22 patients with cavernous malformations. Although DVAs are commonly associated with cavernous malformations, the 2 are distinct cerebral vascular malformations. Our finding of a higher incidence of metabolic abnormality associated with DVAs compared with cavernous malformations suggests that these vascular malformations have differential effects on the brain.

We observed 1 patient (case 22) who had seizure activity shortly after FDG administration, which manifested as extreme focal hypermetabolism in the posterior left temporal lobe, which corresponded to a T2 hyperintense cortical abnormality seen on the MR imaging (Fig 4). The association of DVAs and seizure has been previously reported<sup>23</sup>; however, to the best of our knowledge, this is the first report to observe hypermetabolic activity near the region of a DVA on FDG-PET. The concordance between the PET and MR imaging findings further suggests that DVAs may be epileptogenic. Alternatively, or in addition, the DVA in this case may be associated with a cortical malformation, which supports the hypothesis that DVA may be a marker of developmental abnormality that includes

both vessels and neurons.

The findings of this study have implications for the evaluation of patients with DVAs. We suggest that certain criteria may help to identify DVAs that could be symptomatic and that might warrant further evaluation, especially with FDG-PET. These include the following: 1) symptoms that could localize to the region of the DVA, 2) increased age (older than 50 years), and 3) large size (>4 cm). The presence or absence of brain parenchymal abnormalities on MR imaging was not strongly associated with metabolic abnormalities, so these findings may be less useful in the identification of symptomatic DVAs.

This study has several limitations. Although the number of DVAs included in this study is greater than that of any other DVA study evaluating FDG-PET findings, our collection of cases is relatively small owing to the relative scarcity of DVAs and the infrequency of FDG-PET examinations. Because the patients in this study underwent PET imaging as part of the inclusion criteria, there was a potential selection bias for patients with clinical symptoms that prompted the examination. Consequently, it is possible that the frequency with which hypometabolism is associated with DVAs is higher in our clinical population than in the general population. Nonetheless, the finding of hypometabolism in most cases reported here supports the conclusion that in some patients, the presence of a DVA correlates with and may cause brain parenchymal abnormality. Another limitation in this study is that the method used for measuring DVA size has limited accuracy in characterizing the overall extent of the lesion. DVAs are topologically diverse and not accurately characterized with orthogonal measurements. Furthermore, the PET findings in this study were qualitatively analyzed on the basis of visual inspection. A more quantitative volumetric analysis would better characterize the region of brain parenchyma affected by DVAs. Additionally, such a quantitative approach to the structural data would provide an improved approach to quantitative analysis of the PET data by providing a better defined region of interest for PET analysis.

## CONCLUSIONS

We found that most (more than three-quarters) of the DVAs in our series of 25 cases were associated with metabolic abnormality in the adjacent brain parenchyma, as assessed by FDG-PET, often in the absence of any other structural abnormality. We also found that a more severe degree of DVA-associated hypometabolism was observed in older patients. In light of these findings, we suggest that DVAs may be better regarded as developmental venous aberrancies. A better understanding of the pathogenesis of the parenchymal metabolic abnormality associated with DVAs would be useful in the evaluation and possibly the management of patients with DVAs.

Disclosures: Mykol Larvie—RELATED: Grant: National Institutes of Health\*; UNRELATED: Grants/Grants Pending: National Institutes of Health.\*\*Money paid to the institution.

## REFERENCES

1. Sarwar M, McCormick WF. **Intracerebral venous angioma: case report and review.** *Arch Neurol* 1978;35:323–25
2. Lee M, Kim MS. **Image findings in brain developmental venous anomalies.** *J Cerebrovasc Endovasc Neurosurg* 2012;14:37–43
3. Lasjaunias P, Burrows P, Planet C. **Developmental venous anomalies (DVA): the so-called venous angioma.** *Neurosurg Rev* 1986;9:233–42
4. Saito Y, Kobayashi N. **Cerebral venous angiomas: clinical evaluation and possible etiology.** *Radiology* 1981;139:87–94
5. Valavanis A, Wellauer J, Yaşargil MG. **The radiological diagnosis of cerebral venous angioma: cerebral angiography and computed tomography.** *Neuroradiology* 1983;24:193–99
6. Wilms G, Demaerel P, Robberecht W, et al. **Coincidence of developmental venous anomalies and other brain lesions: a clinical study.** *Eur Radiol* 1995;5:495–500
7. Santucci GM, Leach JL, Ying J, et al. **Brain parenchymal signal abnormalities associated with developmental venous anomalies: detailed MR imaging assessment.** *AJNR Am J Neuroradiol* 2008;29:1317–23
8. Linscott LL, Leach JL, Zhang B, et al. **Brain parenchymal signal abnormalities associated with developmental venous anomalies in children and young adults.** *AJNR Am J Neuroradiol* 2014;35:1600–07
9. Sharma A, Zipfel GJ, Hildebolt C, et al. **Hemodynamic effects of developmental venous anomalies with and without cavernous malformations.** *AJNR Am J Neuroradiol* 2013;34:1746–51
10. Jung HN, Kim ST, Cha J, et al. **Diffusion and perfusion MRI findings of the signal-intensity abnormalities of brain associated with developmental venous anomaly.** *AJNR Am J Neuroradiol* 2014;35:1539–42
11. Iv M, Fischbein NJ, Zaharchuk G. **Association of developmental venous anomalies with perfusion abnormalities on arterial spin labeling and bolus perfusion-weighted imaging.** *J Neuroimaging* 2014 Apr 9. [Epub ahead of print]
12. Matsuda H, Terada T, Katoh M, et al. **Brain perfusion SPECT in a patient with a subtle venous angioma.** *Clin Nucl Med* 1994;19:785–88
13. Schneider SW, Ludwig T, Tatenhorst L, et al. **Glioblastoma cells release factors that disrupt blood-brain barrier features.** *Acta Neuropathol* 2004;107:272–76
14. Malik GM, Morgan JK, Boulos RS, et al. **Venous angiomas: an underestimated cause of intracranial hemorrhage.** *Surg Neurol* 1988;30:350–58
15. Nagatani K, Osada H, Takeuchi S, et al. **Surgical resection of developmental venous anomaly causing massive intracerebral haemorrhage: a case report.** *Br J Neurosurg* 2014;28:116–18
16. Griffiths D, Newey A, Faulder K, et al. **Thrombosis of a developmental venous anomaly causing venous infarction and pontine hemorrhage.** *J Stroke Cerebrovasc Dis* 2013;22:e653–55
17. Chang CL, Chiu NC. **Developmental venous anomaly found by cranial US in a neonate.** *Pediatr Radiol* 2010;40:374
18. Horsch S, Govaert P, Cowan FM, et al. **Developmental venous anomaly in the newborn brain.** *Neuroradiology* 2014;56:579–88
19. Gümüş A, Yildirim SV, Kizilkiliç O, et al. **Case report: seizures in a child caused by a large venous angioma.** *J Child Neurol* 2007;22:787–89
20. Vaitkevicius H, Erdemli HE, Anderson WS, et al. **Biopsy neuropathology of cerebral ischemia associated with a developmental venous anomaly.** *Clin Neurol Neurosurg* 2013;115:621–23
21. Planche V, Chassin O, Leduc L, et al. **Sturge-Weber syndrome with late onset hemiplegic migraine-like attacks and progressive unilateral cerebral atrophy.** *Cephalalgia* 2014;34:73–77
22. Ryvlin P, Mauguière F, Sindou M, et al. **Interictal cerebral metabolism and epilepsy in cavernous angiomas.** *Brain* 1995;118(pt 3):677–87
23. Hon JM, Bhattacharya JJ, Counsell CE, et al. **The presentation and clinical course of intracranial developmental venous anomalies in adults: a systematic review and prospective, population-based study.** *Stroke* 2009;40:1980–85

# Identification of Minimal Hepatic Encephalopathy in Patients with Cirrhosis Based on White Matter Imaging and Bayesian Data Mining

H.-J. Chen, R. Chen, M. Yang, G.-J. Teng, and E.H. Herskovits



## ABSTRACT

**BACKGROUND AND PURPOSE:** White matter abnormalities have been demonstrated to play an important role in minimal hepatic encephalopathy. In this study, we aimed to evaluate whether WM diffusion tensor imaging can be used to identify minimal hepatic encephalopathy among patients with cirrhosis.

**MATERIALS AND METHODS:** Our study included 65 patients with cirrhosis with covert hepatic encephalopathy (29 with minimal hepatic encephalopathy and 36 without hepatic encephalopathy). Participants underwent DTI, from which we generated mean diffusivity and fractional anisotropy maps. We used a Bayesian machine-learning technique, called Graphical-Model-based Multivariate Analysis, to determine WM regions that characterize group differences. To further test the clinical significance of these potential biomarkers, we performed Cox regression analysis to assess the potential of these WM regions in predicting survival.

**RESULTS:** In mean diffusivity or fractional anisotropy maps, 2 spatially distributed WM regions (predominantly located in the bilateral frontal lobes, corpus callosum, and parietal lobes) were consistently identified as differentiating minimal hepatic encephalopathy from no hepatic encephalopathy and yielded 75.4%–81.5% and 83.1%–92.3% classification accuracy, respectively. We were able to follow 55 of 65 patients (median = 18 months), and 15 of these patients eventually died of liver-related causes. Survival analysis indicated that mean diffusivity and fractional anisotropy values in WM regions were predictive of survival, in addition to the Child-Pugh score.

**CONCLUSIONS:** Our findings indicate that WM DTI can provide useful biomarkers differentiating minimal hepatic encephalopathy from no hepatic encephalopathy, which would be helpful for minimal hepatic encephalopathy detection and subsequent treatment.

**ABBREVIATIONS:** FA = fractional anisotropy; GAMMA = Graphical-Model-based Multivariate Analysis; HE = hepatic encephalopathy; HR = hazard ratio; MD = mean diffusivity; MHE = minimal hepatic encephalopathy; NHE = no hepatic encephalopathy

Hepatic encephalopathy (HE) is a serious and frequent complication of cirrhosis,<sup>1</sup> which can increase the risk of death.<sup>2</sup> As the mildest form of HE, minimal hepatic encephalopathy (MHE) is defined by impaired performance on psychometric or neu-

rophysiologic testing, despite normal mental status.<sup>1,3</sup> MHE is associated with impaired quality of life<sup>4</sup> and predicts conversion to overt HE,<sup>5</sup> which can result in subsequent mortality.<sup>2</sup> Meanwhile, MHE represents a treatable and reversible stage of HE<sup>6</sup>; it is, therefore, important to identify MHE to optimize treatment and prognosis.

Abnormalities in brain white matter, such as low-grade edema<sup>7-11</sup> and structural impairments,<sup>12-14</sup> have been well-revealed in MHE by MR imaging. These WM abnormalities are believed to be responsible for poor neurologic performances<sup>12,15,16</sup> and brain dysfunctions<sup>17,18</sup> in MHE and to be associated with HE development,<sup>9,11,16</sup> suggesting that WM imaging may be useful in characterizing potential MHE biomarkers. Of WM imaging techniques, diffusion tensor imaging, measuring the appropriate metrics such as mean diffusivity (MD), reflecting water movement across cell membranes, and fractional anisotropy (FA), reflecting microstructural in-

Received April 29, 2014; accepted after revision September 5.

From the Jiangsu Key Laboratory of Molecular and Functional Imaging (H.-J.C., M.Y., G.-J.T.), Department of Radiology, Zhongda Hospital, Medical School, Southeast University, Nanjing, China; Department of Diagnostic Radiology and Nuclear Medicine (R.C., E.H.H.), University of Maryland School of Medicine, Baltimore, Maryland; and Department of Radiology (H.-J.C.), The First Affiliated Hospital of Nanjing Medical University, Nanjing, China.

This work was supported by the grants from the National Basic Research Program of China (973 Program: No. 2013CB733800, No. 2013CB733803), National Natural Science Foundation of China (No. 30910103905), Jiangsu Provincial Special Program of Medical Science (BL2013029), and Scientific Research Foundation of Graduate School of Southeast University (No. YBJJ1243).

Please address correspondence to Edward H. Herskovits, MD, PhD, Department of Diagnostic Radiology and Nuclear Medicine, University of Maryland School of Medicine, Baltimore, Maryland 21201; e-mail: ehh@ieee.org; or Gao-Jun Teng, MD, Jiangsu Key Laboratory of Molecular and Functional Imaging, Department of Radiology, Zhongda Hospital, Medical School, Southeast University, Nanjing 210009, China; e-mail: gjteng@vip.sina.com

Indicates open access to non-subscribers at [www.ajnr.org](http://www.ajnr.org)

Indicates article with supplemental on-line photo.

<http://dx.doi.org/10.3174/ajnr.A4146>

**Table 1: Demographic and clinical characteristics of subjects**

Characteristic	Patients with NHE (n = 36)	Patients with MHE (n = 29)	P Value
Age (yr)	50.1 ± 8.9	52.8 ± 8.4	.227
Sex (male/female)	34/2	26/3	.471 ( $\chi^2$ test)
Education (yr)	8.5 ± 2.9	7.6 ± 2.3	.158
Etiology of cirrhosis (HBV/alcoholism/ HBV + alcoholism/other)	29/4/1/2	22/0/4/3	–
Child-Pugh stage (A/B/C)	19/12/5	8/10/11	–
Child-Pugh score	7.0 ± 2.2	8.4 ± 2.2	.016
Previous history of overt HE (yes/no)	7/29	10/19	.170
Number Connection Test A (sec)	44.5 ± 10.8	81.4 ± 23.8	<.001
Digit Symbol Test (raw score)	40.2 ± 8.7	23.6 ± 7.7	<.001
Block Design Test (raw score)	29.3 ± 8.8	17.7 ± 6.5	<.001

**Note:**—HBV indicates hepatitis B virus.

tegrity of WM, is demonstrated to reveal the neuropathologic processes of MHE through group-level comparison.<sup>8,9,12,14,15,17</sup> To date, however, there is no study using DTI-derived feature maps to discriminate patients with and without MHE in cirrhosis at the individual level; this discrimination remains an important question for clinicians.<sup>6,19</sup> The only related study is the report of Sugimoto et al,<sup>16</sup> which used a DWI-based metric (apparent diffusion coefficient) instead of DTI to classify patients with or without MHE, but in which patients in the intermediate state were excluded; this method obviously results in inadequate assessment. Few studies to date have been conducted to detect MHE by using FA as a biomarker.

In this study, our goal was to investigate whether DTI feature maps can distinguish patients with cirrhosis with MHE from those without (NHE) by using a Bayesian voxel-based machine-learning technique called Graphical-Model-based Morphometric Analysis (GAMMA; [http://www.nitrc.org/projects/gamma\\_suite](http://www.nitrc.org/projects/gamma_suite)).<sup>20–22</sup> GAMMA is a nonparametric, multivariate, Bayesian approach to modeling structure-function associations, which allows dimension reduction and predictive modeling in a unified framework and has been validated both on structural and functional MR imaging data<sup>21,23</sup> and has been used in several studies related to neurologic diseases.<sup>22,24</sup> To further validate identified biomarkers, we assessed their abilities to predict survival among patients with cirrhosis with covert hepatic encephalopathy, given the relationship between MHE and mortality: The presence of MHE has been observed to have a prognostic impact on mortality among patients with liver cirrhosis.<sup>25,26</sup>

## MATERIALS AND METHODS

### Subjects

This study was approved by the Research Ethics Committee of Affiliated Zhongda Hospital, Southeast University, China; 65 patients with clinically proved cirrhosis with covert HE (29 with MHE and 36 with NHE) were included after written informed consent was obtained (Table 1).

For psychometric assessment, a battery of neuropsychiatric tests, including the Number Connection Test A, Digit Symbol Test, and Block Design Test, were administered to all participants. These 3 neuropsychiatric tests are widely used in MHE detection,<sup>1,3,16</sup> development of new diagnostic methods for MHE,<sup>19,27</sup> and survival analysis of patients with cirrhosis.<sup>16,28</sup> Pa-

tients were identified as having MHE if they had abnormal scores in any of these 3 neurocognitive tests.<sup>19,27</sup>

Exclusion criteria were the presence of overt HE at baseline, known presence of neuropsychiatric diseases, significant nonhepatic diseases (such as decompensated heart and respiratory or renal failure), and uncontrolled endocrine or metabolic diseases (such as diabetes mellitus and thyroid dysfunction). Subjects on psychoactive medications or with alcohol abuse 6 months before the study were also excluded.

### MR Imaging Acquisition

MR imaging was performed by using a 1.5T scanner (Vantage Atlas; Toshiba Medical Systems, Tokyo, Japan). DTI sequences were acquired by using a 6-direction, single-shot, spin-echo EPI sequence, with TR = 9450 ms, TE = 100 ms, FOV = 260 × 260 mm, matrix = 128 × 128, section thickness/gap = 3.0/0 mm,  $b = 1000$  s/mm<sup>2</sup>, and NEX = 3. The 3D high-resolution (1.0 × 1.0 × 1.5 mm) T1-weighted images were also acquired for the registration of DTI.

### DTI Processing

We used the fMRI of the Brain Software Library (FSL; <http://fsl.fmrib.ox.ac.uk/fsl>) to process the DTI data. We corrected the DTI data for head movement and eddy current distortions with the non-diffusion-weighted imaging (the B0 image) as a reference. We fitted diffusion tensor models independently for each voxel and computed MD and FA maps. For the normalization of DTI, we first segmented the high-resolution T1-weighted images into gray matter, WM, and CSF by using the FMRIB Integrated Registration and Segmentation Tool (FIRST; <http://fsl.fmrib.ox.ac.uk/fsl/fslwiki/FIRST>) and spatially normalized these images to the Montreal Neurological Institute coordinate space. By concatenating the transformation from the B0 image to the T1 image with the transformation from the T1 image to the Montreal Neurological Institute space (by using a nonlinear transformation), we obtained normalized FA and MD maps.

### GAMMA

GAMMA is a machine-learning method that detects biomarkers from high-dimensional neuroimaging data. GAMMA has 2 important features: First, it has an embedded dimension-reduction mechanism. For high-dimensional neuroimaging data, the large number of candidate models turns the model inference into an underdetermined computational problem. Dimension reduction can ameliorate this problem. Second, GAMMA can detect multivariate interactions among brain regions characterizing a disorder by considering conditional independence among variables. To date, few neuroimaging data analysis methods have these 2 features.

The goal of GAMMA is to detect a set of brain regions that are jointly predictive of a group-membership variable  $g$ . Toward this end, GAMMA iteratively performs Markov Blanket identification

and voxel-space partitioning. In Markov Blanket identification, GAMMA uses Bayesian methods to search for a set of voxels (called representative voxels) that are jointly predictive of  $g$ . The interactions among representative voxels and  $g$  are described by a Bayesian network model. In voxel-space partitioning, for each representative voxel, GAMMA identifies voxels that are probabilistically equivalent to this representative voxel—that is, GAMMA searches for additional voxels that have similar associations with  $g$ . In this manner, each representative voxel is associated with a region of interest consisting of a representative voxel and its equivalent voxels. The output of GAMMA is a label field and a Bayesian network model. The label field includes a set of brain regions that are jointly most predictive of  $g$ , and each brain region in the label field is a ROI. The interactions among these brain regions and  $g$  are described by the Bayesian network model. Details of the GAMMA algorithm are presented in Chen and Herskovits.<sup>20</sup>

We calculated voxelwise mean and SD values for FA maps and compared each subject's FA map with the mean FA map. Decreased FA in WM has been consistently reported in patients with MHE<sup>12,14,15</sup>; therefore, we used a voxelwise threshold that is at multiple SDs below the mean value to threshold the FA map, resulting in a binary FA map, in which 1 represents an abnormal FA value and zero is normal. To reduce noise, we included only WM voxels with decreased FA value (determined by uncorrected  $P < .05$  in a 2-sample  $t$  test).<sup>29</sup> To ensure model stability, we compared 5 different thresholds: 0 SD, 0.25 SD, 0.50 SD, 0.75 SD, and 1.0 SD below the mean.

We performed similar preprocessing steps to generate binary MD maps. Because previous reports have consistently reported that patients with MHE have increased MD in WM,<sup>8,12,14-17</sup> we set the voxelwise thresholds of the MD value at 0 SD, 0.25 SD, 0.50 SD, 0.75 SD, and 1.0 SD above the mean.

After identifying FA and MD regions of interest that characterize group differences, we used the regional state inference algorithm<sup>20</sup> to infer the state (normal/abnormal) for a particular ROI. Then we built Naive-Bayes classifiers (10-fold cross-validation) to discriminate patients with MHE and NHE on the basis of these regional state variables. The structure of the Naive-Bayes classifier was [group membership  $\rightarrow$  (biomarker 1, ..., biomarker  $m$ )].

### Validation of Detected Biomarkers

We performed 2 experiments to validate the biomarkers detected by GAMMA. For each subject, we extracted the average FA value for each ROI generated by GAMMA; let  $FA(ROI_k)/MD(ROI_k)$  denote the average FA/MD value for the  $k^{\text{th}}$  ROI.

First, we used Pearson correlation analysis to examine the relationship between  $MD(ROI_k)$  or  $FA(ROI_k)$  and the neurologic test score and the Child-Pugh score. Second, we performed survival analysis by using the detected biomarkers. We defined the date of the first DTI examination as day 1, and each patient was followed up every 6 months. Fifty-five of 65 patients with cirrhosis completed follow-up studies until death or the end of the observation period (November 2012). We performed multivariate Cox regression (forward LR method)

analysis to assess the associations of  $MD(ROI_k)$  or  $FA(ROI_k)$  with survival.

## RESULTS

### Neurologic Assessments and Altered DTI Metrics

Patients with MHE showed significantly impaired performance in all neurocognitive tests, compared with those with NHE (Table 1). Relative to patients with NHE, those with MHE showed increased mean MD values throughout the WM globally [NHE:  $(0.805 \pm 0.020) \times 10^{-3}$  mm<sup>2</sup>/s; MHE:  $(0.821 \pm 0.035) \times 10^{-3}$  mm<sup>2</sup>/s;  $P = .025$ ]. Patients with MHE also had reduced mean FA values throughout the WM (NHE:  $0.344 \pm 0.014$ ; MHE:  $0.331 \pm 0.016$ ;  $P < .001$ ). The brain areas with increased MD values in MHE were the bilateral frontal lobes and the corpus callosum, and the areas with decreased FA values included the bilateral frontal, parietal, occipital, and temporal lobes; internal capsule; and corpus callosum (see the Appendix and On-line Figure). Moreover, in the MHE group, there was no area showing decreased MD or increased FA.

Additionally, we performed a post hoc power analysis based on FA. The observed effect size was 0.87, which was considered large by using Cohen criteria. Power analysis with  $\alpha = .05$  demonstrated that this study had power = 0.96.

### Results of GAMMA Analysis

Across different abnormality thresholds for the MD and FA maps, GAMMA consistently identified 2 spatially distributed WM regions that were jointly significantly predictive of the group-membership variable (Figs 1 and 2). Two ROIs identified in MD maps, denoted by  $ROI_1^{\text{MD}}$  and  $ROI_2^{\text{MD}}$ , were predominant in the bilateral frontal lobes, precuneus, and the corpus callosum (Fig 1). Similarly, the 2 ROIs identified in FA maps, denoted by  $ROI_1^{\text{FA}}$  and  $ROI_2^{\text{FA}}$ , included bilateral frontal lobes, the corpus callosum, and the left paracentral lobule (Fig 2). Of note, the ROIs that GAMMA identified from MD and FA maps largely overlapped.

### Results of Classification Analysis

Table 2 shows classification performance based on these ROIs. Using MD maps, GAMMA achieved good classification accuracy (mean, 79.1%; range, 75.4%–81.5%) across 5 distinct thresholds. The optimal classification performance was accuracy = 80.0%, sensitivity = 75.9%, and specificity = 83.3%, with the threshold of 0.25 SD above the mean MD value. Using FA maps, GAMMA yielded higher classification accuracy (mean, 87.1%; range, 83.1%–92.3%) across the different thresholds. The optimal classification result was accuracy = 92.3%, sensitivity = 100%, and specificity = 86.1%, which was obtained at the threshold of 0.75 SD below the mean FA value. The thresholds resulting in best classification result (eg, a threshold of 0.25 SD above the mean MD value or a threshold of 0.75 SD below mean FA value) were chosen and included in the following validation analyses.

### Results of Validation Analysis

Table 3 shows that MD values of WM ROIs [ $MD(ROI_1)$  and  $MD(ROI_2)$ ] were significantly positively correlated with the

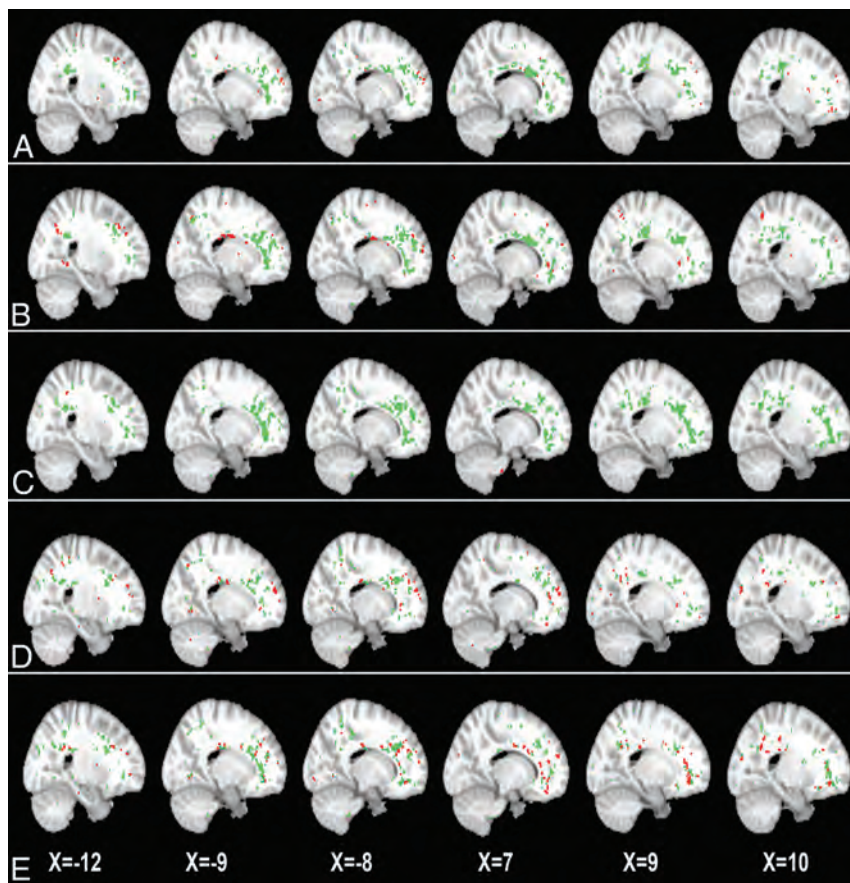


**FIG 1.** Two white matter ROIs generated by GAMMA, which characterize group differences on the MD map on the basis of voxelwise thresholds of the following: 0 SD (A), 0.25 SD (B), 0.50 SD (C), 0.75 SD (D), and 1.0 SD (E) above the mean voxelwise MD value. Green and red indicate the 2 ROIs generated by GAMMA.

result of the Number Connection Test A and negatively correlated with the results of the Digit Symbol Test and Block Design Test. In contrast, FA values of WM ROIs [FA(ROI<sub>1</sub>) and FA(ROI<sub>2</sub>)] were significantly negatively correlated with the Number Connection Test A and positively correlated with the Digit Symbol Test and the Block Design Test scores. Longer time to complete Number Connection Test A and lower scores in the Digit Symbol Test and Block Design Test indicated poorer performance. Patients' Child-Pugh scores were significantly correlated with MD(ROI<sub>1</sub>), MD(ROI<sub>2</sub>), FA(ROI<sub>1</sub>), and FA(ROI<sub>2</sub>).

For survival analysis, the median follow-up period was 18.0 months. By the end of the observation, 15 patients (11 with MHE and 4 with NHE) had died from liver-related complications. Given the consensus that the Child-Pugh score is a variable with prognostic value for survival among patients with cirrhosis,<sup>2,25,26,28</sup> we assessed the predictive values of MD and FA alterations by multivariate Cox regression, taking into account the Child-Pugh score as a covariate. Cox regression showed that MD(ROI<sub>1</sub>) (hazard ratio [HR] = 4.253; 95% CI, 1.218–14.848;  $P = .023$ ) was a predictor of survival, independent of the Child-Pugh score. Similarly, MD(ROI<sub>2</sub>) (HR = 3.948; 95% CI, 1.655–9.420;  $P = .002$ ), FA(ROI<sub>1</sub>) (HR = 0.823; 95% CI, 0.696–0.973;  $P = .022$ ), and FA(ROI<sub>2</sub>) (HR = 0.805; 95% CI, 0.671–0.965;

$P = .019$ ) showed prognostic value on survival as well, in addition to the Child-Pugh assessment.

## DISCUSSION

In this study, by using machine learning, we found that MD values in the bilateral frontal lobes, the precuneus, and the corpus callosum differentiate subjects with MHE and NHE; similarly, FA values in the bilateral frontal lobes, the corpus callosum, and the left paracentral lobule distinguish subjects with MHE from those with NHE. Meanwhile, MD and FA values of WM ROIs had prognostic value for survival, independent of the Child-Pugh score. These findings suggest the utility of measuring WM water molecular diffusivity for MHE detection.

WM edema (reflected by increased MD)<sup>7–11</sup> and impaired cerebral structures<sup>12–14</sup> have been demonstrated to play an important role in the MHE mechanisms. WM edema, which could be extracellular and/or cytotoxic in origin,<sup>8–10</sup> is considered closely associated with a metabolic disorder of ammonia in the brain tissue of patients with MHE.<sup>7,8,10,30</sup> Although the neuropathologic mechanism of decreased FA is not well-understood in the setting of cirrhosis, one possible explanation is demyelination. Osmotic demyelination (due to inappropriate correction of hyponatremia<sup>31</sup>) has been noted in cirrhosis.<sup>32</sup> Moreover, central nervous system inflammation has been shown to play an important role in HE,<sup>33</sup> which may contribute to inflammatory demyelination as observed in other neurologic diseases such as multiple sclerosis.<sup>34</sup> In addition, it has been found that factors released by astrocytes contribute to brain myelination,<sup>35</sup> which would be impaired due to astrocytic dysfunction resulting from Alzheimer type II changes.<sup>7,8,10</sup> Thus, reduction of WM FA may indicate impaired microstructural integrity in MHE.

Indeed, increased MD and decreased FA are also associated with the disruption of brain intrinsic networks,<sup>17,18</sup> which can induce neurologic dysfunction in patients with MHE. In our study, the correlations between altered MD and FA values and psychometric results further suggest that WM abnormalities, especially in the corpus callosum and frontal and parietal lobes, are responsible for neurologic deficits such as psychomotor speed (reflected by the Number Connection Test A), attention and visual memory (reflected by the Digit Symbol Test), and visuospatial motor function (reflected by the Block Design Test).

We identified 2 spatially distributed WM ROIs, predominantly located in the bilateral frontal lobes, the corpus callosum, and bilateral parietal lobe, in MD maps as predictive of MHE. The ROIs identified from FA maps largely overlap those obtained

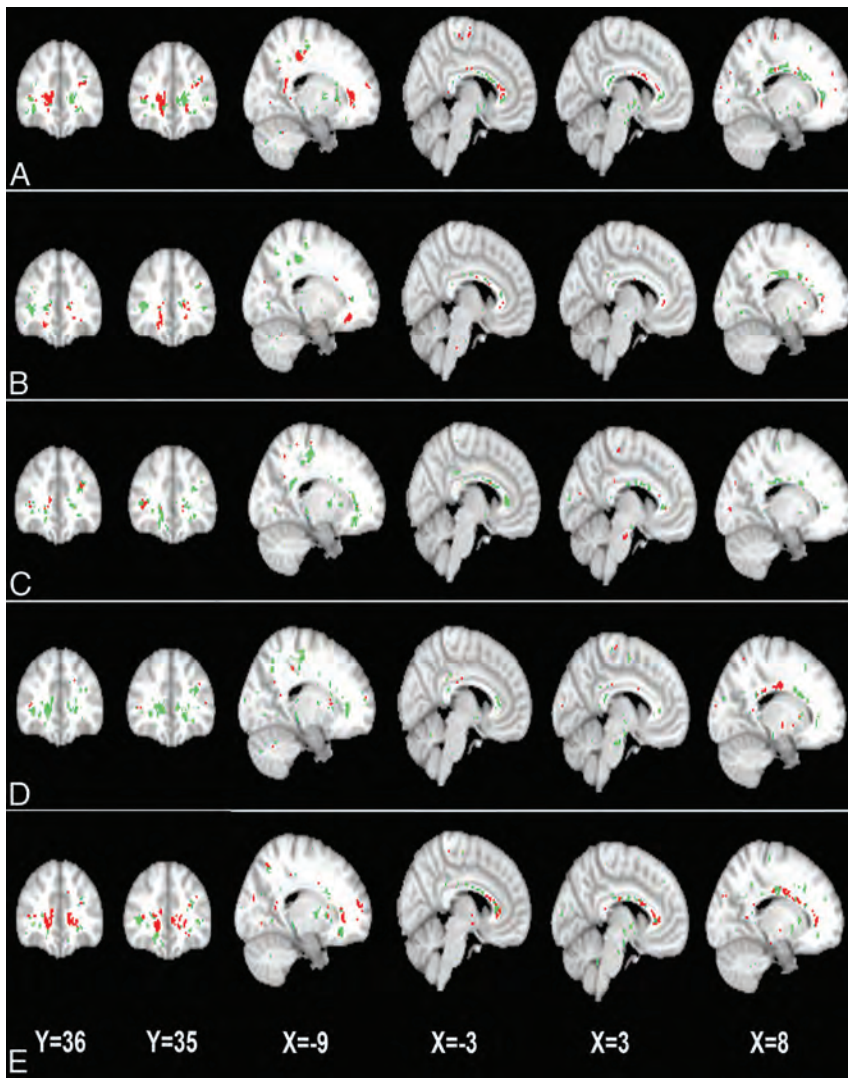


**FIG 2.** The 2 white matter ROIs generated by GAMMA, which characterize group differences in the FA on the basis of voxelwise thresholds of the following: 0 SD (A), 0.25 SD (B), 0.50 SD (C), 0.75 SD (D), and 1.0 SD (E) below the mean voxelwise FA value. Green and red indicate the 2 ROIs.

**Table 2: Classification accuracy between patients with MHE and NHE using a single Bayesian network**

Voxelwise Threshold and Classification Network	Accuracy	Sensitivity	Specificity
<b>MD alone</b>			
0 SD above mean value	78.5%	75.9%	80.6%
0.25 SD above mean value	80.0%	75.9%	83.3%
0.50 SD above mean value	75.4%	58.6%	88.9%
0.75 SD above mean value	81.5%	65.5%	94.4%
1.0 SD above mean value	80.0%	62.1%	94.4%
<b>FA alone</b>			
0 SD below mean value	84.6%	75.9%	91.7%
0.25 SD below mean value	83.1%	79.3%	86.1%
0.50 SD below mean value	89.2%	86.2%	91.7%
0.75 SD below mean value	92.3%	100%	86.1%
1.0 SD below mean value	86.2%	72.4%	97.2%

from MD maps; this overlap indicates that these WM regions are predominantly affected by MHE pathology. Increased ammonia levels have been found to be associated with the increased ADC in the frontal and parietal WM.<sup>16</sup> In addition, positron-emission

tomography studies have indicated that an altered glial cell state, an important cause of MHE, occurs in the frontal WM and in the corpus callosum.<sup>36</sup> The frontal and parietal WM and corpus callosum (particularly the anterior part) are the regions most commonly reported to demonstrate increased water content<sup>11</sup> or diffusivity<sup>9,10,12,15,16</sup> and decreased FA.<sup>15</sup> When patients with cirrhosis in the intermediate state are excluded, Sugimoto et al<sup>16</sup> reported 70%–90% sensitivity and 85%–90% specificity in classification of MHE and NHE, based on a frontal or parietal WM ADC metric. Their results indicate, to some extent, the usefulness of measuring WM diffusion features in MHE detection and are in line with our findings.

Increased regional MD has been found to be predictive of the development of overt HE,<sup>16</sup> which has an ominous prognostic value on survival.<sup>2</sup> Meanwhile, MHE is associated with increased risk of an episode of overt HE.<sup>5</sup> It is believed that MHE (measured by neuropsychological tests) has prognostic value on survival in patients with cirrhosis with covert HE.<sup>25</sup> These progressive patterns of disease may explain why we found increased MD to be predictive of survival for patients with cirrhosis with covert HE. Brain edema has been reported to be fatal, especially in high-grade HE, due to increased intracranial pressure.<sup>37,38</sup> Moreover, our findings regarding the predictive values of MD and FA on survival agree with the consensus that brain edema<sup>9–11</sup> and structural impairment<sup>12,13</sup> progress with advanced disease.

One strength of this study is the application of an advanced machine-learning method, GAMMA, to the detection of MHE-related biomarkers.<sup>20–22</sup> GAMMA is a nonparametric and multivariate Bayesian approach to model complex nonlinear multivariate associations among image features and the clinical variables. GAMMA automatically generates ROIs that can be used to differentiate MHE from NHE; this feature distinguishes our study from previous DWI studies, which relied on prespecified ROIs.<sup>8–10,16</sup> The consistency of classification across distinct thresholds suggests the validity of these results. Moreover, the significance of MD ROIs and FA ROIs in predicting survival provides further evidence regarding the validity of biomarkers detected by GAMMA.

One limitation of our study is that we confined our analysis to WM regions, where brain edema predominantly occurs in MHE<sup>11,15</sup>; however, several studies have indicated that other cerebral regions, such as subcortical nuclei,<sup>9,10</sup> may also manifest

**Table 3: Pearson correlation coefficients of MD and FA values with neurologic performances and Child-Pugh score among patients with cirrhosis and covert hepatic encephalopathy**

Variables	MD Map		FA Map	
	ROI1	ROI2	ROI1	ROI2
Number Connection Test A	0.38 <sup>a</sup>	0.41 <sup>a</sup>	-0.59 <sup>a</sup>	-0.63 <sup>a</sup>
Digit Symbol Test	-0.51 <sup>a</sup>	-0.52 <sup>a</sup>	0.71 <sup>a</sup>	0.68 <sup>a</sup>
Block Design Test	-0.32 <sup>a</sup>	-0.37 <sup>a</sup>	0.51 <sup>a</sup>	0.56 <sup>a</sup>
Child-Pugh score	0.33 <sup>a</sup>	0.37 <sup>a</sup>	-0.27 <sup>b</sup>	-0.34 <sup>a</sup>

<sup>a</sup> $P < .01$ .

<sup>b</sup> $P < .05$ .

low-grade edema. The second limitation is that we used a suboptimal DTI sequence with 6 diffusion-encoding gradient directions, due to the finite capability of our MR imaging scanner. The third limitation is that we only used DTI to generate biomarkers for MHE. Other MR imaging models (eg, resting-state fMRI<sup>39</sup>) have been reported to be useful in distinguishing MHE from NHE as well. DTI may be more readily applicable in the clinical setting because it is more convenient to obtain DTI relative to resting-state fMRI. However, the combination of these MR imaging techniques may yield more accurate classification and is an area for future extension of this research.

## CONCLUSIONS

Combining advanced machine-learning techniques and DTI can generate biomarkers that identify patients with MHE among patients with cirrhosis with covert hepatic encephalopathy; both increased MD and decreased FA are predictive of survival. Our findings may be helpful in detecting MHE and improving subsequent treatment.

## APPENDIX

### Between-Group Comparison

The 2-sample  $t$  tests were performed to determine the regions with an MD/FA difference between 2 groups in a voxelwise way. The statistical threshold was set at  $P < .05$  (the combination of  $P < .005$  for single voxel and a minimum cluster size of 120 voxels), which was determined by Monte Carlo simulations by using the AlphaSim program (<http://afni.nimh.nih.gov/afni>).

Disclosures: Edward H. Herskovits—UNRELATED: Expert Testimony: Medicolegal; Grants/Grants Pending: Microsoft,\* State of Maryland.\* \*Money paid to the institution.

## REFERENCES

1. Ferenci P, Lockwood A, Mullen K, et al. **Hepatic encephalopathy: definition, nomenclature, diagnosis, and quantification—final report of the working party at the 11th World Congresses of Gastroenterology, Vienna, 1998.** *Hepatology* 2002;35:716–21
2. Stewart CA, Malinchoc M, Kim WR, et al. **Hepatic encephalopathy as a predictor of survival in patients with end-stage liver disease.** *Liver Transpl* 2007;13:1366–71
3. Bajaj JS, Wade JB, Sanyal AJ. **Spectrum of neurocognitive impairment in cirrhosis: implications for the assessment of hepatic encephalopathy.** *Hepatology* 2009;50:2014–21
4. Groeneweg M, Quero JC, De Bruijn I, et al. **Subclinical hepatic encephalopathy impairs daily functioning.** *Hepatology* 1998;28:45–49
5. Romero-Gómez M, Boza F, Garcia-Valdecasas MS, et al. **Subclinical hepatic encephalopathy predicts the development of overt hepatic encephalopathy.** *Am J Gastroenterol* 2001;96:2718–23
6. Prasad S, Dhiman RK, Duseja A, et al. **Lactulose improves cognitive**

functions and health-related quality of life in patients with cirrhosis who have minimal hepatic encephalopathy. *Hepatology* 2007;45:549–59

7. Córdoba J, Alonso J, Rovira A, et al. **The development of low-grade cerebral edema in cirrhosis is supported by the evolution of (1)H-magnetic resonance abnormalities after liver transplantation.** *J Hepatol* 2001;35:598–604
8. Chavarria L, Alonso J, Garcia-Martinez R, et al. **Biexponential analysis of diffusion-tensor imaging of the brain in patients with cirrhosis before and after liver transplantation.** *AJNR Am J Neuroradiol* 2011;32:1510–17
9. Kale RA, Gupta RK, Saraswat VA, et al. **Demonstration of interstitial cerebral edema with diffusion tensor MR imaging in type C hepatic encephalopathy.** *Hepatology* 2006;43:698–706
10. Lodi R, Tonon C, Stracciari A, et al. **Diffusion MRI shows increased water apparent diffusion coefficient in the brains of cirrhotics.** *Neurology* 2004;62:762–66
11. Shah NJ, Neeb H, Kircheis G, et al. **Quantitative cerebral water content mapping in hepatic encephalopathy.** *Neuroimage* 2008;41:706–17
12. Chen HJ, Wang Y, Zhu XQ, et al. **White matter abnormalities correlate with neurocognitive performance in patients with HBV-related cirrhosis.** *J Neurol Sci* 2012;321:65–72
13. Guevara M, Baccaro ME, Gomez-Anson B, et al. **Cerebral magnetic resonance imaging reveals marked abnormalities of brain tissue density in patients with cirrhosis without overt hepatic encephalopathy.** *J Hepatol* 2011;55:564–73
14. Qi R, Zhang LJ, Zhong J, et al. **Grey and white matter abnormalities in minimal hepatic encephalopathy: a study combining voxel-based morphometry and tract-based spatial statistics.** *Eur Radiol* 2013;23:3370–78
15. Kumar R, Gupta RK, Elderkin-Thompson V, et al. **Voxel-based diffusion tensor magnetic resonance imaging evaluation of low-grade hepatic encephalopathy.** *J Magn Reson Imaging* 2008;27:1061–68
16. Sugimoto R, Iwasa M, Maeda M, et al. **Value of the apparent diffusion coefficient for quantification of low-grade hepatic encephalopathy.** *Am J Gastroenterol* 2008;103:1413–20
17. Qi R, Xu Q, Zhang LJ, et al. **Structural and functional abnormalities of default mode network in minimal hepatic encephalopathy: a study combining DTI and fMRI.** *PLoS One* 2012;7:e41376
18. Lin WC, Hsu TW, Chen CL, et al. **Connectivity of default-mode network is associated with cerebral edema in hepatic encephalopathy.** *PLoS One* 2012;7:e36986
19. Bajaj JS, Saeian K, Verber MD, et al. **Inhibitory control test is a simple method to diagnose minimal hepatic encephalopathy and predict development of overt hepatic encephalopathy.** *Am J Gastroenterol* 2007;102:754–60
20. Chen R, Herskovits EH. **Graphical model based multivariate analysis (GAMMA): an open-source, cross-platform neuroimaging data analysis software package.** *Neuroinformatics* 2012;10:119–27
21. Chen R, Herskovits EH. **Graphical-model-based morphometric analysis.** *IEEE Trans Med Imaging* 2005;24:1237–48
22. Chen R, Pawlak MA, Flynn TB, et al. **Brain morphometry and intelligence quotient measurements in children with sickle cell disease.** *J Dev Behav Pediatr* 2009;30:509–17
23. Chen R, Herskovits EH. **Graphical-model-based multivariate analysis of functional magnetic-resonance data.** *Neuroimage* 2007;35:635–47
24. Mueller SG, Young K, Hartig M, et al. **A two-level multimodality imaging Bayesian network approach for classification of partial epilepsy: preliminary data.** *Neuroimage* 2013;71:224–32
25. Dhiman RK, Kurmi R, Thumburu KK, et al. **Diagnosis and prognostic significance of minimal hepatic encephalopathy in patients with cirrhosis of liver.** *Dig Dis Sci* 2010;55:2381–90
26. Amodio P, Del Piccolo F, Marchetti P, et al. **Clinical features and survival of cirrhotic patients with subclinical cognitive alterations**

- detected by the number connection test and computerized psychometric tests. *Hepatology* 1999;29:1662–67
27. Bajaj JS, Hafeezullah M, Franco J, et al. **Inhibitory control test for the diagnosis of minimal hepatic encephalopathy.** *Gastroenterology* 2008;135:1591–600.e1
  28. Romero-Gómez M, Grande L, Camacho I. **Prognostic value of altered oral glutamine challenge in patients with minimal hepatic encephalopathy.** *Hepatology* 2004;39:939–43
  29. Bourgon R, Gentleman R, Huber W. **Independent filtering increases detection power for high-throughput experiments.** *Proc Natl Acad Sci U S A* 2010;107:9546–51
  30. Mardini H, Smith FE, Record CO, et al. **Magnetic resonance quantification of water and metabolites in the brain of cirrhotics following induced hyperammonaemia.** *J Hepatol* 2011;54:1154–60
  31. Restuccia T, Gomez-Anson B, Guevara M, et al. **Effects of dilutional hyponatremia on brain organic osmolytes and water content in patients with cirrhosis.** *Hepatology* 2004;39:1613–22
  32. Yu C, Sharma N, Saab S. **Hyponatremia: clinical associations, prognosis, and treatment in cirrhosis.** *Exp Clin Transplant* 2013;11:3–11
  33. Rodrigo R, Cauli O, Gomez-Pinedo U, et al. **Hyperammonemia induces neuroinflammation that contributes to cognitive impairment in rats with hepatic encephalopathy.** *Gastroenterology* 2010;139:675–84
  34. Zhornitsky S, Wee Yong V, Koch MW, et al. **Quetiapine fumarate for the treatment of multiple sclerosis: focus on myelin repair.** *CNS Neurosci Ther* 2013;19:737–44
  35. Ishibashi T, Dakin KA, Stevens B, et al. **Astrocytes promote myelination in response to electrical impulses.** *Neuron* 2006;49:823–32
  36. Cagnin A, Taylor-Robinson SD, Forton DM, et al. **In vivo imaging of cerebral “peripheral benzodiazepine binding sites” in patients with hepatic encephalopathy.** *Gut* 2006;55:547–53
  37. Donovan JP, Schafer DF, Shaw BW Jr, et al. **Cerebral oedema and increased intracranial pressure in chronic liver disease.** *Lancet* 1998;351:719–21
  38. Joshi D, O’Grady J, Patel A, et al. **Cerebral oedema is rare in acute-on-chronic liver failure patients presenting with high-grade hepatic encephalopathy.** *Liver Int* 2014;34:362–66
  39. Chen HJ, Wang Y, Zhu XQ, et al. **Classification of cirrhotic patients with or without minimal hepatic encephalopathy and healthy subjects using resting-state attention-related network analysis.** *PLoS One* 2014;9:e89684

# Strategies of Collateral Blood Flow Assessment in Ischemic Stroke: Prediction of the Follow-Up Infarct Volume in Conventional and Dynamic CTA

S.E. Beyer, K.M. Thierfelder, L. von Baumgarten, M. Rottenkolber, F.G. Meinel, H. Janssen, B. Ertl-Wagner, M.F. Reiser, and W.H. Sommer



## ABSTRACT

**BACKGROUND AND PURPOSE:** Collateral blood flow is an important prognostic marker in the acute stroke situation but approaches for assessment vary widely. Our aim was to compare strategies of collateral blood flow assessment in dynamic and conventional CTA in their ability to predict the follow-up infarction volume.

**MATERIALS AND METHODS:** We retrospectively included all patients with an M1 occlusion from an existing cohort of 1912 consecutive patients who underwent initial multimodal stroke CT and follow-up MR imaging or nonenhanced CT. Collateralization was assessed in both conventional CT angiography and dynamic CT angiography by using 3 different collateral grading scores and segmentation of the volume of hypoattenuation. Arterial, arteriovenous, and venous phases were reconstructed for dynamic CT angiography, and all collateral scores and the volume of hypoattenuation were individually assessed for all phases. Different grading systems were compared by using the Bayesian information criterion calculated for multivariate regression analyses (Bayesian information criterion difference = 2–6, “positive”; Bayesian information criterion difference = 6–10, “strong”; Bayesian information criterion difference = >10, “very strong”).

**RESULTS:** One hundred thirty-six patients (mean age, 70.4 years; male sex, 41.2%) were included. In the multivariate analysis, models containing the volume of hypoattenuation showed a significantly better model fit than models containing any of the 3 collateral grading scores in conventional CT angiography (Bayesian information criterion difference = >10) and dynamic CT angiography (Bayesian information criterion difference = >10). All grading systems showed the best model fit in the arteriovenous phase. For the volume of hypoattenuation, model fit was significantly higher for models containing the volume of hypoattenuation as assessed in the arteriovenous phase of dynamic CT angiography compared with the venous phase (Bayesian information criterion difference = 6.2) and the arterial phase of dynamic CT angiography (Bayesian information criterion difference = >10) and in comparison with conventional CT angiography (Bayesian information criterion difference = >10).

**CONCLUSIONS:** The use of dynamic CT angiography within the arteriovenous phase by using quantification of the volume of hypoattenuation is the superior technique for assessment of collateralization among the tested approaches.

**ABBREVIATIONS:** BIC = Bayesian information criterion; NECT = nonenhanced CT; VH = volume of hypoattenuation

In acute ischemic stroke, leptomeningeal collateral vessels provide blood flow to the ischemic bed of the occluded artery.<sup>1,2</sup> The extent of collateralization is an independent predictor of a small-lesion volume on follow-up imaging<sup>3</sup> and a favorable clinical outcome.<sup>4</sup> It has been further shown to predict response to

intravenous thrombolysis<sup>5</sup> and to determine penumbral tissue loss.<sup>6</sup> Noninvasive imaging of collaterals can be performed by using CT angiography<sup>7,8</sup> or MR angiography.<sup>9</sup> CTA offers the advantages of a wide availability and short scanning times.

One strategy to assess collateral blood flow in CTA is through grading of collateral vessels in the territory of the occluded artery.<sup>4,7,8</sup> Currently, several different grading scores have been published,<sup>10</sup> which differ not only in the number of categories of each score but also in the type of assessment (ie, an assessment relative to the contralateral hemisphere or absolute quantification). The 3 most commonly used scores in the literature include

Received June 14, 2014; accepted after revision August 7.

From the Institute for Clinical Radiology (S.E.B., K.M.T., F.G.M., B.E.-W., M.F.R., W.H.S.), Departments of Neurology (L.v.B.) and Neuroradiology (H.J.), Ludwig Maximilians University Hospital Munich, Munich, Germany; and Department of Medical Informatics, Biometry and Epidemiology (M.R.), Ludwig Maximilians University Munich, Munich, Germany.

S.E. Beyer and K.M. Thierfelder contributed equally to this work.

Please address correspondence to Wieland H. Sommer, MD, MPH, Institute for Clinical Radiology, Ludwig Maximilians University Hospital Munich, Marchioninistr 15, 81377 Munich, Germany; e-mail: Wieland.Sommer@med.uni-muenchen.de

 Indicates article with supplemental on-line tables.

 Indicates article with supplemental on-line photo.

<http://dx.doi.org/10.3174/ajnr.A4131>

the following: 1) an absolute score assessing the percentage of the ischemic bed in which collateral filling is seen,<sup>3</sup> 2) a relative score comparing collateral vessel enhancement within the ischemic bed with similar contralateral vessels,<sup>8</sup> and 3) a detailed relative score comparing collateral vessel enhancement with similar contralateral vessels within each ASPECTS region.<sup>11</sup>

Another strategy to assess collateral blood flow is through quantification of hypoattenuated brain tissue in CTA source images.<sup>12-15</sup> Whereas hypoattenuation in nonenhanced CT (NECT) images represents the brain tissue net water uptake,<sup>16</sup> hypoattenuation in CT angiography suggests an area receiving limited blood flow, which has been shown to correlate with initial diffusion-weighted images<sup>15</sup> and follow-up lesion size.<sup>14</sup> However, this correlation might be heavily influenced by the time point of image acquisition.<sup>13</sup>

Recently, Smit et al<sup>17</sup> demonstrated that conventional CTA can fail to capture delayed collateral enhancement. Delay-insensitive CT angiography with acquisition of multiple timeframes can help overcome this limitation. Its value in assessing the maximal extent of collateralization has been shown in several studies.<sup>5,17,18</sup> However, the time point of image analysis might play an important role in correctly assessing the prognostic value of the collateralization.

The aim of our study was the following: 1) to determine the optimal time-phase for reconstruction of the dynamic CTA images to best predict follow-up lesion volume, and 2) to compare the predictive value of the volume of hypoattenuation with different collateral vessel grading scores.

## MATERIALS AND METHODS

### Study Design and Population

The institutional review board approved the retrospective study and waived the requirement for informed consent. Our initial cohort consisted of 1912 consecutive patients who underwent initial whole-brain CT perfusion for suspected acute ischemic stroke at our institution between April 2009 and April 2014. From this cohort, we included all patients with complete occlusion of the middle cerebral artery in the M1 segment, with or without an occlusion of the internal carotid artery, on both conventional and dynamic CTA. We excluded patients with the following:

- 1) Incomplete or missing whole-brain CTP raw datasets
- 2) Missing follow-up NECT or MR imaging acquired at least 1 day after initial CT perfusion imaging<sup>19</sup>
- 3) Nondiagnostic quality of conventional CTA or dynamic CTA.

Data on the time of symptom onset, treatment with intravenous thrombolysis, and mechanical recanalization were collected by review of the medical charts.

### CT Examination Protocol

The multiparametric CT protocol consisted of an NECT to exclude intracranial hemorrhage, supra-aortic CTA, and whole-brain CT perfusion, all performed by using one of the following CT scanners: Somatom Definition AS+, a 128-section CT scanner; Somatom Definition Flash, a 128-section dual-source CT scanner; and Somatom Definition Edge, a 128-section CT scanner (all by Siemens, Erlangen, Germany).

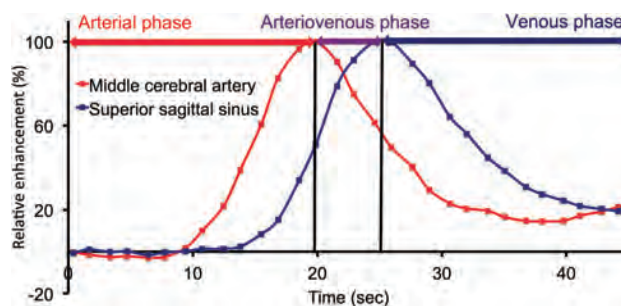


**FIG 1.** Definition of arterial, arteriovenous, and venous phases. Example of the separation the 3 phases by using the time-to-peak contrast enhancement of the contralateral middle cerebral artery and the superior sagittal sinus in a typical patient.

Conventional CT angiography was acquired in a caudocranial direction with a 2-second delay after bolus triggering in the aortic arch (cutoff value = 100 HU). Images of whole-brain CTP were obtained with 0.6-mm collimation and 100-mm scan coverage in the z-axis by using a toggling-table technique. One scan was acquired every 1.5 seconds. Tube voltage and current were 80 kV and 200 mAs, respectively. CT dose index was 276 mGy. A total of 35 mL of iodinated contrast agent was administered at a flow rate of 5 mL/s, followed by a saline flush of 40 mL at 5 mL/s. Thirty-one axial sections were reconstructed per view with a thickness of 10 mm and an increment of 3 mm.

### Dynamic CT Angiography Image Processing

CT perfusion raw datasets were reconstructed as dynamic angiographies by using the syngo CT Dynamic Angio module and syngo via, VA 20 (Siemens). The image processing included motion correction and automated bone removal. Dynamic angiographies were then represented as source images and temporal MIPs. Computation of temporal MIPs included a 4D noise reduction; our approach was previously described by Smit et al.<sup>20</sup> We created 3 different temporal MIPs representing the arterial phase, the arteriovenous phase, and the venous phase, to determine differences in collateral vessel enhancement with time. We created temporal MIPs of the different phases rather than using source images acquired at a single time point, to optimize quality because temporal MIP computation included the aforementioned 4D noise reduction. This process has been shown to increase the signal-to-noise ratio, vessel contour, detail visibility, and overall image quality.<sup>20</sup> For standardization and adjustment for interindividual differences in circulation times and bolus dispersion, we used the time point of peak contrast enhancement of the contralateral MCA to separate arterial and arteriovenous phases and the time point of peak contrast enhancement of the superior sagittal sinus to separate arteriovenous and venous phases (Fig 1).

### Image Analysis of CTA and Dynamic CTA

**Quantification of Regions of Hypoattenuation.** OsiriX, Version 4.0, imaging software (<http://www.osirix-viewer.com>) was used for 3D assessment of regions of hypoattenuation by using a method previously described for CT perfusion deficit assessment.<sup>21</sup> We manually segmented the region of hypoattenuation on every axial section of the temporal MIPs by using the OsiriX Closed Polygon Tool to create a region of interest; thus, the extent

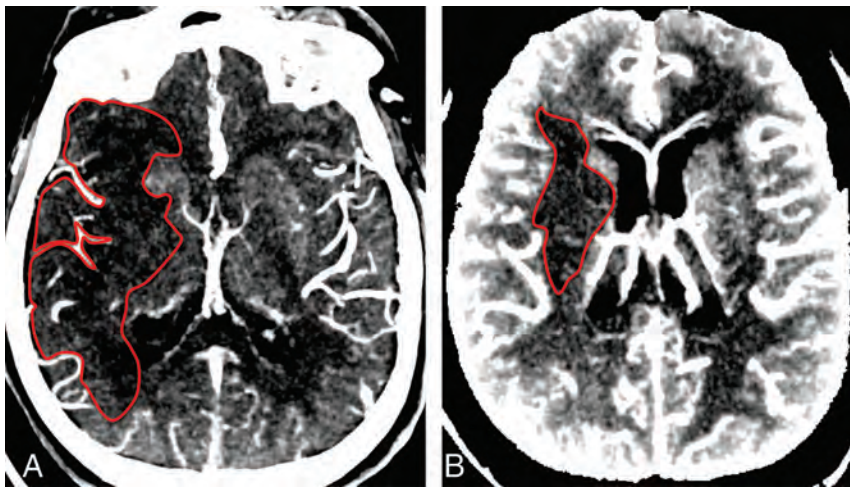


**FIG 2.** Comparison of conventional and dynamic CTA. A, MIP (10-mm) of conventional CTA source images. Volume of hypoattenuation (1 representative section outlined) is 90.5 mL. B, Temporal MIPs (10 mm) of dynamic CTA source images reconstructed for the arteriovenous phase. Volume of hypoattenuation (1 representative section outlined) is 7.5 mL. The follow-up infarct volume was 6.5 mL.

of the hypoattenuation could be evaluated by comparison with the contralateral hemisphere. Figure 2 shows representative examples. The region volume was then calculated by using the OsiriX volume calculation tool. According to previous studies on the quantification of the region of hypoattenuation,<sup>13</sup> window and level settings were adjusted by the reader to increase the contrast between normal and hypoattenuated brain tissue.

**Grading of Collateral Vessels.** All images were reconstructed with a section thickness of 20 mm to increase the visualization of vessel continuity. We assessed collateralization in conventional CT angiography and temporal MIPs of the arterial, arteriovenous, and venous phases. Collateral vessels were graded by using 3 previously described and evaluated scores (On-line Table 1). For relative collateral grading in dynamic CT angiography, we used contralateral arterial vessel status as a reference to prevent venous superimposition. Collaterals were assessed separately for each phase and each score.

In addition, we assessed CT angiographic datasets for an additional ICA occlusion and a visible early temporal branch before the occlusion because these have been shown to affect final infarct size.<sup>22</sup>

### Follow-Up Image Analysis

MR imaging or NECT acquired at least 1 day after the initial multiparametric CT was used to assess follow-up lesion volume. In MR imaging, lesions were assessed as volumes of relatively increased signal in the DWI sequence with a b-value of 1000 s/mm<sup>2</sup> and concomitant decreases in the apparent diffusion coefficient. On NECT, lesions were assessed as volumes of relative hypoattenuation. Volumetric analyses of either MR imaging or NECT datasets were performed by using OsiriX, Version 4.0, as described above, for regions of hypoattenuation analysis.

Image analysis was performed by 2 readers: 1 board-certified radiologist (W.H.S.) with 10 years of experience in neuroimaging, and 1 reader (S.E.B.) with 2 years of experience in acute stroke imaging. Quantitative measurements (eg, drawing of ROIs) were

performed by the less experienced reader. In unclear cases, the more experienced reader was consulted. The readers were blinded to clinical data and follow-up imaging.

### Statistical Analysis

We performed all statistical analyses by using SPSS (Version 22.0; IBM, Armonk, New York) and the open-source R statistical computing software, Version 3.0.3 (<http://www.r-project.org>).

All metric and normally distributed variables are reported as mean  $\pm$  SD; non-normally distributed variables are presented as median with first-third quartiles. Categorical variables are presented as frequency and percentage.

Normal distribution was assessed by using histogram methods for the variable follow-up lesion volume. Square root transformation was performed for nor-

malization of the dependent variable in regression analysis in case of non-normal distribution. Univariate linear regression analysis was used to test the association between predictors and follow-up lesion volume as outcome. The following variables were included as predictors: age, sex, time from symptom onset to initial imaging, time to follow-up imaging, additional ICA occlusion, visible early temporal branch, intravenous thrombolysis, and mechanical recanalization.

Multivariate linear regression was used for adjusted analyses of collateral scores and volume of hypoattenuation for follow-up lesion volume. Variables significantly associated with a favorable outcome ( $P < .2$ ) in the univariate regression were included in the multivariate models with the collateral scores or volume of hypoattenuation. The 4-point absolute and the 5-point relative scores were entered as ordinal variables. Volume of hypoattenuation and the 20-point relative score were entered as continuous variables.  $P$  values  $< .05$  were statistically significant. Residual plots (independent variable: regression standardized predicted value; dependent variable: regression standardized residual) and normal probability-probability plots of regression standardized residuals were generated to evaluate linear regression models.

Multivariate regression models were compared on the basis of the adjusted coefficients of determination (adjusted  $R^2$ ) and the Bayesian information criterion (BIC). Differences in BIC of 2–6 were regarded as “positive”; 6–10, as “strong”; and  $>10$ , as “very strong.”<sup>9</sup>

## RESULTS

### Study Population

Among our cohort of 1912 patients and after exclusion of non-complete raw datasets, 165 patients showed complete M1 occlusion on conventional and dynamic CT angiography and were included in further analyses. Among these, we further excluded 22 patients due to missing follow-up imaging and 7 patients due to nondiagnostic quality of dynamic CTA. The remaining 136 patients constituted the study cohort. Figure 3 illustrates the detailed patient flow chart of the study cohort.

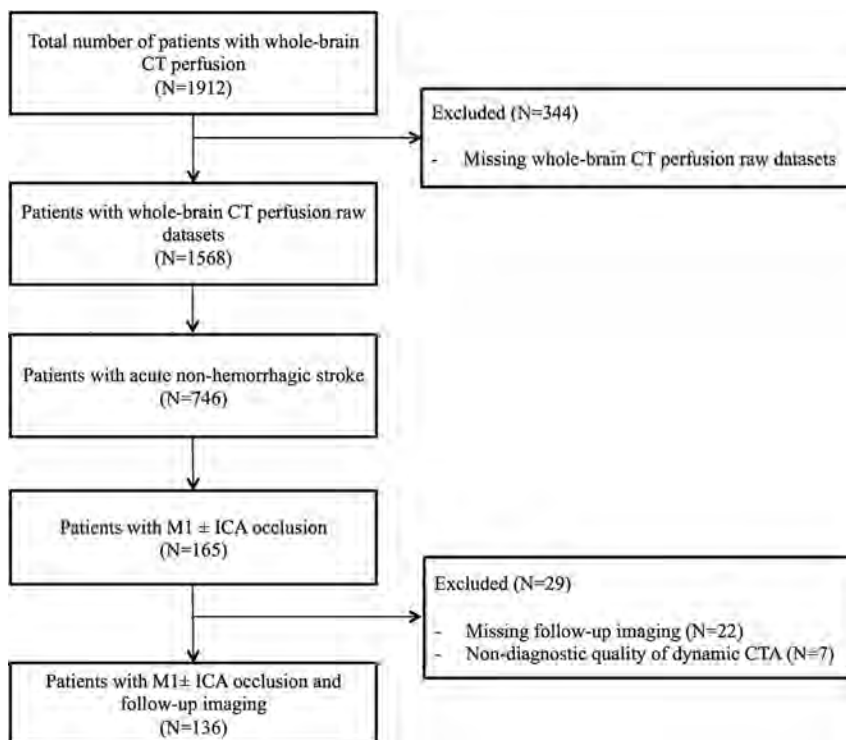


**FIG 3.** Inclusion and exclusion flow chart.

**Table 1: Patient characteristics and univariate linear regression analysis to determine the effect of patient characteristics on follow-up lesion size**

	All Patients (N = 136)	$\beta$ -Coefficient <sup>a</sup>	P Value <sup>a</sup>
Age (yr) <sup>b</sup>	70.4 ± 13.8	$\beta = -0.043$	.235
Male sex (No.) (%)	56 (41.2)	$\beta = 1.434$	.157
Time from symptom onset to initial imaging <sup>c</sup> (min) <sup>d</sup>	139 (89–227)	$\beta = -0.001$	.897
Time to follow-up imaging (days) <sup>d</sup>	3 (1–5)	$\beta = -0.095$	.051
Additional ICA occlusion (No.) (%)	65 (47.8)	$\beta = 4.911$	<.001
Visible early temporal branch (No.) (%)	28 (20.6)	$\beta = -2.431$	.048
IV thrombolysis (No.) (%)	90 (66.2)	$\beta = -3.926$	<.001
Mechanical recanalization (No.) (%)	72 (52.9)	$\beta = -3.776$	<.001
Follow-up lesion volume <sup>e</sup> (mL) <sup>d</sup>	79 (19–218)	N/A	N/A

**Note:**—N/A indicates not available.

<sup>a</sup> Results of univariate linear regression analysis with follow-up lesion volume (square-root-transformed) as a dependent variable. Positive  $\beta$ -values indicate an increase in follow-up lesion volume.

<sup>b</sup> Mean.

<sup>c</sup> Documented for 70 patients.

<sup>d</sup> Median (first-third quartile).

<sup>e</sup> As measured by DWI-MRI ( $b=1000$ ) or NECT.

### Baseline Characteristics

The mean age was 70 ± 14 years (range, 28–97 years). Fifty-six (41.2%) patients were male. Ninety patients (66.2%) were treated with IV thrombolysis, and 72 patients (52.9%) underwent mechanical recanalization. Among these, 57 patients (41.9%) were treated with IV thrombolysis and mechanical recanalization. Median follow-up lesion volume was 79 mL (first-third quartiles = 19–218). Because follow-up lesion volume was not normally distributed, square root transformation was performed for this variable for further analysis. Patient characteristics and the results of univariate linear regression analyses for the square-root-transformed follow-up lesion volume are given in Table 1.

Collateral grades were lowest on conventional CTA. In dynamic

CT angiography, collateral grades were highest in the arteriovenous phase and were slightly lower in the arterial phase than in the venous phase. The volume of hypoattenuation was highest in conventional CTA and decreased continuously from the arterial to the venous phase. The detailed results of collateral vessel grading systems are presented in On-line Table 2.

### Optimal Time-Phase for Collateral Assessment

The models containing collateral grading assessed in the arteriovenous phase of dynamic CTA showed the best model fit (highest adjusted  $R^2$ , Table 2) in multivariate linear regression analyses for follow-up lesion volume controlling for the variables sex, additional ICA occlusion, time to follow-up imaging, early temporal branch, IV thrombolysis, and mechanical recanalization. This was seen independent of whether the models contained the volume of hypoattenuation or any collateral grading score.

For the model containing the volume of hypoattenuation, model fit (adjusted  $R^2$ ) was 0.614 in the arteriovenous phase, compared with 0.483 in conventional CTA (BIC difference = 39.9, indicating a very strong difference between the 2 models), 0.576 in the arterial phase (BIC difference = 15.8, also indicating a very strong difference), and 0.586 in the venous phase (BIC difference = 9.6, indicating a strong difference). Figure 2 presents examples comparing conventional and dynamic CT angiography in a typical patient. On-line Fig 1 illustrates the plots of the residuals of the multivariate regression models.

For the model containing the 4-point absolute score, BIC difference between the arteriovenous phase and the conventional CTA, arterial phase, and venous phase was 16.7 (very strong), 5.7 (positive), and 20.7 (very strong), respectively. For the model

containing the 5-point relative score, the BIC difference between the arteriovenous phase and conventional CTA, arterial phase, and venous phase was 17.1 (very strong), 16.8 (very strong), and 26.5 (very strong), respectively. For the model containing the 20-point relative score, the BIC difference between the arteriovenous phase and conventional CTA, arterial phase, and venous phase was 12.0 (very strong), 15.6 (very strong), and 27.4 (very strong), respectively (Fig 4).

### Volume of Hypoattenuation versus Collateral Vessel Grading Scores

In the multivariate linear regression analysis for follow-up lesion volume controlling for the variables sex, additional ICA occlusion,

**Table 2: Model fit of multivariate linear regression for follow-up lesion volume<sup>a</sup>**

	Dynamic CT Angiography ( $R^2$ )			
	Conventional CTA ( $R^2$ )	Arterial Phase	Arteriovenous Phase	Venous Phase
4-Point absolute	0.392	0.439	0.462	0.374
5-Point relative	0.348	0.349	0.441	0.321
20-Point relative	0.436	0.421	0.483	0.368
Volume of hypoattenuation	0.483	0.567	0.614	0.586

**Note:**— $R^2$  indicates the adjusted coefficient of determination corrected for sex, time to follow-up imaging, additional ICA occlusion, visible early temporal branch, IV thrombolysis, and mechanical recanalization. It is an indicator of model fit; higher values indicate a better explanation of the variance of the outcome variable.

<sup>a</sup> Overall, dynamic CTA allows a better prediction of follow-up lesion volume than conventional CTA. Specifically, model fit was highest for reconstructions of dynamic CTA images within the arteriovenous phase. Models containing the volume of hypoattenuation performed better than models containing any of the collateral vessel grading scores.

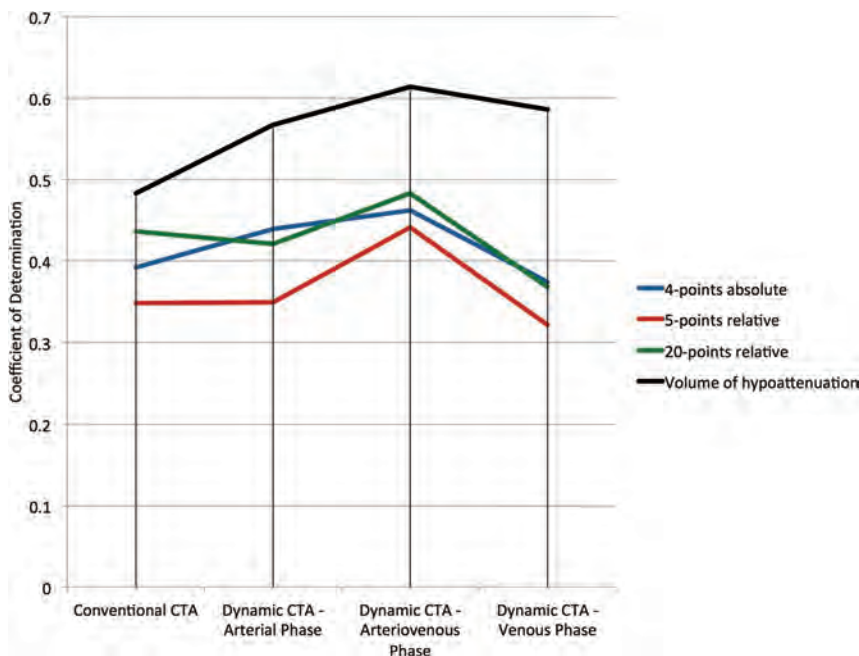


**FIG 4.** Comparison of collateral grading systems. The coefficient of determination is an indicator of model fit. Higher values indicate a better explanation of the variance of the outcome variable.

sion, time to follow-up imaging, early temporal branch, intravenous thrombolysis, and mechanical recanalization, the models containing a volume of hypoattenuation showed a better model fit (adjusted  $R^2$ ) than models containing any of the collateral vessel grading scores (adjusted  $R^2 = 0.483$  versus  $0.392$ – $0.436$  in conventional CTA,  $0.567$  versus  $0.349$ – $0.439$  in the arterial phase,  $0.614$  versus  $0.441$ – $0.483$  in the arteriovenous phase,  $0.586$  versus  $0.321$ – $0.374$  in the venous phase, Table 2). BIC analyses confirmed these results and showed a very strong preference (BIC difference =  $>10$ ) for models containing the volume of hypoattenuation in conventional CTA and in all phases of dynamic CTA.

Among collateral vessel grading scores, the BIC favored the model containing the 20-point relative score in conventional CTA (BIC difference = 17.8, indicating a very strong difference). In dynamic CTA, there was also a preference for the 20-point relative score in the arterial phase (BIC difference = 3.3), in the arteriovenous phase (BIC difference = 13.2, indicating a very strong difference), and in the venous phase (BIC difference = 6.5,

indicating a strong difference). Figure 5 shows 2 examples of the volume of hypoattenuation and collateral vessels in all 3 phases of dynamic CTA and the infarct on follow-up in a typical patient.

## DISCUSSION

Our data demonstrate the volume of hypoattenuation to be a stronger predictor of the follow-up lesion volume than collateral vessel grading scores. Dynamic CTA, particularly if assessed in the arteriovenous phase, was superior to conventional CTA in predicting the follow-up infarction volume.

Our findings are in line with and extend those of prior reports showing that the degree of collateralization is an independent predictor of tissue outcome.<sup>4,5,23</sup> Most of these studies were performed by using conventional CTA for collateral assessment. So far, no consensus has been reached on how to standardize collateral assessment. Different approaches included the quantification of the volume of hypoattenuation in CTA source images<sup>12,13</sup> and the use of different collateral vessel grading scores.<sup>10</sup>

In our study, we demonstrate the volume of hypoattenuation to be a stronger predictor of tissue outcome than collateral vessel grading scores in both conventional and dynamic angiography. While collateral vessels correspond to the macrocirculation within the ischemic bed, attenuation values correlate with parenchymal contrast material arrival and may therefore be considered an indicator of effectiveness of collateral blood supply.<sup>24</sup> This effectiveness may depend on not only the status of the macrocirculation but also other factors such as cerebral perfusion pressure<sup>1</sup> and may therefore be a better prognostic marker.

Another crucial aspect in collateral blood flow imaging by using conventional CT angiography is the time point of image acquisition. Triggered protocols that cover the phase of peak arterial enhancement have already found their way into clinical routine because they reliably detect arterial occlusions, stenoses, and aneurysms.<sup>13,17</sup> However, image acquisition at an early arterial phase can fail to capture delayed collateral contrast material arrival.<sup>17</sup> Using delay-insensitive dynamic CTA, Smit et al<sup>17</sup> could show that the presence of a delayed collateral enhancement may still be an important predictor of a good outcome. While important information has been added to the previously described value of conventional CT angiography,<sup>25</sup> the optimal time point for collateral evaluation has not been assessed. Other studies demonstrated that the application of different CTA acquisition protocols has a substantial effect on the correlation with concur-

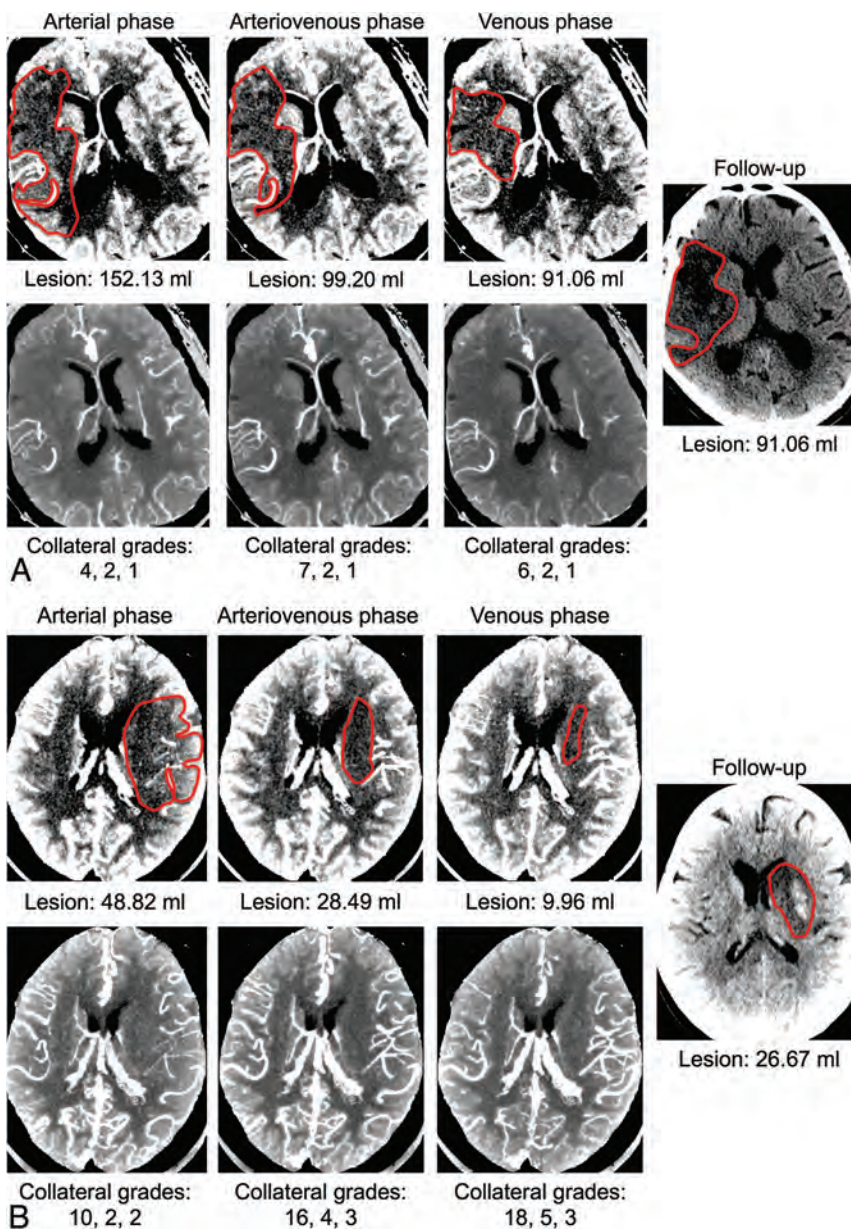


**FIG 5.** Examples of the volume of hypoattenuation and collateral vessels. *A* and *B*, Examples of 2 typical patients. The *top* rows show 10-mm MIPs of each phase in dynamic CTA. The areas of hypoattenuation of these MIPs are outlined, and the total lesion volumes of each phase are given beneath the images. The *bottom* rows show 20-mm MIPs of each phase in dynamic CTA, illustrating the collateral vessels. Collateral grades for each phase are given beneath the images and correspond to (in the order given) the 20-point relative score, the 5-point relative score, and the 4-point absolute score. The area of infarction on follow-up is shown on the right.

rently acquired CT perfusion<sup>26</sup> and MR diffusion-weighted images.<sup>13</sup>

Independent of the approach chosen to evaluate the collateralization status, our results suggest an optimal prognostic value of collateralization when assessed during the arteriovenous phase. Notably, the prognostic value was lowest in conventional CT angiography, which is acquired in a caudocranial direction with a 2-second delay after bolus triggering in the aortic arch (cutoff value = 100 HU) at our institution. This finding is in line with those in previous studies showing that early scan acquisition

might fail to capture the full extent of collateral enhancement.<sup>17</sup>

Furthermore, our results indicate that collateral assessment in dynamic CTA during the venous phase has a worse prognostic value than assessment during an earlier phase. Two possible reasons for a worse prognostic performance of the late venous phase compared with the earlier arteriovenous phase may be an overestimation of collateral blood flow due to concurrent enhancement of venous vessels and an important role of collateral filling time, which cannot be accounted for in the late venous phase. The superiority of the arteriovenous phase may also have important implications for standardization of collateral blood flow assessment by using conventional CT angiography because it might not be necessary to perform image acquisition during a delayed venous phase. Instead, the arteriovenous phase might allow an optimal assessment of occlusions and of collateral blood flow.

Our data should be interpreted in the context of the study design. As a retrospective study, there is a potential for bias in patient selection. The use of a large cohort of consecutive patients and standardized protocols for patients with suspected stroke, however, helped to reduce these confounding factors. Furthermore, although patients with mechanical recanalization and treatment by intravenous rtPA were included, the state of recanalization between initial CT and follow-up imaging was not assessed. Lack of recanalization leads to larger volumes of infarction and reduces the correlation between initial and follow-up lesion volumes.<sup>14</sup> Thus, different rates of recanalization might alter the correlation between the collateral status at different time-phases and the follow-up lesion volume. Finally, assessment was performed in consensus readings. The purpose of this study was

not to test interobserver agreement but to compare the predictive value of different strategies at different time-phases.

## CONCLUSIONS

We demonstrated that the type of collateral blood flow assessment is an important cornerstone for estimating the final infarct volume. Among all strategies tested, the use of dynamic CTA within the arteriovenous phase, including the quantification of the volume of hypoattenuation, is the best-suited technique to assess collateralization. This technique may help to reliably assess the

collateralization status and to make a first prognostic statement in the acute stroke situation.

Disclosures: Maximilian F. Reiser—UNRELATED: Grants/Grants Pending: 1) German Research Society (Deutsche Forschungsgemeinschaft) "Cluster of Excellence";\* 2) Euro-Biolmaging;\* 3) German National Cohort;\* 4) Munich Cluster of Excellence M4 Imaging;\* 5) Federal Ministry of Education and Research German Center for Lung Diseases;\* and 6) Federal Ministry of Education and Research German Center for Cardiovascular Diseases.\* Comments: 1) November 2006–2016 Principal Investigator, Munich Center of Advanced Photonics, Ludwig Maximilians University of Munich, Technical University of Munich, Germany; December 20, 2010–2016 Principal Site Investigator Euro-Biolmaging; European Commission-SP4 Capacities-FP7-Infrastructures-2010-1 (GA 262023). Ludwig Maximilians University of Munich, Germany; 3) 2011–2016 Co-Principal Investigator, German National Cohort, Imaging Working Group—Whole Body MRI Phenotyping, Federal Ministry of Education and Research/Helmholtz Society, Germany; 4) 2011–2016 Co-Principal Investigator: Imaging-Personalized Medicine, a new dimension of drug development; 5) 2010–2015 Principal Investigator; and 6) 2010–2015 Principal Investigator. Birgit Ertl-Wagner—RELATED: Grant: German Research Council (past)\*; UNRELATED: Board Membership: Philips Healthcare (current), Bracco (current), Springer Medical Publishing (current); Consultancy: Munich Medical International (current), Philips Healthcare (current); Grants/Grants Pending: Eli Lilly (current)\*, Genentech (current)\*, Guerbet (current)\*, Merck Serono (current)\*, Novartis (current)\*; Payment for Lectures (including service on Speakers Bureaus): Siemens (ongoing), Bayer-Schering (past); Payment for Manuscript Preparation: Siemens (past); Springer Medical Publishing (ongoing), Thieme Medical Publisher (ongoing), Bracco (ongoing); Royalties: Springer Medical Publishing (ongoing), Thieme Medical Publisher (ongoing); Payment for Development of Educational Presentations: Siemens (past), Bracco (ongoing), Springer (ongoing), Thieme (ongoing); Stock/Stock Options: Siemens (stock owned by spouse, ongoing); Travel/Accommodations/Meeting Expenses Unrelated to Activities Listed: Siemens (ongoing). \*Money paid to the institution.

## REFERENCES

1. Liebeskind DS. Collateral circulation. *Stroke* 2003;34:2279–84
2. Tariq N, Khatri R. Leptomeningeal collaterals in acute ischemic stroke. *J Vasc Interv Neurol* 2008;1:91–95
3. Tan JC, Dillon WP, Liu S, et al. Systematic comparison of perfusion-CT and CT-angiography in acute stroke patients. *Ann Neurol* 2007;61:533–43
4. Miteff F, Levi CR, Bateman GA, et al. The independent predictive utility of computed tomography angiographic collateral status in acute ischaemic stroke. *Brain* 2009;132:2231–38
5. Calleja AI, Cortijo E, Garcia-Bermejo P, et al. Collateral circulation on perfusion-computed tomography-source images predicts the response to stroke intravenous thrombolysis. *Eur J Neurol* 2013;20:795–802
6. Jung S, Gilgen M, Slotboom J, et al. Factors that determine penumbral tissue loss in acute ischaemic stroke. *Brain* 2013;136:3554–60
7. Lima FO, Furie KL, Silva GS, et al. The pattern of leptomeningeal collaterals on CT angiography is a strong predictor of long-term functional outcome in stroke patients with large vessel intracranial occlusion. *Stroke* 2010;41:2316–22
8. Maas MB, Lev MH, Ay H, et al. Collateral vessels on CT angiography predict outcome in acute ischemic stroke. *Stroke* 2009;40:3001–05
9. Campbell BC, Christensen S, Tress BM, et al. Failure of collateral blood flow is associated with infarct growth in ischemic stroke. *J Cerebr Blood Flow Metab* 2013;33:1168–72
10. McVerry F, Liebeskind DS, Muir KW. Systematic review of methods for assessing leptomeningeal collateral flow. *AJNR Am J Neuroradiol* 2012;33:576–82
11. Menon BK, Smith EE, Modi J, et al. Regional leptomeningeal score on CT angiography predicts clinical and imaging outcomes in patients with acute anterior circulation occlusions. *AJNR Am J Neuroradiol* 2011;32:1640–45
12. Schaefer PW, Yoo AJ, Bell D, et al. CT angiography-source image hypoattenuation predicts clinical outcome in posterior circulation strokes treated with intra-arterial therapy. *Stroke* 2008;39:3107–09
13. Pulli B, Schaefer PW, Hakimelahi R, et al. Acute ischemic stroke: infarct core estimation on CT angiography source images depends on CT angiography protocol. *Radiology* 2012;262:593–604
14. Lev MH, Segal AZ, Farkas J, et al. Utility of perfusion-weighted CT imaging in acute middle cerebral artery stroke treated with intra-arterial thrombolysis: prediction of final infarct volume and clinical outcome. *Stroke* 2001;32:2021–28
15. Schramm P, Schellinger PD, Fiebich JB, et al. Comparison of CT and CT angiography source images with diffusion-weighted imaging in patients with acute stroke within 6 hours after onset. *Stroke* 2002;33:2426–32
16. Dzialowski I, Weber J, Doerfler A, et al. Brain tissue water uptake after middle cerebral artery occlusion assessed with CT. *J Neuroimaging* 2004;14:42–48
17. Smit EJ, Vonken EJ, van Seeters T, et al. Timing-invariant imaging of collateral vessels in acute ischemic stroke. *Stroke* 2013;44:2194–99
18. Frölich AM, Wolff SL, Psychogios MN, et al. Time-resolved assessment of collateral flow using 4D CT angiography in large-vessel occlusion stroke. *Eur Radiol* 2014;24:390–96
19. Bivard A, Levi C, Spratt N, et al. Perfusion CT in acute stroke: a comprehensive analysis of infarct and penumbra. *Radiology* 2013;267:543–50
20. Smit EJ, Vonken EJ, van der Schaaf IC, et al. Timing-invariant reconstruction for deriving high-quality CT angiographic data from cerebral CT perfusion data. *Radiology* 2012;263:216–25
21. Thierfelder KM, Sommer WH, Baumann AB, et al. Whole-brain CT perfusion: reliability and reproducibility of volumetric perfusion deficit assessment in patients with acute ischemic stroke. *Neuroradiology* 2013;55:827–35
22. Menon BK, Bal S, Modi J, et al. Anterior temporal artery sign in CT angiography predicts reduced fatal brain edema and mortality in acute M1 middle cerebral artery occlusions. *J Neuroimaging* 2012;22:145–48
23. Kim JJ, Fischbein NJ, Lu Y, et al. Regional angiographic grading system for collateral flow: correlation with cerebral infarction in patients with middle cerebral artery occlusion. *Stroke* 2004;35:1340–44
24. Shuaib A, Butcher K, Mohammad AA, et al. Collateral blood vessels in acute ischaemic stroke: a potential therapeutic target. *Lancet Neurol* 2011;10:909–21
25. Souza LC, Yoo AJ, Chaudhry ZA, et al. Malignant CTA collateral profile is highly specific for large admission DWI infarct core and poor outcome in acute stroke. *AJNR Am J Neuroradiol* 2012;33:1331–36
26. Sharma M, Fox AJ, Symons S, et al. CT angiographic source images: flow- or volume-weighted? *AJNR Am J Neuroradiol* 2011;32:359–64

# Impact of Time-to-Reperfusion on Outcome in Patients with Poor Collaterals

Y.-H. Hwang, D.-H. Kang, Y.-W. Kim, Y.-S. Kim, S.-P. Park, and D.S. Liebeskind



## ABSTRACT

**BACKGROUND AND PURPOSE:** The relationship between reperfusion and clinical outcome is time-dependent, and the effect of reperfusion on outcome can vary on the basis of the extent of collateral flow. We aimed to identify the impact of time-to-reperfusion on outcome relative to baseline angiographic collateral grade in patients successfully treated with endovascular revascularization for acute large-vessel anterior circulation stroke.

**MATERIALS AND METHODS:** Two hundred seven patients were selected for analysis from our prospectively maintained registry. Inclusion criteria were M1 MCA ± ICA occlusions, onset-to-puncture time within 8 hours, and successful endovascular reperfusion. Baseline angiographic collateral grades were independently evaluated and dichotomized into poor (0–1) versus good (2–4). Multivariable analyses were performed to identify the effect of collateral-flow adequacy on favorable outcome on the basis of onset-to-reperfusion time and puncture-to-reperfusion time.

**RESULTS:** In the poor collateral group, the odds of favorable outcome significantly dropped for patients with onset-to-reperfusion time of >300 minutes or puncture-to-reperfusion time of >60 minutes (onset-to-puncture time: ≤300, 59% versus >300, 32%; OR, 0.24;  $P = .011$ ; puncture-to-reperfusion time: ≤60, 73% versus >60, 32%; OR, 0.21,  $P = .011$ ), whereas the probability of favorable outcome in the good collateral group was not significantly influenced by onset-to-reperfusion time or puncture-to-reperfusion time. In the subgroup lesion-volume growth analysis by using DWI, the effect of puncture-to-reperfusion time of >60 minutes was significantly greater compared with the effect of puncture-to-reperfusion time of <60 minutes in the poor collateral group ( $\beta = 41.6 \text{ cm}^3$ ,  $P = .001$ ).

**CONCLUSIONS:** Time-to-reperfusion including onset-to-reperfusion time and puncture-to-reperfusion time in patients with poor collaterals is an important limiting factor for favorable outcome in a time-dependent fashion. Future trials may benefit from a noninvasive imaging technique to detect poor collaterals along with a strategy for rapid reperfusion.

**ABBREVIATIONS:** HI = hemorrhagic infarction; OPT = onset-to-puncture time; ORT = onset-to-reperfusion time; PH = parenchymal hematoma; PRT = puncture-to-reperfusion time

The restoration of antegrade perfusion to the ischemic territory is the principal goal of current acute stroke treatments because it is associated with better clinical outcomes and reduced mortality.<sup>1,2</sup>

Also, the effect of reperfusion on outcome is time-dependent, and onset-to-reperfusion time (ORT) has emerged as an important time metric to show the benefit of endovascular treatment.<sup>3,4</sup>

However, the effect of reperfusion on outcome can vary on the basis of the extent of collateral flow.<sup>5–11</sup> Baseline collateral flow, which is an important determinant of clinical recovery, can mitigate potential injury to ischemic brain tissue.<sup>12</sup> Before adequate reperfusion occurs, the penumbral area can continue to be salvageable depending on the robustness of collateral flow, and its impact on infarct growth and subsequent clinical outcome may be time-dependent, along with reperfusion status. It can be speculated that in patients with poor collaterals, the relationship between reperfusion and clinical outcome may be more dependent on time-to-reperfusion because the odds of potential brain injury may be higher until reperfusion occurs.

We hypothesized that differential clinical response to reperfusion can be driven by the quality of baseline collaterals in a time-

Received June 25, 2014; accepted after revision August 10.

From the Departments of Neurology (Y.-H.H., Y.-W.K., S.-P.P.), Neurosurgery (D.-H.K.), Radiology (D.-H.K., Y.-W.K., Y.-S.K.), and Cerebrovascular Center (Y.-H.H., D.-H.K., Y.-W.K., Y.-S.K.), Kyungpook National University Hospital, Daegu, Korea; School of Medicine (Y.-H.H., D.-H.K., Y.-W.K., Y.-S.K., S.-P.P.), Kyungpook National University, Daegu, Korea; and UCLA Stroke Center (D.S.L.), University of California, Los Angeles, Los Angeles, California.

Y.-H. Hwang and D.-H. Kang contributed equally to this work.

Please address correspondence to Yang-Ha Hwang, MD, PhD, Department of Neurology and Cerebrovascular Center, Kyungpook National University Hospital, 130, Dongduk-ro, Jung-gu, Daegu, 700–721, Republic of Korea; e-mail: yangha.hwang@gmail.com; @yangha73

Indicates open access to non-subscribers at www.ajnr.org

Indicates article with supplemental on-line tables.

Indicates article with supplemental on-line photo.

<http://dx.doi.org/10.3174/ajnr.A4151>

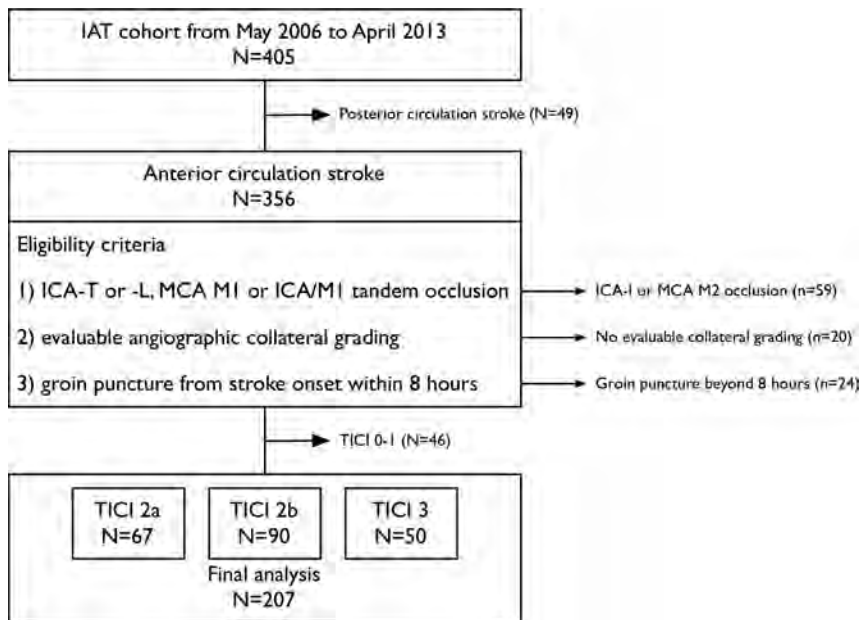


**FIG 1.** Flow chart description of patient selection and exclusion for the study. IAT indicates intra-arterial treatment.

dependent manner. We sought to determine the relationship among time-to-reperfusion, angiographic collateral-flow grade, and clinical and imaging outcome, which may show that there is a narrow therapeutic time window for patients having poor collaterals, despite angiographic reperfusion.

## MATERIALS AND METHODS

Between May 2006 and April 2013, patients were retrospectively selected from a prospectively maintained acute stroke intra-arterial treatment registry at our institution. Eligibility for inclusion in this study was that patients met the following criteria: 1) They had an acute anterior circulation stroke with angiographically confirmed ICA-T or -L (-T or -L indicate the shape of occlusive lesion), MCA M1, or ICA/M1 tandem occlusion; 2) had evaluable angiographic imaging for collateral-flow grading; 3) had arterial puncture in the angiography suite room within 8 hours from time last-known well; and 4) achieved a sufficient angiographic reperfusion, which we defined as a TIIC grades 2–3 (Fig 1).<sup>13</sup> Within the 3-hour time window, intravenous rtPA was used,<sup>14,15</sup> and patients showing a persistent ICA or MCA occlusion despite rtPA on TOF MRA or CTA were selected for endovascular treatment. We excluded patients who revealed well-developed parenchymal hypodensity on CT or hyperattenuation on FLAIR imaging, severe brain edema, intracerebral hemorrhage, or cardiopulmonary compromise. The local institutional review board approved this study for retrospective analysis.

Eligible patients underwent transfemoral cerebral angiography, including injection of both carotid arteries and the dominant vertebral artery through the late venous phase, under local or general anesthesia to define the angioarchitecture of the occluded vessel and to assess collateral flow from all possible sources. If the treatable ICA or MCA occlusion persisted, endovascular treatment was initiated. Treatment strategies were selected on the basis of available therapies at the time of angiography,

which included intra-arterial thrombolytic infusion (urokinase or rtPA), mechanical clot disruption, mechanical thrombectomy including forced arterial suction thrombectomy or Solitaire thrombectomy (Covidien, Irvine, California), rescue intra-/extracranial stent, or a combination.<sup>16–18</sup> Angiographic collateral-flow grade was evaluated with the American Society of Interventional and Therapeutic Neuroradiology/Society of Interventional Radiology collateral-flow grading system on pretreatment angiography. This angiographic scale assigns patients to grades 0–4 according to the completeness and rapidity of collateral filling in a retrograde fashion.<sup>13</sup> The angiographic collateral-flow grade was independently evaluated by an experienced neurologist (Y.-W.K.) and neuroradiologist (D.-H.K.) blinded to patient information and was dichotomized as poor (collateral-flow grades 0–1) and good (2–

4).<sup>19</sup> The  $\kappa$  coefficient for interobserver agreement was 0.864 for each collateral grade. Disagreement was resolved by consensus. Reperfusion status was measured by the same raters and methods for the TIIC scale.<sup>13</sup>

Information on demographic and clinical characteristics, medical history, admission blood pressure, and blood glucose levels was collected at baseline. The onset of stroke was defined as the time when the patient was last observed to be healthy. Stroke severity was assessed by using the NIHSS at baseline. The DWI at baseline was assessed by using ASPECTS.<sup>20</sup> All patients underwent CT or MR imaging at 24–48 hours after the treatment. If there was evidence of hemorrhage, the subtype was classified as hemorrhagic infarction (HI), parenchymal hematoma (PH), SAH, intraventricular hemorrhage, or mixed.<sup>21</sup> Symptomatic intracranial hemorrhage was defined as any type of hemorrhage associated with an increase in the NIHSS score of  $\geq 4$  within 24 hours.<sup>22</sup> A subset of 160 patients had undergone both pretreatment and post-treatment DWI (3–7 days from stroke onset). One experienced neurologist (Y.-W.K.) who was blinded to clinical status performed DWI lesion-volume calculation by using an open source image-analysis software (OsiriX Imaging Software; <http://www.osirix-viewer.com>). Functional status was assessed by using the mRS at 3 months, and favorable outcome was defined as an mRS of  $\leq 2$  or equal to the prestroke mRS if the prestroke mRS was  $> 2$ .<sup>22,23</sup>

## Statistical Analysis

Statistical analysis was performed by using the SPSS statistical package (Version 20.0; IBM, Armonk, New York). Bivariate comparisons were made by using the  $\chi^2$  test or Fisher exact test as appropriate for categorical variables. The Student *t* test was used for continuous variables, and the Mann-Whitney *U* test was used for ordinal and continuous variables that had skewed distributions. Multivariable regression analysis was performed to identify the effect of collateral-flow grade on each outcome or lesion volume

based on prespecified various time cutoff points. The results are presented as OR estimates of relative risk with a 95% CI or  $\beta$  coefficient as appropriate. Probability values  $< .05$  were statistically significant.

## RESULTS

During the study period, 207 patients were included for analysis, and the details of exclusion are described in Fig 1. Overall, 76

patients (37%) were assigned to the poor collateral group (collateral-flow grades, 0–1), and 131 patients (63%), to the good collateral group (collateral-flow grades, 2–4). The baseline characteristics and outcomes are described in the Table (On-line Table 1 in detail). Patients in the poor collateral group had a higher baseline NIHSS score, a lower baseline ASPECTS<sub>DWI</sub>, a higher incidence of ICA-T or -L occlusion, and a lower rate of 3-month favorable outcome, all statistically significant.

### Baseline characteristics, imaging, and clinical outcomes (N = 207)<sup>a</sup>

Characteristics	Collateral-Flow Grade		P Value
	0–1 (n = 76)	2–4 (n = 131)	
Age (yr)	69 (62–76)	67 (58–73)	.105
Male	50 (65.8%)	75 (57.3%)	.226
Baseline NIHSS	17 (13–21)	16 (12–19)	.041
Baseline ASPECTS <sub>DWI</sub> <sup>b</sup>	7 (5–8)	8 (6–9)	.004 <sup>c</sup>
SBP (mm Hg)	148 (131–176)	146 (126–168)	.520
DBP (mm Hg)	82 (72–90)	82 (71–97)	.470
Blood glucose level (mg/dL)	126 (117–156)	126 (111–159)	.861
Occlusion site			.000
ICA-T or ICA-L	38 (50.0%)	22 (16.8%)	
MCA MI	26 (34.2%)	103 (78.6%)	
ICA/MI tandem	12 (15.8%)	6 (4.6%)	
IV rtPA	41 (53.9%)	62 (47.3%)	.359
Onset-to-puncture (min)	220 (160–290)	245 (175–325)	.055
Puncture-to-reperfusion (min)	77 (54–104)	66 (44–90)	.053
Onset-to-reperfusion (min)	297 (224–383)	307 (244–395)	.342
3-Month favorable outcome	35 (46.1%)	82 (62.6%)	.021
Procedure-related complications	4 (5.3%)	8 (6.1%)	1.000 <sup>c</sup>
Symptomatic ICH	4 (5.3%)	6 (4.6%)	1.000 <sup>c</sup>
Ischemic brain edema	7 (9.2%)	8 (6.1%)	.406
Mortality	11 (14.5%)	13 (9.9%)	.324

**Note:**—SBP indicates systolic blood pressure; DBP, diastolic blood pressure; ICH, intracranial hemorrhage.

<sup>a</sup> Numbers in parentheses are median (interquartile range) or number (%).

<sup>b</sup> Two hundred one DWI images at baseline (72 in 0–1 and 129 in 2–4; 97.1% in total) were available for ASPECTS<sub>DWI</sub> analysis.

<sup>c</sup> Fisher exact test for categoric variables/Mann-Whitney U test for continuous variables.

### Time-to-Reperfusion and Favorable Outcome

As shown in Fig 2A, the probability of favorable outcome decreased with every minute increase of ORT in the poor collateral group (OR, 0.99; 95% CI, 0.99–1.00;  $P = .021$ ). The effect of ORT on the probability of favorable outcome in the good collateral group was also time-dependent, but it was not statistically significant (OR, 1.00; 95% CI, 0.99–1.00;  $P = .080$ ). With 30-minute time intervals, the OR magnitude was 0.80 (95% CI, 0.67–0.96;  $P = .015$ ) in the poor collateral group compared with the good collateral group (OR, 0.90; 95% CI, 0.80–1.02;  $P = .096$ ) after adjustment for age, baseline NIHSS score, and posttreatment TICI 2b–3 reperfusion. With a time cutoff point of 300 minutes for ORT, ORT of  $>300$  minutes remained as an independent predictor of decreased odds for favorable outcome in patients with poor collateral flow (OR, 0.24; 95% CI, 0.08–0.72;  $P = .011$ ) compared with good collateral flow (OR, 0.47; 95% CI, 0.21–1.08;  $P = .074$ ) after adjustment for age, baseline NIHSS score, and posttreatment TICI 2b–3 reperfusion (Fig 3A).

We divided the ORT between onset-to-puncture time (OPT) and puncture-to-reperfusion time (PRT) to determine the effects of time spent on endovascular treatment. There was no time-dependent effect on favorable outcome based on a time cutoff point of 240 minutes of OPT. Rather, as shown in Fig 2B, the probability of favorable outcome decreased with every minute

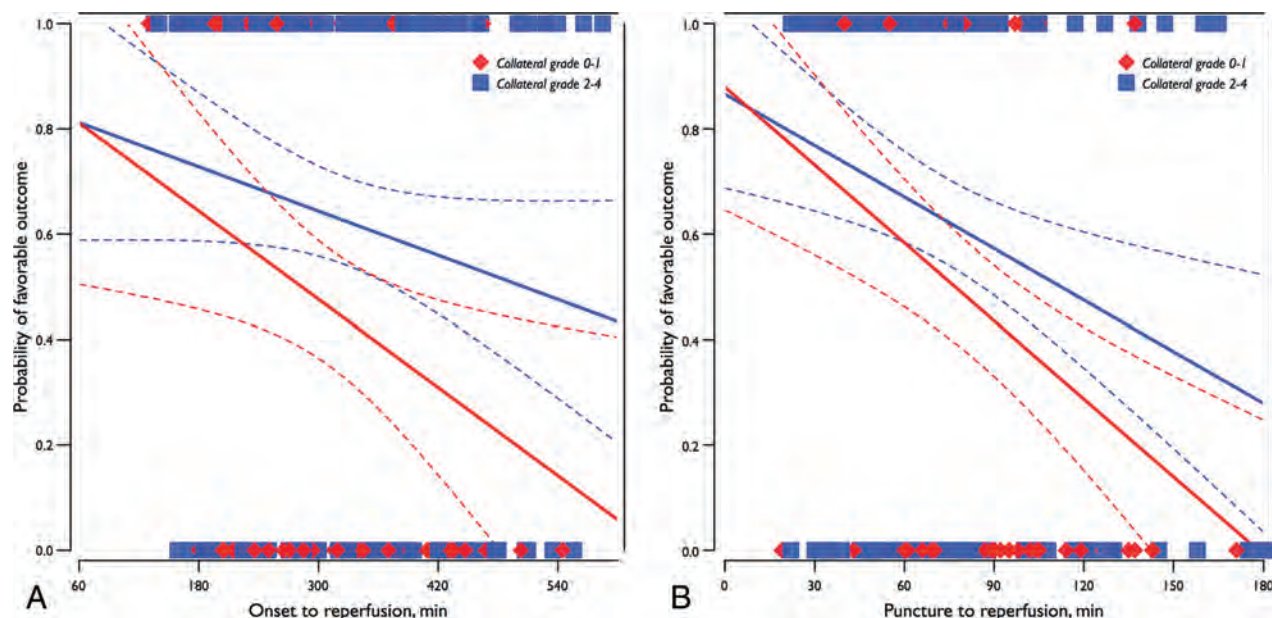


**FIG 2.** Unadjusted predicted probability of favorable outcome at 3 months by time-to-reperfusion based on collateral-flow grades 0–1 (red line) versus 2–4 (blue line). Solid lines represent the probability of favorable outcome over onset-to-reperfusion time (A) and puncture-to-reperfusion time (B) as predicted by an unadjusted logistic regression model based on collateral-flow grade. Dashed lines show the 95% confidence intervals. Outcomes of each observed case are also indicated on the basis of collateral-flow grades 0–1 (red diamond) versus 2–4 (blue square).

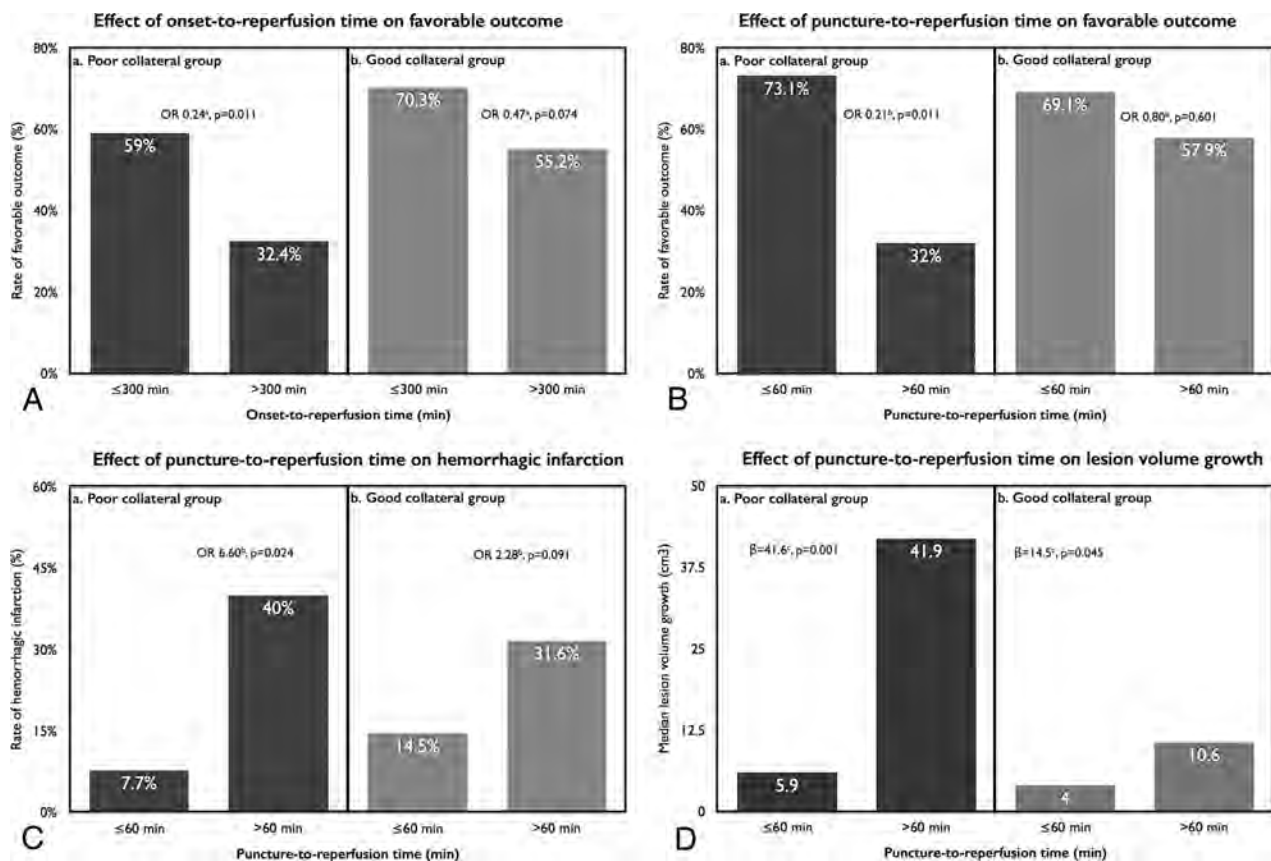


**FIG 3.** A–D, The effect of time-to-reperfusion on clinical and imaging outcomes based on collateral-flow grade. <sup>a</sup> indicates logistic regression analysis adjusted for age, baseline NIHSS score, and posttreatment TICI 2b–3 reperfusion; <sup>b</sup>, logistic regression analysis adjusted for age, baseline NIHSS score, posttreatment TICI 2b–3 reperfusion, and onset-to-puncture time; <sup>c</sup>, linear regression analysis adjusted for age, baseline NIHSS score, posttreatment TICI 2b–3 reperfusion, and onset-to-puncture time.

increase of PRT in the poor collateral group (OR, 0.97; 95% CI, 0.96–0.99;  $P = .001$ ). The effect of PRT on the probability of favorable outcome in the good collateral group was also time-dependent (OR, 0.99; 95% CI, 0.98–1.00;  $P = .005$ ). According to a time cutoff point of 60 minutes, PRT of >60 minutes remained an independent predictor of decreased odds of favorable outcome in patients with poor collateral flow (OR, 0.21; 95% CI, 0.06–0.70;  $P = .011$ ) compared with good collateral flow (OR, 0.80; 95% CI, 0.34–1.85;  $P = .601$ ) after adjustment for age, baseline NIHSS score, posttreatment TICI 2b–3 reperfusion, and OPT (Fig 3B). The cutoff time points for ORT and PRT were chosen on the basis of sensitivity and specificity analyses, and details are described in the On-line Figure.

#### Time-to-Reperfusion and Mortality/Intracerebral Hemorrhage

Unlike the significant relationship between the probability of favorable outcome and time-to-reperfusion, no statistically significant relationship was seen between the probability of mortality and prespecified time metrics based on collateral-flow grade. As to hemorrhage, the rate of HI was significantly increased in patients with ORT of >300 minutes in both the poor and good collateral groups. Likewise, a PRT of >60 minutes also increased the rate of HI, which remained as an independent predictor of increased odds of HI (OR, 6.60; 95% CI, 1.23–34.1;  $P = .024$ ) in the poor collateral group compared with the good collateral

group (OR, 2.28; 95% CI, 0.88–5.95;  $P = .091$ ) after adjustment for age, baseline NIHSS score, posttreatment TICI 2b–3 reperfusion, and OPT (Fig 3C). The rate of PH was not significantly influenced by the prespecified time metrics based on collateral-flow grade (On-line Table 2).

#### Time to Reperfusion and DWI Lesion Volume

A subset of 160 patients (of 207, 77.3%) completed both pretreatment and posttreatment DWI (3–7 days from stroke onset). There was a significant imbalance regarding the completion of both DWIs between patients with a favorable outcome or those without; 108 of 117 (92.3%) in patients with a favorable outcome versus 52 of 90 (57.8%) in patients with an unfavorable outcome ( $P = .000$ ). At baseline, the median DWI lesion volume was 14.6 and 9.8 cm<sup>3</sup> in the poor and good collateral group, respectively ( $P = .115$ ). The median DWI lesion volume at posttreatment and DWI lesion-volume growth were 56.6 cm<sup>3</sup> and 31.1 cm<sup>3</sup> versus 18.4 cm<sup>3</sup> and 7.0 cm<sup>3</sup> in the poor and good collateral groups, respectively ( $P = .002$  and  $.001$ ). Multiple regression analysis was performed to elucidate the effect of prespecified time cutoff points on DWI lesion volume based on collateral-flow grade (On-line Table 3). PRT of >60 minutes in the poor collateral group was an independent predictor of larger final lesion volume ( $\beta = 46.8$  cm<sup>3</sup>;  $P = .004$ ) and lesion-volume growth ( $\beta = 41.6$  cm<sup>3</sup>;  $P = .001$ ) after adjustment for age, baseline NIHSS score, posttreat-

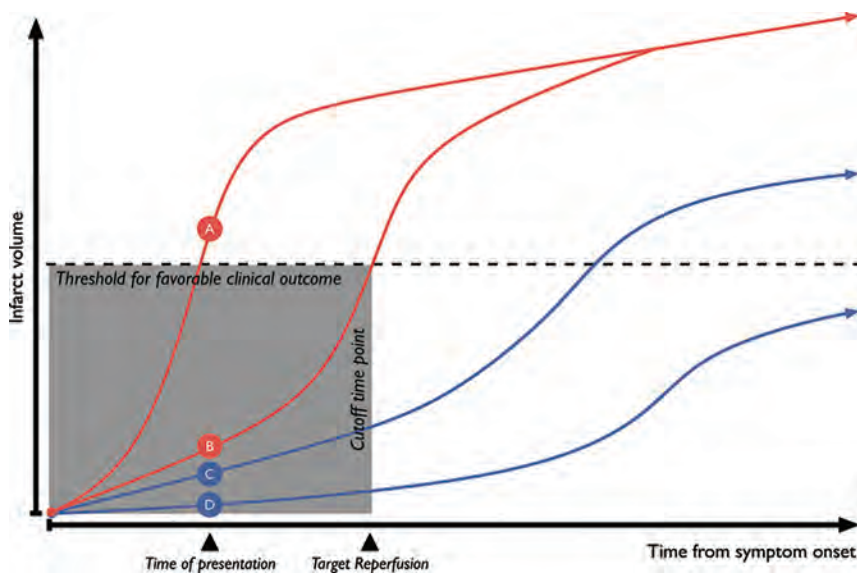


**FIG 4.** Simplified illustration, which represents the unique effect of time-to-reperfusion on clinical outcome based on proposed collateral scenarios (modified from Liebeskind's illustrations<sup>31</sup>). A, Universally good collaterals, which may show large infarcts and severe neurologic deficits at the time of presentation. B, Rapidly failing collaterals, which may show small-to-medium infarcts and severe neurologic deficits at the time of presentation. C, Slowly failing collaterals, which may show small infarcts and moderate-to-severe neurologic deficits at the time of presentation. D, Universally good collaterals, which may show tiny-to-small infarcts and mild-to-moderate neurologic deficits at the time of presentation. In real clinical practice, patients in scenarios B and C can be ideal candidates for endovascular reperfusion. However, the clinical outcome is limited by time-to-reperfusion in scenario B (eg, onset-to-reperfusion within 300 minutes or puncture-to-reperfusion within 60 minutes in this study).

ment TICI 2b–3 reperfusion, and OPT (Fig 3D). In addition, a PRT of >60 minutes was associated with lesion-volume growth ( $\beta = 14.5 \text{ cm}^3$ ,  $P = .045$ ) in the good collateral group, but the magnitude of the increment was not so large compared with the poor collateral group. The effect of final lesion volume and infarct volume growth remained significant from pretreatment DWI to reperfusion of >150 minutes in both groups; however, the magnitude of the increment was larger in the poor collateral group compared with the good collateral group.

## DISCUSSION

In patients with acute ischemic stroke attributable to large-vessel occlusion, selecting a candidate who will benefit most from endovascular revascularization therapy to optimize the practice of endovascular treatment is important for improving clinical outcome.<sup>24</sup> In consideration of that point, defining the optimal timeframe for reperfusion based on collateral-flow adequacy is crucial in averting further ischemic injury.<sup>25,26</sup> Our study demonstrated that the evaluation of the collateral-flow status before the initiation of intra-arterial treatment could be a key marker to determine a timeframe for reperfusion with a probable favorable clinical outcome.

The effect of the quality of collateral flow on clinical outcome has been examined in previous reports, which show that good collateral flow is associated with favorable outcome.<sup>5–11</sup> Also, the ORT in intra-arterial treatment was a main determinant factor in predicting favorable outcome.<sup>3,4</sup> Regarding collateral flow and ORT as determinant factors of favorable outcome, reperfusion of >300 minutes from onset in a poor collateral group was associated with decreased odds of clinical improvement and

favorable outcome from a small retrospective cohort.<sup>27</sup> Our study also showed that ORT is a critical determinant of favorable outcome in a time-dependent fashion (each minute, 30 minutes, or reperfusion of >300 minutes were all associated with a decreased chance of favorable outcome). Among the time variables affecting ORT, PRT was the main determinant of favorable outcome in the poor collateral group, which can be a more practical time metric to proceed or not proceed in the consideration of intra-arterial treatment. In the poor collateral group, PRT of >60 minutes was strongly associated with decreased odds of favorable outcome, which can be a practical marker for the determination of endovascular therapy termination. A previous study showed that the procedural time in intra-arterial treatment is a critical determinant of outcomes,<sup>28</sup> and further negative impact on favorable outcome was shown in the poor collateral group in our study.

The extent of collateral flow has been associated with the rate of hemorrhage in patients with acute stroke undergoing intra-arterial treatment.<sup>19,29</sup> In our

study, the rate of hemorrhagic infarction was increased in the later time window (eg, ORT of >300 minutes and PRT of >60 minutes), especially in the poor collateral group; this change suggests that the ischemic area in the poor collateral group is more susceptible to reperfusion injury in a time-dependent manner. Unlike that previous study,<sup>29</sup> we could not find any significant relationship between collateral-flow grade and parenchymal hematoma.

The status of collateral flow at the time of angiography has been shown to be associated with infarct growth in interaction with reperfusion.<sup>12</sup> We tried to link the 3-month favorable outcome and diffusion lesion volume to explain the inter-relationship between lesion-volume increments based on collateral-flow status. Perhaps because many cases of unfavorable outcome were excluded in this volumetric analysis, the relationship between ORT and lesion volume was not statistically significant on the basis of collateral-flow grade. However, we found that the chance of increased infarct volume is determined by the PRT and imaging-to-reperfusion time.

The main findings of this study were the following: 1) The probability of favorable outcome differed in a time-dependent manner on the basis of collateral-flow adequacy; 2) the rate of hemorrhagic infarction, which is a marker of reperfusion injury, increased with increasing ORT or PRT in the poor collateral group; and 3) lesion-volume enlargement was most prominent in patients with poor collaterals having a longer PRT or imaging-to-reperfusion time.

The results of this study should be interpreted with caution because it was not a randomized, controlled trial. Patients were treated with a variety of reperfusion therapies, including throm-

bolytics and different types of endovascular therapy. Furthermore, although our patients were enrolled prospectively, the decision for endovascular treatment was based on our institutional treatment protocol and the attending physician's decision, so there was a chance of exclusion from our study if the patient had a sizable infarct volume with a large-vessel occlusion despite being within the treatable time window. Therefore, this study was limited by its retrospective nature and inherent case-selection bias. For example, for patients with poor collaterals at baseline, the chance of sizable infarct volume might be higher, and such a patient could be excluded from endovascular treatment. In addition, the exclusion of patients who failed reperfusion despite endovascular treatment might affect the results of our study because the chance of successful reperfusion could be higher in cases of good collaterals.<sup>11,30</sup>

## CONCLUSIONS

In considering endovascular revascularization as a rescue treatment in patients with acute large-vessel occlusion, the status of baseline collateral flow at the time of angiography can be a crucial marker for favorable outcome and a limiting factor for lesion-volume increments in a time-dependent fashion (Fig 4). Therefore, limiting time-to-reperfusion, especially in patients with poor collaterals, is desirable in clinical practice, though our results should be confirmed in randomized trials or large datasets of prospective trials.

## ACKNOWLEDGMENTS

The authors thank Wade Martin of Medical Research International for his critical English revision.

Disclosures: David S. Liebeskind—UNRELATED: Consultancy: consultant for the angiography core laboratory at the University of California, Los Angeles\*; Grants/Grants Pending: National Institutes of Health—National Institute of Neurological Disorders and Stroke.\* \*Money paid to the institution.

## REFERENCES

- Zaidat OO, Suarez JJ, Sunshine JL, et al. **Thrombolytic therapy of acute ischemic stroke: correlation of angiographic recanalization with clinical outcome.** *AJNR Am J Neuroradiol* 2005;26:880–84
- Rha JH, Saver JL. **The impact of recanalization on ischemic stroke outcome: a meta-analysis.** *Stroke* 2007;38:967–73
- Khatri P, Abruzzo T, Yeatts SD, et al. **Good clinical outcome after ischemic stroke with successful revascularization is time-dependent.** *Neurology* 2009;73:1066–72
- Mazighi M, Chaudhry SA, Ribó M, et al. **Impact of onset-to-reperfusion time on stroke mortality: a collaborative pooled analysis.** *Circulation* 2013;127:1980–85
- Kucinski T, Koch C, Eckert B, et al. **Collateral circulation is an independent radiological predictor of outcome after thrombolysis in acute ischaemic stroke.** *Neuroradiology* 2003;45:11–18
- Christoforidis GA, Mohammad Y, Kehagias D, et al. **Angiographic assessment of pial collaterals as a prognostic indicator following intra-arterial thrombolysis for acute ischemic stroke.** *AJNR Am J Neuroradiol* 2005;26:1789–97
- Miteff F, Levi CR, Bateman GA, et al. **The independent predictive utility of computed tomography angiographic collateral status in acute ischaemic stroke.** *Brain* 2009;132:2231–38
- Galimanis A, Jung S, Mono ML, et al. **Endovascular therapy of 623 patients with anterior circulation stroke.** *Stroke* 2012;43:1052–57
- Souza LCS, Yoo AJ, Chaudhry ZA, et al. **Malignant CTA collateral profile is highly specific for large admission DWI infarct core and poor outcome in acute stroke.** *AJNR Am J Neuroradiol* 2012;33:1331–36
- Liebeskind DS, Tomsick TA, Foster LD, et al. **Collaterals at angiography and outcomes in the Interventional Management of Stroke (IMS) III trial.** *Stroke* 2014;45:759–64
- Liebeskind DS, Jahan R, Nogueira RG, et al. **Impact of collaterals on successful revascularization in Solitaire FR with the intention for thrombectomy.** *Stroke* 2014;45:2036–40
- Bang OY, Saver JL, Buck BH, et al. **Impact of collateral flow on tissue fate in acute ischaemic stroke.** *J Neurol Neurosurg Psychiatry* 2008;79:625–29
- Higashida RT, Furlan AJ, Roberts H, et al. **Trial design and reporting standards for intra-arterial cerebral thrombolysis for acute ischemic stroke.** *Stroke* 2003;34:e109–37
- National Institute of Neurological Disorders and Stroke rt-PA Stroke Study Group. **Tissue plasminogen activator for acute ischemic stroke.** *N Engl J Med* 1995;333:1581–87
- Yamaguchi T, Mori E, Minematsu K, et al. **Alteplase at 0.6 mg/kg for acute ischemic stroke within 3 hours of onset: Japan Alteplase Clinical Trial (J-ACT).** *Stroke* 2006;37:1810–15
- Hwang YH, Kang DH, Kim YW, et al. **Outcome of forced-suction thrombectomy in acute intracranial internal carotid occlusion.** *J Neurointerv Surg* 2013;(5 suppl 1):i81–84
- Kang DH, Hwang YH, Kim YS, et al. **Direct thrombus retrieval using the reperfusion catheter of the Penumbra system: forced-suction thrombectomy in acute ischemic stroke.** *AJNR Am J Neuroradiol* 2011;32:283–87
- Kang DH, Kim YW, Hwang YH, et al. **Switching strategy for mechanical thrombectomy of acute large vessel occlusion in the anterior circulation.** *Stroke* 2013;44:3577–79
- Bang OY, Saver JL, Kim SJ, et al. **Collateral flow averts hemorrhagic transformation after endovascular therapy for acute ischemic stroke.** *Stroke* 2011;42:2235–39
- Barber PA, Demchuk AM, Zhang J, et al. **Validity and reliability of a quantitative computed tomography score in predicting outcome of hyperacute stroke before thrombolytic therapy: ASPECTS Study Group—Alberta Stroke Programme Early CT Score.** *Lancet* 2000;355:1670–74
- Hacke W, Kaste M, Fieschi C, et al. **Randomised double-blind placebo-controlled trial of thrombolytic therapy with intravenous alteplase in acute ischaemic stroke (ECASS II).** *Lancet* 1998;352:1245–51
- Saver JL, Jahan R, Levy EI, et al. **Solitaire flow restoration device versus the Merci retriever in patients with acute ischaemic stroke (SWIFT): a randomised, parallel-group, non-inferiority trial.** *Lancet* 2012;380:1241–49
- van Swieten JC, Koudstaal PJ, Visser MC, et al. **Interobserver agreement for the assessment of handicap in stroke patients.** *Stroke* 1988;19:604–07
- Lazzaro MA, Novakovic RL, Alexandrov AV, et al. **Developing practice recommendations for endovascular revascularization for acute ischemic stroke.** *Neurology* 2012;79:S243–55
- Liebeskind DS. **Collateral circulation.** *Stroke* 2003;34:2279–84
- Liebeskind DS, Sanossian N. **How well do blood flow imaging and collaterals on angiography predict brain at risk?** *Neurology* 2012;79:S105–09
- Ribo M, Flores A, Rubiera M, et al. **Extending the time window for endovascular procedures according to collateral pial circulation.** *Stroke* 2011;42:3465–69
- Hassan AE, Chaudhry SA, Miley JT, et al. **Microcatheter to recanalization (procedure time) predicts outcomes in endovascular treatment in patients with acute ischemic stroke: when do we stop?** *AJNR Am J Neuroradiol* 2013;34:354–59
- Christoforidis GA, Karakasis C, Mohammad Y, et al. **Predictors of hemorrhage following intra-arterial thrombolysis for acute ischemic stroke: the role of pial collateral formation.** *AJNR Am J Neuroradiol* 2009;30:165–70
- Bang OY, Saver JL, Kim SJ, et al. **Collateral flow predicts response to endovascular therapy for acute ischemic stroke.** *Stroke* 2011;42:693–99
- Liebeskind DS. **Imaging the future of stroke: I. Ischemia.** *Ann Neurol* 2009;66:574–90

# MS Lesions Are Better Detected with 3D T1 Gradient-Echo Than with 2D T1 Spin-Echo Gadolinium-Enhanced Imaging at 3T

A. Crombé, M. Saranathan, A. Ruet, M. Durieux, E. de Roquefeuil,  J.C. Ouallet, B. Brochet, V. Dousset, and T. Tourdias



## ABSTRACT

**BACKGROUND AND PURPOSE:** In multiple sclerosis, gadolinium enhancement is used to classify lesions as active. Regarding the need for a standardized and accurate method for detection of multiple sclerosis activity, we compared 2D-spin-echo with 3D-gradient-echo T1WI for the detection of gadolinium-enhancing MS lesions.

**MATERIALS AND METHODS:** Fifty-eight patients with MS were prospectively imaged at 3T by using both 2D-spin-echo and 3D-gradient recalled-echo T1WI in random order after the injection of gadolinium. Blinded and independent evaluation was performed by a junior and a senior reader to count gadolinium-enhancing lesions and to characterize their location, size, pattern of enhancement, and the relative contrast between enhancing lesions and the adjacent white matter. Finally, the SNR and relative contrast of gadolinium-enhancing lesions were computed for both sequences by using simulations.

**RESULTS:** Significantly more gadolinium-enhancing lesions were reported on 3D-gradient recalled-echo than on 2D-spin-echo ( $n = 59$  versus  $n = 30$  for the junior reader,  $P = .02$ ;  $n = 77$  versus  $n = 61$  for the senior reader,  $P = .017$ ). The difference between the 2 readers was significant on 2D-spin-echo ( $P = .044$ ), for which images were less reproducible ( $\kappa = 0.51$ ) than for 3D-gradient recalled-echo ( $\kappa = 0.65$ ). Further comparisons showed that there were statistically more small lesions ( $<5$  mm) on 3D-gradient recalled-echo than on 2D-spin-echo ( $P = .04$ ), while other features were similar. Theoretic results from simulations predicted SNR and lesion contrast for 3D-gradient recalled-echo to be better than for 2D-spin-echo for visualization of small enhancing lesions and were, therefore, consistent with clinical observations.

**CONCLUSIONS:** At 3T, 3D-gradient recalled-echo provides a higher detection rate of gadolinium-enhancing lesions, especially those with smaller size, with a better reproducibility; this finding suggests using 3D-gradient recalled-echo to detect MS activity, with potential impact in initiation, monitoring, and optimization of therapy.

**ABBREVIATIONS:** FSPGR = fast-spoiled gradient recalled; GRE = gradient recalled-echo; SE = spin-echo

MR imaging is widely used in multiple sclerosis and has become an established tool not only for diagnosis but also for disease monitoring.<sup>1</sup> MR imaging–defined disease activity, in conjunction with clinical status, can be used to ensure treatment optimization by identifying high-risk patients or poor responders during follow-up,<sup>2,3</sup> which is important given that MS is a chronic

disease for which expensive treatments are now used. There is an urgent need for an accurate and standardized MR imaging methodology among centers to better characterize and follow intrapatient changes longitudinally in personalized medicine and to facilitate analysis of large standardized datasets, which could help define predictors of disease evolution and long-term effects of therapies. Several attempts to improve and standardize MR imaging protocols have been published,<sup>4–6</sup> and several national cohorts are being developed (MAGNetic resonance Imaging in Multiple Sclerosis centers in Europe,<sup>7</sup> L'Observatoire Français de la Sclérose en Plaques in France<sup>8</sup>), all sharing the objective of creating a central library documented by using high-quality homoge-

Received June 25, 2014; accepted after revision September 1.

From the Service de NeuroImagerie Diagnostique et Thérapeutique (A.C., M.D., E.d.R., V.D., T.T.) and Pôle de Neurosciences Cliniques (A.R., J.C.O., B.B.), Centre Hospitalier Universitaire de Bordeaux, Bordeaux, France; Department of Radiology (M.S.), Stanford University, Stanford, California; and INSERM U862 (A.R., B.B., V.D., T.T.), Neurocentre Magendie, Université de Bordeaux, Bordeaux, France.

This work was supported by the FLI (ANR-II-INBS-0006) and the French Agence Nationale de la Recherche within the context of the Investments for the Future Program, referenced ANR-10-LABX-57 and named TRAIL.

Paper previously presented in part at: Annual Meeting of the International Society for Magnetic Resonance in Medicine and European Society for Magnetic Resonance in Medicine and Biology (eposter 6954), May 10–16, 2014; Milan, Italy; and Annual Meeting of the French Society of MS (Association pour la Recherche contre la Sclérose en Plaques), May 23, 2014; Paris, France.

Please address correspondence to Thomas Tourdias, MD, PhD, Service de Neuroimagerie Diagnostique et Thérapeutique, Hôpital Pellegrin, CHU de Bordeaux, Place Amélie Raba Léon, 33076 Bordeaux cedex, France; e-mail: thomas.tourdias@chu-bordeaux.fr

 Indicates open access to non-subscribers at [www.ajnr.org](http://www.ajnr.org)

<http://dx.doi.org/10.3174/ajnr.A4152>

neous MR imaging examinations with demographic and clinical evaluations.

Despite published imaging recommendations,<sup>4-6</sup> recent technical developments suggest a careful re-examination of imaging methods and parameters. One significant development is the successful implementation of single-slab 3D sequences,<sup>9</sup> which have become more commonplace with stronger field strengths (3T), better gradients, and improved receiver coil arrays. For example, the single-slab version of the 3D-T2-FLAIR has been shown to be better than conventional 2D-T2-FLAIR in terms of contrast-to-noise ratio, lesion detection, and homogeneity of CSF suppression.<sup>10-12</sup> Due to its higher sensitivity for lesion detection, 3D-T2-FLAIR is increasingly being used in MS and it also improves comparison across time points through easier registration of images to be displayed within the same geometric frame.<sup>6</sup>

While 3D-T1-weighted imaging sequences such as 3D fast-spoiled gradient recalled (FSPGR) and magnetization-prepared rapid acquisition of gradient echo have been in use for a long time and are widely used in clinical brain imaging,<sup>13</sup> they are not routinely used in MS for visualization of active lesions after gadolinium injection. This practice is likely a result of theoretic<sup>14</sup> and clinical studies<sup>15-17</sup> that demonstrated that 3D gradient recalled-echo (GRE) sequences could miss contrast enhancement compared with “conventional” 2D spin-echo (SE) images. While it is true that there are fundamental differences in the contrast behavior of the GRE and SE techniques,<sup>14</sup> the dogma favoring 2D-SE over 3D-GRE for contrast enhancement of MS lesions comes from early work by using an older generation of imaging hardware and sequences.<sup>15-18</sup> The increased availability of higher SNR 3T imaging systems and the improved contrast effect of gadolinium agents at 3T compared with 1.5T<sup>19-22</sup> suggest a reconsideration of 2D-versus-3D imaging. High-performance imaging hardware and developments in parallel imaging permit whole-brain coverage with thin-section thickness by using 3D-GRE sequences in relatively short scanning times. The multiplanar reformatting capabilities with high SNR and contrast make 3D sequences appealing. In addition, Kakeda et al<sup>23</sup> found significantly more metastases with contrast-enhanced 3D FSPGR than with 2D-SE imaging at 3T, especially small metastases of <3 mm in diameter. A direct comparison of 3D-GRE and 2D-SE T1-weighted sequences to depict active MS lesions after gadolinium injection has not been conducted, to our knowledge.

Consequently, recognizing the need for a standardized optimal detection of MS activity among centers to better guide therapy, we aimed at comparing the detection of gadolinium-enhancing lesions between 3D-GRE and conventional 2D-SE sequences. To achieve this goal, we combined an experimental approach in patients with MS with theoretic models analyzing the contrast-enhancement performance of 3D-GRE versus 2D-SE.

## MATERIALS AND METHODS

### Subjects

Fifty-eight patients with clinically definite MS (48 women and 10 men; mean age, 39.3 years; range, 18–78 years) were prospectively included between March and October 2012. All were scanned when they were admitted to our hospital either to monitor treat-

ment efficacy ( $n = 34$ ) or because of a recent relapse ( $n = 24$ ). Fifty had relapsing-remitting MS, and 8 had secondary-progressive MS. Disease duration ranged from 1 month to 39 years (mean, 10 years), and the median Expanded Disability Status Scale score was 2 (range, 0–8). All patients were already under disease-modifying treatment before MR imaging: Twenty-nine patients were treated with natalizumab; 9, with fingolimod; and the remaining 20 received interferon. Corticosteroids were not administered within 1 month before MR imaging, and even patients presenting with new neurologic symptoms were scanned before steroid administration. Both the patients and their relatives were informed that the patient's data might be used in clinical research studies, and all gave informed consent for their data to be analyzed after anonymization.

### MR Imaging Acquisition

Brain imaging was performed on a whole-body MR imaging system operating at 3T (Discovery MR750w; GE Healthcare, Milwaukee, Wisconsin) equipped with high-performance gradients (maximum slew rate of 200 mT/m/ms and maximum strength of 50 mT/m) and using a 32-channel phased array head coil. The scanning protocol included a T2-FLAIR sequence, a pre-gadolinium 3D T1, and 2 postgadolinium sequences referred to as 2D-SE and 3D-GRE. The gadolinium-containing agent (gadoterate meglumine, Dotarem; Guerbet, Aulnay-sous-Bois, France) was injected manually at 0.2 mL/kg of body weight, and a 5-minute delay was observed before the acquisition of the first postinjection sequence. Because the delay between contrast injection and image acquisition may influence enhancement,<sup>24</sup> the order of the 2D-SE and 3D-GRE was randomly chosen, with half of subjects being scanned with 2D-SE first and the other half, with 3D-GRE first. The following imaging parameters were used after administration of Dotarem—2D-SE refers to an axial T1 spin-echo sequence: 38 sections; thickness = 3 mm; gap = 1 mm; FOV = 22 cm; matrix = 320 × 224; voxel size = 0.7 × 1 × 3 mm<sup>3</sup>; TR/TE = 400/6.8 ms; bandwidth = 50 KHz; echo-train length = 2; refocusing flip angle = 111°; NEX = 2; parallel imaging factor = 1.5; scan time = 2 minutes 16 seconds. The sequence was acquired with flow-compensation gradients. 3D-GRE refers to a single-slab axially acquired T1 FSPGR: 128 sections; thickness = 1.2 mm; no gap; FOV = 24 cm; matrix = 288 × 288; voxel size = 0.8 × 0.8 × 1.2 mm<sup>3</sup>; TR/TE = 7.8/3.2 ms; bandwidth = 31 KHz; refocusing flip angle = 10°; NEX = 1; parallel imaging factor = 2; scan time = 2 minutes 24 seconds.

These parameters were optimized and adjusted for routine clinical imaging, and the matched acquisition times allowed a fair comparison between the 2 sequences.

### Image Analysis

2D-SE and 3D-GRE after gadolinium injection were analyzed randomly and in a blinded fashion, with a minimum interval of 10 days between the 2 readings to avoid any recall bias. The analysis was done by 2 readers, independently, blinded to any clinical information. One reader was a junior radiologist in residency training in radiology with 2 years' experience in MR imaging, including 6 months as a neuroradiology resident (A.C.), and the other was a senior neuroradiologist with >9 years' experience in MR

imaging, especially in neuroimaging (T.T.). Subsequently, a final interpretation was made in consensus, with the addition of a third experienced neuroradiologist (V.D., with >25 years' experience) in case of disagreements.

The readers were asked to count the gadolinium-enhancing lesions and to measure their maximal diameter. The precontrast T2-FLAIR sequence was always available during the interpretation because an enhancing lesion had to be seen on T2 FLAIR and to appear with high signal intensity on postgadolinium T1WI, irrespective of its maximum length or the number of sections in which the lesion was visible. The enhancing lesions were categorized according to their anatomic location in infratentorial, periventricular, juxtacortical, and other deep white matter locations as defined previously.<sup>22</sup> Finally, the pattern of enhancement was also categorized as uniform or ring-like.<sup>5</sup> The 3D-GRE volume could be reformatted in arbitrary planes to assess the presence of lesions, a unique advantage of 3D sequences.

In the subgroup of lesions of >5 mm in diameter that were found to enhance on both the 2D-SE and the 3D-GRE, identical ROIs were placed by 1 reader within the lesion and the adjacent normal-appearing white matter, to compute relative contrast defined as  $(\text{Signal}_{\text{lesion}} - \text{Signal}_{\text{WM}}) / (\text{Signal}_{\text{lesion}} + \text{Signal}_{\text{WM}})$ . This metric was preferred rather than the contrast-to-noise ratio because noise cannot be accurately measured when parallel imaging is used without duplicating the sequence to measure the noise on the image difference.<sup>25</sup>

### Simulations

To understand the theoretic signal and contrast behavior of the sequences used above after gadolinium injection, we performed Matlab (MathWorks, Natick, Massachusetts) simulations of lesion SNR and lesion-WM relative contrast by implementing the signal equation for 2D-SE and 3D-GRE, similar to that of Mugler and Brookeman.<sup>13</sup> We used a T1 value of 1300 ms and a T2 value of 100 ms to define a theoretic MS lesion precontrast at 3T.<sup>26</sup> We used the data of Yu et al<sup>27</sup> to set the relaxivity values of Dotarem at 3T as  $r1 = 5.5 \text{ mmol}^{-1}\text{s}^{-1}$  and  $r2 = 6.25 \text{ mmol}^{-1}\text{s}^{-1}$  and varied the gadolinium concentration values from 0 to 5 mmol/L. We simulated 2 scenarios: 1) The lesion is large and occupies the entire voxel in both the 2D and 3D sequences, and 2) the lesion is small and occupies the entire voxel in 3D but not in 2D sequences (ie, 2D lesion volume < 2D voxel volume and 3D lesion volume = 3D voxel volume). The former is the worst-case scenario, and the latter is more realistic for cases we encountered and the scan parameters we used. Note that the 3D and 2D voxel sizes on the acquired images and used in these simulations were  $0.8 \times 0.8 \times 1.2 \text{ mm}^3$  and  $0.7 \times 1.0 \times 3.0 \text{ mm}^3$ , with 3D voxel volume being ~2.5 times smaller than the 2D voxel volume.

### Statistical Analysis

Nonparametric tests were used because the number of lesions did not follow a Gaussian distribution. Statistical differences in lesion counting were compared patient-wise by using the Wilcoxon signed ranked test for matched pairs. Differences were first tested between 3D-GRE and 2D-SE for the junior and the senior radiol-

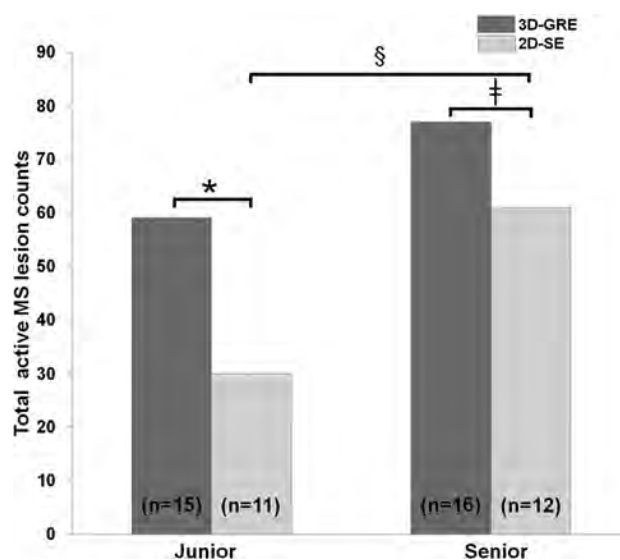


**FIG 1.** Total count of gadolinium-enhancing lesions on 3D-GRE (dark gray) and 2D-SE (light gray) is plotted for the junior and the senior readers. The data in brackets are the number of patients with at least 1 gadolinium-enhancing lesion detected on 3D-GRE (dark gray) or 2D-SE (light gray). The asterisk, double dagger, and section sign indicate corrected *P* values of .021, .017, and .044, respectively, obtained by the Wilcoxon test for matched pairs.

ogists and then between readers for the 3D-GRE and 2D-SE by using Bonferroni corrections to adjust for multiple (4 pair-wise) comparisons. The interreader agreement between the junior and the senior readers with respect to the number of gadolinium-enhancing lesions detected on 3D-GRE and 2D-SE was assessed by calculating the Cohen  $\kappa$  test. Finally, differences in the proportions of gadolinium-enhancing lesions detected with 3D-GRE versus 2D-SE in terms of location, pattern of enhancement, and lesion size were compared with the McNemar test for paired data, while relative contrast values of gadolinium-enhancing lesions detected with 3D-GRE versus 2D-SE were compared with the Wilcoxon signed ranked test. Statistical analyses were performed by using R statistical computing software, Version 3.0.0 (<http://www.r-project.org>). A corrected *P* value  $\leq .05$  was statistically significant.

## RESULTS

### In Vivo Study in Patients

Both the junior and the senior readers consistently reported more gadolinium-enhancing lesions on 3D-GRE compared with 2D-SE (Fig 1). The junior radiologist reported 59 enhancing lesions in 15 patients on 3D-GRE, which was 96% more compared with 2D-SE (30 lesions in 11 patients), while the senior radiologist reported 77 enhancing lesions in 16 patients on 3D-GRE, which was 26% more compared with 2D-SE (61 lesions in 12 patients). For the junior and the senior readers, 4 patients would have been missed as "active" when using only 2D-SE. Patient-wise analysis showed that these differences were statistically significant, with a higher number of patients with more enhancing lesions on 3D-GRE compared with 2D-SE both for the junior and senior radiologists ( $P = .021$  and  $P = .017$ , respectively). All lesions counted on 2D-SE were also seen on 3D-GRE for both readers; thus, 29 and 16

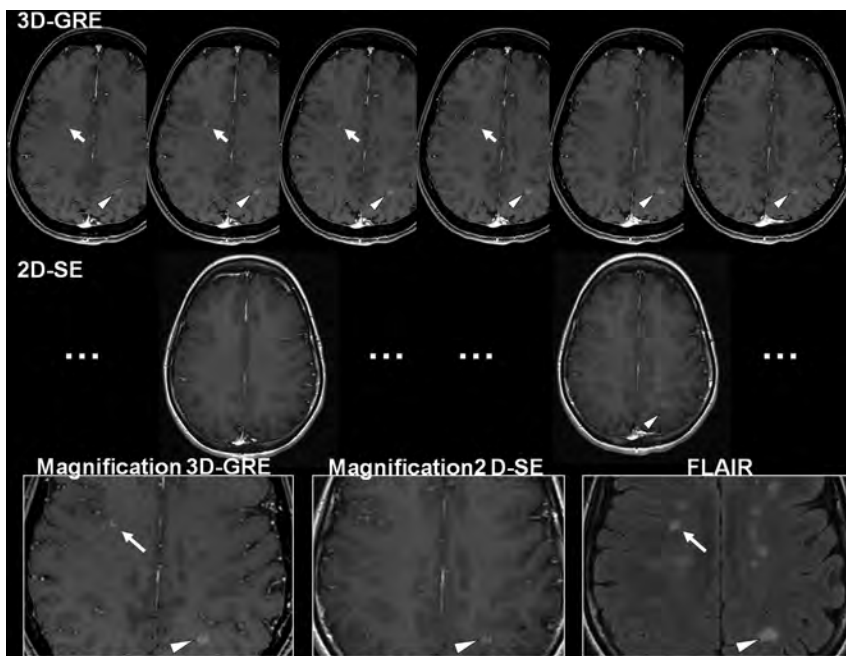


**FIG 2.** Illustrative example of a small right juxtacortical lesion (*arrow*) that was scored as gadolinium-enhancing by the 2 readers on 3D-GRE, being visible on 4 consecutive sections, while it was fully invisible even retrospectively on 2D-SE. The contralateral larger lesion (*arrowhead*) was counted as enhancing on both 3D-GRE and the 2D-SE. In this case, 2D-SE was acquired before 3D-GRE.

lesions for the junior and the senior readers, respectively, were supplementary lesions reported on 3D-GRE only.

The senior reader had a significantly better lesion-detection rate compared with the junior reader on 2D-SE ( $P = .044$ ), while the difference did not reach statistical significance on 3D-GRE ( $P = .078$ ). In line with this observation, the agreement between the 2 readers was better for the 3D-GRE ( $\kappa = 0.65$ , indicating good agreement; 95% confidence interval,  $0.50 < \text{intraclass correlation coefficient} < 0.79$ ) than for the 2D-SE ( $\kappa = 0.51$ , indicating fair agreement; 95% confidence interval,  $0.36 < \text{intraclass correlation coefficient} < 0.64$ ).

To determine which factors could contribute to the higher rate of gadolinium-enhancing lesions detected on the 3D-GRE compared with the 2D-SE, we compared the features of gadolinium-enhancing lesions detected by 3D-GRE and 2D-SE for qualitative and quantitative differences by using the final consensual interpretation.

Qualitatively, the additional gadolinium-enhancing lesions seen on 3D-GRE were sometimes totally invisible on 2D-SE ( $n = 11$ ; Fig 2 for an illustrative example) and sometimes were not scored on the 2D-SE in the first reading while retrospectively detected during the final consensual side-by-side comparison ( $n = 5$ ). Such misdiagnoses on 2D-SE were attributed to difficulty associated with pulsation artifacts in the venous sinus that were less dominant on 3D-GRE (Fig 3) or to confusion with enhancing cortical vessels on 2D-SE. Vessel distinction was not problematic on 3D-GRE due to decreased partial volume effects and 3D reformats that allowed scrolling through images in 3D to distinguish linear vascular structures present in multiple planes from enhancing MS lesions.

Quantitatively, 3D-GRE showed significantly more small lesions ( $< 5$  mm) than 2D-SE in patient-wise analysis ( $P = .04$ ), while there was no difference for larger lesions ( $> 5$  mm). All the

other features were similar for gadolinium-enhancing lesions seen on 2D-SE or 3D-GRE. Specifically, there was no confounding effect induced by the delay of acquisition after the injection<sup>24</sup> because exactly 50% of patients with enhancing lesions were scanned with 3D-GRE first and the other 50%, with 2D-SE first. There was a trend, though not significant, for a higher detection on 3D-GRE, even in the subgroup explored with 3D first ( $n = 46$  versus  $n = 31$ ). Furthermore, the distribution of gadolinium-enhancing lesions was identical between 3D-GRE and 2D-SE in terms of location (for 3D-GRE and 2D-SE, respectively: 20.8% and 21.3% in periventricular; 39% and 42.6% in deep WM; 28.6% and 27.8% in juxtacortical; and 11.6% and 8.3% in infratentorial locations) and pattern of enhancement (for 3D-GRE and 2D-SE, respectively: 56% and 47% with homogeneous enhancement; 44% and 53% with ringlike enhancement). Finally, measurement of the gadolinium-enhancing lesions large enough to avoid any difficulty with region-of-interest placement (diameter of  $> 5$  mm) and seen

with both 3D-GRE and 2D-SE ( $n = 15$  lesions) showed similar relative contrast between gadolinium-enhancing lesions and the adjacent white matter (contrast =  $0.16 \pm 0.08$  on 2D-SE versus  $0.15 \pm 0.07$  on 3D-GRE,  $P = \text{not significant}$ ).

### Simulations and Theoretic Models

Figure 4 summarizes the results of theoretic simulations of SNR and contrast behavior for the 2D and 3D sequences by using the scan parameters in the actual imaging experiments. For a simulated MS lesion occupying the whole voxel on 2D-SE and 3D-GRE, the lesion-SNR and the lesion-to-white matter contrast as a function of the gadolinium concentration within this lesion were close. The 2D-SE still provided slightly better performance for lesions accumulating a small amount of gadolinium (low gadolinium concentration), but even in this situation, there was not a major drop in SNR and contrast on 3D-GRE, despite a voxel size  $> 2.5$  times smaller than that on 2D-SE. If we consider small lesions that occupy the entire 3D-GRE voxel but only a portion of the 2D-SE voxel, the simulations predict a significant decrease in lesion SNR and lesion-to-white matter contrast on 2D-SE (solid red), which was roughly in agreement with our experimental results. While the true gadolinium concentration in vivo in an MS lesion is unknown, some authors have estimated that the typical gadolinium dose of 0.2 mL/Kg of body weight leads to a target tissue concentration of  $\geq 0.5$  mmol/L.<sup>28</sup> At this gadolinium concentration, the models predicted that the SNR of a large lesion on 3D-GRE was decreased by 9.5% compared with 2D-SE but was increased by 46% for a small lesion. Similarly, lesion-WM contrast on 3D-GRE was decreased by 16% compared with 2D-SE for a large lesion but was increased by 45% for a small lesion.

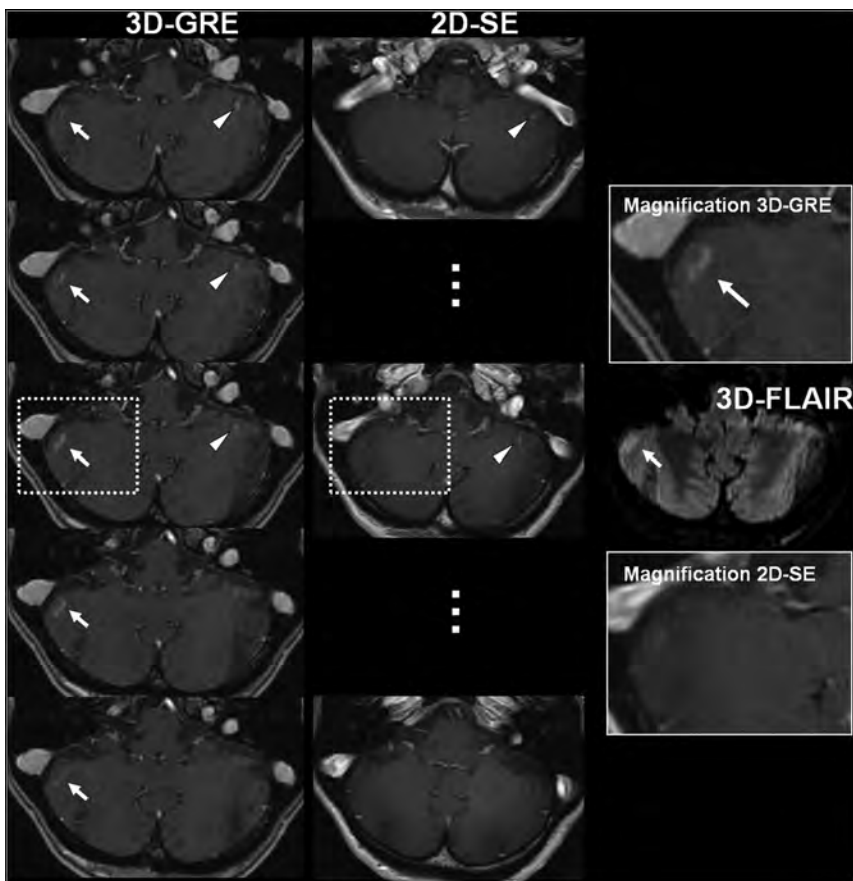


**FIG 3.** Illustrative example of a right cerebellar lesion (arrow) that was scored as gadolinium-enhancing by the 2 readers on the 3D-GRE but not on 2D-SE during the independent blinded reading sessions. Retrospectively, subtle gadolinium enhancement can also be seen on 2D-SE but in a single section (as opposed to 5 sections on 3D-GRE), where it could easily be misdiagnosed as ghosting artifacts induced by the adjacent sinus. The contralateral lesion (arrowhead) was counted as gadolinium-enhancing on both 3D-GRE and the 2D-SE. In this case, 2D-SE was acquired before 3D-GRE.

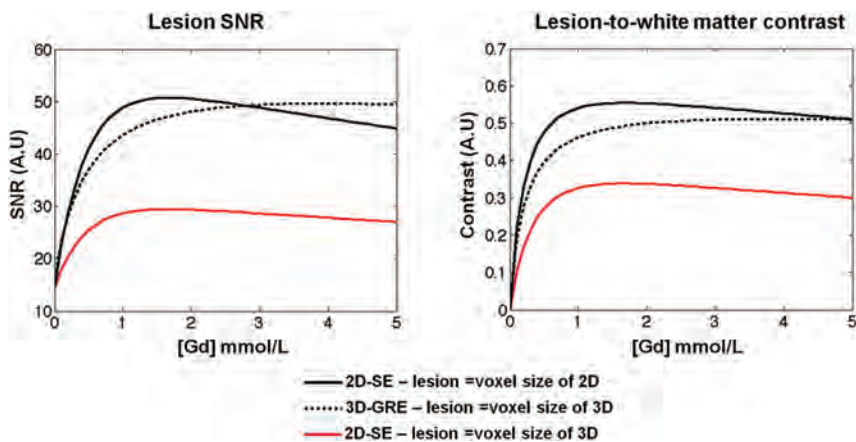


**FIG 4.** Plots of lesion SNR and lesion-to-white matter relative contrast (same definition as that for in vivo experiments (ie,  $[S_{\text{lesion}} - S_{\text{WM}}]/[S_{\text{lesion}} + S_{\text{WM}}]$ ) as a function of the concentration of gadolinium within theoretic MS lesions assumed to fulfill a whole-voxel size in 2D-SE (dark solid line) and 3D-GRE (dark dotted line). If a lesion the size of the 3D voxel is simulated, the dark dotted line still shows the lesion SNR and lesion-to-white matter contrast on 3D-GRE but the 2D-SE shows a far lower signal and contrast (red solid line).

## DISCUSSION

We found that the 3D-GRE sequence after injection of gadolinium in patients with MS detected more enhancing lesions and more patients with enhancing lesions than the standard 2D-SE

sequence, which failed to detect some active lesions. This result is in contrast to earlier ones showing better sensitivity of the 2D SE sequence to contrast enhancement<sup>15,17</sup> and suggests the use of a 3D-GRE-type sequence after gadolinium injection for imaging patients with MS to improve the quality and consistency of routine scanning.

Currently, gadolinium has a pivotal role in MS to assess the radiologic disease activity,<sup>1</sup> which is used in turn for diagnosis,<sup>29</sup> guiding therapeutic strategies,<sup>2,3,30</sup> and as a surrogate marker to evaluate treatment efficacy in clinical trials.<sup>31</sup> After a first clinical event suggestive of MS (clinically isolated syndrome), detection of a single gadolinium-enhancing lesion can argue for “dissemination in time,”<sup>32</sup> which could allow fulfilling diagnostic criteria of MS, which, in turn, could accelerate early therapy. At later stages, a single gadolinium-enhancing lesion can provide a strong argument to optimize therapy by identifying an aggressive course or a suboptimal treatment response at follow-up, both requiring escalation of therapy.<sup>3,30</sup> Any additional sign of activity depicted with 3D-GRE could therefore have a strong impact in clinical practice. Whether the additional sensitivity that we are reporting here translates to such clinical relevance remains a crucial question. The current study could be viewed as the first step to be followed up with larger studies on homogeneous populations to ascertain whether the 3D-GRE could really lead to an earlier diagnosis or have any therapeutic consequences.

While earlier studies reported that contrast enhancement might be less conspicuous on GRE images compared with SE,<sup>15-17</sup> those studies were performed on older scanners. We revisited this possibility, keeping in mind the improvements in scanner hardware and pulse sequences. The higher field strength at 3T affects the relaxation time of both enhanced and nonenhanced tissues, but disproportionately, with a greater relative T1 shortening effect after gadolinium at 3T than at lower field strengths.<sup>21</sup> The linear increase of signal-to-noise ratio with the field strength is another factor that might

improve the quality of higher resolution images such as 3D-GRE and, in turn, the conspicuity of small lesions. The higher field strength also enhances parallel imaging performance by reducing

noise enhancement in reconstruction,<sup>33</sup> which can be further improved by the 32-channel coil. Altogether, the fundamental differences between the contrast behaviors of the SE and GRE techniques reported earlier<sup>14</sup> might not necessarily result in the inferiority of GRE, and the higher spatial resolution of 3D-GRE could even overtake SE for active lesion detection. In our study, the thinner section thickness and reduced partial volume averaging seem to be the main factors associated with 3D-GRE performance regarding the identical experimental values of relative contrast but the significantly higher rate of small lesions of <5 mm on 3D-GRE. Some of the lesions were completely invisible on 2D-SE, even after retrospective reading. In our experimental design, the readers could not be blinded to the sequence type (2D-SE versus 3D-GRE) because it is easily recognizable, and that factor could have potentially biased the results of the reading. Nevertheless, the simulation results, which are consistent with the in vivo data, strengthen our experimental findings. From these simulations, in line with the literature,<sup>14</sup> 2D-SE is expected to provide slightly higher SNR and contrast if the amount of gadolinium is low and the lesion occupies the whole voxel. Nevertheless, no lesions seen on 2D-SE were missed by 3D-GRE. With the parameters of the sequences routinely used in clinical imaging at 3T and assuming a different lesion/volume contribution, which is the case for small lesions fully captured on the 3D voxel but only partly on the 2D voxel, the simulations predict that the SNR and the contrast of an enhancing lesion will be significantly better by using 3D-GRE than 2D-SE.

Moving to 3D datasets for postgadolinium imaging in patients with MS could offer other advantages in addition to its higher sensitivity to enhancing lesions. Such images seem easier to read on the basis of our junior and senior readers' results, with probably less training required to distinguish noise, artifacts, anatomic variants, and true lesions. For example, the pulsatile flow artifacts seen on 2D-SE, even if not fully absent, were reduced on 3D-GRE because of the shorter TEs used in 3D-GRE. Furthermore, with 3D being more amenable to image registration, the 3D images could be easily displayed in a fixed-registration framework, facilitating longitudinal follow-up and standardization. Finally, because noncontrast 3D-GRE is becoming more frequently used in MS to monitor atrophy,<sup>6</sup> it makes sense to use the same sequence after contrast injection for an accurate pre/post comparison.

This study has limitations from the limited number of active lesions, which nevertheless corresponds to the classic recruitment of patients with MS, who are more often controlled by therapy. Such a study also has an intrinsic limitation from the absence of a valid reference standard (histopathologic confirmation) to define which lesions are truly active or inactive. Therefore, we did not compute true sensitivity and specificity, but we compared absolute numbers of lesions detected with each sequence, considering each lesion is truly active, because misdiagnoses can be reasonably excluded during the final consensual interpretation with expert readers. Furthermore, the theoretic approach provides additional evidence to support our experimental findings, even in the absence of a valid criterion standard. Last, we did not use the recently developed class of 3D-TSE sequences, which could combine the advantage of the SE and the 3D acquisitions while using variable flip angles to optimize contrast and reduce the specific

absorption rate.<sup>34,35</sup> While these sequences are promising,<sup>34</sup> they are still less widely available compared with the 3D-GRE we used here, availability being important for standardization of MS imaging protocols among a large number of centers with different vendors. These 3D-TSE sequences are also longer than the 3D-GRE-based T1 and may have more motion artifacts due to subject motion and blurring due to the long echo-trains.<sup>36</sup> 3D-GRE T1 imaging is thus an easy start for improving the MS protocol for clinical routine or research purposes after gadolinium injection.

## CONCLUSIONS

In summary, we have demonstrated that the contrast-enhanced 3D T1 FSPGR sequence can detect significantly more active demyelinating lesions than the conventional axial T1 SE sequence at 3T in patients with MS. We suggest reconsidering a 3D sequence post-gadolinium injection, which can be easily standardized among centers, instead of 2D-SE, to improve routine scanning for personalized medicine and also clinical research studies.

## ACKNOWLEDGMENTS

We thank Alice Doreille for her implication in this MS imaging study.

Disclosures: Monojkumar Saranathan—UNRELATED: Other: research support from GE Healthcare.\* Aurelie Ruet—UNRELATED: Board Membership: Biogen Idec; Consultancy: Teva; Travel/Accommodations/Meeting Expenses Unrelated to Activities Listed: Biogen Idec, Novartis; OTHER RELATIONSHIPS: I am a recipient of a European Committee for Treatment and Research In Multiple Sclerosis fellowship research grant. Bruno Brochet—UNRELATED: Board Membership: Biogen Idec, Teva; Grants/Grants Pending: Teva, Merck Serono, Bayer, Caridian; Payment for Lectures (including service on Speakers Bureaus): Novartis, Teva; Payment for Development of Educational Presentations: Novartis, Genzyme; Travel/Accommodations/Meeting Expenses Unrelated to Activities Listed: Novartis, Teva. \*Money paid to the institution.

## REFERENCES

1. Filippi M, Rocca MA. **MR imaging of multiple sclerosis.** *Radiology* 2011;259:659–81
2. Río J, Comabella M, Montalban X. **Predicting responders to therapies for multiple sclerosis.** *Nat Rev Neurol* 2009;5:553–60
3. Freedman MS, Selchen D, Arnold DL, et al. **Treatment optimization in MS: Canadian MS Working Group updated recommendations.** *Can J Neurol Sci* 2013;40:307–23
4. Simon JH, Li D, Traboulsee A, et al. **Standardized MR imaging protocol for multiple sclerosis: Consortium of MS Centers consensus guidelines.** *AJNR Am J Neuroradiol* 2006;27:455–61
5. Lövblad KO, Anzalone N, Dorfler A, et al. **MR imaging in multiple sclerosis: review and recommendations for current practice.** *AJNR Am J Neuroradiol* 2010;31:983–89
6. Vrenken H, Jenkinson M, Horsfield MA, et al. **Recommendations to improve imaging and analysis of brain lesion load and atrophy in longitudinal studies of multiple sclerosis.** *J Neurol* 2013;260:2458–71
7. MAGNetic resonance In Multiple Sclerosis. MAGNIMS online. <http://www.magnims.eu/>. Accessed April 15, 2014
8. L'Observatoire Français de la Sclérose en Plaques. <http://www.edmus.org/en/proj/observatoire.html>. Accessed April 15, 2014
9. Barkhof F, Pouwels PJ, Wattjes MP. **The Holy Grail in diagnostic neuroradiology: 3T or 3D?** *Eur Radiol* 2011;21:449–56
10. Moraal B, Roosendaal SD, Pouwels PJ, et al. **Multi-contrast, isotropic, single-slab 3D MR imaging in multiple sclerosis.** *Eur Radiol* 2008;18:2311–20
11. Bink A, Schmitt M, Gaa J, et al. **Detection of lesions in multiple**

- sclerosis by 2D FLAIR and single-slab 3D FLAIR sequences at 3.0 T: initial results. *Eur Radiol* 2006;16:1104–10
12. Naganawa S, Koshikawa T, Nakamura T, et al. Comparison of flow artifacts between 2D-FLAIR and 3D-FLAIR sequences at 3 T. *Eur Radiol* 2004;14:1901–08
  13. Mugler JP 3rd, Brookeman JR. Three-dimensional magnetization-prepared rapid gradient-echo imaging (3D MP RAGE). *Magn Reson Med* 1990;15:152–57
  14. Mugler JP 3rd, Brookeman JR. Theoretical analysis of gadopentetate dimeglumine enhancement in T1-weighted imaging of the brain: comparison of two-dimensional spin-echo and three-dimensional gradient-echo sequences. *J Magn Reson Imaging* 1993;3:761–69
  15. Brant-Zawadzki M, Gillan GD, Nitz WR. MP RAGE: a three-dimensional, T1-weighted, gradient-echo sequence: initial experience in the brain radiology. *Radiology* 1992;182:769–75
  16. Chappell PM, Pelc NJ, Foo TK, et al. Comparison of lesion enhancement on spin-echo and gradient-echo images. *AJNR Am J Neuroradiol* 1994;15:37–44
  17. Blüml S, Schad LR, Scharf J, et al. A comparison of magnetization prepared 3D gradient-echo (MP-RAGE) sequences for imaging of intracranial lesions. *Magn Reson Imaging* 1996;14:329–35
  18. Wenz F, Hess T, Knopp MV, et al. 3D MPRAGE evaluation of lesions in the posterior cranial fossa. *Magn Reson Imaging* 1994;12:553–58
  19. Nöbauer-Huhmann IM, Ba-Ssalamah A, Mlynarik V, et al. Magnetic resonance imaging contrast enhancement of brain tumors at 3 Tesla versus 1.5 Tesla. *Invest Radiol* 2002;37:114–19
  20. Ba-Ssalamah A, Nöbauer-Huhmann IM, Pinker K, et al. Effect of contrast dose and field strength in the magnetic resonance detection of brain metastases. *Invest Radiol* 2003;38:415–22
  21. Trattng S, Pinker K, Ba-Ssalamah A, et al. The optimal use of contrast agents at high field MRI. *Eur Radiol* 2006;16:1280–87
  22. Wattjes MP, Lutterbey GG, Harzheim M, et al. Higher sensitivity in the detection of inflammatory brain lesions in patients with clinically isolated syndromes suggestive of multiple sclerosis using high field MRI: an intraindividual comparison of 1.5 T with 3.0 T. *Eur Radiol* 2006;16:2067–73
  23. Kakeda S, Korogi Y, Hiai Y, et al. Detection of brain metastasis at 3T: comparison among SE, IR-FSE and 3D-GRE sequences. *Eur Radiol* 2007;17:2345–51
  24. Uysal E, Erturk SM, Yildirim H, et al. Sensitivity of immediate and delayed gadolinium-enhanced MRI after injection of 0.5 M and 1.0 M gadolinium chelates for detecting multiple sclerosis lesions. *AJR Am J Roentgenol* 2007;188:697–702
  25. Goerner FL, Clarke GD. Measuring signal-to-noise ratio in partially parallel imaging MRI. *Med Phys* 2011;38:5049–57
  26. Kober T, Granziera C, Ribes D, et al. MP2RAGE multiple sclerosis magnetic resonance imaging at 3 T. *Invest Radiol* 2012;47:346–52
  27. Yu SM, Choi SH, Kim SS, et al. Correlation of the R1 and R2 values of gadolinium-based MRI contrast media with the  $\Delta$ Hounsfield unit of CT contrast media of identical concentration. *Current Applied Physics* 2013;13:857–63
  28. Rinck PA, Muller RN. Field strength and dose dependence of contrast enhancement by gadolinium-based MR contrast agents. *Eur Radiol* 1999;9:998–1004
  29. Polman CH, Reingold SC, Banwell B, et al. Diagnostic criteria for multiple sclerosis: 2010 revisions to the McDonald criteria. *Ann Neurol* 2011;69:292–302
  30. Wiendl H, Toyka KV, Rieckmann P, et al. Basic and escalating immunomodulatory treatments in multiple sclerosis: current therapeutic recommendations. *J Neurol* 2008;255:1449–63
  31. Tourdias T, Dousset V. Neuroinflammatory imaging biomarkers: relevance to multiple sclerosis and its therapy. *Neurotherapeutics* 2013;10:111–23
  32. Rovira A, Swanton J, Tintore M, et al. A single, early magnetic resonance imaging study in the diagnosis of multiple sclerosis. *Arch Neurol* 2009;66:587–92
  33. Wiesinger F, Van de Moortele PF, Adriany G, et al. Parallel imaging performance as a function of field strength: an experimental investigation using electrodynamic scaling. *Magn Reson Med* 2004;52:953–64
  34. Hodel J, Outteryck O, Ryo E, et al. Accuracy of postcontrast 3D turbo spin-echo MR sequence for the detection of enhanced inflammatory lesions in patients with multiple sclerosis. *AJNR Am J Neuroradiol* 2014;35:519–23
  35. Saranathan M, Tourdias T, Kerr AB, et al. Optimization of magnetization-prepared 3-dimensional fluid attenuated inversion recovery imaging for lesion detection at 7 T. *Invest Radiol* 2014;49:290–98
  36. Mugler JP 3rd. Optimized three-dimensional fast-spin-echo MRI. *J Magn Reson Imaging* 2014;39:745–67

# Pretreatment Diagnosis of Suprasellar Papillary Craniopharyngioma and Germ Cell Tumors of Adult Patients

H.-J. Lee, C.-C. Wu, H.-M. Wu, S.-C. Hung, J.-F. Lirng, C.-B. Luo, F.-C. Chang, and W.-Y. Guo



## ABSTRACT

**BACKGROUND AND PURPOSE:** Suprasellar papillary craniopharyngiomas and germ cell tumors in adults share some clinical and imaging similarities but have different therapeutic strategies and outcomes. This study aimed to evaluate the pretreatment diagnosis of these 2 tumors to improve the therapeutic outcome.

**MATERIALS AND METHODS:** We retrospectively enrolled 18 adults with papillary craniopharyngiomas and 17 with germ cell tumors. The MR imaging findings were evaluated, including signal change and anatomic extension. The medical records were reviewed to collect clinical findings, management, and outcomes.

**RESULTS:** The clinical findings of papillary craniopharyngiomas versus germ cell tumors were as follows: age:  $46 \pm 13.9$  years versus  $23 \pm 7.1$  years ( $P < .0001$ ); diabetes insipidus: 2/18 (11%) versus 11/17 (65%) ( $P = .001$ ); recurrence 13/16 (81%) versus 4/17 (24%) ( $P = .0031$ ). The MR imaging findings of papillary craniopharyngiomas versus germ cell tumors were as follows—pituitary stalk thickening:  $1.6 \pm 0.4$  mm versus  $5.4 \pm 4.2$  mm ( $P < .0001$ ); vertical infundibular extension: 1/18 (6%) versus 16/17 (94%) ( $P < .0001$ ); sagittal spheric shape: 17/18 (94%) versus 1/17 (6%) ( $P < .0001$ ); diffusion restriction: 1/17 (6%) versus 8/12 (67%) ( $P = .0009$ ).

**CONCLUSIONS:** Younger age, diabetes insipidus, MR imaging characteristics of restricted diffusion, and vertical infundibular extension favor the diagnosis of germ cell tumors. Spheric shape without infundibular infiltration provides clues to papillary craniopharyngiomas, which originate from the pars tuberalis and are located outside the third ventricle. We suggest that suprasellar germ cell tumor is possibly an intraventricular lesion. Appropriate treatment planning can be initiated according to the diagnosis and anatomic location.

**ABBREVIATIONS:** GCT = germ cell tumor; PCP = papillary craniopharyngioma

Except for pituitary macroadenoma, suprasellar tumors are infrequent in adult patients. Some of these suprasellar tumors have specific clinical and imaging features that make them straightforward to diagnose and subsequently manage. These classic features include a dural tail appearance in meningioma; young age; cysts and calcifications in adamantinomatous cranio-

pharyngioma; homogeneous infiltrating mass of hypothalamic/optic pathway gliomas; a midline enhancing lesion in germ cell tumor (GCT); specific locations with signal similar to those of gray matter in hamartoma; and bright signals on DWI in epidermoids.<sup>1-3</sup> However, some suprasellar tumors in adults can mimic each other in some clinical and imaging features, making pretreatment planning difficult.

Papillary craniopharyngiomas (PCPs) and GCTs are 2 unusual suprasellar tumors in adults, with similar clinical and imaging findings in some aspects. Clinically, PCPs and GCTs mostly occur in young adults with visual impairment or pituitary axis dysfunction or diabetes insipidus. They commonly present as predominantly solid or mixed cysts and solid suprasellar lesions with contrast enhancement on MR imaging. However, the treatment and outcomes of both tumor types are quite different.<sup>2,4,5</sup> Surgical resection not only is the main treatment of PCPs but also remarkably affects the outcome.<sup>6</sup> By contrast, complete surgical resection is usually unnecessary in patients with germinoma. This radiosensitive tumor can be well-controlled by radiation therapy alone or

Received July 3, 2014; accepted after revision August 17.

From the Department of Radiology, Taipei Veterans General Hospital, Taipei, Taiwan; and School of Medicine, National Yang-Ming University, Taipei, Taiwan.

This work was supported in part by grants from Taipei Veterans General Hospital (V103C-063, CI-103-3) and the Ministry of Science and Technology (NSC 102-2314-B-075-068).

Paper previously presented in part at: Annual Meeting of the Japanese Society of Neuroradiology, March 21–23, 2014; Yonago, Japan.

Please address correspondence to Feng-Chi Chang, MD, Department of Radiology, Taipei Veterans General Hospital, 201 Shih-Pai Rd, Sec 2, Taipei, Taiwan; e-mail: fcchang374@gmail.com

Indicates open access to non-subscribers at www.ajnr.org

Indicates article with supplemental on-line table.

<http://dx.doi.org/10.3174/ajnr.A4142>

**Table 1: Analysis of clinical symptoms and outcomes of suprasellar papillary craniopharyngioma and suprasellar germ cell tumors**

Variables	PCP (n = 18)	GCT (n = 17)	OR	95% CI	P Value <sup>a</sup>
Age (yr)	46 ± 13.9 (21–70)	23 ± 7.1 (16–43)			<.0001
Sex (male:female)	13:5	13:4	1.3	.27–5.7	.7738
Symptoms					
Visual field deficits	12 (67%)	6 (35%)	.27	.07–1.1	.0634
Hypopituitarism <sup>b</sup>	12 (71%)	12 (75%)	1.3	.27–5.8	.7761
Hyperprolactinemia <sup>c</sup>	14 (93%)	11 (67%)	.16	.02–1.5	.0834
Hypothalamic dysfunction, including diabetes insipidus	2 (11%)	11 (65%)	15	2.5–87	.0010
Initial management					.0303
Total resection	7 (39%)	3 (18%)	1.0	–	
Subtotal resection	6 (33%)	1 (6%)	.39	.03–4.8	
Partial resection or biopsy	3 (17%)	6 (35%)	4.7	.67–32	
Radiation or radiosurgery	2 (11%)	7 (41%)	8.2	1.03–65	
Outcome					
Recurrence <sup>d</sup>	13 (81%)	4 (24%)	.10	.02–.50	.0031
Survival (mean)	39.6 ± 32.02 (2–118)	52.4 ± 40.32 (13–123)			.3815

<sup>a</sup> P = statistical significance as calculated by the log-rank test.

<sup>b</sup> In the PCP group, n = 17; in the GCT group, n = 16.

<sup>c</sup> In the PCP group, n = 15; in the GCT group, n = 16.

<sup>d</sup> In the PCP group, n = 16; in the GCT group, n = 17.

combined with chemotherapy, even without a tissue diagnosis.<sup>7</sup> The preoperative diagnosis of these 2 unusual suprasellar tumors in adults facilitates appropriate treatment planning and avoids associated surgical morbidity. We presumed that the distinct embryology and pathogenesis of the 2 tumors develop unique clinical and MR imaging characteristics. This study was designed to evaluate retrospectively the clinical and MR imaging findings of suprasellar papillary craniopharyngioma and germ cell tumors in adult patients, to obtain a pretreatment diagnosis.

## MATERIALS AND METHODS

### Study Population

This retrospective study was reviewed by an institutional review board. Between 2003 and 2013, 58 patients with craniopharyngioma and 17 patients with germ cell tumors who were older than 16 years of age were diagnosed at our institution. Of the 58 pathologically diagnosed craniopharyngiomas, 21 adamantinomatous craniopharyngiomas and 12 in patients without mention of specific subtypes or mixed type of adamantinomatous and papillary components were excluded. Seven patients with PCPs with incomplete preoperative MR imaging studies were also excluded. We excluded the patients with adamantinomatous craniopharyngiomas because they can usually be diagnosed by their classic imaging findings.<sup>8</sup> Thus, 18 patients with PCP were included in the present study. Among the 17 consecutive patients with a GCT at a suprasellar location, 8 were pathologically diagnosed with a germinoma; 1, with an immature teratoma; 1, with a mixed germ cell tumor; and 7 patients with germinoma were diagnosed on the basis of clinical and neuroradiologic features (Table 1).<sup>9</sup> The medical records of both groups were reviewed to collect demographic information, presenting symptoms, laboratory data, management information, and outcome information.

### Clinical Findings

We included the symptoms of visual field defects, hypopituitarism, and hypothalamic dysfunction. Visual field tests were analyzed by ophthalmologic examination. Hypopituitarism included symptoms of orthostatic hypotension, amenorrhea, impotence, or a decreased level of hypothalamic-pituitary axis hormones

(Table 1). Hypothalamic dysfunction included symptoms of diabetes insipidus or weight gain. The level of prolactin,  $\beta$ -human chorionic gonadotropin, and  $\alpha$ -fetoprotein were also assessed.

### MR Imaging Findings

MR images were retrospectively blindly reviewed by 2 certified neuroradiologists (F.-C.C. and H.-J.L.). All quantitative measurements were made by standard tools in the hospital PACS, and qualitative assessments of lesional characters were made on the basis of consensus. We evaluated the MR imaging findings of the 2 suprasellar tumors regarding the location, extent (largest sagittal diameter), components, signal, shape, involvement of the pituitary stalk and pituitary gland, and other associated findings (Online Table). The locations of the tumors were divided into 3 subgroups: those located at the suprasellar space and extending toward the third ventricle; those located at the suprasellar region with sellar extension, causing displacement of the pituitary gland; and those involving the sellar and suprasellar spaces and third ventricle. The size of the tumor was measured as the largest diameter at the midsagittal plane on contrast-enhanced T1WI. If the solid component of the tumor exceeded 50% of the total tumor volume on both sagittal and coronal imaging, the tumor was defined as having a solid predominance and vice versa. The signal intensities of the solid part of the tumors were further compared with those of the gray matter at the adjacent temporal lobe on T1WI, T2WI, and DWI. The signal changes on noncontrast and post-contrast-enhanced T1WI were also evaluated. The patterns of contrast enhancement were further described as enhancement if the solid component showed strong enhancement and marginal enhancement if there was peripheral enhancement along the margin.

The shape of the tumors was evaluated on sagittal imaging. If the lower end of the tumor appeared as a round or blunted shape in the suprasellar region, the tumor was described as spheric (Figs 1A and 2A). If the low end of the tumor extended vertically down to the sellar region, the tumor was described as transfundibular (Figs 3A and 4B).<sup>10</sup> The diameter of the pituitary stalk was measured at the narrowest part on contrast-enhanced sagittal T1WI.

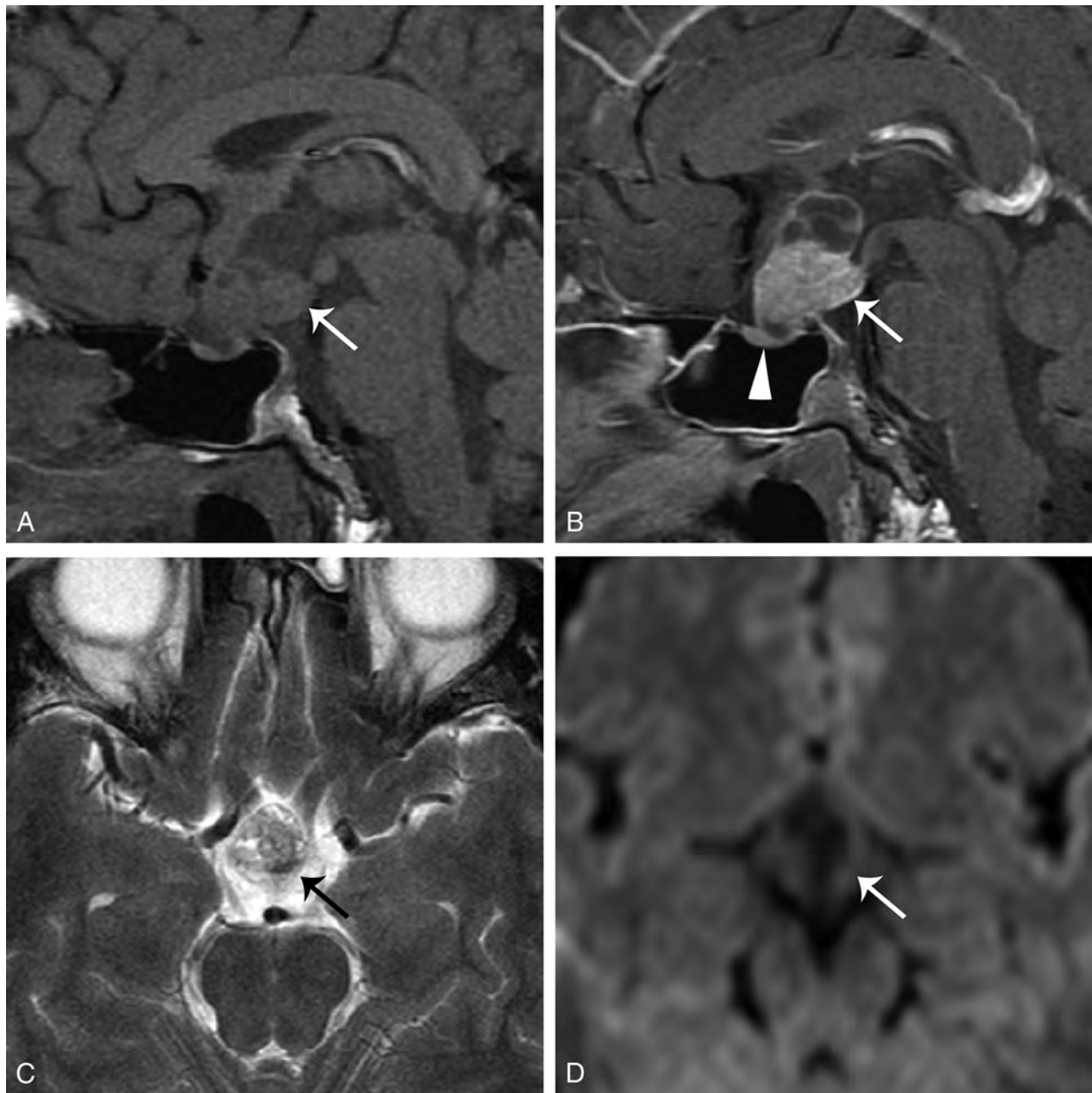


**FIG 1.** A 28-year-old man had bitemporal hemianopsia for several weeks. Surgical resection revealed PCP. *A*, Sagittal T1WI shows a mixed solid and cystic tumor (*arrow*) at the sellar and suprasellar regions. *B*, Contrast-enhanced sagittal T1WI shows strong enhancement at the solid component and its cystic wall (*arrow*). The lower end of the tumor is spherical. The pituitary gland is compressed but intact (*arrowhead*). *C*, Axial T2WI demonstrates that the tumor (*arrow*) has mixed isointense-to-hyperintense signals compared with the adjacent temporal gray matter. *D*, DWI ( $b=800$ ) shows no restricted diffusion in the tumor (*arrow*).

If the diameter of the infundibulum was  $\geq 4$  mm, infundibular thickening was defined.<sup>11</sup> The relationship between the tumor and the pituitary gland was described as infiltrative if there was an indistinct and irregular border between the tumor and the gland on sagittal and coronal imaging (Figs 3 and 4A, -B). When the pituitary gland was compressed but intact, it was described as a compression (Fig 1B). The associated findings of involvement of the optic pathway and hypothalamus and dilation of the ventricles were analyzed (On-line Table).

Except for the 2 patients with GCT who underwent surgical resection, all patients of both groups underwent radiation therapy of the tumor bed or residual tumor and/or the ventricular system.

To check the relationship between suprasellar GCT and the possible origin of the pineal region, we evaluated the interval changes of the pineal gland and suprasellar tumor of both groups. The largest diameter of the pineal gland and/or its associated tumor on contrast-enhanced sagittal T1WI in the initial studies was compared with those in the latest follow-up series, to evaluate the effect of radiation therapy on the pineal gland or its associated tumor (mean,  $36.8 \pm 31.2$  months). If the largest diameter changed  $>25\%$  from the initial one, a significant interval change of volume was defined. The presence of ventricular or subarachnoid tumor seeding was evaluated by contrast-enhanced T1WI.

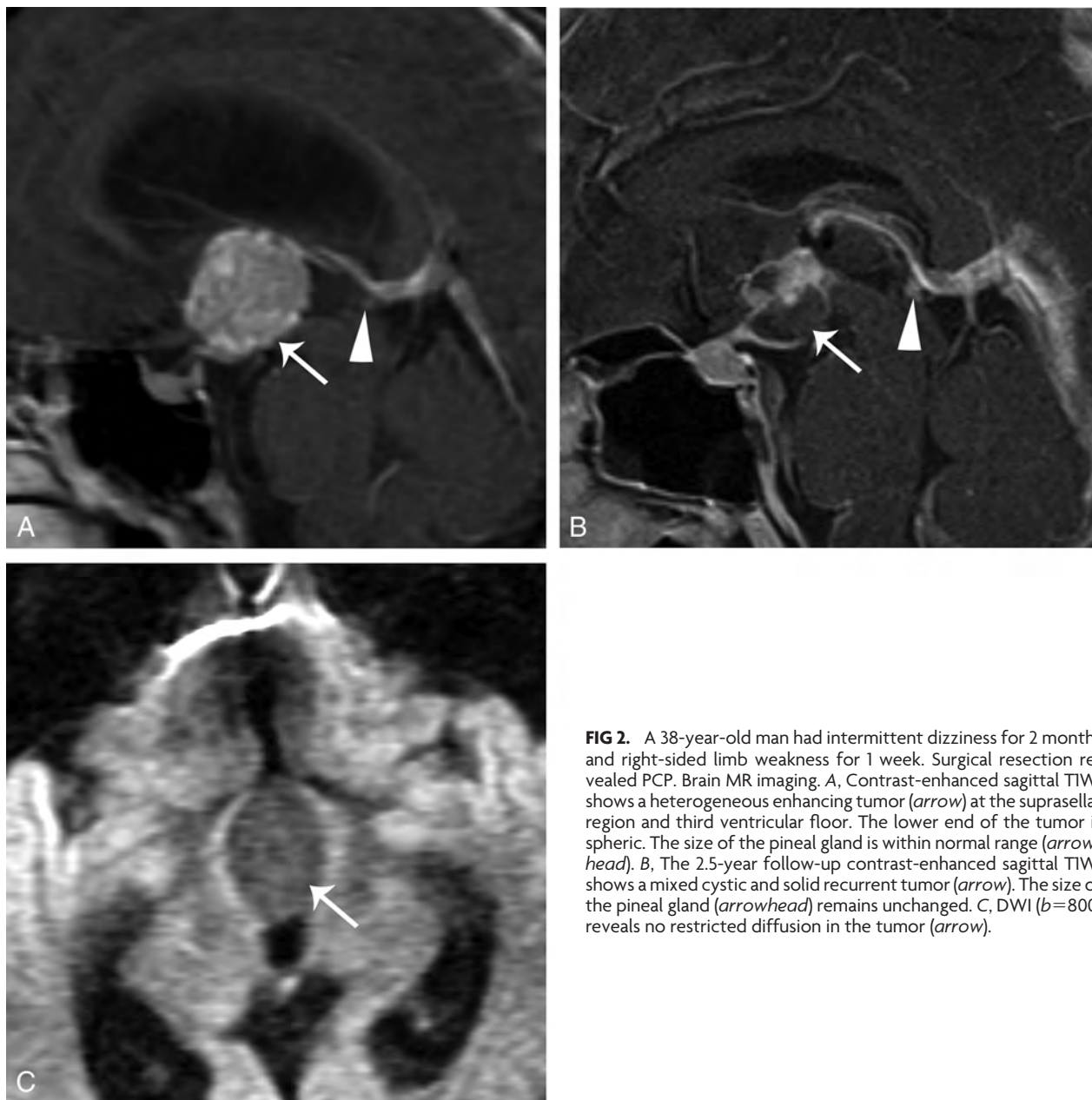


**FIG 2.** A 38-year-old man had intermittent dizziness for 2 months and right-sided limb weakness for 1 week. Surgical resection revealed PCP. Brain MR imaging. *A*, Contrast-enhanced sagittal T1WI shows a heterogeneous enhancing tumor (arrow) at the suprasellar region and third ventricular floor. The lower end of the tumor is spherical. The size of the pineal gland is within normal range (arrowhead). *B*, The 2.5-year follow-up contrast-enhanced sagittal T1WI shows a mixed cystic and solid recurrent tumor (arrow). The size of the pineal gland (arrowhead) remains unchanged. *C*, DWI ( $b=800$ ) reveals no restricted diffusion in the tumor (arrow).

### Management and Outcome

Initial management was determined according to the preoperative diagnosis by the clinical and neuroradiologic findings. The surgical approach included craniotomy or transsphenoidal resection aimed at obtaining tumor removal in all patients with PCP and in 7 with GCT. Postoperative radiation therapy of the residual tumor/tumor bed and/or ventricular system was assigned for both tumor types. Radiation therapy was the initial treatment in 10 patients with GCT when they had a tissue or a clinical diagnosis of germinoma. The initial results of surgical resection were classified as gross total removal, subtotal removal, and partial removal or biopsy of the tumor, which were defined as no tumor left under maximum magnification, residual invaded parenchyma, and persistent macroscopic fragments, respectively.<sup>12</sup> Complications related to the management and any tumor recurrence were recorded to evaluate the outcome. Radiation therapy or gamma

knife radiosurgery was conducted for recurrent tumor. The survival time was also calculated.

### Statistical Analysis

We analyzed the clinical and MR imaging findings of both groups. Demographic features, clinical presentations, management and outcome, and MR imaging findings were examined by using the Fisher exact test. The odds ratios and the accompanying 95% confidence intervals were calculated. For all analyses,  $P < .05$  was statistically significant.

## RESULTS

### Clinical Findings

The demographic and clinical findings of both groups are summarized in Tables 1 and 2. The age of patients with GCT was significantly younger than that in those with PCP ( $P < .0001$ ).

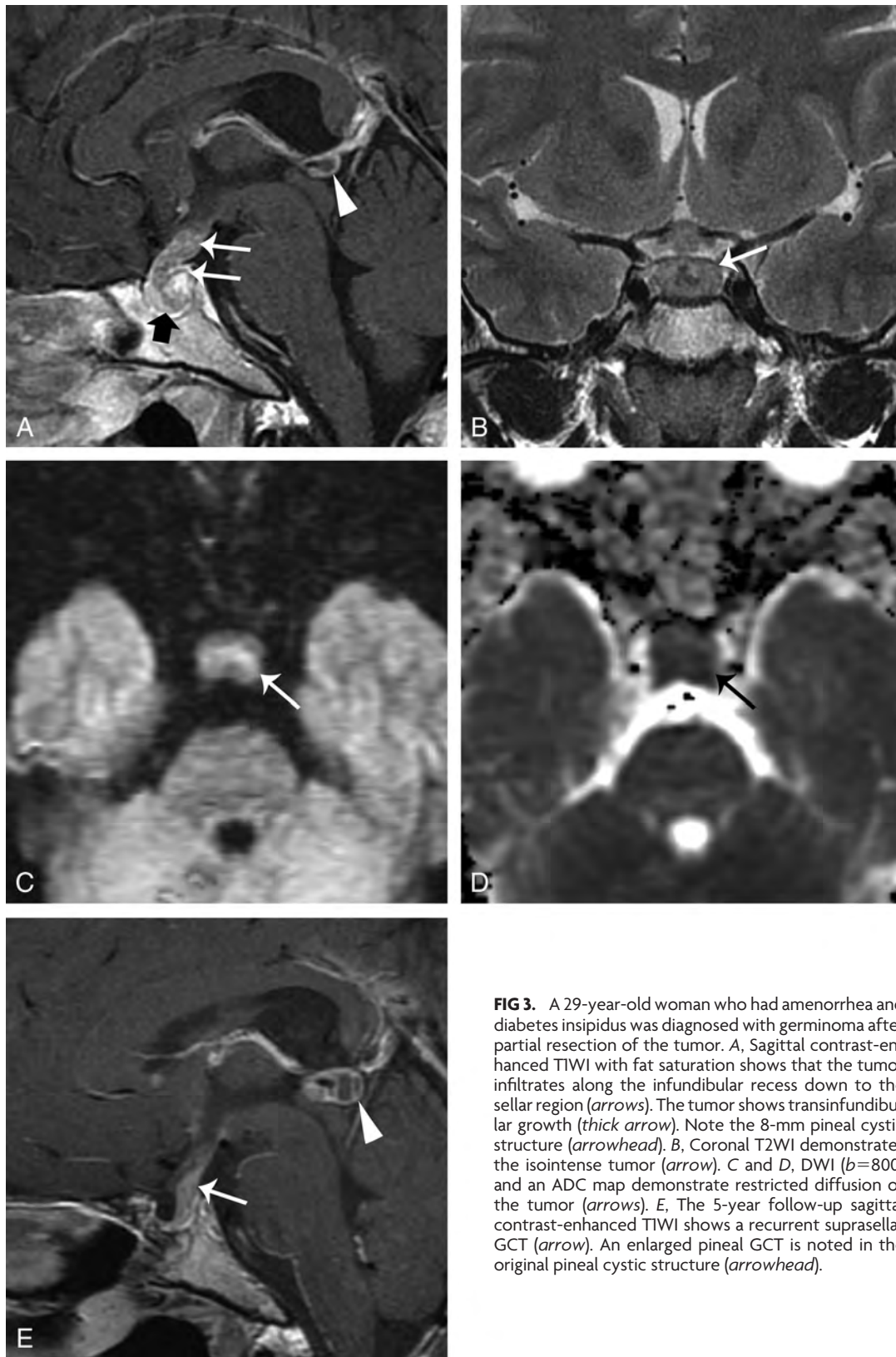


**FIG 3.** A 29-year-old woman who had amenorrhea and diabetes insipidus was diagnosed with germinoma after partial resection of the tumor. *A*, Sagittal contrast-enhanced T1WI with fat saturation shows that the tumor infiltrates along the infundibular recess down to the sellar region (*arrows*). The tumor shows transinfundibular growth (*thick arrow*). Note the 8-mm pineal cystic structure (*arrowhead*). *B*, Coronal T2WI demonstrates the isointense tumor (*arrow*). *C* and *D*, DWI ( $b=800$ ) and an ADC map demonstrate restricted diffusion of the tumor (*arrows*). *E*, The 5-year follow-up sagittal contrast-enhanced T1WI shows a recurrent suprasellar GCT (*arrow*). An enlarged pineal GCT is noted in the original pineal cystic structure (*arrowhead*).

The symptoms related to an impaired visual field and pituitary dysfunction were commonly found in both groups but showed no significant difference. Hypothalamic dysfunction and diabetes insipidus were significantly associated with patients with GCT ( $P = .001$ ; OR, 15; 95% CI, 2.5–87). Besides the 7/17

(41%) patients in the GCT group diagnosed clinically,  $\alpha$ -fetoprotein and  $\beta$ -human chorionic gonadotropin levels were examined in 2/10 (20%) patients of the GCT group and 4/18 (22%) patients of the PCP group before the operation.  $\alpha$ -fetoprotein levels were elevated in 2 patients, including 1 with

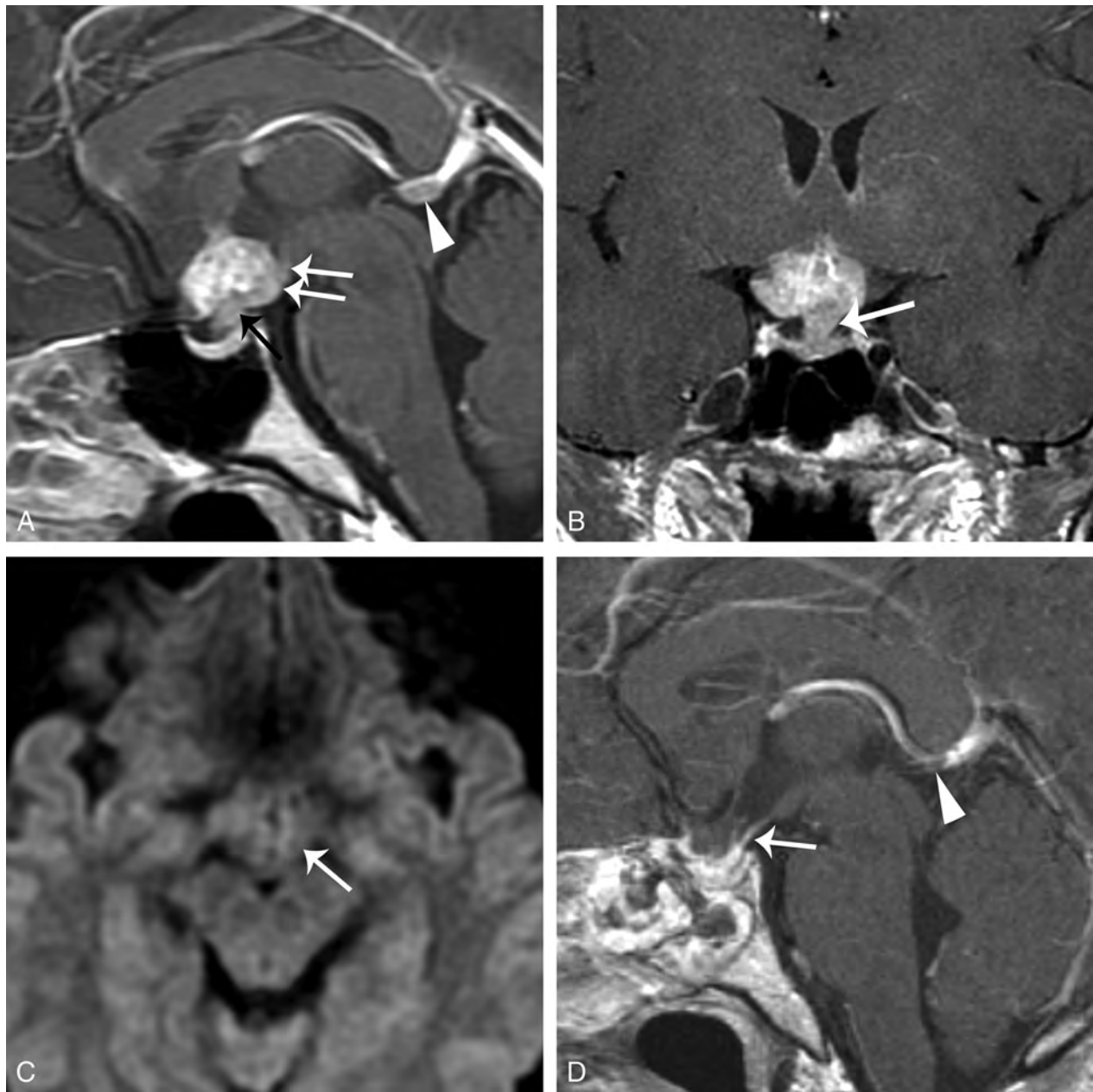


**FIG 4.** A 23-year-old woman had amenorrhea for 2 years and biopsy-proved germinoma. *A*, Sagittal contrast-enhanced T1WI with fat saturation shows a heterogeneous enhancing suprasellar and third ventricular floor tumor (*white arrows*) with infundibular stalk thickening (*black arrow*). The pineal gland is 8 mm in the largest diameter (*arrowhead*). *B*, Coronal contrast-enhanced T1WI shows the growth of the tumor along the infundibular recess (*arrow*) and the indistinct margin between the tumor and pituitary gland. *C*, DWI ( $b=800$ ) demonstrates mildly high signal in the tumor (*arrow*). *D*, The 3-month follow-up sagittal contrast-enhanced T1WI after surgical and radiation treatment shows shrinkage of both the suprasellar (*arrow*) and pineal tumors (*arrowhead*).

mixed germ cell tumor and 1 with immature teratoma;  $\beta$ -human chorionic gonadotropin levels were elevated in 1 patient with immature teratoma and 2 with germinomas.

#### MR Imaging Findings

MR imaging findings of both groups are summarized in the Online Table and Table 2. Both suprasellar tumors could extend to the sellar region and third ventricle. PCPs had a larger size than GCTs at the time of diagnosis, with a mean diameter of 3.18 cm on sagittal images ( $P = .0064$ ). Compared with the predominantly heterogeneous solid characteristics in the GCT groups, PCPs were

mostly well-circumscribed mass lesions with heterogeneous, multicystic components ( $P = .0002$ ; OR, 0.03; 95% CI, 0.003–0.30). The multicystic components of PCPs showed prominent marginal enhancement on contrast-enhanced T1WI compared with the heterogeneous strong enhancement of the solid portion of GCTs ( $P < .0001$ ). Most of the solid parts of both tumors showed isointense signal intensity in the gray matter on T1WI and T2WI, which demonstrated no significant difference ( $P = .2962$  and 0.9616, respectively). On DWI, the solid parts of GCTs revealed higher signal intensity than the adjacent gray matter, and PCPs had lower signal intensity than the gray matter. The signal

**Table 2: Specific clinical findings and MR imaging characteristics favoring papillary craniopharyngiomas or suprasellar germ cell tumors**

	Papillary Craniopharyngioma	Germ Cell Tumor
Clinical findings		
Hypothalamic dysfunction, including diabetes insipidus	—	Yes
MR imaging characteristics		
Component	Cystic predominance	Solid predominance
DWI signals in the solid part	Hypointense	Isointense
Marginal contrast enhancement	Yes	—
Shape	Spheric	Transfundibular
Pituitary stalk	—	Thickening
Tumor seedings	—	Yes
Size change of the pineal gland after radiotherapy	—	Yes
Main management strategy	Surgery	Radiation therapy
Outcomes	Higher recurrence rate	—

**Note:**— indicates the feature was significantly lower or less in the specific tumor group.

intensity was significantly different between both tumor groups ( $P = .0009$ ).

Regarding the shape of the lower part of both tumors on sagittal images, PCPs appeared spheric or blunted in all except 1 patient; additionally, the GCT extended vertically downward along the pituitary stalk in all except 1 patient ( $P < .0001$ ; OR, 272; 95% CI, 16–4724). Infundibular thickening was observed in 13 of 17 GCTs, and the mean diameter of the pituitary stalk was 5.4 mm. Infundibular thickening was not noted in patients with PCPs with a mean value of 1.6 mm ( $P < .0001$ ). Although patients with GCTs involving the pituitary gland were more frequent than those with PCPs, no significant difference was found between the 2 groups ( $P = .1896$ ).

Seeding lesions in the subarachnoid space or ventricle were noted in 8 patients with GCT and in none with PCP ( $P = .0009$ ). Except for 6 patients with PCP, all the other patients of both groups underwent radiation therapy. Thereafter, a significant interval change of the size of the pineal gland was noted in 8 of the 16 patients with GCT (50%), but in none in the patients with PCP ( $P = .0009$ ). These included 7 patients with a reduced size (Fig 4D) and 1 patient with an increased size of the pineal gland (Fig 3E). In both tumor types, some of the optic tract and hypothalamus had edema. However, the PCP group demonstrated more significant compression and displacement of the optic chiasm compared with the GCT group ( $P = .0019$ ; OR, 0.05; 95% CI, 0.01–0.49).

### Management and Outcome

For patients with PCP, the extent of the initial resection was grossly total in 7 patients, subtotal in 6 patients, and partial or only a biopsy in 3 patients. The other 2 patients with PCP underwent radiation therapy initially because the preoperative impression was GCT. They had surgical resection due to poor response to radiation therapy and local recurrence. One underwent a subtotal resection 10 months after initial radiation therapy; the other underwent 3 operations and 1 session of radiosurgery in 10 years. Regarding the treatment outcomes, 2 surgery-related deaths occurred in the PCP group (2/18, 11%). One was caused by intracranial infection 6 days after the surgery; the other patient died of severe extrapontine myelinolysis 1 month after the surgery. Of the other 16 patients in the PCP group, 13 (81%) had residual or recurrent tumors that required adjuvant radiation therapy, radiosurgery, or repeat surgery. Only 3 of the 16 patients (19%) in the PCP group obtained complete tumor removal after initial management.

Ten of the 17 patients of the GCT group received surgical treatment. The surgical results were total tumor removal in 3 patients, subtotal resection in 1 patient, and partial resection or biopsy in 6 patients. Four of the 6 patients had a partial resection or biopsy because the diagnosis of GCT was made on frozen section pathology. The other 7 patients with GCT diagnosed by clinical and MR imaging findings underwent radiation therapy as the initial treatment. No mortality in the GCT group was noted.

After initial management, the recurrence rate in the PCP and GCT groups was 81% versus 24%, respectively ( $P = .003$ ; OR, 0.10; 95% CI, 0.02–0.50). Repeat surgery or adjuvant radiosurgery was performed for the 12 patients with PCP with recurrent tumors. In the GCT group, only 1 patient had recurrent tumors after surgery and radiation therapy. Although the pineal gland was initially normal, recurrent tumors were observed in both the infundibular and pineal regions (Fig 2E). The survival interval was longer in patients with GCT ( $52.4 \pm 40.3$  months) than in those with PCP ( $39.6 \pm 32.0$  months) ( $P = .3815$ ), but it was not statistically significant.

### DISCUSSION

The pituitary gland is divided into 2 anatomic compartments from different ectodermal origins. At the fourth week of gestation, the Rathke pouch forms from the evagination of an ectodermal outpouching of stomodeum immediately in front of the buccopharyngeal membrane. The cells in the anterior wall of the Rathke pouch proliferate rapidly to form the pars anterior. The less active cells in the posterior wall form the pars intermedia. By the 16th week of gestation, the pars tuberalis, a small part of the pars anterior, extends superoventrally and wraps around the pituitary stalk (Fig 5A).<sup>13,14</sup> It was hypothesized that PCPs originated from squamous epithelial cells in the pars tuberalis of adenohypophysis (Fig 5B). The spheric tumor shape of PCPs and upward compression of the optic chiasm were compatible with an origin in the pars tuberalis, which encircles the pituitary stalk (Fig 1B).

The posterior lobe develops from the downward evagination of neuroectodermal tissue originating from the diencephalon, called the “infundibulum.” The neurohypophysis is embryologically and anatomically continuous with the hypothalamus.<sup>15</sup> Intracranial GCTs almost exclusively arise from the diencephalon, primarily the pineal region and hypothalamic-infundibular axis. These 2 regions are regulated by gonadotropins and connected via the accessory optic tract.<sup>16</sup> It was proposed that GCTs originated

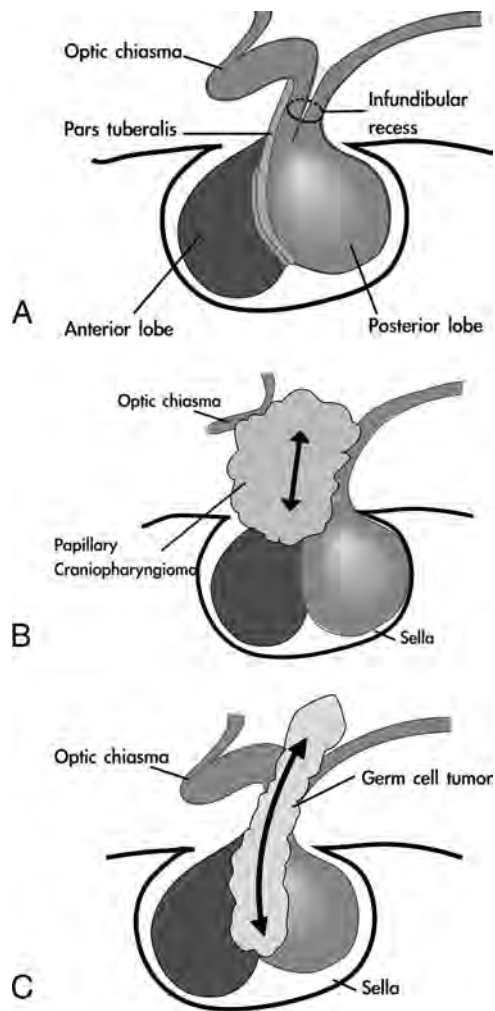


**FIG 5.** Hypothetic pathogenesis of suprasellar GCT and PCP. *A*, Normal anatomy of the sellar and suprasellar regions. The pars tuberalis, a small part of the pars anterior, extends ventrally and wraps around the pituitary stalk; the neurohypophysis is embryologically and anatomically continuous with the hypothalamus. *B*, The PCP originates from squamous epithelial cells in the pars tuberalis of the adenohypophysis and is located extraventricularly. *C*, The GCT originates from the hypothalamic-infundibular axis or pineal region. It is located intraventricularly and infiltrates along the infundibular recess down to the sellar region.

from the abnormal termination of primordial germ cell migration. Most hypophyseal GCTs present with infundibular thickening, which represents the only imaging findings in small tumors.<sup>5,17</sup> This infundibular lesion can extend vertically into the sellar region along the pituitary stalk axis (Figs 3A, 4A, -B, and 5C).

The pineal region is the most common location for GCTs, accounting for 40%–60%.<sup>18</sup> The suprasellar region is the second most common location of GCTs. Between 5% and 10% of intracranial germ cell tumors are found in both the pineal and suprasellar regions at diagnosis. This bifocal disease manifests mostly as germinoma, but its actual spreading or synchronous development remains unclear.<sup>7</sup> We propose that suprasellar GCT presents more commonly as a spreading lesion from the primary pineal lesion than as a lesion with synchronous development or as a primary lesion. Some results of this study support our hypothesis: 1) In our 10 patients with suprasellar GCT who underwent surgi-

cal management, the tumors were identified in the lower portion or floor of the third ventricle. This location implied that the suprasellar GCT had a close relationship with the intraventricular CSF flow dynamics and was influenced by gravity, particularly related to the pineal lesion with intraventricular involvement. 2) The transinfundibular tumor growth, diffuse thickening of the pituitary stalk, and downward infiltration of the pituitary gland on MR imaging suggested that the suprasellar GCT grew intraventricularly along the infundibular recess of third ventricle. This intraventricular location could also explain the common symptom of diabetes insipidus with suprasellar GCT because the hypothalamus has a close relationship with the third ventricle. By contrast, suprasellar PCPs originate outside the ventricle. Suprasellar PCPs presented with spheric tumor growth, displacement of the pituitary stalk, and compression of the optic chiasm. That PCPs had more upward growth toward the third ventricle (50%) than GCTs (24%) also suggests the extraventricular location and the influence of the hard structures of the tuberculum sellae and diaphragm sellae in their floor. 3) In half of the patients with GCT, the size of the pineal gland changed after low-dose radiation therapy. In the patients with recurrent GCT, tumor growth was revealed in the pineal gland and in the suprasellar region. The PCP group showed no significant interval change of the pineal gland, though the pineal gland was included in the field of radiation therapy. We suppose that the structure of the pineal gland in GCTs in the present study, even if the lesion is <1 cm, could be a part of the primary tumor. This radiosensitive tumor can shrink significantly from any low-dose irradiation, such as brain CT, and can regrow in some seeding areas.<sup>19,20</sup> Due to gravity in upright position, the infundibular recess of the third ventricle is one of the most common sites for deposition of a seeding lesion. This seeding hypothesis of suprasellar GCT can corroborate the therapeutic results of pediatric GCT with low-dose irradiation including the ventricular system.<sup>20</sup> Further study to compare the pathology of the pineal gland and suprasellar GCT will help confirm this hypothesis.

PCPs predominated in the older age groups, with bimodal distribution of craniopharyngiomas peaking in the fifth to sixth decades.<sup>6,21</sup> Intracranial suprasellar GCTs were mostly diagnosed between 6 and 15 years of age.<sup>22</sup> In the present study, the patients diagnosed with GCT were younger than those diagnosed with PCP; nevertheless, a 43-year-old man with GCT was identified. Regarding pediatric GCT, pineal tumors showed a male predominance, and suprasellar tumors were equally distributed between both sexes.<sup>7</sup> We found male predominance in the adult patients of both groups in the present study. Both groups also presented with the common clinical symptoms of suprasellar tumors, including headache, visual field defects, decreased visual acuity, and hormone disturbance.<sup>23</sup> However, GCTs commonly caused diabetes insipidus, which was consistent with hypothalamic-neurohypophyseal axis involvement.<sup>4</sup>

Several reports concerned optic pathway edematous changes associated with craniopharyngioma.<sup>24–26</sup> Recently, this finding was also reported in other parasellar tumors, such as pituitary adenoma, GCTs, meningioma, and lymphoma.<sup>27</sup> We also found optic pathway edema in both groups with no significant difference.

Only a few studies concerning MR imaging diffusion of PCPs have been published in the English literature. A case report of a

huge craniopharyngioma showed high signal intensities on both DWI and ADC maps by its complex contents.<sup>28</sup> In our study, the solid component of PCPs on DWI showed hypointense signals, presumably reflecting the character of this low-grade epithelial tumor.<sup>10,29</sup> Intracranial GCTs were thought to demonstrate high nuclear-to-cytoplasmic ratios of tumor cells or high tumor cellularity, showing restricted diffusion on DWI.<sup>30</sup> Routine axial whole-brain DWI may have problems in the evaluation of small suprasellar tumors because of scan gaps or artifacts of the skull base. We suggest sagittal DWI of the sellar region to improve the diagnosis of suprasellar tumors.

Although craniopharyngiomas are classified as grade I tumors by the World Health Organization, multiple recurrences and malignant transformations have been reported. Adhesion or encasement of adjacent cranial nerves or vessels also promotes the association of craniopharyngiomas with significant surgical morbidity. Aggressive surgical resection or conservative surgical treatment combined with adjuvant therapy remains a controversial therapeutic strategy. Regarding GCTs, germinomas respond well to radiation therapy, even without a pathologic diagnosis. Non-germinomatous GCTs require surgery or radiation therapy combined with chemotherapy.<sup>7</sup> These diverse therapeutic strategies and outcomes highlight the importance of presurgical planning of these 2 unusual suprasellar tumors. According to our hypothesis of the extraventricular location of suprasellar PCPs, a transphenoidal or subfrontal approach is a good option for tumor removal. An interhemispheric approach is appropriate for obtaining a pathologic diagnosis of the intraventricular location of suprasellar GCTs.

The major limitation of this study is the small number of cases of GCTs in the adult group. We included patients older than 16 years of age because they are beyond the common age distribution of pediatric GCT.<sup>22</sup> The other limitation is that some cases of GCT did not have a pathologic diagnosis, including the interval change of pineal tissue on serial MR imaging. Further study comparing the pathologic and imaging changes of suprasellar and pineal structures will be helpful to clarify the origin and extension of these tumors and their best management.

## CONCLUSIONS

Younger age, diabetes insipidus, MR imaging characteristics of restriction diffusion, and vertical infundibular extension favor the diagnosis of GCT. MR imaging findings of spheric shape without infundibular infiltration and without diffusion restriction provide clues to PCPs. We suggest that suprasellar GCT is possibly an intraventricular lesion originating from a pineal lesion or the hypothalamic-infundibular axis. Suprasellar PCPs originate from the pars tuberalis and are located outside the third ventricle. On the basis of clinical and MR imaging findings and these anatomic origins, appropriate pretreatment diagnosis and a surgical approach can be planned.

Disclosures: Feng-Chi Chang—RELATED: Grant: Taipei Veterans General Hospital (V103C-063, CI-103-3) and the Ministry of Science and Technology (NSC 102-2314-B-075-068). Comments: I am the Principal Investigator of these projects; Payment for Writing or Reviewing the Manuscript: Taipei Veterans General Hospital (V103C-063, CI-103-3) and the Ministry of Science and Technology (NSC 102-2314-B-075-068). Comments: English editing of this submitted manuscript was supported by these projects. Wan-Yuo Guo—UNRELATED: Other: research collaboration with Siemens

on topics other than the current submission under a contract between Taipei Veterans General Hospital and Siemens Healthcare.

## REFERENCES

1. Dietemann JL, Cromero C, Tajahmady T, et al. **CT and MRI of suprasellar lesions.** *J Neuroradiol* 1992;19:1–22
2. Smith JK. **Parasellar tumors: suprasellar and cavernous sinuses.** *Top Magn Reson Imaging* 2005;16:307–15
3. Karnaze MG, Sartor K, Winthrop JD, et al. **Suprasellar lesions: evaluation with MR imaging.** *Radiology* 1986;161:77–82
4. Fujisawa I, Asato R, Okumura R, et al. **Magnetic resonance imaging of neurohypophyseal germinomas.** *Cancer* 1991;68:1009–14
5. Kanagaki M, Miki Y, Takahashi JA, et al. **MRI and CT findings of neurohypophyseal germinoma.** *Eur J Radiol* 2004;49:204–11
6. Zoicas F, Schofl C. **Craniopharyngioma in adults.** *Front Endocrinol (Lausanne)* 2012;3:46
7. Packer RJ, Cohen BH, Cooney K. **Intracranial germ cell tumors.** *Oncologist* 2000;5:312–20
8. Sartoretti-Schefer S, Wichmann W, Aguzzi A, et al. **MR differentiation of adamantinous and squamous-papillary craniopharyngiomas.** *AJNR Am J Neuroradiol* 1997;18:77–87
9. Ogawa K, Shikama N, Toita T, et al. **Long-term results of radiotherapy for intracranial germinoma: a multi-institutional retrospective review of 126 patients.** *Int J Radiat Oncol Biol Phys* 2004;58:705–13
10. Fernandez-Miranda JC, Gardner PA, Snyderman CH, et al. **Craniopharyngioma: a pathologic, clinical, and surgical review.** *Head Neck* 2012;34:1036–44
11. Hamilton BE, Salzman KL, Osborn AG. **Anatomic and pathologic spectrum of pituitary infundibulum lesions.** *AJR Am J Roentgenol* 2007;188:W223–32
12. Van Effenterre R, Boch AL. **Craniopharyngioma in adults and children: a study of 122 surgical cases.** *J Neurosurg* 2002;97:3–11
13. Zada G, Lin N, Ojerholm E, et al. **Craniopharyngioma and other cystic epithelial lesions of the sellar region: a review of clinical, imaging, and histopathological relationships.** *Neurosurg Focus* 2010;28:E4
14. Sadler TW. *Langman's Medical Embryology.* Philadelphia: Lippincott Williams & Wilkins; 2009:414
15. Nussey S, Whitehead S. *Endocrinology: An Integrated Approach.* Boca Raton: CRC Press; 2001:283–85
16. Glenn OA, Barkovich AJ. **Intracranial germ cell tumors: a comprehensive review of proposed embryologic derivation.** *Pediatr Neurosurg* 1996;24:242–51
17. Liang L, Korogi Y, Sugahara T, et al. **MRI of intracranial germ-cell tumours.** *Neuroradiology* 2002;44:382–88
18. McCarthy BJ, Shibui S, Kayama T, et al. **Primary CNS germ cell tumors in Japan and the United States: an analysis of 4 tumor registries.** *Neuro Oncol* 2012;14:1194–200
19. Yoneoka Y, Tsumanuma I, Jinguji S, et al. **Synchronized multiple regression of diagnostic radiation-induced rather than spontaneous disseminated primary intracranial germinoma in a woman: a case report.** *J Med Case Rep* 2011;5:39
20. Chen YW, Huang PI, Ho DM, et al. **Change in treatment strategy for intracranial germinoma: long-term follow-up experience at a single institute.** *Cancer* 2012;118:2752–62
21. Garnett MR, Puget S, Grill J, et al. **Craniopharyngioma.** *Orphanet J Rare Dis* 2007;2:18
22. Wong TT, Ho DM, Chang KP, et al. **Primary pediatric brain tumors.** *Cancer* 2005;104:2156–67
23. Huang BY, Castillo M. **Nonadenomatous tumors of the pituitary and sella turcica.** *Top Magn Reson Imaging* 2005;16:289–99
24. Higashi S, Yamashita J, Fujisawa H, et al. **“Moustache” appearance in craniopharyngiomas: unique magnetic resonance imaging and computed tomographic findings of perifocal edema.** *Neurosurgery* 1990;27:993–96

25. Nagahata M, Hosoya T, Kayama T, et al. **Edema along the optic tract: a useful MR finding for the diagnosis of craniopharyngiomas.** *AJNR Am J Neuroradiol* 1998;19:1753–57
26. Hirunpat S, Tanomkiat W, Sriprung H, et al. **Optic tract edema: a highly specific magnetic resonance imaging finding for the diagnosis of craniopharyngiomas.** *Acta Radiol* 2005;46:419–23
27. Saeki N, Nagai Y, Matsuura I, et al. **Histologic characteristics of normal perivascular spaces along the optic tract: new pathogenetic mechanism for edema in tumors in the pituitary region.** *AJNR Am J Neuroradiol* 2004;25:1218–22
28. Sener RN, Dzelzite S, Migals A. **Huge craniopharyngioma: diffusion MRI and contrast-enhanced FLAIR imaging.** *Comput Med Imaging Graph* 2002;26:199–203
29. Kono K, Inoue Y, Nakayama K, et al. **The role of diffusion-weighted imaging in patients with brain tumors.** *AJNR Am J Neuroradiol* 2001;22:1081–88
30. Gavrilovic S, Lavrnjic S, Thurnher M, et al. **Proton MR spectroscopy and diffusion-weighted imaging of intracranial germ cell tumors: implications for differentiation from other lesions.** *European Journal of Radiology Extra* 2011;79:e59–e64

# Crossed Cerebrocerebellar Language Lateralization: An Additional Diagnostic Feature for Assessing Atypical Language Representation in Presurgical Functional MR Imaging

C. Méndez Orellana, E. Visch-Brink, M. Vernooij, S. Kalloe, D. Satoer, A. Vincent, A. van der Lugt, and M. Smits



## ABSTRACT

**BACKGROUND AND PURPOSE:** Determining language dominance with fMRI is challenging in patients with brain tumor, particularly in cases of suspected atypical language representation. Supratentorial activation patterns must be interpreted with great care when the tumor is in or near the presumed language areas, where tumor tissue or mass effect can lead to false-negative fMRI results. In this study, we assessed cerebrocerebellar language fMRI lateralization in healthy participants and in patients with brain tumors with a focus on atypical language representation.

**MATERIALS AND METHODS:** Twenty healthy participants and 38 patients with a brain tumor underwent fMRI with a verb-generation task. Cerebral and cerebellar language lateralizations were separately classified as left-sided, right-sided, or symmetric. Electrocortical stimulation was performed in 19 patients. With the McNemar test, we evaluated the dependency between language lateralization in the cerebrum and cerebellum, and with Pearson correlation analysis, the relationship between the cerebral and cerebellar lateralization indices.

**RESULTS:** There was a significant dependency between cerebral and cerebellar language activation, with moderate negative correlation (Pearson  $r = -0.69$ ). Crossed cerebrocerebellar language activation was present in both healthy participants and patients, irrespective of handedness or typical or atypical language representation. There were no discordant findings between fMRI and electrocortical stimulation.

**CONCLUSIONS:** Language lateralization in the cerebellum can be considered an additional diagnostic feature to determine language dominance in patients with brain tumor. This is particularly useful in cases of uncertainty, such as the interference of a brain tumor with cerebral language activation on fMRI and atypical language representation.

**ABBREVIATIONS:** ECS = electrocortical stimulation; HP = healthy participant; LI = lateralization index

Functional MR imaging is a feasible diagnostic neuroimaging tool for determining hemispheric language dominance in patients with brain tumor preoperatively.<sup>1</sup> Nevertheless, it has important limitations when evaluating language lateralization, particularly in patients with brain tumors.<sup>1-3</sup> Activation patterns must be interpreted with great care when the tumor is in or near the presumed language areas, where tumor tissue or mass effect can lead to false-negative fMRI results.<sup>2</sup>

Determining language dominance is additionally challenging in left-handed patients with brain tumor. Left-handers are known to have less well-defined language-lateralization patterns, with more atypical right-sided language lateralization compared with right-handers.<sup>4-6</sup> In patients with brain tumor, the ability of fMRI to confirm Wada-established language lateralization was significantly more specific for right- than for left-handed or ambidextrous patients, presumably due to their higher rate of typical, left-lateralized language representation.<sup>7</sup> In a study evaluating the role of fMRI confirming language dominance in patients with epilepsy, this technique showed higher posttest probability for language dominance in patients with typical language representation than in patients with atypical language representation.<sup>8</sup>

Thus far, studies assessing language lateralization have focused on the supratentorial brain. Prior fMRI studies have shown activation not only in the cerebral hemispheres but also in the cerebellum while performing specific language tasks.<sup>9-11</sup> An example

Received June 21, 2014; accepted after revision August 13.

From the Departments of Radiology (C.M.O., M.V., S.K., A.v.d.L., M.S.), Neurology (C.M.O., E.V.-B.), and Neurosurgery (E.V.-B., D.S., A.V.), Erasmus MC, University Medical Center Rotterdam, Rotterdam, the Netherlands.

Please address correspondence to Marion Smits, MD, PhD, Department of Radiology (Hs-224), Erasmus MC—University Medical Center Rotterdam, PO Box 2040, 3000 CA Rotterdam, the Netherlands; e-mail: marion.smits@erasmusmc.nl; @MarionSmits

Indicates article with supplemental on-line tables.

<http://dx.doi.org/10.3174/ajnr.A4147>

is the verb-generation task, which is preferred to localize language areas in patients with tumor<sup>11-14</sup> and has been properly validated with electrocortical stimulation (ECS).<sup>15</sup> In individuals with left-hemispheric language dominance, this task has been shown to activate the right cerebellum.<sup>9</sup> Some further studies have provided evidence for a so-called crossed cerebrocerebellar language lateralization pattern in healthy individuals, with both typical, left-sided and atypical, right-sided language lateralization.<sup>10,16</sup> This crossed cerebrocerebellar language lateralization may serve as a useful additional diagnostic feature in determining language hemispheric dominance in patients with brain tumor because the cerebellar language activation is generally undisturbed by the tumor localized in or near the presumed supratentorial language areas. Such an additional diagnostic feature may be especially helpful in patients with potentially atypical language representation, namely left-handers.

The purpose of our study was to assess cerebrocerebellar language fMRI lateralization in healthy participants and in patients with brain tumor, with a focus on atypical language representation.

## MATERIALS AND METHODS

### Study Participants

We included 20 healthy participants (HPs) whose functional data were reported in a previous study<sup>17</sup> that investigated the relationship between cerebral functional language lateralization and structural asymmetry of the arcuate fasciculus and 38 patients with brain tumor. Institutional review board approval was obtained for the inclusion of HPs and for the retrospective use of anonymized patient data. We included more left- than right-handed HPs to increase the probability of finding atypical right-lateralized or symmetric language representation. Handedness in healthy participants was assessed with the Oldfield Edinburgh Handedness Inventory.<sup>18</sup> Written informed consent was obtained from all HPs before participation in this study. The institutional review board waived the requirement to obtain written informed consent from patients. Patients were selected from our data base of 205 patients referred for preoperative fMRI by the neurosurgery department at our institution between May 2004 and September 2013. From this data base, we selected all left-handed patients ( $n = 19$ ) who had performed an fMRI language task. We then matched these with 19 right-handed patients for sex, age, and tumor location. Handedness in all patients was assessed by the neurosurgeon at presurgical neurologic examination. All patients were able to perform the language task and were native Dutch speakers except for 1 native German speaker, who was fluent in Dutch after learning this language at 37 years of age. Nineteen patients (9 left-handed) underwent an operation in an awake setting, where direct ECS was performed to identify language functions (biphasic pulse, 50-Hz frequency, 1-ms duration, 6–12 mA).

### Data Acquisition and Preprocessing

Participants performed a verb-generation task.<sup>12</sup> They were instructed to think of a verb related to an auditorily presented noun, and in the control condition, they listened to high (2000-Hz) and low (400-Hz) tones.

Participants were scanned at 1.5T or 3T with an 8-channel head coil. Functional and structural sequences are specified in On-line Table 1. Imaging data were analyzed by using SPM8 software (<http://www.fil.ion.ucl.ac.uk/spm/software/spm8>). Functional images were manually aligned to the anterior commissure, realigned to correct for motion, coregistered with the individual's T1-weighted image,<sup>19</sup> and smoothed with a 3D Gaussian full width at half maximum filter of  $6 \times 6 \times 6$  mm<sup>3</sup>.<sup>20</sup>

Anatomic images of the HPs were segmented and normalized with the functional images to the Montreal Neurological Institute standard brain space by using affine and nonlinear registration. This process resulted in resampled voxel sizes of  $3 \times 3 \times 3$  mm<sup>3</sup> for the functional and  $1 \times 1 \times 1$  mm<sup>3</sup> for the anatomic images. Patient data were not normalized, in line with routine presurgical analysis, but were resliced with preservation of the acquired voxel size.

### Data Analysis

Statistical activation maps were generated with a general linear model, by using a boxcar function convolved with a hemodynamic response function, corrected for temporal autocorrelation and filtered with a high-pass filter of 128-second cutoff. Motion parameters were included as regressors of no interest to reduce potential confounding effects of motion. Individual t-contrast images of language activation (verb-generation > tones) were generated for all participants. Different from the analysis performed with the HPs in our previous study,<sup>17</sup> individual lateralization indices (LIs) were determined by ROIs known to be involved in language processing: the inferior frontal gyrus, superior temporal and middle temporal gyri, angular and supramarginal gyri, and the cerebellum. Furthermore, in this study, the number of activated voxels within these ROIs was calculated by using a threshold-independent method.<sup>21,22</sup> The LI was defined as  $(LH - RH)/(LH + RH)$ , where  $LH$  and  $RH$  are the number of activated voxels in the left and right hemispheres, respectively. Activation was classified for the cerebrum and cerebellum separately as left-lateralized for LI values between 0.1 and 1.0, right-lateralized for LI values between -0.1 and -1.0, or symmetric for LI values between or equal to -0.1 and 0.1.<sup>21</sup>

Patients' individual t-contrast images, thresholded individually but at a minimum t-value of 3.2, were assessed qualitatively by a neuroradiologist with 11 years' experience in presurgical fMRI who was blinded to the handedness of patients and ECS findings. Language activation was assessed in the same predetermined language areas as those quantitatively assessed in the HPs. For each region, activation was categorized as left-lateralized, right-lateralized, symmetric, or no activation, on the basis of which an overall assessment of supratentorial language representation was made. Cerebellar activation was not taken into account when determining overall language lateralization.

For both HPs and patients, when functional language activation in the cerebrum was left-lateralized, we defined this activation as typical language representation. When cerebral language activation was right-lateralized or symmetric, we defined it as atypical language representation. Furthermore, when activation patterns were observed in the left cerebrum and right cerebellum,

### Healthy participant demographics and lateralization indices

Age (yr)	Sex	EHI Score <sup>a</sup>	LI Cerebrum	LI Cerebellum	Lateralization Cerebrum	Lateralization Cerebellum
25	M	-100	0.42	-0.36	L	R
30	M	-100	-0.44	0.34	R	L
33	F	-100	-0.27	0.03	R	S
27	F	-100	0.34	-0.41	L	R
28	F	-100	0.02	-0.43	S	R
35	F	-100	0.24	-0.19	L	R
53	M	-90	-0.18	0.13	R	L
36	F	-90	-0.28	0.07	R	S
30	M	-80	0.13	-0.22	L	R
29	M	-78	0.32	-0.40	L	R
28	F	-20	-0.04	-0.13	S	R
31	M	-20	0.48	0.00	L	S
43	M	0	-0.18	0.00	R	S
30	F	100	0.21	-0.30	L	R
34	F	100	0.16	-0.04	L	S
34	M	100	0.32	-0.12	L	R
34	F	100	0.31	-0.46	L	R
29	F	100	0.42	-0.30	L	R
32	M	100	0.33	-0.09	L	S
28	F	100	0.43	-0.25	L	R

**Note:**—L indicates left-sided; R, right-sided; S, symmetric; EHI, Oldfield Edinburgh Handedness Inventory.

<sup>a</sup> Handedness was assessed with the Oldfield Edinburgh Handedness Inventory.

or vice versa, we defined this relationship as crossed cerebrocerebellar language activation.<sup>23</sup>

### Statistical Analysis

Statistical analysis was performed by using SPSS (Version 20; IBM Armonk, New York). Age differences between left- and right-handed participants were examined by using an independent-samples *t* test. Sex differences between both groups of patients were examined by using the Fisher exact test. To test whether the lateralizations in the cerebrum and in the cerebellum were independent of each other, we performed a McNemar test in HP and patient data. In HPs, the possible relationship between the LIs of the cerebrum and of the cerebellum was investigated with a scatterplot and was tested with Pearson correlation analysis. We used a significance level of  $\alpha = .05$  for all analyses.

## RESULTS

### Participant Characteristics

From the 20 HPs included in the study (mean age, 32.8 years; range, 25–54 years, 9 men), 13 were classified<sup>18</sup> as left-handed and 7, as right-handed (Table). There were no significant differences between the left- and right-handed HPs for age ( $t[18] = -0.416$ ,  $P = .682$ ) or sex ( $P = .374$ , Fisher exact test). Patient characteristics are shown in On-line Table 2. There were no significant differences between the left- and right-handed patients for age ( $t[36] = -0.723$ ,  $P = .474$ ) or sex ( $P = .728$ , Fisher exact test). In 24 patients, tumors were reported as low-grade, and in 13 patients, as high-grade on histopathologic examination. Thirty-two of the 38 patients underwent surgery. ECS was performed in 19 of these, and language regions were identified in 5.

### Cerebrocerebellar Language Lateralization in HPs

The cerebral and cerebellar language lateralizations and LIs in HPs are presented in Fig 1 and the Table. We found a crossed cerebrocerebellar activation in 60% (12/20) of HPs. None of the participants showed language lateralization toward the same

hemisphere in both the cerebrum and cerebellum. Of the 13 left-handed participants, 6 showed typical and 7, atypical language representation: right-lateralized cerebral activation in 5 and symmetric cerebral activation in 2 participants. Crossed cerebrocerebellar language activation was observed in 7 left-handed participants (5/6 with typical and 2/7 with atypical language representation). Of the remaining 6 participants, cerebellar activation was symmetric in 4 and right-lateralized in 2. All 7 right-handed participants showed typical language representation, of whom 5 showed a crossed cerebrocerebellar language activation. The remaining 2 participants showed symmetric activation in the cerebellum.

There was a significant dependency between the cerebral and cerebellar language lateralization patterns with  $\chi^2 (3, n = 20) = 8.533$ ,  $P = .036$ . The scatterplot (Fig 2) indicated a negative direction of this dependency, with a moderate negative correlation between the LIs of the cerebrum and the cerebellum (Pearson  $r(20) = -0.69$ ,  $P = .001$ ).

### Cerebrocerebellar Lateralization in Patients with Tumor

The cerebral and cerebellar language lateralizations in patients are presented in Fig 1 and in On-line Table 2. We found crossed cerebrocerebellar activation in 76% (29/38) of patients. None of the patients showed language lateralization toward the same side in both the cerebrum and cerebellum.

Of the 19 left-handed patients, 13 showed typical, and 6, atypical language representation. Crossed cerebrocerebellar language activation was observed in 12/13 left-handed patients with typical language representation. Of the 6 patients with atypical language representation, cerebral language activation was right-lateralized in 1 and symmetric in 5. Of these, 1 patient with symmetric cerebral language activation showed right-lateralized activation in the cerebellum (Fig 3A). His tumor was localized in the presumed language areas in the left hemisphere, which could have reduced language activation, resulting in a potentially false symmetric language-activation pattern. In addition, this patient was a bilingual speaker whose mother tongue was German. Although he was fluent in Dutch, he performed the verb-generation task in his mother tongue while the task was presented in Dutch. It is known that language activation in bilingual patients may be more symmetric,<sup>24</sup> and his performing the task with the interference of both languages may have contributed to the unexpected language-activation pattern we observed. The other patients showed symmetric (3 patients) or no activation (1 patient) in the cerebellum.

Of the 19 right-handed patients, 17 showed typical and 2, atypical language representation. Crossed cerebrocerebellar language activation was observed in 16 of the 17 patients with typical language representation. Of the 2 patients with atypical language representation, one showed right-lateralized cerebral activation with crossed cerebrocerebellar language representation (Fig 3B) and the other showed symmetric cerebral and cerebellar language activation.

There was a significant dependency between the lateralization in the cerebrum and in the cerebellum [ $\chi^2 (6, n = 38) = 42.06$ ,  $P = .000$ ].

There were no discordant findings between fMRI and ECS, which positively identified language representation in the same

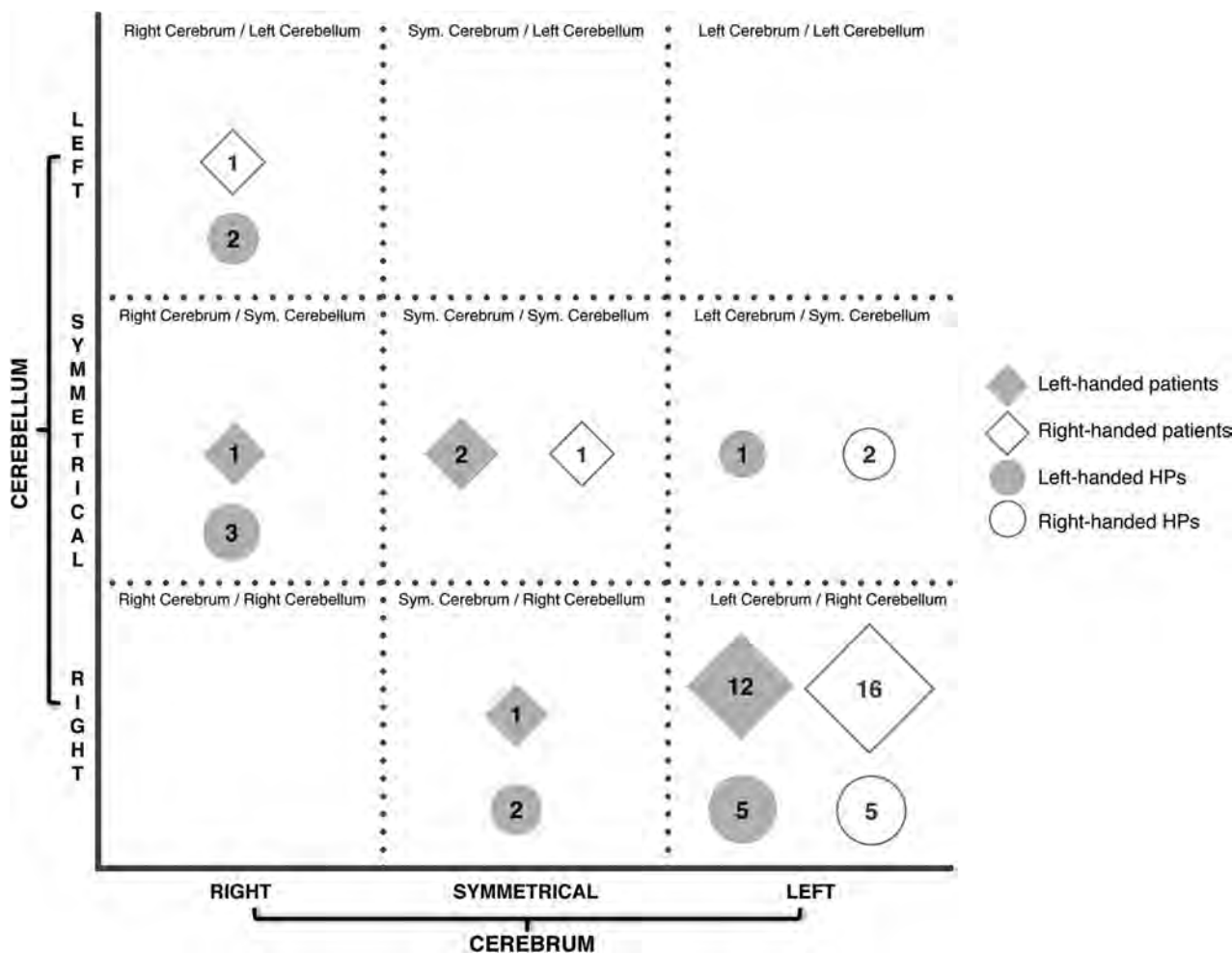


**FIG 1.** Cerebrotal and cerebellar language representation in healthy participants and patients. The 4 patients with no activation in the cerebellum (as described in On-line Table 2) are not represented in this figure. Sym. indicates symmetric.

hemisphere in 5 patients. In one of these patients, fMRI language activation was found to be present in both hemispheres, whereas it was only identified on the operated side with ECS (the contralateral hemisphere was not assessed with ECS).

### DISCUSSION

We found a significant dependency between language lateralization in the cerebrum and in the cerebellum, both in HPs and in patients with brain tumor, in line with previous studies in healthy left- and right-handers with typical language representation.<sup>10,23</sup> Furthermore, we found a moderate inverse correlation of cerebrotal lateralization; in other words, the more strongly language was lateralized toward a cerebral hemisphere, the more strongly it was lateralized to the contralateral cerebellar hemisphere. In almost all cases in which activation in the cerebellum was lateralized, there was a crossed cerebrotal lateralization pattern, irrespective of whether language representation was typical or atypical. This means that as a rule of thumb, in cases of clear cerebellar lateralization, cerebral language lateralization can be assumed contralateral. Language lateralization in the cerebellum may thus serve as an additional diagnostic feature for determining hemispheric language dominance in individuals with either typical or atypical language representation. Cerebellar

activation was found to be symmetric in a minority of HPs and patients. In these cases, there was no clear correlation with cerebral language representation; in some, cerebral language was also symmetric, but in others, cerebral activation was clearly lateralized. In cases in which assessment of cerebral lateralization is hindered by tumor effects and cerebellar activation is symmetric, another examination such as the Wada test or ECS is thus still required to determine language dominance.<sup>1,8</sup>

Neuroimaging studies of the verb-generation task indicated that the cerebellum is involved in generating or maintaining articulatory representation,<sup>25</sup> even though no speech motor output was required. Both lesion and functional neuroimaging studies suggest that the cerebellum contributes to diverse cognitive language components and aspects of language production,<sup>25,26</sup> and cerebellar activation has been reported not only in productive tasks but also in speech-comprehension tasks.<sup>27</sup> The mechanism underlying the observed crossed cerebrotal activation remains to be elucidated. Connectome analyses could be used to attempt to find white matter pathways that may be responsible for these findings.

Irrespective of handedness or the side of lateralization, crossed cerebrotal activation was observed in most cases and par-

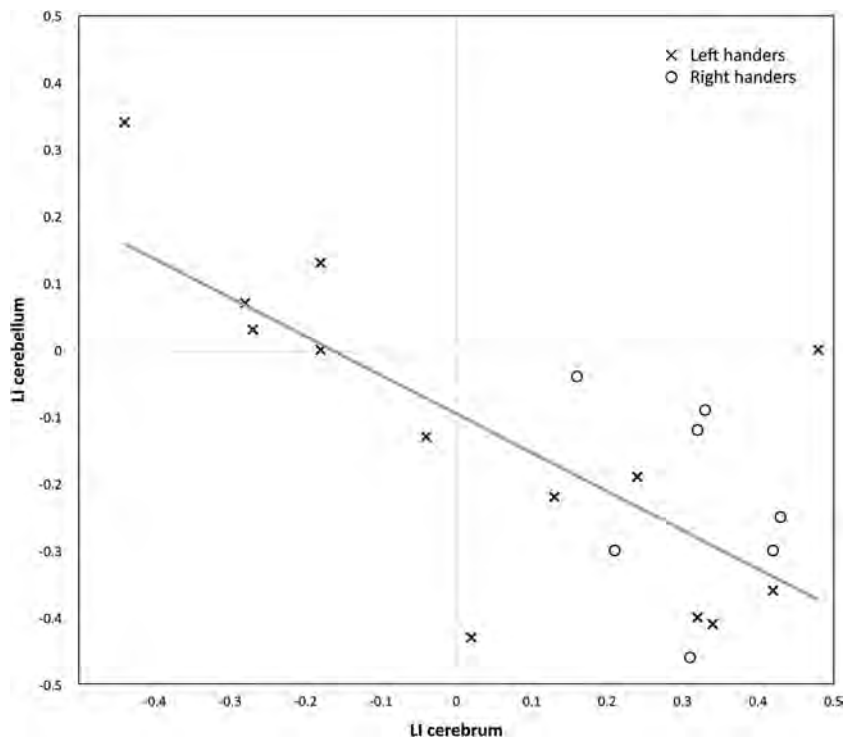


**FIG 2.** Scatterplot of the healthy participant lateralization indices of the cerebrum and cerebellum.

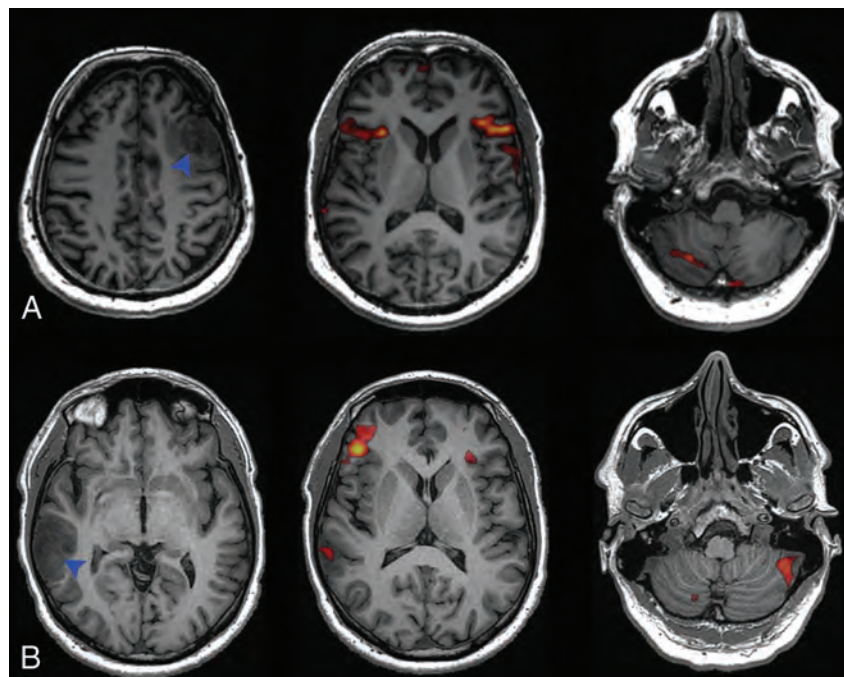


**FIG 3.** A, Language activation of a left-handed, bilingual patient, with tumor in the left middle frontal gyrus (*blue arrowhead*), showing symmetric cerebral activation and right-lateralized cerebellar activation. B, Language activation of a right-handed patient with tumor in the right middle temporal and angular gyri (*blue arrowhead*), showing atypical, right-lateralized cerebral activation and crossed cerebellar lateralization.

ticularly in all patients, except one who was bilingual, in whom cerebellar activation was lateralized. This finding is of particular clinical use in cases in which hemispheric language dominance cannot be assessed because of the interference of lan-

guage activation due to tumor<sup>2,28</sup> and in left-handed patients in whom diagnostic uncertainty is greater due to the increased prevalence of atypical language representation.

To the best of our knowledge, this is the first study confirming crossed cerebrocerebellar activation in a large group of HPs and patients with brain tumor with a high prevalence of atypical language representation. To assess the correlation between cerebral and cerebellar lateralization quantitatively, we used a threshold-independent method, which is less prone to within-subject variability than threshold-dependent LI calculation and generates LIs that are more in agreement with clinical findings.<sup>21</sup> For the assessment of language lateralization in patients with brain tumor, we chose to assess language lateralization qualitatively to remain as close to the clinical routine as possible. Studies comparing quantitative with qualitative assessment of language lateralization have shown that visual inspection by an experienced rater is reliable for presurgical assessment of language lateralization.<sup>29-31</sup> This qualitative approach provided a clinically applicable assessment of the cerebrocerebellar relationship in patients with tumor.

The main limitation of our study, as in many studies assessing functional language lateralization presurgically,<sup>1,32</sup> is the relative lack of a criterion standard. Next to techniques such as the Wada test and ECS that are commonly considered criterion standards, transcranial magnetic stimulation,<sup>33</sup> magnetoencephalography,<sup>34</sup> and fMRI are currently being used as presurgical methods to evaluate language lateralization. In our study, in combination with fMRI, ECS was performed in most of our patients, but in many, no language area was identified. ECS assessment is limited to just the brain region surrounding the tumor, and language areas at some distance from the tumor are thus not identified. Even when a language area is identified, we cannot know for certain whether this is the sole, dominant hemisphere: Bilateral language representation cannot be assessed with certainty. While we found no discordance between ECS and fMRI, the number of patients in whom this could be assessed with certainty was small. A minor limitation of our study is that patients were scanned on several scanners, consistent with

daily clinical practice. Nevertheless, we used a standardized imaging protocol for presurgical fMRI evaluations, maintaining similar image resolution across our MR imaging systems and standardized image analysis. Another minor limitation was the difference in assessment of handedness: In healthy participants, the standardized Oldfield Edinburgh Handedness Inventory was used while in patients, handedness information was obtained from the preoperative neurosurgical evaluation. Finally, patients with both high- and low-grade gliomas were included in this study. Neurovascular decoupling is a potential limitation of fMRI in high-grade tumors. Our study population was too small to allow a formal comparison or a distinction among these tumor grades.

## CONCLUSIONS

Cerebellar activation may provide an additional diagnostic feature to assess hemispheric language dominance, both in typical and atypical language representations. This is particularly useful in left-handed patients with brain tumor, in whom language representation is commonly atypical, resulting in diagnostic uncertainty, especially when there is potential interference of the tumor with language activation. When cerebellar activation is found to be lateralized, we can, as a rule of thumb, assume that there is contralateral hemispheric language dominance. This crossed cerebrocerebellar pattern of activation could be included as a diagnostic tool in future guidelines of clinical fMRI examinations, which should further specify that a language task that is known to involve the cerebellum is used.

Disclosures: Aad van der Lugt—UNRELATED: Grants/Grants Pending: General Electric Healthcare\*; Payment for Lectures (including service on Speakers Bureaus): General Electric Healthcare.\* Marion Smits—UNRELATED: Grants/Grants Pending: Erasmus MC,\* Coolsingel Foundation\*; Payment for Lectures (including service on Speakers Bureaus): European Society for Magnetic Resonance in Medicine and Biology\*; Travel/Accommodations/Meeting Expenses Unrelated to Activities Listed: Radiological Society of North America, European Congress of Radiology, European Society for Magnetic Resonance in Medicine and Biology. \*Money paid to the institution.

## REFERENCES

1. Stippich C, Rapps N, Dreyhaupt J, et al. **Localizing and lateralizing language in patients with brain tumors: feasibility of routine preoperative functional MR imaging in 81 consecutive patients.** *Radiology* 2007;243:828–36
2. Smits M. **Functional magnetic resonance imaging (fMRI) in brain tumour patients.** *Eur Assoc NeuroOncol Mag* 2012;2:123–28
3. Petrella JR, Shah LM, Harris KM, et al. **Preoperative functional MR imaging localization of language and motor areas: effect on therapeutic decision making in patients with potentially resectable brain tumors.** *Radiology* 2006;240:793–802
4. Knecht S, Dräger B, Deppe M, et al. **Handedness and hemispheric language dominance in healthy humans.** *Brain* 2000;123(pt 12):2512–18
5. Szafarski JP, Binder JR, Possing ET, et al. **Language lateralization in left-handed and ambidextrous people: fMRI data.** *Neurology* 2002;59:238–44
6. Tzourio-Mazoyer NN, Josse G, Crivello F, et al. **Interindividual variability in the hemispheric organization for speech.** *Neuroimage* 2004;21:422–35
7. Dym RJR, Burns JJ, Freeman KK, et al. **Is functional MR imaging assessment of hemispheric language dominance as good as the Wada test? A meta-analysis.** *Radiology* 2011;261:446–55
8. Medina LS, Bernal B, Ruiz J. **Role of functional MR in determining**

**language dominance in epilepsy and nonepilepsy populations: a Bayesian analysis.** *Radiology* 2007;242:94–100

9. Binder JR, Frost JA, Hammeke TA, et al. **Human brain language areas identified by functional magnetic resonance imaging.** *J Neurosci* 1997;17:353–62
10. Hubrich-Ungureanu PP, Kaemmerer NN, Henn FAF, et al. **Lateralized organization of the cerebellum in a silent verbal fluency task: a functional magnetic resonance imaging study in healthy volunteers.** *Neurosci Lett* 2002;319:91–94
11. Frings M, Dimitrova A, Schorn CF, et al. **Cerebellar involvement in verb generation: an fMRI study.** *Neurosci Lett* 2006;409:19–23
12. Smits M, Visch-Brink EG, Schraa-Tam CK, et al. **Functional MR imaging of language processing: an overview of easy-to-implement paradigms for patient care and clinical research.** *Radiographics* 2006;26:S145–58
13. Wise RJ, Chollet F, Hadar U, et al. **Distribution of cortical neural networks involved in word comprehension and word retrieval.** *Brain* 1991;114(pt 4):1803–17
14. Ojemann JG, Ojemann GA, Lettich E. **Cortical stimulation mapping of language cortex by using a verb generation task: effects of learning and comparison to mapping based on object naming.** *J Neurosurg* 2002;97:33–38
15. Bizzi A, Blasi V, Falini A, et al. **Presurgical functional MR imaging of language and motor functions: validation with intraoperative electrocortical mapping.** *Radiology* 2008;248:579–89
16. FitzGerald DB, Cosgrove GR, Ronner S, et al. **Location of language in the cortex: a comparison between functional MR imaging and electrocortical stimulation.** *AJNR Am J Neuroradiol* 1997;18:1529–39
17. Vernooij MW, Smits M, Wielopolski PA, et al. **Fiber density asymmetry of the arcuate fasciculus in relation to functional hemispheric language lateralization in both right- and left-handed healthy subjects: a combined fMRI and DTI study.** *Neuroimage* 2007;35:1064–76
18. Oldfield RC. **The assessment and analysis of handedness: the Edinburgh inventory.** *Neuropsychologia* 1971;9:97–113
19. Friston KJ, Holmes AP, Poline JB, et al. **Analysis of fMRI time-series revisited.** *Neuroimage* 1995;2:45–53
20. Friston KJ, Zarahn E, Josephs O, et al. **Stochastic designs in event-related fMRI.** *Neuroimage* 1999;10:607–19
21. Suarez RO, Whalen S, Nelson AP, et al. **Threshold-independent functional MRI determination of language dominance: a validation study against clinical gold standards.** *Epilepsy Behav* 2009;16:288–97
22. Branco DM, Suarez RO, Whalen S, et al. **Functional MRI of memory in the hippocampus: laterality indices may be more meaningful if calculated from whole voxel distributions.** *Neuroimage* 2006;32:592–602
23. Jansen A, Flöel A, Van Randenborgh J, et al. **Crossed cerebro-cerebellar language dominance.** *Hum Brain Mapp* 2005;24:165–72
24. Abutaleb J. **Neural aspects of second language representation and language control.** *Acta Psychologica* 2008;128:466–78
25. Mariën P, Ackermann H, Adamaszek M, et al. **Consensus paper: language and the cerebellum: an ongoing enigma.** *Cerebellum* 2014;13:386–410
26. O'Halloran CJ, Kinsella GJ, Storey E. **The cerebellum and neuropsychological functioning: a critical review.** *J Clin Exp Neuropsychol* 2012;34:35–56
27. Londei A, D'Ausilio A, Basso D, et al. **Sensory-motor brain network connectivity for speech comprehension.** *Hum Brain Mapp* 2010;31:567–80
28. Ulmer JL, Hacein-Bey L, Mathews VP, et al. **Lesion-induced pseudodominance at functional magnetic resonance imaging: implications for preoperative assessments.** *Neurosurgery* 2004;55:569–79; discussion 580–81
29. Fernández G, de Greiff A, von Oertzen J, et al. **Language mapping in less than 15 minutes: real-time functional MRI during routine clinical investigation.** *Neuroimage* 2001;14:585–94

30. Jones SE, Mahmoud SY, Gonzalez-Martinez J, et al. **Application of a computerized language lateralization index from fMRI by a group of clinical neuroradiologists.** *AJNR Am J Neuroradiol* 2013;34:564–69
31. Gutbrod K, Spring D, Degonda N, et al. **Determination of language dominance: Wada test and fMRI compared using a novel sentence task.** *J Neuroimaging* 2012;22:266–74
32. Jones SE, Mahmoud SY, Phillips MD. **A practical clinical method to quantify language lateralization in fMRI using whole-brain analysis.** *Neuroimage* 2011;54:2937–49
33. Rösler J, Niraula B, Strack V, et al. **Language mapping in healthy volunteers and brain tumor patients with a novel navigated TMS system: evidence of tumor-induced plasticity.** *Clin Neurophysiol* 2014;125:526–36
34. Stufflebeam SM. **Clinical magnetoencephalography for neurosurgery.** *Neurosurg Clin N Am* 2011;22:153–67

# Conscious Sedation versus General Anesthesia during Endovascular Acute Ischemic Stroke Treatment: A Systematic Review and Meta-Analysis

W. Brinjikji, M.H. Murad, A.A. Rabinstein, H.J. Cloft, G. Lanzino, and D.F. Kallmes



## ABSTRACT

**BACKGROUND AND PURPOSE:** A number of studies have suggested that anesthesia type (conscious sedation versus general anesthesia) during intra-arterial treatment for acute ischemic stroke has implications for patient outcomes. We performed a systematic review and meta-analysis of studies comparing the clinical and angiographic outcomes of the 2 anesthesia types.

**MATERIALS AND METHODS:** In March 2014, we conducted a computerized search of MEDLINE and EMBASE for reports on anesthesia and endovascular treatment of acute ischemic stroke. Using random-effects meta-analysis, we evaluated the following outcomes: recanalization rate, good functional outcome (mRS  $\leq 2$ ), asymptomatic and symptomatic intracranial hemorrhage, death, vascular complications, respiratory complications, procedure time, time to groin, and time from symptom onset to recanalization.

**RESULTS:** Nine studies enrolling 1956 patients (814 with general anesthesia and 1142 with conscious sedation) were included. Compared with patients treated by using conscious sedation during stroke intervention, patients undergoing general anesthesia had higher odds of death (OR = 2.59; 95% CI, 1.87–3.58) and respiratory complications (OR = 2.09; 95% CI, 1.36–3.23) and lower odds of good functional outcome (OR = 0.43; 95% CI, 0.35–0.53) and successful angiographic outcome (OR = 0.54; 95% CI, 0.37–0.80). No difference in procedure time ( $P = .28$ ) was seen between the groups. Preintervention NIHSS scores were available from 6 studies; in those, patients receiving general anesthesia had a higher average NIHSS score.

**CONCLUSIONS:** Patients with acute ischemic stroke undergoing intra-arterial therapy may have worse outcomes with general anesthesia compared with conscious sedation. However, the difference in stroke severity at the onset may confound the comparison in the available studies; thus, a randomized trial is necessary to confirm this association.

**ABBREVIATION:** ICH = intracranial hemorrhage

Intra-arterial recanalization for acute ischemic stroke is commonly used in patients with large-vessel occlusion.<sup>1</sup> Timely recanalization of the occluded vessel with either IV-tPA or intra-arterial therapy is essential in preventing neuronal death and improving patient outcome.<sup>2</sup> A number of factors affect patient outcomes following endovascular recanalization, possibly including choice of anesthetic agent during the procedure. Moderate conscious sedation and general anesthesia with intubation are the

2 most commonly used anesthesia techniques for patients with acute ischemic stroke undergoing endovascular recanalization.<sup>3</sup> General anesthesia is often the preferred method due to the perceptions of improved procedural safety and efficacy.<sup>3</sup> However, conscious sedation and local anesthesia allow operators to monitor neurologic status during the procedure and avoid delays in procedure initiation.<sup>4</sup> Furthermore, conscious sedation may be associated with improved hemodynamic stability compared with general anesthesia. Due to the continuing debate regarding anesthesia choices during intra-arterial treatment of acute ischemic stroke, we performed a meta-analysis of studies comparing outcomes of patients with stroke receiving general anesthesia and conscious sedation during the procedures.<sup>5,6</sup>

## MATERIALS AND METHODS

### Literature Search

To identify comparative studies on general anesthesia versus conscious sedation during endovascular treatment of acute ischemic stroke, we searched 3 databases from 1990 to March 2014: Ovid

Received June 11, 2014; accepted after revision September 6.

From the Departments of Radiology (W.B., H.J.C., G.L., D.F.K.), Neurology (A.A.R.), and Neurosurgery (H.J.C., G.L., D.F.K.), and Center for the Science of Healthcare Delivery and the Division of Preventive Medicine (M.H.M.), Mayo Clinic, Rochester, Minnesota.

Please address correspondence to Waleed Brinjikji, MD, 200 1st St SW, Rochester, MN 55905; e-mail: brinjikji.waleed@mayo.edu



Indicates article with supplemental on-line photo.



Evidence-Based Medicine Level 1.

<http://dx.doi.org/10.3174/ajnr.A4159>

MEDLINE, Ovid EMBASE, and the Web of Science. Ovid MEDLINE and Ovid EMBASE use controlled vocabulary. The Web of Science is text word-based but tends to be more current and multidisciplinary. The initial search terms were conscious sedation, general anesthesia, and intracranial embolism and thrombosis or stroke. These were combined with treatment techniques: endovascular, fibrinolytic agents, thromboembolism, catheter, transcatheter, thrombolysis, fibrinolysis, recanalization, embolectomy, or thrombectomy (subject heading available in EMBASE, but not MEDLINE). We also searched references from multiple articles to find any additional studies on anesthesia and outcomes of endovascular treatment of acute ischemic stroke not found in the initial literature search.

Identified studies from the literature search were then further evaluated for inclusion in the meta-analysis. Inclusion criteria were the following: 1) studies comparing outcomes of the 2 groups: general anesthesia and conscious sedation/local anesthesia; 2) studies reporting separate angiographic and clinical outcomes for the general anesthesia and conscious sedation/local anesthesia groups. Exclusion criteria were the following: 1) case reports, 2) studies not separating outcomes by anesthesia type, 3) noncomparative studies (ie, studies with only 1 group: general anesthesia or conscious sedation). Two authors reviewed the articles for inclusion. Following selection of the articles, the data were abstracted by 1 author.

### **Quality Assessment**

Quality assessment of the studies was performed by using the Newcastle-Ottawa Scale. This tool is used for assessing the quality of nonrandomized studies included in systematic reviews and/or meta-analyses. Each study is judged on 8 items categorized into 3 groups: 1) selection of the study groups, 2) comparability of the study groups, and 3) ascertainment of the outcome of interest. One star is awarded for each quality item; 4 stars are the maximum for the selection of groups, 2 stars are the maximum for comparability, and 3 stars are the maximum for ascertainment of outcome. The highest quality studies are awarded up to 9 stars.<sup>7</sup>

### **Outcome Variables**

Good functional outcome, defined as a modified Rankin Scale score of  $\leq 2$  at 90 days following endovascular treatment, was the primary end point of this study. Other studied outcomes included mortality, successful recanalization/angiographic outcome (Thrombolysis in Myocardial Infarction  $\geq 2$  or TICI 2b/3), asymptomatic intracranial hemorrhage (ICH), symptomatic ICH, other vascular complications including dissections and vessel perforations, respiratory complications including respiratory failure and pneumonia, procedure time, time from symptom onset to revascularization, and time from arrival at the hospital to groin puncture.

### **Statistics**

From each study, we extracted a  $2 \times 2$  table for binary outcomes, the mean group sample size, and a measure of variability for continuous outcomes. Random-effects meta-analysis was used for pooling across studies.<sup>8</sup> The  $I^2$  statistic was used to express the proportion of inconsistency that was not attributable to chance.<sup>9</sup>

Meta-analysis results were expressed as odds ratio for binary outcomes and weighted mean difference for continuous outcomes with respective 95% confidence intervals. When assessing continuous outcomes, some studies reported mean values with corresponding SDs, while others reported median values with interquartile ranges. If a median and interquartile range were reported, these were converted to a mean and SD on the basis of the assumption of a log-normal distribution of the original measure. We planned to explore the impact of publication bias by constructing funnel plots and testing their symmetry if a sufficient number of studies ( $>20$ ) were available. Meta-analysis was conducted by using Comprehensive Meta-Analysis, Version 2.2 (Comprehensive Meta-Analysis, Englewood, New Jersey).

Because the study subjects were not randomized by anesthesia type, we were concerned about a lack of similarity between the 2 study groups (ie, patients with worse prognosis receiving 1 of the 2 interventions). Therefore, we planned to conduct metaregression, in which the dependent outcome was the effect size (log of the OR of the primary outcome, the odds of good neurologic outcome), and the explanatory variables (independent variables) were initial stroke severity categorized by the baseline average NIHSS score and the type of anesthesia (general anesthesia versus conscious sedation). Studies were weighted in metaregression by using their precision. The results of the metaregression were presented as an odds ratio adjusted for NIHSS score. Metaregression was conducted by using STATA, Version 12.1 (StataCorp, College Station, Texas). We also performed a sensitivity analysis examining the comparative outcomes, including only those studies that reported baseline NIHSS scores.

## **RESULTS**

### **Literature Search**

One hundred twenty-three articles were found on the initial literature search. Of these, 102 (82.9%) were excluded after reading the abstracts alone because they were not found to be relevant to our study. Of the remaining 21 articles, 3 (2.4%) were excluded because they mixed outcomes of endovascular stroke treatment with other endovascular procedures (ie, stent placement, aneurysm coiling, and so forth); 5 articles (4.1%) were excluded because they only included 1 treatment group; and 4 articles (3.3%) were excluded because they were review articles. In total, 9 articles (7.3%) with 1956 patients (814 with general anesthesia and 1142 with conscious sedation) were included in this study. No studies randomized patients to general anesthesia or conscious sedation. The largest study had 1079 patients (428 with general anesthesia and 651 with conscious sedation), and the smallest study had 66 patients (9 with general anesthesia and 57 with conscious sedation). All studies had at least 7 stars on the Newcastle-Ottawa scale. A summary of included studies is provided in Table 1.

### **Outcomes**

General anesthesia was associated with a lower odds of favorable functional outcome (ie, mRS  $\leq 2$ ) compared with conscious sedation (OR = 0.43; 95% CI, 0.35–0.53;  $P < .01$ ) (Figure). General anesthesia was also associated with a lower odds of successful recanalization (OR = 0.54; 95% CI, 0.37–0.80;  $P < .01$ ). Patients

**Table 1: Studies included in the meta-analysis**

Authors, Year	No. with GA	No. with CS	Type of Endovascular Treatment	Selection	Comparability	Outcome
Abou-Chebl et al, 2014 <sup>28</sup>	196	85	Solitaire stent <sup>a</sup>	★★★★ <sup>b</sup>		★★★
Davis et al, 2012 <sup>12</sup>	48	48	IA tPA and mechanical thrombectomy	★★★★	★	★★★
Hassan et al, 2012 <sup>21</sup>	53	83	Endovascular technique not specified	★★★★		★★★
Jumaa et al, 2010 <sup>17</sup>	53	73	IA tPA and mechanical thrombectomy	★★★★	★	★★★
Langner et al, 2013 <sup>26</sup>	19	105	Mechanical thrombectomy	★★★★	★	★★★
Li et al, 2014 <sup>25</sup>	35	74	Mechanical thrombectomy, IA tPA	★★★★	★	★★★
Nichols et al, 2010 <sup>27</sup>	26	49	IA tPA, low-energy ultrasound	★★★★	★	★★★
Sugg et al, 2010 <sup>30</sup>	9	57	Mechanical thrombectomy	★★★★	★	★★★
Abou-Chebl et al, 2010 <sup>16</sup>	428	651	IA tPA, mechanical thrombectomy, stent	★★★★	★	★★★

**Note:**—GA indicates general anesthesia; CS, conscious sedation; IA, intra-arterial.

<sup>a</sup> Covidien, Irvine, California.

<sup>b</sup> One star is awarded for each quality item; 4 stars are the maximum for selection of groups, 2 stars are the maximum for comparability, and 3 stars are the maximum for ascertainment of outcome.

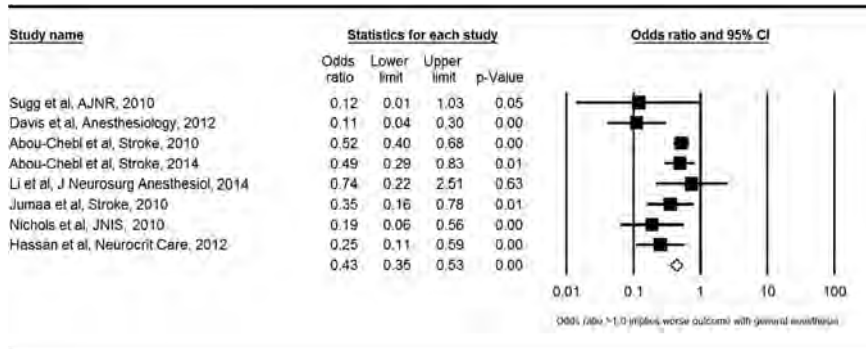


**FIG 1.** Forest plot of meta-analysis results for good functional outcome (mRS ≤ 2).

**Table 2: Meta-analysis results: categoric outcomes**

	OR GA vs CS	95% CI	P Value
Death	2.59	1.87–3.58	<.01
Good functional outcome <sup>a</sup>	0.43	0.35–0.53	<.01
Successful recanalization	0.49	0.33–0.72	<.01
sICH	1.34	0.95–1.87	.09
aICH	1.24	0.94–1.62	.12
Other vascular complications	1.22	0.68–2.18	.5
Respiratory complications	2.09	1.36–3.23	<.01

**Note:**—aICH indicates asymptomatic intracranial hemorrhage; sICH, symptomatic intracranial hemorrhage.

<sup>a</sup> Modified Rankin scale score of ≤2.

receiving general anesthesia had higher odds of mortality (OR = 2.59; 95% CI, 1.87–3.58;  $P < .01$ ) and respiratory complications (OR = 2.09; 95% CI, 1.36–3.23;  $P < .01$ ). There was no significant difference in the odds of asymptomatic ICH (OR = 1.24; 95% CI, 0.94–1.62;  $P = .12$ ), symptomatic ICH (OR = 1.34; 95% CI, 0.95–1.87;  $P = .09$ ), or other vascular complications (OR = 1.22; 95% CI, 0.68–2.18;  $P = .50$ ) between groups. These findings are summarized in Table 2. Forest plots for other measures are included in On-line Figs 1–6.

Mean time to groin was 136 minutes 20 seconds ± 54 minutes for general anesthesia compared with 117 minutes 20 seconds ± 56 minutes 20 seconds for conscious sedation ( $P = .24$ ). Mean procedure time was 104 minutes 20 seconds for general anesthesia compared with 89 minutes ± 44 seconds for conscious sedation ( $P = .28$ ). Mean time from symptom onset to revascularization was 329 minutes 43 seconds ± 173 minutes for general anesthesia compared with 354 minutes 51 seconds ± 265 minutes for conscious sedation ( $P = .17$ ).

**Study Heterogeneity**

$I^2$  values were <50% for the following outcomes: asymptomatic ICH ( $I^2 = 41\%$ ), death ( $I^2 = 0\%$ ), other vascular complications ( $I^2 = 8\%$ ), recanalization success ( $I^2 = 11\%$ ), respiratory complications ( $I^2 = 0\%$ ), and symptomatic ICH ( $I^2 = 0\%$ ).  $I^2$  values were >50% (indicating substantial heterogeneity) for the following outcomes: mRS ≤ 2 ( $I^2 = 55\%$ ), time to revascularization ( $I^2 = 60\%$ ), time to groin puncture ( $I^2 = 83\%$ ), and procedure time ( $I^2 = 91\%$ ).

**Metaregression and Publication Bias**

Adjusting for NIHSS score by using metaregression for the main outcome (odds of having good functional outcomes) yielded an odds ratio of 0.38; which was similar to the unadjusted estimate of 0.43; however, the 95% CI became statistically insignificant (0.12, 1.22). The number of included studies in this analysis (with an available NIHSS score) was only 6; therefore, this adjustment is not reliable and likely underpowered.

Evaluation of publication bias was not possible due to the small number of included studies.

**Sensitivity Analysis**

Outcomes from our sensitivity analysis, including only those studies that reported baseline NIHSS scores, are provided in Table 3. Similar to the results in the overall analysis, in the sensitivity analysis, general anesthesia was associated with higher odds of death (OR = 2.22; 95% CI, 1.54–3.20) and respiratory complications (OR = 2.03; 95% CI, 1.12–3.68). General anesthesia was associated with lower odds of recanalization (OR = 0.48; 95% CI, 0.30–0.76) and lower odds of good neurologic outcome (OR = 0.38; 95% CI, 0.25–0.60). No differences in procedure time ( $P = .69$ ), time to groin ( $P = .77$ ), or time to revascularization ( $P = 1.00$ ) were seen.

**DISCUSSION**

Our meta-analysis demonstrated that patients receiving conscious sedation had higher rates of good functional outcome and recanalization and decreased rates of mortality and respiratory complications compared with those receiving general anesthesia. No difference in procedure times, time to recanalization, or time

**Table 3: Sensitivity analysis excluding studies without baseline NIHSS data: categorical outcomes**

	No. of Studies	OR GA vs CS	95% CI	P Value	I <sup>2</sup>
alCH	2	1.17	0.89–1.54	.27	NA
Death	5	2.22	1.54–3.20	.00	0
mRS ≤ 2	6	0.38	0.25–0.60	.00	56
Other vasc comp	3	1.66	0.56–4.93	.36	37
Recan (TIMI ≥ 2)	4	0.55	0.35–0.87	.01	0
Resp comp	3	2.03	1.12–3.68	.02	0
sICH	5	1.21	0.83–1.75	.32	0

**Note:**—NA indicates not applicable; vasc comp, vascular complications; Recan, recanalization; Resp comp, respiratory complications; TIMI, Thrombolysis in Myocardial Infarction; GA, general anesthesia; CS, conscious sedation; alCH, asymptomatic intracranial hemorrhage; sICH, symptomatic intracranial hemorrhage.

to groin was seen between groups. Rates of ICH and vascular complications were similar between the 2 groups as well. Following adjustment for the baseline NIHSS score, general anesthesia was associated with lower, but not statistically significant, odds of good functional outcome. Because only 6 of the 9 studies in this meta-analysis included information on the baseline NIHSS score, the lack of significance of the association in the adjusted analysis may have been related to the decreased statistical power. Given the superior outcomes of patients receiving conscious sedation compared with those receiving general anesthesia, these data suggest that conscious sedation should generally be the anesthesia technique of choice during endovascular recanalization for treatment of acute ischemic stroke.

A number of factors likely contributed to the higher morbidity and mortality rates seen in the general anesthesia group. Inhalational anesthetic agents are associated with a higher risk of cerebral hypoperfusion and increased ischemic injury.<sup>10,11</sup> Davis et al<sup>12</sup> found that patients with ischemic stroke receiving endovascular recanalization had higher rates of intraprocedural hypotension with general anesthesia than with conscious sedation. Inhalational anesthetic agents, such as isoflurane, have been found to steal flow from ischemic areas with poor autoregulation by inducing cerebral vasodilation.<sup>10,13</sup> Induction and recovery phases of general anesthesia are often associated with significant hemodynamic changes (hypotension and rapid blood pressure fluctuations) that could exacerbate ischemic injury.<sup>14</sup> It is possible that the poor autoregulation and higher rates of intraprocedural hypotension with general anesthesia contribute to the markedly lower recanalization rates compared with conscious sedation seen in this meta-analysis.

General anesthesia remains widely used for intra-arterial treatment of acute ischemic stroke. The main argument in favor of general anesthesia is decreased intraprocedural patient movement.<sup>5</sup> Patients who are awake during endovascular treatment may move during endovascular therapy, which could compromise the safety and efficacy of the intervention.<sup>15</sup> Patient movement during the procedure can lead to wire perforation, resulting in intracranial hemorrhage or vascular injury in the form of dissection. However, no studies have demonstrated that conscious sedation is associated with higher rates of wire perforation, dissection, or intracranial hemorrhage than general anesthesia.<sup>16,17</sup> Many practitioners cite perceived procedural safety, specifically avoiding emergent endotracheal intubation, as an advantage of general anesthesia over conscious sedation.<sup>3</sup>

Emergent intubation is associated with various complications including airway trauma, aspiration, and death.<sup>18,19</sup> However, many studies have suggested that the rate of emergent endotracheal intubation among patients with conscious sedation receiving neuroendovascular therapies is very low.<sup>17,20–22</sup> The findings of this meta-analysis that conscious sedation was actually associated with higher rates of recanalization and no increase in intraprocedural complications should assuage concerns about the perceived disadvantages of conscious sedation for the interventionalist.

In contrast to general anesthesia, conscious sedation allows intraprocedural monitoring of neurologic deficits, allowing operators to adjust the treatment strategy if needed.<sup>23</sup> Dynamic cerebral autoregulation is preserved with midazolam sedation, resulting in decreased volatility in intraprocedural cerebral perfusion.<sup>24</sup> While some studies have found that conscious sedation is associated with more rapid reperfusion, our study found no difference in procedure time, time to groin, or time from symptom onset to reperfusion between the general anesthesia and conscious sedation groups.<sup>25,26</sup>

Most previously published studies have demonstrated superior outcomes for patients undergoing endovascular recanalization therapy receiving conscious sedation relative to those receiving general anesthesia. General anesthesia is generally associated with higher rates of poor neurologic outcome at 90 days and higher mortality compared with conscious sedation.<sup>12,16,17,25,27</sup> The use of general anesthesia was independently associated with worse outcomes despite comparable rates of recanalization among patients included in the North American SOLITAIRE Acute Stent Retriever Registry.<sup>28</sup> One recently published study demonstrated that >80% of patients undergoing mechanical thrombectomy could be safely treated while under conscious sedation, with high rates of good neurologic outcome.<sup>29</sup> These studies, along with the findings from our study, suggest that conscious sedation is safe and effective in the setting of mechanical thrombectomy for acute ischemic stroke and should be preferred when deemed feasible.

### Limitations

This study has several limitations. None of the available studies were randomized by anesthesia type. In general, average baseline NIHSS scores were higher for patients receiving general anesthesia than for those receiving conscious sedation. Adjustment for this variable was likely unreliable because of the small number of available studies with this information. Worse initial stroke severity could contribute to the higher rates of posttreatment morbidity and mortality seen in the general anesthesia group. However, the odds ratios found in this meta-analysis were not marginal, which strongly suggests that conscious sedation does lead to improved outcomes. Still, the higher baseline NIHSS scores underscore the possibility of selection bias because it is likely that patients with more severe strokes received general anesthesia or were intubated before the procedure due to an inability to preserve airway patency. We did not stratify outcomes on the basis of stroke location (anterior/posterior circulation) or initial ASPECTS.

The site of vascular occlusion is another determinant of outcomes and a potential confounder in this analysis. For example, carotid occlusions, carotid bifurcation occlusions, and basilar ar-

tery occlusions typically have worse outcomes. It is possible that the lower recanalization rates with general anesthesia seen in this meta-analysis were the result of a higher proportion of more challenging vascular occlusions in the general anesthesia group. Although some of the studies included in our meta-analysis represented earlier experience with endovascular stroke therapy and may have lower rates of recanalization and higher risk of complications than those in current practice, this caveat should apply similarly to both anesthesia types. We were not able to evaluate the presence of publication bias because our study incorporated 9 studies and measures of publication bias are only reliable if  $\geq 10$  studies are included in a meta-analysis.

## CONCLUSIONS

This systematic review and meta-analysis demonstrates that patients with acute stroke receiving conscious sedation had significantly lower rates of morbidity and mortality and higher recanalization rates compared with patients receiving general anesthesia. However, these findings are based solely on studies that did not randomize patients by anesthesia type; differences in baseline patient characteristics, such as stroke severity, may confound the association. Therefore, a randomized controlled trial is needed to confirm whether general anesthesia is associated with higher rates of complications and impaired neurologic outcome in patients receiving endovascular therapy for acute ischemic stroke. In the meantime, when possible, it is reasonable to favor conscious sedation over general anesthesia during acute endovascular stroke therapy on the basis of available collective evidence.

Disclosures: Giuseppe Lanzino—UNRELATED: Consultancy: Covidien,\* Codman/Johnson & Johnson,\* Edge Therapeutics.\* David F. Kallmes—UNRELATED: Board Membership: GE Healthcare (advisory board); Consultancy: ev3.\* Comments: planning and implementing clinical trials; Grants/Grants Pending: ev3,\* MicroVention,\* Sequent Medical,\* Surmodics.\* Codman/Johnson & Johnson,\* Comments: preclinical and clinical research; Royalties: University of Virginia Patent Foundation (spine fusion). \*Money paid to the institution.

## REFERENCES

1. Brinjikji W, Rabinstein AA, Kallmes DF, et al. **Patient outcomes with endovascular embolectomy therapy for acute ischemic stroke: a study of the National Inpatient Sample: 2006 to 2008.** *Stroke* 2011; 42:1648–52
2. Saver JL. **Time is brain—quantified.** *Stroke* 2006;37:263–66
3. McDonagh DL, Olson DM, Kalia JS, et al. **Anesthesia and sedation practices among neurointerventionalists during acute ischemic stroke endovascular therapy.** *Front Neurol* 2010;1:118
4. Molina CA, Selim MH. **General or local anesthesia during endovascular procedures: sailing quiet in the darkness or fast under a daylight storm.** *Stroke* 2010;41:2720–21
5. Brekenfeld C, Mattle HP, Schroth G. **General is better than local anesthesia during endovascular procedures.** *Stroke* 2010;41:2716–17
6. Gupta R. **Local is better than general anesthesia during endovascular acute stroke interventions.** *Stroke* 2010;41:2718–19
7. Deeks JJ, Dinnes J, D'Amico R, et al. **Evaluating non-randomised intervention studies.** *Health Technol Assess* 2003;7:iii–x, 1–173
8. DerSimonian R, Laird N. **Meta-analysis in clinical trials.** *Control Clin Trials* 1986;7:177–88
9. Higgins JP, Thompson SG, Deeks JJ, et al. **Measuring inconsistency in meta-analyses.** *BMJ* 2003;327:557–60
10. Messick JM Jr, Newberg LA, Nugent M, et al. **Principles of neuroan-**

- esthesia for the nonneurosurgical patient with CNS pathophysiology. *Anesth Analg* 1985;64:143–74
11. Steen PA. **Inhalational versus intravenous anesthesia: cerebral effects.** *Acta Anaesthesiol Scand Suppl* 1982;75:32–35
12. Davis MJ, Menon BK, Baghirzada LB, et al. **Anesthetic management and outcome in patients during endovascular therapy for acute stroke.** *Anesthesiology* 2012;116:396–405
13. Petersen KD, Landsfeldt U, Cold GE, et al. **Intracranial pressure and cerebral hemodynamic in patients with cerebral tumors: a randomized prospective study of patients subjected to craniotomy in propofol-fentanyl, isoflurane-fentanyl, or sevoflurane-fentanyl anesthesia.** *Anesthesiology* 2003;98:329–36
14. Rosenberg M, Weaver J. **General anesthesia.** *Anesth Prog* 1991;38: 172–86
15. Rossitti S, Pfister M. **3D road-mapping in the endovascular treatment of cerebral aneurysms and arteriovenous malformations.** *Interv Neuroradiol* 2009;15:283–90
16. Abou-Chebl A, Lin R, Hussain MS, et al. **Conscious sedation versus general anesthesia during endovascular therapy for acute anterior circulation stroke: preliminary results from a retrospective, multicenter study.** *Stroke* 2010;41:1175–79
17. Jumaa MA, Zhang F, Ruiz-Ares G, et al. **Comparison of safety and clinical and radiographic outcomes in endovascular acute stroke therapy for proximal middle cerebral artery occlusion with intubation and general anesthesia versus the nonintubated state.** *Stroke* 2010;41:1180–84
18. Jabre P, Avenel A, Combes X, et al. **Morbidity related to emergency endotracheal intubation: a substudy of the KETamine SEDation trial.** *Resuscitation* 2011;82:517–22
19. Li J, Murphy-Lavoie H, Bugas C, et al. **Complications of emergency intubation with and without paralysis.** *Am J Emerg Med* 1999; 17:141–43
20. Chaczuk AJ, Ogilvy CS, Snyder KV, et al. **Elective stenting for intracranial stenosis under conscious sedation.** *Neurosurgery* 2010;67: 1189–93; discussion 1194
21. Hassan AE, Chaudhry SA, Zacharatos H, et al. **Increased rate of aspiration pneumonia and poor discharge outcome among acute ischemic stroke patients following intubation for endovascular treatment.** *Neurocrit Care* 2012;16:246–50
22. Qureshi AI, Suri MF, Khan J, et al. **Endovascular treatment of intracranial aneurysms by using Guglielmi detachable coils in awake patients: safety and feasibility.** *J Neurosurg* 2001;94:880–85
23. Abou-Chebl A, Krieger DW, Bajzer CT, et al. **Intracranial angioplasty and stenting in the awake patient.** *J Neuroimaging* 2006; 16:216–23
24. Ogawa Y, Iwasaki K, Aoki K, et al. **The different effects of midazolam and propofol sedation on dynamic cerebral autoregulation.** *Anesth Analg* 2010;111:1279–84
25. Li F, Deshaies EM, Singla A, et al. **Impact of anesthesia on mortality during endovascular clot removal for acute ischemic stroke.** *J Neurosurg Anesthesiol* 2014;26:286–90
26. Langner S, Khaw AV, Fretwurst T, et al. **Endovascular treatment of acute ischemic stroke under conscious sedation compared to general anesthesia: safety, feasibility and clinical and radiological outcome [in German].** *Rofo* 2013;185:320–27
27. Nichols C, Carrozzella J, Yeatts S, et al. **Is periprocedural sedation during acute stroke therapy associated with poorer functional outcomes?** *J Neurointerv Surg* 2010;2:67–70
28. Abou-Chebl A, Zaidat OO, Castonguay AC, et al. **North American SOLITAIRE Stent-Retriever Acute Stroke Registry: choice of anesthesia and outcomes.** *Stroke* 2014;45:1396–401
29. Soize S, Kadziolka K, Estrade L, et al. **Mechanical thrombectomy in acute stroke: prospective pilot trial of the Solitaire FR device while under conscious sedation.** *AJNR Am J Neuroradiol* 2013;34:360–65
30. Sugg RM, Jackson AS, Holloway W, et al. **Is mechanical embolectomy performed in nonanesthetized patients effective?** *AJNR Am J Neuroradiol* 2010;31:1533–35

# The Computational Fluid Dynamics Rupture Challenge 2013— Phase I: Prediction of Rupture Status in Intracranial Aneurysms

G. Janiga, P. Berg, S. Sugiyama, K. Kono, and D.A. Steinman



## ABSTRACT

**BACKGROUND AND PURPOSE:** Rupture risk assessment for intracranial aneurysms remains challenging, and risk factors, including wall shear stress, are discussed controversially. The primary purpose of the presented challenge was to determine how consistently aneurysm rupture status and rupture site could be identified on the basis of computational fluid dynamics.

**MATERIALS AND METHODS:** Two geometrically similar MCA aneurysms were selected, 1 ruptured, 1 unruptured. Participating computational fluid dynamics groups were blinded as to which case was ruptured. Participants were provided with digitally segmented lumen geometries and, for this phase of the challenge, were free to choose their own flow rates, blood rheologies, and so forth. Participants were asked to report which case had ruptured and the likely site of rupture. In parallel, lumen geometries were provided to a group of neurosurgeons for their predictions of rupture status and site.

**RESULTS:** Of 26 participating computational fluid dynamics groups, 21 (81%) correctly identified the ruptured case. Although the known rupture site was associated with low and oscillatory wall shear stress, most groups identified other sites, some of which also experienced low and oscillatory shear. Of the 43 participating neurosurgeons, 39 (91%) identified the ruptured case. None correctly identified the rupture site.

**CONCLUSIONS:** Geometric or hemodynamic considerations favor identification of rupture status; however, retrospective identification of the rupture site remains a challenge for both engineers and clinicians. A more precise understanding of the hemodynamic factors involved in aneurysm wall pathology is likely required for computational fluid dynamics to add value to current clinical decision-making regarding rupture risk.

**ABBREVIATIONS:** CFD = computational fluid dynamics; OSI = oscillatory shear index; Re = Reynolds; RRT = relative residence time; TAWSS = temporal-averaged wall shear stress; WSS = wall shear stress

In case of a weakened cerebral vasculature, dilations of the vessel walls may form. It has been estimated that such intracranial aneurysms are present in approximately 2%–5% of the Western

population.<sup>1,2</sup> Slightly <1% of these aneurysms rupture annually, but with mostly severe consequences.<sup>3</sup> The mortality rate is up to 40%, and even if treatment were available within hours, irreversible disabilities may remain afterward.<sup>4,5</sup>

However, if aneurysms are detected incidentally, the attending physician needs to suggest to the patient whether a treatment is necessary or a repeated observation is the best choice. Especially in complex case scenarios, the risk that treatment complications occur could be even higher than the potential risk of an aneurysm rupture itself. Therefore, any reliable assistance that can support the physician's therapy planning can improve the outcome for the patient.

During the past years, there has been success in using computational fluid dynamics (CFD) to predict intracranial aneurysm rupture status on the basis of a nominal relationship between local hemodynamics (notably wall shear stress, [WSS]) and aneurysmal wall remodeling and degradation.<sup>6–9</sup> However, the retrospective prediction of rupture status (and, by extension, the prospective prediction of rupture risk) in intracranial aneurysms is

Received March 7, 2014; accepted after revision September 9.

From the Department of Fluid Dynamics and Technical Flows (G.J., P.B.), University of Magdeburg, Magdeburg, Germany; Department of Neurosurgery (S.S.), Tohoku University Graduate School of Medicine, Miyagi, Japan; Department of Neurosurgery (K.K.), Wakayama Rosai Hospital, Wakayama, Japan; and Department of Mechanical and Industrial Engineering (D.A.S.), University of Toronto, Toronto, Ontario, Canada.

This work was partly funded by the Federal Ministry of Education and Research in Germany within the Research Campus STIMULATE under grant number 03FO16102A.

P.B. was supported by the International Max Planck Research School Magdeburg. D.A.S. was supported by a MidCareer Investigator award from the Heart and Stroke Foundation of Ontario.

Please address correspondence to Gábor Janiga, PhD, Laboratory of Fluid Dynamics and Technical Flows, University of Magdeburg "Otto von Guericke," Germany, Universitätsplatz 2, D-39106 Magdeburg, Germany; e-mail: janiga@ovgu.de

Indicates open access to non-subscribers at [www.ajnr.org](http://www.ajnr.org)

Indicates article with supplemental on-line tables.

Indicates article with supplemental on-line photo.

<http://dx.doi.org/10.3174/ajnr.A4157>

controversially discussed in the literature. Xiang et al<sup>10</sup> found that rupture status correlated with significantly lower WSS and a higher oscillatory shear index (OSI). In contrast, Cebal et al<sup>11</sup> found that high maximum WSS and concentrated impingement regions might be responsible for an aneurysm rupture. In both studies, >100 intracranial aneurysms were investigated, and the authors tried to find correlations between hemodynamic or morphologic parameters and the known rupture status. Both studies agreed that ruptured aneurysms present complex flow structures and concentrated inflow. Recently, Meng et al<sup>12</sup> and Xiang et al<sup>13</sup> published a 2-part review summarizing the various criteria for rupture status predictions and introducing a hypothesis that both high and low WSS might lead to aneurysm rupture.

In the present study, we wanted to produce a snapshot of whether engineering groups are able to predict the event of an aneurysm rupture. Two of the authors (G.J. and D.A.S.) decided to propose a new computational challenge addressing 2 main questions: First, can an aneurysm rupture be predicted by using CFD? Second, along the lines of the previous American Society of Mechanical Engineering aneurysm CFD challenge,<sup>14</sup> how broad is the variability of the different solution strategies used for the computations?

In Phase I, the participants were asked to predict which of the 2 provided aneurysms was ruptured and where the rupture site was located. The study was completely blinded; none of the CFD participants had information about the cases, and the source of the data was not communicated. For the second phase, participants were provided with prescribed viscosity and patient-specific mean velocity boundary conditions and were asked to repeat the simulations to separate solution variations from boundary condition variations. In the current work, only Phase I of this challenge and the corresponding results are presented. The variability of the CFD solutions is discussed in a complementary article.<sup>15</sup>

## MATERIALS AND METHODS

### Case Details

One of the major difficulties was to find unpublished appropriate datasets in which the rupture site is known. One of the authors (S.S.) was able to provide 2 cases: an unruptured aneurysm with MRA examination every 6 months during 5 years and a ruptured one with a documented site of rupture. They were chosen on the basis of similar geometric characteristics of the MCA segments. The 2 intracranial aneurysms that were part of this rupture challenge were both located at the left M1 segment. On-line Table 1 summarizes the characteristics of both cases, which were not provided to participating CFD groups.

**Clinical Presentation of Case 1.** A 77-year-old female patient underwent a medical checkup of the brain, and MR angiography revealed an unruptured aneurysm (approximately 10 mm) at the bifurcation of the left middle cerebral artery. Thereafter, the patient was followed up by MR angiography at 6-month intervals. Gradual growth of the aneurysm was observed during a 5-year follow-up; its form changed from spheric to irregular shape. Coil embolization was performed, considering the risk of rupture.

**Clinical Presentation of Case 2.** The chief symptom of the case 2 patient was sudden headache. CT examination determined the diagnosis of an SAH (Hunt and Kosnik grade II/World Federation

of Neurosurgical Societies grade I). During the neck clipping surgery, the aneurysm was completely exposed except for the ruptured site, which was covered with a thick fibrin cap. The fibrin cap was removed gradually with much caution, but accidentally, intraoperative rupture occurred. Fig 1A shows an image acquired during the intervention, with the rupture bleed clearly visible. Fig 1B shows the reconstructed aneurysm model in a lateral view to visualize the nominal rupture site.

### Vascular Reconstruction

The image acquisition was performed by using 3D digital subtraction angiography. Digital segmentation was performed in Magdeburg, Germany, to fix the computational geometry for all participants.<sup>16</sup> A neuroradiologist reviewed the virtual geometries afterward to check the plausibility of the reconstructed shapes. The obtained surface geometries were provided to the participants as surface triangulation mesh files. On-line Fig 1 shows the 2 investigated cases.

### Participating Groups

The first phase of the CFD Rupture Challenge 2013 started on July 1, and all groups that were willing to participate had the opportunity to submit the requested data until August 23. The complete announcement can be accessed on [http://www.ovgu.de/isut/LSS/CFD/CFD\\_Challenge.html](http://www.ovgu.de/isut/LSS/CFD/CFD_Challenge.html). More than 30 groups from academia and industry accepted the challenge and asked for the reconstructed surface geometries. Ultimately, 26 submitted a short abstract describing the details of their computations and their rupture predictions. They were from 15 countries and 4 different continents; therefore, the challenge indeed represented a worldwide snapshot in computational hemodynamics of intracranial aneurysms. The participating groups are listed in On-line Table 2.

### CFD Methods

Often in CFD challenges, very strict conditions are provided (see, eg, Steinman et al<sup>14</sup>) to test the variability of the solution in the absence of other sources of measurement variability. However, because a variety of rupture-status-predicting approaches exist throughout the literature, we decided in advance to provide the surface models of the intracranial aneurysms exclusively. Therefore, each group had the freedom to choose any desired volume mesh with arbitrary types of elements and resolution, flow/velocity boundary conditions, solver methodology, blood rheology, and so forth. With this flexibility, the participants were asked solely to report which of the 2 cases had ruptured and where the site of rupture was located.

Most the simulations (16/26) were performed by using commercial CFD solvers, but open-source and in-house codes were also applied. Ten groups decided to use steady-state computations; 14 groups used unsteady simulations for their predictions, while 2 groups performed both. The unsteady computations were performed by using various time-steps in the range of  $\Delta t = 1 \times 10^{-5}$  seconds to  $5 \times 10^{-3}$  seconds (ie, 100,000 down to 200 time-steps per cardiac cycle) with a median of  $7.5 \times 10^{-4}$  seconds (~1300 steps per cardiac cycle). The reported mesh sizes were in the range of 283,000 to 17.97 million linear elements (median, 2.1 million). These figures included 3 groups that used quadratic tet-

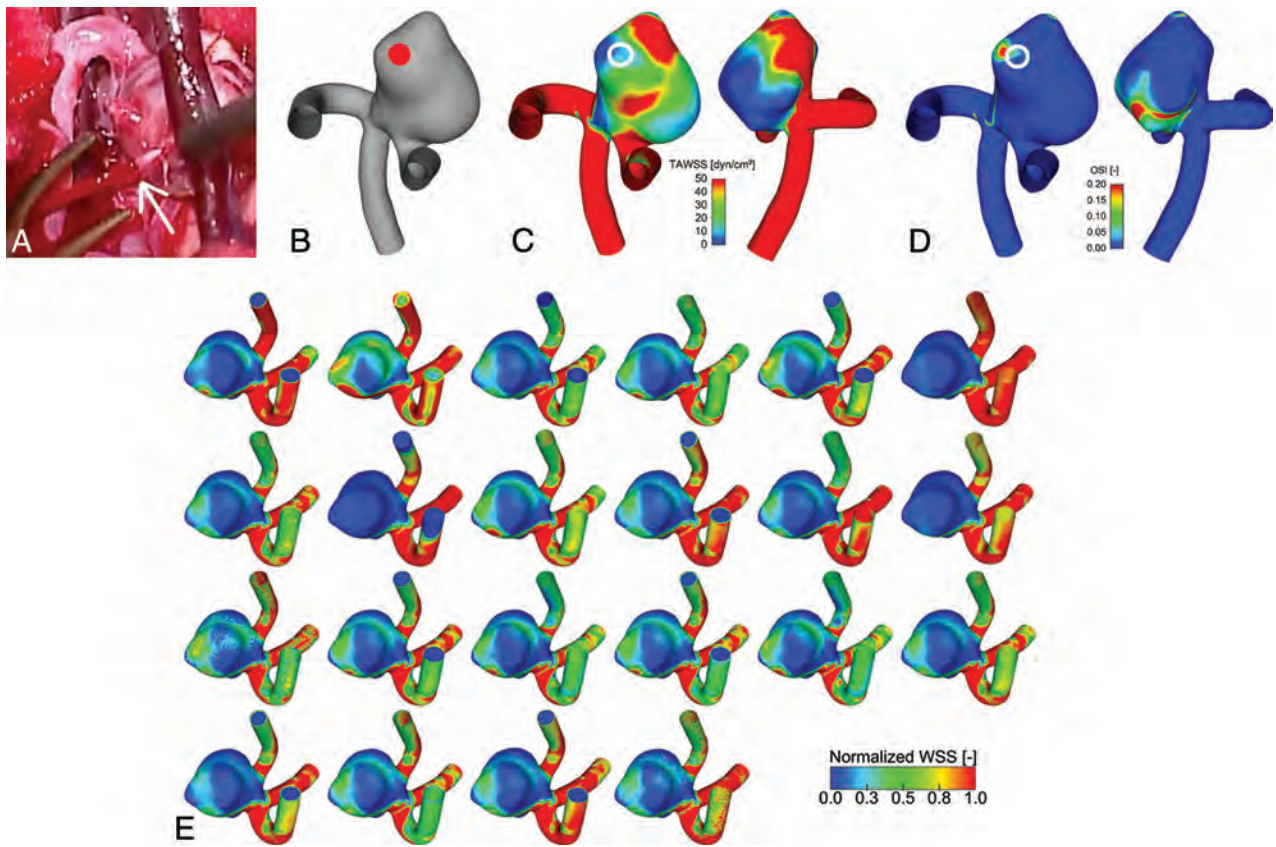


**FIG 1.** A, Live image acquired during open surgery showing the rupture that occurred in case 2. The *white arrow* indicates the rupture site from which blood is streaming. B, Reconstructed surface model of case 2 indicating the ruptured site. C, Temporal averaged wall shear stress. D, Oscillatory shear index from 1 representative group, in 2 opposite perspectives. The site of rupture is indicated by a *white circle*. A low shear and elevated oscillating shear area are present. E, Sagittal view of the normalized wall shear stress distribution in the ruptured case 2 predicted by 22 groups with different simulation settings. Although most of the solutions qualitatively agree, considerable differences in the shear patterns are visible, depending on the type of simulation.

rahedral elements, in which case their number of elements was multiplied by 8 to indicate the effective number of linear elements. Mesh-dependency studies were reported by 5 groups.

As a preparation of the hemodynamic simulation, 7 groups extruded the inlet. Sixteen groups imposed a uniform (plug) velocity profile at the inlet of the computational domain, while 7 groups used Poiseuille (parabolic) velocity profiles and 3 groups used Womersley profiles. Nineteen groups reported their chosen flow rates, inlet velocities, or Reynolds (Re) numbers. Most applied cycle-average flow rates ranging from 0.9 to 11.36 mL/s with a median of 3.5 mL/s. The corresponding inlet velocities were between 0.25 and 1.51 m/s (median, 0.61 m/s) with the minimum/maximum/median Re numbers of 134/815/326. Unrealistic values were also reported (eg, Reynolds number, 1; inlet velocity, 10 m/s). The corresponding patient-specific flow rates were provided in the second phase of the CFD challenge. The cycle-averaged flow rates were 1.76 mL/s for case 1 and 2.5 mL/s for case 2, whereas the peak systolic flow rates were 2.61 and 3.88 mL/s, respectively. See the Phase II study<sup>15</sup> for further details regarding the flow measurements.

Regarding the outlet boundary condition, nearly one-half ( $n = 12$ ) defined zero pressure at all outlets. Another 12 groups applied an explicit flow splitting through the 2 outlets (eg, 50–50, or based on Murray's law). Only 2 groups implemented a 3-element Windkessel model for the downstream microvasculature.

Most of the participants ( $n = 18$ ) assumed blood to be an incompressible Newtonian fluid, with a dynamic viscosity ranging from 3.5 to 4.01 mPa · s (median, 4 mPa · s). The other groups described the shear dependency of blood with a Carreau-Yasuda, Cross, or power law model. The survey of all abstracts revealed that a wide variety of approaches was chosen; therefore, the field of CFD was highly represented.

#### **Prediction of Rupture Status and Rupture Site**

Various criteria were selected for the rupture-status assessment and, in consequence, the prediction of the rupture site. The most common variable was temporal-averaged wall shear stress (TAWSS) or just WSS in case of steady computations, but in some predictions, uncommon criteria (eg, the maximum velocity at the ostium) were selected. A few groups applied a single criterion for their prediction, while most combined 2 or 3 criteria simultaneously. The parameters that were used to predict the explicit rupture site are summarized in the Table. Redundant variables were also selected (ie, high relative residence time [RRT] is a direct consequence of low WSS [and high OSI]).<sup>17</sup>

#### **Wall Shear Stress Computation**

In addition to the rupture prediction, all participants were asked to submit their solution of the 3D TAWSS distribution. There-

fore, the variability of the WSS computation could be assessed directly. Another purpose was to ensure that the participating groups had actually performed the simulations that informed their prediction of rupture status and site. The submitted WSS distributions have shown very different maximum values, possibly due to the different near-wall resolutions but more likely because of the very different flow rates applied at the inlet. Because the results could not be compared dimensionally, each dataset was cropped at a chosen location of the parent artery and the calculated WSS field was normalized by the maximum value in the sac, to compare the relative qualitative distributions of WSS.

### Neurosurgeon Challenge

One of the authors (K.K.), who performs endovascular treatments, open skull surgery, and CFD simulations on cerebral aneurysms, thought that it would be interesting to know the prediction of the ruptured aneurysm and the rupture site by neurosurgeons versus computer simulations. A single-page questionnaire (On-line Fig 3) was created providing only 3D images of the 2 aneurysms in 4 different angles. The questionnaire included the following: maximum size, neck size, height, diameters of the aneurysm in 3 axes, and size of the parent arteries. No other information, including the patient data, risk factors, and treatments

### Hemodynamic parameters that were used to predict the rupture site after the ruptured case was selected

No. of Parameters	Parameter	No. of Groups
1	Low (TA)WSS	6
	High (TA)WSS	3
	High pressure	1
	Maximum velocity	1
2	Low (TA)WSS, high pressure	3
	Low (TA)WSS, high OSI	3
	High (TA)WSS, pressure gradient	2
	Low TAWSS, complex flow	1
	High TAWSS, complex flow	1
	High TAWSS, direct impingement	1
3	Low TAWSS, high OSI, high RRT	1
	TAWSS distribution, complex flow, flow diversion	1
	Direct impingement, pressure gradient, high WSS	1

Note.—TAWSS indicates time-averaged WSS values; (TA)WSS, both steady-state as well as time-dependent results.

presented in On-line Table 1, was available. As noted above, both aneurysms had been carefully selected in advance to have comparable dimensions. K.K. asked 43 neurosurgeons in Japan to predict the ruptured aneurysm and the rupture site using the questionnaire. Additionally, they were asked to report the years of experience as a neurosurgeon and the reasons for the prediction of the ruptured aneurysm and the rupture point. The questionnaire had been completed before the CFD simulations were performed and the ruptured case identified. Thus, this questionnaire was performed in a double-blinded fashion.

## RESULTS

### Prediction of Rupture Status and Rupture Site

Regarding the challenge in Phase I, 4 groups predicted rupture for case 1, 21 groups chose case 2, and 1 group was unsure and therefore did not contribute any predictions. The ruptured aneurysm was case 2 as described above, so most, 21 of 26 groups (81%), predicted the ruptured aneurysm correctly. As illustrated in Fig 2, the predictions of the site of rupture for case 1 concentrated on 2 locations. Three of the 4 groups decided that the impingement zone had the highest probability of being the rupture site (B, blue). High WSS and an elevated pressure gradient were associated with this area. Only 1 group suggested low WSS at the dome of the first aneurysm to be responsible for the rupture (A, green). A broader variability was present for (the ruptured) case 2. Here, the majority ( $n = 10$ ) derived from their computations that the rupture occurred at the small bleb, which was located at the dome of case 2 (C, blue) and exposed to low WSS and elevated pressure. The second highest number of predictions picked the neck region that was aligned with the entering flow jet (F, red). For all 4 of those groups, the decision was based on high WSS, whereby 2 groups added the pressure gradient as a criterion for rupture. Another 4 groups associated the site of rupture with areas between the neck and dome of the aneurysm (E, green, and G, purple). They made their choice on the basis of areas of low WSS and high OSI, whereby multiple spots with high oscillatory shear were identified (Fig 1D). Two more groups selected the impingement zone where the entering flow jet is directed to the aneurysm wall (D, cyan). Finally, 1 group chose the end of the parent artery

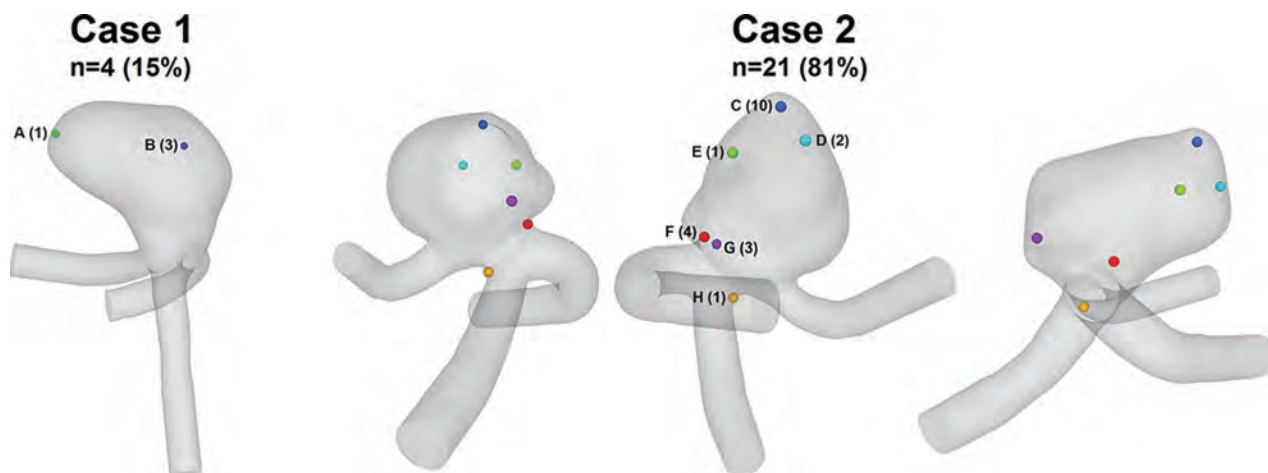


FIG 2. Sites of rupture predicted by the participating groups for case 1 and case 2 (3 perspectives). From the 26 submissions, 4 chose case 1 and 21 decided that case 2 was ruptured. One group was unsure and declined to provide a decision.

because the highest velocities were present due to the smallest vessel diameter (*H*, orange). However, after we reviewed the submitted abstract of this particular group, the results can be classified as unrealistic (peak velocity as rupture criterion; peak-systolic inflow velocity of 10 m/s for both cases).

Throughout the complete challenge period, both the participants and the organizers were blinded regarding the rupture solution to ensure objective conditions. Afterward, author S.S. revealed the ruptured case.

The known site of rupture can now be compared with hemodynamic parameters that are typically used to characterize aneurysmal flow. We focused on TAWSS and OSI as major representatives of the predictions (Table). The results of wall shear stress and the oscillatory shear index were taken from a group that implemented inflow conditions that have been close to patient-specific. As indicated in Fig 1C, the ruptured site is located in an area that experiences rather low TAWSS compared with the parent artery with values well above 50 dyn/cm<sup>2</sup>. In the indicated region, TAWSS ranges between 0.1 and 19 dyn/cm<sup>2</sup>. Furthermore, elevated OSI is visible within the region of interest (Fig 1D). However, very low WSS (<5 dyn/cm<sup>2</sup>) and high oscillatory shear with values up to 0.42 are present beside this area.

### WSS Distributions

WSS distributions contributed by the participants are shown in Fig 1E (for the ruptured case 2). The WSS distributions for the unruptured case 1 are presented in On-line Fig 4. The WSS patterns on the aneurysm surface are obtained from 22 participants that used different assumptions to calculate the hemodynamic parameters. The normalized values demonstrate qualitative similarities, but differences regarding, for example, the size of different regions can also be observed. These differences show the variability of CFD and might explain the variability of rupture site prediction.

The different WSS predictions revealed the importance of realistic boundary conditions such as patient-specific measurements. This information was provided to all participants in a second phase along with further simulation conditions. The corresponding results, which represent the inherent variability of the CFD solutions among all groups, are not discussed in this article but are extensively described in the complementary work.<sup>15</sup>

### Neurosurgeon Predictions

The mean experience of neurosurgeons was 14.5 ± 9.4 years. Most of the neurosurgeons (39/43) correctly predicted that the case 2 aneurysm was the ruptured one because of blebs (56%) or irregular shape (44%). The predictions of the rupture site were split (On-line Fig 2). The main reasons for prediction of the rupture site in case 2 were impact zone (42%) or tip of the aneurysm (58%) for point B (red) and the irregular and sharp bleb (75%) or the flow stagnation area (15%) for point C (blue), respectively. None predicted the rupture site correctly.

## DISCUSSION

The results of the challenge were first presented in a plenary talk at the IntraCranial Stent Meeting, which was held as a joint meeting

with the World Federation of Interventional and Therapeutic Neuroradiology Congress in November 2013 in Buenos Aires. At the beginning of the talk, only the attending neurosurgeons and neuroradiologists from the whole audience were polled to predict the rupture status before seeing the results of the challenge. Five selected case 1, while >20 chose case 2. The clinicians from the audience were shown only the geometry of both cases and On-line Table 1 (without the geometric information). That table was not available for the participants during the challenge (engineers and neurosurgeons). Case 1 is slightly larger, while for case 2, smoking and hypertension should be mentioned. This information might have influenced the ad hoc on-site poll. The ratio of the predictions was very similar regarding both the engineering participants from the CFD challenge and the clinicians at the conference and from the independent neurosurgeon questionnaire.

One of the goals of CFD research is to make CFD simulations clinically useful. However, CFD simulations still seem far from clinical use. There are only a few reports in which CFD simulations are used for designing treatment strategy.<sup>18</sup> CFD simulations would not become helpful if they predict a rupture in the same aneurysms as clinicians already do. CFD simulations can be useful only when they change neurosurgeons' decisions or treatment strategy or add helpful hemodynamic information that is inaccessible to physicians. In the current CFD and neurosurgeon challenge, which consists of 2 cases only, prediction by computers and neurosurgeons was comparable. Prediction by CFD simulations took hours, while prediction by neurosurgeons took <1 minute. Thus, in this particular situation at least, neurosurgeons would not use CFD in the clinical field. One method to clarify possible clinical applications of computer simulations is to examine in what situations computer simulations can exceed clinicians' experience or decisions. In addition, clinicians should learn possible clinical applications and limitations of computational simulations, and engineers should provide this information. Then, clinicians using CFD simulations may provide better treatment to patients in selected situations.

Regarding the second task of the CFD challenge, the specific predictions of the site of rupture were distributed throughout the second aneurysm, with the groups defining 6 different locations. One essential reason might be that only a few hemodynamic studies about rupture points are available.<sup>19,20</sup> In general, ruptured-versus-unruptured aneurysms are compared, but no information regarding the real rupture site can be derived. In addition, hemodynamic studies addressing thin walls and blebs do not necessarily indicate actual rupture sites. Another reason can be seen in the potential level of experience regarding hemodynamic simulations in intracranial aneurysms. Although some groups were highly experienced in other fields of engineering, the survey of the abstracts revealed that unrealistic inflow rates or velocities were applied. For instance, one group defined an inflow velocity of 10 m/s, whereas another group used a turbulence model that was developed for industrial flows and has not been well-tested on aneurysm-type flows. Another concern is related to the spatial and temporal resolution because some groups used coarse meshes and/or large time-steps in their computations.<sup>21</sup>

Proponents of both the low and the high WSS theory were able to predict the ruptured case. It was found for the group with

boundary conditions close to the patient-specific that case 2 had lower area-averaged WSS and higher maximum WSS than case 1 (averaged WSS1 = 32.1 dyn/cm<sup>2</sup> versus averaged WSS2 = 27.8 dyn/cm<sup>2</sup>; maximum WSS1 = 203.2 dyn/cm<sup>2</sup> versus maximum-WSS2 = 244.4 dyn/cm<sup>2</sup>). Therefore, the different results (low-versus-high WSS) may not contradict each other. Although at the ruptured site, relatively low WSS and partly elevated OSI were detected, the groups who used these parameters to predict the location did not necessarily succeed in choosing the correct rupture site. Because multiple areas throughout the aneurysm sac fulfilled these conditions, other, even stronger, spots were picked by the corresponding groups (Fig 1C, -D).

Most interesting, RRT is prolonged on the rupture site and the flow stagnation area on the opposite side. Live images acquired during the intervention revealed the presence of atherosclerosis in this stagnation area, which supports recent findings.<sup>17</sup> However, no thickening of the aneurysm wall was observed at the rupture site. In that study,<sup>17</sup> the thick wall had prolonged RRT, but prolonged regions with RRT did not necessarily show a thick wall. Because the results of the second phase<sup>15</sup> demonstrate that almost all groups are capable of generating nearly identical flow fields under the prescribed boundary conditions, the importance of a realistic numeric setup and model parameters is emphasized once again. Hence, if CFD is integrated in clinical routines some day, guidelines that have evolved from years of experience (eg, spatial and temporal discretization, flow rates, and so forth) should be provided. Such guidelines for hemodynamic simulations in intracranial aneurysms need to address the choice of inflow boundary condition (eg, idealized versus patient-specific<sup>22</sup>), flow splitting through multiple outlet sections, wall treatment, blood modeling, and the consideration of pulsatile flow (steady versus unsteady<sup>23</sup>), and so forth.

Overall, the following knowledge can be derived from this CFD challenge, which should be considered a snapshot of the current state-of-the-art regarding hemodynamic simulations. Twenty-one of the 26 participants could predict the correct aneurysm and therefore demonstrated that the applied methods are capable of differentiating between the provided cases. Because the particular predictions of the rupture site were relatively diverse, it is not possible to state that CFD can be used to detect the rupture point with high probability currently. To reach this aim, investigating the nature and magnitude of forces that give rise to aneurysm wall remodeling and degradation is necessary. Additionally, CFD should be considered as only 1 aspect besides, for example, patient history or shape analyses within the treatment planning. As a numerical method, it just provides help and not a decision for the attending clinician.

### **Limitations of the Study**

Although precise predictions of the site of rupture in intracranial aneurysms were performed, this study does not claim that a reliable virtual rupture prediction is possible now. Still, the numeric models underlie too many assumptions, and it is unclear how strongly they affect the real hemodynamics. First, this study involved only 2 aneurysms. Because this study is the first of its kind, participants focused on 2 aneurysms with similar geometric properties and were aware that one had ruptured. This number of cases

and prior knowledge are not representative and need to be improved in the future to decide how reliably computational models can predict rupture status. Selected cases from private or open data bases should be considered.

A second limitation is related to the implemented outlet boundary conditions. Some groups applied flow splitting through the different outflows or used Windkessel and resistance models to improve on the assumption of a constant pressure at the outlets. However, the lack of knowledge regarding the real temporal pressure/flow variation at the outlet cross-section certainly leads to inaccuracies of the blood flow simulations.

As a third aspect, rigid vessel walls were assumed for all simulations performed within this study. Although Oubel et al<sup>24</sup> found that the actual wall motion does not influence the hemodynamics predicted by CFD and the lack of elastin of aneurysms, which is the essential component to enable flexibility, generally strong differences regarding the wall thickness were observed.<sup>25</sup> In consequence, the resistance against the imposed flow structures is not equally distributed over the complete aneurysm sac. Therefore, a better understanding of the interaction between the flow and the wall response is required. Vessel wall information such as thickness and strength should be included in future studies if reliable measurements by using, for example, optical coherence tomography or intraoperative microscopy<sup>26</sup> are possible.

The actual rupture was observed intraoperatively and was thought to be a rerupture of the spontaneous rupture that occurred before the intervention.

Finally, a broad range of skill and experience was detected among the CFD participants, representing a possible state-of-the-art of the current status in the field of computational hemodynamics for intracranial aneurysms. The neurosurgeons who completed the questionnaire have years of experience and can be considered experts. This heterogeneity among the biomedical engineers might have an influence on the comparison of both communities.

### **CONCLUSIONS**

Many groups throughout the world apply numerical methods to investigate cerebral hemodynamics. Challenging these groups by asking them to predict the rupture status of an intracranial aneurysm revealed that approximately 80% were able to choose the correct aneurysm on the basis of their computations. In particular, low and oscillatory shear was associated with the site of rupture correctly. However, the determination of the rupture site remained challenging if CFD (or, indeed, geometry) was used for the decision exclusively; the predictions were distributed throughout the entire aneurysm sac. Reviewing the participating groups and their submitted abstracts indicates that though great experience concerning engineering problems exists, it might not be sufficient for the investigation of aneurysmal hemodynamics. Therefore, it is of enormous importance that groups have experience in simulating cerebrovascular flows before conclusions are drawn from computational results.

Future challenges in the retrospective prediction of the rupture status in intracranial aneurysms might include more biological aspects. This step will be a necessary one toward the prospective rupture risk assessment. In particular, aneurysm wall

information and the formation of blood clots or even thrombi should be considered within the numerical modeling. However, because reliable information is not available up to now, the rupture-prediction challenge might be expanded to more cases to test the consistency of the CFD groups.

## ACKNOWLEDGMENTS

The authors express their gratitude to all participants of the CFD Rupture Challenge 2013. The large number of contributions enabled us to reflect the current state-of-the-art in the field of virtual aneurysm research. Additionally, we thank Pedro Lylyk (Interventional Neuroradiology, Clinical Institute ENERI, Buenos Aires, Argentina) and Juan R. Cebral (George Mason University, Fairfax, Virginia) for providing the opportunity to present the results in a plenary session at the IntraCranial Stent Meeting 2013 in Buenos Aires. Furthermore, the authors warmly acknowledge the fruitful discussions with Oliver Beuing (Department of Neuroradiology, University Hospital of Magdeburg, Germany). Special thanks are addressed to Mathias Neugebauer (Department of Simulation and Graphics, University Magdeburg, Magdeburg, Germany) who performed the 3D reconstruction of the patient-specific aneurysms. S.S. thanks Ayako Nadia Aoyagi (Tohoku University Hospital, Japan) for her technical support on this study.

## REFERENCES

- Bonneville F, Sourour N, Biondi A. **Intracranial aneurysms: an overview.** *Neuroimag Clin N Am* 2006;16:371–82, vii
- Curtis SL, Bradley M, Wilde P, et al. **Results of screening for intracranial aneurysms in patients with coarctation of the aorta.** *AJNR Am J Neuroradiol* 2012;33:1182–86
- Morita A, Kirino T, Hashi K, et al. **The natural course of unruptured cerebral aneurysms in a Japanese cohort.** *N Engl J Med* 2012; 366:2474–82
- Teunissen LL, Rinkel GJ, Algra A, et al. **Risk factors for subarachnoid hemorrhage: a systematic review.** *Stroke* 1996;27:544–49
- Bederson JB, Connolly ES Jr, Batjer HH, et al. **Guidelines for the management of aneurysmal subarachnoid hemorrhage: a statement for healthcare professionals from a special writing group of the Stroke Council, American Heart Association.** *Stroke* 2009;40: 994–1025
- Qian Y, Takao H, Umezumi M, et al. **Risk analysis of unruptured aneurysms using computational fluid dynamics technology: preliminary results.** *AJNR Am J Neuroradiol* 2011;32:1948–55
- Takao H, Murayama Y, Otsuka S, et al. **Hemodynamic differences between unruptured and ruptured intracranial aneurysms during observation.** *Stroke* 2012;43:1436–39
- Goubergrits L, Schaller J, Kertzscher U, et al. **Statistical wall shear stress maps of ruptured and unruptured middle cerebral artery aneurysms.** *J R Soc Interface* 2012;9:677–88
- Zhang Y, Mu S, Chen J, et al. **Hemodynamic analysis of intracranial aneurysms with daughter blebs.** *Eur Neurol* 2011;66:359–67
- Xiang J, Natarajan SK, Tremmel M, et al. **Hemodynamic-morphologic discriminants for intracranial aneurysm rupture.** *Stroke* 2011;42:144–52
- Cebral JR, Mut F, Raschi M, et al. **Aneurysm rupture following treatment with flow-diverting stents: computational hemodynamics analysis of treatment.** *AJNR Am J Neuroradiol* 2011;32:27–33
- Meng H, Tutino VM, Xiang J, et al. **High WSS or low WSS? Complex interactions of hemodynamics with intracranial aneurysm initiation, growth, and rupture: toward a unifying hypothesis.** *AJNR Am J Neuroradiol* 2014;35:1254–62
- Xiang J, Tutino VM, Snyder KV, et al. **CFD: computational fluid dynamics or confounding factor dissemination? The role of hemodynamics in intracranial aneurysm rupture risk assessment.** *AJNR Am J Neuroradiol* 2014;35:1849–57
- Steinman DA, Hoi Y, Fahy P, et al. **Variability of computational fluid dynamics solutions for pressure and flow in a giant aneurysm: the ASME 2012 Summer Bioengineering Conference CFD Challenge.** *J Biomech Eng* 2013;135:021016
- Berg P, Roloff C, Beuing O, et al. **The Computational Fluid Dynamics Rupture Challenge 2013—Phase II: variability of hemodynamic simulations in two intracranial aneurysms.** *J Biomech Eng*. In press
- Neugebauer M, Lawonn K, Beuing O, et al. **Automatic generation of anatomic characteristics from cerebral aneurysm surface models.** *Int J Comput Assist Radiol Surg* 2013;8:279–89
- Sugiyama S, Niizuma K, Nakayama T, et al. **Relative residence time prolongation in intracranial aneurysms: a possible association with atherosclerosis.** *Neurosurgery* 2013;73:767–76
- Kono K, Shintani A, Fujimoto T, et al. **Stent-assisted coil embolization and computational fluid dynamics simulations of bilateral vertebral artery dissecting aneurysms presenting with subarachnoid hemorrhage: case report.** *Neurosurgery* 2012;71:E1192–200; discussion E1200–01
- Kono K, Fujimoto T, Shintani A, et al. **Hemodynamic characteristics at the rupture site of cerebral aneurysms: a case study.** *Neurosurgery* 2012;71:E1202–08; discussion 1209
- Omodaka S, Sugiyama S, Inoue T, et al. **Local hemodynamics at the rupture point of cerebral aneurysms determined by computational fluid dynamics analysis.** *Cerebrovasc Dis* 2012;34:121–29
- Valen-Sendstad K, Steinman DA. **Mind the gap: impact of computational fluid dynamics solution strategy on prediction of intracranial aneurysm hemodynamics and rupture status indicators.** *AJNR Am J Neuroradiol* 2014;35:536–43
- Jansen IG, Schneiders JJ, Potters WV, et al. **Generalized versus patient-specific inflow boundary conditions in computational fluid dynamics simulations of cerebral aneurysmal hemodynamics.** *AJNR Am J Neuroradiol* 2014;35:1543–48
- Babiker MH, Gonzalez LF, Albuquerque F, et al. **An in vitro study of pulsatile fluid dynamics in intracranial aneurysm models treated with embolic coils and flow diverters.** *IEEE Trans Biomed Eng* 2013;60:1150–59
- Oubel E, DeCraene M, Putman CM, et al. **Analysis of intracranial aneurysm wall motion and its effects on hemodynamic patterns.** *Proc SPIE* 2007;6511:65112A
- Frösen J, Tulamo R, Paetau A, et al. **Saccular intracranial aneurysm: pathology and mechanisms.** *Acta Neuropathol* 2012;123:773–86
- Kadasi LM, Dent WC, Malek AM. **Cerebral aneurysm wall thickness analysis using intraoperative microscopy: effect of size and gender on thin translucent regions.** *J Neurointerv Surg* 2013;5:201–06

# Patency of the Anterior Choroidal Artery after Flow-Diversion Treatment of Internal Carotid Artery Aneurysms

W. Brinjikji, D.F. Kallmes, H.J. Cloft, and G. Lanzino

## ABSTRACT

**BACKGROUND AND PURPOSE:** Treatment of cerebral aneurysms with flow diverters often mandates placement of the device across the ostia of major branches of the internal carotid artery. We determined the patency rates of the anterior choroidal artery after placement of flow-diversion devices across its ostium.

**MATERIALS AND METHODS:** We analyzed a consecutive series of patients in whom a Pipeline Embolization Device was placed across the ostium of an angiographically visible anterior choroidal artery while treating the target aneurysm. Patency of the anterior choroidal artery after Pipeline Embolization Device placement was determined at immediate postoperative and follow-up angiography. Data on pretreatment aneurysm rupture status, concomitant coiling, number of Pipeline Embolization Devices used, neurologic status at follow-up, and follow-up MR imaging/CT findings were collected.

**RESULTS:** Fifteen patients with 15 treated aneurysms were included in this study. In the immediate postprocedural setting, the anterior choroidal artery was patent on posttreatment angiography for all 15 patients. Of the 14 patients with follow-up angiography at least 6 months after Pipeline Embolization Device placement, 1 (7%) had occlusion of the anterior choroidal artery and 14 had a patent anterior choroidal artery (93%). No patients had new neurologic symptoms or stroke related to anterior choroidal artery occlusion at follow-up. Of the 9 patients with follow-up CT or MR imaging, none had infarction in the vascular territory of the anterior choroidal artery.

**CONCLUSIONS:** In this small study, placement of a Pipeline Embolization Device across the anterior choroidal artery ostium resulted in occlusion of the artery in only 1 patient. It was not associated with ischemic changes in the distribution of the anterior choroidal artery in any patient.

**ABBREVIATIONS:** AchoA = anterior choroidal artery; PED = Pipeline Embolization Device

Flow-diverter devices such as the Pipeline Embolization Device (PED; Covidien, Irvine, California) are increasingly being used in the embolization of intracranial aneurysms as both alternatives and adjuncts to endovascular coiling.<sup>1-4</sup> Flow diverters limit aneurysmal blood flow but maintain blood flow into large vessels and perforating vessels covered by the device.<sup>5</sup> Although many in vitro and experimental models have demonstrated long-term patency rates of branch vessels covered by the PED, the long-term patency of major branch vessels is not well-established.<sup>6-8</sup> In this study, we assessed the immediate and long-term patency rates of

the anterior choroidal artery (AchoA) in patients following the placement of a PED across the AchoA ostium.

## MATERIALS AND METHODS

After institutional review board approval, we examined a consecutive series of patients undergoing treatment of intracranial aneurysms with the PED, in which the PED was placed across the ostium of the anterior choroidal artery, from January 2010 to December 2013. Current on-label use of PEDs is for aneurysms of >10 mm in diameter with a neck of >4 mm in the ICA up to but not including the posterior communicating artery. In this study, we used the PED off-label for wide-neck aneurysms considered likely to require stent coiling.

All patients undergoing treatment were premedicated with aspirin and clopidogrel, and full anticoagulation was maintained during the procedure (target activated clotting time between 250 and 300 seconds). Following the procedure, patients were maintained on dual antiplatelet therapy for 3 months. After 3 months,

Received May 29, 2014; accepted after revision August 13.

From the Departments of Radiology (W.B., D.F.K., H.J.C., G.L.) and Neurosurgery (D.F.K., H.J.C., G.L.), Mayo Clinic, Rochester, Minnesota.

Please address correspondence to Waleed Brinjikji, MD, Department of Radiology, Mayo Clinic, 200 1st St SW, Rochester, MN 55901; e-mail: Brinjikji.waleed@mayo.edu

<http://dx.doi.org/10.3174/ajnr.A4139>

**Table 1: Patient characteristics**

Patient No.	Presentation	Side	Aneurysm Location	Prior Coiling	Aneurysm Size (mm)
1	VF deficit	Left	Carotid terminus	Yes	25
2	Headache	Left	PcomA	No	27
3	SAH	Left	ICA blister	No	4
4	Asymptomatic	Right	PcomA	No	3
5	Prior SAH	Left	Paraclinoid	Yes	13
6	Headache	Left	PcomA	Yes	16
7	Prior SAH	Left	Carotid terminus	Yes	20
8	Asymptomatic	Left	PcomA	No	7
9	Asymptomatic	Left	AchoA	No	11
10	Symptomatic	Left	PcomA	No	20
11	Prior SAH	Right	PcomA	Yes	10
12	Asymptomatic	Left	PcomA	No	11
13	Asymptomatic	Left	Paraclinoid	No	13
14	Prior SAH	Left	Paraclinoid	Yes	16
15	Asymptomatic	Right	PcomA	No	4

**Note:**—VF indicates visual field; PcomA, posterior communicating artery.

clopidogrel was discontinued and aspirin was continued indefinitely. This antiplatelet regimen was the same in all patients, and no platelet responsiveness studies were used in these cases. All the procedures were performed with the patient under general endotracheal anesthesia. A bi- or triaxial access technique and, in all cases, a Marksman microcatheter (Covidien) were used to obtain distal access past the segment of the vessel harboring the target aneurysm. Pipeline Embolization Devices were sized to match the maximum diameter of the target vessel. One or multiple devices were used at the discretion of the operators to maximize the changes of complete aneurysm occlusion and/or to ensure adequate coverage of the aneurysm neck and a segment of the parent artery proximal and distal to it. Digital subtraction angiography was performed at 2 frames per section before and following placement of the PED.

Determination of AchoA patency by all authors was made for each patient immediately after the original procedure and at the follow-up angiography performed furthest from the initial procedure. Note was also made of any subjectively determined change in flow patterns (slowing of angiographic flow after PED deployment and/or at follow-up). All patients underwent a detailed clinical examination before the procedure, immediately after the procedure, the following day, and at each corresponding follow-up angiography. In addition to AchoA patency, patient age, sex, presentation, aneurysm size, previous coiling, neurologic status on last follow-up, and follow-up MR imaging and CT results were collected. Postoperative follow-up CT and MR imaging results were divided into 2 time periods: 1) within 1 month of the procedure, and 2) >1 month after the procedure. Infarction location in the AchoA distribution was defined as infarctions localized to the posterior limb of the internal capsule and thalamus as described by Damasio.<sup>9</sup> All images were reviewed by 2 neuroradiologists. Patient neurologic status on last follow-up was scored by using the modified Rankin Scale and was assessed on follow-up with the Neurosurgery Department.

### Statistical Analysis

Summary statistics are presented for all data available by using means  $\pm$  SDs for continuous variables and frequency tabulations

for categorical variables. All statistical analyses were performed by using JMP 9.0 (SAS Institute, Cary, North Carolina).

## RESULTS

### Patient and Aneurysm Characteristics

Fifteen patients (12 women and 3 men) with 15 PED-treated aneurysms were included in this study. Mean patient age was  $56.0 \pm 14.4$  years (range, 34–75 years). Aneurysm sizes ranged from 3 to 27 mm with a mean of  $13.0 \pm 7.4$  mm. Twelve aneurysms were unruptured; 3 were previously ruptured and were treated with coil embolization in the acute phase and staged Pipeline placement after patients had recovered from the acute SAH. Two

patients had their aneurysm treated after it was discovered during treatment of a different, ruptured aneurysm. Three patients with unruptured aneurysms had prior aneurysm coiling. One PED was placed in 11 patients. These data are summarized in Table 1.

### Clinical and Angiographic Follow-Up

Initial postoperative angiography demonstrated patency of the AchoA in all 15 patients. One patient (patient 3) died 10 days after PED placement from intraparenchymal hemorrhage but had a follow-up angiography on postprocedural day 1, which demonstrated a patent AchoA. Of the remaining 14 patients, angiographic follow-up times ranged from 6 to 30 months, with a mean follow-up of  $12.0 \pm 7.2$  months. Of these 14 patients, 13 had a patent AchoA (93%) and 1 had occlusion of the AchoA (7%) (Figure). There were no instances of slowing of flow in the AchoA.

The mean clinical follow-up time was  $12 \pm 8.6$  months, with a minimum follow-up of 10 days and a maximum follow-up of 30 months. One patient (patient 3) presented with SAH resulting from an ICA blister aneurysm and was treated in the acute phase with a PED. One day following the procedure, this patient was found to have multiple watershed infarcts in the bilateral anterior cerebral artery/MCA distribution and a large frontal lobe intraparenchymal hematoma ipsilateral to the treated aneurysm. This patient died 10 days after the procedure because of the intraparenchymal hematoma. Of the remaining patients, the mRS scores at last follow-up ranged from 0 to 2 (mean =  $1 \pm 0.76$ ). None of these patients had neurologic complications related to the procedure. No patients had clinical strokes in the perioperative period or during long-term follow-up. The most common cause for an mRS of >0 was headache. The 1 patient with occlusion of the AchoA had an mRS of zero at 6 months and experienced no symptoms related to AchoA occlusion. These data are summarized in Table 2.

### MR Imaging/CT Follow-Up

Eight patients had postoperative MR imaging or CT within 1 month of PED placement. Patient 3, described above, had an intraparenchymal hemorrhage with multiple bilateral watershed infarcts on CT on postoperative day 1. Seven patients underwent early postoperative MRI (1–5 days postopera-

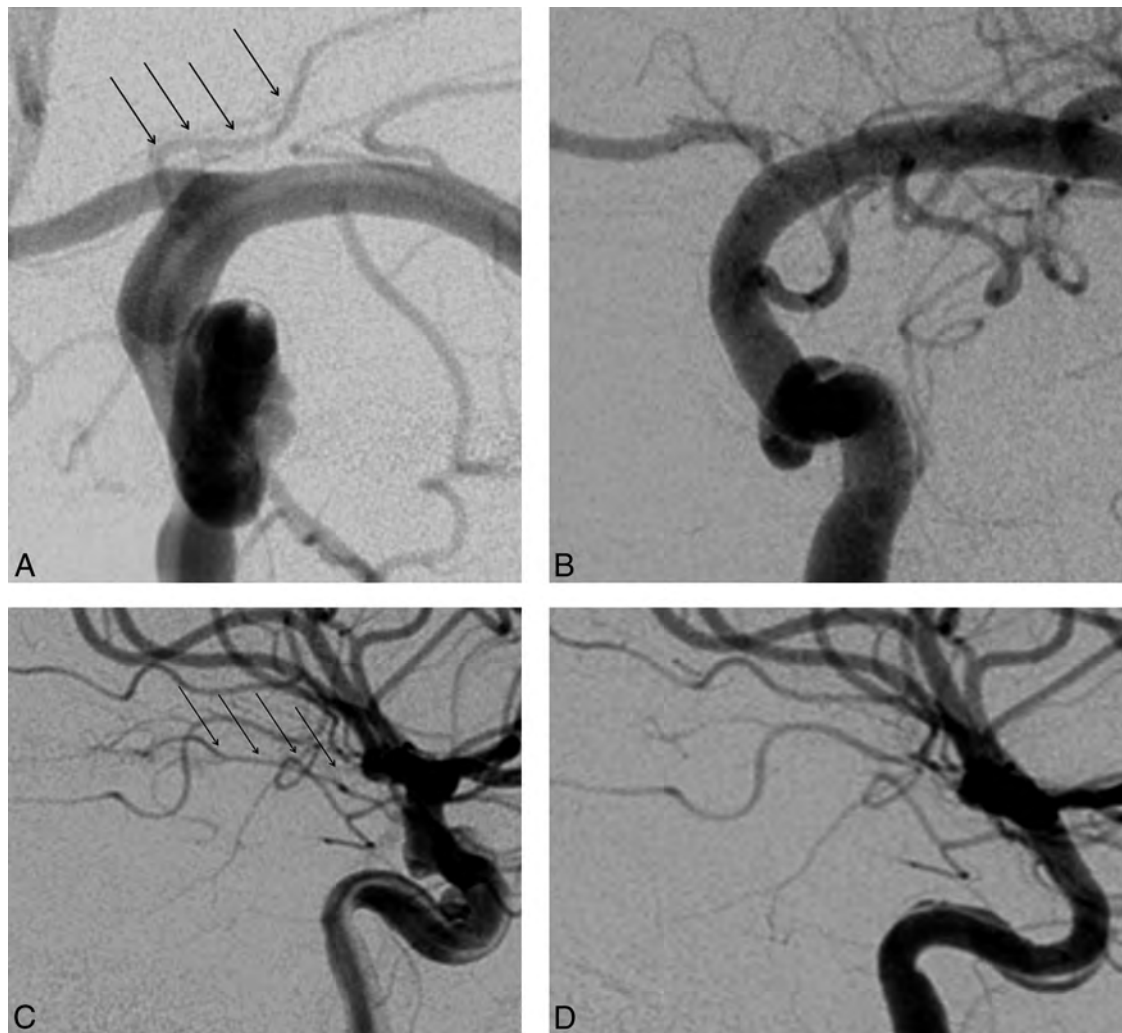


**FIGURE.** Occlusion of anterior choroidal artery on follow-up angiography. *A*, Anteroposterior view of the anterior choroidal artery on pretreatment angiography demonstrates a patent anterior choroidal artery (*black arrows*). *B*, Follow-up angiogram 7 months posttreatment demonstrates absence of filling of the anterior choroidal artery. *C*, Lateral view of the anterior choroidal artery on pretreatment angiography demonstrates that it is patent (*black arrows*). *D*, Follow-up angiogram 7 months posttreatment demonstrates absence of filling of the anterior choroidal artery.

**Table 2: Angiographic results**

Patient No.	No. of Devices	Immediate Postangiography AchoA Patency	Long-Term Patency	Angiographic Follow-Up (mo)	Aneurysm Occlusion, Last Follow-Up
1	3	Patent	Patent	14	Occluded
2	2	Patent	Patent	30	Residual aneurysm
3	1	Patent	NA	1 day	NA
4	2	Patent	Patent	25	Residual aneurysm
5	1	Patent	Patent	13	Residual neck
6	1	Patent	Patent	6	Residual neck
7	1	Patent	Patent	9	Occluded
8	1	Patent	Patent	12	Residual aneurysm
9	1	Patent	Patent	12	Residual aneurysm
10	2	Patent	Patent	12	Residual aneurysm
11	1	Patent	Patent	6	Occluded
12	1	Patent	Patent	6	Occluded
13	1	Patent	Patent	12	Occluded
14	1	Patent	Patent	6	Occluded
15	1	Patent	Occluded	7	Occluded

**Note:**—NA indicates not available; patient died within 10 days of treatment.

tively). Seven patients demonstrated multiple small infarcts, generally in the MCA distribution. No patients had infarcts in the AchoA distribution. Eight patients underwent postopera-

tive MR imaging or CT at >1 month after PED placement. No patients had permanent neurologic deficits corresponding to the infarct location. These findings are summarized in Table 3.

## DISCUSSION

Our study demonstrated that the ostium of the AchoA can be covered with the PED for aneurysm treatment without resulting in neurologic complications related to AchoA occlusion. Following flow-diverter placement across its ostium, the AchoA was patent in 13 of 14 patients who underwent follow-up angiography at least 6 months after the procedure. Of the patients who underwent postoperative CT or MR imaging, none experienced infarctions

that were definitely in the territory of the AchoA. The rarity of angiographic occlusion of the AchoA and lack of neurologic sequelae following placement of the PED across its ostium are

**Table 3: Clinical and MRI/CT Results**

Patient No.	mRS at Last Follow-Up	Reason for mRS	Clinical Follow-Up Time (mo)	Follow-Up MRI/CT Findings at <1 Month	Follow-Up Imaging Findings at >1 Month
1	2	Headaches	27	MRI: tiny silent infarcts, none in AchoA territory	MRI: no new infarcts
2	1	Abdominal pain	30	NA	CT: tiny infarcts, none in AchoA territory
3	6	Death	0.3	CT: watershed infarcts, intraparenchymal hemorrhage	
4	0	—	25	NA	NA
5	2	CN IV paresis, double vision	13	MRI: tiny silent infarcts, none in AchoA territory	CT: no new infarcts
6	0	—	6	MRI: tiny silent infarcts, none in AchoA territory	MRI: no new infarcts
7	1	Shoulder pain	9	MRI: tiny silent infarcts, none in AchoA territory	MRI: no new infarcts
8	0	—	12	NA	NA
9	1	Headaches	12	NA	NA
10	1	Headaches	12	MRI: tiny silent infarcts, none in AchoA territory	MRI: no new infarcts
11	0	—	6	NA	NA
12	0	—	6	NA	NA
13	0	—	12	NA	CT: no new infarcts
14	0	—	6	MRI: tiny silent infarcts, none in AchoA territory	NA
15	0	—	7	MRI: tiny silent infarcts, none in AchoA territory	MRI: no new infarcts

**Note:**—NA indicates not available; CN, cranial nerve.

particularly important, given the large number of aneurysms in the supraclinoid ICA that are amenable to flow-diverter treatment.<sup>10</sup>

Previous clinical, animal, and computational studies have examined the propensity for branch artery occlusion following flow-diversion implantation.<sup>5,6,11,12</sup> Kallmes et al<sup>13,14</sup> found that on occlusion of lumbar branch vessels in the rabbit aorta with overlapping flow-diversion devices, these perforating vessels remained patent on follow-up. While a device placed across the origin of a perforating vessel (traditionally considered end vessels with no distal collaterals) may maintain flow across the ostium due to a pressure gradient across its ostium, the same is not true when larger vessels like the ophthalmic artery and the posterior communicating artery (which often have significant distal collateral potential) are covered by these devices. In such cases, the pressure gradient across the device struts is not enough to maintain patent flow due to the opposing effect of the distal collateral flow, which creates a neutral gradient and angiographic occlusion. Puffer et al<sup>15</sup> examined ophthalmic artery patency rates following flow-diverter placement and found that nearly 25% of ophthalmic arteries were occluded on long-term follow-up with no clinical sequelae. Brinjikji et al<sup>16</sup> demonstrated a long-term occlusion rate of the posterior communicating artery of approximately 27%, with no patients experiencing focal neurologic deficits.

In the case of the anterior choroidal artery, prior studies have demonstrated collateral flow in the setting of chronic ICA occlusion from the lateral posterior choroidal artery, posterior cerebral artery, and posterior communicating artery. Takahashi et al<sup>17</sup> described 7 cases of retrograde filling of the anterior choroidal artery on vertebral angiography. In most cases, this retrograde filling was demonstrated following thrombotic occlusion of the supraclinoid ICA. The normal AchoA has anastomoses with the posterior com-

municating artery and the posterior cerebral artery. Anastomoses with the posterior circulation occur at the level of the choroid plexus, lateral geniculate body, or proximal portions of the posterior cerebral artery.<sup>18,19</sup>

All 6 patients who had MR imaging in the immediate postoperative period had small foci of restricted diffusion. These findings are consistent with those of the coiling literature, in which up to 75% of patients have high-signal lesions on DWI, most of which are silent infarcts. In a series of 34 consecutive patients undergoing elective coiling for unruptured aneurysms, Matsushige et al<sup>20</sup> reported that 76% of patients had high-signal spots on DWI. Hahnemann et al<sup>21</sup> found that nearly two-thirds of patients undergoing stent-assisted coiling had postprocedural ischemic lesions on DWI in a series of 75 patients. Our study is considerably smaller, and further studies reporting the incidence of DWI changes following PED placement are necessary. In all cases, these infarcts were clinically silent.

There was 1 death in our series. The patient had a small ruptured blister aneurysm and was treated in the acute phase with a PED. One day following the procedure, this patient was found to have multiple watershed infarcts in the bilateral anterior cerebral artery/MCA distribution and a large frontal lobe intraparenchymal hematoma ipsilateral to the treated aneurysm. Ruptured blister aneurysms have a very poor natural history and are generally associated with poor clinical outcomes regardless of treatment technique. However, the PED is emerging as a valid therapeutic option for ruptured blister aneurysms of the ICA. Yoon et al<sup>22</sup> reported a series of 11 patients treated with the PED for ruptured blister ICA aneurysms. In this series, 3 patients (27%) had major perioperative ischemic complications and 1 patient died. Further research is needed to determine the role of the PED in the treatment of blister aneurysms.

Our study was limited by the relatively small number of treated aneurysms. Given the rarity of angiographic occlusion of the anterior choroidal artery in the patients included in our study, we could not determine which variables were associated with anterior choroidal artery occlusion. Therefore, we did not perform any statistical comparisons in our study. Lack of angiographic opacification of a vessel may not indicate complete absence of flow through the vessel. On follow-up angiography, most patients did not have vertebral artery injections; thus, filling of the AchoA from the posterior circulation could not be appreciated. Platelet responsiveness, a potentially important factor in determining arterial patency following PED placement, was not examined in this study. A mean follow-up of approximately 12 months may not have been enough time to determine the long-term patency of the AchoA in these patients; however, the 1 case of angiographic occlusion of the AchoA was demonstrated at the 6-month follow-up.

Another important limitation is our lack of consistent imaging follow-up. Only 9 patients underwent posttreatment imaging. This small number makes it difficult to understand why no patients with a jailed AchoA had an infarct in the AchoA territory. As discussed in an article by Hanley and Lippman-Hand,<sup>23</sup> a zero numerator does not necessarily mean “no risk.” In this article, Hanley and Lippman-Hand discuss the concept of “the rule of 3,” essentially stating that the 95% confidence interval estimate of the risk of an event occurring when the numerator is 0 is, at most, 3 in  $n$  ( $n$  = denominator). Thus, with the rule of 3, the 95% confidence interval for risk of AchoA territory infarction in our study ranges from 0.0% (0/9) to 33.3% (3/9). These results suggest that further larger studies with consistent imaging follow-up are needed to determine the risk of AchoA territory infarct when the artery is jailed by flow-diverter devices. Last, while none of the silent infarcts seen on MR imaging were in the traditional territory of the AchoA, vascular territories are known to be inexact. However, all images were reviewed by 2 neuroradiologists, and in no cases were there definite findings of AchoA-related infarct.

## CONCLUSIONS

In this small study, placement of a Pipeline Embolization Device across the AchoA ostium resulted in occlusion of the artery in only 1 patient. It was not associated with ischemic changes in the distribution of the AchoA in any patient.

Disclosures: David F. Kallmes—UNRELATED: Board Membership: GE Healthcare, Comments: Advisory Board membership; Consultancy: ev3, Comments: planning and implementation of clinical trials; Grants/Grants Pending: ev3,\* Sequent Medical,\* Codman,\* MicroVention,\* NeuroSigma,\* Comments: funding for preclinical and clinical research; Royalties: University of Virginia Patent Foundation, Comments: Spine Fusion. Harry J. Cloft—UNRELATED: Grants/Grants Pending: Cordis Endovascular,\* Comments: Site Principal Investigator at enrolling site for Stenting and Angioplasty with Protection in Patients and High Risk for Endarterectomy registry sponsored by Cordis Endovascular. Giuseppe Lanzino—UNRELATED: Consultancy: Covidien\*; Payment for Development of Educational Presentations: Codman/Johnson & Johnson. \*Money paid to the institution.

## REFERENCES

1. Brinjikji W, Murad MH, Lanzino G, et al. Endovascular treatment of intracranial aneurysms with flow diverters: a meta-analysis. *Stroke* 2013;44:442–47
2. Deutschmann HA, Wehrschiuetz M, Augustin M, et al. Long-term

- follow-up after treatment of intracranial aneurysms with the Pipeline embolization device: results from a single center. *AJNR Am J Neuroradiol* 2012;33:481–86
3. Fischer S, Vajda Z, Aguilar Perez M, et al. Pipeline embolization device (PED) for neurovascular reconstruction: initial experience in the treatment of 101 intracranial aneurysms and dissections. *Neuroradiology* 2012;54:369–82
4. Saatci I, Yavuz K, Ozer C, et al. Treatment of intracranial aneurysms using the Pipeline flow-diverter embolization device: a single-center experience with long-term follow-up results. *AJNR Am J Neuro-radiol* 2012;33:1436–46
5. D’Urso PI, Lanzino G, Cloft HJ, et al. Flow diversion for intracranial aneurysms: a review. *Stroke* 2011;42:2363–68
6. Geremia G, Haklin M, Brennecke L. Embolization of experimentally created aneurysms with intravascular stent devices. *AJNR Am J Neuroradiol* 1994;15:1223–31
7. Lieber BB, Livescu V, Hopkins LN, et al. Particle image velocimetry assessment of stent design influence on intra-aneurysmal flow. *Ann Biomed Eng* 2002;30:768–77
8. Trager AL, Sadasivan C, Seong J, et al. Correlation between angiographic and particle image velocimetry quantifications of flow diverters in an in vitro model of elastase-induced rabbit aneurysms. *J Biomech Eng* 2009;131:034506
9. Damasio H. A computed tomographic guide to the identification of cerebral vascular territories. *Arch Neurol* 1983;40:138–42
10. Brinjikji W, Cloft HJ, Fiorella D, et al. Estimating the proportion of intracranial aneurysms likely to be amenable to treatment with the Pipeline embolization device. *J Neurointerv Surg* 2013;5:45–48
11. Appanaboyina S, Mut F, Löhner R, et al. Computational modelling of blood flow in side arterial branches after stenting of cerebral aneurysms. *Int J Comput Fluid Dynamics* 2008;22:669–76
12. Seong J, Wakhloo AK, Lieber BB. In vitro evaluation of flow diverters in an elastase-induced saccular aneurysm model in rabbit. *J Biomech Eng* 2007;129:863–72
13. Kallmes DF, Ding YH, Dai D, et al. A new endoluminal, flow-disrupting device for treatment of saccular aneurysms. *Stroke* 2007;38:2346–52
14. Kallmes DF, Ding YH, Dai D, et al. A second-generation, endoluminal, flow-disrupting device for treatment of saccular aneurysms. *AJNR Am J Neuroradiol* 2009;30:1153–58
15. Puffer RC, Kallmes DF, Cloft HJ, et al. Patency of the ophthalmic artery after flow diversion treatment of paraclinoid aneurysms. *J Neurosurg* 2012;116:892–96
16. Brinjikji W, Lanzino G, Cloft HJ, et al. Patency of the posterior communicating artery after flow diversion treatment of internal carotid artery aneurysms. *Clin Neurol Neurosurg* 2014;120:84–88
17. Takahashi S, Tobita M, Takahashi A, et al. Retrograde filling of the anterior choroidal artery: vertebral angiographic sign of obstruction in the carotid system. *Neuroradiology* 1992;34:504–07
18. Morandi X, Brassier G, Darnault P, et al. Microsurgical anatomy of the anterior choroidal artery. *Surg Radiol Anat* 1996;18:275–80
19. Takahashi S, Suga T, Kawata Y, et al. Anterior choroidal artery: angiographic analysis of variations and anomalies. *AJNR Am J Neuro-radiol* 1990;11:719–29
20. Matsushige T, Kiura Y, Sakamoto S, et al. Multiple antiplatelet therapy contributes to the reversible high signal spots on diffusion-weighted imaging in elective coiling of unruptured cerebral aneurysm. *Neuroradiology* 2013;55:449–57
21. Hahnemann ML, Ringelstein A, Sandalcioglu IE, et al. Silent embolism after stent-assisted coiling of cerebral aneurysms: diffusion-weighted MRI study of 75 cases. *J Neurointerv Surg* 2014;6:461–65
22. Yoon JW, Siddiqui AH, Dumont TM, et al. Feasibility and safety of Pipeline embolization device in patients with ruptured carotid blister aneurysms. *Neurosurgery* 2014;75:419–29
23. Hanley JA, Lippman-Hand A. If nothing goes wrong, is everything all right? *JAMA* 1983;249:1743–45

# Silk Flow-Diverter Stent for the Treatment of Intracranial Aneurysms: A Series of 58 Patients with Emphasis on Long-Term Results

B. Lubicz, O. Van der Elst, L. Collignon, B. Mine, and F. Alghamdi

## ABSTRACT

**BACKGROUND AND PURPOSE:** The Silk flow-diverter stent is increasingly used to treat complex intracranial aneurysms including wide-neck, fusiform aneurysms. Sparse data are available concerning long-term results of this technique. We report our 5-year experience with Silk stent treatment of intracranial aneurysms.

**MATERIALS AND METHODS:** A retrospective review of our prospectively maintained database identified all patients treated by the Silk stent in 2 institutions. Clinical charts, procedural data, and angiographic results were reviewed.

**RESULTS:** Between July 2009 and May 2014, we identified 58 patients with 70 intracranial aneurysms. Endovascular treatment was successful in 93% of patients with 32 treated with the first-generation Silk stent and 26 with the new Silk+ stent. Mean follow-up in 47 patients was 22 months. Despite an 11% delayed complication rate, overall permanent neurologic morbidity was 5.5%. All complications were seen with the first-generation Silk stent. There was no procedure-related mortality. Long-term anatomic results showed 73% with complete occlusion, 16% with neck remnants, and 11% with incomplete occlusion. No recanalization or retreatment was performed. The midterm intrastent stenosis rate was 57%, of which 60% improved or disappeared, 28% were stable, and 12% led to vessel occlusion. Seventy-four percent of stenosis and all vessel occlusions occurred with the first-generation Silk stent.

**CONCLUSIONS:** Endovascular treatment of complex intracranial aneurysms with the Silk stent is an effective therapeutic option. Despite a high rate of delayed complications with the first-generation stents, the current Silk+ stent appears safer. This treatment achieves a high rate of adequate and stable occlusion at long-term follow-up.

**ABBREVIATIONS:** CLARITY = Clinical and Anatomical Results in the Treatment of Ruptured Intracranial Aneurysms; PAO = parent artery occlusion

Endovascular treatment is now the first-intention treatment for both ruptured and unruptured intracranial aneurysms.<sup>1-4</sup> However, endovascular treatment of complex intracranial aneurysms (wide-neck and fusiform) remains technically challenging. On the other hand, aneurysm coil recanalization is an important issue in endovascular therapy, with approximately 20% of coiled aneurysms recanalized and 10% retreated.<sup>5</sup> As previously shown, wide-neck aneurysms are highly prone to recanalization.<sup>6</sup>

These relative limitations of standard coiling have contributed to the development of new endovascular approaches, including balloon-assisted coiling, stent-assisted coiling, flow diversion,

and flow disruption. Flow-diverter stents have been developed, and they offer the potential of aneurysm occlusion related to flow disruption. Recently, several flow-diverter stents, such as the Silk flow diverter (Balt Extrusion, Montmorency, France), have been released, and short- and midterm results have been published.<sup>7-15</sup> Notwithstanding the early promise of these devices, important shortcomings have been reported. First, delayed complications, either hemorrhagic or thromboembolic, are not uncommon; second, the flow-diverter stent tolerance might be considered poor because of the relatively high rates of intrastent stenosis and parent artery occlusion (PAO) during follow-up.<sup>7-15</sup> To the best of our knowledge, sparse data are available about the long-term results of this technique, including stability of aneurysm occlusion and stent tolerance. These data are mandatory to define the place of flow-diverter stents in the therapeutic armamentarium of intracranial aneurysms. Therefore, the aim of our study was to report our 5-year experience with Silk stent treatment of intracranial aneurysms with an emphasis on long-term results.

Received July 9, 2014; accepted after revision September 3.

From the Department of Neuroradiology (B.L., O.V.d.E., B.M., F.A.), Erasme University Hospital, Brussels, Belgium; and Department of Radiology (L.C.), Centre Hospitalier Régional Citadelle, Liège, Belgium.

Please address correspondence to Boris Lubicz, MD, PhD, Hôpital Erasme, 808 Route de Lennik, 1070 Bruxelles, Belgium; e-mail: blubicz@ulb.ac.be

<http://dx.doi.org/10.3174/ajnr.A4143>

## MATERIALS AND METHODS

This retrospective study was approved by our institutional ethics committee. Between July 2009 and May 2014, we retrospectively identified in our prospectively maintained database all patients treated with the Silk stent for 1 or multiple intracranial aneurysms in 2 institutions. All patients underwent conventional angiography of both internal carotid arteries and vertebral arteries. Then, 3D-rotational angiography was performed to depict the aneurysm morphology. These aneurysms were classified as saccular or fusiform and as small (<10 mm), large (between 10 and 24 mm), or giant ( $\geq 25$  mm). For saccular aneurysms, the neck was classified as wide (neck width of  $>4$  mm or dome-to-neck ratio of  $<1.6$ ) or small (neck width of  $\leq 4$  mm and dome-to-neck ratio of  $\geq 1.6$ ).

In all patients, endovascular treatment was performed with the patient under general anesthesia and systemic heparinization. The adequacy of systemic anticoagulation was monitored by repeated measurements of the activated clotting time. A baseline activated clotting time was obtained before the 5000-IU bolus infusion of heparin and hourly thereafter. The bolus infusion was followed by a continuous drip (1500–2500 IU/h) to double the baseline activated clotting time. At the end of the procedure, systemic heparinization was maintained for 24 hours in most patients. All procedures were performed by 2 senior interventional neuroradiologists (B.L., B.M.). The aim of endovascular treatment was to deliver only 1 Silk stent at the aneurysm site. In case of misplacement, a second stent was used to fully cover the aneurysm neck. In all patients, we used a telescopic access system: a long IVA guiding introducer (Balt), a Fargo (Balt) or Neuron (Penumbra, Alameda, California) access catheter, and the delivery Vasco catheter (Silk). From July 2009 to November 2011, the first generation of the Silk stent was used. Then, only the second generation of the stent named “Silk+” was used. In all cases, the Silk stent was first half-deployed and an angiographic control was performed to evaluate the stent tolerance within the parent vessel. If the control was satisfactory, the Silk was fully delivered; if not, the device was removed and other treatments were performed. For planned procedures, a loading dose of 300 mg of clopidogrel and 320 mg of aspirin was administered 1 day before and on the day of endovascular treatment. When stent placement was decided during the procedure, intravenous abciximab was administered a few minutes before stent deployment with a bolus of 0.25 mg/kg followed by a continuous perfusion of 0.125  $\mu\text{g}/\text{kg}/\text{min}$  for 12 hours. Additional coiling was performed according to the treating physician’s judgment. In these cases, a coiling microcatheter was first placed within the aneurysmal sac and then jailed following Silk stent delivery. After endovascular treatment, control DSA was performed, including working, frontal, and lateral views. Patients were then transferred to the intensive care unit; fluid balance, neurologic status, and blood pressure were carefully monitored. In all patients, clopidogrel was maintained for 12 months (75 mg/day), whereas aspirin (160 mg/day) was administered forever. Our antiplatelet treatment remained the same throughout the study.

Procedural and early postprocedural (within 48 hours) complications were recorded. The clinical course was recorded, in-

cluding worsening of symptoms and death. Clinical outcome was evaluated according to the modified Rankin Scale.<sup>16</sup>

Patients were evaluated by angiography at the end of the procedure. Anatomic outcome was classified according to the Oxford Grading Scale.<sup>17</sup>

On the basis of clinical chart review, we recorded delayed complications, retreatments, and aneurysm ruptures.

Our imaging follow-up protocol for flow-diverter stents includes DSA every 3 months until aneurysm occlusion. At 12 months (or later if the aneurysm is still not completely occluded), a last DSA and a concurrent MR angiography, which serves as a baseline comparative noninvasive technique, are performed. Then, patients are followed up only by MRA every year (ruptured aneurysms) or every 2 years (unruptured aneurysms). Both time-of-flight and contrast-enhanced MRA are performed. Imaging follow-up duration was defined as the delay between Silk stent placement and the most recent DSA or MRA. We considered follow-up to be short- to-midterm when the latest control examination was performed before 12 months. At  $\geq 12$  months, we considered the patient to have undergone a long-term anatomic follow-up.

Two senior neuroradiologists who did not participate in endovascular treatment and 1 medical student (last year of training) reviewed all imaging examinations. Anatomic outcome was classified as complete occlusion (no contrast filling the aneurysm), neck remnant (residual contrast filling the aneurysmal neck), and incomplete occlusion (residual contrast filling the aneurysmal body). Intrastent stenosis was classified as nonsignificant if it was  $<50\%$  and significant or severe if it was  $>50\%$ . Parent artery occlusion was also noted. The readers reached a consensus regarding aneurysm occlusion and stent tolerance. The latest available imaging follow-up was compared with the immediate result after endovascular treatment. The evolution of intrastent stenosis was also evaluated and judged stable, improved, or worsened.

## RESULTS

Fifty-eight patients with 70 intracranial aneurysms were identified. There were 40 women and 18 men with a mean age of 48.5 years (range, 14–82 years). Forty-one patients were asymptomatic, whereas 17 were symptomatic. Clinical presentation is detailed in the Table.

Aneurysms were located in the anterior circulation in 59 cases and in the posterior circulation in 11 cases. There were 52 small aneurysms, 17 large aneurysms, and 1 giant aneurysm. Mean aneurysm diameter was 7 mm (range, 1–46 mm).

There were 51/70 saccular aneurysms, among which 46 had a wide neck. The remaining aneurysms were fusiform ( $n = 11$ ), blood blister-like ( $n = 6$ ), and dissecting ( $n = 2$ ). Two aneurysms were partially thrombosed.

Embolization was successfully performed in 54 patients with 66 aneurysms (93%), and failure occurred in 4 patients (7%). In these 4 patients, the Silk stent could not be delivered because of high friction within the delivery microcatheter in 2 cases or because the angiographic controls showed that the stent was not tolerated (nonopacification of the parent artery) in 2 cases. Among these failures, three-fourths occurred with the first-gen-

**Clinical presentation in 58 patients with 70 IAs**

	No. of Patients
Asymptomatic	
Incidental	21
Previous SAH	16
Other IAs to be treated	7
Post-EVT recanalization	4
Postclipping remnant	3
Postclipping regrowth	2
Familial history	3
Recanalization	1
Symptomatic	
SAH	9
WFNS grade 1	2
WFNS grade 2	1
WFNS grade 3	1
WFNS grade 4	5
TIA-stroke	4
Neurologic deficit	4
Decreased visual acuity	1
Ophthalmoplegia	1
Transient tetraparesis	1
Progressive tetraparesis	1

**Note:**—IA indicates intracranial aneurysm; EVT, endovascular treatment; WFNS, World Federation of Neurosurgical Societies.

eration Silk stent. Overall, 32 patients were treated with the Silk stent and 26 with the Silk+ stent.

Among 54 treated patients, 48 had only Silk stent placement and 6 had additional coil placement. These 6 patients presented with SAH or a large unruptured aneurysm. All Silk stents could be fully deployed, and no balloon had to be used because no stenosis was encountered. Only 1 technical complication occurred in a patient in whom a cavernous ICA tear occurred due to the access guiding catheter. Two Silk stents were finally placed to occlude the tear, but it failed. Therefore, a test occlusion was performed during endovascular treatment, showing a good tolerance of this ICA occlusion. We stopped heparin, so the aneurysm and the ICA both occluded without any clinical impact.

Clinical complications occurred in 8 patients (8/54, 15%). Five patients developed a femoral, a retroperitoneal, or cervical hematoma; 1 of these patients experienced a stroke and a hemiparesis due to severe hypotension. Among the 3 remaining patients, 1 had a transient hemiparesis without a clear identifying cause, 1 had a contralateral basal ganglia hematoma 24 hours after uneventful endovascular treatment due to a known severe and uncontrolled hypertension, and 1 had an SAH and a contralateral frontoparietal hematoma a few hours after an uneventful procedure. Among these latter 2 patients, 1 with the basal ganglia hematoma died because of severe intracranial hypertension and the other had no deficit.

Among 54 treated patients (38 asymptomatic, 16 symptomatic), 49 were unchanged, 1 had a severe hemiparesis (mRS = 4), and 4 died. In these latter 4 patients, 3 died because of the initial clinical presentation (2 severe SAHs and 1 case of severe pneumonia in a patient who presented with progressive tetraparesis from a giant compressive vertebrobasilar aneurysm) and 1 patient died of intracranial hypertension due to a hypertensive contralateral basal ganglia hematoma. The overall immediate neurologic morbidity rate was thus 1.9% (1/54). There was no procedure-related mortality.

Among 54 treated patients with 66 aneurysms, immediate aneurysm occlusion was graded 0 in 53 cases (80.3%), 1 in 6 cases (9.1%), 2 in 1 case (1.5%), 3 in 2 cases (3%), and 4 in 4 cases (6.1%). There was 1 parent artery occlusion (1/54, 1.9%). The aneurysms graded 3 and 4 were those treated by the Silk stent and coils.

Among 50 treated patients, clinical and imaging follow-up were available in 47, ranging from 3 to 56 months (mean = 22 months). Three patients were lost to follow-up. Thirty-six patients had a long-term follow-up, and 11, a short-to-midterm follow-up.

Among 47 patients with follow-up, 5 (5/47, 10.6%) experienced a delayed thromboembolic complication 11 days to 4 months after endovascular treatment. In 4 cases, the antiplatelet medication was doubled for 12 months, and in 1 patient, an angioplasty was performed to treat a significant intrastent stenosis. Of these patients, 2 kept a slight neurologic deficit (1 with mRS = 1, and 1 with mRS = 2) and 3 were completely recovered at follow-up. All of these 5 patients were treated with the first-generation Silk stent. No delayed complications occurred because we used the Silk+ stent. There was no aneurysmal rupture.

Overall permanent neurologic morbidity was 5.5% (1 patient at the immediate phase and 2 at follow-up, 3/54 patients). There was no procedure-related mortality.

Among 47 patients with follow-up with 59 aneurysms, 3 patients with 4 aneurysms experienced an asymptomatic PAO (3/47, 6.4%). These 3 patients were treated with the first-generation Silk stent and were excluded from the long-term aneurysm occlusion evaluation.

At the latest available imaging examination in 55 aneurysms, 40 were completely occluded (73%), 9 had a neck remnant (16%), and 6 were incompletely occluded (11%). Adequate occlusion (complete + neck remnant) was thus 89%. No recanalization was observed.

At short-to-midterm follow-up in 47 patients, there were 27 intrastent stenoses (57%). Only 5/27 (18.5%) stenoses were severe. Twenty stenoses of 27 (74%) occurred in patients treated with the Silk stent, whereas 7 (26%) occurred in patients treated with the Silk+ stent. At long-term follow-up in 25 cases, 15 stenoses improved and/or completely resolved (60%), 7 were stable (28%), and 3 asymptomatic PAOs (12%) occurred. These PAOs were seen in patients treated with the first generation of the Silk stent. In 1 patient with a basilar artery dissection, there was already a significant parent artery stenosis before endovascular treatment. In 1 patient, there was a severe stenosis at short-term follow-up. In the last patient, there was a nonsignificant stenosis at short-term follow-up.

**DISCUSSION**

This study shows that endovascular treatment of complex intracranial aneurysms with the Silk stent is an effective therapeutic option. Despite a relatively high rate of delayed complications (thromboembolic event, intrastent stenosis, PAO) with the first-generation stents, the current Silk+ stent appears safer. Moreover, this endovascular approach achieved a high rate of adequate and stable aneurysm occlusion at long-term follow-up.

This study included all consecutive patients treated in our in-

stitutions with the Silk stent since its release in 2009 in our country. Despite an obvious learning curve, the rate of successful embolization was very high (93%). Moreover, 3 of 4 failures occurred with the first-generation Silk stent, which is no longer available. With the new Silk+ stent, only 1 failure occurred, suggesting a better stent tolerance at the acute phase of endovascular treatment. The recent introduction of intermediate access catheters (Neuron, Fargo) also helps facilitate the endovascular procedure by adding significant support, for easier and better stent delivery. Our high rate of successful endovascular treatment is in concordance with previous series.<sup>7-15</sup>

It is now generally admitted, and even recommended by the Balt company, that additional coiling be performed in very large or giant unruptured intracranial aneurysms to prevent delayed bleeding.<sup>18</sup> Our results confirm these findings because we did not observe any bleeding in the present series, with most of our patients having mid-to-long-term follow-up. In our daily practice, we always add coils in ruptured aneurysms and in very large or giant unruptured aneurysms.

The rate of immediate and delayed complications is a major concern with the use of flow-diverter stents. With the first-generation Silk stent, we encountered a high rate of these complications. Since the release of the Silk+ stent, none of our patients have experienced a clinical complication. Overall, the long-term clinical follow-up showed a low rate (5.5%) of patients with permanent neurologic morbidity and no direct procedure-related mortality. One of our patients died from a contralateral hypertensive hematoma 24 hours after uneventful Silk treatment. We agree that the size of the hematoma was probably increased by the antiplatelet therapy that she had before endovascular treatment, but the severe arterial hypertension was clearly responsible for this complication and not the Silk stent itself. Our good clinical outcome compares favorably with the recent meta-analysis from Murthy et al.<sup>14</sup> It might be partially explained by the fact that our series included <25% of large/giant intracranial aneurysms, whereas Murthy et al included almost two-thirds of these aneurysms. Indeed, the rate of delayed complications is significantly higher in larger intracranial aneurysms in which additional coiling is now recommended.<sup>18</sup>

Another reason might be related to the learning curve with a new device. Indeed, all our permanent complications occurred in our first 20 patients. It is obvious that this technique requires being very familiar with intracranial stent placement. In our referral institutions, 250 intracranial aneurysms are treated by an endovascular approach among which two-thirds are treated with a stent. Therefore, the complete process from the premedication to endovascular treatment and follow-up of patients in the intensive care unit is our daily routine. Last but not least, the Silk stent has been significantly improved with the release of the Silk+ stent, which has flared ends, a higher radial force, and a higher radio-opacity. These features have clearly improved its behavior. Indeed, since we started using the Silk+ stent, we have not experienced any clinical complications both during the periprocedural phase and at follow-up.

The present series shows that in this group of complex intracranial aneurysms, adequate occlusion was obtained in a high percentage of cases in long-term results (89%). Moreover, the

treatment was stable with time, with no worsening of the occlusion status. These findings are in concordance with the meta-analysis reported by Murthy et al.<sup>14</sup> It has been previously shown that neck size is a critical factor for aneurysm recanalization and mid-to-long-term anatomic results in intracranial aneurysms treated with coils.

In the Clinical and Anatomical Results in the Treatment of Ruptured Intracranial Aneurysms (CLARITY) study, aneurysm neck size was identified as the single most important factor in the quality of aneurysm occlusion at midterm follow-up after standard endovascular treatment.<sup>4,6</sup> In this series, adequate occlusion was obtained in the whole population (narrow and wide-neck aneurysms) and in 80.4% at midterm follow-up after bare platinum coil treatment. In wide-neck aneurysms, the rate of adequate occlusion was 68.2%, which is much lower than the 89% observed in the present series. Also in the Ferns et al<sup>5</sup> review dealing with narrow and wide-neck aneurysms, the rate of adequate occlusion at follow-up was only 83.4%, lower than the percentage in the present series. With Silk stent treatment, adequate aneurysm occlusion was stable at long-term follow-up and compares favorably with conventional endovascular coiling. Indeed, in CLARITY, worsening of aneurysm occlusion was observed in 51.1% of aneurysms in the whole group and in 62.1% of wide-neck aneurysms. Moreover, no retreatment was performed in the present series, and that is a major advantage compared with what was reported in CLARITY (6.2%) and in the Ferns et al review (10.3%).<sup>4-6</sup> These anatomic results are very satisfying because of our selected population that included mostly wide-neck and fusiform intracranial aneurysms.

Stent tolerance is another major concern with flow-diverter stents. Our series showed a very high rate (57%) of intrastent stenosis at short- and midterm follow-ups. Most stenoses were asymptomatic, but our rate is significantly superior compared with that in previous series.<sup>7-15</sup> Indeed, the incidence of intrastent stenosis was 7.8% in the Berge et al series,<sup>10</sup> 6% in the Byrne et al series,<sup>10</sup> and 5% in the Murthy et al meta-analysis.<sup>14</sup> Nevertheless, the only series that is almost comparable with ours is that of Cohen et al,<sup>15</sup> which was also focused on this precise evaluation. In this latter study, the rate of intrastent stenosis at the first follow-up examination was 38%. A possible explanation is that we asked 2 neuroradiologists who were not involved in endovascular treatment to evaluate our results to avoid any underestimation. Most interesting, 76% of these stenoses were seen with the use of the first-generation stents. These anatomic findings are well-correlated to our clinical results, which are much better with the Silk+ stent. Even more important is that these stenoses improved or disappeared in 60% of cases. This phenomenon has previously been reported,<sup>10</sup> but our series, with a large number of patients having long-term follow-up until 56 months, brings additional data to highlight the remarkable nature of these stenoses. This particular behavior of improving/disappearing intrastent stenosis should now be better understood by more fundamental research. Nevertheless, this information is of great interest when physicians are facing such problems. Last but not least, PAOs were also seen in the present series, and all occurred with the first-generation stents. Risk factors for PAO are not very well-identified, but pre-existing stenosis seems to be one of them.<sup>7-15</sup> Larger series with

long-term follow-up are needed to better define patients who are at risk of such pejorative evolution.

Our study has several limitations. First, it was retrospective with a small number of patients. However, all patients were consecutively included and analyzed. Second, imaging follow-up was incompletely homogeneous because it included MRA and DSA. Indeed, MRA has recently been reported to be reliable for the follow-up of intracranial aneurysms treated with flow-diverter stents, but it underestimates the luminal diameter of the reconstructed artery compared with DSA.<sup>19</sup> However, in our imaging protocol, contemporaneous DSA and MRA are performed when the aneurysm is completely occluded, and these examinations serve as the baseline study for the follow-up. Therefore, the following MRA examinations are compared with the baseline study to detect a decrease of the parent artery diameter.

## CONCLUSIONS

This series shows that endovascular treatment of complex intracranial aneurysms with the Silk stent is effective and is associated with an acceptable neurologic morbidity. Despite a relatively high rate of delayed complications (thromboembolic event, intrastent stenosis, PAO) with the first-generation stents, the current Silk+ stent appears safer. Moreover, this endovascular approach achieves a high rate of adequate and stable aneurysm occlusion at long-term follow-up.

Disclosures: Boris Lubicz—UNRELATED: Consultancy: MicroVention, Codman, Covidien, Sequent.

## REFERENCES

1. Molyneux A, Kerr R, Stratton I, et al; International Subarachnoid Aneurysm Trial (ISAT) Collaborative Group. **International Subarachnoid Aneurysm Trial (ISAT) of neurosurgical clipping versus endovascular coiling in 2143 patients with ruptured intracranial aneurysms: a randomised trial.** *Lancet* 2002;360:1267–74
2. McDougall CG, Spetzler RF, Zabramski JM, et al. **The Barrow Ruptured Aneurysm Trial.** *J Neurosurg* 2012;116:135–44
3. Cognard C, Pierot L, Anxionnat R, et al; Clarity Study Group. **Results of embolization used as the first treatment choice in a consecutive non selected population of ruptured aneurysms: clinical results of the Clarity GDC study.** *Neurosurgery* 2011;69:837–41
4. Pierot L, Spelle L, Vitry F; ATENA Investigators. **Immediate clinical outcome of patients harbouring unruptured intracranial aneurysms treated by endovascular approach: results of the ATENA study.** *Stroke* 2008;39:2497–504
5. Ferns SP, Sprengers MES, van Rooij WJ, et al. **Coiling of intracranial aneurysms: a systematic review on initial occlusion and reopening and retreatment rates.** *Stroke* 2009;40:e523–29
6. Pierot L, Cognard C, Anxionnat R, et al; CLARITY Investigators. **Endovascular treatment of ruptured intracranial aneurysms: factors affecting mid-term quality anatomic results: analysis in a prospective multicenter series of patients (CLARITY).** *AJNR Am J Neuroradiol* 2012;33:1475–80
7. Lubicz B, Collignon L, Raphaeli G, et al. **Flow-diverter stent for the endovascular treatment of intracranial aneurysms: a prospective study in 29 patients with 34 aneurysms.** *Stroke* 2010;41:2247–53
8. Byrne JV, Beltechi R, Yarnold JA, et al. **Early experience in the treatment of intra-cranial aneurysms by endovascular flow diversion: a multicentre prospective study.** *PLoS One* 2010;5:pii: e12492
9. Tähtinen OI, Manninen HI, Vanninen RL, et al. **The Silk flow-diverting stent in the endovascular treatment of complex intracranial aneurysms: technical aspects and midterm results in 24 consecutive patients.** *Neurosurgery* 2012;70:617–23
10. Berge J, Biondi A, Machi P, et al. **Flow-diverter Silk stent for the treatment of intracranial aneurysms: 1-year follow-up in a multicenter study.** *AJNR Am J Neuroradiol* 2012;33:1150–55
11. Wagner A, Cortsen M, Hauerberg J, et al. **Treatment of intracranial aneurysms: reconstruction of the parent artery with flow-diverting (Silk) stent.** *Neuroradiology* 2012;54:709–18
12. Velioglu M, Kizilkilic O, Selcuk H, et al. **Early and midterm results of complex cerebral aneurysms treated with Silk stent.** *Neuroradiology* 2012;54:1355–65
13. Cirillo L, Leonardi M, Dall'olio M, et al. **Complications in the treatment of intracranial aneurysms with Silk stents: an analysis of 30 consecutive patients.** *Interv Neuroradiol* 2012;18:413–25
14. Murthy SB, Shah S, Shastri A, et al. **The Silk flow diverter in the treatment of intracranial aneurysms.** *J Clin Neurosci* 2014;21:203–06
15. Cohen JE, Gomori JM, Moscovici S, et al. **Delayed complications after flow-diverter stenting: reactive in-stent stenosis and creeping stents.** *J Clin Neurosci* 2014;21:1116–22
16. Bonita R, Beaglehole R. **Modification of Rankin scale: recovery of motor function after stroke.** *Stroke* 1988;19:1497–500
17. Kamran M, Yarnold J, Grunwald IQ, et al. **Assessment of angiographic outcomes after flow diversion treatment of intracranial aneurysms: a new grading schema.** *Neuroradiology* 2011;53:501–08
18. Kulcsár Z, Houdart E, Bonafé A, et al. **Intra-aneurysmal thrombosis as a possible cause of delayed aneurysm rupture after flow-diversion treatment.** *AJNR Am J Neuroradiol* 2011;32:20–25
19. Boddu SR, Tong FC, Dehkharghani S, et al. **Contrast-enhanced time-resolved MRA for follow-up of intracranial aneurysms treated with the Pipeline embolization device.** *AJNR Am J Neuroradiol* 2014;35:2112–18

# Comparison of Modern Stroke Thrombectomy Approaches Using an In Vitro Cerebrovascular Occlusion Model

M. Mokin, S.V. Setlur Nagesh, C.N. Ionita, E.I. Levy, and A.H. Siddiqui



## ABSTRACT

**BACKGROUND AND PURPOSE:** A new in vitro cerebrovascular occlusion model of the intracranial circulation was developed recently for testing thrombectomy devices. Using this model, we compared recanalization success associated with different modern endovascular thrombectomy approaches.

**MATERIALS AND METHODS:** Model experiments were performed in 4 thrombectomy test groups: 1) primary or direct Stentriever thrombectomy with a conventional guide catheter (control group), 2) primary Stentriever thrombectomy with a balloon-guide catheter, 3) combined Stentriever–continuous aspiration approach, and 4) direct aspiration alone. Successful recanalization was defined as a TIC1 score of 2b or 3.

**RESULTS:** Seventy-one thrombectomy experiments were conducted. Similar rates of TIC1 2b–3 scores were achieved with balloon-guide and conventional guide catheters ( $P = .34$ ). The combined Stentriever plus aspiration approach and the primary aspiration thrombectomy resulted in significantly higher rates of TIC1 2b or 3 than the conventional guide-catheter approach in the control group ( $P = .008$  and  $P = .0001$ , respectively). The primary Stentriever thrombectomy with the conventional guide catheter showed the highest rate of embolization to new territories (53%).

**CONCLUSIONS:** Data from our in vitro model experiments show that the Stentriever thrombectomy under continuous aspiration and primary aspiration thrombectomy approaches led to the highest degree of recanalization.

**ABBREVIATIONS:** ADAPT = direct aspiration first pass technique; EDT = embolization in distal territory; ENT = embolization in new territory; SWIFT = Solitaire FR With the Intention for Thrombectomy; TREVO 2 = Thrombectomy REvascularization of large Vessel Occlusions in acute ischemic stroke

Since the publication of the Solitaire FR With the Intention for Thrombectomy (SWIFT) and Thrombectomy REvascularization of large Vessel Occlusions in acute ischemic stroke (TREVO 2) randomized clinical trials, Stentriever (Trevo; Stryker, Kalamazoo, Michigan) have become widely used for endovascular treatment of stroke.<sup>1,2</sup> Postmarketing experience

indicates that in modern clinical practice, Stentriever are often used in conjunction with another device such as an aspiration thrombectomy catheter or a balloon-guide catheter.<sup>3–5</sup> Moreover, direct aspiration thrombectomy by using recently developed large-bore aspiration catheters has shown promise as an effective alternative approach for intra-arterial revascularization.<sup>6,7</sup> However, the recanalization effectiveness of these types of thrombectomy devices has not been compared in a randomized trial, to our knowledge.

A novel in vitro intracranial cerebrovascular occlusion model for testing thrombectomy devices was developed recently.<sup>8,9</sup> This 3D printed model is uniquely constructed on the basis of patient-specific anatomies to mimic a typical intracranial circulation by the presence of robust collaterals through both anterior and posterior communicating arteries and the typical tortuosity encountered in the intracranial circulation. In addition, the modulus of the model is closer to normal physiologic vessels than typical silicone models, allowing a feel and device deformation that are similar to those in a real clinical situation.<sup>10,11</sup> Here, we com-

Received June 22, 2014; accepted after revision September 6.

From the Departments of Neurosurgery (M.M., E.I.L., A.H.S.), Biomedical Engineering (S.V.S.N., C.N.I.), Electrical Engineering (S.V.S.N.), Mechanical and Aerospace Engineering (S.V.S.N.), and Radiology (E.I.L., A.H.S.) and Toshiba Stroke and Vascular Research Center (C.N.I., E.I.L., A.H.S.), University at Buffalo, State University of New York, Buffalo, New York; and Jacobs Institute (A.H.S.), Buffalo, New York.

Devices were provided by Covidien, Stryker, and Penumbra. All data collection, analysis, and interpretation were performed by the authors, independent of company input or interpretation.

Please address correspondence to Adnan H. Siddiqui, MD, PhD, University at Buffalo Neurosurgery, 100 High St, Suite B4, Buffalo, NY 14203; e-mail: asiddiqui@ubns.com

Indicates open access to non-subscribers at www.ajnr.org

<http://dx.doi.org/10.3174/ajnr.A4149>

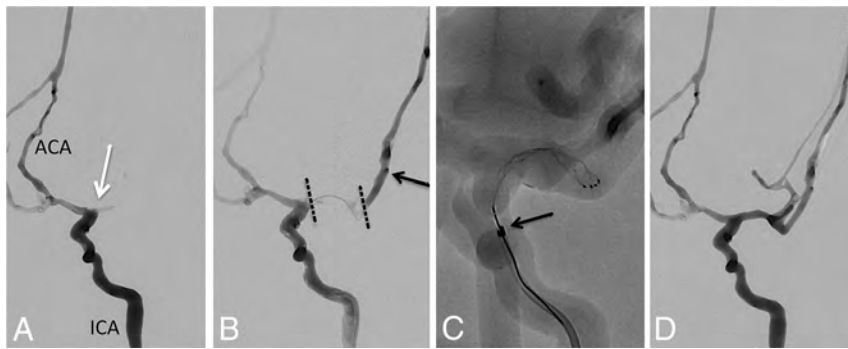


**FIG 1.** Combined Stentriever plus aspiration approach to thrombectomy. A, Baseline angiogram, anteroposterior view, left ICA injection, demonstrating occlusion at the MCA origin (white arrow). ACA indicates anterior cerebral artery. B, Combined left ICA and microcatheter injection shows the extent of the thrombus within the left MCA (dotted black lines). Black arrow points to the tip of the microcatheter within an M2 branch of the MCA. C, Solitaire FR stent retriever is deployed within the M1 MCA segment. Black arrow points to the distal tip of the 5MAX ACE reperfusion catheter. D, Final angiogram after successful thrombectomy shows robust filling of the left MCA branches except for some distal superior trunk vessels. The final recanalization grade is TIC1 2b.

pare primary Stentriever thrombectomy with the aforementioned other modern thrombectomy approaches by using this in vitro model.

**Ethics Statement.** The collection of clinical data for the model design was approved by the University at Buffalo institutional review board.

## MATERIALS AND METHODS

### Model Description

The in vitro model of the intracranial cerebrovascular occlusion has been described in detail previously.<sup>8,9</sup> This model closely resembles the human intracranial circulation and consists of 3 separate inflow channels mimicking the basilar artery and the 2 intracranial ICA branches. The design includes the MCA branches (M1–M4 segments with the smallest vessels of 1 mm in diameter), bilateral A1 anterior cerebral artery segments connected to a single anterior cerebral artery, and a single posterior communicating artery (right side), allowing near-complete circle of Willis circulation. The circulating fluid (40% glycerol, 60% water) was maintained at 37°C. A pulsatile pump (Masterflex; Cole-Parmer, Vernon Hills, Illinois) was used to simulate cardiac output.

Fresh clots were prepared by mixing 4 mL of fresh swine blood (no anticoagulant), 32 mg of fibrinogen from bovine plasma (Sigma-Aldrich, St. Louis, Missouri; catalog No. F8630), and 1 U of thrombin from bovine plasma (Sigma-Aldrich, catalog No. T4648) in a 5-mL syringe for at least 3 minutes. The mixture was placed into plastic tubing (4-mm-diameter) and incubated at room temperature for at least 60 minutes. Clots were then cut into 10-mm-length pieces and were introduced into the flow loop through a 9F sheath. The clots were navigated into the M1 or M2 MCA segment with antegrade flow of the circulatory fluid. Pressure measurements of the intracranial vessels by using the conventional guide catheter before and after clot introduction were reported in our initial publication describing the model.<sup>9</sup> Inflation of the balloon-guide catheter resulted in a

3-mm Hg decrease in pressure immediately proximal to the clot.

### Thrombectomy Procedures

After placing the clot into the target vessel (either the M1 or proximal M2 MCA segment), we performed baseline angiography injections to confirm the occlusion site. A single thrombectomy attempt was allowed for each experiment in the 4 groups described below.

The control group (group 1) consisted of thrombectomy cases performed by using a conventional guide catheter. For these experiments, we used a 6F Shuttle (Cook Medical, Bloomington, Indiana), which was placed into the segment corresponding to the cervical ICA. A 0.021-inch microcatheter was delivered over a 0.014-inch wire

to cross the clot under fluoroscopy and road-mapping guidance. A microinjection through the microcatheter was performed to document the extent of occlusion distally. A Solitaire FR device (Covidien, Irvine, California) or a Trevo ProVue Stentriever (Stryker) was delivered by using the 0.021-inch microcatheter, deployed at the occlusion site, left in place for 5 minutes, and then retrieved.

For experiments testing the balloon-guide-catheter approach (group 2), thrombectomy was performed with an 8F catheter (Concentric Medical, Mountain View, California) or an 8F Cello Balloon-Guide Catheter (Covidien). The balloon was inflated before the Stentriever was withdrawn, and manual aspiration through the guide catheter was applied by using a 20-mL syringe.

For experiments testing the combined Stentriever and aspiration approach (group 3), an intermediate catheter (5MAX ACE Reperfusion Catheter; Penumbra, Alameda, California) and the 6F Cook Shuttle were used. The Stentriever was withdrawn into the reperfusion catheter under continuous aspiration by using the Aspiration Pump (Penumbra). Figure 1 shows an example of this experiment.

For experiments testing the primary aspiration approach, no Stentriever was used (group 4). The 5MAX ACE catheter was delivered over the microcatheter (always attempting not to cross the clot with the microcatheter-microwire construct) and advanced to the level of the thrombus, according to the previously described direct aspiration first pass technique (ADAPT).<sup>6</sup> Aspiration through the Penumbra Aspiration Pump was applied while the aspiration catheter was gently pushed forward to ensure complete contact with the clot. After 2 minutes of continuous aspiration, if no clot was collected, the aspiration catheter was withdrawn under continuous aspiration.

While performing thrombectomy, we continuously monitored the clot and thrombectomy devices via gross observation and high-definition video recording to document the location of any clot breakdown. Primary outcomes included the degree of recanalization (based on the TIC1 grading scale) and the occurrence of emboli. Successful recanalization was defined as a TIC1 score of 2b or 3. Embolization in new territory (ENT) was defined

## Radiographic outcomes of thrombectomy experiments

	Conventional Guide + Stentriever (n = 19)	Balloon-Guide + Stentriever (n = 20)	Stentriever + Aspiration (n = 17)	Direct Aspiration (n = 15)
TICI score				
0 (No.) (%)	7 (37%)	8 (40%)	0 (0%)	0 (0%)
1 (No.) (%)	2 (11%)	0 (0%)	1 (6%)	0 (0%)
2a (No.) (%)	3 (16%)	1 (5%)	2 (12%)	0 (0%)
2b (No.) (%)	2 (11%)	3 (15%)	3 (18%)	2 (13%)
3 (No.) (%)	5 (26%)	8 (40%)	11 (65%)	13 (87%)
2b or 3 (No.) (%)	7 (37%)	11 (55%)	14 (82%)	15 (100%)
Embolic events				
Embolization of new territories (No.) (%)	10 (53%)	2 (10%)	2 (12%)	0 (0%)
Embolization of distal territories (No.) (%)	3 (16%)	3 (15%)	4 (24%)	2 (13%)

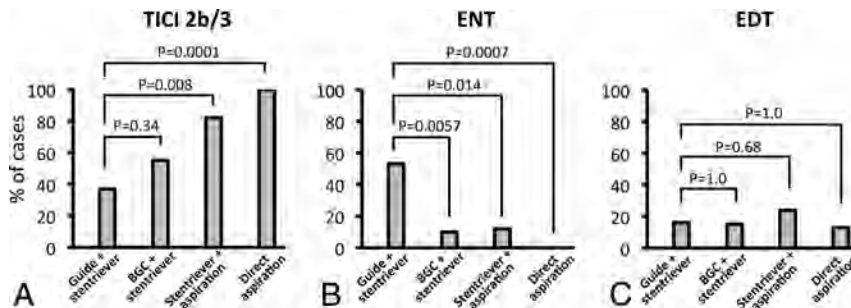


**FIG 2.** A, Rates of TICI 2b or 3 recanalization achieved with different thrombectomy approaches. “Guide + Stentriever” represents the primary Stentriever approach by using a conventional guide catheter. “BGC + Stentriever” represents the primary Stentriever approach by using a balloon-guide catheter. “Stentriever + aspiration” represents the combined Stentriever plus continuous aspiration approach. “Direct aspiration” represents thrombectomy performed by using the direct aspiration approach without the use of a Stentriever. B, Rates of embolization of new territories with different thrombectomy approaches. C, Rates of embolization of distal territories with different thrombectomy approaches.

as emboli observed on postthrombectomy angiography within previously unaffected territories. Embolization in distal territory (EDT) was defined as emboli seen within the territory of the vessel where the thrombus was originally placed. Final TICI scores and postthrombectomy embolic events were analyzed blinded to the type of thrombectomy approach.

### Statistical Analysis

Analysis of variables was performed by using the Fisher exact test.  $P < .05$  was statistically significant.

### RESULTS

We conducted 71 thrombectomy experiments: 19 primary Stentriever thrombectomies by using a conventional guide catheter, 20 primary Stentriever thrombectomies by using a balloon-guide catheter, 17 combined Stentriever plus continuous aspiration thrombectomies, and 15 primary aspiration thrombectomies. The Table summarizes angiographic outcomes in each group. There was no significant difference in achieving TICI 2b or 3 with a balloon-guide catheter versus a conventional catheter for primary Stentriever thrombectomy ( $P = .34$ ; Fig 2A). The combined Stentriever plus continuous aspiration approach and primary aspiration thrombectomy resulted in significantly higher rates of TICI 2b or 3 than the primary Stentriever thrombectomy with the conventional guide catheter ( $P = .008$  and  $P = .0001$ , respectively; Fig 2A).

The primary Stentriever thrombectomy with the conventional guide catheter showed the highest rate of ENT (53%) (Table). The rate of ENT after Stentriever thrombectomy was significantly reduced with the balloon-guide catheter or continuous direct aspiration, compared with thrombectomy by using the conventional guide catheter ( $P = .0057$  and  $P = .0014$ , respectively; Fig 2B). The most significant reduction in ENT rates was seen in cases of primary aspiration thrombectomy versus Stentriever thrombectomy with the conventional guide catheter ( $P = .0007$ ; Fig 2B). There was no difference in the rate of EDT events among the studied approaches (Fig 2C).

### DISCUSSION

Our study showed that the highest degree of revascularization was achieved with the use of the combined Stentriever–aspiration thrombectomy or primary aspiration techniques. The use of the balloon-guide catheter for Stentriever thrombectomy did not result in significant improvement in recanalization, though a trend toward higher TICI scores was noted. Embolic events can occur in up to 12% of cases of Stentriever thrombectomy and are associated with a 2-fold increase in mortality compared with cases without embolic complications.<sup>12</sup> In our experiments, we observed the presence of substantial ENT with all approaches except for direct aspiration; however, regarding EDT events, no technique protects effectively from this occurrence.

Nguyen et al<sup>13</sup> published their experience with the use of the balloon-guide catheter in conjunction with Solitaire FR stent retriever thrombectomy. Although TICI 3 recanalization was seen more often in cases in which the balloon-guide catheter was used (54% with the balloon-guide catheter versus 33% without;  $P < .001$ ), overall rates of TICI 2b or 3 recanalization were similar (76% with versus 71% without,  $P = .3$ ). Occurrence of distal emboli or emboli in new territories was also similar. Of importance, the discharge NIHSS score and 3-month favorable clinical outcome were significantly higher in the balloon-guide catheter group. It is possible that with a higher number of thrombectomy experiments in our study, we could have achieved a significant difference in obtaining higher recanalization results with the bal-

loon-guide catheter because a trend toward higher TIC1 2b–3 was observed in this group.

Our in vitro results with direct aspiration or the combined Stentriever-aspiration approach are different from those of the real-world clinical experience. Direct aspiration alone resulted in TIC1 2b or 3 recanalization in 75%–78% of cases, whereas the addition of Stentriever improved the rate of successful recanalization to 95%, according to the 2 recent studies of the direct-aspiration approach to stroke thrombectomy.<sup>6,7</sup> EDT prompting additional aspiration was noted in 16% of cases in the initial experience with direct aspiration.<sup>6</sup> In the ADAPT FAST series, the rate of EDT was also high (10%) but no cases of ENT were observed.<sup>7</sup> In our model, the rate of TIC1 2b or 3 recanalization reached 100%, which is remarkably higher than that previously reported in clinical data. However, the 13% EDT rate is similar to rates reported in the ADAPT and ADAPT FAST studies. Turk et al<sup>7</sup> compared radiographic outcomes from the real-world experience in the ADAPT FAST, SWIFT, TREVO, and North American Solitaire Stent-Retriever Acute Stroke studies, which can further help readers when matching our model data to the clinical results.

Our results should be interpreted with caution. First, this model is likely representative of an embolic stroke-type of large-vessel occlusion, in which aspiration thrombectomy could be highly effective. The design of the model did not simulate intracranial atherosclerosis, thrombotic plaque, or embolic debris from a ruptured extracranial plaque, for which a Stentriever rather than primary aspiration thrombectomy might be of more benefit. Approximately one-third of large-vessel-occlusion strokes are of noncardioembolic origin (eg, 31% in TREVO 2<sup>1</sup>). Another limitation is that intimal damage or occlusion of perforators, which can be evaluated in animal stroke models with the use of different thrombectomy devices, cannot be tested in our in vitro model.<sup>14</sup>

Second, only a single thrombectomy attempt was performed in each experiment, whereas in clinical practice multiple thrombectomy attempts are often required to achieve recanalization. It would also be interesting to study how the mode of aspiration affects revascularization success in our model. Simon and Grey<sup>15</sup> demonstrated that manual aspiration with syringes can provide a substantially higher dynamic pressure at the catheter tip than the Penumbra aspiration system. We are planning to investigate this finding in future experiments. Third, because the smallest MCA M4 branches in the model were 0.5 mm in diameter, we did not account for embolization that could have occurred with debris under that size, which could further affect our final TIC1 score interpretation.

## CONCLUSIONS

Data from these experiments indicate that the Stentriever thrombectomy under continuous aspiration and primary aspiration thrombectomy approaches lead to the highest degree of recanalization. However, embolization in nonaffected territories and in distal territories remains a major issue, which could affect eventual clinical outcomes. Such data might prove helpful in clinical practice when estimating radiographic outcomes with different endovascular treatment approaches.

## ACKNOWLEDGMENTS

The authors thank Stephen Rudin, PhD, for guidance; Liza Pope, BS, for clot preparation; Paul H. Dressel, BFA, for illustration preparation; and Debra J. Zimmer, for editorial assistance.

Disclosures: Ciprian N. Ionita—RELATED: Grant: National Institutes of Health\*; Other: grants from the National Institutes of Health (2ROIEB002873; for partial support of student and faculty) and Toshiba (equipment) in conjunction with the present study; UNRELATED: Grants/Grants Pending: National Institutes of Health.\* Elad I. Levy—UNRELATED: Stock/Stock Options: shareholder/ownership interests in Intratech Medical, Mynx/Access Closure, Blockade Medical LLC; Other: National Principal Investigator on the Covidien US SWIFT PRIME Trials (no compensation involved); compensation from Abbott for carotid training for physicians. Maxim Mokin—UNRELATED: Grants/Grants Pending: Toshiba (stroke research grant)\* Adnan H. Siddiqui—RELATED: Other: Covidien, Stryker, Penumbra. Comments: Devices were provided by Covidien, Stryker, and Penumbra, Inc. All data collection, analysis, and interpretation were performed by the authors, independent of company input or interpretation; UNRELATED: Board Membership: Codman & Shurtleff, Covidien Neurovascular. Comments: Advisory Board member; Consultancy: Codman & Shurtleff, Concentric Medical, ev3/Covidien, Guidepoint Global Consulting, Penumbra, Stryker, Pulsar Vascular, MicroVention, Lazarus Effect, Blockade Medical; Grants/Grants Pending: National Institutes of Health (coinvestigator: National Institute of Neurological Disorders and Stroke 1ROINS064592–01A1; National Institute of Biomedical Imaging and Bioengineering 5ROIEB002873–07), University at Buffalo (Research Development Award). Comments: research grants; Payment for Lectures (including service on Speakers Bureaus): Codman & Shurtleff (Speakers Bureau and honoraria), Abbott Vascular (honoraria), Penumbra (honoraria); Stock/Stock Options: Hotspur Technologies, Intratech Medical, StimSox, Valor Medical, Blockade Medical, Lazarus Effect. Comments: financial interests; Other: Penumbra, Covidien, MicroVention. Comments: National Steering Committee member for Separator 3D Trial of Penumbra; SWIFT PRIME trial of Covidien, and FRED trial of MicroVention. No compensation. \*Money paid to the institution.

## REFERENCES

1. Nogueira RG, Lutsep HL, Gupta R, et al. **Trevo versus Merci retrievers for thrombectomy revascularisation of large vessel occlusions in acute ischaemic stroke (TREVO 2): a randomised trial.** *Lancet* 2012;380:1231–40
2. Saver JL, Jahan R, Levy EI, et al. **Solitaire flow restoration device versus the Merci Retriever in patients with acute ischaemic stroke (SWIFT): a randomised, parallel-group, non-inferiority trial.** *Lancet* 2012;380:1241–49
3. Humphries W, Hoit D, Doss VT, et al. **Distal aspiration with retrievable stent assisted thrombectomy for the treatment of acute ischemic stroke.** *J Neurointerv Surg* 2015;7:90–94
4. Mokin M, Dumont TM, Veznedaroglu E, et al. **Solitaire flow restoration thrombectomy for acute ischemic stroke: retrospective multicenter analysis of early postmarket experience after FDA approval.** *Neurosurgery* 2013;73:19–25; discussion 25–26
5. Zaidat OO, Castonguay AC, Gupta R, et al. **North American Solitaire Stent Retriever Acute Stroke registry: post-marketing revascularization and clinical outcome results.** *J Neurointerv Surg* 2014;6:584–88
6. Turk AS, Spiotta A, Frei D, et al. **Initial clinical experience with the ADAPT technique: a direct aspiration first pass technique for stroke thrombectomy.** *J Neurointerv Surg* 2014;6:231–37
7. Turk AS, Frei D, Fiorella D, et al. **ADAPT FAST study: a direct aspiration first pass technique for acute stroke thrombectomy.** *J Neurointerv Surg* 2014;6:260–64
8. Ionita CN, Mokin M, Varble N, et al. **Challenges and limitations of patient-specific vascular phantom fabrication using 3D Polyjet printing.** *Proc SPIE* 2014;9038:90380M
9. Mokin M, Ionita CN, Setlur Nagesh SV, et al. **Primary stentriever versus combined stentriever plus aspiration thrombectomy approaches: in vitro stroke model comparison.** *J Neurointerv Surg* 2014 Apr 30. [Epub ahead of print]

10. Claes E, Atienza JM, Guinea GV, et al. **Mechanical properties of human coronary arteries.** *Conf Proc IEEE Eng Med Biol Soc* 2010;2010:3792–95
11. Teng Z, Tang D, Zheng J, et al. **An experimental study on the ultimate strength of the adventitia and media of human atherosclerotic carotid arteries in circumferential and axial directions.** *J Biomech* 2009;42:2535–39
12. Gascou G, Lobotesis K, Machi P, et al. **Stent retrievers in acute ischemic stroke: complications and failures during the perioperative period.** *AJNR Am J Neuroradiol* 2014;35:734–40
13. Nguyen TN, Malisch T, Castonguay AC, et al. **Balloon guide catheter improves revascularization and clinical outcomes with the Solitaire device: analysis of the North American Solitaire Acute Stroke Registry.** *Stroke* 2014;45:141–45
14. Gralla J, Schroth G, Remonda L, et al. **A dedicated animal model for mechanical thrombectomy in acute stroke.** *AJNR Am J Neuroradiol* 2006;27:1357–61
15. Simon SD, Grey CP. **Hydrodynamic comparison of the Penumbra system and commonly available syringes in forced-suction thrombectomy.** *J Neurointerv Surg* 2014;6:205–11

# Double Solitaire Mechanical Thrombectomy in Acute Stroke: Effective Rescue Strategy for Refractory Artery Occlusions?

J. Klisch, V. Sychra, C. Strasilla, C.A. Taschner, M. Reinhard, H. Urbach, and  S. Meckel



## ABSTRACT

**BACKGROUND AND PURPOSE:** Mechanical thrombectomy by using a single stent retriever system has demonstrated high efficacy for recanalization of large-artery occlusions in acute stroke. We aimed to evaluate the feasibility, safety, and efficacy of a novel double Solitaire stent retriever technique as an escalating treatment for occlusions that are refractory to first-line single stent retriever mechanical thrombectomy.

**MATERIALS AND METHODS:** All patients treated with the double stent retriever technique by using the Solitaire system were retrospectively selected from 2 large neurointerventional centers. Time to recanalization, angiographic (TICI) and clinical outcomes (mRS), and complications were assessed.

**RESULTS:** Ten patients (median NIHSS score, 16; mean age, 70 years) with MCA M1 segment ( $n = 5$ ) and terminal ICA ( $n = 5$  including 2 ICA tandem) occlusions were included. Prior single stent retriever mechanical thrombectomy had been performed in 9 patients (median number of passes, 3). Median time to recanalization was 60 minutes (interquartile range, 45–87 minutes). Procedure-related complications occurred in 1 patient; overall mortality was 20%. Recanalization of the target vessel (TICI 2b/3) was achieved in 80%. Good clinical outcome (mRS 0–2) was 50%.

**CONCLUSIONS:** In this preliminary feasibility study, the double Solitaire stent retriever technique proved to be an effective method for recanalization of anterior circulation large-artery occlusions refractory to standard stent retriever mechanical thrombectomy.

**ABBREVIATIONS:** DAC = distal-access catheter; ICAT = internal carotid artery terminus; MT = mechanical thrombectomy; SR = stent retriever

In acute ischemic stroke, recanalization of an occluded cerebral artery is strongly linked with improved clinical outcome and reduced mortality.<sup>1</sup> The potential of IV thrombolysis for achieving successful vessel recanalization is significantly limited by the extent of clot burden in proximal cerebral artery occlusions.<sup>2</sup> With the recent introduction of stent retrievers (SR) for mechanical thrombectomy (MT), fast, safe, and efficient large-artery recanalization treatment can be achieved, and their superiority over older MT devices has been demonstrated in randomized controlled trials.<sup>3,4</sup>

Despite considerable recanalization rates of 61%–86% (Thrombolysis in Myocardial Infarction/TICI scores of  $\geq 2/2b$ ),<sup>3–5</sup> up to

33.3% of patients are still left without sufficient recanalization after standard SR MT.<sup>6</sup> In these refractory cases, different rescue treatments have been proposed with variable rates of success.<sup>4,5,7–10</sup> These include local intra-arterial fibrinolysis, MT with the Penumbra device (Penumbra, Alameda, California), mechanical thrombus disruption, thromboaspiration through a distal-access catheter (DAC), balloon angioplasty, and/or stent placement.

Here, we describe a novel escalating strategy for MT by using 2 Solitaire SR devices (Covidien, Irvine, California), hence termed the “double Solitaire SR technique,” for proximal anterior circulation occlusions that are refractory to first-line single SR MT. In a retrospective series of patients from 2 large neurointerventional centers, we assessed the feasibility, safety, and angiographic and clinical outcomes of this technique.

## MATERIALS AND METHODS

### Patient Selection

In this retrospective study, a consecutive series of patients was identified from in-hospital stroke databases that included patients with acute stroke due to large cerebral artery occlusions undergo-

Received June 29, 2014; accepted after revision August 13.

From the Institute of Diagnostic und Interventional Radiology and Neuroradiology (J.K., V.S., C.S.), Helios Klinikum, Erfurt, Germany; and Departments of Neuroradiology (C.A.T., H.U., S.M.) and Neurology (M.R.), University Hospital Freiburg, Freiburg, Germany.

Please address correspondence to Stephan Meckel, MD, Department of Neuroradiology, University Hospital Freiburg, Breisacher Str 64, D-79106 Freiburg, Germany; e-mail: stephanmeckel@gmail.com

 Indicates article with supplemental on-line table.

<http://dx.doi.org/10.3174/ajnr.A4133>

ing MT treatments. We collected all patients treated with the double Solitaire SR technique between its introduction in December 2012 and May 2014 from 2 large tertiary neurointerventional centers. At both centers, a total of 234 MT treatments for anterior circulation occlusions were performed. The eligibility criteria for these MT treatments were the following: 1) NIHSS  $\geq$  8; 2) confirmed proximal anterior circulation cerebral artery occlusion (ICA including tandem lesions, eg, proximal ICA stenosis and ICA terminus [ICAT] or the MCA M1 segment) with a TICI score of 0 or 1; and 3) initiation of MT treatment within 6 hours of symptom onset. In general, written consent is not obtained from all patients undergoing MT treatments in the emergency setting of an acute stroke at both involved centers. The choice of MT treatment is made as an interdisciplinary decision between the on-call attending neurointerventionalist and neurologist on an individual basis, considering relevant inclusion/exclusion criteria that are documented in the patient's file. Approval by the ethics committee was waived because the double Solitaire SR technique represented a rescue treatment in case of failure of the approved standard MT technique using a single SR device, which was performed at the individual operator's decision (see below).

Baseline investigations included the assessment of NIHSS by an experienced on-call stroke neurologist, independent of this study. When no other contraindications were present, a bridging IV thrombolysis treatment was started directly after cranial imaging.

### **MT Procedures**

All procedures were performed with the patient under general anesthesia. Standard first-line MT with a single SR was performed either by using a balloon-guide catheter or a DAC as described previously.<sup>11-13</sup> The Solitaire device was used in all MT procedures either as a single device or for the double SR technique. The sizes of the Solitaire devices used included Solitaire AB, 3  $\times$  20 mm, and Solitaire FR or Solitaire Two, 4  $\times$  20 mm and 6  $\times$  30 mm. In case of insufficient target-vessel recanalization (TICI score, 0 and 1), the SR sequence was repeated on the basis of the individual operator's decision until the double Solitaire SR technique was initiated. This decision was influenced by several factors, including clot load/length of the occluded arterial segment, size and composition of the already retrieved clot fragments, the amount of clot extension into the bifurcation limbs, and the duration of multiple single SR passages.

### **Double Solitaire SR Technique**

With the use of an 8F balloon-guide catheter (Merci; Concentric Medical, Mountain View, California; or Cello; Covidien), two 0.021-inch internal-diameter microcatheters (Prowler Select Plus; Codman & Shurtleff, Raynham, Massachusetts; or Rebar-18; Covidien) were navigated sequentially into the occluded vessel. They were either placed parallel to each other with at least 1 tip distal to the thrombus or in a Y-type configuration with both tips beyond the thrombus, ending in separate bifurcation limbs (eg, the superior and inferior MCA trunks). The parallel configuration of the SRs may enable retrieval of large and/or long thrombi, with both SR devices placed beside each other, also allowing distal device overlap. The latter may potentially increase the area of

thrombus catchment in long segmental occlusions extending from the MCA bifurcation to the terminal ICA. Then, 2 Solitaire devices of similar or different sizes (eg, 4  $\times$  20 and 6  $\times$  30 mm) were delivered from each microcatheter in a sequential fashion to cover the whole extent of the thrombus. A control angiography was performed after unfolding the SRs to evaluate re-establishment of flow. Both SRs were left deployed for 3–10 minutes depending on the degree of flow in the target vessel at the individual operator's discretion. The detachment zones of both SR devices were covered by the tips of the microcatheters to prevent inadvertent detachment during the retrieval maneuver. Then, both devices were slowly recovered by simultaneously pulling them together into the balloon-guide catheter under continuous aspiration and fluoroscopic imaging control. After recovery, both stent devices were found entangled in each other, in some cases with the thrombus embedded between the struts; however, they usually could be carefully released and cleaned of thrombus fragments.

With the use of a DAC (Penumbra 54; Penumbra; or Navien 0.058; Covidien), parallel placement of 2 microcatheters is not possible. Therefore, 1 microcatheter was first placed with its tip distal enough within 1 arterial limb so that the proximal end of the SR did not cover the bifurcation, to avoid an inadvertent placement of the second SR through the struts of the first one. After unfolding the first SR, we removed the microcatheter completely from the DAC, leaving a bare Solitaire device inside the DAC. Then, the second bifurcating limb was catheterized with a microcatheter, and the second SR device was unfolded in a standard fashion. The detachment zone of the proximal SR was left covered by the tip of the microcatheter so that in case of inadvertent detachment of the more distally placed SR during retrieval, the proximal one could still be recovered. Both SRs were subsequently recovered as described above while aspiration was performed directly through the DAC. Thereby, the tip of the DAC was placed as close as possible to the clot (eg, into the terminal ICA or orifice of the M1 segment, depending on the length of the clot), to achieve an optimal aspiration result without clot fragmentation during the retrieval maneuver.

The time from symptom onset to the start of the MT procedure (first angiographic image) and total recanalization time (first angiographic image to the image demonstrating final recanalization) were recorded.

### **Outcome Analysis and Follow-Up**

The degree of target-vessel recanalization was assessed by using the TICI score by 2 experienced interventional neuroradiologists independently from the procedures. Functional outcome was assessed by using the mRS score on discharge from the rehabilitation center (usually at days 60–90 after stroke onset) from respective patient files, determined by experienced neurologists blinded to the treatment details of the double Solitaire SR procedure. Furthermore, we recorded the following procedural parameters: use of a DAC or balloon-guide catheter, use of a bridging IVT, use of carotid stent placement for treatment of proximal ICA stenosis/occlusion, the number of unsuccessful single SR passes before application of the double SR technique, additional escalating techniques, and complications associated with MT procedures including proce-

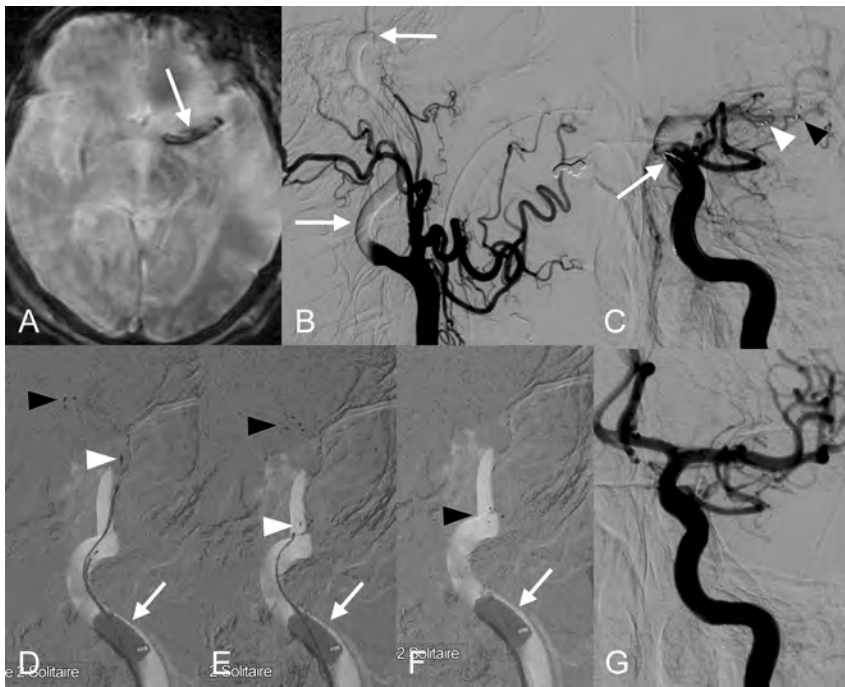


**FIG 1.** Double Solitaire SR maneuver in patient 1 with a left ICAT occlusion. Large M1 thrombus (arrow in A, gradient recalled-echo image) and proximal ICA contrast media stasis (arrows in B) are shown. Two Solitaire SRs are placed parallel (arrow in C, proximal markers) with 1 extending to the MCA bifurcation (black arrowhead, 6 × 30 mm) and 1 into the mid-M1 segment (white arrowhead, 4 × 20 mm). Three consecutive fluoroscopic images (D–F) depict simultaneous retrieval of both SRs; during this maneuver, the distal tip markers of the longer SR device (black arrowheads) follow the shorter one (white arrowheads), with retrieval of a large thrombus inside the tip of the inflated balloon-guide catheter (arrows). After double Solitaire SR MT, complete recanalization is demonstrated (G).

dural complications and postprocedural hemorrhage of any cause associated with a poor clinical outcome (mRS >2).

## RESULTS

We included 10 consecutive patients (7 men, 3 women; mean age, 70 years; range, 51–88 years). These included 5 patients treated for MCA M1 occlusion; 3, for ICAT occlusion; and 2, for ICA tandem occlusion, which overall represented 4.3% of all patients undergoing anterior circulation MT procedures during the analyzed time (see above). The median baseline NIHSS score was 16 (interquartile range, 13–19), and the median time from symptom onset to the start of the MT procedure was 168 minutes (interquartile range, 150–179 minutes). For both ICA tandem occlusions, proximal ICA stent placement was performed before MT. Nine patients were treated by a single SR MT before the double Solitaire SR technique, with a median number of 3 (range, 1–4) unsuccessful passes. In 1 patient (patient 9), the double Solitaire SR technique was performed as a primary MT treatment to avoid thrombus fragmentation during retrieval because superselective microcatheter injection had demonstrated exceptionally long thrombi extending from the ICAT via M1 to both the superior and inferior M2 trunks. The details of all patients including therapy, complications, and outcome are summarized in the On-line Table.

With the double Solitaire SR technique, both SRs were placed in a parallel configuration from M1 into the terminal ICA in 1 patient (Fig 1). In the remaining 9 patients, a Y-type SR configuration was used (Fig 2). Of these, both SRs extended into 2 MCA

divisions in 8 patients and into the M1 and A1 segments in 1 patient (patient 8). Before retrieval of both SRs, control angiograms disclosed variable degrees of re-established target-vessel flow in all patients. In 8 patients, a single pass with both SRs was performed. In 2 patients (patients 7 and 9), the double Solitaire SR technique was applied twice. In 2 patients, we performed additional escalating therapies: In patient 4, a residual M2 trunk occlusion was treated with an intravenous bolus of eptifibatid (glycoprotein IIb/IIIa antagonist) and another pass with a single SR. In patient 8, a refractory ICAT occlusion due to an underlying terminal ICA stenosis was finally treated with unsuccessful balloon angioplasty (a noncompliant balloon was used because wall-adherent thrombus and partially thrombosed atherosclerotic stenosis could initially not be discerned), and stent placement could not be performed due to difficult vascular access.

The median total recanalization time was 60 minutes (interquartile range, 45–87 minutes), including all additional procedures such as ICA stent placement. Overall complete recanalization (TICI 2b/3) was achieved in 8 patients (80%),

and good clinical outcome (mRS ≤2) was observed in 5 patients (50%). There were 2 fatalities (20%): One was a related malignant infarct following failed recanalization of an ICAT occlusion (patient 8, see above). The other (patient 6) had successful recanalization of an ICAT occlusion with initial neurologic improvement and then secondary deterioration 3 weeks later, with aphasia and hemiparesis due to presumed re-infarction (it was not further investigated due to the patient's documented provision, which only became apparent after the initial treatment).

We observed 1 procedural complication: Patient 4 had a residual proximal M2 occlusion after 2 unsuccessful single SR passes and 1 double SR pass. Contrast extravasation from the M2 segment was observed after further therapy escalation with IV eptifibatid and another single SR pass (see above). The ruptured segment was temporarily occluded with a single coil until active bleeding had stopped angiographically. Following decompressive craniectomy due to a malignant MCA infarct the next day, the outcome was poor (mRS 4). Inadvertent SR detachment during retrieval of both devices was not observed.

Mild vasospasm after the double Solitaire SR maneuver was encountered in 7 patients (70%). No severe vasospasm or arterial dissection was encountered.

## DISCUSSION

Our experience with this new off-label simultaneous use of 2 Solitaire SRs has been encouraging due to its ease of use and ability to achieve effective recanalization in refractory cases (TICI 2b/3 in 60% and

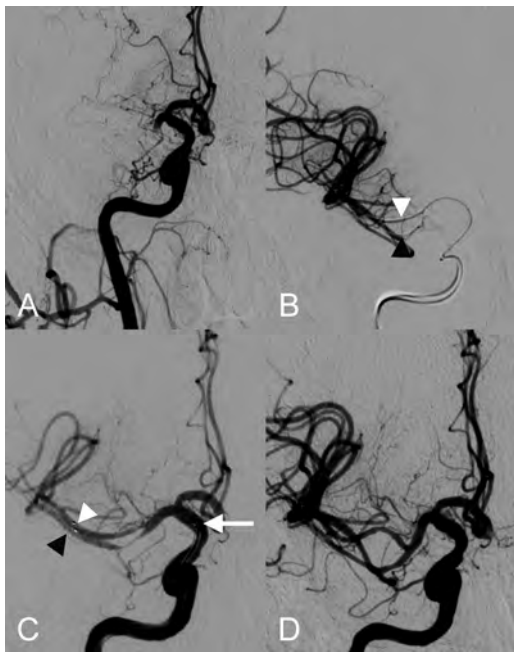


**FIG 2.** Double Solitaire SR maneuver with SRs in a Y-type configuration in patient 2 with MCA M1 occlusion. Following 3 single SR passes, there is refractory M1 occlusion (A). Simultaneous injection of 2 microcatheters being placed in the superior (*white arrowhead*) and inferior (*black arrowhead*) MCA divisions is shown in B. C, ICA injection after unfolding of 2 Solitaire devices (4 × 20 mm), which extend from both M2 segments (distal markers in the superior and inferior divisions, *white and black arrowheads*, respectively) to the terminal ICA (attachment zones, *white arrow*), demonstrates re-establishment of flow within both MCA trunks. D, After simultaneous retrieval of both SRs by using proximal occlusion and aspiration through a balloon-guide catheter, both MCA trunks are recanalized. Mild vasospasm of ICA and MCA vessels is depicted.

80% after 1 and 2 passes with the double Solitaire SR technique, respectively). The median total recanalization times of 60 minutes (interquartile range, 45–87 minutes) were increased compared with those reported in standard MT procedures with a single SR (range, 20–48 minutes).<sup>3,5,9–11</sup> However, given that these procedural times also included a median number of 3 unsuccessful single SR passes, the extra procedural time appears tolerable. The overall good clinical outcome (50%) was comparable with the results of larger series/trials with the standard single SR MT technique (40%–58%).<sup>3–5</sup> The Y-type configuration of the 2 SRs appears particularly useful for retrieving riding emboli at arterial bifurcations such as M1 emboli that extend into both M2 trunks. This technique may also be applied to refractory basilar artery occlusions due to emboli extending into both posterior cerebral arteries. Likewise, Clarençon et al<sup>14</sup> reported a case of an acute basilar artery occlusion that was treated successfully with double Merci retriever devices in a Y-type configuration via a bilateral vertebral artery approach.

In previous studies, other rescue therapies were usually applied in patients in whom adequate recanalization (TICI ≥ 2b) could not be achieved following several passes with a single SR (usually 3–5 passes at the individual operator’s discretion).<sup>3–5,9,11</sup> However, the success rates of various rescue treatments including intra-arterial pharmacologic thrombolysis, other MT devices, thromboaspiration (Penumbra), balloon angioplasty, or intracranial stent placement remain limited.<sup>5,9–11</sup> For example, patients who received a rescue therapy in the Solitaire FR Thrombectomy

for Acute Revascularization (STAR) study showed a significantly lower rate of favorable outcome compared with those who did not (33.3% versus 60.3%).<sup>5</sup> Likewise, Kurre et al<sup>10</sup> recently reported a significantly lower rate of adequate recanalization in patients who had rescue treatments compared with those with a maximum of 3 passes with a single SR device.

Cervical or intracranial vessel trauma remains a potentially serious procedure-related adverse event, which occurs at a low incidence with the use of the standard single SR MT technique.<sup>3,5,10,15,16</sup> In the Solitaire FR With the Intention For Thrombectomy trial, the reported incidences of arterial dissection, symptomatic cerebral hemorrhage, and SAH were 4.5%, 1.1%, and 1.1%, respectively.<sup>15</sup> The use of 2 parallel SRs within the MCA or ICA vessel lumen may potentially increase the force on the endothelium during the retrieval maneuver. We observed only 1 vessel trauma occurring after several single SR passes, 1 double SR pass, and further escalating therapy (see above). Within the limited experience of this feasibility study, therapeutic escalation beyond the double Solitaire SR technique should thus be made with caution.

In our series, we included a single case in which the double Solitaire SR technique was performed as a primary treatment for MT of an ICAT occlusion due to exceptionally long thrombi. However, on the basis of these preliminary results, this technique should be reserved only as a rescue treatment for cases refractory to standard single SR MT until further data on the safety and outcome are available. In general, the decision to extend the procedure after several unsuccessful retrieval attempts with a single SR device should only be made after careful consideration of individual factors defining the likelihood of a clinical success. Such factors may include the time from stroke onset, the extent of baseline infarct core, or the presence of underlying intracranial artery stenosis. The application of this technique with a second SR device will potentially add a significant increase in hospital costs to an already expensive acute stroke treatment. On the other hand, this may be considered worthwhile in light of high costs for care in cases of futile recanalization therapy resulting in a poor clinical outcome. However, the analysis of cost effectiveness was far beyond the scope of this feasibility study.

The limitations of the study relate to its small sample size and retrospective nature, which was designed to provide evidence of the feasibility and safety of this novel rescue technique for MT. The angiographic and clinical outcome data are promising but require further confirmation in larger prospective studies to demonstrate a possible improvement in clinical outcome related to the application of this MT escalating strategy compared with standard single SR MT only. Until the risk/benefit ratio has been further determined in such studies, practitioners are advised to proceed with extreme caution when applying this technique.

## CONCLUSIONS

In this preliminary feasibility study, the double Solitaire SR technique for MT therapy proved to be an effective rescue method for rapid recanalization of refractory anterior circulation occlusions. The technique showed a low complication rate and a high rate of target-vessel recanalization with 50% favorable clinical outcome. Further pro-

spective studies are required to demonstrate the clinical benefit for the subgroup of patients with refractory cerebral artery occlusion.

Disclosures: Joachim Klisch—UNRELATED: Consultancy: Sequent Medical.\* Christian A. Taschner—UNRELATED: Board Membership: MircoVention,\* Acandis\*; Consultancy: Stryker Neurovascular. Stephan Meckel—UNRELATED: Travel/Accommodations/Meeting Expenses Unrelated to Activities Listed: Stryker, MicroVention, Comments: travel expenses and Congress fees. \*Money paid to the institution.

## REFERENCES

1. Rha JH, Saver JL. **The impact of recanalization on ischemic stroke outcome: a meta-analysis.** *Stroke* 2007;38:967–73
2. Riedel CH, Zimmermann P, Jensen-Kondering U, et al. **The importance of size: successful recanalization by intravenous thrombolysis in acute anterior stroke depends on thrombus length.** *Stroke* 2011;42:1775–77
3. Nogueira RG, Lutsep HL, Gupta R, et al. **Trevo versus Merci retrievers for thrombectomy revascularisation of large vessel occlusions in acute ischaemic stroke (TREVO 2): a randomised trial.** *Lancet* 2012;380:1231–40
4. Saver JL, Jahan R, Levy EI, et al. **Solitaire flow restoration device versus the Merci retriever in patients with acute ischaemic stroke (SWIFT): a randomised, parallel-group, non-inferiority trial.** *Lancet* 2012;380:1241–49
5. Pereira VM, Gralla J, Davalos A, et al. **Prospective, multicenter, single-arm study of mechanical thrombectomy using Solitaire flow restoration in acute ischemic stroke.** *Stroke* 2013;44:2802–07
6. Gascou G, Lobotesis K, Machi P, et al. **Stent retrievers in acute ischemic stroke: complications and failures during the perioperative period.** *AJNR Am J Neuroradiol* 2014;35:734–40
7. Brekenfeld C, Schroth G, Mordasini P, et al. **Impact of retrievable stents on acute ischemic stroke treatment.** *AJNR Am J Neuroradiol* 2011;32:1269–73
8. Miteff F, Faulder KC, Goh AC, et al. **Mechanical thrombectomy with a self-expanding retrievable intracranial stent (Solitaire AB): experience in 26 patients with acute cerebral artery occlusion.** *AJNR Am J Neuroradiol* 2011;32:1078–81
9. Yoon YH, Yoon W, Jung MY, et al. **Outcome of mechanical thrombectomy with Solitaire stent as first-line intra-arterial treatment in intracranial internal carotid artery occlusion.** *Neuroradiology* 2013;55:999–1005
10. Kurre W, Aguilar-Perez M, Schmid E, et al. **Clinical experience with the pREset stent retriever for the treatment of acute ischemic stroke—a review of 271 consecutive cases.** *Neuroradiology* 2014;56:397–403
11. Dávalos A, Pereira VM, Chapot R, et al. **Retrospective multicenter study of Solitaire FR for revascularization in the treatment of acute ischemic stroke.** *Stroke* 2012;43:2699–705
12. Roth C, Papanagiotou P, Behnke S, et al. **Stent-assisted mechanical recanalization for treatment of acute intracerebral artery occlusions.** *Stroke* 2010;41:2559–67
13. Möhlenbruch M, Seifert M, Okulla T, et al. **Mechanical thrombectomy compared to local-intraarterial thrombolysis in carotid T and middle cerebral artery occlusions: a single center experience.** *Clin Neuroradiol* 2012;22:141–47
14. Clarençon F, Blanc R, Gallas S, et al. **Thrombectomy for acute basilar artery occlusion by using double Merci retriever devices and bilateral temporary vertebral artery flow reversal: technical note.** *J Neurosurg* 2009;111:53–56
15. Akins PT, Amar AP, Pakbaz RS, et al. **Complications of endovascular treatment for acute stroke in the SWIFT trial with Solitaire and Merci devices.** *AJNR Am J Neuroradiol* 2014;35:524–28
16. Gory B, Bresson D, Kessler I, et al. **Histopathologic evaluation of arterial wall response to 5 neurovascular mechanical thrombectomy devices in a swine model.** *AJNR Am J Neuroradiol* 2013;34:2192–98

# Small Pipes: Preliminary Experience with 3-mm or Smaller Pipeline Flow-Diverting Stents for Aneurysm Repair prior to Regulatory Approval

A.R. Martin, J.P. Cruz, C. O'Kelly, M. Kelly, J. Spears, and T.R. Marotta



## ABSTRACT

**SUMMARY:** Flow diversion has become an established treatment option for challenging intracranial aneurysms. The use of small devices of  $\leq 3$ -mm diameter remains unapproved by major regulatory bodies. A retrospective review of patients treated with Pipeline Embolization Devices of  $\leq 3$ -mm diameter at 3 Canadian institutions was conducted. Clinical and radiologic follow-up data were collected and reported. Twelve cases were treated with  $\geq 1$  Pipeline Embolization Device of  $\leq 3$ -mm diameter, including 2 with adjunctive coiling, with a median follow-up of 18 months (range, 4–42 months). One patient experienced a posttreatment minor complication (8%) due to an embolic infarct. No posttreatment hemorrhage or delayed complications such as in-stent stenosis/thrombosis were observed. Radiologic occlusion was seen in 9/12 cases (75%) and near-occlusion in 2/12 cases (17%). Intracranial aneurysm treatment with small-diameter flow-diverting stents provided safe and effective aneurysm closure in this small selected sample. These devices should be further studied and considered for regulatory approval.

**ABBREVIATIONS:** PED = Pipeline Embolization Device; PICA = posterior inferior cerebellar artery

Endovascular flow diversion by using devices such as the Pipeline Embolic Device (PED; Covidien, Irvine, California) has gained acceptance as a viable option for endovascular treatment of intracranial aneurysms not amenable to more conventional therapies. This technique has been established mainly in the treatment of proximal unruptured aneurysms in relatively large parent vessels, with a paucity of data describing the use of small devices.<sup>1</sup> Health Canada has only approved PED use in parent vessels of  $\geq 3.25$  mm in diameter,<sup>2</sup> perhaps due to concern that smaller devices might be prone to complications such as access difficulties, kinking, or in-stent thrombosis. The US FDA did not specify a size constraint in its approval letter but specified that the PED was only approved for ICA aneurysms from the petrous segment to the superior hypophyseal segment.<sup>3</sup> This limited approval also effectively restricts PED use to larger devices because it is extremely rare for the ICA to measure  $< 3$  mm. Furthermore, distal-vessel aneurysms frequently have wide-neck or fusiform morphology, making them difficult to treat with conventional

techniques such as coiling and potentially good candidates for flow diversion. Therefore, it is imperative that the safety profile of small flow-diversion devices be well-studied so that challenging aneurysms in small-diameter parent vessels can be properly evaluated for potential use of this emerging treatment option.

## MATERIALS AND METHODS

We conducted a retrospective review at 3 institutions of all endovascular cases using PEDs between June 2008 and July 2013. Patients that were treated with one or more small stents ( $\leq 3.00$  mm in diameter) were included in our analysis. Data including demographics; aneurysm type, size, and location; procedural details; clinical presentation; subsequent imaging; and clinical outcome, including the most recent follow-ups, were collected. Our results are expressed in medians and interquartile ranges, given the small sample size (non-normal distribution).

The decision to treat was made for each case by a multidisciplinary team, including vascular neurosurgeons and interventional neuroradiologists, and Health Canada approval was individually obtained under an appeal for compassionate use. Informed consent was obtained from patients or substitute decision-makers. Pretreatment antiplatelet therapy included both acetylsalicylic acid (325 mg) and a total dose of 600 mg of clopidogrel before the procedure (initiated 5 days prior for unruptured aneurysms or within 24 hours for ruptured aneurysms). Testing of in vitro platelet function for clopidogrel response was not performed (not approved by Health Canada). In cases presenting with SAH, extraventricular drains were placed before initiation of

Received April 8, 2014; accepted after revision August 23.

From the Division of Neurosurgery (A.R.M., J.S.), Department of Surgery, and Department of Radiology (J.P.C., T.R.M.), University of Toronto, Toronto, Ontario, Canada; Division of Neurosurgery (C.O.), Department of Surgery, University of Alberta, Edmonton, Alberta, Canada; and Division of Neurosurgery (M.K.), Department of Surgery, College of Medicine, University of Saskatchewan, Saskatoon, Saskatchewan, Canada.

Please address correspondence to Allan R. Martin, MD, 4th Floor, West Wing, 399 Bathurst St, Toronto, Ontario, Canada, M5T2S8; e-mail: allan.martin@utoronto.ca



Indicates article with supplemental on-line table.

<http://dx.doi.org/10.3174/ajnr.A4170>

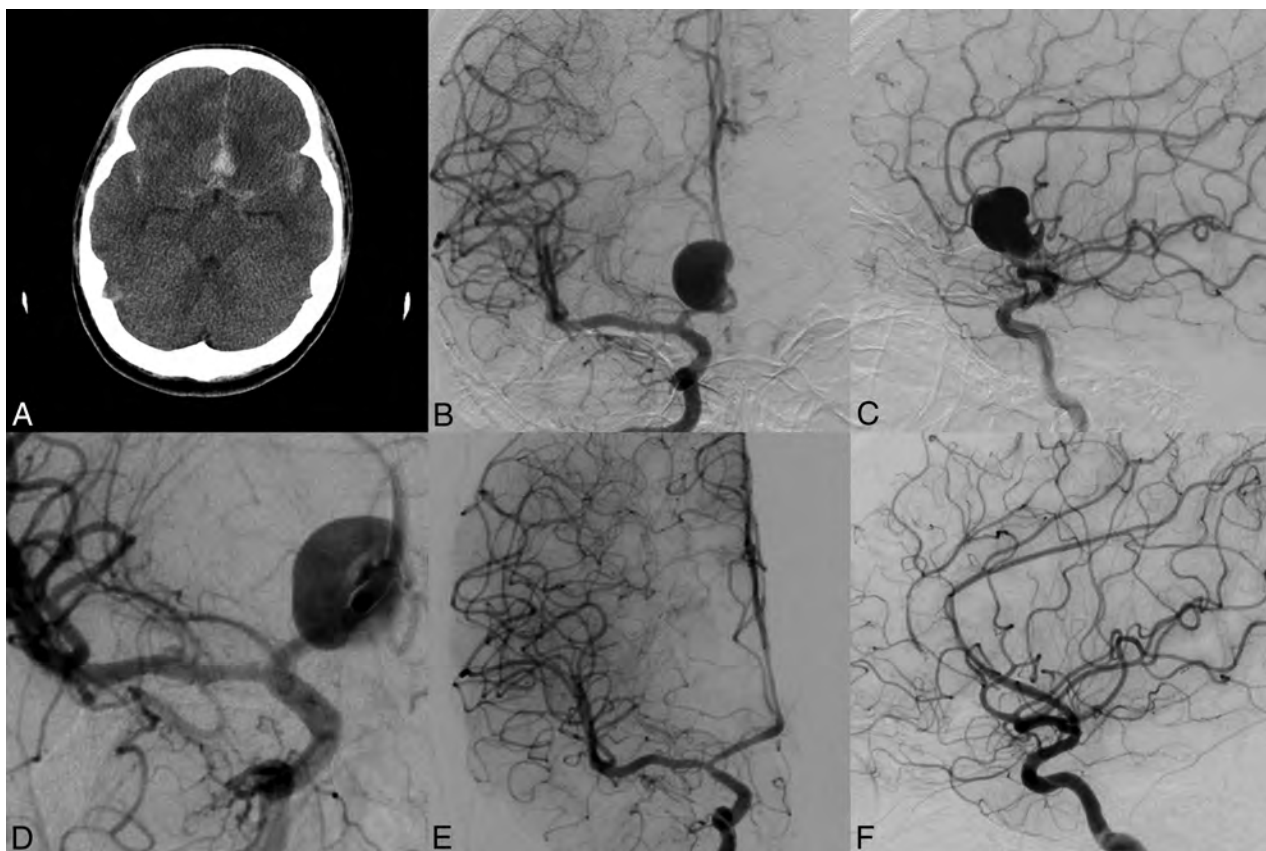


**FIG 1.** Representative images for case 6. *A*, Noncontrast CT demonstrates an acute SAH centered in the interhemispheric fissure. *B* and *C*, Anteroposterior and lateral projections, right ICA injections, pretreatment, show a right A2 fusiform aneurysm. *D*, Oblique projection, right ICA injection, immediately postdeployment, shows the flow effect and position of the stent. *E* and *F*, Anteroposterior and lateral projections, right ICA injections, at 2 months posttreatment show complete aneurysm occlusion.

dual antiplatelet therapy if indicated. Intraprocedural heparin was administered to achieve a targeted activated clotting time of 250–300 seconds.

All procedures were performed with the patient under general anesthesia in a biplane angiography suite. Standard transfemoral access was obtained, and a triaxial approach was used for all anterior circulation aneurysms and for those posterior circulation aneurysms in which the dominant vertebral artery was of sufficient size to allow these devices. A 0.027-inch microcatheter (Marksman; Covidien) was used to gain a distal position across the neck of the aneurysm. In cases in which adjuvant coiling was planned, a 0.014- or 0.018-inch microcatheter was placed into the aneurysm lumen before stent deployment, by using a 5F guide catheter via contralateral femoral access. PED sizes were selected on the basis of the proximal and distal diameters of the parent vessel. One or more PEDs were then deployed to reconstruct the parent artery, depending on the degree of inflow reduction. In coiling cases, loose-packed coils would be placed until the primary operator was satisfied with the result.

All patients were monitored postprocedure in a dedicated neurosurgical intensive care unit. Patients typically underwent postprocedural MRA within 48 hours. After discharge, clinical and imaging follow-up varied on the basis of the treating physician's discretion and the patient's wishes. Radiologic follow-up consisted of DSA or noninvasive imaging (MRA or CTA) and was usually performed at 4–6 months. Dual antiplatelet therapy was

strictly continued for a minimum of 6 months. After this, discontinuation of clopidogrel was based on imaging findings and the discretion of the treating physician, and the patient was maintained on aspirin only.

## RESULTS

The results are summarized in the On-line Table, with representative images displayed in Figs 1 and 2. The median diameter was 18 mm (range, 2–38 mm). Among the aneurysms treated, 6/12 (50%) were located in the anterior circulation, and 6/12, (50%) in posterior circulation (Table). Three patients were treated in the acute phase of SAH; 1 patient, in the subacute phase; and 1, with remote SAH. Five patients had previous treatment with coiling or a standalone stent and experienced subsequent recanalization before their treatment with flow diversion. Two patients (17%) were treated with both coiling and flow diversion.

One patient (8%) experienced technical complications with access and required preexisting angioplasty of the parent vessel so that the device could cross the aneurysm. One patient (8%) experienced a clinically significant procedure-related complication, with a distal posterior inferior cerebellar artery (PICA) stroke, which was detected in the immediate postprocedure period with mild dysmetria and limb ataxia, which improved to a minimal deficit during several days. This stroke was seen on postprocedure MR imaging, and the mechanism appeared to be embolic on the basis of its distal territory, most likely occurring during catheter

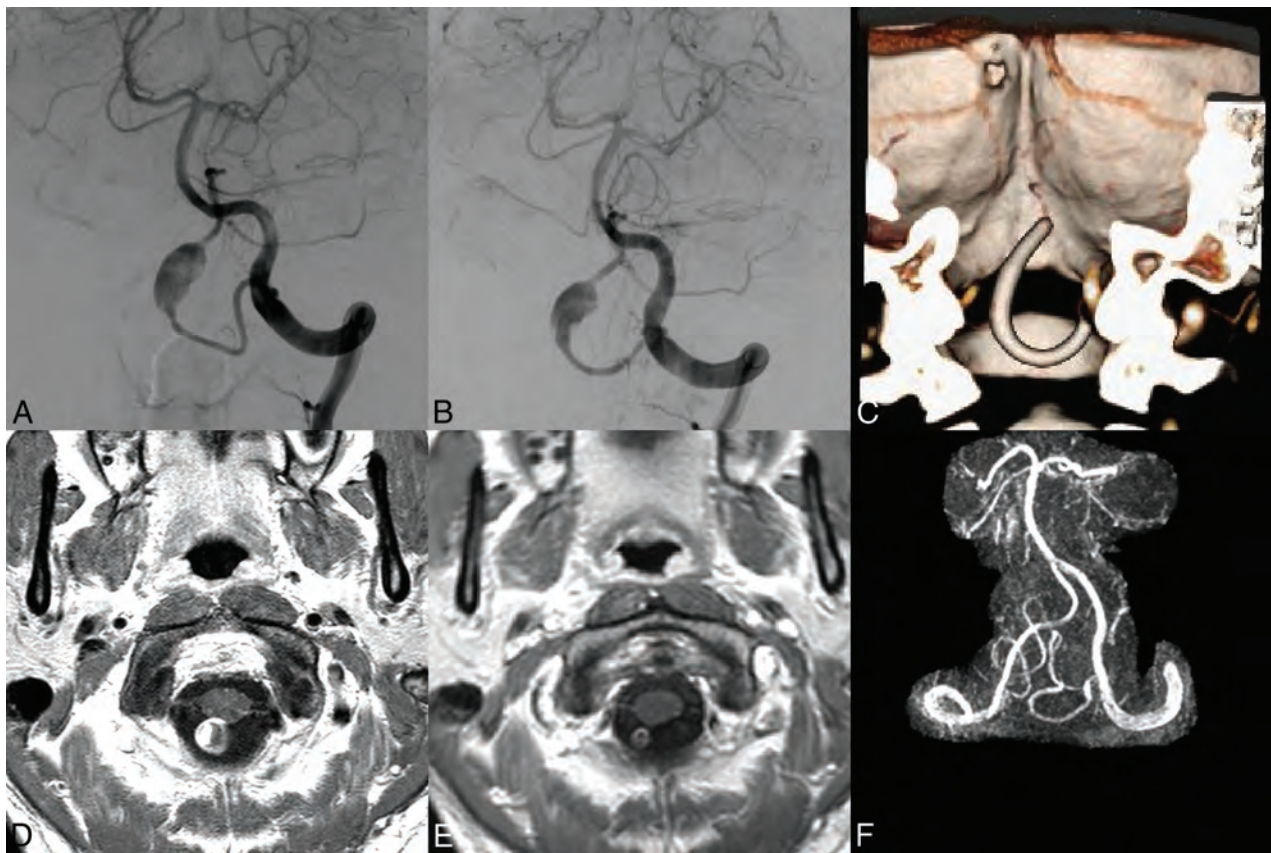


**FIG 2.** Representative images for case 7. *A* and *B*, Anteroposterior projections, left vertebral artery injections, pretreatment and immediately post-PED deployment, respectively, show persistent filling with a minor flow effect. *C*, 3D reconstruction of CTA at 4 months postprocedure shows placement of the stent entirely in the PICA. *D* and *E*, Axial T1 MR imaging with gadolinium, postoperative day 1 and at 1-year follow-up, respectively, shows delayed aneurysm occlusion. *F*, 3D reconstruction of the MRA at 1-year follow-up shows patency of the parent vessel.

**Summary of aneurysm characteristics by size/location**

Location	<7 mm	7–12 mm	13–24 mm	>24 mm
Anterior (ICA/MCA/ACA)	2	1	2	1
Posterior (vertebrobasilar, PcomA, PCA)	1	2	2	1

**Note:**—PcomA indicates posterior communicating artery; PCA, posterior cerebral artery; ACA, anterior cerebral artery.

navigation, because the aneurysm was located at the superior cerebellar artery takeoff. One additional patient (8%) had clinically asymptomatic infarcts seen on postprocedural MR imaging (day 1), not requiring any specific treatment or rehabilitation. This patient was further assessed by early DSA, and it was found that the frontopolar artery, which was covered by the PED, was now occluded, whereas it was patent in the immediate postdeployment angiogram. No patients had a periprocedural decrease in the Glasgow Outcome Score. No delayed complications were seen at a median follow-up of 1.5 years (range, 6 months to 3.5 years), including no cases of in-stent stenosis/thrombosis or rerupture.

The results at latest follow-up included a complete occlusion rate of 9/12 (75%), a near-occlusion rate of 2/12 (17%), and a residual filling rate of 1/12 (8%). The timing of follow-up imaging and the choice of technique were variable, with 5/12 (42%) undergoing only noninvasive imaging postprocedure. Among the cases that showed complete occlusion, the median time for first documentation of occlusion was 6 months (range, 1 day to 8 months). The 2 cases of near-occlusion were both first documented at 6 months. The

case that had residual filling was documented on MRA at 1 day, and this was persistently seen on several follow-up studies including DSA at 1.5 years and MRA at 2.5 years.

**DISCUSSION**

The use of  $\leq 3$ -mm diameter flow-diversion devices is not currently approved in North America, and there is a paucity of published literature that describes their use. Pistocchi et al<sup>1</sup> reported a series of 26 patients, most of whom were treated with flow-diversion devices of  $\leq 3$  mm, with good outcomes including an occlusion rate of 83% and a neurologic complication rate of 4% with no hemorrhage. Yavuz et al<sup>4</sup> recently reported 25 cases of MCA aneurysms located at the bifurcation or more distally, with an occlusion rate of 84% and only 1 case of long-term neurologic impairment, which was mild (mRS 1). Presumably, many of the cases in this series involved small-diameter parent vessels and PEDs, but these specific data were not reported. Most larger flow-diversion series either did not report any cases of devices of  $\leq 3$  mm, or they did not include documentation of the parent vessel or device size.<sup>4,6-8</sup> Our current series of 12 patients demonstrated that the use of these small devices is technically feasible and safe, with excellent clinical and radiologic outcomes at a median latest follow-up of 1.5 years. The rates of occlusion (75%) and near- or complete occlusion (92%) are similar to overall data published for flow-diversion treatment (76% complete occlusion at 1 year),<sup>9</sup> and our current series comprises 50% posterior circulation aneu-

rysms, which are known to carry higher rates of complications. The early morbidity rate of 8% is similar to the established 5%–7% seen in overall data,<sup>9,10</sup> and no aneurysm ruptures or delayed complications were observed among these data, whereas published data suggest a late morbidity of 3% and mortality of 1%.<sup>10</sup> Therefore, the overall safety profile of this small series appears grossly in line with the results of Pistocchi et al<sup>1</sup> and the overall published flow-diversion data.<sup>4–10</sup>

The timing of follow-up imaging and the choice of imaging technique varied greatly among the cases in this series, on the basis of the discretion of the treating clinician. It was thought that performing follow-up DSA was unnecessary in cases with good clinical status and a satisfactory noninvasive radiologic result. In cases without any coils present, it was thought that CTA was the superior noninvasive technique in assessing in-stent stenosis, but MRA was generally acceptable for assessing patency. For cases with any concerning features such as suspected stenosis, DSA remains the optimal technique for detailed assessment.

The use of flow diversion in small and/or distal vessels has unique technical challenges that may increase the risk of ischemic or hemorrhagic complications during both access and deployment. Access in small and/or distal vessels is likely to be more difficult in comparison with that in larger and/or proximal flow diversion because the device is delivered in a large and relatively stiff microcatheter and tortuosity or sharp corners can pose serious roadblocks. Establishing a distal position with a microwire sometimes requires using a larger microwire (0.018 inch) or a buddy wire technique (0.008/0.010 and 0.014 inch). The distal landing zone may be of particularly small caliber, increasing the risk of dissection or perforation by the wire or the microcatheter. Smaller vessels also pose a risk of clot formation or distal spasm because the microcatheter may slow or occlude flow. These risks are also of concern during deployment when the pusher wire may appear in small distal branches. However, our early experience did not demonstrate an increased risk of vessel dissection, perforation, or spasm.

Another technical challenge is deploying the device with a smaller margin of error on the proximal and distal landing zones, because the surrounding vessels are likely to have nearby branches. Proper sizing becomes a critical factor in smaller vessels to maximize coverage across the aneurysm but avoid too much coverage over branches/perforators because fully expanded devices provide higher surface area coverage in small vessels. In addition, we found that it was sometimes more difficult to unscrew the release coil while maintaining the intended delivery position in these smaller devices than in their larger counterparts, because the proximal vascular loops decrease the torque of the delivery system. However, all of these issues were found to be manageable, and difficulties diminished as greater experience deploying small PEDs was acquired.

An important topic in flow diversion is the covering, or jailing, of sidewall or branch arteries by the flow-diverting stent. This topic has been widely discussed in the flow-diversion literature, with the consensus suggesting that branch occlusions are not uncommon but are often clinically silent.<sup>5,11,12</sup> It remains unclear whether small-diameter flow diverters have a greater propensity to cause occlusion or symptomatic flow reduction to covered arterial branches, but the series by Yavuz et al<sup>4</sup> showed relatively

high rates of branch occlusion (3/21, 14%) and a reduced caliber of the covered branch (6/21, 29%) among 21 MCA bifurcation aneurysms treated.<sup>12</sup> Our series demonstrated 1 case (8%) of a jailed branch artery occlusion (frontopolar artery) with an associated area of diffusion restriction on MR imaging (postprocedure day 1) suggestive of infarct, but this was clinically silent. There was no radiologic evidence in our series of other infarcts or significant branch occlusions on MR imaging or DSA that were attributable to jailed branches, but in the retrospective review of our cases, it was difficult to accurately determine the patency of smaller jailed branches and perforators. Future study of flow diversion in small vessels would likely benefit from a careful analysis of all jailed vessels, such as a comparison among predeployment, immediate postdeployment, and delayed follow-up by using 3D DSA or 2D images with precisely matched projections.

In-stent stenosis and thrombosis have been cited as important concerns with flow-diversion devices, which occur in 5%–10% of cases,<sup>9</sup> and these may be even more of a concern with small devices because there is less room available for stenosis to occur before complete thrombosis occurs.<sup>13</sup> Pistocchi et al<sup>1</sup> reported 1 case of in-stent thrombosis (4%) in their series, which was treated with angioplasty in a subsequent procedure that restored flow, but the patient still had a clinical infarct. Delayed ischemia due to intimal hyperplasia is also a possibility, and if this occurs so that a vessel diameter is reduced by 1–2 mm, it could theoretically lead to a critical flow effect in stents of <3 mm. Furthermore, in-stent stenosis may be more difficult to detect in small-caliber stents due to a lack of imaging resolution and the presence of metal artifacts. In our series, we did not observe any cases of significant in-stent stenosis and there were no cases of thrombosis, but further data are needed to know whether these small devices pose a greater risk of this complication.

The use of intravascular metal stents requires dual antiplatelet therapy, which is commonly recommended for at least 6 months before reduction to a single antiplatelet agent, though variations in practice exist.<sup>8</sup> The preprocedural regimen and postprocedural duration remain controversial, especially in the setting of SAH. Our series included 3 cases that were treated in the acute phase of SAH with none of these experiencing early rerupture, similar to previous results.<sup>14,15</sup> The optimal timing likely depends on the degree of epithelialization of the metal device, which, in turn, depends on various factors such as flow characteristics, aneurysm occlusion, length, and the presence of endoleaks.<sup>11,16</sup> All of these variables may be even more important in small-sized vessels. One possibility is that higher resolution imaging such as vessel wall MRA will eventually be able to provide evidence of epithelialization, but until then, controversy will likely continue.

## CONCLUSIONS

Flow diversion with small-diameter devices ( $\leq 3$  mm) remains unapproved by Health Canada, and the US FDA effectively imposes a similar constraint. Our current results document the safe and effective use of small-diameter flow diverters in a small selected sample, without evidence of higher-than-published complication rates such as in-stent stenosis/thrombosis, dissection, or rerupture. As such, this treatment option should be further studied and potentially considered for broader regulatory approval.

Disclosures: Cian O’Kelly—RELATED: Consulting Fee or Honorarium: Covidien, Comments: proctor for Pipeline cases; UNRELATED: Grants/Grants Pending: National Institutes of Health trial Minimally Invasive Surgery plus rt-PA for ICH Evacuation,\* Comments: due to start October 2014; we receive an amount to our institution per patient enrolled. Michael Kelly—RELATED: Support for Travel to Meetings for the Study or Other Purposes: Covidien,\* Comments: 2014 Flow Diversion Meeting, Toronto, Ontario, Canada (April 10, 2014); OTHER RELATIONSHIPS: I am a shareholder of Blockade Medical, Inc. Thomas R. Marotta—RELATED: Consulting Fee or Honorarium: proctor for Pipeline (Canada); Fees for Participation in Review Activities such as Data Monitoring Boards, Statistical Analysis, Endpoint Committees, and the Like: Flow Redirection Endoluminal Device study, China Endovascular Course, Low-profile Visualized Intraluminal Support device study data and safety monitoring board; UNRELATED: Consultancy: As above, Pipeline proctor; Patents (planned, pending or issued): My invention, eclips, endovascular clip systems, flow diverter for bifurcation aneurysms. \*Money paid to the institution.

## REFERENCES

1. Pistocchi S, Blanc R, Bartolini B, et al. **Flow diverters at and beyond the level of the circle of Willis for the treatment of intracranial aneurysms.** *Stroke* 2012;43:1032–38
2. Health Canada. Summary of basis of decision: Pipeline embolization device. [http://www.hc-sc.gc.ca/dhp-mps/prodpharma/sbd-smd/md-im/sbd\\_smd\\_2010\\_pipeline\\_embolization\\_148227-eng.php](http://www.hc-sc.gc.ca/dhp-mps/prodpharma/sbd-smd/md-im/sbd_smd_2010_pipeline_embolization_148227-eng.php). Accessed March 24, 2014
3. US Food and Drug Administration. Pipeline embolization device approval letter. [http://www.accessdata.fda.gov/cdrh\\_docs/pdf10/p100018a.pdf](http://www.accessdata.fda.gov/cdrh_docs/pdf10/p100018a.pdf). Accessed March 24, 2014
4. Yavuz K, Geyik S, Saatci I, et al. **Endovascular treatment of middle cerebral artery aneurysms with flow modification with the use of the Pipeline embolization device.** *AJNR Am J Neuroradiol* 2014;35:529–35
5. Fiorella D, Woo HH, Albuquerque FC, et al. **Definitive reconstruction of circumferential, fusiform intracranial aneurysms with the Pipeline embolization device.** *Neurosurgery* 2008;62:1115–20; discussion 1120–21
6. Kulcsár Z, Wetzel SG, Augsburg L, et al. **Effect of flow diversion treatment on very small ruptured aneurysms.** *Neurosurgery* 2010; 67:789–93
7. Deutschmann HA, Wehrschutz M, Augustin M, et al. **Long-term follow-up after treatment of intracranial aneurysms with the Pipeline embolization device: results from a single center.** *AJNR Am J Neuroradiol* 2012;33:481–86
8. McAuliffe W, Wenderoth JD. **Immediate and midterm results following treatment of recently ruptured intracranial aneurysms with the Pipeline embolization device.** *AJNR Am J Neuroradiol* 2012;33:487–93
9. Brinjikji W, Murad MH, Lanzino G, et al. **Endovascular treatment of intracranial aneurysms with flow diverters: a meta-analysis.** *Stroke* 2013;44:442–47
10. Arrese I, Sarabia R, Pintado R, et al. **Flow-diverter devices for intracranial aneurysms: systematic review and meta-analysis.** *Neurosurgery* 2013;73:193–99; discussion 199–200
11. Kallmes DF, Ding YH, Dai D, et al. **A new endoluminal, flow-disrupting device for treatment of saccular aneurysms.** *Stroke* 2007;38:2346–52
12. Saatci I, Yavuz K, Ozer C, et al. **Treatment of intracranial aneurysms using the Pipeline flow-diverter embolization device: a single-center experience with long-term follow-up results.** *AJNR Am J Neuroradiol* 2012;33:1436–46
13. Liou TM, Li YC. **Effects of stent porosity on hemodynamics in a sidewall aneurysm model.** *J Biomech* 2008;41:1174–83
14. Martin AR, Cruz JP, Matouk CC, et al. **The Pipeline flow-diverting stent for exclusion of ruptured intracranial aneurysms with difficult morphologies.** *Neurosurgery* 2012;70(1 suppl operative):21–28; discussion 28
15. Cruz JP, O’Kelly C, Kelly M, et al. **Pipeline embolization device in aneurysmal subarachnoid hemorrhage.** *AJNR Am J Neuroradiol* 2013;34:271–76
16. Dai D, Ding YH, Kadirvel R, et al. **Patency of branches after coverage with multiple telescoping flow-diverter devices: an in vivo study in rabbits.** *AJNR Am J Neuroradiol* 2012;33:171–74

# Attenuation of Blood Flow Pulsatility along the Atlas Slope: A Physiologic Property of the Distal Vertebral Artery?

T. Schubert, M. Pansini, O. Bieri, C. Stippich, S. Wetzel, S. Schaedelin, A. von Hessling, and F. Santini

## ABSTRACT

**BACKGROUND AND PURPOSE:** Physiologic and pathologic arterial tortuosity may attenuate blood flow pulsatility. The aim of this prospective study was to assess a potential effect of the curved V3 segment (Atlas slope) of the vertebral artery on arterial flow pulsatility. The pulsatility index and resistance index were used to assess blood flow pulsatility.

**MATERIALS AND METHODS:** Twenty-one healthy volunteers (17 men, 4 women; mean age, 32 years) were examined with a 3T MR imaging system. Blood velocities were measured at 2 locations below (I and II) and at 1 location above the V3 segment (III) of the vertebral artery by using a high-resolution 2D-phase-contrast sequence with multidirectional velocity-encoding.

**RESULTS:** Pulsatility and resistance indices decreased along all measurement locations from proximal to distal. The pulsatility index decreased significantly from location II to III and from I to II. However, the decrease was more pronounced along the Atlas slope than in the straight-vessel section below. The decrease of the resistance index was highly significant along the Atlas slope (location II to III). The decrease from location I to II was small and not significant.

**CONCLUSIONS:** The pronounced decrease in pulsatility and resistance indices along the interindividually uniformly bent V3 segment compared with a straight segment of the vertebral artery indicates a physiologic attenuating effect of the Atlas slope on arterial flow pulsatility. A similar effect has been described for the carotid siphon. A physiologic reduction of pulsatility in brain-supplying arteries would be in accordance with several recent publications reporting a correlation of increased arterial flow pulsatility with leukoencephalopathy and lacunar stroke.

**ABBREVIATIONS:** PC = phase-contrast; PI = pulsatility index; RI = resistance index; Vmax = maximum blood velocity; Vmean = mean blood velocity; Vmin = minimum blood velocity

The flow waveform in an arterial vessel is affected by many factors. Main influencing parameters are inflow determinants (cardiac function), outflow determinants (downstream tissue), and resistance presented by the vessel wall.<sup>1-4</sup>

Due to the different functions of large and small arteries, arterial flow waveforms undergo changes along the vascular tree. The large conduit arteries have an elastic wall to minimize longitudinal impedance.<sup>5</sup> In contrast, the distal arteries that regulate the demand for blood of the downstream tissue have a more muscular wall to effectively change lumen size.

The elasticity of the large arteries has a buffering function, which decreases pressure and flow pulsatility by taking up energy during systole and releasing it during diastole (Windkessel effect), thus delivering blood in a more continuous stream to peripheral vascular beds.<sup>6</sup> Due to increased wall stiffness, waveform changes occur with normal aging but also in pathologies that affect vascular compliance.<sup>7</sup> Recent studies with large patient cohorts indicate that the brain is vulnerable to increased arterial pulsatility, reflected by a higher number of white matter hyperintensities and a greater incidence of lacunar strokes.<sup>8-10</sup>

The most important techniques for noninvasive flow measurements and therefore flow wave characterization are Doppler sonography and phase-contrast (PC) MR imaging. Both techniques are important clinical tools. Doppler sonography has the advantage of a widely available method with very high spatial and temporal resolution; however, it is user-dependent and restricted to sonography-accessible vessel locations.<sup>11</sup> Phase-contrast MR imaging, in turn, has the advantage of providing blood flow measurements independent of the user without an-

Received June 18, 2014; accepted after revision September 6.

From the Divisions of Neuroradiology (T.S., C.S., A.v.H.) and Radiological Physics (O.B., F.S.), Clinic of Radiology and Nuclear Medicine, and Clinical Trial Unit (S.S.), Basel University Hospital, Basel, Switzerland; Department of Radiology (M.P.), Bruderholz Cantonal Hospital, Basel, Switzerland; and Department of Neuroradiology (S.W.), Hirslanden Clinic, Zurich, Switzerland.

Please address correspondence to Tilman Schubert, MD, Division of Neuroradiology, Clinic of Radiology and Nuclear Medicine, Basel University Hospital, Petersgraben 4, 4031 Basel, Switzerland; e-mail: Tilman.Schubert@usb.ch

<http://dx.doi.org/10.3174/ajnr.A4148>

atomic restrictions, however, with lower spatial and temporal resolution.<sup>12-14</sup>

Regarding PC-MR imaging, a 2D-PC sequence with unidirectional velocity-encoding is routinely applied. This sequence is fast and robust; however, due to its unidirectional vessel encoding, it may underestimate flow velocities due to placement errors.<sup>15</sup> Newer techniques such as 4D-PC-MR imaging and 2D-PC-MR imaging with multidirectional velocity-encoding have been shown superior to 2D-PC-MR imaging with unidirectional velocity-encoding in curved vessel sections.<sup>16-19</sup>

The aim of the present study was to evaluate blood flow characteristics along the curved vessel section of the distal vertebral artery, extending from the transverse foramen C2 to the dura mater cranial to the Atlas vertebra (Atlas slope), to evaluate the effect of a tortuous vessel geometry on blood flow pulsatility. For blood flow and velocity measurements, a

2D-PC sequence with multidirectional velocity-encoding has been applied.

## MATERIALS AND METHODS

### Study Population

Forty-two vertebral arteries of 21 healthy volunteers without pre-existing conditions (17 male; mean age,  $32 \pm 5.2$  years; range, 23–40 years) were prospectively investigated.

For each vessel, time-resolved measurements of blood velocities and flow volume were acquired at 2 locations below (location I, level of the cervical vertebral body 6; location II, level of the upper cervical vertebral body 3 immediately below the Atlas slope) and at 1 location above the V3 segment (location III, intradural V4 segment) of the vertebral artery (Fig 1). The study was approved by the local ethics review committee, and written informed consent was obtained from all subjects.

### MR Imaging Measurements

Data were acquired on a 3T MR imaging system (Magnetom Verio; Siemens, Erlangen, Germany). After localizer measurements, a time-of-flight angiography was used to identify the vertebral artery segments and to plan the subsequent velocity-encoded acquisitions. The velocity-encoded MR imaging consisted of *k*-space segmented 2D radiofrequency-spoiled gradient-echo sequences with prospective electrocardiography gating and interleaved 3-directional velocity-encoding. The applied 2D-PC acquisition with 3D-velocity-encoding used a  $187 \times 151$  mm<sup>2</sup> rectangular FOV and a spatial resolution of  $0.5 \times 0.5 \times 5$  mm<sup>3</sup>. Data acquisition resulted in a series of datasets representing the components of the velocity vector in consecutive timeframes within the cardiac cycle with a temporal resolution of 68 ms. The total acquisition times were approximately 90 seconds with variability depending on the patient's individual heart rate (10–16 acquired cardiac cycles). Velocity-encoding sensitivity was 80 cm/s along all 3 encoding directions. Further imaging parameters were the following: TR/TE, 8.5/5.7 ms; flip angle, 30°; bandwidth, 460 Hz/pixel. The velocity distributions for each voxel and time point within the cardiac cycle were reconstructed from data acquired over numerous cardiac cycles throughout the total acquisition period.

Further imaging parameters were the following: TR/TE, 8.5/5.7 ms; flip angle, 30°; bandwidth, 460 Hz/pixel. The velocity distributions for each voxel and time point within the cardiac cycle were reconstructed from data acquired over numerous cardiac cycles throughout the total acquisition period.

### Postprocessing

Semiautomated postprocessing of the datasets was performed by using an in-house software tool developed with Matlab (MathWorks, Natick, Massachusetts) for the definition of ROIs based on manual region selection and signal thresholding of the magnitude images.<sup>20-22</sup>

### Outcome Measures

Minimum and maximum velocities were extracted from individual flow-velocity curves (Fig 2). Mean velocity was calculated by dividing the sum of velocities by the time points.

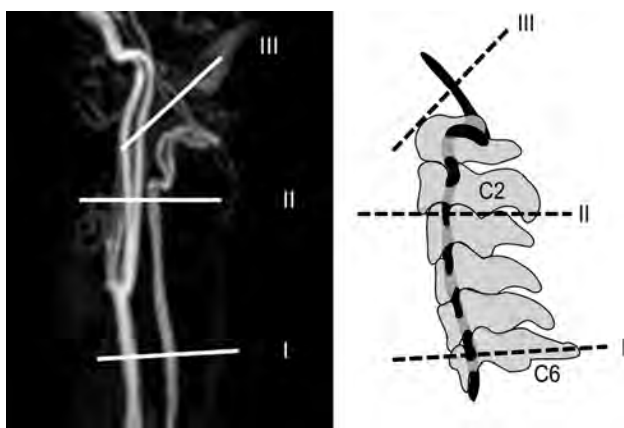


**FIG 1.** Measurement locations along the vertebral artery (I–III) depicted on a contrast-enhanced MRA (left) and on a schematic image in relation to the bony anatomy (right).

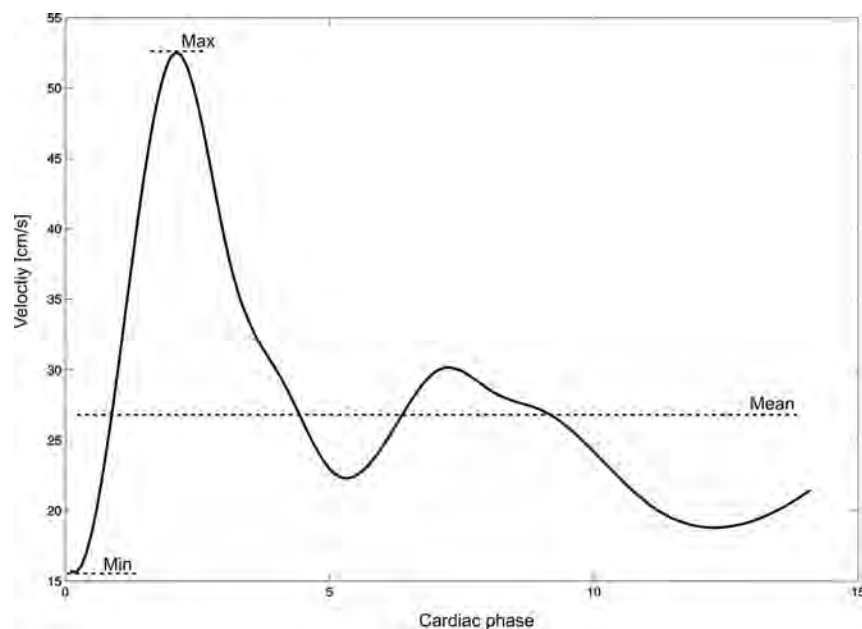


**FIG 2.** Depiction of a flow-velocity waveform with the calculated mean velocity indicated. X-axis: centimeters per second; Y-axis: cardiac phases.

**Table 1: Measured velocities at locations I–III**

Variable	Mean	Median	Minimum	Maximum	SD
Vmin I	13.3	12.7	8.4	21.6	3.0
Vmax I	39.3	40	27.8	52.5	6.7
Vmean I	23	22.4	15.7	30.8	4.1
Vmin II	12.6	12.4	5.6	21.2	3.5
Vmax II	36.3	36.5	18.5	55	6.7
Vmean II	23.9	24.3	10.2	34.2	5
Vmin III	17.4	16.9	8.9	32.9	4.8
Vmax III	41	37.8	19.4	72.6	10.4
Vmean III	29.7	28.9	14	52.9	7.2

**Table 2: Descriptive characterization of the parameters PI and RI**

Variable	Mean	SD
PI I	1.15	0.22
PI II	1.01	0.18
PI III	0.79	0.13
RI I	0.66	0.06
RI II	0.65	0.07
RI III	0.57	0.07

For quantification of pulsatility, the pulsatility index (PI) and resistance index (RI) were applied.

The pulsatility index and resistance index were calculated according to the following formulas by using blood velocities<sup>23,24</sup>:

$$\text{Pulsatility Index: PI} = \frac{V_{\max} - V_{\min}}{V_{\text{mean}}}$$

$$\text{Resistance Index: RI} = \frac{V_{\max} - V_{\text{enddiastolic}}}{V_{\max}}$$

**Statistical Analysis**

Both end points, PI (primary end point) and RI, were calculated for the left and right vertebral arteries at the 3 locations (I, II, and III) as described above for 21 healthy volunteers:

For the end points PI and RI and for minimum blood velocity (Vmin), maximum blood velocity (Vmax), and mean blood velocity (Vmean), a linear mixed-effects model was fit with segment location as mixed-effect, and volunteer and side (nested within volunteer), as random effects for which separate intercepts were fit. The significance of mixed-effects was calculated by using a *t* test with Satterthwaite approximation for *df*.

**RESULTS**

**Pulsatility and Resistance Indices**

**Calculation of Indices.** Vmin was invariably found before the systolic upslope of the flow curve; therefore, Vmin conformed to blood velocity at end of diastole in our measurements, which was then used to calculate the resistance index.

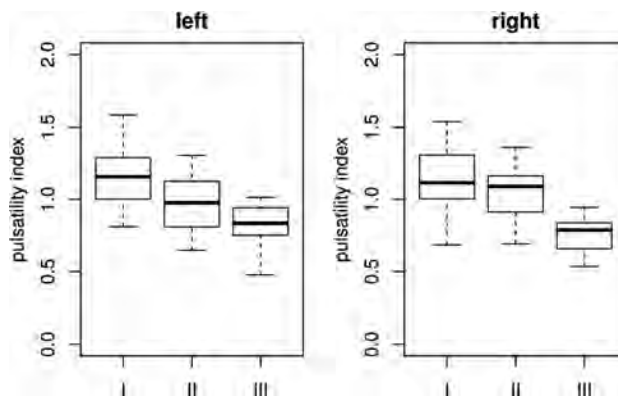
In general, the mean values for PI and RI decreased from proximal to distal. Both PI and RI showed a pronounced decrease between the segments II and III (Tables 1 and 2).

Table 3 shows the descriptive statistics for the parameters PI and RI. Boxplots of the indices are given in Figs 3 and 4.

**Table 3: Estimates and confidence interval for the mixed-effect “location” and the end point pulsatility index<sup>a</sup>**

	Estimate	SD	95% CI	T	P
(Intercept)	1.01	0.03	(0.9–1.07)	33.8	<.001
I	0.14	0.03	(0.08–0.2)	4.67	<.001
III	–0.22	0.03	(–0.27–0.16)	–7.42	<.001

<sup>a</sup> Location II is taken as base. This means that the estimate of the decrease from I (respectively III) to II is calculated by comparing the pulsatility index at segment I (respectively III) with the pulsatility index at segment II (Intercept), which explains the negative sign for the estimate in sections II to III. The estimated variances between volunteers and those between left and right side measurements are negligible.



**FIG 3.** Boxplots of pulsatility indices per location on both sides.

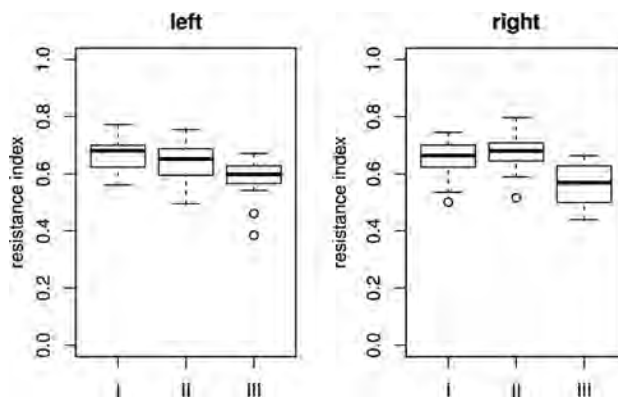


**FIG 4.** Boxplots of resistance indices per location on both sides.

**Table 4: Estimates and confidence interval for the mixed-effect “location” and the end point resistance index<sup>a</sup>**

	Estimate	SD	95% CI	T	P
(Intercept)	0.65	0.01	(0.63–0.67)	59.16	<0.001
I	0.007	0.012	(–0.02–0.03)	0.61	0.54
III	–0.08	0.012	(–0.1 to –0.05)	–6.54	<0.001

<sup>a</sup> Location II is taken as base. This means that the estimate of the decrease from I (respectively III) to II is calculated by comparing the pulsatility index at segment I (respectively III) with the pulsatility index at segment II (Intercept), which explains the negative sign for the estimate in sections II to III. The estimated variances between volunteers and those between left and right side measurements are negligible.

**Pulsatility Index**

The pulsatility index median was lower at the distal segment III than at the proximal segments I and II (Fig 3). According to the results of the mixed-effects models (Table 3), the decrease of PI was highly significant from II to III and from I to II, but the effect size was much higher in the section between II and III (average decrease of 0.22) than in the section between I and II (average decrease of 0.14).

The estimated variances between volunteers and left and right side measurements were negligible.

### Resistance Index: Model

The resistance index median was lower at distal segment III than at proximal segments I and II (Fig 4). According to the results of the mixed-effects models (Table 4), the decrease of RI was highly significant from segments II to III (average decrease of 0.08). The

**Table 5: Estimates and confidence interval for the fixed-effect "location" and the end point minimal blood velocity<sup>a</sup>**

	Estimate	SD	95% CI	T	P
(Intercept)	12.6067	0.59	(11.44–13.78)	21.24	<0.001
I	0.81	0.57	(-0.32–1.94)	1.4	0.16
III	4.75	0.56	(3.64–5.86)	8.4	<0.001

<sup>a</sup> Location II is taken as base. This means that the estimate of the increase/decrease from I (respectively III) to II is calculated by comparing the blood velocity at segment I (respectively III) with the blood velocity at segment II (Intercept).

**Table 6: Estimates and confidence interval for the fixed-effect "location" and the end point mean velocity<sup>a</sup>**

	Estimate	SD	95% CI	T	P
(Intercept)	23.85	0.86	(22.15–25.55)	27.47	<0.001
I	-0.67	0.80	(-2.26–0.9)	-0.84	0.4
III	5.87	0.79	(4.32–7.43)	7.41	<0.001

<sup>a</sup> Location II is taken as base. This means that the estimate of the increase/decrease from I (respectively III) to II is calculated by comparing the mean velocity at segment I (respectively III) with the mean velocity at segment II (Intercept).

**Table 7: Estimates and confidence interval for the fixed-effect "location" and the end point maximum velocity<sup>a</sup>**

	Estimate	SD	95% CI	T	P
(Intercept)	36.32	1.26	(33.84–38.8)	28.68	<0.001
I	3.31	1.3	(0.76–5.86)	2.55	0.013
III	4.69	1.27	(2.19–7.2)	3.67	<0.001

<sup>a</sup> Location II is taken as base. This means that the estimate of the increase/decrease from I (respectively III) to II is calculated by comparing the maximum velocity at segment I (respectively III) with the maximum velocity at segment II (Intercept).

decrease from segments I to II was small and not significant ( $P = <.001$ ).

The estimated variances between volunteers and left- and right-side measurements were negligible.

### Peak Velocities: Model

**Minimum Velocity.** According to the mixed-effects model results in Table 5, the increase in minimal velocity was highly significant from segments II to III. A decrease was found between segments I and II. Due to small effect size, this decrease was not significant.

**Mean Velocity.** According to the mixed-effects model results in Table 6, the increase in mean velocity is highly significant from segments II to III. A small increase was found between segments I and II. Due to small effect size, this increase was not significant.

**Maximum Velocity.** According to the mixed-effects model results in Table 7, the increase in minimal blood velocity is highly significant from segments II to III. A significant decrease was found between segments I and II.

Blood velocities per location are summarized in Table 1; box-plots are shown in Fig 5.

## DISCUSSION

The main finding of the present study is a highly significant reduction of arterial flow pulsatility along the upper part of the vertebral artery, the Atlas slope.

The measured blood velocities ( $V_{min}$ ,  $V_{max}$ , and  $V_{mean}$ ) and indices (PI, RI) showed a nonlinear behavior along the 3 measurement locations (Fig 5). From segments I to II, only  $V_{max}$  showed a significant change (decrease), reflected by the decrease in RI. From segments II to III, all velocities increased significantly. However,  $V_{min}$  and  $V_{mean}$  increased relatively more strongly compared with  $V_{max}$ .

How the velocities changed along the vessel course was reflected by a clearly higher decrease of PI from locations II to III than from I to II. RI, in turn, stayed almost constant from locations I to II and showed a strong decrease from locations II to III, which indicates a greater effect on flow pulsatility of the Atlas slope compared with the straight-vessel section below.

The pulsatility index and resistance index are mainly used to describe the arterial resistance of a downstream capillary bed<sup>25</sup> and upstream vessel stenoses.<sup>26</sup> However, it is known that vascular compliance can also affect these indices.<sup>6–9</sup> In our study, we measured blood velocities under the same circumstances of the downstream capillary bed at relatively close locations along the vertebral artery. Therefore, changes in PI and RI were most likely induced by the local vessel properties.

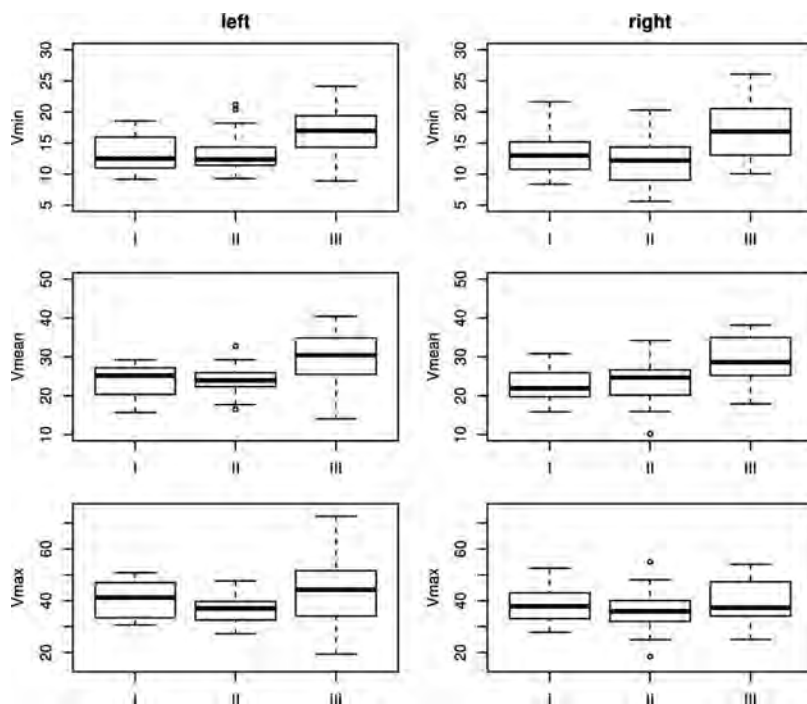


**FIG 5.** Boxplots of blood velocities per location on both sides.

The distinct reduction in flow pulsatility appeared along a geometrically complex, tortuous vessel section with high interindividual uniformity. The main function of this physiologic elongation of the vertebral artery is to provide the high range of motion of the upper cervical spine. However, the characteristic shape of the Atlas slope may be an explanation of the pronounced attenuation of blood flow pulsatility. The results are underlined by the theoretic consideration that in contrast to a straight vessel, a fluid running through a curved vessel generates a centrifugal force,<sup>27</sup> leading to an energy transfer from the current to the vessel wall. With regard to a physiologic pulsatile current, energy transfer from the current to the vessel wall takes place at peak systolic velocity and vice versa in the diastolic phase. The elastic vessel wall can react on the applied force with a distension during systole and a retraction during diastole, laminarizing downstream pulsatile flow appropriate to a Windkessel reservoir.<sup>18,28</sup>

The results of the present study are plausible because the acquired values are consistent with low intersubject variability. The acquired values of blood velocity, PI, and RI are in good accordance with Doppler sonography measurements reported in the literature.<sup>29</sup> In the present study, a 2D-PC sequence with multidirectional velocity-encoding and high spatial resolution was chosen to accurately capture blood flow of both vertebral arteries within a single measurement. A lower temporal resolution was taken into account to achieve this.

Physiologically, the measured decrease in arterial pulsatility along the carotid siphon may be meaningful for the cerebral circulation. The brain has a low-resistance capillary bed without protective precapillary sphincters.<sup>7</sup> Moreover, a physiologic dampening of arterial flow pulsatility has already been described in the anterior cerebral circulation. Here, a marked attenuation of blood flow pulsatility occurs along a short-but-curved vessel section with comparable uniformity to the Atlas slope, the carotid siphon.<sup>18</sup>

During recent years, there has been increasing evidence about the negative impact of increased arterial flow pulsatility on the brain.

Recent large collective longitudinal studies have shown that increased PI and RI correlate significantly with cerebral white matter hyperintensities.<sup>8</sup> In this context, PI correlated strongest with white matter hyperintensities as radiologic correlates of microvascular disease of the evaluated parameters.<sup>9</sup> Another recent study of patients with ischemic stroke showed significantly higher PI and RI in patients with lacunar stroke based on cerebral microvascular disease compared with other stroke subtypes.<sup>10</sup> These new data are in accordance with previous studies of patients with type 2 diabetes mellitus in whom increased arterial pulsatility correlated with a higher degree of cerebral microangiopathy.<sup>30,31</sup> Bateman et al<sup>32</sup> have also shown that early vascular dementia is associated with increased blood flow pulsation.

A shortcoming of the present study is the absence of patient data. However, our intention was primarily to evaluate a potential physiologic function of the Atlas slope and to establish baseline values in terms of pulsatility changes. Shortcomings of the applied MR imaging sequence are a lower temporal resolution and slightly increased scanning time due to multidirectional velocity-encoding compared with a standard unidirectionally encoded 2D-PC

sequence. In contrast, 4D-PC-MR imaging shows even less underestimation of flow velocities compared with a 2D-PC acquisition with 3D velocity-encoding. However, a 4D-PC sequence with the necessary spatial resolution would have resulted in extensive scanning time. Nevertheless, we think that the applied technique is advantageous, if the paired cervical arteries are measured within 1 planar sequence. This advantage is underlined by the accordance of the measured values with sonography data.<sup>29</sup>

## CONCLUSIONS

On the basis of the observation that increased arterial pulsatility appears to harm the brain parenchyma, the measured attenuation of pulsatility along the Atlas slope seems plausible. How arterial stiffness affects the demonstrated pulsatility attenuation along the Atlas slope and whether there is a difference between healthy elderly and individuals with white matter hyperintensities are interesting questions for future study. In this context, the pulsatility attenuation may also be evaluated as a surrogate marker for white matter hyperintensities.

Disclosures: Tilman Schubert—*RELATED: Grant:* Basel University Research Grant (grant No. DMS 2180)\*; *UNRELATED: Grants/Grants Pending:* Swiss Atrial Fibrillation Study (grant pending)\*. Christoph Stippich—*OTHER RELATIONSHIPS:* general support to the radiology department, *Comments:* The Department of Radiology, University Hospitals Basel, Switzerland receives financial support from Bayer Healthcare, Bracco, and Guerbet and has a research agreement with Siemens. The submitted work is not related to these agreements. C. Stippich receives no other financial support related to the submitted work. \*Money paid to the institution.

## REFERENCES

1. Boutouyrie P, Tropeano AI, Asmar R, et al. **Aortic stiffness is an independent predictor of primary coronary events in hypertensive patients: a longitudinal study.** *Hypertension* 2002;39:10–15
2. Chavhan GB, Parra DA, Mann A, et al. **Normal Doppler spectral waveforms of major pediatric vessels: specific patterns.** *Radiographics* 2008;28:691–706
3. Laurent S, Katsahian S, Fassot C, et al. **Aortic stiffness is an independent predictor of fatal stroke in essential hypertension.** *Stroke* 2003;34:1203–06
4. Nelson TR, Pretorius DH. **The Doppler signal: where does it come from and what does it mean?** *AJR Am J Roentgenol* 1988;151:439–47
5. Westerhof N, Lankhaar JW, Westerhof BE. **The arterial Windkessel.** *Med Biol Eng Comput* 2009;47:131–41
6. O'Rourke MF, Safar ME. **Relationship between aortic stiffening and microvascular disease in brain and kidney: cause and logic of therapy.** *Hypertension* 2005;46:200–04
7. Safar ME. **Arterial stiffness: a simplified overview in vascular medicine.** *Adv Cardiol* 2007;44:1–18
8. Aribisala BS, Morris Z, Eadie E, et al. **Blood pressure, internal carotid artery flow parameters, and age-related white matter hyperintensities.** *Hypertension* 2014;63:1011–18
9. Webb AJ, Simoni M, Mazzucco S, et al. **Increased cerebral arterial pulsatility in patients with leukoaraiosis: arterial stiffness enhances transmission of aortic pulsatility.** *Stroke* 2012;43:2631–36
10. Wohlfahrt P, Krajcoviechova A, Jozifova M, et al. **Large artery stiffness and carotid flow pulsatility in stroke survivors.** *J Hypertens* 2014;32:1097–103
11. Niederer PF. **Ultrasound imaging and Doppler flow velocity measurement.** *Technol Health Care* 2010;18:245–65
12. Caroff J, Biere L, Trebuchet G, et al. **Applications of phase-contrast velocimetry sequences in cardiovascular imaging.** *Diagn Interv Imaging* 2012;93:159–70
13. Schneiders JJ, Ferns SP, van Ooij P, et al. **Comparison of phase-contrast MR imaging and endovascular sonography for intracra-**

- nial blood flow velocity measurements. *AJNR Am J Neuroradiol* 2012;33:1786–90
14. Wählin A, Ambarki K, Birgander R, et al. **Measuring pulsatile flow in cerebral arteries using 4D phase-contrast MR imaging.** *AJNR Am J Neuroradiol* 2013;34:1740–45
  15. Schubert T, Bieri O, Pansini M, et al. **Peak velocity measurements in tortuous arteries with phase contrast magnetic resonance imaging: the effect of multidirectional velocity encoding.** *Invest Radiol* 2014;49:189–94
  16. Markl M, Chan FP, Alley MT, et al. **Time-resolved three-dimensional phase-contrast MRI.** *J Magn Reson Imaging* 2003;17:499–506
  17. Markl M, Frydrychowicz A, Kozerke S, et al. **4D flow MRI.** *J Magn Reson Imaging* 2012;36:1015–36
  18. Schubert T, Santini F, Stalder AF, et al. **Dampening of blood-flow pulsatility along the carotid siphon: does form follow function?** *AJNR Am J Neuroradiol* 2011;32:1107–12
  19. Wetzel S, Meckel S, Frydrychowicz A, et al. **In vivo assessment and visualization of intracranial arterial hemodynamics with flow-sensitized 4D MR imaging at 3T.** *AJNR Am J Neuroradiol* 2007;28:433–38
  20. Bock J KB, Hennig J, Markl M. **Optimized preprocessing of time-resolved 2D and 3D phase contrast MRI data.** In: *Proceedings of the Annual Joint Meeting of the International Society for Magnetic Resonance in Medicine and the European Society for Magnetic Resonance in Medicine and Biology*, Berlin, Germany. May 19–25, 2007
  21. Buonocore MH. **Visualizing blood flow patterns using streamlines, arrows, and particle paths.** *Magn Reson Med* 1998;40:210–26
  22. Walker PG, Cranney GB, Scheidegger MB, et al. **Semiautomated method for noise reduction and background phase error correction in MR phase velocity data.** *J Magn Reson Imaging* 1993;3:521–30
  23. Arbeille P, Asquier E, Moxhon E, et al. **Study of fetal and placental circulation by ultrasound. New technic in the surveillance of pregnancy [in French].** *J Gynecol Obstet Biol Reprod (Paris)* 1983;12:851–59
  24. Gosling RG, King DH. **Arterial assessment by Doppler-shift ultrasound.** *Proc R Soc Med* 1974;67:447–49
  25. Gosling RG, Lo PT, Taylor MG. **Interpretation of pulsatility index in feeder arteries to low-impedance vascular beds.** *Ultrasound Obstet Gynecol* 1991;1:175–79
  26. Mukherjee D, Bhatt DL, Robbins M, et al. **Renal artery end-diastolic velocity and renal artery resistance index as predictors of outcome after renal stenting.** *Am J Cardiol* 2001;88:1064–66
  27. Kundu PK. *Fluid Mechanics*. San Diego: Elsevier Academic Press; 2004
  28. Nichols W, O'Rourke M, Vlachopoulos D, eds. *McDonald's Blood Flow in Arteries: Theoretical, Experimental and Clinical Principles*. London: Hodder Arnold; 2005
  29. Albayrak R, Degirmenci B, Acar M, et al. **Doppler sonography evaluation of flow velocity and volume of the extracranial internal carotid and vertebral arteries in healthy adults.** *J Clin Ultrasound* 2007;35:27–33
  30. Lee KY, Sohn YH, Baik JS, et al. **Arterial pulsatility as an index of cerebral microangiopathy in diabetes.** *Stroke* 2000;31:1111–15
  31. Matsumoto K, Sera Y, Nakamura H, et al. **Correlation between common carotid arterial wall thickness and ischemic stroke in patients with type 2 diabetes mellitus.** *Metabolism* 2002;51:244–47
  32. Bateman GA, Levi CR, Schofield P, et al. **The venous manifestations of pulse wave encephalopathy: Windkessel dysfunction in normal aging and senile dementia.** *Neuroradiology* 2008;50:491–97

# Early Postoperative Imaging and Image-Guided Procedures on Patients with Face Transplants

T.C. Lee, T. Chansakul, R.Y. Huang, G.L. Wrubel, S. Mukundan, D.J. Annino, J.J. Pribaz, and B. Pomahac



## ABSTRACT

**SUMMARY:** Face transplantation is being performed with increasing frequency. Facial edema, fluid collections, and lymphadenopathy are common postoperative findings and may be due to various etiologies, some of which are particular to face transplantation. The purpose of this study was to demonstrate how postoperative imaging and image-guided minimally invasive procedures can assist in diagnosing and treating complications arising from face transplantation. Retrospective evaluation of 6 consecutive cases of face transplantation performed at Brigham and Women's Hospital between April 2009 and March 2014 was performed with assessment of postoperative imaging and image-guided procedures, including aspiration of postoperative fluid collection, lymph node biopsy, and treatment of salivary gland leak. Through these cases, we demonstrate that early postoperative imaging and image-guided procedures are key components for the management of complications following face transplantation.

Since the first face transplantation in 2005, 31 cases have been performed worldwide,<sup>1,2</sup> including the most recent case performed at our institution. Face transplantation provides functional and aesthetic restoration to severely disfigured patients with reported outcomes that surpass those achieved with conventional reconstructions.<sup>3-6</sup> This revolutionary operation replaces damaged or missing facial units such as forehead, eyelids, nose, lips, chin, and cheeks with functional and aesthetically equivalent allografts.<sup>7,8</sup> Face transplantation is a complex surgical procedure because patients typically have extremely complex anatomy secondary to severe injury or prior reconstructive attempts. A multidisciplinary team and extensive preoperative planning are required, for which imaging plays a vital role. As previously described in the literature, preoperative imaging aids in determining the facial defects and planning of arterial and venous anastomoses.<sup>9-11</sup> Postoperative imaging has been useful in identifying and diagnosing postsurgical complications.

Following face transplantation, facial swelling, fluid collections, and lymphadenopathy are common. Differential diagnoses

for these findings are broad. Major differential considerations for postoperative fluid collection include seroma, hematoma, lymphocele, abscess, and salivary gland leak. Differential considerations for postoperative lymphadenopathy include rejection, inflammation, posttransplantation lymphoproliferative disease, and infection. Image-guided aspiration has readily triaged these patients with face transplants.

## CASE SERIES

### Patient Population

We reviewed medical records, pre- and posttransplantation imaging studies, posttransplantation image-guided procedures, and microbiology, chemistry, and pathology results for 6 consecutive face transplantations performed at the Brigham and Women's Hospital between April 2009 and March 2014. This sample comprises the first partial face transplantation, the next 4 full-face transplantations, and the sixth face transplantation, which was partial. The investigation was approved by our institutional review board and is Health Insurance Portability and Accountability Act-compliant. Written informed consent was obtained from each patient.

### Image-Guided Procedures

The procedures, including fluid aspiration, lymph node biopsy, and botulinum toxin injection were performed with sonography, CT, or MR imaging guidance. The choice of imaging technique was based on which one best demonstrated the target and adjacent structures. For instance, sonography was chosen for aspiration of a superficial fluid collection. CT was chosen if a target was deep or behind a bony structure, and MR imaging was chosen in cases in which precise soft-tissue characterization was required

Received July 1, 2014; accepted after revision August 23.

From the Section of Neuroradiology, Department of Radiology (T.C.L., T.C., R.Y.H., G.L.W., S.M.), Division of Otolaryngology, Department of Surgery (D.J.A.), and Division of Plastic Surgery, Department of Surgery (J.J.P., B.P.), Brigham and Women's Hospital, Boston, Massachusetts.

Please address correspondence to Thomas C. Lee, MD, Department of Radiology, Brigham and Women's Hospital, 75 Francis St, Boston, MA 02115; e-mail: tclee@post.harvard.edu

Indicates open access to non-subscribers at [www.ajnr.org](http://www.ajnr.org)

<http://dx.doi.org/10.3174/ajnr.A4141>

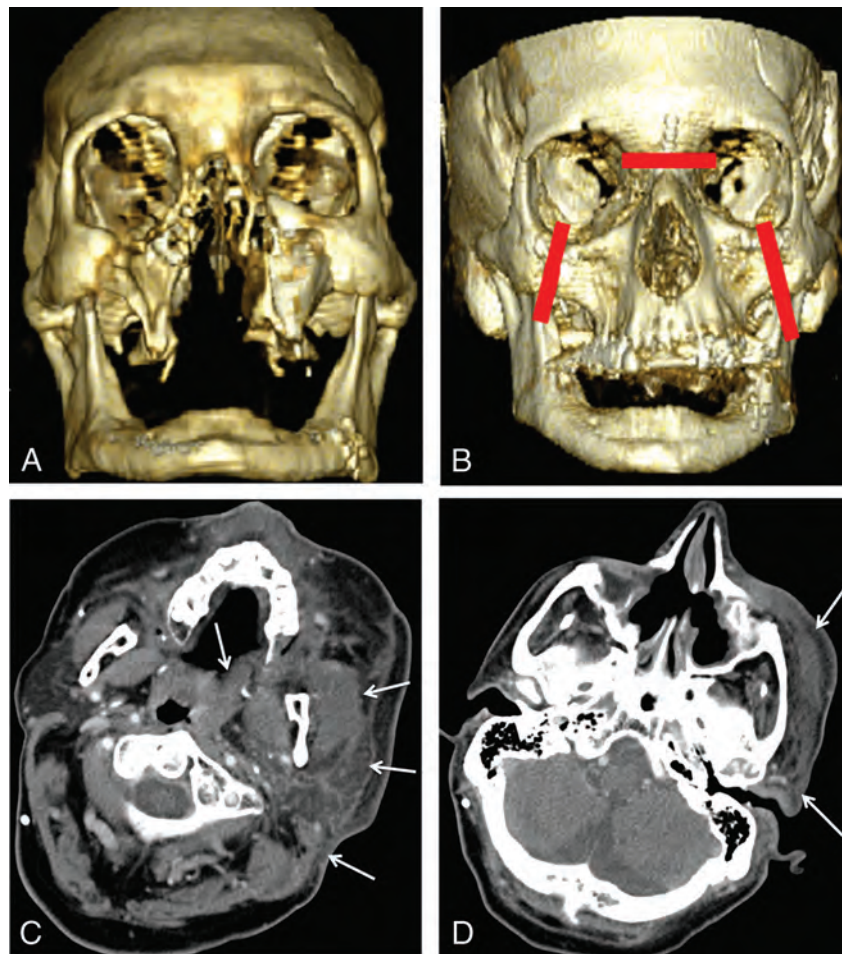


**FIG 1.** A, Preoperative 3D volume-rendered CT image shows posttraumatic and postreconstruction changes including absent nasal bones, anterior walls of the maxillary antra, and most of the hard palate. B, Postoperative 3D volume-rendered image shows fixations of the nasion and bilateral zygoma (*red lines*). C and D, Postoperative CT shows soft-tissue swelling of the left masseter, sternocleidomastoid muscle, parotid gland, and left lateral pharyngeal wall (*arrows*). The degree of swelling is more prominent in recipient native tissues than in the allograft. These findings resolved with antibiotic treatment.

(eg, evaluation of a potentially displaced native salivary gland and point of salivary leak). All diagnostic study interpretations and interventional procedures shown were performed by a board-certified neuroradiologist (T.C.L.).

Image-guided aspiration and lymph node biopsy were performed with standard image-guided techniques following administration of local anesthesia. Aspiration was performed with 25-, 22-, and 20-ga needles and was sent for microbiology and chemistry testing. Lymph node biopsy was performed with an 18-ga core-needle-biopsy device and was submitted to pathology. In cases of salivary gland leak, 0.4 mL (40 U) of botulinum toxin followed by 0.1 mL of saline was administered in each salivary gland at the suspected point of leakage. After all needles were removed, postbiopsy imaging was performed with the same technique, to evaluate immediate postoperative complications.

#### **Patient 1**

Patient 1 underwent the first face transplantation in the Northeast or East Coast in the United States in April 2009 after sustaining massive third- and fourth-degree facial burns secondary to a high-voltage subway rail injury (Fig 1A, -B). There was significant facial swelling and erythema in the immediate postoperative period

without fever. A skin-punch biopsy was performed, showing patchy perivascular chronic inflammation with foci of lymphocytic vasculopathy, consistent with early grade I acute rejection. The patient had 2 more episodes of acute rejection, both of which presented clinically with facial swelling and erythema. All bouts of rejection were responsive to pulse steroids and immunosuppressive therapy.

Five months following the transplantation, the patient presented with left orbital and nasal bridge pain and increased left-face swelling in the setting of low-grade fever preceded by a viral upper respiratory infection. CT performed at this time revealed extensive soft-tissue edema throughout the left periorbital region and left face (Fig 1C, -D), extending caudally to the level of the thyroid gland. There was no soft-tissue gas or drainable collection. The patient was placed on broad-spectrum antibiotics with rapid improvement of symptoms, favoring cellulitis or parotitis as the underlying diagnosis.

#### **Patient 2**

Patient 2 sustained a high-voltage injury to the face and left hip in November 2008 with fourth-degree facial burns and bilateral blindness (Fig 2A). Full-face transplantation was performed in

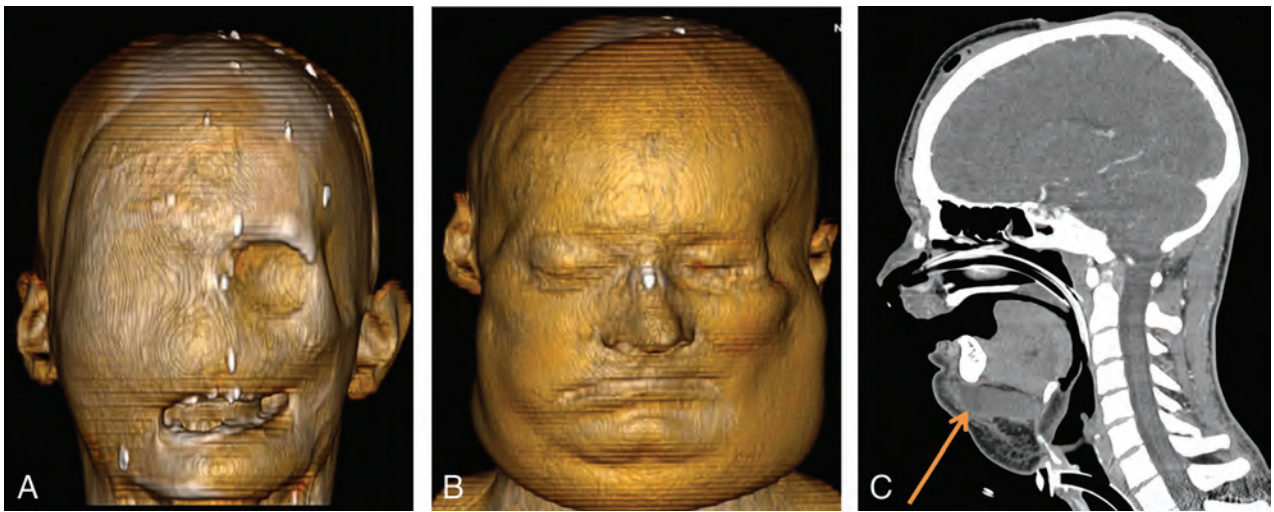


**FIG 2.** A, Preoperative 3D volume-rendered CT image demonstrates posttraumatic changes from a severe electrical burn. B, Postoperative 3D volume-rendered CT image shows facial swelling. C, Postoperative CT image demonstrates a submental fluid collection (orange arrow). Sonography-guided needle aspiration of this fluid collection yielded high amylase and low pH, consistent with salivary collection from donor submandibular glands. The fluid collection was subsequently treated with botulinum toxin injection.

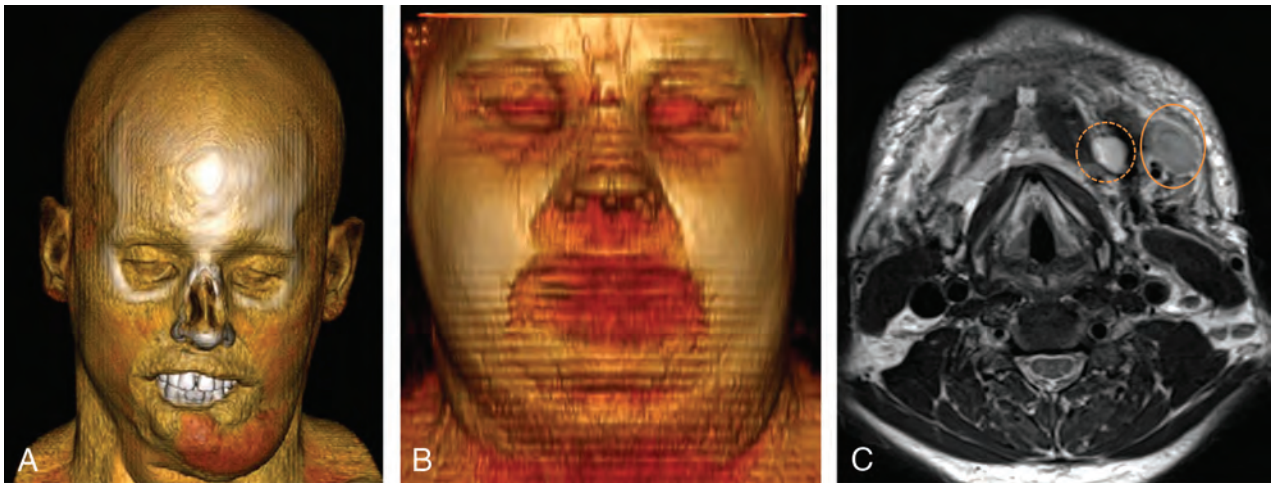


**FIG 3.** A, Preoperative 3D volume-rendered CT scan demonstrates a severely disfigured face. Note a detachable prosthetic nose. B, Postoperative 3D volume-rendered MR imaging performed 3 weeks following the transplantation demonstrates facial swelling. C, Postoperative T2-weighted MR imaging shows a small left submandibular fluid collection, presumed seroma (circle with dotted line), and an enlarged left submandibular lymph node (circle with solid line). A skin-punch biopsy was consistent with grade I/II rejection. The patient's symptoms resolved with pulse steroid therapy.

March 2011. The immediate postoperative period was uneventful. On postoperative day 8, the patient developed leukocytosis, facial swelling, and focal fullness along the left lower margin of the facial allograft (Fig 2B). CT performed at this time demonstrated a large submental fluid collection, a preauricular fluid collection, and multiple enlarged submandibular and submental lymph nodes. A stitch along the left lower margin of the allograft was removed, and the fluid obtained was sent for culture, which later grew *Candida albicans* and *Pseudomonas aeruginosa*. The patient was subsequently treated with cefepime and micafungin. A repeat CT performed 2 weeks following the operation showed that the submental collection was more conspicuous (Fig 2C), prompting sonography-guided aspiration, which yielded 25 mL of sanguineous fluid with a high amylase level and low pH, compatible with salivary gland leak. Culture grew *C albicans*, and the antibiotic was switched to fluconazole. Finally, both submandibular glands were injected with botulinum

toxin under CT guidance (not shown), which successfully treated the salivary gland leak.

### Patient 3

Patient 3 sustained high-voltage facial injury in a motor vehicle collision from a fallen telephone pole (Fig 3A). The patient did well in the immediate postoperative period but presented 3 weeks following the transplant with low-grade fever, facial swelling, and facial erythema (Fig 3B). MR imaging was performed and revealed a small left-sided submandibular fluid collection with 2 adjacent enlarged lymph nodes (Fig 3C). On physical examination, facial edema and erythema were not localized to this left submandibular fluid collection, and there was no focal tenderness at this site. Aspiration of this fluid collection was, therefore, not performed, because this was thought to represent postoperative seroma rather than infection. As with all patients post-face transplantation pre-

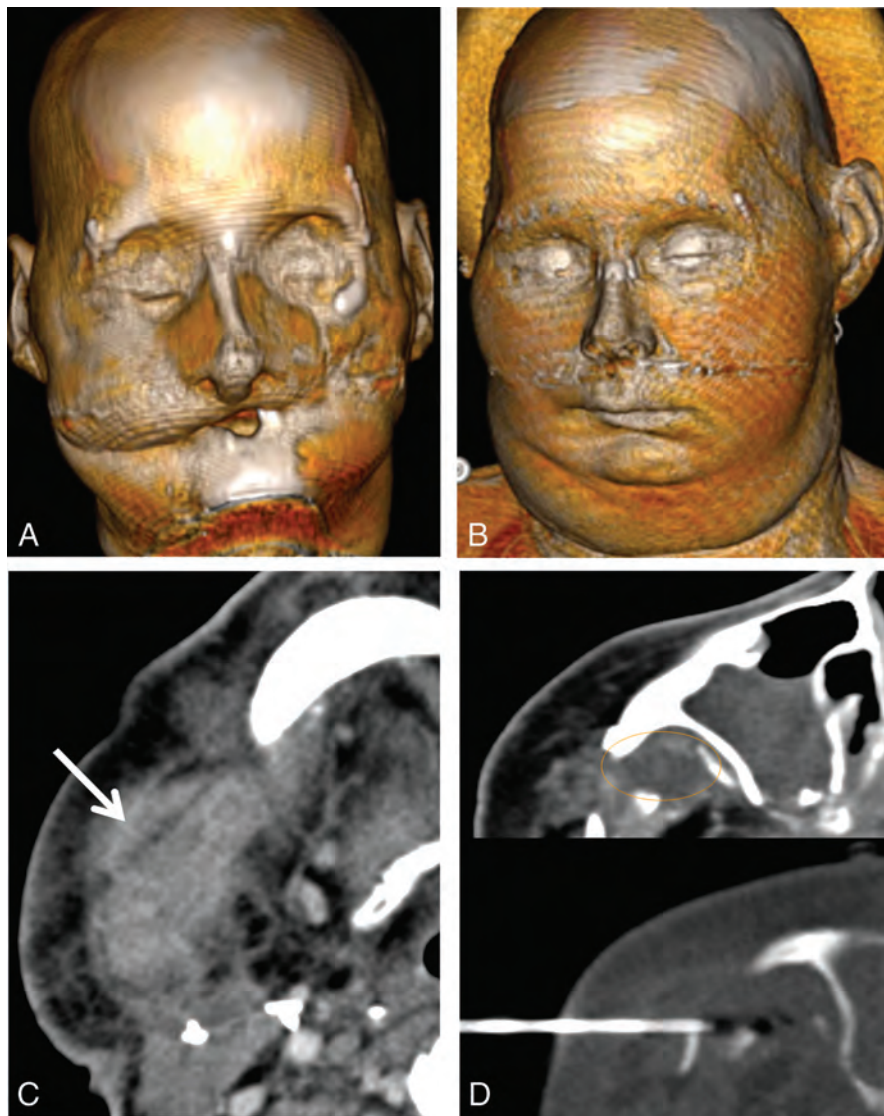


**FIG 4.** A, Preoperative 3D volume-rendered CT image of the patient whose face was mauled by a chimpanzee. B, Postoperative 3D volume-rendered CT image obtained for persistent fever and facial swelling 4 weeks following the surgery demonstrates facial swelling. C, Postoperative CT scan shows a necrotic-appearing right submandibular lymph node (arrow). CT-guided biopsy of this lymph node showed inflammation without evidence of infection or rejection. D, Postoperative CT also demonstrates a small fluid collection adjacent to the native right zygoma (circle), which was aspirated under CT guidance. Culture grew *Enterococcus* species.

senting with facial edema, a skin-punch biopsy was performed, which, in this case, demonstrated grade I/II rejection. The patient's symptoms subsequently resolved with pulse steroid therapy.

#### **Patient 4**

Patient 4 was attacked by a chimpanzee, sustaining severe facial injuries (Fig 4A). Full-face transplantation was performed in May 2011. Four weeks following the transplantation, the patient presented with facial swelling and erythema (Fig 4B). CT revealed a 4-cm conglomerate nodal mass with low-attenuation necrosis in the right submandibular region (Fig 4C). There was also a 1.8-cm fluid collection deep to the right zygoma with surrounding stranding and a 1.5-cm rim-enhancing fluid collection within the left submandibular region. CT-guided biopsy of the necrotic right submandibular mass was obtained, yielding inflammation without evidence of pus, rejection, or infec-

tion. CT-guided aspiration of the fluid collection deep to the native right zygoma was also performed (Fig 4D). Cultures grew *Enterococcus* species. The patient was placed on amoxicillin/clavulanic acid.

#### **Patient 5**

Patient 5 was a female with extensive burn injuries in 2007 after an assault with industrial lye (Fig 5A). Full-face transplantation was performed in February 2013. Two weeks following the surgery, the patient presented with facial swelling (Fig 5B). CT showed soft-tissue edema, lymphadenopathy, but no drainable fluid collection (Fig 5C, -D). Skin biopsy was consistent with grade I/II rejection, which was treated with plasma exchange.

#### **Patient 6**

Patient 6 had a remote gunshot injury to the face (Fig 6A). Partial face transplantation was performed in March 2014. In the first

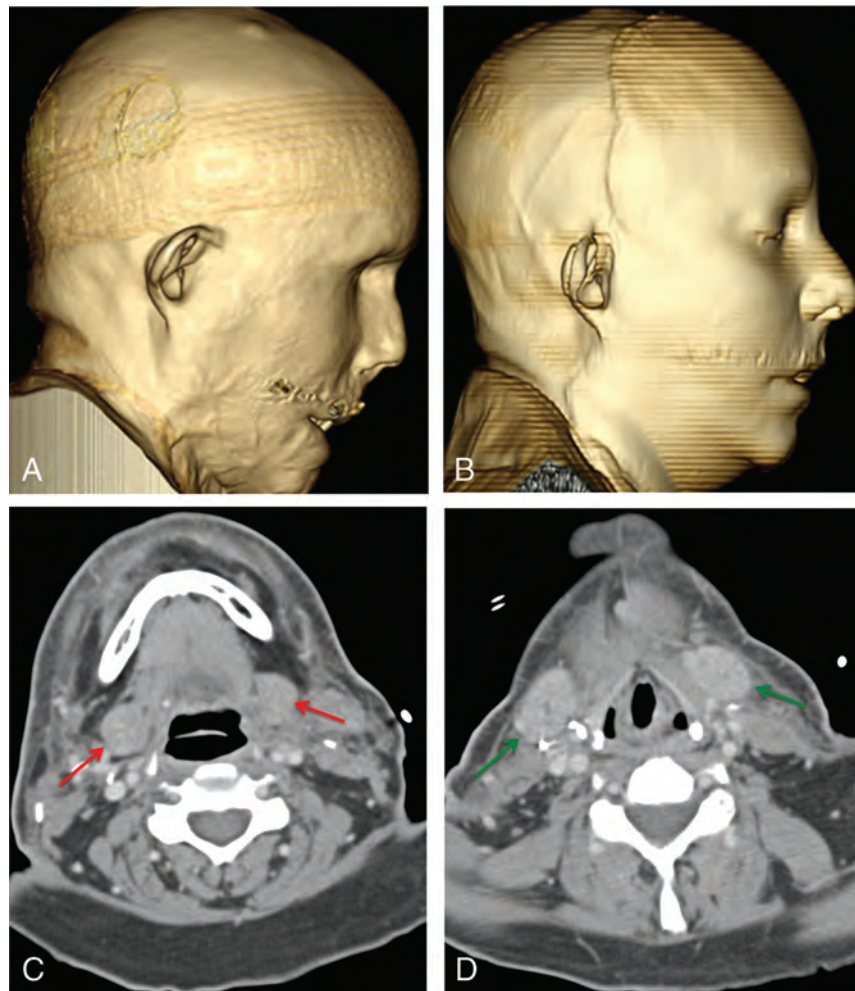


**FIG 5.** A, Preoperative 3D volume-rendered CT image demonstrates facial deformity due to a severe lye burn. B, Postoperative 3D volume-rendered CT image shows mild facial swelling. C and D, Postoperative axial CT images show edema without a fluid collection. Note the normal-sized recipient submandibular glands (red arrows) and, more caudally, the symmetrically swollen bilateral donor submandibular glands (green arrows), which had been injected with botulinum toxin at the time of transplantation.

week following face transplantation, the patient developed increasing swelling of the right neck (Fig 6B). An enhanced CT scan of the head and neck revealed no rim-enhancing collection to suggest abscess; however, there was a large ill-defined fluid collection around the possibly posteriorly displaced native right submandibular gland extending to the right parotid gland (Fig 6C). Because the suspected right submandibular gland was altered in both shape and position, a differential consideration at the time included an enlarged lymph node. Review of the preoperative imaging, however, confirmed that the right submandibular gland was still present, while the left was absent, presumably due to the injury. There was no significant fluid around the 2 donor submandibular glands, which were treated with botulinum toxin injection at the time of transplantation. MR imaging-guided aspiration yielded fluid with a high amylase level, in keeping with a salivary leak (Fig 6D). MR imaging-guided botulinum toxin injection was performed at the right parotid gland and the suspected posteriorly displaced native right submandibular gland (Fig 6E, -F). Right-neck swelling subsequently resolved.

## DISCUSSION

Prior literature on face transplant imaging has focused on preoperative imaging for planning of vascular anastomoses. In this article, we describe how early post-face transplantation imaging plays a vital role in identifying potential postoperative complications, particularly facial edema, fluid collections, and lymphadenopathy. Early postoperative imaging demonstrated facial edema and lymphadenopathy in all 6 cases and fluid collection in 4 cases.

Postoperative facial edema can be explained by a variety of etiologies, including lack of postsurgical lymphatic drainage, inflammation, infection, salivary gland leak, and rejection. Correlation with clinical examination and skin biopsy is helpful in making the diagnosis. At our institution, skin biopsy is obtained post-face transplantation on all patients who develop facial swelling, to evaluate rejection. Imaging with either sonography, CT, or MR imaging should be performed to evaluate the presence of a loculated fluid collection, which would favor an infectious process or salivary leak, in which case, the patient will likely benefit from image-guided aspiration for a definitive diagnosis.

Image-guided aspiration of a fluid collection was performed in

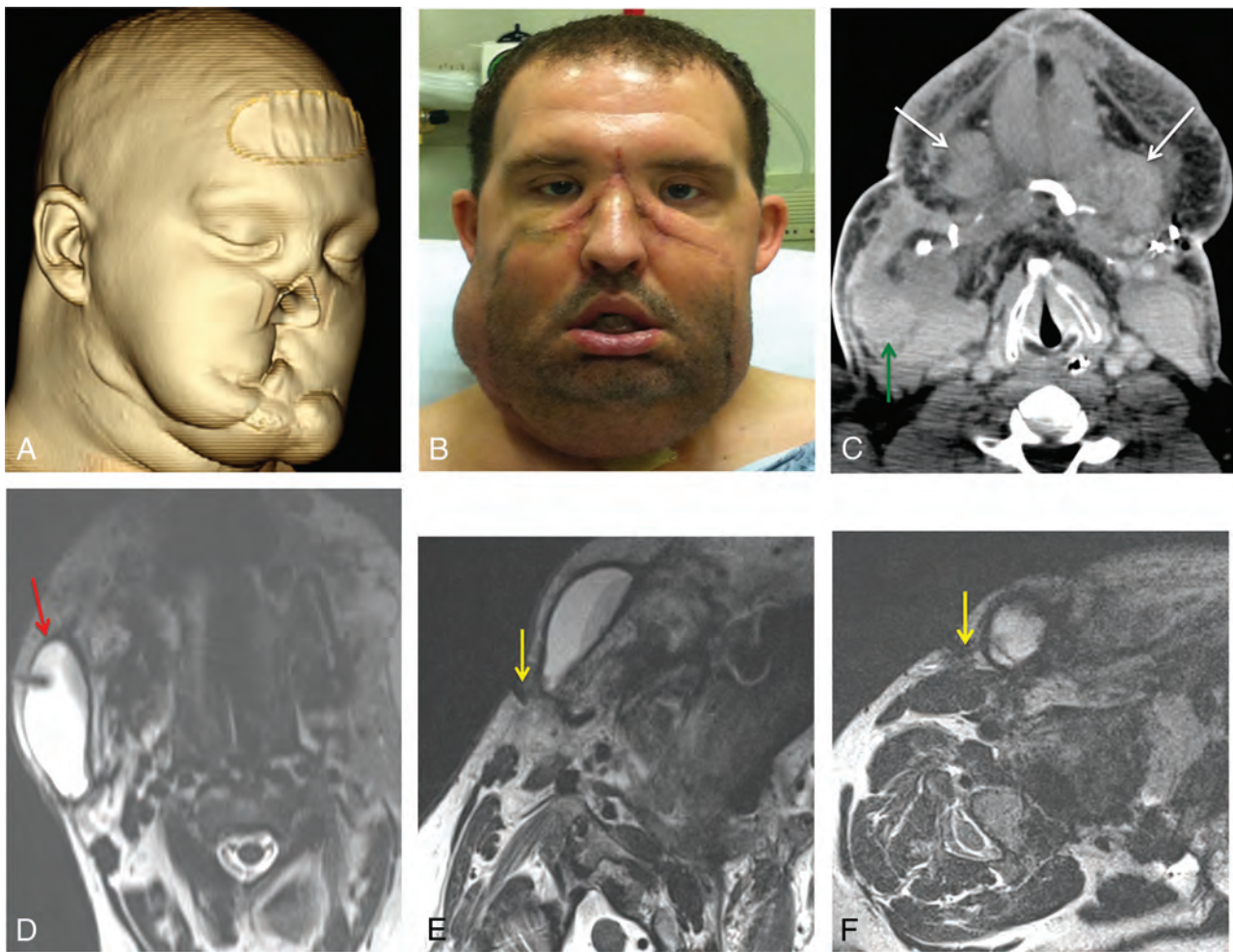


**FIG 6.** A, Preoperative 3D volume-rendered CT demonstrates facial deformity from a gunshot injury. B, Frontal photograph of the patient at 1 week following partial face transplantation shows right lower face and neck swelling. C, Posttransplantation CT demonstrates bilateral donor submandibular glands (*white arrows*), which had been injected with botulinum toxin at the time of transplantation. CT also shows a possible posteriorly displaced native right submandibular gland (*green arrow*), surrounded by fluid. Because the gland is altered in both shape and position, a differential consideration at this point includes an enlarged lymph node. D, Axial T2-weighted image obtained during MR imaging-guided aspiration of the fluid collection (*red arrow*). Aspirated fluid had a high amylase level, in keeping with salivary leak. E and F, Axial T2-weighted images obtained as the needles (*yellow arrows*) were advanced for botulinum toxin injection in the superficial right parotid gland at the site of suspected leak, determined by a tapered narrowing of the fluid collection toward the lateral aspect of the gland (E), and in the suspected posteriorly displaced native right submandibular gland (F). Injection of the native right submandibular gland was targeted at its anterior portion, closest to the adjacent fluid collection.

3 patients, yielding definitive diagnoses in all cases, demonstrating either infection and/or salivary gland leak. In 2 patients in whom infection was identified, broad-spectrum antibiotics or antifungal agents could subsequently be tailored to the isolated organism.

Lymph node enlargement was observed in all patients with face transplants. Lymphadenopathy may be related to graft-versus-host reaction, infection, inflammation, or lymphatic stasis. While lymphoproliferative disorders have not been observed in our patient population, Epstein Barr virus-related lymphoma has previously been reported in the literature.<sup>12</sup> Both lymph node enlargement and facial swelling were noted to resolve in all patients 6 weeks to 2 months following surgery. In the absence of rejection and infection, this resolution in lymphadenopathy is likely secondary to restoration of postsurgical lymphatic channels.

Salivary gland leak is a surgical complication particularly re-

lated to face transplantation. Patient 2, the first patient with a full transplant, was found to have a salivary gland leak, which was treated successfully with bilateral submandibular gland botulinum toxin injection. This injection has previously been used in the setting of sialorrhea secondary to Parkinson disease, stroke, head and neck cancer, and neurodegenerative disease.<sup>13</sup> Given our success in this treatment with post-face transplantation salivary leak, all subsequent full-face transplantations performed at our institution had intraoperative submandibular gland botulinum toxin injection without image guidance as a preventive therapy. None of the subsequent cases of face transplantation experienced salivary leak except patient 6, in whom the salivary leak may have been related to particularly difficult intraparotid facial nerve dissection and/or suspected remnants of a native right submandibular gland posteriorly displaced by the allograft. Botulinum toxin injection is directed at the site of leaking if this can be identified at imaging by the relationship of the fluid collection to the

gland. For instance, in patient 6, there appeared to be a tapered narrowing of the fluid collection toward the lateral aspect of the right superficial parotid gland, and botulinum toxin injection was targeted at this site.

## CONCLUSIONS

Face transplantation is a complex procedure, which is being performed with increasing frequency. Early postoperative face transplantation complications are varied, including rejection, infection, abscess, lymphocele, hematoma, and salivary gland leak. Postoperative sonography, CT, or MR imaging can easily identify discrete fluid collections in the setting of postoperative facial swelling. Once a fluid collection is identified, image-guided aspiration is a minimally invasive technique, which provides a rapid definitive diagnosis that guides therapeutic management. Image-guided botulinum toxin injection has been effective as a preventive and therapeutic procedure for salivary leak.

Disclosures: T.C. Lee—UNRELATED: *Payment for Development of Educational Presentations*: Elsevier, *Comments*: Atlas coauthor. Srinivasan Mukundun—RELATED: *Grant*: Department of Defense,\* *Comments*: sponsors portions of face transplant program; UNRELATED: *Grants/Grants Pending*: National Institutes of Health,\* *Comments*: received shared instrument grant to buy a preclinical 7T MRI scanner; *Payment for Development of Educational Presentations*: Elsevier, *Comments*: Atlas textbook coauthor; *Stock/Stock Options*: consultant, *Comments*: Alzeca, MKT, and Marval. I received stock options for consultant work. These are separate startup companies without a clinical product. D.J. Annino—RELATED: *Grant*: Department of Defense,\* *Comments*: partial salary support from research contract, #W911QY-09-C-0216. J.J. Pribaz—RELATED: *Grant*: Department of Defense,\* *Comments*: partial salary support from research contract, #W911QY-09-C-0216. B. Pomahac—RELATED: *Grant*: Department of Defense,\* *Comments*: partial salary support from research contract, #W911QY-09-C-0216. \*Money paid to the institution.

## REFERENCES

1. Altman LK. **An about-face on a risky transplant.** *New York Times*. April 29, 2014:D1
2. Khalifian S, Brazio PS, Mohan R, et al. **Facial transplantation: the first 9 years.** *Lancet* 2014;384:2153–63
3. Lantieri L, Meningaud JP, Grimbert P, et al. **Repair of the lower and middle parts of the face by composite tissue allotransplantation in a patient with massive plexiform neurofibroma: a 1-year follow-up study.** *Lancet* 2008;372:639–45
4. Petruzzo P, Testelin S, Kanitakis J, et al. **First human face transplantation: 5 years outcomes.** *Transplantation* 2012;93:236–40
5. Pomahac B, Pribaz J, Eriksson E, et al. **Restoration of facial form and function after severe disfigurement from burn injury by a composite facial allograft.** *Am J Transplant* 2011;11:386–93
6. Pomahac B, Pribaz J, Eriksson E, et al. **Three patients with full facial transplantation.** *N Engl J Med* 2012;366:715–22
7. Barret JP, Gavalda J, Bueno J, et al. **Full face transplant: the first case report.** *Ann Surg* 2011;254:252–56
8. Jeung IS, Lee S, Kim HS, et al. **Effect of botulinum toxin injection into the salivary glands for sialorrhea in children with neurologic disorders.** *Ann Rehabil Med* 2012;36:340–46
9. Sisk GC, Kumamaru KK, Schultz K, et al. **Cine computed tomography angiography evaluation of blood flow for full face transplant surgical planning.** *Eplasty* 2012;12:e57
10. Soga S, Pomahac B, Wake N, et al. **CT angiography for surgical planning in face transplantation candidates.** *AJNR Am J Neuroradiol* 2013;34:1873–81
11. Soga S, Wake N, Bueno EM, et al. **Noninvasive vascular images for face transplant surgical planning.** *Eplasty* 2011;11:e51
12. Siemionow M, Ozturk C. **Face transplantation: outcomes, concerns, controversies, and future directions.** *J Craniofac Surg* 2012;23:254–59
13. Lengelé BG. **Current concepts and future challenges in facial transplantation.** *Clin Plas Surg* 2009;36:507–21

# Physiologic Pineal Region, Choroid Plexus, and Dural Calcifications in the First Decade of Life

M.T. Whitehead, C. Oh, A. Raju, and  A.F. Choudhri

## ABSTRACT

**BACKGROUND AND PURPOSE:** Calcifications of the pineal, habenula, choroid plexus, and dura are often physiologic. In the modern CT era with thin-section images and multiplanar reformats, intracranial calcifications have become more conspicuous. We aimed to discover the CT prevalence of pineal region, choroid plexus, and dural calcifications in the first decade of life.

**MATERIALS AND METHODS:** Five hundred head CTs from different patients (age range, 0–9 years) encountered during a consecutive 6-month period at a single academic children's hospital were reviewed retrospectively after excluding examinations with artifacts and pineal region masses/hemorrhage. All studies were performed on a 320-detector CT, with 0.5-mm collimation and a 512 × 512 matrix. Five-millimeter reformatted axial, sagittal, and coronal images were analyzed for location and extent of intracranial calcifications.

**RESULTS:** The mean age was 3.5 ± 5.7 years (range, 0–9 years). There were 285 males (57%) and 215 females (43%). Pineal calcifications were present in 5% (*n* = 25; age range, 3.2–8.9 years; median, 7 years). Habenular calcifications were found in 10% (*n* = 50; age range, 2.8–8.8 years; median, 7 years). Twelve percent (*n* = 58) had choroid plexus calcifications, (age range, 0.1–8.8 years). Dural calcifications were rare, present in 1% (*n* = 6; age range, 2.9–8.7 years).

**CONCLUSIONS:** Physiologic intracranial calcifications may be found in the first decade, principally in children older than 5 years. Most epthalamic calcifications are habenular. Pineal and habenular calcifications were never present in children younger than 3 and 2 years, respectively. Choroid plexus calcifications may be present in the very young. Dural calcifications are rare.

Physiologic intracranial calcifications become increasingly prevalent with advancing age but can be found in children and adults. Pineal region calcification is known to be present histologically from fetal life to adulthood.<sup>1</sup> Benign calcifications in the pineal gland, habenula, choroid plexus, and dura should not be mistaken for hemorrhage or pathologic tumoral or metabolic mineralization. Thus, it is important to know where physiologic intracranial calcification is expected, and the age when it becomes detectable on imaging.

The widely held dictum that pineal region calcifications found

in those younger than 6 years of age are always pathologic no longer holds true in the modern CT era.<sup>2</sup> Previous imaging studies that generated the currently established age thresholds examined intracranial calcifications on more primitive CT scanners with smaller matrices and thicker sections. Furthermore, sparse literature exists regarding the prevalence of dural and choroid plexus calcifications on head CTs in children. We sought to discover the prevalence of intracranial calcifications in the pineal gland, habenula, choroid plexus, and dura in the first decade of life by using contemporary CT technology.

## MATERIALS AND METHODS

This Health Insurance Portability and Accountability Act–compliant retrospective study was performed after institutional review board approval. The imaging database at a single academic children's hospital was searched for all noncontrast head CTs from separate patients younger than 10 years of age obtained during a consecutive 6-month period. The search yielded 507 examinations. Patients with entities known to be associated with calcifications were excluded. Examinations with excessive motion artifacts, pineal region masses, or evaluation-limiting hemorrhage were also excluded. All examinations were performed on a

Received July 17, 2014; accepted after revision September 5.

From the Departments of Radiology (M.T.W., C.O., A.R., A.F.C.) and Neurosurgery (A.F.C.), University of Tennessee Health Science Center, Memphis, Tennessee; Department of Radiology (M.T.W., A.R., A.F.C.), Le Bonheur Children's Hospital, Memphis, Tennessee; and Department of Radiology (M.T.W.), Children's National Medical Center, Washington, DC.

Paper previously presented at: American Society of Neuroradiology Annual Meeting and the Foundation of the ASNR Symposium; May 17–22, 2014; Montreal, Quebec, Canada.

Please address correspondence to Asim F. Choudhri, MD, Department of Radiology, Le Bonheur Children's Hospital, 848 Adams St-G216, Memphis, TN 38103; e-mail: achoudhri@uthsc.edu

<http://dx.doi.org/10.3174/ajnr.A4153>

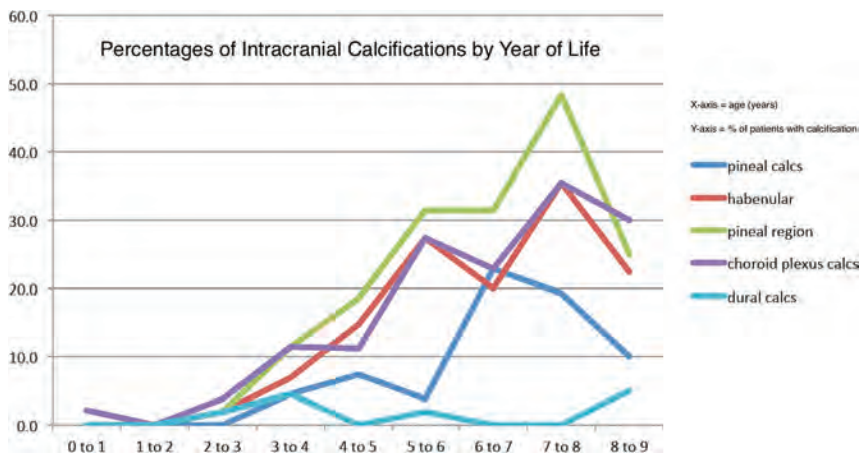


**FIG 1.** Chart depicting the percentage of patients with calcifications (y-axis) in various regions by year of life (x-axis).

#### Location of specific intracranial calcifications

Location of Calcification	No. of Patients	Age Range (yr)
Pineal gland	25/500 (5%)	3.2–8.9 (median, 6.7)
Habenula	50/500 (10%)	2.8–8.8 (median, 6.5)
Pineal region	63/500 (13%)	2.8–8.9 (median, 6.5)
Choroid plexus	58/500 (12%)	0.1–8.8 (median, 6.3)
Dural	6/500 (1%)	2.9–8.7 (median, 4.5)

320-detector CT scanner (Aquilion ONE; Toshiba Medical Systems, Tokyo, Japan) with 0.5-mm collimation and a 512 × 512 matrix. The epithalamus, choroid plexus, and dura were analyzed for calcifications on 5-mm axial, coronal, and sagittal reformatted images in each case. Epithalamic calcifications included either pineal, habenular, or both. Epithalamic calcifications were also subdivided into pineal or habenular on the basis of their distinct location; focal pineal parenchymal or pineal wall calcifications were classified as “pineal,” while pineal adjacent calcifications were considered “habenular.” The latter are generally localizable anterolateral to the pineal gland along the medial thalamic margins.

Calcification positivity was defined as hyperattenuating material respective to gray matter. In addition to group analysis, we evaluated patient subsets on the basis of age. We recorded the total number of patients in each year of life and calculated the percentages of pineal, habenular, choroid plexus, and dural calcifications in patients of each age (range, 0–9 years). Pineal calcifications were classified as punctate and/or single or larger and/or numerous (>1). All encountered pineal cysts were recorded and manually measured by calipers on a PACS in the maximal diameter; mean pineal cyst sizes were then calculated. Dural and choroid plexus calcifications were grouped by location. Choroid plexus calcifications were classified as either punctate and/or few or large and/or multiple. The potential relationship between choroid plexus and pineal calcifications was explored.

Images were retrospectively reviewed in a blinded manner by 2 fellowship-trained neuroradiologists with American Board of Radiology subspecialty certificates in neuroradiology (M.T.W. and A.F.C.). Both readers had >3 years of clinical experience after board certification. A consensus reading was reached in all cases. Each patient’s electronic medical record was researched for pre-

senting symptomatology, demographic information, and pertinent physical examination findings.

Five hundred patients met the inclusion criteria, with a mean age of 3.5 ± 5.7 years (median, 2.5 years; range, 0.0–9 years). The percentages of patients with intracranial calcifications in each age group are shown in Fig 1. There were 285 males (57%) and 215 females (43%). The most common clinical indications for the examinations were trauma (*n* = 209), seizures (*n* = 66), shunt (*n* = 57), and headache (*n* = 41). None of the patients had undergone prior therapeutic radiation, and no histories of metabolic disorders, endocrinopathies, or renal diseases could cause calcium-phosphate imbalance and

premature or excessive intracranial calcification. One patient had a history of tuberous sclerosis but had no intracranial calcification. None of the patients had documented histories of TORCH infection or neurofibromatosis type 1, entities known to be associated with calcifications in or around the choroid plexus.<sup>3</sup>

#### Data Collection and Statistics

Data were stored and analyzed in a spreadsheet (Excel 2011; Microsoft, Redmond, Washington) and in SPSS (Version 20.0; IBM, Armonk, New York). Discrete variables were evaluated by using the  $\chi^2$  or Fisher exact test, as appropriate. Continuous variables were analyzed for significance by using the Kruskal-Wallis test with a nonparametric posttest. Correlations were made by using the Pearson product-moment correlation coefficient. *P* values < .05 were considered significant.

#### RESULTS

Age and intracranial calcification presence were positively correlated (*P* < .0001) (Fig 1). Most (97%) intracranial calcifications were found in patients older than 5 years. There was no significant difference in sex (*P* = .41) or race (*P* = .28) of patients with and without calcifications. A summary of location-specific intracranial calcifications is provided in the Table.

#### Epithalamus

Epithalamus (pineal and/or habenular) calcifications were present in 13% (63/500). Pineal and habenular calcifications were positively correlated (*P* < .0001). Pineal calcifications were present in 5% (*n* = 25; age range, 3.2–8.9 years; median, 7 years). One percent (6/500) of patients were younger than 6 years of age (Fig 2). Pineal calcifications were single and/or punctate in 71% (17/24) and larger and/or more numerous in 29% (7/24; range, 7–9 years).

Pineal cysts were found in 3% (*n* = 15; age range, 0.7–7.5 years; median, 2.6 years). These ranged from 4 to 15 mm (median, 5 mm). Four of these 15 patients had epithalamic calcifications involving the habenula (*n* = 4) and/or pineal gland (*n* = 1).

Habenular calcifications were found in 10% (*n* = 50; age range, 2.8–8.8 years; median, 7 years; Fig 2).



**FIG 2.** A, Midline sagittal head CT image from an 8-year-old child obtained for headache, demonstrating calcifications in both the pineal gland (*large arrow*) and habenular complex (*small arrow*). Habenular calcifications are centered anterosuperior and lateral to the pineal base. B, Axial head CT image through the epithalamus from an 8-year-old child performed for headache, showing pineal gland (*large arrow*) and habenular (*small arrow*) calcifications. Habenular calcifications are centered anterolateral to the pineal base.

#### **Choroid Plexus**

Twelve percent of subjects ( $n = 58$ ) had choroid plexus calcifications (age range, 0.1–8.8 years; median, 6 years; Fig 3). All choroid plexus calcifications were localized to the lateral ventricular glomus. Most choroid plexus calcifications were punctate and/or few ( $n = 54$ ). The 4 remaining patients with large and/or numerous choroid plexus calcifications were 8 ( $n = 3$ ) and 3 ( $n = 1$ ) years of age. There was a significant association between patients with choroid plexus and pineal calcifications ( $P = .003$ ).

#### **Dura**

Dural calcifications were rare, present in only 1% ( $n = 6$ ; age range, 2.9–8.7 years; median, 6 years; Fig 4). The tentorium was the most common dural site to calcify ( $n = 4$ ) followed by the falx cerebri ( $n = 2$ ).

## **DISCUSSION**

#### **Epithalamus**

The epithalamus comprises the pineal gland and habenular complex. We chose to examine the prevalence of epithalamic, pineal,

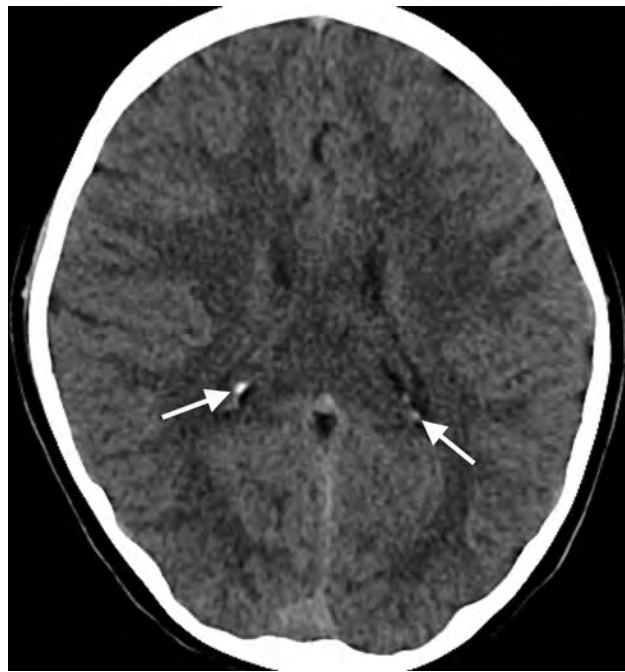


**FIG 3.** Axial head CT image from an 8-year-old child obtained for seizure, at the level of the lateral ventricular atria, depicting choroid plexus glomus calcifications (*arrows*).

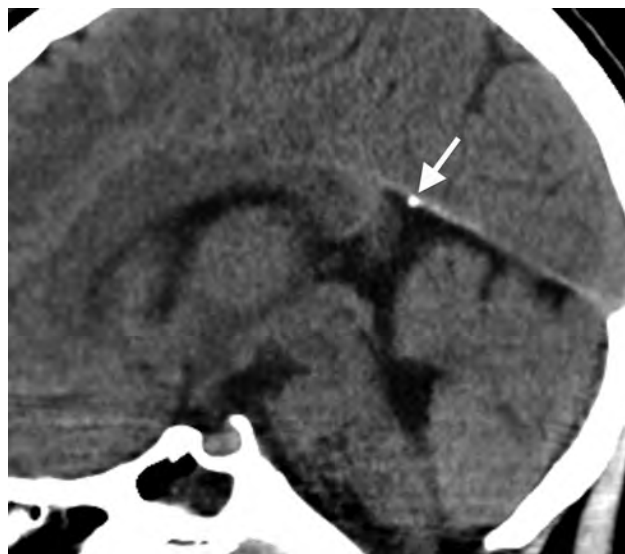


**FIG 4.** Midline sagittal head CT image from an 8-year-old child obtained for headache, demonstrating dural calcifications along the anterior margin of the cerebellar tentorium (*arrow*).

and habenular calcifications separately for several reasons. First, we think pineal and habenular calcifications can be accurately distinguished in most circumstances with modern CT technology and thin-section images. Second, we suspect that in the past, many habenular calcifications were misclassified as being pineal. Because these structures are functionally unique, we think that they deserve to be analyzed separately.

#### **Pineal Gland**

The pineal gland is a conical organ situated in the quadrigeminal cistern between the posterior and habenular commissures. Pi-

nocytes, glial cells, neurons, and perivascular phagocytes constitute the bulk of its internal structure.<sup>4</sup> After a period of initial growth, the size of the pineal gland has been shown to remain stable beyond the first 1–2 years of life.<sup>5–7</sup> Knowledge of normal pineal gland size/volume is relevant in the evaluation of pineal region pathology. Pineal calcifications that would be considered benign in isolation are suspicious for neoplasia if there is concurrent glandular enlargement.

Why does the pineal gland calcify, and where is the calcium localized? Calcified concretions called “corpora arenacea” or “brain sand” found within the pineal gland primarily comprise calcium and magnesium salts.<sup>8</sup> Exophytic membrane debris, a by-product of pineal neuronal and glial polypeptide exocytosis, forms the skeleton of the corpora arenacea around which calcifications are laid.<sup>9</sup> Early calcifications found in younger patients are globular and localize near pinealocytes; whereas in older patients, calcifications tend to be more concentric and are associated with glial cells.<sup>10</sup> In a study of older adults (age range, 62–80 years), Kim et al<sup>11</sup> found multiple concentrically calcified areas distributed throughout the pineal gland with centrally concentrated larger aggregates. Perivascular, tryptase-secreting mast cells have been found in areas where intrapineal calcium deposits originate, implicating these mast cells in the calcification process.<sup>1</sup> Calcium also tends to localize along cell membranes.<sup>8</sup> The outer pineal gland membrane may calcify, generally in a laminated manner.<sup>8,10</sup> The laminated pineal calcifications that are found in older individuals may be related to circannual calcium level changes.<sup>8</sup> However, the underlying cause of pineal calcium deposition remains elusive. It could represent a physiologic, maturational, or degenerative process.

In 1982, Zimmerman and Bilaniuk<sup>2</sup> studied a large series of 725 patients (age range, 0–20 years) to define the incidence of pineal calcifications in the first 2 decades of life. In that study, the incidence of physiologic pineal calcifications was 11%; 13% of these were found in the first decade, with the youngest patient being 6.5 years. Because the study used CT parameters that would be considered primitive by today’s standards, including a relatively small matrix (160 × 160 or 320 × 320) and large section thickness (8 mm), the incidence of pineal calcifications was likely underestimated. Other literature contradicts the low range of 6.5 years. One study indicated a 3% frequency of pineal calcifications in the first 12 months.<sup>12</sup> A more recent study by Doyle and Anderson<sup>13</sup> demonstrated pineal calcifications in 8% of patients 0–10 years of age by using CT with a 512 × 512 matrix and 8-mm section thickness in nearly all cases. The youngest patient with pineal calcification was 3 years of age, and 1% of patients younger than 6 years had pineal calcifications, identical to our study results. Early pineal glandular calcium deposition has also been shown in the histopathology literature, where microscopic calcifications in the human pineal gland have been documented even before birth.<sup>1</sup>

We found pineal calcifications in 5%. While most of these patients were older than 5 years, a few were younger (youngest, 3 years). The apparent decrease in the percentage of patients with pineal region calcifications between 7 and 9 years of age is likely attributable to fewer patients in older patient subsets (Fig 1). The mantra that no pineal gland calcification should be visible in pa-

tients younger than 6 years is no longer relevant in the modern CT age.<sup>2</sup> However, pineal calcifications were single and punctate in all of our patients younger than 7 years of age. Occasional cases of larger and more numerous pineal calcifications were seen only in patients older than 7 years. Therefore, we advise cautious scrutiny in those patients younger than 7 years manifesting large and/or excessive pineal calcifications. Suspicious calcifications (pre-mature, large, or excessive) should prompt a glandular volume analysis.<sup>5–7</sup> A detailed clinical and biochemical assessment should be undertaken. Follow-up imaging should also be considered to exclude early presentation of a pineal tumor.

### **Habenula**

The habenula is a small, bilaterally paired nuclear complex located along the inferior dorsomedial thalami. It is structurally connected to many deep brain structures, including the pineal gland, hypothalamus, midbrain, basal ganglia, and septal area, to name a few. Thus, it has a multitude of functions, mainly serving as a relay and processing center between the limbic system and midbrain through the stria medullaris thalami (afferent) and habenulointerpeduncular tract (efferent), ultimately influencing dopamine and serotonin elaboration.<sup>14</sup> The habenular complex also participates in the sleep-wake cycle. The retinohypothalamic reflex is the process by which light-induced retinal activation recognized in the hypothalamus signals the pineal gland to decrease melatonin production by way of the sympathetic chain. One function of melatonin is to inhibit the habenular complex. In the absence of melatonin-induced habenular inhibition, dopamine inhibition, normally mediated by the habenula, is eliminated, and dopamine excretion increases.<sup>14,15</sup> Because the pineal gland and habenula are in proximity and share at least 1 common function, it is understandable that they may calcify at similar times, whether degenerative, physiologic, or otherwise. The substance of these calcifications is similar in makeup to that found in the pineal gland; the calcifications contain both calcium and magnesium salts.<sup>8</sup>

To our knowledge, the potential association between sleep dysfunction and habenular calcification has not been systematically examined. However, there may be a link between habenular calcification and pathophysiology, ultimately disrupting the aversion/reward process. For instance, pineal and habenular calcifications have been noted as frequent findings in patients with schizophrenia.<sup>16,17</sup> Because patients with schizophrenia often have difficulty learning from errors, habenular dysfunction has been implicated.<sup>18</sup> Habenular calcifications were the most common epithalamic calcification in our cohort, present in 10% and in none younger than 2 years of age.

### **Choroid Plexus**

The choroid plexus is an intraventricular organ comprising cuboidal epithelial cells, vasculature, and connective tissue. It has multifaceted functionality, chiefly serving in CSF volume modulation with productive, absorptive, and filtering capability. Its bulk resides in the lateral ventricular atria, called the glomus. During the human life span, the choroid plexus tends to accumulate physiologic calcifications. Because most choroid plexus is concentrated in the ventricular atria, it is here that calcifications are

most frequently evident. Pathologic processes such as prior intraventricular infection, inflammation, and hemorrhage and chronic calcium and phosphate imbalance can cause premature or excessive choroid plexus mineralization. Therefore, knowledge of a normally expected calcification time range would be helpful in distinguishing physiology from pathology.

The prevalence of choroid plexus calcification increases with age.<sup>19,20</sup> However, few studies have examined choroid plexus calcifications in children. In a large retrospective CT study from 18,000 consecutive children (0–15 years of age) performed with early CT technology (EMI 1010 CT) by Kendall and Cavanagh,<sup>20</sup> choroid calcifications were found in 2% of patients younger than 8 years of age. Another CT study that examined scans obtained with 8-mm section thickness and a 256 × 256 matrix demonstrated the prevalence of choroid plexus calcification in the first decade to be 0.5%.<sup>3</sup> More recently, Doyle and Anderson<sup>13</sup> found choroid plexus calcifications to be more prevalent, present in 16% of their patients. Indeed, choroid plexus psammoma bodies have been described in children histopathologically.<sup>21</sup> Dystrophic calcification associated with the arachnoid cells and collagen fibers is thought to be causative.<sup>22</sup>

We discovered choroid plexus calcifications in 12% of patients in our cohort. In accordance with findings described by Doyle and Anderson,<sup>13</sup> we found a significant positive association of choroid plexus and pineal calcifications. Choroid calcifications were visible in patients across all age ranges, from younger than 1 month to 10 years. A variety of clinical scenarios brought these patients to imaging, mainly trauma and headache. In all cases, the choroid plexus glomus was calcified in isolation, either unilaterally or bilaterally. Typically, calcifications were punctate and few. Therefore, choroid plexus calcifications occurring outside the glomus or in excess should be viewed with suspicion for underlying pathology in patients younger than 9 years of age. Minimal choroid plexus calcium deposition is probably physiologic at any age, including early childhood.

### Dura

Thick connective tissue composing the dura envelops the central nervous system deep to the skeleton. Dura partitions the intracranial compartment into various subsections, forms the walls of the major dural venous sinuses, and serves as a conduit for neurovascular connections.

Although extremely rare, the CT prevalence of childhood dural calcifications remains a subject without strong support in the literature. In a series of 970 trauma patients, Ratcliffe et al<sup>23</sup> found dural calcifications in >20% of men older than 30 years and women older than 50 years on skull radiography; attenuated calcifications were present in less than 2% of those younger than 40 years. Kendall and Cavanagh<sup>20</sup> found dural calcifications in 0.8% of patients 0–15 years of age. Dural calcifications were rare in our study, occurring in 1%. Posttraumatic dural calcifications rarely occur but are not unexpected after a calvarial breach from penetrating trauma and surgical intervention. Indeed, most of our patients with dural calcifications had previous craniotomies (4/6). The other 2 presented with headache (9 years of age) and head trauma (4 years of age). The tentorium was the most common area to calcify. Extensive dural calcifications in young patients

should raise suspicion for pathologic conditions, including basal cell nevus syndrome, meningiomas, sequelae of prior subdural or epidural hemorrhage, and calcium/phosphate imbalance.<sup>24</sup>

This study has several limitations. Calcium detection is inherently limited by CT section thickness; therefore, intracranial calcifications may have been underestimated. However, we believe this underestimation to be of little clinical importance because thinner section soft-tissue algorithm images are not currently part of most practices. Despite their distinctive locations, pineal and habenular calcifications can sometimes be difficult to separate visually; this problem could have resulted in misclassification in some instances (Fig 2). Pineal cysts are common in the age group in our study and can distort regional anatomy.<sup>7</sup> We found pineal cysts in 3% of our patient cohort, ranging from 4 to 15 mm; however, only 4 of these patients had epithalamic calcifications.

### CONCLUSIONS

Physiologic intracranial calcifications may be found in the first decade, principally in children older than 5 years. Most epithalamic calcifications are habenular in location. Pineal and habenular calcifications were never present in children younger than 3 and 2 years, respectively. Dural calcifications are rare; they are not present in those younger than 2 years of age. Choroid plexus calcifications may be present in the very young (younger than 1 year).

### REFERENCES

1. Maślińska D, Laure-Kamionowska M, Deręgowski K, et al. **Association of mast cells with calcification in the human pineal gland.** *Folia Neuropathol* 2010;48:276–82
2. Zimmerman RA, Bilaniuk LT. **Age-related incidence of pineal calcification detected by computed tomography.** *Radiology* 1982;142:659–62
3. Modic MT, Weinstein MA, Rothner AD, et al. **Calcification of the choroid plexus visualized by computed tomography.** *Radiology* 1980;135:369–72
4. Nieuwenhuys R, Voogd J, van Huijzen C. *The Human Central Nervous System*. 4th ed. Berlin: Springer-Verlag; 2008:247–50
5. Schmidt F, Penka B, Trauner M, et al. **Lack of pineal growth during childhood.** *J Clin Endocrinol Metab* 1995;80:1221–25
6. Sumida M, Barkovich J, Newton TH. **Development of the pineal gland: measurement with MR.** *AJNR Am J Neuroradiol* 1996;17:233–36
7. Whitehead MT, Oh C, Choudhri AF. **Incidental pineal cysts in children who undergo 3-T MRI.** *Pediatr Radiol* 2013;43:1577–83
8. Vigh B, Szel A, Debreceni K, et al. **Comparative histology of the pineal gland.** *Histol Histopathol* 1998;13:851–70
9. Lukaszuk A, Rieter RJ. **Histopathological evidence for the secretion of polypeptides by the pineal gland.** *Am J Anat* 1975;143:451–64
10. Koshy S, Vettivel SK. **Varying appearance of calcification in human pineal gland: a light microscopic study.** *J Anat Soc India* 2001;50:17–18
11. Kim J, Kim HW, Chang S, et al. **Growth patterns for acervuli in human pineal gland.** *Sci Rep* 2012;2:984
12. Helmke K, Winkler P. **Incidence of pineal calcification in the first 18 years of life [in German].** *Rofo* 1986;144:221–26
13. Doyle AJ, Anderson GD. **Physiologic calcification of the pineal gland in children on computed tomography: prevalence, observer reliability and association with choroid plexus calcification.** *Acad Radiol* 2006;13:822–26
14. Bianco I, Wilson SW. **The habenular nuclei: a conserved asymmetric relay station in the vertebrate brain.** *Philos Trans R Soc Lond B Biol Sci* 2009;364:1005–20

15. Kunz D, Schmitz S, Mahlberg R, et al. **A new concept for melatonin deficit: on pineal calcification and melatonin excretion.** *Neuropsychopharmacology* 1999;21:765–72
16. Sandyk R. **Pineal and habenular calcification in schizophrenia.** *Int J Neurosci* 1992;67:19–30
17. Caputo A, Chiringheli L, Dieci M, et al. **Epithalamus calcifications in schizophrenia.** *Eur Arch Psychiatry Clin Neurosci* 1998;248:272–76
18. Shepard PD, Holcomb HH, Gold JM. **Schizophrenia in translations: the presence of absence: habenular regulation of dopamine neurons and the encoding of negative outcomes.** *Schizophr Bull* 2006;32:417–21
19. Admassie D, Mekonnen A. **Incidence of normal pineal and chroids plexus calcification on brain CT (computerized tomography) at Tikur Anbessa Teaching Hospital Addis Ababa, Ethiopia.** *Ethiop Med J* 2009;47:55–60
20. Kendall B, Cavanagh N. **Intracranial calcification in paediatric computed tomography.** *Neuroradiology* 1986;28:324–30
21. Korzhevskii DE. **The formation of psammoma bodies in the choroid plexus of the human brain.** *Morfologiya* 1997;111:46–49
22. Alcolado JC, Moore IE, Weller RO. **Calcification in the human choroid plexus, meningiomas and pineal gland.** *Neuropathol Appl Neurobiol* 1986;12:235–50
23. Ratcliffe JF, Shanley S, Ferguson J, et al. **The diagnostic implication of falcine calcification on plain skull radiographs of patients with basal cell naevus syndrome and the incidence of falcine calcification in their relatives and two control groups.** *Br J Radiol* 1995; 68:361–68
24. Makariou E, Patsalides AD. **Intracranial calcifications.** *Appl Radiol* 2009;38:48–60

# Comparing 3T T1-Weighted Sequences in Identifying Hyperintense Punctate Lesions in Preterm Neonates

D. Tortora, V. Panara, P.A. Mattei, A. Tartaro, R. Salomone, S. Domizio, A.R. Cotroneo, and M. Caulo

## ABSTRACT

**BACKGROUND AND PURPOSE:** The loss of contrast on T1-weighted MR images at 3T may affect the detection of hyperintense punctate lesions indicative of periventricular leukomalacia in preterm neonates. The aim of the present study was to determine which 3T T1-weighted sequence identified the highest number of hyperintense punctate lesions and to explore the relationship between the number of hyperintense punctate lesions and clinical outcome.

**MATERIALS AND METHODS:** The presence of hyperintense punctate lesions was retrospectively evaluated in 200 consecutive preterm neonates on 4 axial T1-weighted sequences: 3-mm inversion recovery and spin-echo and 1- and 3-mm reformatted 3D-fast-field echo. Statistically significant differences in the number of hyperintense punctate lesions were evaluated by using a linear mixed-model analysis. Logistic regression analysis was used to assess the relation between the number of hyperintense punctate lesions and neuromotor outcome at 3 months.

**RESULTS:** Thirty-one neonates had at least 1 hyperintense punctate lesion indicative of periventricular leukomalacia in at least 1 of the 4 sequences. The 1-mm axial reformatted 3D-fast-field echo sequence identified the greatest number of hyperintense punctate lesions ( $P < .001$ ). No statistically significant differences were found among the 3-mm T1-weighted sequences. The greater number of hyperintense punctate lesions detected by the 1-mm reformatted T1 3D-fast-field echo sequence in the central region of the brain was associated with a worse clinical outcome.

**CONCLUSIONS:** At 3T, the 1-mm axial reformatted T1 3D-fast-field echo sequence identified the greatest number of hyperintense punctate lesions in the central region of preterm neonate brains, and this number was associated with neuromotor outcome.

**ABBREVIATIONS:** FFE = fast-field echo; IR = inversion recovery; HPL = hyperintense punctate lesion; ICC = intraclass correlation coefficient; PN = preterm neonate; PVL = periventricular leukomalacia; SE = spin-echo

Periventricular white matter injury is a major form of brain damage and the leading cause of chronic neurologic disability in survivors of preterm births.<sup>1,2</sup> Periventricular white matter injury includes a spectrum of cerebral damage that ranges from focal necrotic lesions (periventricular leukomalacia [PVL]) to diffuse myelination disturbances (diffuse periventricular white matter injury).<sup>3-5</sup> PVL is pathologically characterized by foci of

coagulation necrosis in the periventricular white matter, which results in degeneration of cellular elements and, in particular, the premyelinating oligodendrocytes. The physiopathologic mechanism underlying PVL remains an important unresolved question.<sup>6</sup>

Classic MR imaging signs of PVL are hyperintense punctate lesions (HPLs) on T1-weighted sequences, which infrequently may also appear hypointense on T2-weighted images.<sup>7</sup> More severe presentations of PVL are either cavitation (cystic PVL) or glial scars and may be accompanied by a conspicuous reduction in white matter volume and ventricular enlargement.<sup>5</sup> The causes determining the shortening of T1 and T2 signals in punctate PVL have not been completely established. Some authors hypothesized that signal shortening was determined by the presence of focal hemorrhages. Other studies hypothesized that the characteristic hyperintense signal on T1-weighted sequences was due to the contemporary presence of hemosiderin deposition, lipids from myelin breakdown, and dystrophic calcifications.<sup>7</sup>

Received March 10, 2014; accepted after revision August 14.

From the Radiology Unit (D.T., V.P., A.R.C., M.C.), Ophthalmology Clinic (P.A.M.), and Neonatology and Neonatal Intensive Care Unit (R.S., S.D.), University Hospital of Chieti, Chieti, Italy; and ITAB-Institute of Advanced Biomedical Technologies (D.T., V.P., A.T., M.C.) and Department of Neuroscience and Imaging (A.T., A.R.C., M.C.), University "G. d'Annunzio" of Chieti, Chieti, Italy.

Preliminary results previously presented at: Annual Meeting of the European Congress of Radiology, March 7-11, 2013; Vienna, Austria.

Please address correspondence to Massimo Caulo, MD, PhD, ITAB-Institute of Advanced Biomedical Technologies, University "G. d'Annunzio," Via Dei Vestini 33, 66100 Chieti, Italy; e-mail: caulo@unich.it

<http://dx.doi.org/10.3174/ajnr.A4144>

**Table 1: MRI sequence parameters**

Sequence	Section Thickness (mm)	Intersection (mm)	TR (ms)	TE (ms)	T1 (ms)	FA	SAR (W/Kg)	dB
Axial T1 SE	3	0.5	663	11	—	—	<0.2	−6.5
Axial T1 IR	3	0.5	4938	15	400	—	<0.1	7.2
T1 3D-FFE	1 and 3	0	9.2	4.3	—	10°	0.0	5.4
Axial T2-TSE	3	0.5	3000	80	—	—	<0.2	6.5
Axial DWI	4	1	2380	65	—	—	<0.1	9.5

**Note:**—SAR indicates specific absorption rate; FA, flip angle.

Preterm children with PVL present a high incidence of neurodevelopmental disabilities such as cerebral palsy; mental retardation; and psychologic, developmental, behavioral, and emotional disorders.<sup>8</sup> Currently, an accurate method of identifying all preterm neonates (PNs) at risk of poor developmental outcome is not available, to our knowledge. Clinical risk factors, cranial sonography, and electroencephalography are used to study PNs around birth but are not optimal predictors of long-term outcome.<sup>9,10</sup> MR imaging can provide prognostic information concerning neuropsychological development. For example, PNs with a greater number of HPLs at MR imaging subsequently presented a worse motor and neurocognitive outcome. More specifically, the presence of HPLs in white matter regions traversed by the motor pathway was shown to be a useful predictor of motor outcome.<sup>11,12</sup> However, the use of MR imaging to screen PNs has been relatively limited because of the availability of the MR imaging systems, the complex management of neonates, and, above all, the low prognostic accuracy when no lesions are identified.<sup>13,14</sup>

To date, most MR imaging studies on PVL were performed by using MR imaging systems operating at 1.5T or lower field strengths. Liauw et al<sup>15</sup> concluded that the spin-echo (SE) T1-weighted sequence scored best for detecting the presence of HPLs.

Recently, the benefits from the improved signal-to-noise ratio and higher spatial resolution of MR imaging systems operating at 3T indicated the potential of this high magnetic field system for studying the neonatal brain, though the elongation of the T1 relaxation time at higher magnetic field strengths<sup>16</sup> may bias the use of 3T scanners in preterm neonates due to the potential reduction of the sensitivity of T1 images for identifying HPLs.

The aim of the present study was to determine which 3T T1-weighted sequence identified the highest number of HPLs in PNs studied at term-corrected age and to explore the relationship between the number/location of HPLs and the clinical outcome.

## MATERIALS AND METHODS

### Patients

The institutional review board approved our retrospective study and waived informed consent. The brain MR imaging acquisitions of 200 consecutive PNs acquired from January 2010 to December 2012 within 5 days of term-corrected age as part of an ongoing screening of premature neonates (study approved by the Ethics Committee of “G. D’Annunzio” University of Chieti and Azienda Sanitaria Locale n.2 of Lanciano-Vasto-Chieti) were included in this study. Parents or legal guardians of the neonates always gave written informed consent to the MR imaging study.

### Neuromotor Outcome

Neurologic examinations of the PNs were routinely performed at 3 months of corrected age by a pediatric neurologist who assigned the

infant to 1 of the 3 following groups, according to the classification of development by the World Health Organization: 1) “normal” (normal neurologic examination findings); 2) “mildly abnormal” (mild hypertonia, hypotonia, and/or asymmetry); and 3) “definitely abnormal” (cerebral palsy).<sup>17</sup> Results were obtained from patient records.

### MR Imaging

MR imaging was performed by using a 3T whole-body system (Achieva 3.0T X-Series; Philips Healthcare, Best, the Netherlands) with a dedicated 8-channel head coil. Neonates were fed and sedated with 10-mg oral chloral hydrate per kilogram of body weight. During the scan, the neonates were laid in a supine position and swaddled in blankets. Molded foam was placed around the body of the neonate to minimize head movement. Ear protection was always used and consisted of commercially available neonatal earmuffs (MiniMuffs; Natus Medical, San Carlos, California) and adapted ear-canal plugs. Heart rate and oxygen saturation were monitored during the MR imaging study by an experienced intensive care neonatologist. All neonates underwent the same MR imaging protocol. Details of the MR imaging sequences are reported in Table 1.

### MR Image Analysis

**Phase 1.** Two neuroradiologists, with 15 and 5 years of experience in neonatal neuroimaging, reviewed, in consensus, the MR imaging studies of the 200 neonates. They performed a preliminary image-quality assessment of the acquired sequences by using a 3-point scale (0, nondiagnostic images; 1, diagnostic image with limitations; and 2, fully diagnostic). Assessed parameters included general visual image quality, image noise, and the presence of artifacts. Only MR imaging sequences with scores of at least 2 were included in subsequent analyses.

**Phase 2.** Four weeks later, the same 2 neuroradiologists independently reviewed the MR imaging studies selected in phase 1. They focused on the presence of HPLs on the 4 T1-weighted sequences (3-mm axial SE, 3-mm axial inversion recovery [IR], and 3- and 1-mm axial reformatted 3D-fast-field echo [FFE]). An HPL was defined as a hyperintense punctate lesion on T1 with a diameter of <5 mm that did not necessarily present a corresponding decreased signal intensity on T2-weighted images.

A standardized system of visual assessment was used. The 2 readers, blinded to neonate identity, clinical history, and gestational age at birth, used a workstation equipped with a professional DICOM viewer (OsiriX Imaging Software; <http://www.osirix-viewer.com>). They evaluated the T1-weighted sequences for the following characteristics: 1) number of HPLs, 2) location: anterior to the frontal horn of the lateral ventricles (anterior re-

gion), posterior to the trigon (posterior region), or in the centrum semiovale and/or corona radiata (central region traversed by the motor pathway).<sup>5</sup> The sequences of all neonates were randomly presented.

**Phase 3.** Four weeks later the same 2 neuroradiologists jointly reviewed all the MR imaging studies in which at least 1 HPL was detected during phase 2. They were asked to reach a consensus on a global HPL evaluation (number and location). This consensus reading was considered the reference standard for statistical analysis.

### Statistical Analysis

Statistical analysis was performed by using SPSS Statistics for Mac, Version 21.0 (IBM, Armonk, New York). The level of significance was set at  $P < .05$ .

Linear mixed-model analysis was performed to evaluate the presence of significant differences between the overall number of HPLs identified in each T1-weighted sequence and the number of HPLs identified in each location (anterior, posterior, and central/motor).

The presence of a relationship between the neuromotor outcome at 3 months and the number of HPLs was tested by using logistic regression with a backward stepwise conditional method.

Intraclass correlation coefficients (ICCs) were used to study the agreement between the 2 readers in visualizing the number of HPLs with each T1 sequence. An ICC of  $<0.40$  indicated a poor agreement;  $0.40-0.75$ , fair-to-good (moderate); and  $0.76-1.00$ , excellent agreement.<sup>18</sup> To analyze the performance of each MR imaging sequence in showing the presence of HPLs, we calculated the ICC between the individual assessments and the reference standard.

## RESULTS

### Patients

The MR imaging studies of 184/200 (92%) PNs were scored as at least 2 at the preliminary image-quality analysis and therefore were included in the analysis. Thirty-one of 184 (16.8%) PNs (12 females; average gestational age,  $32.5 \pm 2.5$  weeks; range, 28–36 weeks) presented with at least 1 HPL on at least 1 T1-weighted sequence and were included in subsequent statistical analysis. In 4 of these neonates, T1 SE images were not obtained due to patient awakening. In 1 neonate, both SE and T1 IR images were not obtained.

### Neuromotor Outcome

At 3 months, 20/31 (64.5%) preterm infants presented with a mildly abnormal motor development (spasticity), 9/31 (29.0%) presented with a normal motor development, none of the patients presented with cerebral palsy, and 2/31 (6.5%) PNs were lost to follow-up.

### Number of HPLs

In consensus reading, the 1-mm reformatted 3D-FFE sequence detected the greatest overall number of HPLs ( $n = 386$  lesions); 3-mm reformatted 3D-FFE, T1 IR, and T1 SE sequences identified 218, 152, and 151 HPLs, respectively. In 7 PNs, the presence of

**Table 2: HPLs identified in consensus reading**

Patient	Sex	Outcome	Overall			
			3-mm T1 FFE	1-mm T1 FFE	3-mm T1 IR	3-mm T1 SE
1	F	1	4	7	0	NA
2	F	0	3	7	0	NA
3	F	1	12	20	6	NA
4	F	0	3	8	6	NA
5	M	1	8	12	5	4
6	F	1	16	35	8	16
7	M	0	9	12	6	7
8	M	1	17	19	10	11
9	M	1	12	25	9	9
10	F	1	9	11	11	10
11	M	0	3	5	2	4
12	F	NA	5	14	7	4
13	M	1	6	9	11	11
14	M	1	21	30	9	9
15	M	1	15	29	17	15
16	M	1	6	13	8	14
17	M	NA	4	9	NA	NA
18	F	0	8	11	0	0
19	M	0	6	9	1	2
20	F	1	6	12	5	6
21	M	0	4	9	0	0
22	M	1	4	8	3	4
23	M	1	2	4	2	2
24	F	1	4	10	3	1
25	M	1	1	7	5	2
26	M	1	15	15	9	13
27	M	0	5	10	3	3
28	M	0	2	5	0	0
29	M	1	2	8	0	0
30	F	1	1	5	0	0
31	F	1	5	8	6	4
Total			218	386	152	151

**Note:**—NA indicates not available.

HPLs was identified exclusively on the reformatted 3D-FFE sequences and not on SE and IR. Results are summarized in Table 2.

The consensus reading of the location-related number of HPLs indicated that in the central/motor location, 1- and 3-mm reformatted 3D-FFE sequences detected 227 and 115 HPLs. The T1 IR and T1 SE sequences identified 67 and 71 HPLs, respectively. In the anterior location, 1- and 3-mm reformatted 3D-FFE sequences detected 26 and 18 HPLs. The IR and SE sequences identified 18 and 12 HPLs, respectively. In the posterior location, 1- and 3-mm reformatted 3D-FFE sequences detected 133 and 85 HPLs. The IR and SE sequences identified 67 and 68 HPLs, respectively.

The linear mixed-model analysis showed a statistical difference among the overall number of lesions detected by the 4 T1-weighted sequences ( $P < .01$ ). Comparison of the means indicated that the 1-mm reformatted T1 3D-FFE sequence identified a significantly greater overall number of HPLs than 3-mm reformatted T1 3D-FFE, SE, and IR sequences. No statistical differences were observed among the overall number of lesions detected by 3-mm sequences ( $P > .05$ ) (Fig 1).

Linear mixed-model analysis showed a statistical difference among the number of HPLs detected by the 4 T1-weighted sequences in the central/motor location ( $P < .01$ ). Comparison of the means indicated that the 1-mm reformatted T1 3D-FFE sequence identified a significantly greater number of HPLs than the SE and IR sequences ( $P < .01$ ), whereas no differences were ob-

## LOCATIONS

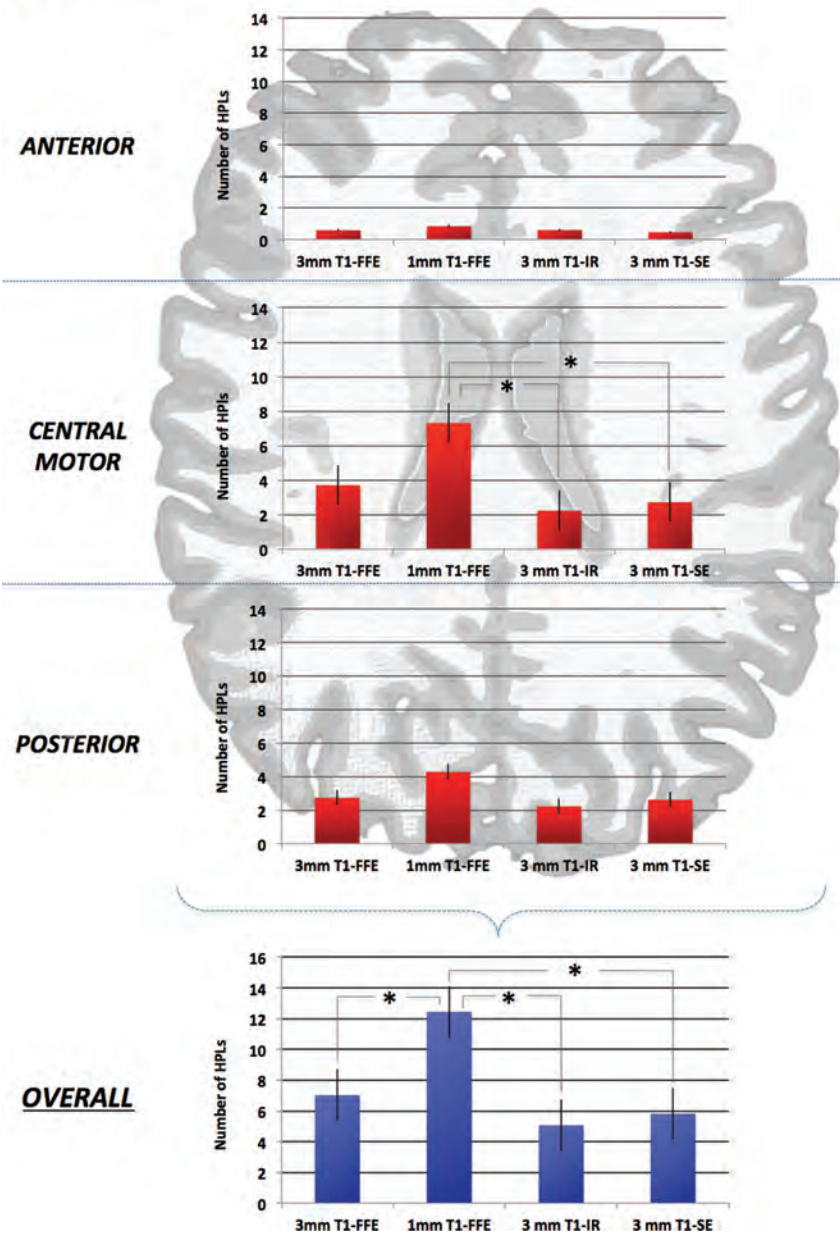


**FIG 1.** Schematic representation of a typical neonatal brain. Only the central (motor) location on the 1-mm reformatted T1 3D-FFE sequence scored a significantly greater number of HPLs compared with IR and SE sequences. The 1-mm axial reformatted T1 3D-FFE sequence identified a significant overall greater number of HPLs than other 3-mm sequences ( $P < .01$ ).

served with the 3-mm reformatted 3D-FFE sequence ( $P > .05$ ). Statistically significant differences were not observed among the number of HPLs identified by the 4 T1-weighted sequences in anterior and posterior locations (Fig 1).

### Relationship between Neuromotor Outcome and the Number of HPLs

To test the clinical implication of the only significant difference in the detection score of the HPLs by the 4 different T1-weighted sequences, we tested the relationship between the number of HPLs in the central region and the neuromotor outcome at 3 months. The number of HPLs detected by each T1-weighted

sequence was included in the primary logistic regression analysis, and 3-mm reformatted T1 3D-FFE, IR, and SE sequences were removed from the backward stepwise model. The number of HPLs detected by the 1-mm T1 3D-FFE sequence was an independent predictive factor for neuromotor outcome (odds ratio = 1.690; 95% CI, 1.017–2.807;  $P = .04$ ).

### Interreader Agreement Analysis

A moderate-to-excellent interreader agreement was observed for all the sequences. The greatest agreement was reached by using the 1-mm axial reformatted T1 3D-FFE sequence (ICC = 0.986). Results of the interreader agreement analysis are summarized in Table 3.

The ICCs of each T1-weighted sequence in relation to the reference standard indicated that the 1-mm axial reformatted T1 3D-FFE sequence yielded the best results (excellent agreement) for both readers. The agreement between the 3-mm T1-weighted sequences and the criterion standard yielded a higher ICC for the 3D-FFE (excellent agreement) than for the SE and IR sequences (moderate agreement) for both readers (Table 3).

## DISCUSSION

Despite the recent availability of an ever-increasing number of 3T scanners, specific indications for the identification of HPLs in PNs are still lacking. Therefore, in this 3T study, we evaluated the contribution of different T1-weighted sequences for the identification and localization of HPLs in a group of PNs. The results indicated that axial reformatted T1 3D-FFE scored better than T1 IR and T1 SE sequences for detecting HPLs, though only the 1-mm sequence differed significantly from the others. These findings can be explained by the combination of thinner

section thickness and the intrinsically higher sensitivity of T1-weighted FFE sequences for hyperintense lesions compared with SE. Wintersperger et al<sup>19</sup> demonstrated that T1 3D-FFE sequences showed a higher signal-to-noise ratio compared with T1 SE sequences at both 1.5T and 3T. Edelman et al<sup>20</sup> recently reinforced this finding by demonstrating that at 3T the T1 3D-FFE presented a significantly higher quality compared with the 2D T1-SE images, providing a higher contrast-to-noise ratio for discriminating gray and white matter structures, reducing artifacts, and improving imaging efficiency with reformatted images in orthogonal orientations. In the present study, the same reasons can be given to explain the difference in scoring HPLs observed between the T1 3D-FFE and T1 IR se-

quences—that is, the T1 IR sequence had the same spin magnetization refocusing of the T1 SE. This aspect was also confirmed by the lack of a significant difference in HPL detection between the T1 SE and T1 IR sequences.

In addition to the intrinsically higher SNR of FFE compared with SE sequences, the section thickness and the possibility of obtaining an isotropic voxel are important in increasing the sensitivity of FFE sequences.

The T1 3D-FFE sequence with a section thickness of 1 mm scored better in identifying HPLs than the other 3-mm T1-weighted sequences ( $P < .01$ ). In particular, the difference between 1- and 3-mm axial reformatted T1 3D-FFE sequences ( $P < .01$ ) demonstrated that decreasing the section thickness can significantly increase the detection rate of punctate lesions. This outcome is because the use of thinner sections allowed the separation of contiguous lesions that were seen as confluent with thicker sections (ie, cluster-organized HPLs could be identified as multiple lesions at 1 mm, while they appeared as a single lesion at 3 mm) (Fig 2).

The importance of using a 3D-FFE sequences was reinforced by the overall greater number of appropriately identified PVLs by using both the 1- and 3-mm reformatted images compared with SE and IR sequences.

**Table 3: Interreader agreement and pulse sequence performances<sup>a</sup>**

Pulse Sequences	Agreement of Reader 1 and Reference Standard	Agreement of Reader 2 and Reference Standard	Interreader Agreement
3-mm T1 FFE	0.893	0.822	0.844
1-mm T1 FFE	0.988	0.992	0.986
3-mm T1 IR	0.776	0.631	0.653
3-mm T1 SE	0.793	0.797	0.820

<sup>a</sup> Data are intraclass correlation coefficients.

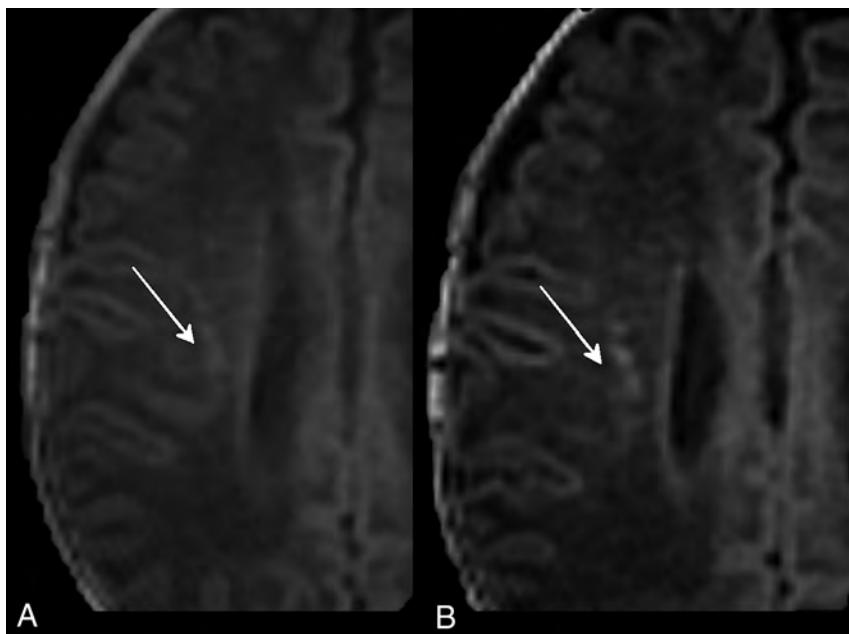


**FIG 2.** Three-millimeter (A) and 1-mm (B) axial reformatted T1 3D-FFE sequences of PNs affected by PVL. The thinner sections (B) separated lesions that were seen as confluent with the thicker sections (A).

As a second step, we classified HPLs according to their location (posterior, central, and anterior).<sup>12</sup> We observed that the 1-mm reformatted 3D-FFE sequence scored a statistically significantly greater number of HPLs compared with the IR and SE sequences only in the central (motor) location. This finding may be attributed to the intrinsically higher contrast-to-noise ratio of T1 3D-FFE sequences that discriminated HPLs from the relatively higher T1 signal intensity of the myelinated cortical spinal tract of neonates. On the other hand, the absence of statistically significant differences in the anterior and posterior locations among the different T1-weighted sequences may be attributed to the lower T1-signal intensity of the unmyelinated white matter, which increased the contrast with HPLs.

On the basis of the findings reported by Nanba et al,<sup>12</sup> subsequent analysis focused on the central (motor) location. We evaluated the relationship between the number of HPLs detected by each sequence and the neuromotor outcome at 3 months. The greater number of HPLs detected by the 1-mm reformatted T1 3D-FFE sequence positively correlated to a worse clinical outcome, thus suggesting that this sequence should be used in routine clinical use for PNs.

The ICCs of interreader agreement in the detection of HPLs were moderate to excellent for all the T1-weighted sequences except for IR, which had the lowest score performance (ICC = 0.63) and interobserver agreement (ICC = 0.66). These results seem to contradict a previous 3T study by Stehling et al,<sup>21</sup> which evaluated differences in contrast-to-noise ratio, artifacts, gray-white differentiation, image noise, and overall diagnostic quality among FFE, IR, and SE sequences. They demonstrated a higher contrast-to-noise ratio and a better gray-white matter differentiation with a higher overall diagnostic quality of both FFE and IR compared with SE sequences. We hypothesize that this discrepancy was related to the lower negative influence of the inhomogeneous myelination of the white matter of PNs on the FFE sequences.<sup>20,21</sup>

The highest interreader agreement was obtained with the 1-mm reformatted T1 3D-FFE sequence. This result could be related to the higher HPL conspicuity on this sequence, due to the higher intrinsic SNR and thinner section thickness. In addition, the higher interreader agreement obtained with T1 3D-FFE compared with T1 IR and T1 SE sequences demonstrated that the detection of HPLs by using the T1 3D-FFE sequence was less influenced by reader experience.

Another important advantage of 3D-FFE sequences is their intrinsic lower specific absorption rate compared with SE. The specific absorption rate level increases with field strength and is higher in T1 SE sequences due to the refocusing pulses and in T1 IR sequences because of their intense radiofrequency pulse.<sup>21</sup> The possibility of using lower specific absorption rate levels is particularly important in neonates due to their immature thermoregulatory abilities.

The main limitation of this study was the lack of a direct comparison between 1.5 and 3T sequences. For ethical reasons, we decided not to repeat the MR imaging studies at different magnetic field intensities.

An additional limit of this study was its retrospective design. The only clinical outcome that was consistently available from patient records for the study group was the neuromotor one at 3 months. In addition, our study population lacked cases with the most unfavorable neuromotor outcome (cerebral palsy). These points should be addressed in future studies. In addition, 4 neonates had incomplete MR imaging studies because they did not undergo axial T1-SE and one did not undergo T1 IR.

All nonisometric sequences were acquired on the axial plane; thus, a comparison with sagittal and coronal reformatted 3D-FFE sequences was not possible.<sup>12</sup> The patient population imposed a rigid limit to the duration of the acquisition, thus excluding the possibility of also acquiring all sequences in the coronal plane. Nonetheless, an evaluation of the effect of the acquisition plane was beyond the scope of this study.

## CONCLUSIONS

This study demonstrated that with 3T scanners, the 1-mm axial reformatted T1 3D-FFE sequence identified the greatest number of HPLs in the central region of PN brains, and this number was predictive of neuromotor outcome at 3 months.

## REFERENCES

1. Volpe JJ. *Neurology of the Newborn*. Philadelphia: W.B. Saunders; 2000
2. Ferriero DM. **Neontal brain injury**. *N Engl J Med* 2004;351:1985–95
3. Volpe JJ. **Neurobiology of periventricular leukomalacia in the premature infant**. *Pediatr Res* 2001;50:553–62
4. Rezaie P, Dean A. **Periventricular leukomalacia, inflammation and white matter lesions within the developing nervous system**. *Neuropathology* 2002;22:106–32
5. Back SA, Riddle A, McClure MM. **Maturation-dependent vulnerability of perinatal white matter in premature birth**. *Stroke* 2007;38(2 suppl):724–30
6. Distefano G, Praticò AD. **Actualities on molecular pathogenesis and repairing processes of cerebral damage in perinatal hypoxic-ischemic encephalopathy**. *Ital J Pediatr* 2010;16:36:63
7. Cornette LG, Tanner SF, Ramenghi LA, et al. **Magnetic resonance imaging of the infant brain: anatomical characteristics and clinical significance of punctate lesions**. *Arch Dis Child Fetal Neonatal Ed* 2002;86:F171–77
8. Olsén P, Paakkii E, Vainionpää L, et al. **Magnetic resonance imaging of periventricular leukomalacia and its clinical correlation in children**. *Ann Neurol* 1997;41:754–61
9. Ment LR, Hirtz D, Huppi PS. **Imaging biomarkers of outcome in the developing preterm brain**. *Lancet Neurol* 2009;8:1042–55
10. Leijser LM, de Bruïne FT, van der Grond J, et al. **Is sequential cranial ultrasound reliable for detection of white matter injury in very preterm infants?** *Neuroradiology* 2010;52:397–406
11. Hintz SR, O’Shea M. **Neuroimaging and neurodevelopmental outcomes in preterm infants**. *Semin Perinatol* 2008;32:11–19
12. Namba Y, Matsui K, Aida N, et al. **Magnetic resonance imaging regional T1 abnormalities at term accurately predict motor outcome in preterm infants**. *Pediatrics* 2007;120:e10–19
13. Bax M, Tydeman C, Flodmark O. **Clinical and MRI correlates of cerebral palsy: the European Cerebral Palsy Study**. *JAMA* 2006;296:1602–08
14. Back SA, Miller SP. **Brain injury in premature neonates: a primary cerebral dysmaturation disorder?** *Ann Neurol* 2014;75:469–86
15. Liauw L, van der Grond J, van den Berg-Huysmans AA, et al. **Hypoxic-ischemic encephalopathy: diagnostic value of conventional MR imaging pulse sequences in term-born neonates**. *Radiology* 2008;247:204–12
16. Williams LA, Gelman N, Picot PA, et al. **Neonatal brain: regional variability of in vivo MR imaging relaxation rates at 3.0T—initial experience**. *Radiology* 2005;235:595–603
17. Rosenbaum P, Stewart D. **The World Health Organization international classification of functioning, disability and health: a model to guide clinical thinking, practice and research in the field of cerebral palsy**. *Semin Pediatr Neurol* 2004;11:5–10
18. Fleiss JL. *Statistical Methods for Rates and Proportion*. 2nd ed. New York: John Wiley; 1981
19. Wintersperger BJ, Runge VM, Biswas J, et al. **Brain tumor enhancement in MR imaging at 3 Tesla: comparison of SNR and CNR gain using TSE and GRE techniques**. *Invest Radiol* 2007;42:558–63
20. Edelman RR, Dunkle E, Koktzoglou I, et al. **Rapid whole-brain magnetic resonance imaging with isotropic resolution at 3 Tesla**. *Invest Radiol* 2009;44:54–59
21. Stehling C, Niederstadt T, Krämer S. **Comparison of a T1-weighted inversion-recovery-, gradient-echo- and spin-echo sequence for imaging of the brain at 3.0 Tesla [in German]**. *Rofa* 2005;177:536–42

# Intramedullary Spinal Cord Metastases: Prognostic Value of MRI and Clinical Features from a 13-Year Institutional Case Series

F.E. Diehn, J.B. Rykken, J.T. Wald, C.P. Wood, L.J. Eckel, C.H. Hunt, K.M. Schwartz, R.K. Lingineni, R.E. Carter, and T.J. Kaufmann

## ABSTRACT

**BACKGROUND AND PURPOSE:** In patients with intramedullary spinal cord metastases, the impact of MR imaging and clinical characteristics on survival has not been elucidated. Our aim was to identify MR imaging and clinical features with prognostic value among patients with intramedullary spinal cord metastases from a large retrospective series.

**MATERIALS AND METHODS:** The relevant MR imaging examination and baseline clinical data for each patient from a consecutive group of patients with intramedullary spinal cord metastases had previously been reviewed by 2 neuroradiologists. Additional relevant clinical data were extracted. The influence of clinical and imaging characteristics on survival was assessed by Kaplan-Meier survival curves and log-rank tests for categorical characteristics.

**RESULTS:** Forty-nine patients had 70 intramedullary spinal cord metastases; 10 (20%) of these patients had multiple metastases. From the date of diagnosis, median survival for all patients was 104 days (95% CI, 48–156 days). One clinical feature was associated with decreased median survival: lung or breast primary malignancy (57 days) compared with all other malignancy types (308 days;  $P < .001$ ). Three MR imaging features were associated with decreased median survival: multiple intramedullary spinal cord metastases (53 versus 121 days,  $P = .022$ ), greater longitudinal extent of cord T2 hyperintensity (if  $\geq 3$  segments, 111 days; if  $\leq 2$ , 184 days;  $P = .018$ ), and ancillary visualization of the primary tumor and/or non-CNS metastases (96 versus 316 days,  $P = .012$ ).

**CONCLUSIONS:** Spinal cord edema spanning multiple segments, the presence of multifocal intramedullary spinal cord metastases, and ancillary evidence for non-CNS metastases and/or the primary tumor are MR imaging features associated with decreased survival and should be specifically sought. Patients with either a lung or breast primary malignancy are expected to have decreased survival compared with other primary tumor types.

**ABBREVIATION:** ISCM = intramedullary spinal cord metastasis

Recent studies have elucidated the imaging features of intramedullary spinal cord metastases (ISCMs). MR imaging findings specific to these secondary compared with primary tumors of the spinal cord have been described.<sup>1</sup> Moreover, multiple MR imaging characteristics have been characterized in detail<sup>2</sup> and correlated with findings on physiologic imaging with PET.<sup>3</sup> However, the prognostic value of MR imaging and clinical findings has not been assessed, to our knowledge. A recent literature review of

301 patients noted that there are no evidence-based treatment guidelines for ISCMs and that the various therapeutic options do not generally considerably affect survival.<sup>4</sup> Thus, identification of pretreatment factors that may affect outcomes is relevant. The purpose of this retrospective study was to identify MR imaging and clinical features with prognostic value among patients with ISCMs from a large retrospective series.

## MATERIALS AND METHODS

Institutional review board approval with waived consent was obtained for this Health Insurance Portability and Accountability Act–compliant retrospective research study.

## Subjects

As detailed in a prior study,<sup>2</sup> the pathologic, surgical, clinical, and radiologic data bases at our single institution were queried to identify a group of consecutive patients with ISCMs ( $n = 58$ , 1999–2011). Exclusion criteria were patients in whom ISCM was

Received June 16, 2014; accepted after revision September 6.

From the Division of Neuroradiology (F.E.D., J.B.R., J.T.W., C.P.W., L.J.E., C.H.H., K.M.S., T.J.K.), Department of Radiology, and Department of Health Sciences Research (R.K.L., R.E.C.), Mayo Clinic, Rochester, Minnesota.

Paper previously presented at: American Society of Neuroradiology Annual Meeting and the Foundation of the ASNR Symposium, May 17–22, 2014; Montreal, Quebec, Canada.

Please address correspondence to Felix E. Diehn, MD, Department of Radiology, Mayo Clinic, 200 First St SW, Rochester, MN 55905; e-mail: diehn.felix@mayo.edu

<http://dx.doi.org/10.3174/ajnr.A4160>

never formally clinically diagnosed, patients in whom alternative diagnoses were suspected clinically, and patients without available pretreatment digital MR images. This group of patients with ISCMs is from the same 58 patients in whom we recently described 2 specific enhancement features of ISCM on postgadolinium MR imaging that may help to differentiate it from primary cord masses.<sup>1</sup> Five (9%) of these 58 patients were again excluded due to a lack of available pretreatment MR imaging examinations. Additional details of the study population were as reported in the prior studies<sup>1,2</sup>; specifically, 4 (8%) of the remaining 53 patients “were excluded because alternative diagnoses were being considered clinically and ISCM was never formally diagnosed.”<sup>1</sup> Thus, only patients with a clinical diagnosis of ISCM were included on the basis of review of available clinical, pathologic, and imaging data. The resultant final ISCM study population was 49 with 70 ISCMs, with solitary ISCMs in 39 and multiple in 10. In 5 (10%) of these 49 patients, the diagnosis of ISCM was confirmed by cord mass biopsy/resection. In 44 (90%) of the 49 patients with ISCM, “pathologic proof of the systemic malignancy had been obtained from the primary site or a metastatic site outside of the spinal cord.”<sup>1,2</sup>

### **MR Imaging Review**

Two radiologists had previously reviewed all MR imaging examinations in consensus at an electronic workstation (one [F.E.D.], a staff neuroradiologist with American Board of Radiology certification and a Certificate of Added Qualification in neuroradiology, and the other [J.B.R.], a neuroradiology fellow with American Board of Radiology certification).<sup>2</sup> The MR imaging examinations were predominantly from our institution, but some were from outside facilities. Given this range of institutions and the >10-year timeframe of this retrospective study, no single, consistent MR imaging platform or protocol was used. At our institution, a typical MR imaging protocol for a patient suspected of having a spinal cord neoplasm during the timeframe of the study consisted of the following sequences, at 1.5T field strength: precontrast sagittal T1WI, T2WI, and optional STIR optimized for spinal cord signal abnormality (TI ~ 110 ms); axial T2WI; optional axial gradient recalled-echo and axial T1WI; and post-contrast sagittal and axial T1WI.

The results of this detailed radiologic review have been published in a separate study.<sup>2</sup> Previously analyzed radiologic features that are relevant for the present study are the following: number of ISCMs per patient, and for each ISCM: 1) maximal size of the enhancing lesion in millimeters (measured anteroposterior, transverse [axial images required], and superoinferior), 2) maximal longitudinal extent of the enhancing lesion in a number of vertebral segments, 3) maximal longitudinal extent of spinal cord T2 hyperintensity in a number of vertebral segments (sagittal T2 images required), 4) position within the cord on axial images (central, eccentric, exophytic), 5) cord expansion (absent versus present), 6) T2 signal intensity (hyper-, hypo-, or isointense to spinal cord), 7) T1 signal intensity (hyper-, hypo-, or isointense to spinal cord), 8) convincing evidence of cystic change (absence or presence of nonenhancing fluid signal on T1- and T2-weighted images), 9) convincing evidence of intratumoral hemorrhage (absence or presence of nonenhancing T1 hyperintensity and/or

marked T1 hypointensity and corresponding T2 hypointensity and/or “blooming” magnetic susceptibility artifacts on gradient recalled-echo sequences, if available), and 10) gadolinium enhancement pattern (absent, or if present, homogeneous versus heterogeneous versus ring).<sup>2</sup> Presence or absence of postgadolinium features highly specific for ISCM (“rim” and “flame” signs) was also based on previously obtained data.<sup>1</sup> As per that prior report, the definitions of these signs are the following: rim sign, “a complete or partial thin peripheral rim of gadolinium enhancement more intense than the central enhancement of a noncystic/necrotic lesion”; flame sign, “an ill-defined flame-shaped region of gadolinium enhancement at the superior and/or inferior margin of an otherwise well-defined lesion”; and “both the rim and flame signs can be present in the same lesion.”<sup>1</sup> The ratio of the length of spinal cord T2 hyperintensity to the length of the ISCM was calculated for each lesion.

For each patient, the reference spinal MR imaging had previously been reviewed for ancillary evidence of the primary tumor and/or extraspinal, non-CNS metastases and any other spinal column and/or CNS metastases not involving the spinal column (including vertebral column, leptomeninges, and visualized intracranial contents).<sup>2</sup> When available, follow-up spinal MR imaging examinations had also been reviewed for the development of additional ISCMs.<sup>2</sup> A previous study had categorized the presence or absence of uptake of these ISCMs on PET, when this was available, within 60 days prior or 14 days after the correlative pretreatment diagnostic MR imaging.<sup>3</sup>

Note that a previously published analysis<sup>2</sup> of the 70 ISCMs in the current study demonstrated that most of the lesions had a convincing appearance of being intramedullary rather than leptomeningeal in origin. Specifically, only 4 of the lesions were exophytic on MR imaging, and in all 4 of these cases, the interpreting radiologist had described an intramedullary mass extending exophytically, rather than a leptomeningeal mass invading the parenchyma. Only 3 lesions (4% of 70 ISCMs) appeared to be potentially leptomeningeal in origin, with 2 occurring in the same patient.<sup>2</sup>

### **Clinical Review**

The electronic medical records of each patient with ISCM were reviewed. The primary tumor type and the dates of the primary tumor diagnosis, ISCM clinical presentation, and ISCM diagnosis had previously been noted.<sup>2</sup> The date of death (if applicable) was identified for each patient. We calculated 2 relevant intervals: survival from ISCM clinical presentation and survival from ISCM diagnosis.

### **Statistical Analysis**

The statistical evaluation consisted of performing analyses on all subjects (having either solitary or multiple ISCMs) and on subjects with only solitary ISCMs. Median survival (days, [95% CI]) from the date of the ISCM diagnosis was calculated for each of the following variables by using the Kaplan-Meier product limit estimator for the following: 1) clinical variables: age, primary malignancy type, lung/breast versus nonlung/nonbreast primary malignancy, melanoma versus nonmelanoma primary malignancy, CNS versus non-CNS primary malignancy, and ISCM diagnosis preceding primary malignancy diagnosis; and 2) MR imaging variables: solitary versus multifocal ISCMs, non-spinal cord CNS

**Table 1: Survival analysis of clinical features for all patients with ISCM (N = 49)**

Variable	Median Survival (days <sup>a</sup> ) (95% CI)	Hazard Ratio (95% CI)	P Value <sup>b</sup>
Age at diagnosis (yr) (N = 49)	108 (48–156)	1.02 (0.99–1.04)	.091
Primary malignancy			.005
Lung (n = 24)	58 (31–120)	–	
Breast (n = 7)	48 (21–456)	–	
Melanoma (n = 5)	87 (15–734)	–	
CNS (n = 4)	763 (19–1261)	–	
Renal (n = 3)	299 (231–643)	–	
Other (n = 6)	503 (24–884)	–	
Lung/breast primary malignancy			<.001
Nonlung/nonbreast (n = 18)	308 (87–689)	–	
Lung/breast (n = 31)	57 (33–117)	–	
Melanoma			.635
Nonmelanoma (n = 44)	115 (40–166)	–	
Melanoma (n = 5)	87 (15–734)	–	
CNS primary malignancy			.018
Non-CNS (n = 45)	104 (42–127)	–	
CNS (n = 4)	763 (19–1261)	–	
ISCM diagnosis precedes primary malignancy diagnosis			.361
No (n = 44)	104 (42–184)	–	
Yes (n = 5)	127 (21–187)	–	

**Note:**— indicates not applicable.

<sup>a</sup> From the date of ISCM diagnosis.

<sup>b</sup> P values are for log-rank tests for categorical variables and Wald tests for continuous variables.

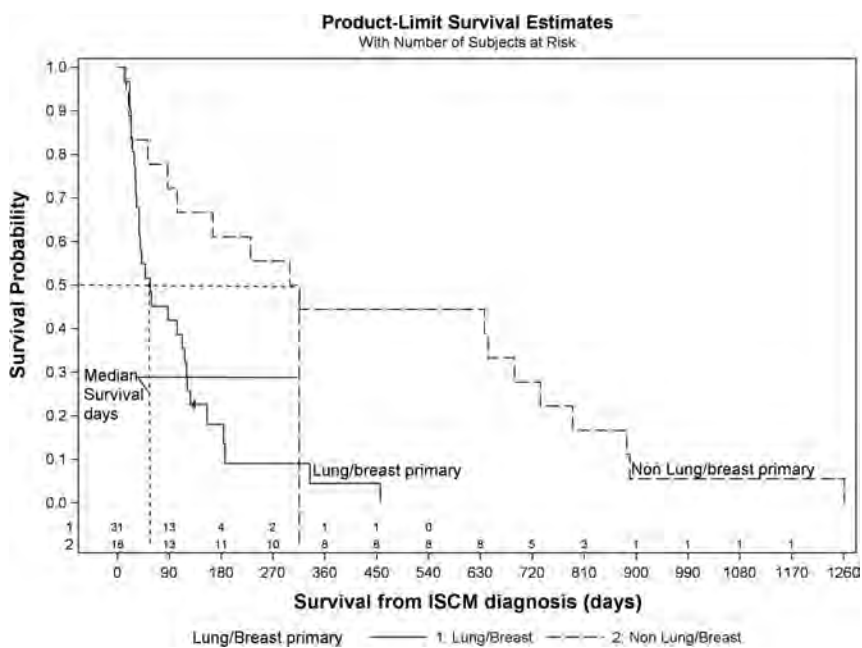


**FIG 1.** Kaplan-Meier plot. Decreased survival for patients with lung or breast primary malignancy compared with all other types of primary malignancy. The median survival for patients with lung or breast primaries was 57 days and for patients with nonlung/nonbreast primaries was 308 days ( $P < .001$ , log-rank test;  $N = 49$  patients).

and/or spinal metastases, leptomeningeal metastases, primary tumor and/or non-CNS metastases, longitudinal extent of spinal cord T2 hyperintensity (treated both as continuous and categorical [ $\geq 2$  and  $\geq 3$  segments] variables), ISCM enhancement size (millimeters, superior/inferior), ISCM enhancement longitudinal extent (number of segments), ratio of the extent of longitudinal cord T2 hyperintensity to longitudinal ISCM enhancement, and presence/absence of rim and flame signs (alone or in combination).

The rationale for analyzing lung/breast primary malignancy

compared with others was that the 10 cases of multiple ISCMs in this patient population occurred only with these 2 malignancies.<sup>2</sup> In addition, this grouping of lung and breast primary malignancies was driven by both the relatively small number of patients with breast primary malignancy ( $n = 7$ ), and the apparent clustering of the shorter survival curves for these 2 primary malignancies and clustering of longer survival curves of the other primary malignancies at initial statistical analysis. The rationale for analyzing melanoma primary malignancy compared with others was that prior studies have suggested improved survival in patients with melanoma.<sup>5,6</sup> The rationale for using the date of ISCM diagnosis rather than the date of ISCM presentation was the following: 1) The former was deemed the more relevant time index from a patient care perspective and has been used in other studies such as the recent comprehensive literature review by Sung et al<sup>4</sup>; 2) there was a median survival difference of only 4 days by using these 2 different time indices; and 3) although the granular data are not included herein, the results were comparable between the 2 dates. Log-rank tests and large sample tests of the hazard ratios (Wald tests) were used, respectively, to compare the potential effect on survival of each of these categorical and continuous variables. The hazard ratios were estimated from a Cox model. For the T2 signal abnormality and ISCM enhancement characteristics in patients with multiple ISCMs, the length of the longest lesion was used, and the rim and flame signs were considered to be positive if present in any 1 of the multiple ISCMs. Patients who were still alive or lost to follow-up were censored at the last known date alive for the analysis.

Statistical analyses were conducted by using SAS, Version 9.3 (SAS Institute, Cary, North Carolina). Statistical significance was defined by  $P < .05$ .

## RESULTS

### Survival

The date of death was known in 96% (47/49) of patients; 4% of patients (2/49) were either still alive ( $n = 1$ ) or lost to follow-up ( $n = 1$ ) by the end of the analysis period. From the dates of ISCM diagnosis and presentation, median survival for all patients was 104 days (3.5 months; 95% CI, 48–156 days) and 108 days (3.6 months; 95% CI, 77–166 days), respectively.

**Table 2: Survival analysis of MRI features for patients with solitary ISCMs (n = 39)**

Variable	Median Survival (days <sup>a</sup> ) (95% CI)	Hazard Ratio (95% CI)	P Value <sup>b</sup>
No. of ISCMs			.022
Solitary (n = 39)	121 (42–187)	–	
Multiple (n = 10)	53 (12–88)	–	
Noncord CNS/spinal metastases			.879
No (n = 19)	166 (87–334)	–	
Yes (n = 20)	79 (26–184)	–	
Leptomeningeal metastases			.274
No (n = 27)	127 (38–231)	–	
Yes (n = 12)	113 (24–790)	–	
Primary tumor/non-CNS metastases			.012
No (n = 15)	316 (38–790)	–	
Yes (n = 24)	96 (32–166)	–	
Cord T2 hyperintensity ≥2 segments <sup>c</sup>			.037
No (n = 10)	184 (24–884)	–	
Yes (n = 28)	111 (38–166)	–	
Cord T2 hyperintensity ≥3 segments <sup>c</sup>			.018
No (n = 12)	184 (24–790)	–	
Yes (n = 26)	111 (38–166)	–	
Cord T2 hyperintensity (No. of segments) <sup>c</sup> (n = 38)	121 (42–187)	1.02 (0.96–1.09)	.541
ISCM enhancement, superior/inferior size (mm) <sup>c</sup> (n = 35)	120 (42–187)	1.01 (0.99–1.02)	.138
ISCM enhancement, extent (No. of vertebral segments) <sup>c</sup> (n = 35)	120 (42–187)	1.08 (0.85–1.38)	.524
Ratio, longitudinal extent of cord T2 hyperintensity to enhancement <sup>c</sup> (n = 34)	119 (40–187)	1.03 (0.94–1.13)	.477
Rim sign <sup>c</sup>			.621
No (n = 18)	79 (26–643)	–	
Yes (n = 17)	127 (40–299)	–	
Flame sign <sup>c</sup>			.068
No (n = 19)	127 (42–734)	–	
Yes (n = 16)	96 (26–299)	–	
Rim/flame signs <sup>c</sup>			.143
Neither (n = 13)	121 (32–884)	–	
Rim sign only (n = 6)	147 (21–790)	–	
Flame sign only (n = 5)	26 (15–643)	–	
Both signs (n = 11)	120 (38–316)	–	

**Note:** — indicates not applicable.

<sup>a</sup> From date of ISCM diagnosis.

<sup>b</sup> P values are for log-rank tests for categoric variables and Wald tests for continuous variables.

<sup>c</sup> Missing patients (n < 39) due to MRI not having sagittal T2- or gadolinium-enhanced sagittal T1-weighted images.

### Prognostic Value of Clinical Features

Table 1 demonstrates the impact of various clinical features on survival from the date of ISCM diagnosis, considering all 49 patients. The median survival of patients with ISCMs with lung or breast primary malignancies (1.9 months) was shorter than that of patients with all other types of primary malignancy (10.3 months) ( $P < .001$ ). This association was maintained when the analysis was performed on only the 39 patients with solitary ISCMs ( $P = .002$ , with respective median survival of 3.5 months for lung/breast primaries [ $n = 21$ ] and 10.3 months for nonlung, nonbreast primaries [ $n = 18$ ]). A Kaplan-Meier plot for all patients with ISCMs demonstrates the shorter survival period for patients with lung/breast primary malignancies (Fig 1). When analyzed by each primary malignancy individually, the different distribution, with both lung and breast each having shorter survival, maintained statistical significance, though most of the individual primary types had a small sample size (Table 1,  $P = .005$ ). This statistical significance was also maintained when the analysis was performed on only the 39 patients with solitary ISCMs ( $P = .017$ , with respective median survival of 3.9 months for lung primaries [ $n = 17$ ] and 1.3 months for breast primaries [ $n = 4$ ]). Additional median survivals based on primary malignancy considering both solitary and multiple ISCMs were the following:

lung (1.9 months,  $n = 24$ ), breast (1.6 month,  $n = 7$ ), melanoma (2.9 months,  $n = 5$ ), all nonmelanoma primaries (3.8 months,  $n = 44$ ), CNS (25.4 months,  $n = 4$ ), renal (10.0 months,  $n = 3$ ), and other (16.8 months,  $n = 6$ ). The median survival of patients with ISCMs with non-CNS primary malignancies (3.5 months) was shorter than that of patients with CNS primary malignancy (25.4 months) ( $P = .018$ ), though the sample size of CNS primaries was small. None of the following features significantly correlated with survival: age at ISCM diagnosis (mean and median, 58 years), melanoma-versus-non-melanoma primary malignancy, and ISCM diagnosis preceding primary malignancy diagnosis.

### Prognostic Value of MR Imaging Features

Patients with multiple ISCMs experienced shorter median survivals from the date of ISCM diagnosis than those with solitary ISCMs (1.8 versus 4.0 months, respectively;  $P = .022$ ) (Table 2 and Fig 2). Table 2 also demonstrates the impact of various additional categoric and continuous MR imaging findings on patient survival, considering only the 39 patients with solitary ISCMs. Two other MR imaging features were associated with statistically significant shorter survival periods: 1) greater longitudinal extent of T2 signal abnormality ( $P = .037$  if at least 2 segments,  $P = .018$  if at least 3 segments) (Fig 3); and 2) ancillary presence of the primary tumor and/or non-CNS metastases on the reference MR imaging ( $P = .012$ ) (Fig 4). The correlation between these 2 MR imaging features and a shorter survival period was maintained when the analysis was performed on all 49 patients with either solitary or multiple ISCMs (respective  $P$  values for T2 signal abnormality on at least 2 segments, .042; T2 signal abnormality on at least 3 segments, .022; and primary tumor/non-CNS metastases, .012). Regarding the longitudinal extent of the T2 signal abnormality, patients with at least 3 segments of spinal cord T2 hyperintensity associated with the solitary ISCM had median and mean survival durations of 111 days (3.7 months) and 157 days (5.2 months), compared with 184 days (6.1 months) and 436 days (14.5 months), respectively, in patients with  $\leq 2$  segments of cord T2 hyperintensity. A Kaplan-Meier plot for all patients with solitary ISCMs demonstrated the shorter survival associated with  $\geq 3$  segments of cord T2 hyperintensity (Fig 5). When treated as a continuous rather than categoric variable, the number of segments of T2 signal abnormality did not significantly correlate with survival (hazard ratio, 1.02; 95% CI, 0.96–1.09;  $P = .541$ ).

In patients with solitary ISCMs, the presence of a flame sign on

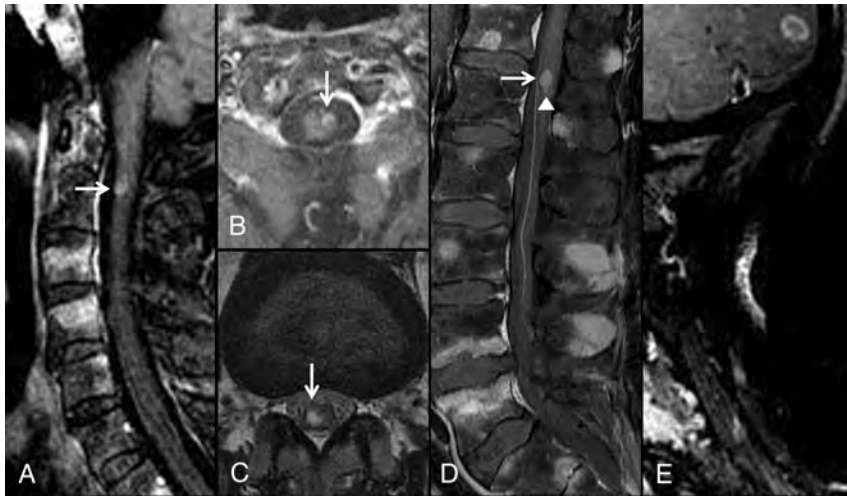


**FIG 2.** The presence of multiple ISCMs was a poor prognostic indicator. A 76-year-old man with metastatic non-small cell lung cancer. Lung or breast carcinoma was a poor prognostic feature compared with all other primary malignancy types. MR images of the cervical and lumbar spine with postcontrast fat-saturated sagittal (A, D, and E) and axial (B) T1-weighted and axial T2-weighted (C) images are shown. ISCMs are present at C2 (arrows, A and B) and L1 (arrows, C and D). Compared with solitary ISCMs, multiple ISCMs were associated with decreased survival. This patient survived 59 days from the diagnosis of ISCMs. The median survival of patients with multiple ISCMs was 53 days, compared with 121 days for those with a solitary ISCM. The conus lesion demonstrates the flame sign<sup>1</sup> inferiorly (arrowhead, D); the presence of this sign was associated with a non-statistically significant trend toward shorter survival. Note that multiple enhancing noncord CNS and spinal (osseous) metastases are present, including in the cerebellum (E); their presence did not correlate with a shorter survival.

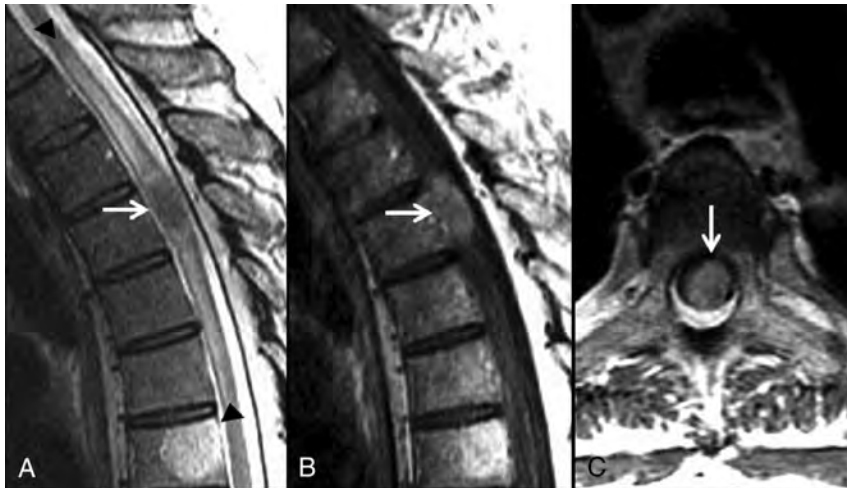


**FIG 3.** The presence of extensive edema was a poor prognostic indicator. A 55-year-old man with metastatic cerebral glioblastoma. MR images of the thoracic spine with sagittal T2- (A) and postcontrast T1-weighted sagittal (B) and axial (C) images are shown. An ISCM is present at T4 (arrows, A–C). Extensive edema for lesion size spans 5 vertebral segments, from the T1–T2 to T6–T7 levels (arrowheads, A). Spinal cord edema spanning multiple segments was associated with decreased survival in this series. This patient survived 19 days from the diagnosis of ISCMs. The median survival of patients with cord edema spanning  $\geq 3$  segments was 111 days, compared with 184 days for patients in whom it spanned  $\leq 2$  (note that the T7 vertebral body lesion is an incidental hemangioma).

postgadolinium T1-weighted imaging<sup>1</sup> may be associated with shorter survival; this possible association approached but did not reach statistical significance ( $P = .068$ ). The following MR imaging findings were not predictive of survival: noncord CNS and/or spinal metastases ( $P = .879$ ), the presence of leptomeningeal metastases ( $P = .274$ ), size or extent of ISCM enhancement ( $P = .138$ ;  $P = .524$ ), ratio of cord T2 hyperintensity to

enhancement ( $P = .477$ ), or the rim sign ( $P = .621$ ).<sup>1</sup> Several additional imaging features not shown in Table 2 did not correlate with survival, when considering the 39 patients with solitary ISCMs: position within the cord ( $P = .854$ ), cord expansion ( $P = .169$ ), T2 signal intensity ( $P = .090$ ), T1 signal intensity ( $P = .467$ ), cystic change ( $P = .583$ ), intratumoral hemorrhage ( $P = .601$ ), and gadolinium enhancement pattern ( $P = .326$ ). In the small group of patients with solitary ISCMs who had available PET examinations ( $n = 9$ ), uptake on PET ( $n = 6$ ) did not correlate with survival ( $P = .702$ ).

The visualization of additional ISCMs on follow-up MR imaging occurred in 11 of 49 (22%) patients, 10 of whom initially had solitary ISCMs. When we considered all 49 patients, this feature was associated with longer survival:  $P = .001$ , with respective median survival of 21.2 months for patients in whom this did occur ( $n = 11$ ) and 1.9 months for patients in whom it did not ( $n = 38$ ). This association was maintained when the analysis was performed on only the 39 patients with solitary ISCMs ( $P = .007$ , with respective median survival of 21.2 months [ $n = 10$ ] and 3.5 months [ $n = 29$ ]).

## DISCUSSION

The current study highlights that in a large series of patients, several clinical and MRI features of ISCMs have prognostic value. Patients with lung or breast primary tumor type have decreased survival compared with patients with all other primary malignancies, a finding that was evident when these primary malignancies were analyzed both as grouped and individual variables. On reference MR imaging, features associated with decreased survival are the following: 1) multiple ISCMs, 2) longitudinally extensive spinal cord T2 hyperintensity, and 3) ancillary presence of the primary tumor and/or non-CNS metastases.

Familiarity with these prognostically relevant clinical and imaging features of ISCMs is relevant to both radiologists and the referring clinicians. For any spinal cord mass, but particularly when ISCM is strongly considered, MR imaging should be scrutinized for the ancillary presence of the primary tumor/non-CNS metastases to assist with the differential diagnosis and evaluate evidence of widely metastatic disease. The visualized lungs should be specifically carefully evaluated on MR imaging because lung cancer is the most com-



**FIG 4.** The ancillary presence of primary malignancy and/or non-CNS metastases on reference MR imaging was a poor prognostic indicator. A 39-year-old man with metastatic non-small cell lung cancer. MR images of the cervical, thoracic, and lumbar spine with sagittal T2- (A), post-contrast T1-weighted (B), fat-saturated T1-weighted (C), and axial T2-weighted (D) images, and an axial postcontrast chest CT image (E) are shown. An ISCM is present at C3 (arrows, A and B). The primary lung carcinoma is visualized in the right upper lobe (arrowheads, D and E), as are several presumed pulmonary metastases (eg, arrows, D and E). The presence of the primary malignancy and/or non-CNS metastases was associated with decreased survival in this series. This patient survived 24 days from the diagnosis of ISCM. The median survival of patients with visible primary malignancy/non-CNS metastases was 96 days, compared with 316 days for patients in whom these were not visible. Note that leptomeningeal metastases are present (block arrows, B and C); their presence did not correlate with a shorter survival.

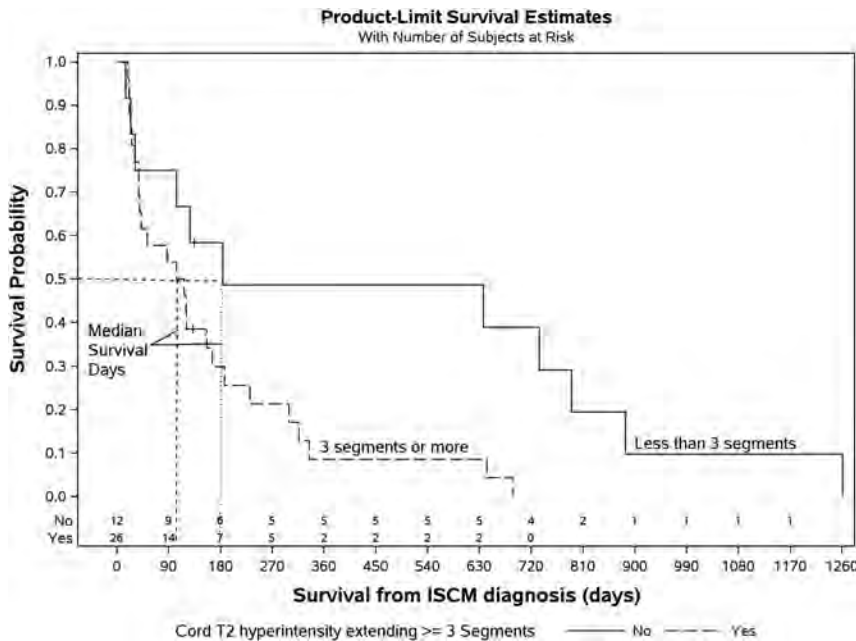


**FIG 5.** Kaplan-Meier plot. Decreased survival of patients with ISCM-related cord T2 hyperintensity extending  $\geq 3$  spinal segments. The median survival for T2 hyperintensity of  $\geq 3$  segments was 111 days and for  $< 3$  segments was 184 days ( $P = .018$ , log-rank test;  $n = 38$  patients with solitary ISCMs with available sagittal T2WI).

mon primary malignancy and imparts a worse prognosis compared with other nonlung/nonbreast malignancies. The presence of both extensive spinal cord T2 hyperintensity and additional ISCMs should be specifically sought. Evaluating these MR imaging features not only assists with the differential diagnosis but also offers prognostic value, because patients whose MR imaging examinations have these features have decreased survival.

The decreased survival of those patients with MR imaging evidence of multiple ISCMs and those with the ancillary presence of the primary tumor and/or non-CNS metastases on the reference MR imaging, while intuitive, has not, to our knowledge, been reported in the literature. Although not specifically evaluated in our study, presumed causes for the decreased survival are that these findings represent a particularly aggressive type of advanced (stage IV) metastatic disease, recalcitrance of the disease (either the primary and or the metastases) to therapy, and/or in select cases, the tendency for clinicians and their patients to choose palliative therapy. Likely a complex interplay of factors such as inherent disease aggressiveness, responsiveness to treatment, patient comorbidities, and patient immune system status underlies a patient's ability to have prolonged survival, but the current study, by its very design, cannot shed discriminatory light on these features. It would be interesting to explore these in future studies. The decreased survival associated with greater spinal cord edema extent has also, to our knowledge, not been described, and precise conclusions cannot be drawn about the reason for this association. Presumably such a finding either directly impairs the ability of the patient to survive (eg, perhaps spinal cord functional impairment, possibly due to a more locally infiltrative phenotype) and/or it serves as a marker for a more aggressive disease state (eg, perhaps disease less likely to respond to therapy and/or aggressive metastatic disease to sites outside the spinal cord).

We cautiously interpret the apparent decreased survival of patients with non-CNS versus CNS primary neoplasms as merely an observed possible association, given the very small ( $n = 4$ ) number of patients in the CNS primary neoplasm group and the several CNS histologies that are represented (as previously reported,<sup>1</sup> 2 medulloblastomas, 1 esthesioneuroblastoma, and 1 cerebral glioblastoma). Similarly, the apparent association of visualization of subsequent ISCMs with improved survival must be carefully interpreted. At least in part, this should simply reflect the longer survival of these patients who are being imaged again, allowing documentation of additional ISCM development. Potentially, having imaging of the initial ISCM at an earlier disease state could also contribute to this presumed statistical artifact. Most interest-

ing, the presence of leptomeningeal disease on MR imaging was not associated with shorter survival. While speculative, a potential explanation is that perhaps such metastatic disease might not impair vital functions as much as a metastasis elsewhere, such as in the spinal cord parenchyma or in other vital organs. The lack of correlation of ISCM diagnosis preceding primary malignancy diagnosis with shorter survival is also interesting. However, even if such a statistical association were present, it would likely be difficult to ascribe significance because of the very small sample size of 5 patients.

The lack of a convincing association of the recently described rim and flame signs<sup>1</sup> with survival in the current study has yet to be reported. Likewise, the decreased survival of patients with ISCMs with lung or breast primary tumors has not been specifically described. Note that 2 studies previously reported that patients with melanoma had significantly longer survival compared to patients with nonmelanoma histology,<sup>5,6</sup> a finding not corroborated by our present data, which included 5 patients with melanoma. The latter of the 2 studies based this assertion on the combination of a single patient with melanoma combined with 4 others from the literature, while the former included 2 patients with melanoma. Similarly, the reported longer survival of patients with breast cancer compared with those with lung cancer described in a prior study of 12 patients with ISCMs<sup>7</sup> was not confirmed in the present study. A similarity between our series and the recent comprehensive literature review by Sung et al<sup>4</sup> is the short survival of patients with ISCMs (median, 3.5 months versus 4 months in that review).

Limitations include the retrospective nature of our study. Despite this group being the largest published single institution series of patients with ISCM to our knowledge, the 49-patient sample size is, nonetheless, a limitation. Similarly, the lack of a standard MR imaging technique, given that the examinations were performed during more than a decade and at >1 institution, is a weakness. Admittedly, visualization of the primary tumor on spinal MR imaging is not possible in all cases of ISCM due to the area of interest being either not well-included or not being included at all. Multiple possible confounding variables could influence the survival analyses and were not considered, such as extent of metastatic disease clinically at the time of reference MR imaging, comorbidities, and treatment. Because the purpose was to assess the prognostic value of baseline clinical and MR imaging

findings irrespective of subsequent therapies, this study did not assess the impact on survival of the various treatment modalities for ISCM or how treatment may or may not have been affected by clinicians' knowledge of the existence of ISCMs. Interested readers are referred to the aforementioned recent comprehensive literature review by Sung et al<sup>4</sup>; note that even in that review, median survival between surgically and conservatively treated patients was not considerably different (6 versus 5 months, respectively, with solitary-versus-multiple ISCM status not provided).

## CONCLUSIONS

We describe the prognostic value of pertinent clinical and MR imaging features in a large series of patients with ISCMs. Spinal cord edema spanning multiple segments, the presence of multifocal ISCMs, and ancillary evidence for non-CNS metastases and/or the primary tumor should be specifically sought because these MR imaging features are associated with decreased survival. Patients with either a lung or breast primary malignancy have decreased survival compared with other primary tumor types.

Disclosures: Timothy J. Kaufmann—UNRELATED: Consultancy: SpineThera, Comments: medical advisory board; I have received no fees to date but will.

## REFERENCES

1. Rykken JB, Diehn FE, Hunt CH, et al. **Rim and flame signs: postgadolinium MRI findings specific for non-CNS intramedullary spinal cord metastases.** *AJNR Am J Neuroradiol* 2013;34:908–15
2. Rykken JB, Diehn FE, Hunt CH, et al. **Intramedullary spinal cord metastases: MRI and relevant clinical features from a 13-year institutional case series.** *AJNR Am J Neuroradiol* 2013;34:2043–49
3. Mostardi PM, Diehn FE, Rykken JB, et al. **Intramedullary spinal cord metastases: visibility on PET and correlation with MRI features.** *AJNR Am J Neuroradiol* 2014;35:196–201
4. Sung WS, Sung MJ, Chan JH, et al. **Intramedullary spinal cord metastases: a 20-year institutional experience with a comprehensive literature review.** *World Neurosurg* 2013;79:576–84
5. Wilson DA, Fusco DJ, Uschold TD, et al. **Survival and functional outcome after surgical resection of intramedullary spinal cord metastases.** *World Neurosurg* 2012;77:370–74
6. Connolly ES Jr, Winfree CJ, McCormick PC, et al. **Intramedullary spinal cord metastasis: report of three cases and review of the literature.** *Surg Neurol* 1996;46:329–37; discussion 337–38
7. Lee SS, Kim MK, Sym SJ, et al. **Intramedullary spinal cord metastases: a single-institution experience.** *J Neurooncol* 2007;84:85–89

# Correlation of the Patient Reported Outcomes Measurement Information System with Legacy Outcomes Measures in Assessment of Response to Lumbar Transforaminal Epidural Steroid Injections

L. Shahgholi, K.J. Yost, R.E. Carter, J.R. Geske, C.E. Hagen, K.K. Amrami, F.E. Diehn, T.J. Kaufmann, J.M. Morris, N.S. Murthy, J.T. Wald, K.R. Thielen, D.F. Kallmes, and T.P. Maus

## ABSTRACT

**BACKGROUND AND PURPOSE:** The Patient Reported Outcomes Measurement Information System is a newly developed outcomes measure promulgated by the National Institutes of Health. This study compares changes in pain and physical function–related measures of this system with changes on the Numeric Rating Pain Scale, Roland Morris Disability Index, and the European Quality of Life scale 5D questionnaire in patients undergoing transformational epidural steroid injections for radicular pain.

**MATERIALS AND METHODS:** One hundred ninety-nine patients undergoing transforaminal epidural steroid injections for radicular pain were enrolled in the study. Before the procedure, they rated the intensity of their pain by using the 0–10 Numeric Rating Pain Scale, Roland Morris Disability Index, and European Quality of Life scale 5D questionnaire. Patients completed the Patient Reported Outcomes Measurement Information System Physical Function, Pain Behavior, and Pain Interference short forms before transforaminal epidural steroid injections and at 3 and 6 months. Seventy and 43 subjects replied at 3- and 6-month follow-up. Spearman rank correlations were used to assess the correlation between the instruments. The minimally important differences were calculated for each measurement tool as an indicator of meaningful change.

**RESULTS:** All instruments were responsive in detecting changes at 3- and 6-month follow-up ( $P < .0001$ ). There was significant correlation between changes in Patient Reported Outcomes Measurement Information System scores and legacy questionnaires from baseline to 3 months ( $P < .05$ ). There were, however, no significant correlations in changes from 3 to 6 months with any of the instruments.

**CONCLUSIONS:** The studied Patient Reported Outcomes Measurement Information System domains offered responsive and correlative psychometric properties compared with legacy instruments in a population of patients undergoing transforaminal epidural steroid injections for radicular pain.

**ABBREVIATIONS:** EQ-5D = European Quality of Life scale 5D questionnaire; NRS = Numeric Rating Pain Scale; PROMIS = Patient Reported Outcomes Measurement Information System; RMDI = Roland-Morris Disability Index; TFESI = transforaminal epidural steroid injection

Spinal pain is one of the most common types of chronic pain worldwide.<sup>1</sup> The epidemiology of low back pain has been investigated comprehensively in adults. A recent epidemiologic review noted lifetime prevalence estimates ranging from 12.2% to 43%; annual prevalence estimates were 2.2% to 34%.<sup>2</sup> When there is both compression and inflammation of neural elements, low back pain may be accompanied by radicular pain. Patients with

radicular pain tend to have poorer outcomes, consume more health care resources, and have greater disability than patients with back pain alone. Transforaminal epidural steroid injections (TFESI) have become a common intervention in the treatment of radicular pain; the procedure has shown efficacy in explanatory trials<sup>3</sup> and clinical effectiveness in large retrospective series.<sup>4</sup> A recent systematic literature review demonstrated a consensus of support for TFESIs, but historically, there have been conflicting reports regarding their efficacy.<sup>5</sup> Systematic literature reviews are made more challenging and their interpretation is confounded by the use of a host of different measurement tools including the Numeric Rating Pain Scale (NRS), Roland-Morris Disability Index (RMDI), Oswestry Disability Index, European Quality of Life scale 5D questionnaire (EQ-5D), finger-to-floor distance, and the Oswestry and Nottingham Health Profile Verbal Rating Scale.<sup>6</sup>

Although the NRS is a familiar mechanism for measuring pain for most patients, it cannot assess the more complex construct of

Received June 23, 2014; accepted after revision September 1.

From the Departments of Physical Medicine and Rehabilitation (L.S.) and Radiology (K.K.A., F.E.D., T.J.K., J.M.M., N.S.M., J.T.W., K.R.T., D.F.K., T.P.M.), Mayo Clinic and Foundation, Rochester, Minnesota; and Division of Epidemiology (K.J.Y.) and Division of Biomedical Statistics and Informatics (R.E.C., J.R.G., C.E.H.), Department of Health Sciences Research, Mayo Clinic, Rochester, Minnesota.

Please address correspondence to Leili Shahgholi, MD, Department of Physical Medicine and Rehabilitation, Mayo Clinic and Foundation, 200 First St SW, Rochester, MN 55905; e-mail: leili.shahgholi@neurology.uf.edu

 Indicates article with supplemental on-line appendix.

<http://dx.doi.org/10.3174/ajnr.A4150>

a patient's functional disability and overall quality of life. The RMDI as a measure of functional disability has 23 questions with dichotomized choices. The EQ-5D is a measure of quality of life and addresses 5 different domains of mobility, self-care, usual work, and pain, though its 3-choice format may seem insufficient to quantitate the complicated effects of pain on a patient's life.<sup>7</sup> The need for a multiplicity of questionnaires and the variety of options leads to both excessive patient burden in assessment and challenges in comparison among studies when different measurement tools have been chosen.

To overcome these shortcomings, which apply across many different fields of medicine, a new Patient Reported Outcomes Measurement Information System (PROMIS) has been developed. The PROMIS initiative is the National Institutes of Health-funded effort to produce widely applicable standardized measurement tools, covering a variety of domains, which can be used across many disciplines while minimizing the patient burden. The PROMIS study group has developed short-form measures of multiple domains, which should perform well in a TFESI procedural population. The PROMIS measures currently require clinical testing to compare them with established measures in a variety of clinical populations with different characteristics (including type

of pain). They need to be compared with established measures (ie, "legacy" measures) with respect to responsiveness, reliability, and validity. Currently, the NRS, 23-point RMDI, and EQ-5D are performed in our practice before TFESI and at 3-, 6-, 9-, and 12-month follow-up as standard quality assurance measures. The follow-up measurements occur by machine-read forms; these are given to the patient at dismissal from the procedure area with instructions to complete them at the indicated times and return them via the postage-paid envelope provided. If the questionnaires are not returned, an attempt is made to reach patients via telephone to give them the option of sending back the completed forms or completing the data via a telephone interview. The PROMIS tools are designed to measure pain and functional and quality-of-life domains with less patient burden. The goal of this study was to compare the reliability and responsiveness of PROMIS short forms with the NRS, 23-point RMDI, and EQ-5D after lumbar transforaminal epidural steroid injections.

## MATERIALS AND METHODS

Our institutional review board approved this prospective Health Insurance Portability and Accountability Act-compliant study, and written consent of all study participants was obtained. Between May 2010 and June 2012, 200 patients were enrolled who had been evaluated by the Mayo multidisciplinary Spine Center and referred to the radiology pain-management practice for lumbar transforaminal epidural steroid injections for radicular pain with or without radiculopathy. Patients were considered for enrollment in the study if they had lumbar radicular pain unresponsive to conservative therapy and were able to answer the questions in English. We excluded patients who were unable to consent or cooperate, had myelopathy or progressive neurologic deficits, were using anticoagulant medication, had a systemic infection or local skin infection in the lumbar region, or were pregnant.

In the first evaluation, following the physician's procedural explanation and consent process and after the study coordinator's explanation of how to answer the questions, patients completed the PROMIS short forms measuring 3 different domains relevant to their radicular pain, including Physical Function, Pain

**Table 1: Demographic characteristic of patients at baseline, 3 months, and 6 months**

	Baseline (n = 199)	3 Months (n = 71)	6 Months (n = 43)
Age at injection (yr)			
Mean (SD)	63.1 (14.7)	66.5 (14.8)	68.3 (12.4)
Median	65	70	71
Q1, Q3	55.0, 74.0	62, 75	62.0, 77.0
Range	25.0–90.0	25–90	37.0–90.0
Sex			
Female	101 (50.8%)	43 (60.6%)	30 (69.8%)
Male	98 (49.2%)	28 (39.4%)	13 (30.2%)
Race			
American Indian/Alaskan Native	1 (0.5%)	0 (0%)	0 (0%)
African American	4 (2.0%)	0 (0%)	0 (0%)
White	188 (94.5%)	71 (100%)	43 (100%)
Other	3 (1.5%)	0 (0%)	0 (0%)
Asian	1 (0.5%)	0 (0%)	0 (0%)
Unknown	2 (1.0%)	0 (0%)	0 (0%)
Ethnicity			
Mexican	1 (0.5%)	0 (0%)	0 (0%)
Not Hispanic or Latino	182 (91.5%)	68 (95.8%)	39 (90.7%)
Unknown	14 (7.0%)	3 (4.2%)	4 (9.3%)
Chose not to disclose	2 (1.0%)	0 (0%)	0 (0%)
Marital status			
Divorced	21 (10.6%)	7 (9.9%)	5 (11.6%)
Married	143 (71.9%)	49 (69.0%)	29 (67.4%)
Life partnership	1 (0.5%)	0 (0%)	0 (0%)
Single	16 (8.0%)	5 (7.0%)	3 (7.0%)
Unknown	1 (0.5%)	1 (1.4%)	1 (2.3%)
Widowed	17 (8.5%)	9 (12.7%)	5 (11.6%)

**Note:**—Q1 indicates first quartile; Q3, third quartile.

**Table 2: Continuous outcomes data**

	Baseline (Mean) (Range)	95% CI	3 Months (Mean) (Range)	95% CI	6 Months (Mean) (Range)	95% CI
RMDI	12.37 ± 5.71 (1–23)	11.56–13.17	9.92 ± 5.87 (1–22)	8.72–11.13	9.61 ± 5.73 (1–21)	8.27–10.94
EQ-5D	0.60 ± 0.19 (0.26–0.83)	0.57–0.63	0.69 ± 0.19 (1–23)	0.65–0.73	0.70 ± 0.17 (0.31–1)	0.66–0.74
NRS	5.85 ± 2.44 (0–10)	5.5–6.19	4.41 ± 2.53 (0–10)	3.89–4.93	4.34 ± 2.50 (0–10)	3.76–4.92
PF	36.71 ± 5.78 (22.4–55.3)	35.9–37.52	37.99 ± 6.92 (26.2–61.7)	36.38–39.6	38.06 ± 6.41 (26.2–50.8)	36.18–39.93
PI	64.55 ± 5.39 (48.5–74.4)	63.79–65.32	61.17 ± 6.39 (41–78.3)	59.69–62.65	60.34 ± 6.41 (41–74.4)	58.22–62.47
PB	60.01 ± 3.38 (52.1–72.1)	59.53–60.48	58.44 ± 4.38 (36.7–66.6)	57.43–59.45	57.80 ± 6.14 (36.7–75.9)	55.98–59.61

**Note:**—PB indicates PROMIS Pain Behavior Scale; PF, PROMIS Physical Function Scale; PI, Pain Interference.

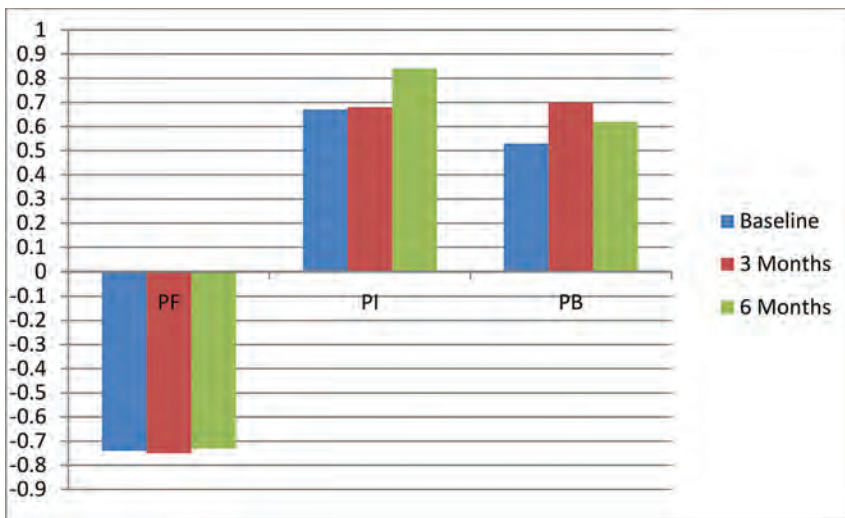


**FIG 1.** Spearman correlation coefficients between PROMIS scores and RMDI on the first day and at 3- and 6-month evaluations in the TFESI group.

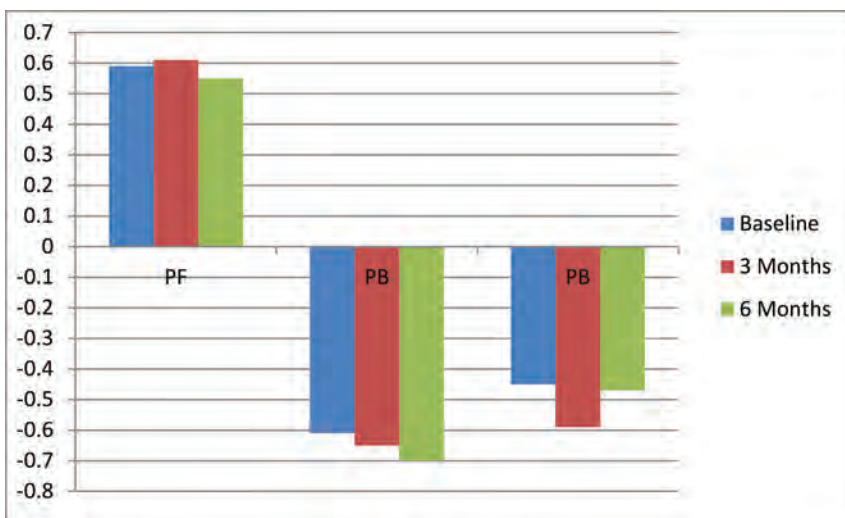


**FIG 2.** Spearman correlation coefficients between PROMIS scores and EQ-5D on the first day and from 3- and 6-month evaluations in the TFESI group.

Behavior, and Pain Interference. Patients who were able to complete the forms themselves did so; the study coordinator was available to assist if necessary. Two more sets of questionnaires were given to the patient at dismissal from the procedure area with instructions to complete them at 3 and 6 months and return them in prepaid, preaddressed envelopes.

The PROMIS forms included the 10-question Physical Function Short Form, which is focused on the ability to perform various daily activities from self-care (bathing and dressing) to vigorous physical activities (running, strenuous sports) (On-line Appendix, Fig A). The 6-question Pain Interference Short Form is focused on pain interference with mental, physical, and social aspects of daily living (On-line Appendix, Fig B). The 7-question Pain Behaviors Short Form focuses on verbal, facial, and bodily expressions of pain (On-line Appendix, Fig C). Completing each questionnaire takes approximately 2.5 minutes. Responses to PROMIS questions on a given short form were summed for raw scores; responses entered into the on-line PROMIS data base provided *t*-scores. The *t*-score scale

has a mean score of 50 and an SD of 10 in the US general population.<sup>8</sup> For example, a person who has a PROMIS pain interference score of 70 is reporting adverse pain interference 2 SDs worse than the general population mean. Higher *t*-scores indicate greater levels of the construct being measured. Thus, for pain behavior and pain interference, higher scores reflect worse pain, whereas for physical function, higher scores indicate better functioning. Participants also rated the intensity of their pain in the past 24 hours by using a pain NRS from 0 to 10, with zero indicating no pain and 10 indicating the worst imaginable pain. The 23-item modified RMDI and 5-item EQ-5D, 2 widely used functional outcome scales, were also administered. The EQ-5D survey assesses 5 dimensions with the possible score range for each of the dimensions of 1–3, in which 1 = no problems, 2 = moderate problems, and 3 = extreme problems. Each unique health state described by the instrument has an associated 5-digit descriptor ranging from 11111 for perfect health to 33333 for the worst possible state. The resulting descriptive system defines 243 (3<sup>5</sup>) health states.<sup>9</sup>

#### Power, Sample Size, and Statistical Analysis

The study was a prospective registry, and the sample size was justified before the start of the study on the basis of the estimated precision for the agreement of the PROMIS and legacy scales. These calculations supported a range of sample sizes and incorporated up to a 50% attrition rate during follow-up (the assumed survey nonresponse rate). Briefly, agreement between the 2 approaches of measuring pain was estimated to be >0.8. We wanted to rule out agreement <0.6. For sample-size planning purposes, 55% of the patients were assumed to have a decrease in disability as measured by the RMDI at 3 months. Furthermore, it was assumed that 50% (40%) of the patients would have a decrease (increase) on both the RMDI and the PROMIS scales. The remaining 10% were assumed discordant cases (response on either RMDI or PROMIS but not both). On the basis of these estimates,  $\kappa$  was estimated to be 0.80; and provided 100 completed assessments were available, the 95% CI for  $\kappa$  would span 0.682–0.918. This would provide sufficient precision to rule out the null value of 0.6. To account for drop-out, we administratively selected a sample size of 200 to be sufficient to describe the primary aim.

Statistical tests on secondary aims were performed on an exploratory basis. Categorical data are presented as counts and per-

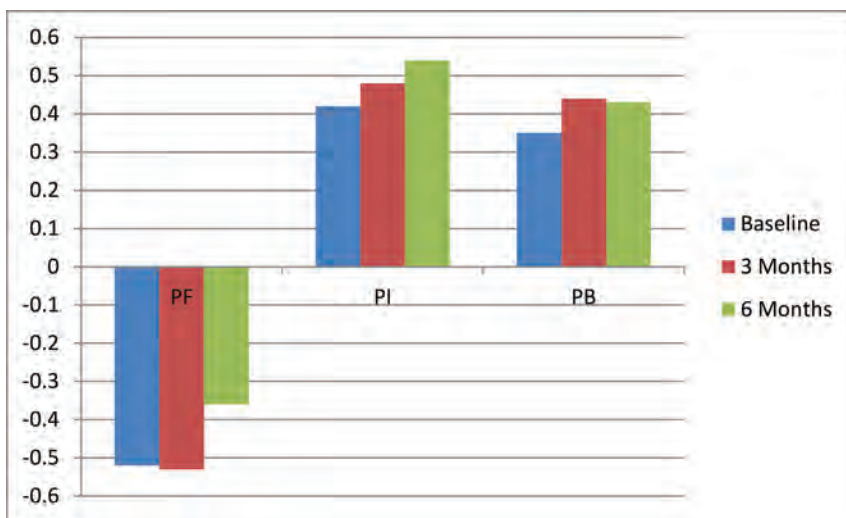


**FIG 3.** Spearman correlation coefficients between PROMIS scores and NRS on the first day and from 3- and 6-month evaluations in the TFESI group.

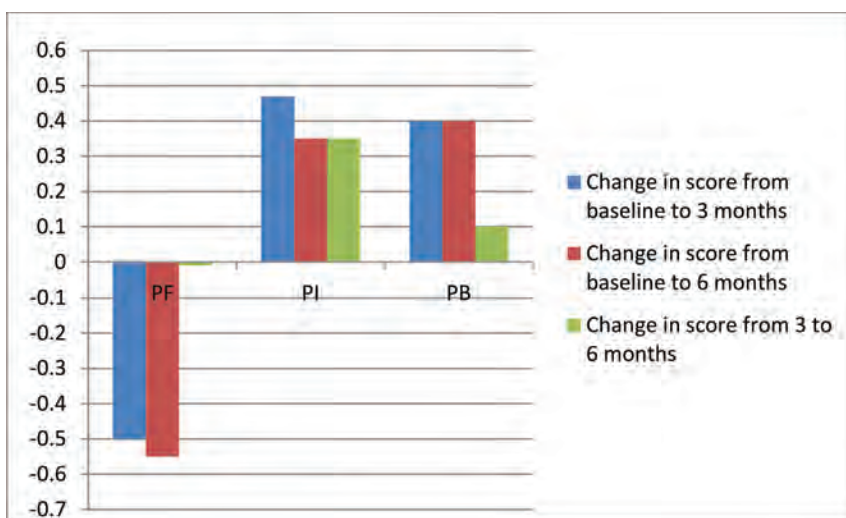


**FIG 4.** Spearman correlation coefficients between changes in PROMIS scores and those in RMDI on the first day and from 3- and 6-month evaluations in the TFESI group.

centages. Continuous data are presented by using mean, median, SD, and range as appropriate. The minimally important differences were calculated as reliable change index  $\times 1.96$  for the multi-item measurement tools by using baseline data. Reliable change index is calculated as  $\sqrt{2} \times$  standard error of measurement.<sup>8,10</sup> The standard error of measurement is calculated as  $SD\sqrt{(1-r)}$ , where SD is the standard deviation of the sample and r is reliability.<sup>10</sup> Instrument reliability used in standard error of measurement calculations was estimated with Cronbach  $\alpha$  measured at baseline. Changes exceeding 2 points on the pain NRS were considered clinically meaningful.<sup>7</sup>

The minimally important difference served as another means of comparing instruments. Specifically, we assessed whether the proportion of individuals identified as having experienced meaningful change (defined as a change greater than or equal to the minimally important difference) was similar across measures. All correlations presented are Spearman rank correlation coefficients; associated significant *P* values indicate nonzero correla-

tion. Criteria for an adequate cross-sectional and longitudinal Spearman correlation were set at  $>0.5$  and  $>0.3$ , respectively.<sup>11</sup> *P* values  $\leq .05$  were statistically significant. Statistical comparisons of the model-based estimates were configured to test changes from baseline to 3 months, baseline to 6 months, and 3–6 months postprocedure. SAS 9.3 (SAS Institute, Cary, North Carolina) was used in all data analyses.

## RESULTS

### Study Participants

Two hundred patients met the enrollment criteria and underwent TFESIs. One patient canceled the research authorization after 1 day, leaving the cohort with 199 research-authorized patients. All patients were able to complete the forms without assistance. Demographic characteristics are presented in Table 1. The sample consisted of 98 (49.2%) men and 101 (50.8%) women. Subject ages ranged from 25 to 90 years (mean,  $63.1 \pm 14.7$  years). One hundred twenty-nine patients were lost to follow-up at the 3-month time point; and from the remaining 70 patients, 43 subjects replied at 6-month follow-up. At the 3- and 6-month time points, 7 and 10 patients completed the forms with a telephone interview versus 63 and 33 that were self-administered, respectively. This process left a cohort of 70/199 (35%) at 3 months following injection and 43/199 (22%) at 6 months following the procedure. Although our standard clinical quality assurance follow-up continued through 9 and 12 months, there was a continued decline in the rate of return of the outcomes forms, so that evaluation at these data points was not considered useful.

### Numeric Rating Pain Scale, PROMIS T-Score, RMDI, and EQ-5D

Table 2 presents baseline and 3- and 6-month scores. All instruments were responsive to detect changes at 3- and 6-month follow-up ( $P < .0001$ ). Mean scores for all domains demonstrated improvement at 3 and 6 months (eg, less pain, better physical function). Correlations between RMDI, EQ-5D, or NRS and PROMIS scores were significant in all cross-sectional measurements ( $P < .0001$ ,  $P < .005$ , and  $P < .05$  respectively; Figs 1–3). Correlations between changes with time in PROMIS scores and changes with time both in EQ-5D and RMDI scores were significant at 3 and 6 months ( $P < .05$ ; Figs 4–6). Although there was significant correlation between changes in the PROMIS scores and the pain NRS from baseline to 3 months ( $P < .05$ ), the changes from 3 to 6 months were not significantly correlated.

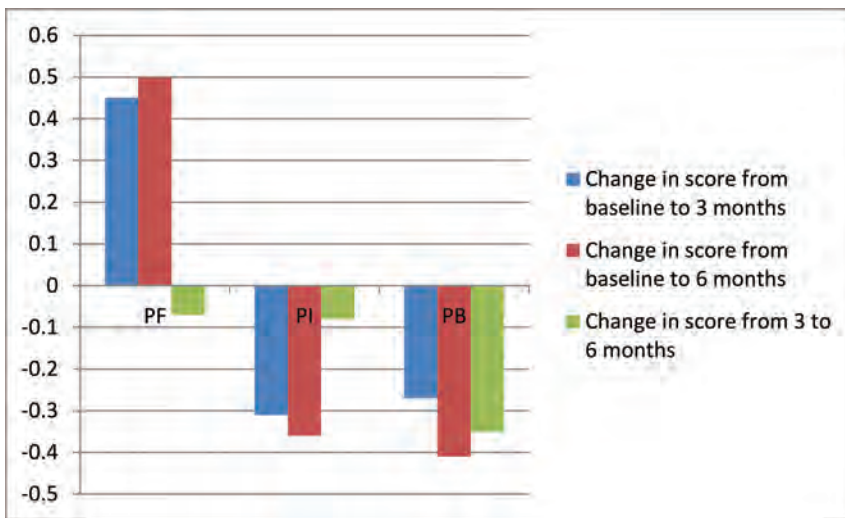


**FIG 5.** Spearman correlation coefficients between changes in PROMIS scores and those in EQ-5D from baseline to 3 months, baseline to 6 months, and 3–6 months in the TFESI group.

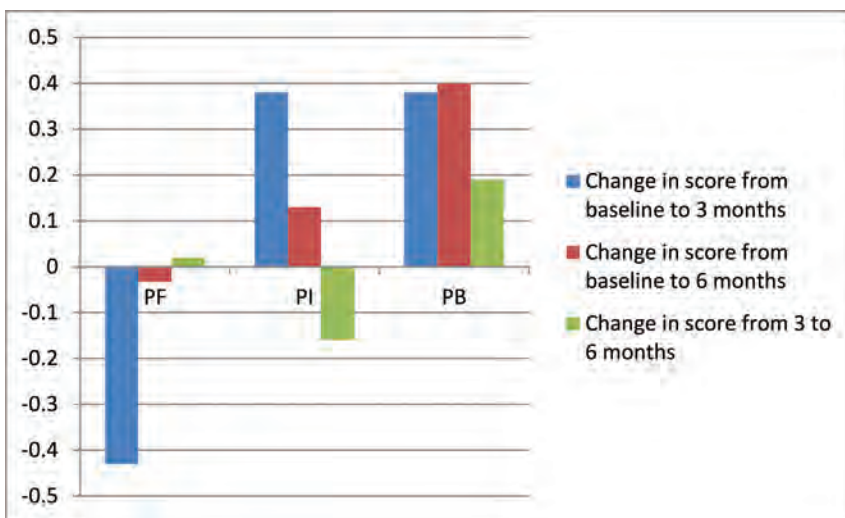


**FIG 6.** Spearman correlation coefficients between changes in PROMIS scores and those in NRS on the first day and from 3- and 6-month evaluations in the TFESI group.

There were no significant correlations in changes from 3 to 6 months with any of instruments.

On the basis of the minimally important difference calculation ( $1.96 \times$  reliable change index), patients who had changes of 5.2 points for the RMDI, 0.3 points for EQ-5D, 6.2 points for Physical Function, 4.5 points for Pain Interference, and 4.4 points for Pain Behavior were considered to have experienced meaningful improvement. At 3 and 6 months, the proportion of patients achieving improvement in the 3 PROMIS domains and EQ-5D and RMDI were, respectively, 1%–10% and 2%–5%. The improvements were much higher in pain NRS either at 3 (42%) or 6 (41%) months. The direction of change (decline versus improvement) at 3-month follow-up of RMDI and PROMIS Physical Function, Pain Interference, Pain Behavior, and EQ-5D was the same in 65 (93%), 32 (46%), 63 (91%), 69 (98.5%), and 58(83%) patients, respectively. At 6-month follow-up, proportionately more patients exhibited a decline in RMDI (25%) compared with those showing a decline in the PROMIS Physical Function (9%) or Pain

Behavior (9%) domains. A similar proportion (27%) showed a decline in the PROMIS Pain Interference domain (Table 3).

## DISCUSSION

Using a cohort of patients who underwent TFESI, we found moderate-to-high degrees of correlation among PROMIS Physical Function, Pain Interference, and Pain Behavior domains and legacy instruments. All PROMIS domains were moderately-to-highly responsive to change and correlated with the RMDI, EQ-5D, and NRS, which have been validated in patients with low back pain and lower extremity radicular pain. Correlation between PROMIS domains and RMDI was high at any cross-sectional or longitudinal measurement and was highest for PROMIS Physical Function. There was not a strong correlation between the EQ-5D and the PROMIS Physical Function domain, which was expected because the RMDI focuses on physical activity, while the EQ-5D simultaneously assesses mood and physical function. In assessing post-TFESI improvement with legacy instruments, we saw the greatest improvement in the NRS (42% had meaningful improvement), while there were few patients showing meaningful improvement in either legacy or PROMIS functional scales. This finding could reflect the advanced age of this study population or could be an artifact of the small sample size. That the measurements of the PROMIS domains remained concordant with the legacy instruments in no way undermines the primary study result.

Other recent studies have evaluated the PROMIS scales in focused clinical populations. Shahgholi et al<sup>7</sup> studied 50 patients undergoing vertebroplasty following osteoporotic compression fractures and showed a strong correlation between PROMIS physical function and RMDI. Fries et al<sup>12</sup> studied 451 patients with chronic rheumatoid arthritis and showed a strong correlation between PROMIS physical function and the Health Assessment Questionnaire or the Health Assessment Questionnaire Disability Index in patients with chronic rheumatoid arthritis. In our current study, correlations between RMDI and PROMIS scales were stronger than those of Shahgholi et al<sup>7</sup> and Fries et al.<sup>12</sup> We also observed good longitudinal correlation of change in scores.

This study thus provides additional, incremental validation of the PROMIS outcome measures in a clinical population of subjects undergoing a therapeutic intervention. As such validation studies accumulate, PROMIS methodology may achieve the goal of the National Institutes of Health of widespread use, enhancing comparability of studies within and across multiple fields of med-

**Table 3: Minimally important differences at 3- and 6-month follow-up**

	Reliability (Cronbach $\alpha$ )	Criterion for Meaningful Change	Patients Experiencing Meaningful Improvement (No.) (%)	Patients Experiencing No Change (No.) (%)	Patients Experiencing Meaningful Decline (No.) (%)
RMDI					
3 mo	0.88	5.2	4 (4%)	67 (74%)	19 (21%)
6 mo			2 (2%)	50 (71%)	18 (25%)
EQ-5D					
3 mo	0.56	0.3	1 (1%)	74 (85%)	12 (13%)
6 mo			2 (2%)	57 (82%)	10 (14%)
NRS					
3 mo	N/A	2.0	38 (42%)	41 (45%)	11 (12%)
6 mo			29 (41%)	34 (48%)	7 (10%)
PF					
3 mo	0.88	6.2	6 (8%)	56 (82%)	6 (8%)
6 mo			4 (9%)	35 (81%)	4 (9%)
PI					
3 mo	0.91	4.5	7 (10%)	41 (59%)	21 (30%)
6 mo			5 (11%)	26 (60%)	12 (27%)
PB					
3 mo	0.79	4.4	3 (4%)	61 (85%)	7 (9%)
6 mo			2 (4%)	37 (86%)	4 (9%)

**Note:**—PB indicates PROMIS Pain Behavior Scale; PF, PROMIS Physical Function Scale; PI, Pain Interference.

icine. The PROMIS instruments have also been formulated for computer adaptive testing; this change could further reduce the testing burden.

The study has limitations, the primary one being the number of subjects lost to follow-up. This is a product of the study design, relying on subjects to return materials distant in time from the intervention; supplying the surveys at the time of the procedure may have also diminished the rate of return. No useful data could be obtained at 9- and 12-month follow-up due to the failure of participants to return the study materials. Because the object of the study was correlation of measurement instruments, not assessment of outcomes, this lack of feedback reduces our precision, but does not confound the results. The lost-to-follow-up data may have introduced bias into the correlation summary. The results of this study will provide data for power analysis of future, more robust correlative studies as PROMIS scales are applied to additional therapeutic interventions.

## CONCLUSIONS

The PROMIS domains used in this study offered responsive and comparable psychometric properties to legacy instruments in a population of patients undergoing TFESI for radicular pain. The advantages of using PROMIS instruments are their ability to compare the results in a study cohort with the general US population, the ease of scoring, lesser patient burden while maintaining responsiveness and precision, and lack of licensure costs. As PROMIS instruments become more widely used, there will be the opportunity to compare the impact of disease burden and therapeutic interventions across medical specialties.

**Disclosures:** Timothy J. Kaufmann—UNRELATED: Consultancy: I am on the medical advisory board of SpineThera. I have not yet received any remuneration for this but anticipate such. Kent R. Thielen—UNRELATED: Royalties: Nevro. David F. Kallmes—UNRELATED: Board Membership: GE Healthcare, Comments: Cost-Effectiveness Board membership; Consultancy: ev3,\* Comments: planning and implementation of clinical trials; Grants/Grants Pending: MicroVention,\* Sequent,\* SurModics,\* ev3,\* Codman,\* Comments: clinical and preclinical research; Royalties: University of Vir-

ginia Patent Foundation (Spine Fusion). Timothy P. Maus—UNRELATED: Board Membership: International Spine Intervention Society, Comments: travel reimbursement for meetings of the Board of Directors of the International Spine Intervention Society and as an instructor at its Bio-Skills courses. \*Money paid to the institution.

## REFERENCES

- Hoy D, Brooks P, Blyth F, et al. **The epidemiology of low back pain.** *Best Pract Res Clin Rheumatol* 2010;24:769–81
- Konstantinou K, Dunn KM. **Sciatica: review of epidemiological studies and prevalence estimates.** *Spine* 2008;33:2464–72
- Ghahreman A, Ferch R, Bogduk N. **The efficacy of transforaminal injection of steroids for the treatment of lumbar radicular pain.** *Pain Med* 2010;11:1149–68
- Kaufmann TJ, Geske JR, Murthy NS, et al. **Clinical effectiveness of single lumbar transforaminal epidural steroid injections.** *Pain Med* 2013;14:1126–33
- MacVicar J, King W, Landers MH, et al. **The effectiveness of lumbar transforaminal injection of steroids: a comprehensive review with systematic analysis of the published data.** *Pain Med* 2013;14:14–28
- Roberts ST, Willick SE, Rho ME, et al. **Efficacy of lumbosacral transforaminal epidural steroid injections: a systematic review.** *PM R* 2009;1:657–68
- Shahgholi L, Yost KJ, Kallmes DF. **Correlation of the National Institutes of Health patient reported outcomes measurement information system scales and standard pain and functional outcomes in spine augmentation.** *AJNR Am J Neuroradiol* 2012;33:2186–90
- Jacobson NS, Truax P. **Clinical significance: a statistical approach to defining meaningful change in psychotherapy research.** *J Consult Clin Psychol* 1991;59:12–19
- Shaw JW, Coons SJ, Foster SA, et al. **Responsiveness of the Smoking Cessation Quality of Life (SCQoL) questionnaire.** *Clin Ther* 2001; 23:957–69
- King MT. **A point of minimal important difference (MID): a critique of terminology and methods.** *Expert Rev Pharmacoecon Outcomes Res* 2011;11:171–84
- Revicki DA, Chen WH, Harnam N, et al. **Development and psychometric analysis of the PROMIS pain behavior item bank.** *Pain* 2009;146:158–69
- Fries JF, Witter J, Rose M, et al. **Item response theory, computerized adaptive testing, and PROMIS: assessment of physical function.** *J Rheumatol* 2014;41:153–58

# Percutaneous Injection of Radiopaque Gelified Ethanol for the Treatment of Lumbar and Cervical Intervertebral Disk Herniations: Experience and Clinical Outcome in 80 Patients

M. Bellini, D.G. Romano, S. Leonini, I. Grazzini, C. Tabano, M. Ferrara, P. Piu, L. Monti, and A. Cerase



## ABSTRACT

**BACKGROUND AND PURPOSE:** Chemonucleolysis represents a minimally invasive percutaneous technique characterized by an intradiskal injection of materials under fluoroscopic or CT guidance. Recently, a substance based on radiopaque gelified ethanol has been introduced. The purpose of this study was to describe the indications, procedure, safety, and efficacy of radiopaque gelified ethanol in the percutaneous treatment of cervical and lumbar disk herniations.

**MATERIALS AND METHODS:** Between September 2010 and August 2013, 80 patients (32 women and 48 men; age range, 18–75 years) were treated for 107 lumbar disk herniations (L2–L3,  $n = 1$ ; L3–L4,  $n = 15$ ; L4–L5,  $n = 53$ ; and L5–S1,  $n = 38$ ) and 9 cervical disk herniations (C4–C5,  $n = 2$ ; C5–C6,  $n = 2$ ; C6–C7,  $n = 3$ ; and C7–D1,  $n = 2$ ) by percutaneous intradiskal injection of radiopaque gelified ethanol under fluoroscopic guidance. Thirty-six patients underwent a simultaneous treatment of 2 disk herniations. Patient symptoms were resistant to conservative therapy, with little or no pain relief after 4–6 weeks of physical therapy and drugs. All patients were evaluated by the Visual Analog Scale and the Oswestry Disability Index.

**RESULTS:** Sixty-two of 73 (85%) patients with lumbar disk herniations and 6/7 (83%) patients with cervical disk herniations obtained significant symptom improvement, with a Visual Analog Scale reduction of at least 4 points and an Oswestry Disability Index reduction of at least 40%. Leakage of radiopaque gelified ethanol in the surrounding tissues occurred in 19 patients, however without any clinical side effects.

**CONCLUSIONS:** In our experience, percutaneous intradiskal injection of radiopaque gelified ethanol is safe and effective in reducing the period of recovery from disabling symptoms.

**ABBREVIATIONS:** CDH = cervical disk herniation; LDH = lumbar disk herniation; ODI = Oswestry Disability Index; RGE = radiopaque gelified ethanol; VAS = Visual Analog Scale

Cervical disk herniation (CHD) and lumbar disk herniation (LDH) generally have a favorable natural history, often with long-term resolution of symptoms.<sup>1,2</sup> However, pain can be debilitating, resulting in long absences from work or daily activities. Treatment is targeted at reducing both symptoms and the patient's recovery time. The first therapeutic approach is usually pharmacologic and physical; however, the clinical condition may not improve within a reasonable time.<sup>1</sup>

Chemonucleolysis is a minimally invasive percutaneous technique allowing intradiskal injection of various materials under fluoroscopic or CT guidance, to “digest” or dehydrate disk portions. Materials include chymopapain,<sup>3</sup> now abandoned because of frequent allergic reactions,<sup>4</sup> and oxygen-ozone,<sup>5</sup> whose results have still not been completely demonstrated. Recently, a newly developed substance, radiopaque gelified ethanol (RGE), has been introduced into clinical practice.<sup>6–10</sup> RGE is a viscous solution containing ethyl alcohol and cellulose derivative products associated with a contrast agent (tungsten). Clinical outcomes seem to be encouraging, with a high reduction of possible collateral effects.<sup>4</sup> The purpose of this article is to describe the results of our study in percutaneous intradiskal injection of RGE for CDH and LDH.

## MATERIALS AND METHODS

### Population

Between September 2010 and August 2013, 80 patients (32 women and 48 men; age range, 18–75 years) were treated for 107 LDHs (L2–L3,  $n = 1$ ; L3–L4,  $n = 15$ ; L4–L5,  $n = 53$ ; and L5–S1,

Received July 7, 2014; accepted after revision September 6.

From the Neuroimaging and Neurointerventional Unit - NINT (M.B., D.G.R., S.L., M.F., L.M., A.C.) and Unit of Neurology (P.P.), Department of Neurological and Neurosensory Sciences, Hospital “Santa Maria alle Scotte,” Siena, Italy; Department of Medical, Surgical and Neuro Sciences, Diagnostic Imaging (I.G.), University of Siena, Siena, Italy; and Unit of Radiology (C.T.), Hospital of Arzignano, Vicenza, Italy.

There has not been any financial support from commercial sources or pecuniary interest in such enterprises that could pose a conflict of interest, including consultations for any product or process mentioned in the submission.

Please address correspondence to Matteo Bellini, MD, Azienda Ospedaliera Universitaria Senese, Uoc NINT Neuroimmagini e Neurointerventistica, Viale Bracci n.16, 53100 Siena, Italy; e-mail: matteo.bellini@icloud.com

<http://dx.doi.org/10.3174/ajnr.A4166>

$n = 38$ ), and 9, for CDH (C4–C5,  $n = 2$ ; C5–C6,  $n = 2$ ; C6–C7,  $n = 3$ ; and C7–D1,  $n = 2$ ) by percutaneous intradiskal injection of RGE. This retrospective evaluation of clinical and neuroradiologic data was in accordance with the rules of local institutional review boards.

### Indications

Treatment was reserved for patients with recurrent drug-resistant neck or low back pain with brachialgia or sciatica (also incomplete) and no or minimal pain reduction after 4–6 weeks of physical therapy including resistive capacitive energy transfer, clinical neurodynamics, manual therapy, and global postural re-education. Clinical evaluation included Lasègue, Slump, and Wassermann tests.

Sixty-seven patients underwent MR imaging; 13 patients underwent CT due to contraindications or claustrophobia. All patients with LDH showed at least 1 disk herniation at a metameric level consistent with symptoms. All patients with CDH and 18 with LDH underwent electromyography because of multiple disk herniations and uncertainty of the disk to be treated.

Inclusion criteria were disk herniations contained, without complete annulus tear, and not contained, with posterior longitudinal ligament integrity and no free fragments assessed with MR imaging<sup>11</sup> or CT. Because of the risk of adhesions or epidural fibrosis, treatment was not performed in patients who had already undergone surgery at a clinical symptom level, with the exception of 1 patient with a recurrent LDH in whom gadolinium-enhanced MR imaging ruled out fibrous scar tissue.

Exclusion criteria were high disk degeneration (ie, the so-called “black disk” or a disk height loss of more than two-thirds), free isolated disk herniation fragments, stenosis of the intervertebral foramina or spinal canal, asymptomatic disk bulging, primary tumor or metastatic disease involving the level to be treated, active local or systemic infections, pregnancy, hemorrhagic diathesis, and anticoagulant therapy if not stopped before surgery.

CDHs were treated after neck color Doppler sonography, to rule out any anatomic variations or abnormalities of vessels, trachea, or esophagus.

All patients provided informed consent on the day before the procedure.

### Procedure

Treatment was performed with the patient under local anesthesia, in “day-surgery” (71 patients) or short hospitalization (9 patients) regimens. If the patient was under antiplatelet or anticoagulant therapy, this was stopped 6 days before the procedure and converted to subcutaneous low-molecular-weight heparin.

Intravenous injection of short-term broad-spectrum antibiotic therapy including 2 g of amoxicillin/clavulanic acid (Augmentin) or 1 g of ceftriaxone disodium (Sirtap) was performed immediately before the procedure. Local anesthesia was by subcutaneous lidocaine 2% (SELF SpA). Fluoroscopic guidance was by a digital biplanar rotational angiography (Innova 3131IQ; GE Healthcare, Milwaukee, Wisconsin). Under a sterile surgical regimen, a percutaneous approach was performed by using a spinal-type 20-ga needle (Spinocan; B. Braun Melsungen, Melsungen, Germany) for CDH and a Chiba 18-ga needle included in the RGE

kit (DiscoGel; Gelscom SAS, Caen, France) for LDH. Needle insertion was monitored by fluoroscopic anteroposterior and lateral projections.

Patients with CDH were placed in a supine position, with a hyperextended neck. A right paravertebral approach was preferred due to a greater risk of esophageal lesions by a left approach. Lidocaine 2% (1–2 mL) was injected in the superficial subcutaneous tissue. Medial to the right sternocleidomastoid muscle, the operator exerted sufficient pressure with the index and middle fingers of the left hand on the neck for lateral displacement of the common carotid artery and internal jugular vein, pushing the skin as close as possible to the intervertebral space, thus minimizing the needle tract and making the needle entry site “safe.” Once penetrating the annulus, the needle was advanced until it reached the central portion of the disk.

Patients with LDH were placed in a prone position, usually by positioning an air-inflated cushion under the abdomen, to reduce the lumbar lordosis. Lidocaine 2% (5–10 mL) was injected subcutaneously. The approach to the disks between L1 and L5 was posterior paravertebral, ipsilateral to the symptomatic side. Anatomic landmarks were identified by a 45° lateral oblique projection, following the “scotty dog” technique. A Chiba needle was introduced at a paramedian entry point, 8–10 cm from the midline; it was directed parallel to the intervertebral space and anterior to the superior articular process (ie, “scotty dog” ear), to avoid puncturing the nerve root. The approach to the L5–S1 disk was technically more complex and partially limited by the iliac wing. At 45°, the needle was positioned with a high cranial C-arm inclination, tilted obliquely toward a narrow triangular area realized by the radiologic overlap of some skeletal structures, including the iliac wing, sacral wing, and corresponding superior articular process.

Intradiskal advancement of the needle was monitored by anteroposterior and lateral projections, because the tip has to reach the central portion of the nucleus pulposus. Crossing the annulus may result in a mild, hard elastic resistance, with possible patient’s pain sensation, because it represents the only innervated zone. In all the LDHs, a mixture of triamcinolone acetonide (Triamvirgi) and ropivacaine HCl (Naropin) was injected near the nerve root, as a pharmacologic blockade, just before needle entrance in the disk.

### Preparation and Injection of RGE

Inside its container, RGE is an attenuated liquid, which must be accurately shaken before being injected. The RGE solution should be injected slowly under continuous fluoroscopic guidance to check for extradiskal leakage (Fig. 1). The recommended dose is 0.8 mL for lumbar disks and 0.2 mL for cervical disks.

CT targeted to the treatment site was performed after the procedure in all the patients, with the exception of a young woman for radioprotection; this procedure was to verify the RGE distribution and rule out extradiskal leakage.

### Clinical Monitoring

All patients were given the Visual Analog Scale (VAS) preoperatively and immediately after the treatment and 3 months later and a questionnaire concerning the quality of life based on the Os-

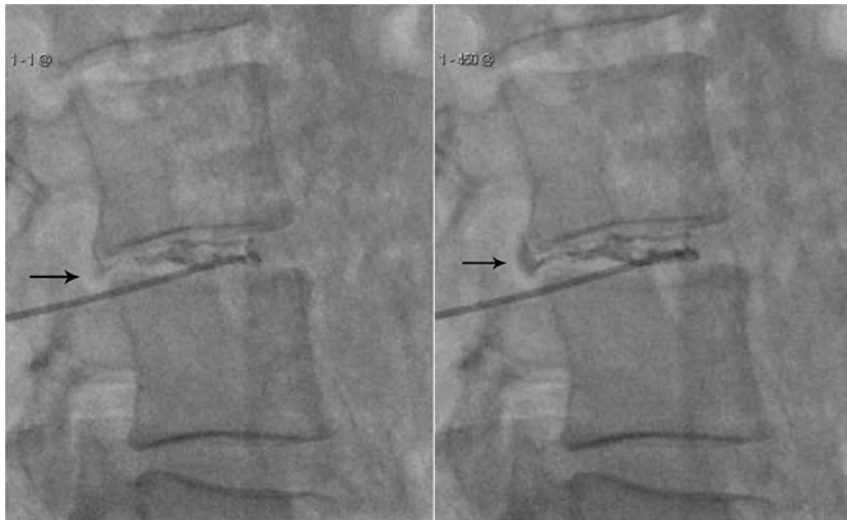


**FIG 1.** Progressive intervertebral disk filling of RGE. Real-time fluoroscopic images showing RGE inside the nucleus pulposus and in the herniated disk (arrows). Tungsten allows proper visualization of the material, including monitoring of possible leakage.

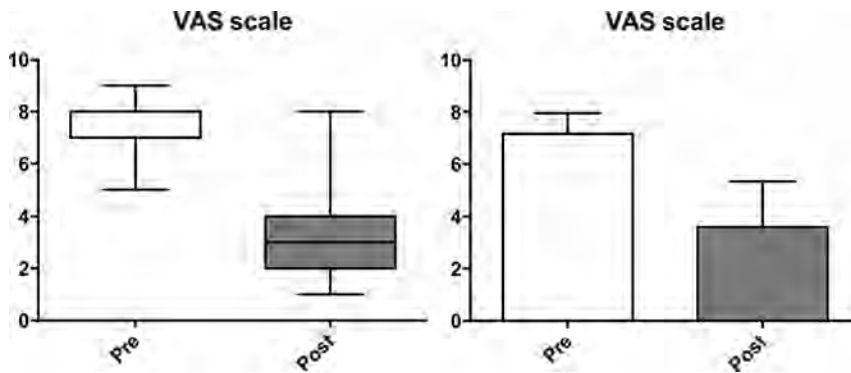


**FIG 2.** VAS scores recorded before and after percutaneous intradiscal injection of RGE. The left panel displays the boxplot of the data. Before treatment, the VAS scores were mostly concentrated on the upper values of the scale (median = 7; 25th percentile = 7; 75th percentile = 8); therefore, this distribution was negatively skewed (skewness =  $-0.29$ ). The distribution of the VAS scores in the posttreatment survey (median = 3; 25th percentile = 2; 75th percentile = 4) became positively skewed (skewness =  $0.91$ ). No outliers were identified. The reduction of 4 points in the median of the VAS scores between pre- and posttreatment was significant for the nonparametric Wilcoxon matched-pairs signed rank test ( $W = -3076$ ;  $P < .0001$ ). The barplots in the right panel show the means and SDs of the data. The decrease of the means of the VAS scores from  $7.16 \pm 0.79$  to  $3.61 \pm 1.72$  was significant under the paired  $t$  test with 78  $df$  ( $t = 17.61$ ;  $P < .0001$ ).

westry Disability Index (ODI)<sup>12</sup> before treatment and 3 months later.

### Statistical Analysis

Analysis was performed on the VAS and ODI score values collected from all patients before treatment and at the 3-month follow-up. Their descriptive statistics such as mean, SD, median, and interquartile range are shown in Figs 2 and 3. To detect statistically significant change of the VAS and ODI in the posttreatment period compared with the pretreatment one, we used a paired  $t$  test and Wilcoxon matched-pairs signed rank test. The null hypothesis of no difference between observed values before and after the treatment was then assumed for each series of scores. The series of ODI scores were labeled according to the canonical standing<sup>12</sup> and then cross-tabulated to represent the pre- to posttreatment

transition. In correspondence to each rank detected before RGE injection and the percentage of the patients who have recovered after the treatment, the best rank (ie, minimal disability with the ODI score not  $>20\%$ ) was calculated.

Statistical analysis was assessed by commercial software (GraphPad Prism; GraphPad Software, San Diego, California; and Matlab; MathWorks, Natick, Massachusetts).

### RESULTS

Thirty-four patients with LDH and 2 with CDH underwent simultaneous treatment of 2 disks. Seven patients with large LDHs either not contained or migrated were selected for RGE (Fig. 4).

Treatment was technically successful in all patients for all the 116 disk herniations (Figs 4 and 5). The procedure for a single disk required no more than 10–12 minutes from anesthesia to the end of the RGE injection. No relevant complications related to treatment occurred in any patient. There were no allergic reactions to RGE or other drugs. There were no cases of local or systemic iatrogenic infection.

Eight patients with LDH presented with temporary pain during treatment, locally or at the lower limb ipsilateral to the treated level, caused by passage of the needle close to a nerve root or during penetration of the annulus. In all these cases, symptoms resolved spontaneously a few minutes after treatment.

Postoperative CT showed a subtle extradiscal leakage of RGE in 14 patients with LDH (epidural,  $n = 2$ ; periradicular space,  $n = 4$ ; and posterior muscle tissues,  $n = 10$ ). None reported any symptoms. In 62 (85%) of the 73 patients treated for LDH and in 6 (83%) of the 7 patients treated for CDH, there was relevant pain reduction, usually within the first month after the procedure.

Statistical analysis indicated a significant difference in the scores between pre- and posttreatment conditions (Figs 2 and 3).

The mean decrease of the VAS index was  $-3.557$  with a 95% confidence interval, 3.959 to  $-3.155$ . The mean decrease of the ODI score was 30.38 with a 95% confidence interval, 33.79 to  $-26.96$ .

The percentage of success was  $>75\%$  in the class of severe disability. Even 2 subjects in the sample with crippling back pain regained the minimal disability class. A reduction of at least 4 points in the VAS scale ( $P < .0001$ ) and at least 40% in the ODI score ( $P < .0001$ ) (Fig 2) occurred in the first 2 months after

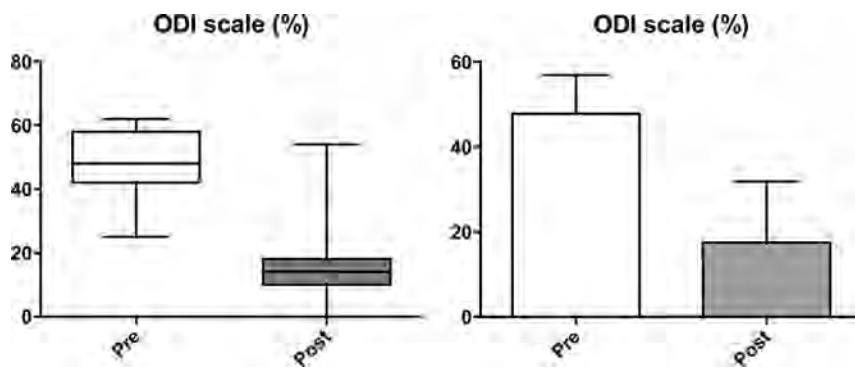


**FIG 3.** ODI scores recorded before and after percutaneous intradiscal injection of RGE. The index is expressed in percentage points and ranges from 0% to 100%. The lower limit corresponds to the absence of disability; the upper limit, to the maximum degree of disability (patients are bed-bound). The left panel displays the boxplot of the data. Before treatment, the distribution of ODI scores (median = 48%; 25th percentile = 42%; 75th percentile = 58%) was slightly negatively skewed (skewness =  $-0.05$ ), and it became positively skewed (skewness =  $1.21$ ) in the posttreatment survey (median = 14%; 25th percentile = 10%; 75th percentile = 18%). No outliers were identified. Between the pre- and posttreatment periods, the medians of the VAS scores dropped by 34 percentage points. This decline was significant for the nonparametric Wilcoxon matched-pairs signed rank test ( $W = -3076$ ;  $P < .0001$ ). The barplots in the right panel show the means and SDs of the data. The decrease of the mean of the ODI scores from  $47.85 \pm 9.05$  to  $17.47 \pm 14.41$  was significant with the paired  $t$  test with 78  $df$  ( $t = 17.71$ ,  $P < .0001$ ).

treatment in 64 (80%) patients and by the third month for the remaining 4 (5%) patients who presented with large disk herniations, extruded or migrated (Fig 4). The patients reporting improvement resumed their normal activities within 1–3 months after treatment.

Twelve patients did not obtain relevant pain reduction within 6 months following treatment. Four underwent surgical discectomy; the remaining 8 underwent other percutaneous treatments ( $n = 6$ ) or tried other conservative therapy ( $n = 2$ ), including anesthesiologist pain management.

## DISCUSSION

DiscoGel (RGE) is a chemonucleolytic agent introduced for the first time in 2007 by Theron et al,<sup>6</sup> containing ethyl alcohol, a cellulose derivative product, added to a radiopaque element (tungsten), causing dehydration of the nu-

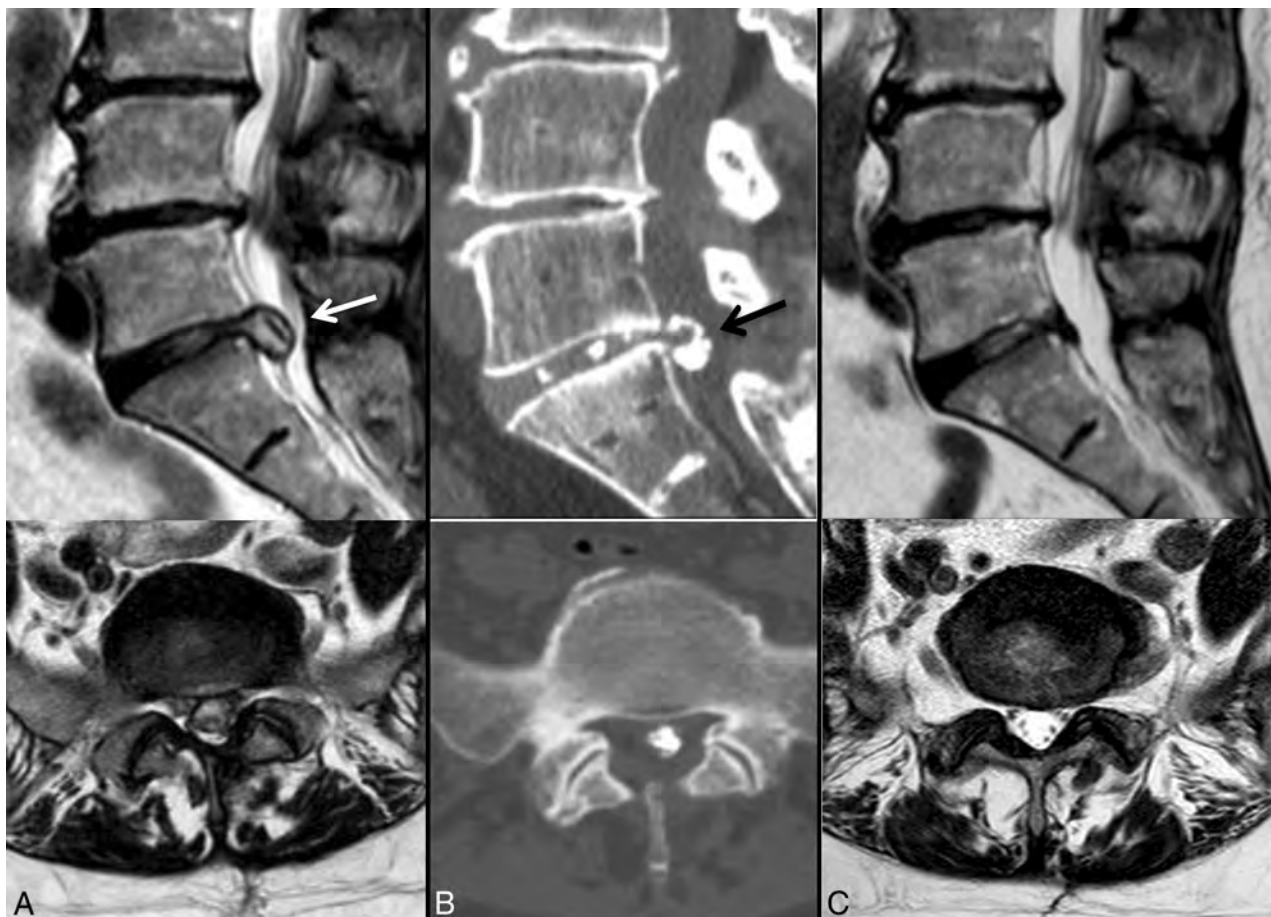


**FIG 4.** Treatment of a very large extruded LDH in a 58-year-old woman with left sciatica (VAS = 8). A, In a preoperative MR imaging study, sagittal and axial T2 sequences show a large uncontained and partially migrated disk herniation at L5–S1 (median left posterolateral), with considerable root involvement (white arrow). B, CT control shows the optimal distribution of RGE in a disk herniation without leakage (black arrow). The patient did not have significant symptoms (VAS = 3). C, MR imaging study obtained 6 months later shows complete dehydration and retraction of disk herniation. The patient was completely asymptomatic (VAS = 0).

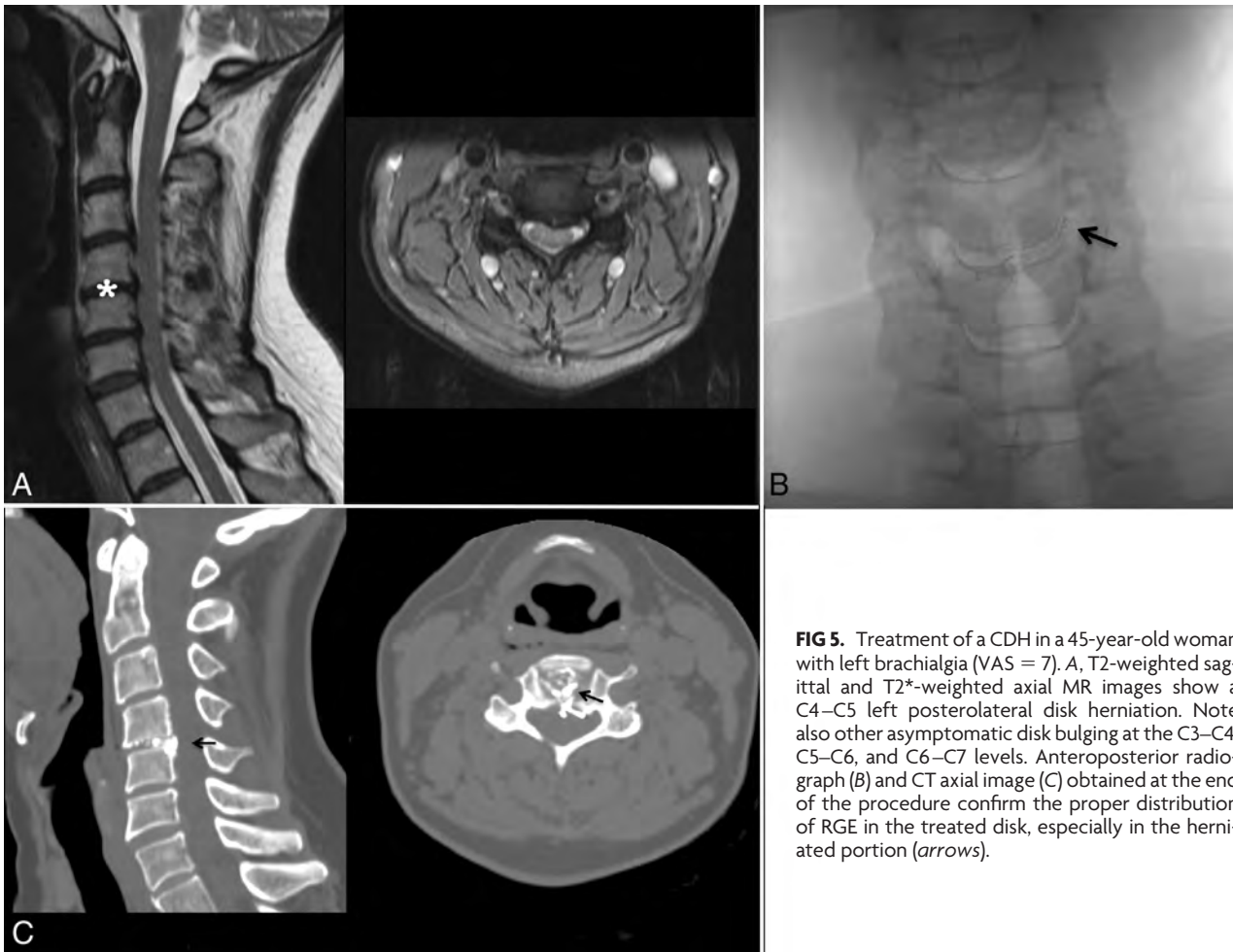


**FIG 5.** Treatment of a CDH in a 45-year-old woman with left brachialgia (VAS = 7). A, T2-weighted sagittal and T2\*-weighted axial MR images show a C4–C5 left posterolateral disk herniation. Note also other asymptomatic disk bulging at the C3–C4, C5–C6, and C6–C7 levels. Anteroposterior radiograph (B) and CT axial image (C) obtained at the end of the procedure confirm the proper distribution of RGE in the treated disk, especially in the herniated portion (arrows).

nucleus pulposus and resulting in disk herniation retraction. In LDH, Volpentesta et al<sup>10</sup> reported excellent and good results in 80.4% of 72 patients, despite complications in 5.45%. Theron et al<sup>6</sup> reported a success rate of 91.4% in a group of 221 patients and a complication rate of <0.5%, while Stagni et al<sup>8</sup> achieved a therapeutic success in 24 of 32 treated patients (75%) without complications. In CDHs, Theron et al<sup>7</sup> reported a success rate of 89.5% in 57 patients without complications.

Our experience has the following considerations.

Percutaneous intradiscal injection of RGE was simple and rapid, due to a biplanar digital rotational angiographic suite, which allowed an easier needle insertion, especially for CDH. The procedure can also be executed by CT or CT fluoroscopy; however, the advantages of fluoroscopic guidance are known and include rapidity, real-time evaluation of RGE distribution and possible leakage, and dose reduction.

In both LDH and CDH, we had no complications. Discomfort was minimal for most patients. They were questioned at the end of treatment and reported tolerating the procedure well. Even patients treated for CDH did not experience perceptible discomfort during the procedure, despite the lower amount of local anesthetic injected only at skin surface. Pain was greater in subjects with osteophytes or with a greatly reduced intervertebral space, making the needle insertion more complex, especially at the L5–S1 level.

We did not treat free fragments or highly degenerated disks.

Free fragments were separated from the disk and could not be reached by RGE injection. Highly degenerated disks, or “black disk” according to grade V of the Pfirrmann classification, are collapsed, without distinction between the nucleus and annulus, and are associated with reduced positive prognosis due to severe morphostructural changes.<sup>13</sup> Moreover, RGE may result in further disk thinning due to its chemonucleolytic effects. Additionally, we think that the gelling effect is reduced in highly degenerated disks because this process is directly correlated to the presence of water in the nucleus pulposus. In “black disks,” radicular pain may also be related to marked reduction of the foraminal space in association with disk calcification and/or bulging or osteophytes. Thus, we usually prefer to perform a periradicular and intradiscal steroid and anesthetic injection and/or to propose an interspinous spacer implant.

We did not perform pretreatment diskography because an iodinated contrast agent may limit proper visualization of RGE, and RGE contacting fluids immediately gels, with the risk of occluding the needle or inducing a rapid premature gelling effect in the disk. Diskography has been performed before pure ethanol injection because of the relative difficulty in the control of its diffusion and leakage. RGE, instead, makes the alcohol solution much easier to handle and reduces the need for diskography.<sup>8</sup> Notably, even in the largest herniations that are potentially “surgical,” we did not consider the annulus integrity necessary, because RGE can spread

to the more isolated disk compartments, leading to good results. In this subset of patients, the results have been encouraging, with convincing symptom improvement. Instead, verifying the annulus integrity is a critical factor in other percutaneous techniques, including mechanical or thermal decompression: These techniques are based on the principle of obtaining an annulus elastic return, especially at the herniated portion. This is possible only for contained disk herniations without an annulus tear.

The recommended dose of RGE is 0.8 mL for LDH and 0.2 mL for CDH. In CDH, the maximum recommended dose was always injected without leakage. In LDH, the amount ranged from 0.5 mL to 0.8 mL, depending on the disk space amplitude and relative disk capacity to accommodate the RGE and to avoid important leakages. We always stopped injection at the observation of initial epidural or foraminal space leakage. It is also important to avoid any possible irritative effect on soft paravertebral tissues, though it is well-demonstrated that no morphostructural changes were caused by intradiscal, intraforaminal, and epidural RGE.<sup>14</sup>

Technically, >2 levels could be treated in the same session, in the absence of specific recommendations by the manufacturer. Three treated levels in a patient but in 2 separate sessions have been recently reported.<sup>10</sup> Currently, the literature does not report a case of 4 disks treated. The main reasons are that most patients would not tolerate a simultaneous multilevel treatment in the same procedure, and an increased number of treated levels would heighten the risk of complications and exposure to x-rays for both patient and operator. Additionally, preliminary clinical and neuroradiologic evaluation in most cases established the levels to be treated. Finally, we agree with those authors<sup>10</sup> who propose treating >2 levels in different sessions, to verify whether the first treatment was the most appropriate.

RGE leakage occurred in extradiscal tissues, in the epidural space, or in the periradicular space, after LDH treatment; this was caused by reflux through the trajectory of the needle. It has been asymptomatic and reported by other authors.<sup>14</sup> In daily clinical practice, we agree to propose follow-up CT only in patients with unchanged or worsening symptoms, to better understand the RGE distribution.

In most patients, clinical improvement occurred during the first month after treatment. Improvement occurred earlier in CDH than in LDH, despite the lower amount of drugs. In LDH, patients with a faster reduction in symptoms were those with a single herniation and treated at the L4–L5 or L5–S1 levels without other associated factors (ie, canal or foramina stenosis). Only in cases of larger and extruded herniated disks and in recurring herniation did improvement take longer (approximately 3 months).

Clinical benefits could be partially due to the gelling effect of RGE that, spontaneously engaging the herniation breach, should prevent a greater disk excursion under axial loading. This hypothesis might be demonstrated by pre- and postoperative orthostatic spinal MR imaging.<sup>15</sup> Possible, but not proved, is the potential effect of ethanol on the reduction of local inflammatory mechanisms generated by the herniation itself (ie, mediated by the release of cytokines and other endogenous substances). This may affect, in part, the favorable development of such treatment clinically.<sup>1</sup>

In Europe, the cost of RGE is higher than that of other chemonucleolytic agents, like oxygen-ozone; however, it is similar to

that of nucleoplasty or decompressive treatment. In our hospital, the cost is less than a third of that of a single-level surgical discectomy. Additionally, compared with surgery, percutaneous RGE may take only 1 day of hospitalization.

## CONCLUSIONS

In our experience, percutaneous RGE for the treatment of CDH and LDH was safe and reduced morbidity, with good clinical results (in some cases even in the very early stages after the treatment). Due to its minimally invasive nature, this technique reduced the recovery period from the disabling symptoms typical of disk herniations.

## ACKNOWLEDGMENTS

We thank Prof. Alessandro Rossi, chief of the Neurologic and Neurosensorial Sciences Department (“Santa Maria alle Scotte” University Hospital, Siena, Italy), for his invaluable help and comments.

Disclosures: Alfonso Cerase—UNRELATED: Board Membership: *Journal of Pediatric Neuroradiology* (editorial board).

## REFERENCES

1. Benoit M. **The natural history of lumbar disc herniation and radiculopathy.** *Joint Bone Spine* 2002;69:155–60
2. Bozzao A, Gallucci M, Masciocchi C, et al. **Lumbar disk herniation: MR imaging assessment of natural history in patients treated without surgery.** *Radiology* 1992;185:135–41
3. Nordby EJ, Wright PH. **Efficacy of chymopapain in chemonucleolysis: a review.** *Spine (Phila Pa 1976)* 1994;19:2578–83
4. Sussman BJ. **Inadequacies and hazards of chymopapain injections as treatment for intervertebral disc disease.** *J Neurosurg* 1975;42:389–96
5. Muto M, Andreula C, Leonardi M. **Treatment of herniated lumbar disc by intradiscal and intraforaminal oxygen-ozone (O2–O3) injection.** *J Neuroradiol* 2004;31:183–89
6. Theron J, Guimaraens L, Casasco A, et al. **Percutaneous treatment of lumbar intervertebral disk hernias with radiopaque gelified ethanol: a preliminary study.** *J Spinal Disord Tech* 2007;20:526–32
7. Theron J, Cuellar H, Sola T, et al. **Percutaneous treatment of cervical disk hernias using gelified ethanol.** *AJNR Am J Neuroradiol* 2010;31:1454–56
8. Stagni S, de Santis F, Cirillo L, et al. **A minimally invasive treatment for lumbar disc herniation: DiscoGel® chemonucleolysis in patients unresponsive to chemonucleolysis with oxygen-ozone.** *Interv Neuroradiol* 2012;18:97–104
9. de Sèze M, Saliba L, Mazaux JM. **Percutaneous treatment of sciatica caused by a herniated disc: an exploratory study on the use of gaseous discography and Discogel® in 79 patients.** *Ann Phys Rehabil Med* 2013;56:143–54
10. Volpentesta G, De Rose M, Bosco D, et al. **Lumbar percutaneous intradiscal injection of radiopaque gelified ethanol (“Discogel”) in patients with low back and radicular pain.** *J Pain Relief* 2014;3:145
11. Oh KJ, Lee JW, Yun BL, et al. **Comparison of MR imaging findings between extraligamentous and subligamentous disk herniations in the lumbar spine.** *AJNR Am J Neuroradiol* 2013;34:683–87
12. Fairbank JC, Pynsent PB. **The Oswestry Disability Index.** *Spine (Phila Pa 1976)* 2000;25:2940–52; discussion 2952
13. Mwale F, Iatridis JC, Antoniou J. **Quantitative MRI as a diagnostic tool of intervertebral disc matrix composition and integrity.** *Eur Spine J* 2008;17(suppl 4):432–40
14. Guarneri G, De Dominicis G, Muto M. **Intradiscal and intramuscular injection of Discogel®: radiopaque gelified ethanol—pathological evaluation.** *Neuroradiology J* 2010;23:249–52
15. Tarantino U, Fanucci E, Iundusi R, et al. **Lumbar spine MRI in upright position for diagnosing acute and chronic low back pain: statistical analysis of morphological changes.** *J Orthop Traumatol* 2013;14:15–22

# T1 $\rho$ and T2 Mapping of the Intervertebral Disk: Comparison of Different Methods of Segmentation

R. Menezes-Reis, C.E.G. Salmon, C.S. Carvalho, G.P. Bonugli, C.B. Chung, and M.H. Nogueira-Barbosa



## ABSTRACT

**BACKGROUND AND PURPOSE:** Intervertebral disk biochemical composition could be accessed in vivo by T1 $\rho$  and T2 relaxometry. We found no studies in the literature comparing different segmentation methods for data extraction using these techniques. Our aim was to compare different manual segmentation methods used to extract T1 $\rho$  and T2 relaxation times of intervertebral disks from MR imaging. Seven different methods of partial-disk segmentation techniques were compared with whole-disk segmentation as the reference standard.

**MATERIALS AND METHODS:** Sagittal T1 $\rho$  and T2 maps were generated by using a 1.5T MR imaging scanner in 57 asymptomatic volunteers 20–40 years of age. Two hundred eighty-five lumbar disks were separated into 2 groups: nondegenerated disk (Pfirrmann I and II) and degenerated disk (Pfirrmann III and IV). In whole-disk segmentation, the disk was segmented in its entirety on all sections. Partial-disk segmentation methods included segmentation of the disk into 6, 5, 4, 3, and 1 sagittal sections. Circular ROIs positioned in the nucleus pulposus and annulus fibrosus were also used to extract T1 $\rho$  and T2, and data were compared with whole-disk segmentation

**RESULTS:** In the nondegenerated group, segmentation of  $\geq 5$  sagittal sections showed no statistical difference with whole-disk segmentation. All the remaining partial-disk segmentation methods and circular ROIs showed different results from whole-disk segmentation ( $P < .001$ ). In the degenerated disk group, all methods were statistically similar to whole-disk segmentation. All partial-segmentation methods, including circular ROIs, showed strong linear correlation with whole-disk segmentation in both the degenerated and nondegenerated disk groups.

**CONCLUSIONS:** Manual segmentation showed strong reproducibility for T1 $\rho$  and T2 and strong linear correlation between partial- and whole-disk segmentation. Absolute T1 $\rho$  and T2 values extracted from different segmentation techniques were statistically different in disks with Pfirrmann grades I and II.

**ABBREVIATIONS:** AAF = anterior annulus fibrosus; AF = annulus fibrosus; CROI = circular ROIs; ICC = intraclass correlation coefficient; NP = nucleus pulposus; PAF = posterior annulus fibrosus; PDS = partial-disk segmentation; WDS = whole-disk segmentation

MR imaging is considered the best noninvasive method to study intervertebral disks. MR imaging allows the visualization of clearly different anatomic disk subregions, including the nucleus pulposus (NP) and the annulus fibrosus (AF).<sup>1,2</sup> However, routine clinical images provide a qualitative or semiquantitative assessment made by an expert.<sup>3</sup> The need for a better understanding of physiologic and pathologic processes in the disk

led to the application of quantitative techniques in MR imaging such as T1 $\rho$  and T2 mapping.<sup>3,4</sup>

For the extraction of quantitative data from a given region of interest, it is necessary to perform segmentation procedures that involve selecting the region to be analyzed.<sup>5</sup> This segmentation can be manual, semiautomatic, or automatic. In studies assessing the lumbar intervertebral disk composition, different authors used different methods to perform disk segmentation with subsequent data extraction. The most common method in the literature with regard to T1 $\rho$  and T2 is to acquire small regions of interest that are anatomically based.<sup>6–9</sup> Authors have used standard ROIs, delineating subregions within the intervertebral disk to extract quantitative data specifically from the NP and AF.<sup>6,7</sup> Additional intermediate ROIs on boundaries between the nucleus and annulus have also been used.<sup>8,9</sup> In the latter, intermediate ROIs were implemented to compensate for the increased steps for segmentation in each image. These studies analyzed a limited

Received June 30, 2014; accepted after revision August 15.

From the Division of Radiology (R.M.-R., G.P.B., C.S.C., M.H.N.-B.), Ribeirão Preto Medical School, and Department of Physics (C.E.G.S.), Ribeirão Preto Philosophy and Sciences School, University of São Paulo, São Paulo, Brazil; and Department of Radiology (C.B.C.), VA San Diego Healthcare System, San Diego, California.

Please address correspondence to Rafael Menezes-Reis, MD, Radiology Division, Ribeirão Preto Medical School, University of São Paulo–USP, Av Bandeirantes, 3900, Ribeirão Preto, São Paulo, Brazil, 14049-090; e-mail: rafaelmenezesreis@gmail.com

Indicates open access to non-subscribers at www.ajnr.org

<http://dx.doi.org/10.3174/ajnr.A4125>

number of MR imaging sections. The segmentation using a few MR imaging sections and regional ROIs allows the extraction of data more quickly than segmenting the whole intervertebral disk. Other authors chose to perform the segmentation of the disk as a whole, with the region of interest covering the NP and AF simultaneously.<sup>10,11</sup> The use of segmentation of only the central MR imaging sagittal section to extract quantitative data from the intervertebral disk is also very common in the literature.<sup>12,13</sup>

The intervertebral disk structure is nonuniform with differences in hydration and collagen content between NP and AF. Therefore, the extraction of different T1 $\rho$  and T2 relaxation times may be expected depending on the segmentation method used.<sup>10,14</sup> Despite the potential importance of using different segmentation methods in the evaluation of the intervertebral disk composition, we have not found studies comparing the accuracy, reliability, and reproducibility of the results generated by different segmentation methods. Our hypothesis is that partial segmentation of intervertebral disks, especially through standard geometric regional ROIs, will result in the extraction of different T1 $\rho$  and T2 relaxation times compared with full segmentation.

## MATERIALS AND METHODS

### Population Sample

This study was approved by the institutional review board. The volunteers were recruited through institutional review board–approved local advertisement and were selected on the basis of the inclusion criteria. We recruited 57 asymptomatic adults (25 men and 32 women), with a mean age of 26.54  $\pm$  5.0 years (range, 20–40 years); mean height, 1.69  $\pm$  0.08 m (1.53–1.90 m); mean weight, 67.52  $\pm$  13.85 kg (range, 46.5–105 kg); and mean body mass index, 23.5  $\pm$  3.4 kg/m<sup>2</sup> (range, 15.9–30.3 kg/m<sup>2</sup>). The inclusion criteria for the volunteers were the following: 20–40 years of age with an Oswestry Dysfunction Index score <10. Volunteers with persistent low back pain for at least 6 months; an Oswestry Dysfunction Index score >10; or previous spinal pathology, significant scoliosis, or surgery were excluded from the study.

All 5 lumbar disks of the 57 volunteers were studied; therefore, we evaluated 285 disks. The intervertebral disks were graded according to the Pfirrmann et al classification.<sup>14</sup> After classification by the Pfirrmann grading system, we divided the intervertebral disks into 2 subgroups: nondegenerated (grades I and II) = 224 disks and degenerated (grades III and IV) = 61 disks. In our sample, we found no grade V intervertebral disks according to the Pfirrmann et al classification.

### MR Imaging

All MR imaging examinations were performed by using a 1.5T scanner (Achieva; Philips Healthcare, Best, the Netherlands). We used a 16-channel spine coil (SENSE-SPINE; Philips). Volunteers were kept still in a supine position with the lower limbs extended and relaxed. The study protocol included a 2D fast spin-echo sequence with the following characteristics: orientation = sagittal, FOV = 22  $\times$  22 cm, thickness = 4 mm, number of sections = 16, matrix = 256  $\times$  256 and no intersection gap. For the segmentation process, we acquired a T2-weighted sagittal sequence, with TE = 120 ms and TR = 3900 ms. Spin-echo sequences were acquired to generate quantitative T1 $\rho$  and T2 maps. We used the

following parameters—T2 multiecho sequence: TE = 20/40/60/80/100/120/140/160 ms and TR = 3000 ms; T1 $\rho$  multilocker times sequence: TE = 20 ms, TR = 2000 ms, Tlock = 2/10/20/40/60 ms. The total MR imaging acquisition time was 13 minutes.

### Image Evaluation

The Display software (McConnell Brain Imaging Center, Montreal, Quebec, Canada) was used for image analysis and segmentation. The segmentation process was performed on the sagittal plane according to the illustrations in Figs 1 and 2. The segmentation of 285 disks was performed by 2 independent and blinded observers, taking care not to include regions of subchondral bone. They were previously trained for 2 months in manual spinal MR imaging segmentation and were supervised by a senior radiologist with 15 years' experience in musculoskeletal radiology and spine MR imaging. First, full manual segmentation of the whole intervertebral disk, encompassing NP and AF, for each disk in all 12 sections was performed for all lumbar disks of each volunteer (whole-disk segmentation [WDS]). Partial-disk segmentation (PDS) methods were performed by using 6 different techniques according to the illustration in Fig 1 by using the following: 6 sections (PDS-6), 5 sections (PDS-5A and PDS-5B), 4 sections (PDS-4), 3 sections (PDS-3), and only 1 central section (PDS-1). Extraction of T1 $\rho$  and T2 relaxation times was also performed by using 3 circular ROIs (CROI) placed on the NP, anterior annulus fibrosus (AAF), and posterior annulus fibrosus (PAF) by using 3 distinct sagittal sections as shown in Fig 2. The most central region of the NP was marked by using a region of interest with an area of 26.77 mm<sup>2</sup>. This region was labeled regardless of the presence or absence of a nuclear cleft. ROIs with 12.75 mm<sup>2</sup> each were used in the regions of AAF and PAF. We placed ROIs on the most anterior and posterior regions of the annulus, avoiding selecting the transition regions between the AF and NP.

The main researcher was the first observer, responsible for the segmentation of all 285 lumbar disks. One hundred disks were randomly selected for intra- and interobserver reproducibility analysis, 50 from the degenerated group and 50 from the nondegenerated group. These disks were segmented a second time by the first and second observer with an interval of 2 months after the first segmentation.

### Statistical Analysis

The analysis of intra- and interobserver variability was performed by the intraclass correlation coefficient (ICC) with 99% confidence intervals for all lumbar levels.

To analyze the distribution of T2 and T1 $\rho$  relaxation times, the Shapiro-Wilk test (99% significance level) was used for each segmentation method. The WDS was chosen as the reference standard with which all PDS methods and CROI were compared. Repeated-measures ANOVA with the Dunnett posttest was used for parametric samples. For the nonparametric samples, we used the Friedman test with the Dunn posttest. *P* values < .05 were statistically significant. We also performed a linear regression and correlation to verify that the relaxation times of partial segmentation methods showed a linear relationship to the WDS values. For statistical analysis and for the creation of graphs and tables, we used GraphPad Prism software, Version 5 (GraphPad Software,

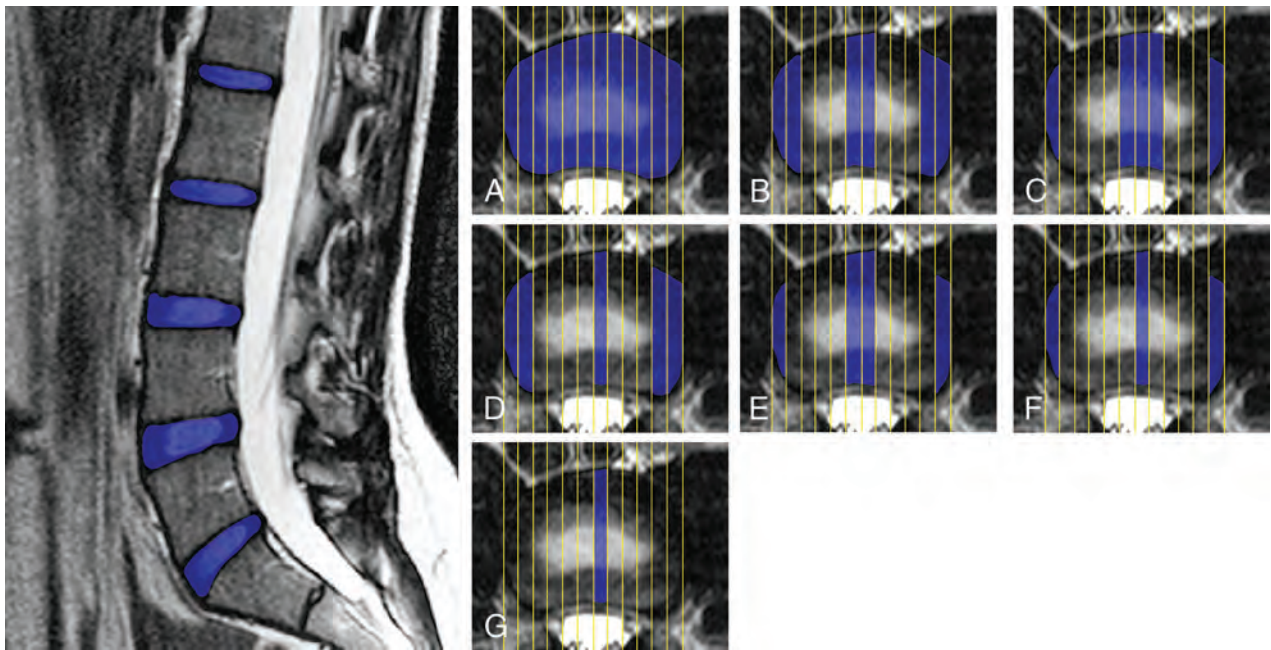


**FIG 1.** On the left is a sagittal T2-weighted image representing the segmented region of the intervertebral disk. On the right is the number of sections used in partial segmentation methods. *A*, Whole-disk segmentation. *B*, Partial-disk segmentation using 6 sections (PDS-6). *C*, Partial-disk segmentations using 5 sections, method A (PDS-5A). *D*, Partial disk segmentation using 5 sections, method B (PDS-5B). *E*, Partial-disk segmentation using 4 sections (PDS-4). *F*, Partial disk segmentation using 3 sections (PDS-3). *G*, Partial-disk segmentation using 1 central section (PDS-1).

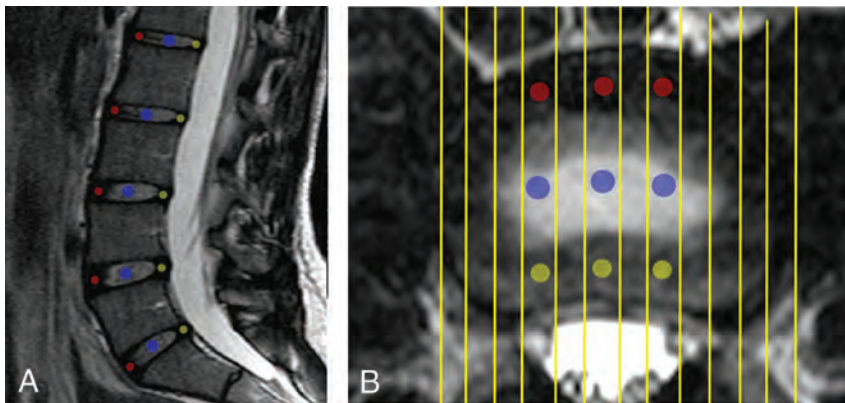


**FIG 2.** *A*, The CROI subregions are indicated in a T2-weighted image in the sagittal plane of a volunteer: blue for the nucleus pulposus, red for the anterior annulus fibrosus, and yellow for the posterior annulus fibrosus. *B*, Axial image in which the CROI method was used.

San Diego, California). To calculate the ICC, we used SPSS, Version 20 (IBM, Armonk, New York).

## RESULTS

The values of T2 and T1 $\rho$  relaxation times of the regions of the disk are shown in Table 1. In the nondegenerated group, in both T2 and T1 $\rho$  mapping, the methods PDS-6 and PDS-5B showed the average nearest to WDS, also with a lower SD. In the segmentation techniques with fewer sections, the average relaxation times extracted were more distanced from the results obtained with WDS and had a larger SD. In the degenerated disk subgroup, on the other hand, the values obtained from both T2 and T1 $\rho$  mappings were similar and did not differ statistically between the WDS, PDS, and CROI.

In Tables 2 and 3 are the results of intraclass correlation coefficients and confidence intervals for each technique in the nonde-

generated and degenerated groups. The ICC was higher for T1 $\rho$  and T2 in the NP and whole disk than for AAF and PAF. These results of intraobserver and interobserver reproducibility were similar between degenerated and nondegenerated disk groups.

The ANOVA test for T2 relaxometry and the Friedman test for T1 $\rho$  relaxometry were used to evaluate whether the relaxation times obtained by different segmentation methods were similar. Our results showed statistically significant differences between the results of different segmentation techniques of nondegenerated cases (T2:  $P < .0001$ ,  $F = 74.33$ ; T1 $\rho$ :  $P < .0001$ , Friedman =

299.2). The exception occurred for the PDS-6 and PDS-5B methods, in which relaxation times extracted for both T2 and for the T1 $\rho$  were not statistically different from those of WDS. The degenerated group showed a different behavior, in which there was no statistical difference among WDS, PDS, and CROI for both T2 ( $P = .45$ ,  $F = 0.97$ ) and T1 $\rho$  mapping ( $P = .14$ , Friedman = 64.41).

Table 4 presents the correlations between the partial-segmentation methods and WDS. The  $R$  values were higher in the methods that used more sections. Comparing T1 $\rho$  and T2 mapping, one could see that the values of T2 relaxation times were discretely more scattered compared with those of T1 $\rho$  relaxation times. In both mappings, the number of sections used decreased and the confidence intervals were larger. All methods also showed a significant positive correlation with WDS (Table 4) ( $P < .0001$ ). The

values were much higher in NP compared with AF in the nondegenerated group for the both T1 $\rho$  and T2 relaxometry. In the degenerated disk group, the relaxation times of NP and AF had a more similar behavior in relation to the whole disk. This result was more evident for T1 $\rho$  mapping.

## DISCUSSION

In this research, we studied different techniques of extraction of T2 and T1 $\rho$  relaxation times from the lumbar intervertebral disks and compared various PDS methods with the WDS. Our results suggest that the choice of the segmentation method can influence

the absolute results obtained. For practical reasons, most previous studies have used small geometric ROIs for degenerative disk disease.<sup>9,15</sup> We did not find any previous study in vivo that explored the segmentation of the intervertebral disk to its full extent.

Our results (Tables 2 and 3) showed a high intra- and interobserver reproducibility for T2 and T1 $\rho$ , both for the nondegenerated and degenerated groups. The intra- and interobserver ICCs were stronger for NP and WDS. AF ICC values were moderate because the placement of ROIs in AF tends to be a bit more difficult. This is especially true in cases of severely degenerated disks, when the border zone between the NP and AF becomes indistinct with progressive incorporation of nucleus pulposus material into the interior of the annular lamellae.<sup>16-18</sup>

PDS-6 and PDS-5B results for T2 and T1 $\rho$  were statistically similar to those of WDS in the nondegenerated group. Our results suggest that about 50% of the disk structure needs to be segmented so that the results would be comparable with those extracted via WDS on intervertebral disks with Pfirrmann grades I and II. As previously described in the literature,<sup>3,11,19</sup> if the extraction of T2 and T1 $\rho$  emphasizes the central sec-

**Table 1: Values of the T2 and T1 $\rho$  relaxation times (ms) expressed as average and SD for each experimental method (n = 285 disks)**

Method	T2 Mapping		T1 $\rho$ Mapping	
	Nondegenerated	Degenerated	Nondegenerated	Degenerated
WDS	118.3 $\pm$ 13.30	104.3 $\pm$ 14.95	49.04 $\pm$ 6.82	48.48 $\pm$ 9.36
NP	129.7 $\pm$ 22.55	99.07 $\pm$ 25.53	52.06 $\pm$ 10.39	46.10 $\pm$ 12.05
PAF	110.3 $\pm$ 28.42	96.70 $\pm$ 72	42.70 $\pm$ 9.5	46.56 $\pm$ 15.01
AAF	104.2 $\pm$ 22.63	99.98 $\pm$ 21.87	47.60 $\pm$ 10.04	41.74 $\pm$ 13.84
CROI	114.6 $\pm$ 16.78	101.8 $\pm$ 17.58	49.00 $\pm$ 7.0	47.77 $\pm$ 8.58
PDS-6	118.1 $\pm$ 13.62	105.3 $\pm$ 14.30	49.70 $\pm$ 7.23	48.59 $\pm$ 9.18
PDS-5A	121.8 $\pm$ 17.31	103.6 $\pm$ 22.75	48.72 $\pm$ 7.07	48.67 $\pm$ 9.05
PDS-5B	116.0 $\pm$ 14.50	105.7 $\pm$ 15.06	49.81 $\pm$ 7.20	49.16 $\pm$ 9.40
PDS-4	123.0 $\pm$ 14.11	107.5 $\pm$ 14.76	49.57 $\pm$ 7.14	48.81 $\pm$ 8.75
PDS-3	121.6 $\pm$ 15.89	108.5 $\pm$ 16.36	45.7 $\pm$ 11.91	49.80 $\pm$ 9.42
PDS-1	128.6 $\pm$ 17.60	105.6 $\pm$ 15.76	48.92 $\pm$ 7.21	49.26 $\pm$ 14.41

**Table 2: ICCs and 99% CIs for intra- and interobserver analysis of quantitative techniques (n = 50) used in the nondegenerated group**

	T2 Mapping				T1 $\rho$ Mapping			
	Intraobserver		Interobserver		Intraobserver		Interobserver	
	ICC	CI	ICC	CI	ICC	CI	ICC	CI
NP	0.97	0.96–0.99	0.97	0.94–0.99	0.96	0.96–0.99	0.97	0.96–0.98
AAF	0.80	0.75–0.87	0.77	0.72–0.90	0.91	0.64–0.97	0.83	0.70–0.93
PAF	0.85	0.72–0.91	0.78	0.64–0.86	0.79	0.64–0.87	0.80	0.79–0.93
Whole disk	0.92	0.87–0.95	0.92	0.85–0.95	0.98	0.96–0.99	0.93	0.72–0.96

**Table 3: ICCs and 99% CIs for intra- and interobserver analysis of quantitative techniques (n = 50) used in the degenerated group**

	T2 Mapping				T1 $\rho$ Mapping			
	Intraobserver		Interobserver		Intraobserver		Interobserver	
	ICC	CI	ICC	CI	ICC	CI	ICC	CI
NP	0.94	0.90–0.96	0.96	0.94–0.97	0.98	0.93–0.99	0.98	0.93–0.99
AAF	0.87	0.39–0.73	0.81	0.70–0.88	0.83	0.64–0.95	0.82	0.41–0.93
PAF	0.79	0.46–0.77	0.66	0.48–0.79	0.79	0.56–0.86	0.80	0.47–0.90
Whole disk	0.92	0.87–0.95	0.86	0.77–0.91	0.98	0.96–0.99	0.93	0.65–0.99

**Table 4: Correlation between whole-disk and partial-disk segmentation methods<sup>a</sup>**

	Nondegenerated Group				Degenerated Group			
	T2 Mapping		T1 $\rho$ Mapping		T2 Mapping		T1 $\rho$ Mapping	
	R	CI 99%	R	CI 99%	R	CI 99%	R	CI 99%
WDS $\times$ PDS-6	0.96	0.95–0.97	0.97	0.96–0.97	0.97	0.95–0.98	0.97	0.95–0.98
WDS $\times$ PDS-5A	0.75	0.69–0.81	0.96	0.95–0.97	0.69	0.53–0.80	0.96	0.94–0.98
WDS $\times$ PDS-5B	0.91	0.88–0.93	0.95	0.93–0.96	0.94	0.90–0.96	0.93	0.89–0.96
WDS $\times$ PDS-4	0.90	0.88–0.93	0.95	0.94–0.96	0.94	0.91–0.96	0.95	0.92–0.97
WDS $\times$ PDS-3	0.83	0.78–0.86	0.90	0.87–0.92	0.89	0.82–0.93	0.89	0.82–0.93
WDS $\times$ PDS-1	0.73	0.67–0.79	0.80	0.75–0.84	0.74	0.61–0.84	0.78	0.66–0.86
WDS $\times$ CROI	0.74	0.67–0.79	0.88	0.85–0.91	0.82	0.71–0.88	0.83	0.72–0.89
WDS $\times$ NP	0.72	0.65–0.72	0.80	0.74–0.84	0.77	0.63–0.85	0.76	0.63–0.85
WDS $\times$ PAF	0.42	0.30–0.52	0.59	0.49–0.67	0.48	0.25–0.66	0.65	0.47–0.77
WDS $\times$ AAF	0.40	0.28–0.51	0.58	0.48–0.66	0.50	0.27–0.67	0.54	0.33–0.70

<sup>a</sup> The result of the correlation is expressed by R confidence intervals of 99%.

tions, it may overestimate the glycosaminoglycan content of the disk.

In the degenerated disk group, partial segmentation methods and CROI showed results similar to those of the full segmentation. This outcome may have occurred by the accentuated loss of proteoglycans and water and replacement by type I collagen in NP.<sup>20</sup> Thus, in degenerated disks, the relaxation time of NP became very close to that of AF because the disk composition becomes more homogeneous.<sup>15,21</sup>

In cases of severe scoliosis, disk degeneration may occur unevenly in different regions of the disk.<sup>22-24</sup> The presence of volunteers with scoliosis could potentially affect our results of comparison between different segmentation techniques, but it did not occur because we had no case of scoliosis. Panoramic radiographs were available for each case due to another research project in progress from our group. The presence of osteophytes should also be considered carefully so that the segmentation does not encompass these regions.<sup>25</sup> Other accentuated postural changes, vertebral fractures, listhesis, or extruded disk herniation could also result in uneven disk degeneration,<sup>24,26</sup> so that using only central sagittal sections for data extraction could result in a different composition assessment of the disk. Our sample had no volunteer with deformities, fractures, or disk herniation.

Our results support the use of partial segmentation methods in the study of intervertebral disk composition because PDS and CROI methods showed, in general, excellent correlation to the WDS method (Table 4). However, the comparison among results of different studies that used different segmentation methods should be done with caution.<sup>15,27</sup> Our results demonstrate that the use of different segmentation techniques may result in measurement of different values of intervertebral disk relaxation times.

Regarding the comparison of our results with the literature, the NP T2 relaxation times were very close to those reported in previous studies.<sup>9,28,29</sup> For the AF T2, our results were similar to those of Stelzeneder et al<sup>28</sup> and Welsch et al,<sup>29</sup> and slightly higher than those of Trattng et al.<sup>9</sup> With respect to the T1 $\rho$  relaxation times, the values encountered for the NP and AF in our study were lower than those found in the literature.<sup>12,30-32</sup> We hypothesize that at least in part, this difference may be due to different magnetic field strengths, because most of the previous studies used 3T MR imaging.<sup>12,31,32</sup> In common with authors of other studies, we found that a greater degree of degeneration implies lower T2 and T1 $\rho$  relaxation times.

When we compared the individual relaxation times of NP, AAF, and PAF, all 3 regions showed statistical correlation with the WDS values. In the nondegenerated group, the NP values had a stronger correlation with WDS, suggesting that their influence on the relaxation time of the whole disk is larger than that from AF, as has already been described in the literature.<sup>19,20</sup> The annulus fibrosus also follows the uniform changes of the whole disk, but less than the nucleus.<sup>33</sup> However, in the degenerated group, the relaxation times of NP and AF showed a more similar behavior in relation to the whole disk. Antoniou et al<sup>21</sup> used MR imaging quantitative techniques and also a mechanical test to study the intervertebral disks and found similarities in the NP and AF behavior over the degenerative processes. This finding shows that both regions are affected evenly, especially at the beginning of

the degeneration. This phenomenon was more evident in T1 $\rho$  mapping because this method has proved more affinity with loss of proteoglycan content, which has been suggested as a major trigger of the degenerative process, resulting in a low relaxation time.<sup>12,13</sup>

Most studies in the literature preferred segmentation of NP and AF individually.<sup>28-32,34</sup> In intervertebral disks with Pfirrmann grades I and II, segmenting these structures separately usually makes it possible to distinguish them better. If the degeneration increases to grades III and IV, this distinction becomes more difficult.<sup>14</sup> Thus, a relative advantage of performing segmentation of the whole area or the whole volume of the disk is to enable a more secure comparison among disks with different degrees of degeneration.

A relative limitation of our study is that we included only young and asymptomatic volunteers; therefore, the results may not be extended to the symptomatic population. We also did not have Pfirrmann grade V intervertebral disks. This probably is not an important practical limitation in the research field because composition studies from quantitative MR imaging are less likely to be applied to severely degenerated disks.

Numerous researchers have used quantitative MR imaging to improve the understanding of intervertebral disk degeneration. During the past 10 years, the use of quantitative MR imaging techniques, especially T2 and T1 $\rho$  relaxometry, have allowed the evaluation of the intervertebral disk composition in vivo. However, the lack of standardization for data collection may impair the comparison of results from different studies. Despite the growing importance of relaxometry for in vivo evaluation of intervertebral disk biochemical composition and disk degeneration, we did not find studies concerned with the comparison of different segmentation techniques. When one envisions future research about the etiology and risk factors for disk degeneration, the standardization of T2 and T1 $\rho$  mapping may assume a great importance.

## CONCLUSIONS

Manual segmentation showed strong reproducibility for degenerated and nondegenerated disks. The segmentation methods we compared showed excellent linear correlation with each other. Absolute T1 $\rho$  and T2 values extracted from different segmentation techniques were statistically different in intervertebral disks with Pfirrmann grades I and II.

## ACKNOWLEDGMENTS

The authors acknowledge the funding support from CNPq, CAPES and FINEP.

Disclosures: Rafael Menezes-Reis—RELATED: Grant: Coordenação de Aperfeiçoamento de Pessoal de Nível Superior, Comments: Masters scholarship; Support for Travel to Meetings for the Study or Other Purposes: Council for Scientific and Technological Development, Comments: support provided by CNPq. Camila Silva de Carvalho—RELATED: Grant: scientific initiation scholarship from R-USP, Comments: from August 1, 2012, to July 31, 2013, \$400.00. Gustavo P. Bonugli—UNRELATED: Board Membership: Coordenação de Aperfeiçoamento de Pessoal de Nível Superior. Christine B. Chung—UNRELATED: Grants/Grants Pending: National Institutes of Health.\* Comments: NIDCR TMJ grant. Marcello H. Nogueira-Barbosa—RELATED: Grant: FINEP.\* Comments: funding sources: Financiadora de Estudos e Projetos, Brazil, Coordenação de Aperfeiçoamento de Pessoal de Nível Superior. \*Money paid to the institution.

## REFERENCES

1. Maus TP, Aprill CN. Lumbar diskogenic pain, provocation diskography, and imaging correlates. *Radiol Clin North Am* 2012;50:681–704
2. Wassenaar M, van Rijn RM, van Tulder MW, et al. Magnetic resonance imaging for diagnosing lumbar spinal pathology in adult patients with low back pain or sciatica: a diagnostic systematic review. *Eur Spine J* 2012;21:220–27
3. Lotz JC, Haughton V, Boden SD, et al. New treatments and imaging strategies in degenerative disease of the intervertebral disks. *Radiology* 2012;264:6–19
4. Majumdar S. Magnetic resonance imaging and spectroscopy of the intervertebral disc. *NMR Biomed* 2006;19:894–903
5. Pham DL, Xu C, Prince JL. Current methods in medical image segmentation. *Annu Rev Biomed Eng* 2000;2:315–37
6. Mwale F, Iatridis JC, Antoniou J. Quantitative MRI as a diagnostic tool of intervertebral disc matrix composition and integrity. *Eur Spine J* 2008;17(suppl 4):432–40
7. Marinelli NL, Haughton VM, Anderson PA. T2 relaxation times correlated with stage of lumbar intervertebral disc degeneration and patient age. *AJNR Am J Neuroradiol* 2010;31:1278–82
8. Haneder S, Apprich SR, Schmitt B, et al. Assessment of glycosaminoglycan content in intervertebral discs using chemical exchange saturation transfer at 3.0 Tesla: preliminary results in patients with low back pain. *Eur Radiol* 2013;23:861–68
9. Trattinig S, Stelzeneder D, Goed S, et al. Lumbar intervertebral disc abnormalities: comparison of quantitative T2 mapping with conventional MR at 3.0 T. *Eur Radiol* 2010;20:2715–22
10. Michopoulou S, Costaridou L, Vlychou M, et al. Texture-based quantification of lumbar intervertebral disc degeneration from conventional T2-weighted MRI. *Acta Radiol* 2011;52:91–98
11. Chan WC, Sze KL, Samartzis D, et al. Structure and biology of the intervertebral disk in health and disease. *Orthop Clin North Am* 2011;42:447–64, vii
12. Blumenkrantz G, Li X, Han ET, et al. A feasibility study of in vivo T1rho imaging of the intervertebral disc. *Magn Reson Imaging* 2006;24:1001–07
13. Auerbach JD, Johannessen W, Borthakur A, et al. In vivo quantification of human lumbar disc degeneration using T1(rho)-weighted magnetic resonance imaging. *Eur Spine J* 2006;15(suppl 3):S338–44
14. Pfirrmann CW, Metzendorf A, Zanetti M, et al. Magnetic resonance classification of lumbar intervertebral disc degeneration. *Spine (Phila Pa 1976)* 2001;26:1873–78
15. Stelzeneder D, Welsch GH, Kovács BK, et al. Quantitative T2 evaluation at 3.0T compared to morphological grading of the lumbar intervertebral disc: a standardized evaluation approach in patients with low back pain. *Eur J Radiol* 2012;81:324–30
16. Sharma A, Parsons M, Pilgram T. Temporal interactions of degenerative changes in individual components of the lumbar intervertebral discs: a sequential magnetic resonance imaging study in patients less than 40 years of age. *Spine (Phila Pa 1976)* 2011;36:1794–800
17. Del Grande F, Maus TP, Carrino JA. Imaging the intervertebral disk: age-related changes, herniations, and radicular pain. *Radiol Clin North Am* 2012;50:629–49
18. Issy AC, Castania V, Castania M, et al. Experimental model of intervertebral disc degeneration by needle puncture in Wistar rats. *Braz J Med Biol Res* 2013;46:235–44
19. Antoniou J, Pike GB, Steffen T, et al. Quantitative magnetic resonance imaging in the assessment of degenerative disc disease. *Magn Reson Med* 1998;40:900–07
20. Zuo J, Joseph GB, Li X, et al. In vivo intervertebral disc characterization using magnetic resonance spectroscopy and T1rho imaging: association with discography and Oswestry Disability Index and Short Form-36 Health Survey. *Spine (Phila Pa 1976)* 2012;37:214–21
21. Antoniou J, Epure LM, Michalek AJ, et al. Analysis of quantitative magnetic resonance imaging and biomechanical parameters on human discs with different grades of degeneration. *J Magn Reson Imaging* 2013;38:1402–14
22. Ding WY, Yang DL, Cao LZ, et al. Intervertebral disc degeneration and bone density in degenerative lumbar scoliosis: a comparative study between patients with degenerative lumbar scoliosis and patients with lumbar stenosis. *Chin Med J (Engl)* 2011;124:3875–78
23. Homminga J, Lehr AM, Meijer GJ, et al. Posteriorly directed shear loads and disc degeneration affect the torsional stiffness of spinal motion segments: a biomechanical modeling study. *Spine (Phila Pa 1976)* 2013;38:E1313–19
24. Gervais J, Périé D, Parent S, et al. MRI signal distribution within the intervertebral disc as a biomarker of adolescent idiopathic scoliosis and spondylolisthesis. *BMC Musculoskelet Disord* 2012;13:239
25. Igbinedion BO, Akhigbe A. Correlations of radiographic findings in patients with low back pain. *Niger Med J* 2011;52:28–34
26. Iguchi T, Nishida K, Ozaki T, et al. Grade three disc degeneration is a critical stage for anterior spondylolisthesis in lumbar spine. *Eur Spine J* 2012;21:2134–39
27. Borthakur A, Maurer PM, Fenty M, et al. T1rho magnetic resonance imaging and discography pressure as novel biomarkers for disc degeneration and low back pain. *Spine (Phila Pa 1976)* 2011;36:2190–96
28. Stelzeneder D, Welsch GH, Kovács BK, et al. Quantitative T2 evaluation at 3.0T compared to morphological grading of the lumbar intervertebral disc: a standardized evaluation approach in patients with low back pain. *Eur J Radiol* 2012;81:324–30
29. Welsch GH, Trattinig S, Paternostro-Sluga T, et al. Parametric T2 and T2\* mapping techniques to visualize intervertebral disc degeneration in patients with low back pain: initial results on the clinical use of 3.0 Tesla MRI. *Skeletal Radiol* 2011;40:543–51
30. Zobel BB, Vadalà G, Del Vecovo R, et al. T1rho magnetic resonance imaging quantification of early lumbar intervertebral disc degeneration in healthy young adults. *Spine (Phila Pa 1976)* 2012;37:1224–30
31. Wang YX, Zhao F, Griffith JF, et al. T1rho and T2 relaxation times for lumbar disc degeneration: an in vivo comparative study at 3.0-Tesla MRI. *Eur Radiol* 2013;23:228–34
32. Wang YX, Zhao F, Yuan J, et al. Accelerated T1rho relaxation quantification in intervertebral disc using limited spin-lock times. *Quant Imaging Med Surg* 2013;3:54–58
33. Pattappa G, Li Z, Peroglio M, et al. Diversity of intervertebral disc cells: phenotype and function. *J Anat* 2012;221:480–96
34. Niu G, Yang J, Wang R, et al. MR imaging assessment of lumbar intervertebral disc degeneration and age-related changes: apparent diffusion coefficient versus T2 quantitation. *AJNR Am J Neuroradiol* 2011;32:1617–23

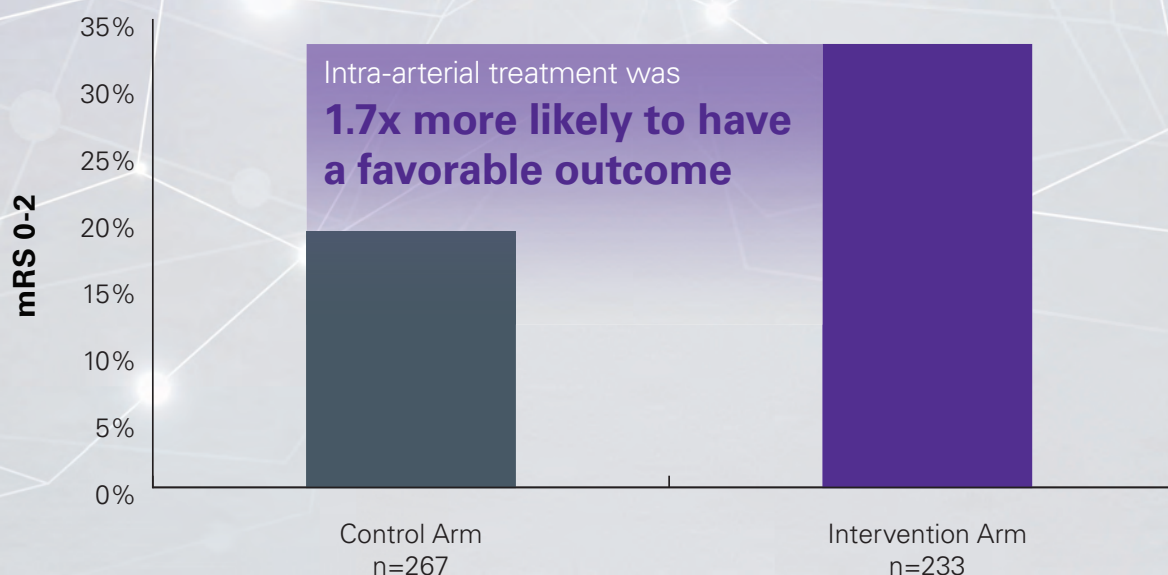
# Congratulations to the MR CLEAN Investigators!

**stryker**<sup>®</sup>  
Neurovascular

## Intra-arterial treatment plus usual care results in better outcomes than usual care alone\*†

- Increase in functional independence in daily life, with no increase in mortality at 90 days
- **Stent retrievers were used in 97% of patients** (190/196) treated with intra-arterial therapy

### Effect of Intervention on Primary Outcome at 90 days<sup>1</sup>



\* Intra-arterial treatment included mechanical thrombectomy (stent retrievers, Merci Retriever<sup>®</sup>, wire disruption, thromboaspiration) and IA lytic. Usual care defined as intravenous administration of alteplase.

† In patients with acute ischemic stroke caused by proximal intracranial occlusion of the anterior circulation, treated within 6 hours after stroke onset.

1. O.A. Berkhemer et. al. A Randomized Trial for Intraarterial Treatment for Acute Ischemic Stroke. *N Eng J Med* 2014.



## Trevo<sup>®</sup> XP

PROVUE RETRIEVER

### Take Control. Capture More.

The newly designed Trevo<sup>®</sup> XP ProVue Retriever takes proven Trevo Retriever performance to new levels for **easy delivery**, **easy placement**, and **easy visualization**.

When you're in control, it's amazing what you can capture.

**stryker**<sup>®</sup>  
Neurovascular

# COILING OPTIMIZED



**NOW AVAILABLE**

**BARRICADE COMPLEX  
FINISHING COIL**

- ◆ Extremely soft profile of The Barricade Finishing coil now in a complex shape
- ◆ Excellent microcatheter stability for confident coil placement
- ◆ Available in a size range of 1mm-5mm

## BARRICADE™ COIL SYSTEM



MADE IN AMERICA

The Barricade Coil System is intended for the endovascular embolization of intracranial aneurysms and other neurovascular abnormalities such as arteriovenous malformations and arteriovenous fistulae. The System is also intended for vascular occlusion of blood vessels within the neurovascular system to permanently obstruct blood flow to an aneurysm or other vascular malformation and for arterial and venous embolizations in the peripheral vasculature. Refer to the instructions for use for complete product information.

18 TECHNOLOGY DRIVE #169, IRVINE CA 92618

p: 949.788.1443 | f: 949.788.1444

[WWW.BLOCKADEMEDICAL.COM](http://WWW.BLOCKADEMEDICAL.COM)

MKTG-031 Rev. A



**BLOCKADE**  
M E D I C A L